BioMed Research International

Technical Advancement of Radiation Therapy

Guest Editors: Tsair-Fwu Lee, Jack Yang, Eng-Yen Huang, Chung-Chi Lee, Maria F. Chan, and An Liu

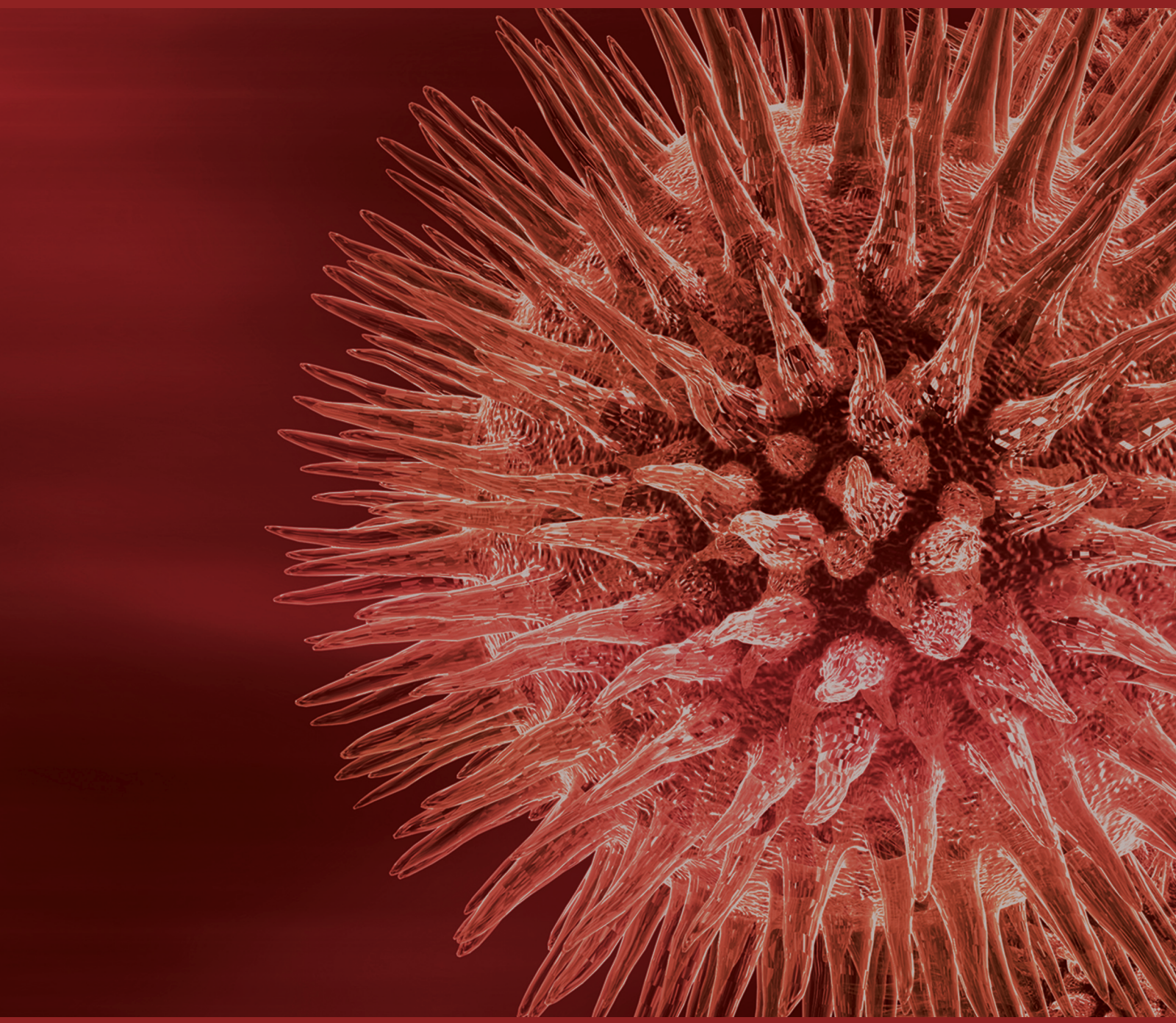

Technical Advancement of Radiation Therapy

BioMed Research International

Technical Advancement of Radiation Therapy

Guest Editors: Tsair-Fwu Lee, Jack Yang, Eng-Yen Huang, Chung-Chi Lee, Maria F. Chan, and An Liu

Contents

Hindawi Publishing Corporation
BioMed Research International
Volume 2014, Article ID 797412, 3 pages
http://dx.doi.org/10.1155/2014/797412

Editorial

Technical Advancement of Radiation Therapy

Tsair-Fwu Lee,[1] Jack Yang,[2] Eng-Yen Huang,[3] Chung-Chi Lee,[4] Maria F. Chan,[5] and An Liu[6]

[1] *Medical Physics and Informatics Laboratory, Department of Electronics Engineering, National Kaohsiung University of Applied Sciences, Kaohsiung 807, Taiwan*
[2] *Department of Radiation Oncology, Institute for Advanced Radiation Oncology, Monmouth Medical Center, Barnabas Health, Long Branch, NJ 07740, USA*
[3] *Department of Radiation Oncology, Kaohsiung Chang Gung Memorial Hospital, Chang Gung University, College of Medicine, Kaohsiung 833, Taiwan*
[4] *Department of Medical Imaging and Radiological Sciences, Chang Gung University, Taoyuan 333, Taiwan*
[5] *Medical Physics Department, Memorial Sloan-Kettering Cancer Center, 136 Mountain View Boulevard, Basking Ridge, NJ 07920, USA*
[6] *Department of Radiation Oncology, City of Hope National Medical Center, Duarte, CA 91010, USA*

Correspondence should be addressed to Tsair-Fwu Lee; tflee@kuas.edu.tw and Jack Yang; jyang@barnabashealth.org

Received 25 November 2013; Accepted 25 November 2013; Published 11 February 2014

Radiation therapy is an integrated part of the modern comprehensive cancer management. It has been proven that treatment effectiveness leads to curing various types of cancers. For example, radiotherapy can result in a 2-year progression-free (PF) survival and overall survival rate to 72.7% and 80.2%, respectively, using IMRT techniques for dose painting of nasopharyngeal carcinoma [1]; this is a very sensitive type of tumor to DNA killing by radiation beams. However, the cure rate for very advanced tumors and certain cancers such as glioblastoma multiforme is still pessimistic. Currently, strategies to improve efficacy of radiation therapy are being studied. One of the major improvements of radiation therapy is to increase the treatment dose to the tumor. However, the main limiting factor to higher dosage delivery to tumor cells is normal tissue tolerances. To overcome this limitation, one can reduce treatment volume to normal tissue or sculpt the target dose as an increment with dose to the tumor [2]. This can be achieved by improving the definition of target volume and the precision of dosimetry delivery with advanced treatment techniques.

One of the major advancements in radiation oncology in early 1990s was the development of conformal three-dimensional (3D) radiation therapy. In this technique, the prescribed dose volume was made to conform to the target volume and spare more normal tissues. Furthermore, radiation dosimetry based on 3D conformal therapy has been studied more accurately and Monte Carlo methodology [3] has been also introduced into the current calculation for patient dosimetry. In the last decade, much interest has been generated in other forms of conformal treatment planning, that is, intensity modulated radiation therapy (IMRT) and stereotactic radiosurgery and radiotherapy (SRS and SRT). IMRT involves the delivery of optimized, nonuniform irradiation beam intensities. A uniform dose distribution can be created around the tumor by either modulating the intensity of the beam during its journey through the linear accelerator or by using multileaf collimators. The resultant dose distributions are highly conformal. This technology provides the potential of improved tumor irradiation and sparing of the organ in the vicinity of the target to an extent that was not possible before, especially for concave target volume usually seen in head and neck cancers. In head and neck cancers, tumor dose is often limited by the surrounding critical structures such as spinal cord. Tight dose gradients around the target volume also enable higher doses to be delivered to the tumor while reducing the dose to surrounding critical organs and radiosensitive tissues such as salivary glands, ears, optic chiasm, and hippocampi. Lee et al. [4] in early days reported a locoregional recurrence-free survival of 97% at a median followup of 31 months for

67 nasopharyngeal carcinoma patients treated with IMRT. At 24-month followup, 92% patients had grade 0-1 xerostomia. Other late toxicities were not assessed for the follow-up period. This has indicated that with newer technology and with optimal dose distribution, impressive clinical outcome could be achieved.

While radiotherapy treatment planning technique is matured to a level with precise dosimetry distribution, however, the inaccuracy of CT definition of tumors and normal structures could likely hinder the accurate target delineation and dose calculations. To overcome those limitations, fusion with other imaging techniques, for example, MRI and PET, is being implemented. MRI has been shown to have better differentiation between normal tissues and many different types of tumors. Image fusion studies with FDG-PET and CT scan have shown encouraging results. A significant impact of PET-derived contours on treatment planning has been shown in 30–60% of the plans with respect to the CT-only target volume [5].

SRS and SRT are forms of the 3D technique that deliver radiation doses in one fraction or hypofractionated scheme to a small intracranial target or targets close to critical structure such as spinal cord or brain stem. Both SRS and SRT combine the contemporary principles of neurosurgery and radiotherapy. Patient's head is attached securely to a fixation device. Radiotherapy can be delivered with 3 methods, namely, heavy charged particles (i.e., protons), gamma irradiation emitted from Co-60, and high energy photon irradiation produced with linear accelerators. Conformal radiotherapy is achieved by the use of multiple noncoplanar arcs. SRS and SRT have been proven to be effective in the treatment for controlling tumor growth or even the benign intracranial and extracranial diseases.

With the improvement of treatment imaging modalities, to adjust patient localization in a nearly real-time basis becomes feasible. The on-treatment cone/fan beam CT, with patient immobilized at the treatment position, while repositioning correlation based on correlation to the planning CT has become a standard image guided radiation therapy (IGRT) in modern centers. This process has been proven to avoid any positional discrepancy while performing daily patient treatment. Furthermore, with the improvement of CPU/GPU power of current computing technology, the real-time calculation has been making good process. Li [6] has introduced an extensive summary publication on how to approach these adaptive radiation treatment techniques.

There are many topics in the radiation therapy which could be addressed in more details. Also there have been various treatment devices and methodologies introduced to clinical treatment with efficacy, hopefully, reaching better clinical outcomes. The main focus of this special issue is focusing on the new development in cancer treatment, quality control, treatment techniques, and radiation dosimetry with related topics. The special issue covers the most recent developments and ideas in radiation oncology in a broad spectrum, with special emphasis given to the clinical progress with new technologies. This special issue included various topics which have been discussed by researchers as follows:

(i) clinical trials and outcome research,

(ii) new technologies development and implementation,

(iii) treatment delivery techniques,

(iv) disease specific treatment discussion,

(v) radiation dosimetry analysis,

(vi) radiation protection, shielding and design,

(vii) clinical therapy physics review and applications,

(viii) molecular imaging application in Radiation Therapy,

(ix) medical imaging,

(x) professional issues in medical, clinical and biomedical physics,

(xi) radiobiology,

(xii) quality control and assurance,

(xiii) computing algorithm and optimization,

(xiv) quality of life analysis,

(xv) radiation safety.

This editorial provides comprehensive introduction to these new technology advancements in radiation therapy and many important topics associated with implementing the technologies. In conclusion, the technological advancements in radiotherapy in the last two decades have been immense. There are tremendous amounts of information available via modern technological implementation. Clinical data on these new technologies are proven by many institutions. Again, there will be more technical breakthroughs on cell or even at the molecular levels, which may present another challenge for researchers.

Tsair-Fwu Lee
Jack Yang
Eng-Yen Huang
Chung-Chi Lee
Maria F. Chan
An Liu

References

[1] N. Lee, J. Harris, A. S. Garden et al., "Intensity-modulated radiation therapy with or without chemotherapy for nasopharyngeal carcinoma: radiation therapy oncology group phase II trial 0225," *Journal of Clinical Oncology*, vol. 27, no. 22, pp. 3684–3690, 2009.

[2] H. Suit, "The gray lecture 2001: coming technical advances in radiation oncology," *International Journal of Radiation Oncology ∗ Biology ∗ Physics*, vol. 53, no. 4, pp. 798–809, 2002.

[3] S. E. Goiten and G. Lewis, "An overview of Monte Carlo treatment planning for radiotherapy radiat," *Radiation Protection Dosimetry*, vol. 131, no. 1, pp. 123–129, 2008.

[4] N. Lee, P. Xia, J. M. Quivey et al., "Intensity-modulated radiotherapy in the treatment of nasopharyngeal carcinoma: an update of the UCSF experience," *International Journal of Radiation Oncology ∗ Biology ∗ Physics*, vol. 53, no. 1, pp. 12–22, 2002.

[5] C. Greco, K. Rosenzweig, G. L. Cascini, and O. Tamburrini, "Current status of PET/CT for tumour volume definition in radiotherapy treatment planning for non-small cell lung cancer (NSCLC)," *Lung Cancer*, vol. 57, no. 2, pp. 125–134, 2007.

[6] X. A. Li, *Adaptive Radiation Therapy*, Taylor and Francis, Boca Raton, Fla, USA, 2011.

Hindawi Publishing Corporation
BioMed Research International
Volume 2014, Article ID 485067, 6 pages
http://dx.doi.org/10.1155/2014/485067

Research Article

Investigating the Feasibility of Rapid MRI for Image-Guided Motion Management in Lung Cancer Radiotherapy

Amit Sawant,[1] Paul Keall,[2] Kim Butts Pauly,[3] Marcus Alley,[3] Shreyas Vasanawala,[3] Billy W. Loo Jr.,[3] Jacob Hinkle,[4] and Sarang Joshi[4]

[1] *University of Texas, Southwestern Medical Center, Dallas, TX 75235, USA*
[2] *University of Sydney, Sydney, NSW 2006, Australia*
[3] *Stanford University, Stanford, CA 95305, USA*
[4] *University of Utah, Salt Lake City, UT 84112, USA*

Correspondence should be addressed to Amit Sawant; amit.sawant@utsouthwestern.edu

Received 17 April 2013; Revised 6 November 2013; Accepted 7 November 2013; Published 12 January 2014

Academic Editor: Jack Yang

Cycle-to-cycle variations in respiratory motion can cause significant geometric and dosimetric errors in the administration of lung cancer radiation therapy. A common limitation of the current strategies for motion management is that they assume a constant, reproducible respiratory cycle. In this work, we investigate the feasibility of using rapid MRI for providing long-term imaging of the thorax in order to better capture cycle-to-cycle variations. Two nonsmall-cell lung cancer patients were imaged (free-breathing, no extrinsic contrast, and 1.5 T scanner). A balanced steady-state-free-precession (b-SSFP) sequence was used to acquire cine-2D and cine-3D (4D) images. In the case of Patient 1 (right midlobe lesion, ~40 mm diameter), tumor motion was well correlated with diaphragmatic motion. In the case of Patient 2, (left upper-lobe lesion, ~60 mm diameter), tumor motion was poorly correlated with diaphragmatic motion. Furthermore, the motion of the tumor centroid was poorly correlated with the motion of individual points on the tumor boundary, indicating significant rotation and/or deformation. These studies indicate that image quality and acquisition speed of cine-2D MRI were adequate for motion monitoring. However, significant improvements are required to achieve comparable speeds for truly 4D MRI. Despite several challenges, rapid MRI offers a feasible and attractive tool for noninvasive, long-term motion monitoring.

1. Introduction

Respiratory motion causes significant uncertainties in tumor delineation, radiotherapy (RT) dose calculations, and delivery, particularly in the case of thoracic tumors (e.g., lung, liver) [1]. The management of respiratory motion has been an active area of research over the last decade. Several investigational as well as clinically implemented respiratory motion management strategies have been described in the literature [1]. However, a common limitation of most of these strategies is that they rely on image-guidance techniques that make simplifying assumptions about respiratory motion and do not adequately capture cycle-to-cycle variations which invariably occur in all patients. Modern motion-managed radiotherapy typically uses four-dimensional computed tomography (4DCT) as the tool of choice for pretreatment anatomic imaging (also termed as "CT simulation" or "CT-sim" in the literature). In this technique, CT projections are acquired over several respiratory cycles from successive "slabs" in the body. At the same time, an external surrogate (e.g., an optical marker) records the amplitude of respiration. Based on the surrogate motion trace, the reconstructed slices are sorted into 6–10 volumes over a single respiratory average cycle, where each volume represents a specific phase of respiration (inhalation through exhalation) [2–4]. This retrospectively reconstructed "movie" of a single respiratory cycle serves as the anatomical ground truth for all subsequent stages of radiotherapy (contouring, treatment planning, and dose delivery).

It is well recognized, however, that respiratory motion is far more complex than can be characterized by a single average cycle. Cycle-to-cycle variations such as baseline

shifts and changes in the amplitude and/or frequency of the respiratory waveform are inadequately accounted for in 4DCT-based planning and can lead to significant geometric and therefore dosimetric errors [5]. Furthermore, binning CT projection data acquired over several cycles into a single cycle leads to severe image artifacts. For example, Yamamoto et al. found that 45 of 50 patients had at least one artifact, with mean magnitude of 11.6 mm (range: 4.4–56.0 mm) [6]. In a separate study, Persson et al. found that 4DCT artifacts caused significant uncertainties in the delineation of the gross tumor volume (GTV) in 16 out of 19 patients [7]. Finally, the equivalent dose for 4DCT is quite high (29–40 mSv), about 4 times higher than that for 3DCT (3–10 mSv) [8]. Such high imaging dose discourages long-term monitoring and frequent imaging. Due to these limitations, 4DCT-based image guidance provides an incomplete picture of respiration-induced spatial and temporal changes in the thoracic anatomy.

The aim of this work is to investigate the feasibility of using rapid magnetic resonance imaging (MRI) as a nonionizing imaging modality to capture long-term and/or frequent information about respiratory motion and its effects on the movement and deformation of lung tumors and surrounding critical organs. The fundamental difference and, therefore, advantage of cine MRI are that, unlike 4DCT, the MR image (i.e., slice or volume) is acquired prospectively, thereby capturing an actual instance of the patient anatomy, which is closer to reality compared to an average estimate of the anatomical state that is represented by 4DCT. Prospective acquisition also enables MRI to overcome the two main challenges that limit the utility of 4DCT images, namely, the ability to capture cycle-to-cycle variations and elimination of binning-related image artifacts. In addition, due to the fact that MRI does not involve ionizing radiation, there is no dose penalty for repeated imaging (as opposed to 4DCT).

The use of rapid cine-2D as well as 4D MRI for radiotherapy guidance has been previously reported in the literature. In cine-2D MRI, a slice of the anatomy is selected, at arbitrary orientation, and imaged repeatedly in time. 4D MRI is conceptually similar, except that in this case an entire volume is selected and imaged. Plathow et al. have reported cine-2D imaging of lung cancer patients at ~3 frames per second (fps) [9] and 4D imaging of malignant pleural mesothelioma patients at ~1 volume/s [10], under slow-breathing conditions using a 1.5 T scanner. Von Siebenthal et al. have reported on a 4D MR imaging technique using retrospective stacking of cine-2D slices [11]. Biederer et al. report 4D MRI of a ventilated chest phantom that uses porcine lung with embedded agarose nodules to simulate tumors [12]. More recently, Cai et al. have reported a 4D MRI study of a moving phantom using a technique that uses retrospective sorting of cine-2D slices [13]. To our knowledge, there has been no systematic study of rapid lung MRI in the context of image-guided radiotherapy (IGRT) motion management under realistic (prospective acquisition, free-breathing human subjects) conditions.

In this work, we present a pilot investigation of prospective rapid cine-2D and cine-3D (commonly termed as "4D" in radiotherapy and the MRI literature) MRI of two nonsmall-cell lung cancer (NSCLC) patients under free-breathing conditions, without externally administered contrast. Subsequently, we compute and analyze the motion trajectories of tumors and structures of interest. Our current goal is to demonstrate the feasibility and the utility of rapid MR imaging to monitor respiratory motion over multiple cycles and obtain guidance information about the motion, deformation, and the interplay between lung tumors and surrounding critical organs. Our long-term goal (beyond the current scope) is to use the information obtained from rapid MRI to augment and potentially correct 4DCT images.

2. Methods

2.1. Imaging of NSCLC Patients. Two NSCLC patients were imaged following informed consent. Patient number 1 was a 67-year old female with an ~40 mm diameter right midlobe tumor. Patient number 2 was an 80-year old male with an ~60 mm diameter left upper-lobe tumor. Both patients were scanned on a 1.5 T scanner (GE Signa). Both patients were scanned in the supine position, under free-breathing conditions and without externally administered contrast. For each patient, a 4-channel cardiac coil was centered around the tumor. cine-2D time series in the coronal and sagittal planes were acquired using a balanced steady-state free precession (b-SSFP) sequence and the images were reconstructed using the vendor's in-built software. In all cases except one (Patient number 1, coronal series), half-Fourier acquisition was used in order to achieve higher imaging speed. In the case of Patient number 2 an additional 3D+t (4D) scan of a tumor-inclusive coronal slab (8 slices, each 5 mm thick) was acquired using the b-SSFP sequence in the 3D mode and in conjunction with parallel imaging (acceleration = 4). The 4D images were reconstructed using the autocalibrating reconstruction for Cartesian imaging (ARC) algorithm [14]. Table 1 summarizes the image acquisition parameters for the cine-2D and the 4D acquisitions.

2.2. Motion Analysis. For each time series from Table 1, the motion trajectories of the tumor and structures of interest were determined as follows. A fluid-flow-based deformable image registration, previously validated for RT applications [15–17], was applied to each time series to compute deformation vector fields (DVFs) across the temporal dimension. In order to reduce errors and achieve high computation speed (i.e., fewer iterations), the registration was performed in two stages-rigid registration which accounted for gross translation and affine transformations of the tumor and organs, followed by deformable registration, which accounted mainly for tumor and organ deformation. For each time series, a reference image was selected (typically at mid-inhale) and ~15 points each on the tumor boundary and the diaphragm were manually selected. Subsequently, the motion trajectory of each pixel on a contour was determined from the DVFs. The validity of using diaphragmatic motion as a surrogate for tumor motion was examined by calculating the correlation between the average motion trajectory of the pixels comprising the diaphragm boundary with the average trajectory of

Table 1: Summary of image acquisition parameters for rapid MRI of NSCLC patients.

	Image orientation	Acquisition (cine-2D/4D)	Voxel size (mm^3)	FOV (mm^2)	TE/TR (ms)	Flip angle (deg)	N_{avg}	T_{acq} (s)
Patient 1	Coronal	cine-2D	$2 \times 3 \times 5$	240×240	1.70/3.41	50	1.0	0.273
	Sagittal	cine-2D	$2 \times 3 \times 5$	240×240	1.70/3.41	50	0.5	0.164
Patient 2	Coronal	cine-2D	$2.4 \times 3 \times 5$	240×240	1.68/3.16	50	0.5	0.165
	Sagittal	cine-2D	$2.4 \times 3.3 \times 5$	240×240	1.68/3.16	50	0.5	0.152
	Coronal (slab)	4D (//accn = 4)	$2.4 \times 3 \times 5$	240×240 (8 slices)	1.91/3.82	50	0.5	1.561

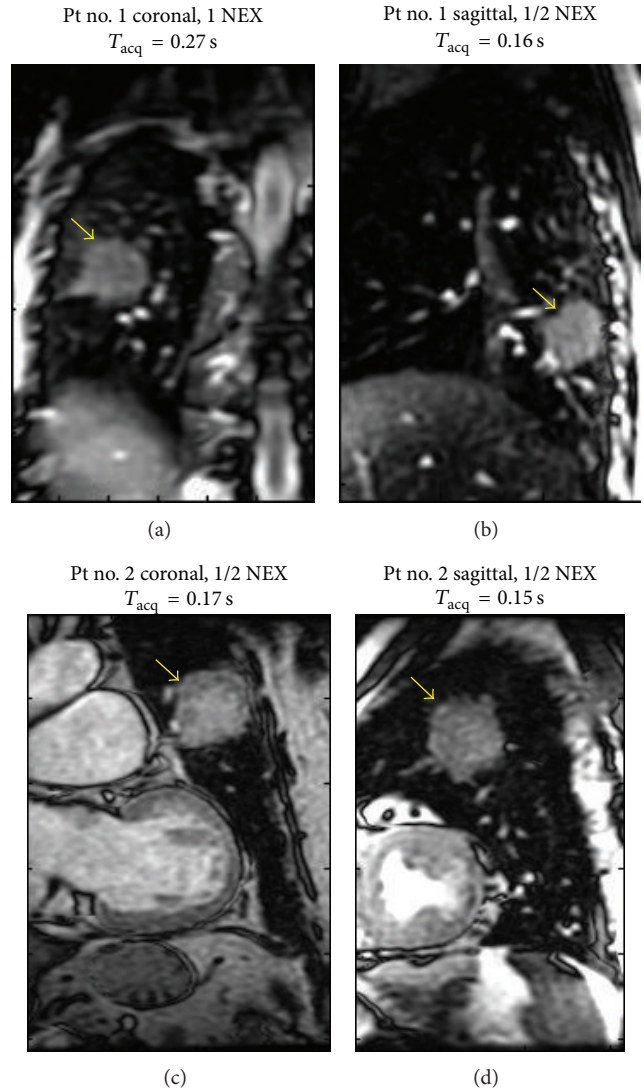

Figure 1: (a) Coronal and (b) sagittal real time MR images acquired from Patient number 1 with an ~40 mm diameter tumor (indicated by the arrows) in the right lower lobe. (c) Coronal and (d) sagittal real-time MR images from Patient number 2 with an ~60 mm diameter tumor in the left upper lobe.

the pixels comprising the tumor boundary. The presence of complex motion such as tumor rotation and/or deformation was tested by comparing the motion trajectory of the tumor centroid with those of the selected points on the tumor boundary.

3. Results and Discussion

Figure 1 shows MR images acquired from Patient number 1 (Figures 1(a) and 1(b)) and Patient number 2 (Figures 1(c) and 1(d)). The acquisition times per image ranged from ~0.15

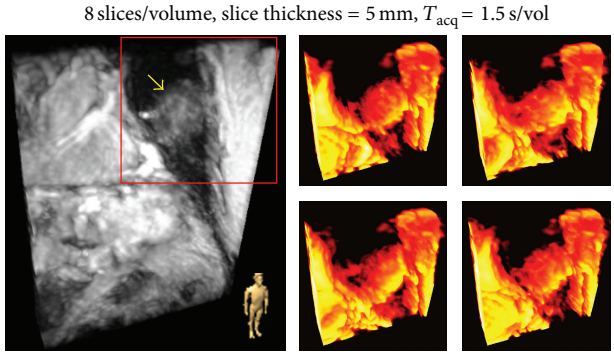

Figure 2: (a) bSSFP, 3D acquisition with parallel imaging (accn = 4) from Patient number 2. The arrow indicates tumor and the icon in the right bottom corner indicates the display orientation. (b) Surface-rendered volume of interest (red box in (a)) for four different respiratory phases.

to 0.27 s—speeds adequate for monitoring most respiratory motion. In each case, the tumor mass (indicated by an arrow) can be clearly delineated against the background of lung parenchyma. Figure 2(a) shows a frame from the 4D acquisition from Patient number 2. A surface rendered tumor-inclusive volume-of-interest in four different respiratory phases is shown in Figure 2(b). Both the tumor as well as the surrounding anatomy exhibit significant deformation from phase to phase.

Figure 3 shows motion trajectories extracted from two time series, one from each patient. MRI-based monitoring over multiple respiratory cycles yields some interesting observations. In the case of Patient number 1, there is little cycle-to-cycle variation in the respiratory pattern, as evidenced by the motion trajectory of the diaphragm. Furthermore, the motion of the tumor centroid is well correlated with the motion of the diaphragm (Figure 3(a); $R^2 = 0.99$) indicating that, in this case, diaphragmatic motion is an appropriate surrogate for tumor motion. Finally, the motion of individual points on the tumor boundary (i.e, pixels comprising the edges of the tumor mass) is well correlated with that of the tumor centroid (Figure 3(b); $R^2 = 0.9$ to 1.0), indicating the absence of any significant rotation or deformation in the tumor mass. In the case of Patient number 2, while the respiratory pattern is quite regular (as seen from the motion trajectory of the diaphragm), the motion of the tumor centroid is very poorly correlated with diaphragmatic motion (Figure 3(c); $R^2 = 0.16$) and shows significant cycle-to-cycle variation. This behavior indicates that, in this case, diaphragmatic motion is a poor surrogate for tumor motion. Furthermore, the motion of the tumor centroid is also relatively poorly correlated with that of individual points on the tumor boundary (Figure 3(d); $R^2 = 0.56$ to 0.94) indicating the occurrence of significant rotation/deformation of the tumor mass. The complex motion observed in Patient number 2 is likely due to the proximity of tumor to the cardiac wall, which almost touches the edge of the tumor (Figure 1(c)) and serves as a second actuator of motion (the first being the diaphragm). These results demonstrate that the current clinical practice of using the motion of the diaphragm (or external or internal surrogates for diaphragmatic motion) has significant limitations when the tumor mass is located in the proximity of other moving structures.

The goal of this work was to demonstrate the feasibility and the potential advantages of using rapid MRI as a pretreatment image-guidance tool for lung RT. These early results from rapid MRI of NSCLC patients show that, for guidance-quality imaging, the inherent contrast presented by the tumor mass and critical structures against the signal-poor lung parenchyma enables us to sacrifice SNR in order to achieve adequate acquisition speed to capture respiratory motion. Furthermore, in the case of Patient number 2, we observe that through long-term, prospective MR imaging, one can capture spatiotemporal effects that are not captured by 4DCT. This is due to the fact that 4DCT projections are sorted using an external surrogate for diaphragmatic motion, thereby implicitly assuming that a perfect correlation exists between diaphragmatic motion and tumor motion.

The choice of a 1.5 T scanner for this work was motivated by the fact that several lung motion investigations have been performed at this field strength [12, 18]. Observer studies comparing 1.5 T and 3 T scanners for lung MRI show that there is no significant difference in overall image quality [19, 20], suggesting that the expected benefits of higher SNR at 3 T are somewhat mitigated due to the accompanying increase in susceptibility artifacts. Furthermore, at this initial stage, we chose to use existing coils and sequences. As seen from the results, while this strategy was adequate for cine-2D imaging, very large improvements in acquisition speed are required for truly 4D MRI. This is evidenced by the fact that, even with the use of parallel acceleration = 4, the acquisition time for the 4D time series shown in Figure 2 was ~1.5 s/volume. Thus, there is much room for exploration of other rapid MRI sequences and for developing sequences specifically optimized for RT guidance. In particular, we expect the largest improvements in imaging speed to come from strategies based on sparse sampling and reconstruction such as k-t Broad-use Linear Acquisition Speed-up Technique (k-t BLAST) and its parallel imaging version, k-t SENSitivity Encoding (k-t SENSE).

Beyond the current scope, it is expected that the information obtained from rapid MRI (cine-2D or 4D) can be merged with that from 3DCT or 4DCT to create a fused pretreatment 4D image that combines the soft-tissue contrast and temporally dense information from MRI with the spatial accuracy and electron density information from CT. Admittedly, this is a nontrivial problem because one has to account for MRI artifacts, correct for geometric distortions of the anatomy due to the relatively narrow bore of the magnet, and develop robust multimodality image registration tools. Furthermore, since this was a feasibility study, the patients were not asked to lie in the treatment position for the MRI scan. However, for future studies which aim to fuse the MRI with CT, patients will be required to do so. However, if these challenges are addressed, fused 4D images would provide a more realistic picture of the behavior of thoracic anatomy over multiple respiratory cycles. Such guidance would enable

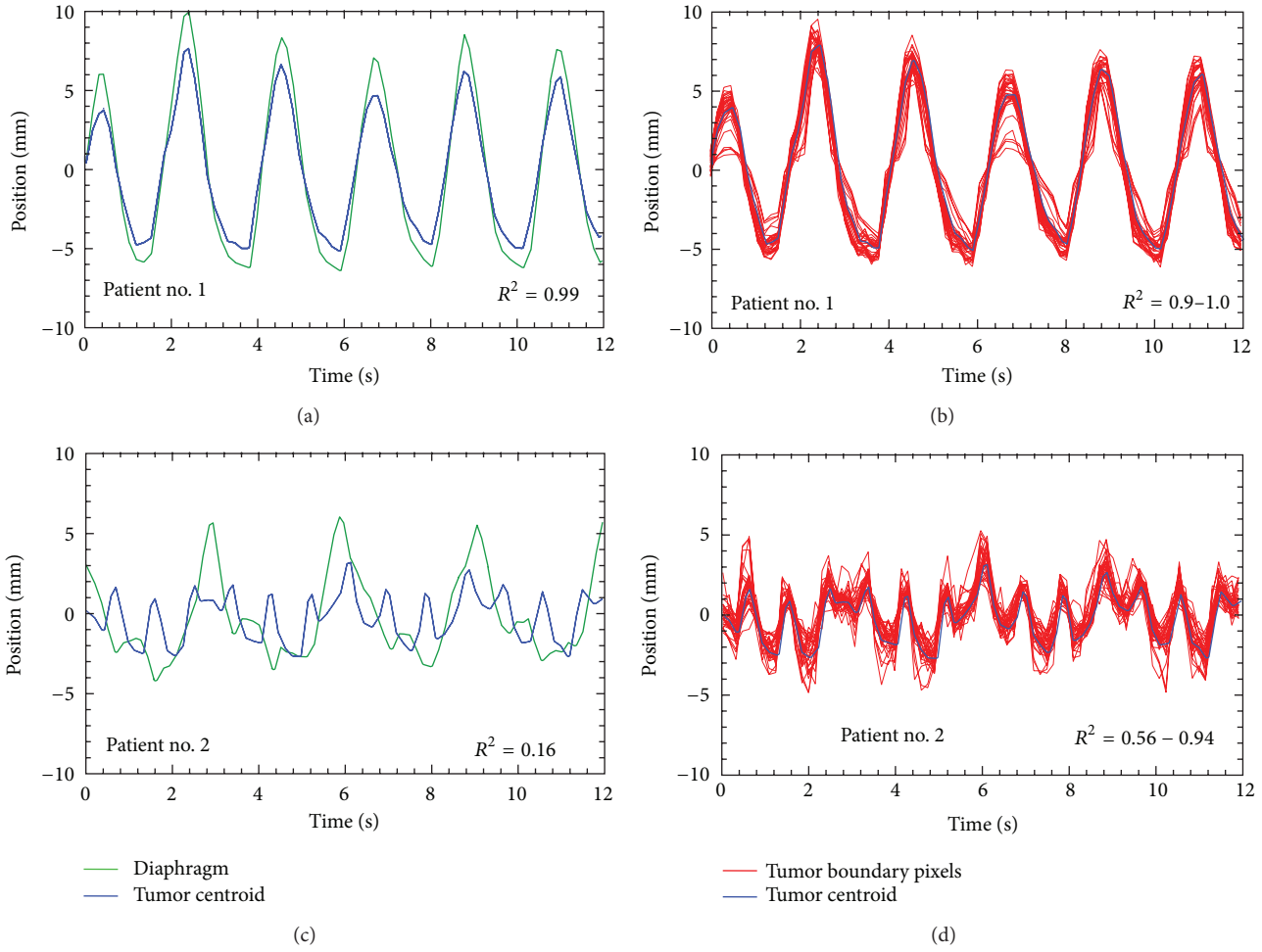

Figure 3: Motion trajectories of extracted from sagittal MRI time series from Patients number 1 and number 2 (Figures 1(b) and 1(d), resp.). ((a) and (c)) Mean-subtracted motion trajectories of the tumor centroid and the dome of the diaphragm for Patient number 1 and Patient number 2, respectively. ((b) and (d)) Trajectories of the tumor centroid and 15 points on the tumor boundary for Patient number 1 and Patient number 2, respectively.

the development of novel 4D treatment planning paradigms that explicitly account for effects such as baseline shifts and changes in abdominal versus thoracic breathing. Finally, several investigators are working on integrated MRI+linac designs [21–23]. Online prospective 4D MRI would enable such systems to perform real-time monitoring and, potentially, real-time beam adaptation.

4. Conclusion

We have investigated the feasibility of rapid MRI as a modality for image-based guidance in lung radiotherapy. While the acquisition speeds of cine-2D imaging are adequate for capturing most respiratory motion, significant further improvements are required to achieve comparable speeds for truly 4D MRI acquisition. Nevertheless, these early results indicate that rapid MRI offers a highly attractive, noninvasive imaging tool for respiratory motion management. The ability to perform dose-free, long-term monitoring over multiple respiratory cycles yields valuable information that is not currently available with 4DCT. We expect that such image-guidance will lay the groundwork for significantly better respiratory motion management in lung radiotherapy.

Conflict of Interests

The authors declare that there is no conflict of interests regarding the publishing of this paper.

Acknowledgments

This work was partially supported by the American Association of Physicists in Medicine (AAPM) Research Seed Funding Grant 2008.

References

[1] P. J. Keall, G. S. Mageras, J. M. Balter et al., "The management of respiratory motion in radiation oncology report of AAPM Task Group 76," *Medical Physics*, vol. 33, no. 10, pp. 3874–3900, 2006.

[2] G. S. Mageras, A. Pevsner, E. D. Yorke et al., "Measurement of lung tumor motion using respiration-correlated CT," *International Journal of Radiation Oncology Biology Physics*, vol. 60, no. 3, pp. 933–941, 2004.

[3] P. Keall, "4-Dimensional Computed Tomography Imaging and Treatment Planning," *Seminars in Radiation Oncology*, vol. 14, no. 1, pp. 81–90, 2004.

[4] N. M. Wink, C. Panknin, and T. D. Solberg, "Phase versus amplitude sorting of 4D-CT data," *Journal of Applied Clinical Medical Physics*, vol. 7, no. 1, pp. 77–85, 2006.

[5] J. Cai, P. W. Read, and K. Sheng, "The effect of respiratory motion variability and tumor size on the accuracy of average intensity projection from four-dimensional computed tomography: an investigation based on dynamic MRI," *Medical Physics*, vol. 35, no. 11, pp. 4974–4981, 2008.

[6] T. Yamamoto, U. Langner, B. W. Loo Jr., J. Shen, and P. J. Keall, "Retrospective analysis of artifacts in four-dimensional CT images of 50 abdominal and thoracic radiotherapy patients," *International Journal of Radiation Oncology Biology Physics*, vol. 72, no. 4, pp. 1250–1258, 2008.

[7] G. F. Persson, D. E. Nygaard, C. Brink et al., "Deviations in delineated GTV caused by artefacts in 4DCT," *Radiotherapy and Oncology*, vol. 96, no. 1, pp. 61–66, 2010.

[8] S. Mori, S. Ko, T. Ishii, and K. Nishizawa, "Effective doses in four-dimensional computed tomography for lung radiotherapy planning," *Medical Dosimetry*, vol. 34, no. 1, pp. 87–90, 2009.

[9] C. Plathow, H. Hof, S. Kuhn et al., "Therapy monitoring using dynamic MRI: analysis of lung motion and intrathoracic tumor mobility before and after radiotherapy," *European Radiology*, vol. 16, no. 9, pp. 1942–1950, 2006.

[10] C. Plathow, S. Ley, C. Fink et al., "Analysis of intrathoracic tumor mobility during whole breathing cycle by dynamic MRI," *International Journal of Radiation Oncology Biology Physics*, vol. 59, no. 4, pp. 952–959, 2004.

[11] M. Von Siebenthal, G. Székely, U. Gamper, P. Boesiger, A. Lomax, and P. Cattin, "4D MR imaging of respiratory organ motion and its variability," *Physics in Medicine and Biology*, vol. 52, no. 6, article 1547, 2007.

[12] J. Biederer, J. Dinkel, G. Remmert et al., "4D-imaging of the lung: reproducibility of lesion size and displacement on helical CT, MRI, and cone beam CT in a ventilated ex vivo system," *International Journal of Radiation Oncology Biology Physics*, vol. 73, no. 3, pp. 919–926, 2009.

[13] J. Cai, Z. Chang, Z. Wang, W. Paul Segars, and F.-F. Yin, "Four-dimensional magnetic resonance imaging (4D-MRI) using image-based respiratory surrogate: a feasibility study," *Medical Physics*, vol. 38, no. 12, pp. 6384–6394, 2011.

[14] A. C. S. Brau, P. J. Beatty, S. Skare, and R. Bammer, "Comparison of reconstruction accuracy and efficiency among autocalibrating data-driven parallel imaging methods," *Magnetic Resonance in Medicine*, vol. 59, no. 2, pp. 382–395, 2008.

[15] M. Foskey, A. Gash, Q. Han et al., "A software toolkit for multi-image registration and segmentation in IGRT and ART," *Medical Physics*, vol. 34, article 2351, 2007.

[16] K. Wijesooriya, E. Weiss, V. Dill et al., "Quantifying the accuracy of automated structure segmentation in 4D CT images using a deformable image registration algorithm," *Medical Physics*, vol. 35, no. 4, pp. 1251–1260, 2008.

[17] R. Kashani, M. Hub, J. M. Balter et al., "Objective assessment of deformable image registration in radiotherapy: a multi-institution study," *Medical Physics*, vol. 35, no. 12, pp. 5944–5953, 2008.

[18] C. Plathow, M. Schoebinger, C. Fink et al., "Quantification of lung tumor volume and rotation at 3D dynamic parallel MR imaging with view sharing: preliminary results," *Radiology*, vol. 240, no. 2, pp. 537–545, 2006.

[19] C. Fink, M. Puderbach, J. Biederer et al., "Lung MRI at 1.5 and 3 tesla: observer preference study and lesion contrast using five different pulse sequences," *Investigative Radiology*, vol. 42, no. 6, pp. 377–383, 2007.

[20] U. I. Attenberger, M. Ingrisch, O. Dietrich et al., "Time-resolved 3D pulmonary perfusion MRI: comparison of different k-space acquisition strategies at 1.5 and 3 T," *Investigative radiology*, vol. 44, no. 9, pp. 525–531, 2009.

[21] A. J. E. Raaijmakers, B. W. Raaymakers, and J. J. W. Lagendijk, "Integrating a MRI scanner with a 6 MV radiotherapy accelerator: dose increase at tissue-air interfaces in a lateral magnetic field due to returning electrons," *Physics in Medicine and Biology*, vol. 50, no. 7, pp. 1363–1376, 2005.

[22] G. Fallone, M. Carlone, B. Murray, S. Rathee, and S. Steciw, "Investigations in the design of a novel Linac-MRI system," *International Journal of Radiation Oncology Biology Physics*, vol. 69, no. 3, p. S19, 2007.

[23] D. E. Constantin, R. Fahrig, and P. J. Keall, "A study of the effect of in-line and perpendicular magnetic fields on beam characteristics of electron guns in medical linear accelerators," *Medical Physics*, vol. 38, no. 7, pp. 4174–4185, 2011.

Hindawi Publishing Corporation
BioMed Research International
Volume 2013, Article ID 701514, 8 pages
http://dx.doi.org/10.1155/2013/701514

Research Article

Contour Propagation Using Feature-Based Deformable Registration for Lung Cancer

Yuhan Yang, Shoujun Zhou, Peng Shang, En Qi, Shibin Wu, and Yaoqin Xie

Key Laboratory for Health Informatics, Shenzhen Institutes of Advanced Technology, Chinese Academy of Sciences, Shenzhen 518055, China

Correspondence should be addressed to Yaoqin Xie; yq.xie@siat.ac.cn

Received 29 May 2013; Revised 13 September 2013; Accepted 20 October 2013

Academic Editor: Chung-Chi Lee

Accurate target delineation of CT image is a critical step in radiotherapy treatment planning. This paper describes a novel strategy for automatic contour propagation, based on deformable registration, for CT images of lung cancer. The proposed strategy starts with a manual-delineated contour in one slice of a 3D CT image. By means of feature-based deformable registration, the initial contour in other slices of the image can be propagated automatically, and then refined by active contour approach. Three algorithms are employed in the strategy: the Speeded-Up Robust Features (SURF), Thin-Plate Spline (TPS), and an adapted active contour (Snake), used to refine and modify the initial contours. Five pulmonary cancer cases with about 400 slices and 1000 contours have been used to verify the proposed strategy. Experiments demonstrate that the proposed strategy can improve the segmentation performance in the pulmonary CT images. Jaccard similarity (JS) mean is about 0.88 and the maximum of Hausdorff distance (HD) is about 90%. In addition, delineation time has been considerably reduced. The proposed feature-based deformable registration method in the automatic contour propagation improves the delineation efficiency significantly.

1. Introduction

Carcinoma of the lung is one of the most common cancers, which has the highest mortality rate all over the world [1]. Radiotherapy is an effective option for carcinoma treatment. How to maintain adequate sparing of the sensitive structures is one of the biggest challenges in radiotherapy, which can be faced by means of treatment planning [2, 3]. The precise target delineation is an essential prerequisite for treatment planning; this, in fact, provides dose escalation to the tumor [4]. In the conventional radiotherapy planning, the clinical contour delineation is manually conducted by physicians slice by slice; however, this is a tedious and time-consuming procedure. Consequently, some fully automatic methods on each slice, such as the traditional water-based segmentation and level set active contour, have been proposed. These techniques mainly rely on local image features, such as intensity and gradient variations. However, these methods are unable to generate accurate target contour in absence of distinctive local image feature, such as in the tissues of mediastinum, hilus pulmonis, or pulmonary artery.

For target delineation of metastatic lung cancer, the hilus pulmonis should be embraced in the lung. Some statistical model-based approaches, such as the classical active shape models [5] or active appearance models [6], have been proposed by adding superior contour constraints in procrustes analysis and principal component analysis. However, lung morphology varies from patient to patient; several efforts have been made to solve this issue by providing prior knowledge by means of three-dimensional views [7–10]. For example, Brown et al. [7] presented an automatic knowledge-based method for segmenting chest CT datasets. Then, Zhang et al. [8] used an anatomic pulmonary atlas, encoded with a priori information on the pulmonary anatomy, to automatically segment the oblique lobar fissures. Qazi et al. [9] presented a fully automatic hybrid approach and combined deformable registration with the model-based approach to accurately segment normal tissues and target from head and neck CT images. Additionally, Collins et al. [10] presented a 3D model-based segmentation method for the automatic identification and delineation of gross anatomical structures of the human brain. However, since these methods partially depended on

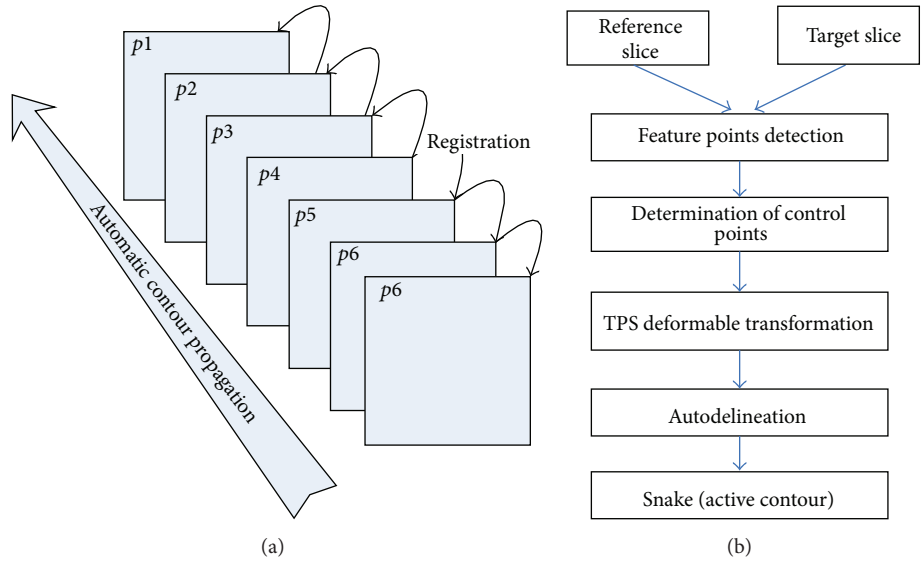

Figure 1: Flowchart of the automatic contour propagation method. (a) General flowchart of the automatic contour propagation; (b) flowchart of the automatic contour delineation between adjacent slices on (a).

a massive patient model dataset and complicated statistical analysis, the necessary work tends to be extensive, and it may result in potential errors arising from the reliability of the selection of the optimal model. In addition, three-dimensional image processing is a time-consuming procedure, and its accuracy hardly reaches the two-dimensional processing accuracy because of the deformation due to respiratory movement. As any error at this step is systematic and would affect the whole course of radiotherapy, manual delineation method is required.

In this paper, a 2D contour propagation method is proposed. Feature-based deformable registration method was employed by using an initial manual delineated contour slice as the prior knowledge; in this way the interaction time compared to the fully manual delineation method can be greatly reduced.

2. Materials and Methods

2.1. Overview of the Automatic Target Delineation. The flowchart of the proposed automatic contour propagation is shown in Figure 1(a). In this study, a template-based registration method was introduced from the research of brain functional area [11], in which a standard brain is used as template to determine the brain functional area for clinical cases through deformable registration. To reduce user interaction time, one slice of the 3D CT image is manually delineated as prior model and then other contours are automatically and recursively delineated by using deformable registration. As shown in Figure 1(b), the previous slice is set as template image, and the next slice is set as target image. The first two steps, feature points detection and association, are conducted by Speeded-Up Robust Features (SURF) [12]. These points contain the local features and also keep invariant to the environment variation. Then, Thin-Plate Spline (TPS) [13] is employed to generate the deformation vector field (DVF) based on the displacement vectors of associated feature points. In the fourth step, the contour transformation is obtained from the DVF. Finally, Snake is introduced as refinement and modification approach to drive the initial contours towards the desired segmented object in the image.

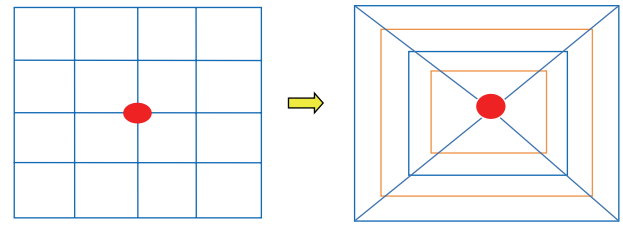

Figure 2: The SURF descriptor (left) and GDLOH descriptor (right). The GDLOH regards a concentric rectangle grid different radius and 4 in angular direction.

2.2. Tissue Feature Detection and Association. Detection and association of distinct tissue feature points on two images play an important role in contour propagation [14]. SURF detector is the accelerated version of the classical Scale-Invariant Feature Transform (SIFT) [15], with the same matching quality. This is considered a beneficial approach because of its distinctive invariant features and robustness to affine distortion, noise, and intensity changes.

With regard to the feature descriptor, an improved version of SURF, gradient distance-location-orientation histogram (GDLOH) [16], is considered to be more distinctive. GDLOH descriptor, as shown in Figure 2, contains 16 square subregions with four principal characters: the frame center

coordination (x, y), the scale σ, and the orientation θ. For each square, the Haar wavelet responses in horizontal direction and vertical direction are computed and summed. In this way, the histogram of 16 frames with 4 dimension gradient vector around the center can obtain 64 dimensional feature descriptors.

The descriptor is employed to search the best association candidate for each feature point by identifying its nearest neighbor in the database of points from testing images. The nearest neighbor is defined as points' minimum Euclidean distance. In this method, interrelationship among the descriptor's elements is also considered in the distance calculation. The expression can be defined as follows:

$$D(P,Q) = \left(\sum P^2[i] + \sum Q^2[i]\right) * \frac{\sum (P[i] - Q[i])^2}{(2 * \sum P[i] * Q[i])}. \quad (1)$$

In Cartesian coordinates, $P = (p_1, p_2, \ldots, p_n)$ is the descriptor of the feature point $P(x, y)$, and $Q = (q_1, q_2, \ldots, q_n)$ is the descriptor of the feature point $Q(x, y)$. Furthermore, the coordinates of the points P, Q can be confined in $10 * 10$ pixels according to the image rotation.

2.3. TPS Transformation. Thin-Plate Splines (TPS) were introduced in geometric designs by Duchon [17]. This has been widely used as deformable transformation model in image registration. In the proposed method, TPS transformation warps the template image to match the target image pixel-by-pixel. Mathematically, this consists in an optimization problem, in which a set of transformation parameters transform the pixels in the template image to their corresponding pixels in the target image.

To find the transformation matrix a TPS deformable model $T(X)$ was employed to map an arbitrary pixel from the template image to that on the target image [18]. The function was defined as

$$f\left(u', v'\right) = a_1 + a_u u + a_v v + \sum_{i=0}^{n-1} w_i U\left(\left|p_i - (u, v)\right|\right), \quad (2)$$

where P_i are control points coordinates in the template image and U is a basis function for measuring the distance. $W = (w_1, w_2, \ldots, w_n)$ and a_1, a_u, a_v stand for the weighting vector and the coefficients, which were computed from series of matrices. These matrices were constructed using a pair of matched control points in the template image (x_i, y_i) and the target image (u_i, v_i). Major steps are presented as follows.

(1) $P_1 = (x_1, y_1)$, $P_2 = (x_2, y_2), \ldots, P_n = (x_n, y_n)$ are n control points in the template image; the distance between point i and j is defined as $r_{ij} = |P_i - P_j|$.Consider the following:

$$P = \begin{bmatrix} 1 & x_1 & y_1 \\ 1 & x_2 & y_2 \\ \vdots & \vdots & \vdots \\ 1 & x_n & y_n \end{bmatrix},$$

$$K = \begin{bmatrix} 0 & U(r_{12}) & \cdots & U(r_{1n}) \\ U(r_{21}) & 0 & \cdots & U(r_{2n}) \\ \vdots & \vdots & \vdots & \vdots \\ U(r_{n1}) & U(r_{n2}) & \cdots & 0 \end{bmatrix}, \quad (3)$$

$$L = \begin{bmatrix} K & P \\ P^T & 0 \end{bmatrix},$$

where O represents $4 * 4$ matrix of zeros and U is a basic function $U(r) = \sqrt{r^2 \log r^2}$.

(2) $Q_1 = (u_1, v_1)$, $Q_2 = (u_2, v_2), \ldots, Q_n = (u_n, v_n)$ represent n corresponding control points in target image. Construct matrices

$$V = \begin{bmatrix} u_1 & u_2 & \cdots & u_n \\ v_1 & v_2 & \cdots & v_n \end{bmatrix},$$
$$Y = \left(V \mid \begin{array}{ccc} 0 & 0 & 0 \end{array}\right)^T. \quad (4)$$

The weighting vector $W = (w_1, w_2, \ldots, w_n)$ and the coefficients a_1, a_u, a_v can be computed by the equation

$$L^{-1}Y = \left(W \mid \begin{array}{ccc} a_1 & a_u & a_v \end{array}\right)^T. \quad (5)$$

(3) The elements of $L^{-1}Y$ can be used to define a function $f(u, v)$.

2.4. Active Contour (Snake). The above contour propagation was based on the manual delineation and deformable registration; this could cause some potential artifacts or distortion. Adapted active contour was proposed to solve this issue. This model is an energy-minimizing spline guided by internal and external forces, which are responsible for driving the contour to the desired local minimum or pulling it towards features such as lines or edges. Its energy function can be represented as

$$E^*_{\text{snake}} = \int_0^1 \left(\alpha^* E_{\text{cont}}(v(s)) + \beta^* E_{\text{curv}}(v(s)) + \gamma^* E_{\text{image}}(v(s))\right) ds, \quad (6)$$

where $v(s) = (x(s), y(s))$ stands for the contour parameter, E_{cont} stands for the continuity energy, E_{curv} stands for the internal energy of the spline due to bend and smooth, E_{image} stands for the external image forces, and the three parameters α, β, and γ stand for the weight coefficient of E_{cont}, E_{curv}, and E_{image}, and they all range from 0 to 1. The optimization of the parameters has been conducted by experiments with 3 parameters α, β, and γ equal to 0.15 ± 0.08, 0.2 ± 0.08, and 0.85 ± 0.06, respectively. Moreover, a band was employed to limit the range of contour motion. According to the experiment results, a band width of 3 to 9 pixels has been proposed for $512 * 512$ lung CT image.

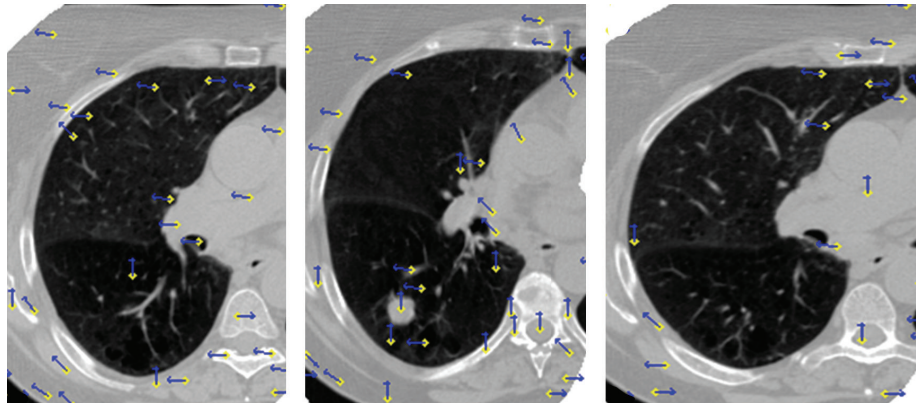

Figure 3: Displacement vectors of control points generated by the TPS transformation in three axial images. The yellow points stand for the control points, and the blue arrows stand for the displacement direction.

2.5. Case Study and Evaluation. The CT images were acquired with a GE Discovery-ST CT scanner (GE Medical System, Milwaukee, WI, USA). The proposed method was developed using the Insight Segmentation and Registration Toolkit (ITK) [19] and Open Source Computer Vision (OpenCV) [20]. ITK is an open-source and cross-platform image processing software developed by the National Library of Medicine. OpenCV is a library of programming functions developed by Intel. In addition, VOLVIEW [21], PARAVIEW [22], and The Visualization ToolKit (VTK) [23] have been used for image visualization. The image sets for all the patients were reconstructed with a 2.5 mm slice thickness. Each CT slice was discretized into $512 * 512$ pixels. About 400 slices and nearly 1000 contours were tested in the evaluation.

To quantitatively evaluate the accuracy of our method, the Jaccard similarity (JS) [24, 25] between the automatic and manual segmentation was calculated as follows:

$$\mathrm{JS} = \left(\frac{S_{\mathrm{auto}} \bigcap S_{\mathrm{manual}}}{S_{\mathrm{auto}} \bigcup S_{\mathrm{manual}}} \right), \tag{7}$$

where S_{auto} is the area of the autosegmentation and S_{manual} is the area of the manual segmentation. The value of JS is defined from 0 to 1, where 0 indicates no overlapped regions and 1 indicates that these two regions are the perfect overlap. Area measures, such as JS, can give a good estimate of expert agreement; however, they are much insensitive to boundary errors in the segmentation. To provide additional information, Hausdorff distance (HD) [26] between autodelineation and the manual delineation is given for estimating mismatch degree. HD measures the maximum and minimum distance between two contour sets, and it can be used as metric of similarity between two contours superimposed together.

3. Results

Figure 3 shows the displacement vectors of the control points generated by the TPS transformation; the three images show three different lung slices. The yellow points represent the control points, and the blue arrows stand for the displacement direction. At least 30 control points were obtained in each slice; this has satisfied the requirement of the TPS transformation [27].

Normal tissue must be considered in radiotherapy plan, whose radiation sensitivity influences the prescribed radiation. In case of lung cancer, the organs at risk (OAR) mainly include lungs and spinal cord [28]. Figure 4 shows the process of the contour propagation and refinement, starting from the initial manual delineation to the final automatic contour. The three images represent a set of sequential slices. The cyan lines represent the manual delineation, the red lines represent the initial contour by SURF-TPS registration, and the yellow lines represent the final contour refined by Snake. It is clear that the yellow lines have much better consistency with the cyan lines as compared with the red lines, especially near the pleura. Since distribution of the pulmonary artery and bronchia is cluttered, distinctive local features are not easily discriminated by the fully automatic approach. Furthermore, after the initial propagation, the JS between the reds and cyans has reached 0.93 ± 0.08.

Figure 5 shows three lung segmented results conducted by fully automatic methods compared with the manual standard. Here, three classical algorithms have been chosen: watershed, flood fill, and active contour. The active contour used in the experiment, which has added the narrow band constraint proposed by Mille [29], is one of the popular extensions of the original Snake. The cyan contour represents the manual standard delineated manually, the yellow region in (a) is generated by flood fill algorithm, the red region in (b) is by active contour, and the blue region in (c) is by watershed algorithm. Notice that all three regions failed to embrace the hilus pulmonis near the mediastinum, indicated by the black ellipse, while our proposed method can reach the requirement (as shown in Figure 4). In addition, as these automatic algorithms highly depend on the initial seeds to start the driving, the selection of the seeds should be much more careful. In this way, it would raise potential delineation time and risk. The JS between the segmented region and the cyan surrounded one can only reach 0.85 ± 0.06; this value is much lower than the one found with the proposed method. In the experiment, since active contour and watershed algorithms, which highly rely on the intensity

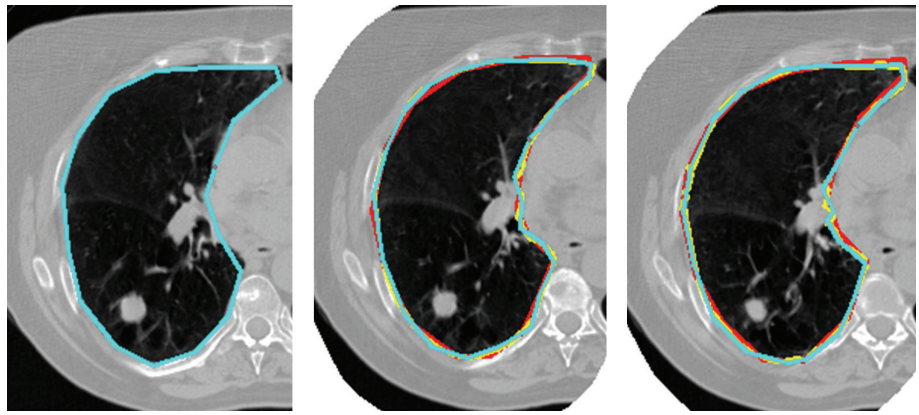

Figure 4: Process of the contour propagation and refinement, from the manual delineation to the final automatic contour. Three images stand for three sets of sequential slices. The cyan lines stand for the manual delineation, the red lines stand for the initial contour by SURF-TPS registration, and the yellow lines stand for the final contour refined by Snake. Yellow contours match the cyan better.

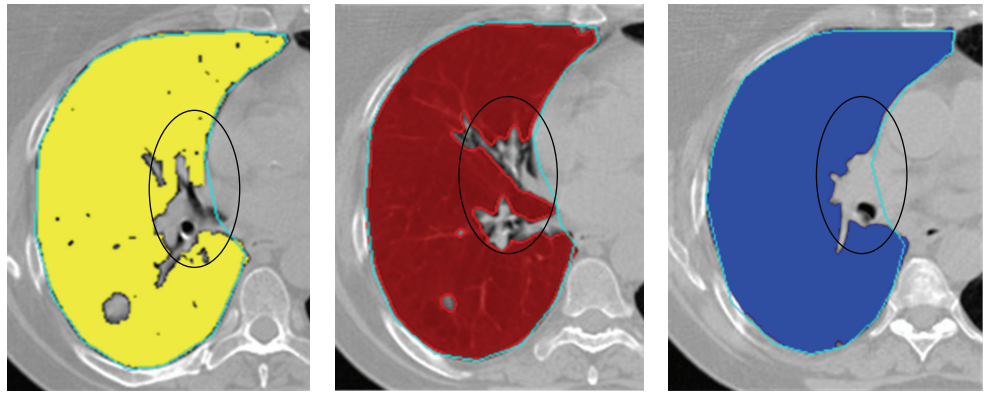

(a) (b) (c)

Figure 5: Comparison between fully automatic segmented methods and the manual delineation. The cyan contours were manual delineated contours. (a) Flood fill algorithm (yellow); (b) active contour (red); (c) watershed algorithm (blue). The region embraced by the black ellipse failed to be delineated by these automatic segmentations.

and seed information, do not perform well in the spinal cord and tumor delineation, we will mainly introduce the flood fill algorithm in the following to compare it with the results of our proposed method.

With respect to the spinal cord, which is more sensitive to the radiation injury, more precise delineation was needed. Figure 6 shows three cases of delineation results obtained from the proposed method and the flood fill method, respectively. As shown in Figure 5, better results were achieved by using flood fill method and then active contour method and watershed method. In Figure 6, the red region is generated by the flood fill method, the yellow contour is delineated by our proposed method, and the cyan contour stands for the manually delineated contour. It has been found that the yellow contours can better fit the cyan contours as compared to the red contours. In addition, as the intensity information is distributed differently from slice to slice, the parameter settings of the flood fill algorithm should be changed. For example, the optimal local scale parameter for lung is 12 ± 2, but for spinal cord it is reduced to 5 ± 1, which results in some uncertainty. The JS between the red region and the cyan surrounded region is about 0.65 ± 0.08, which is much lower than what the yellow contains.

Figure 7 shows three cases of lung tumor segmentation obtained from our proposed method and the flood fill algorithm, respectively. The cyan contour represents the manual delineation, the yellow contour is generated by our proposed method, and the red region is generated by flood fill algorithm. These three tumors are located on the bronchia, hilus pulmonis, and lobe, respectively. As there is no obvious intensity difference among the tumor, bronchia, and hilus, the red contour tends to be more inconsistent with the cyan contour, while the yellow contour that can better fit the cyan contour well overcomes this problem. The JS between the yellows and the cyan is nearly 0.88 ± 0.5, which is much higher than the JS between the reds and the cyan.

Since the contour delineation of tumor and organ at risk (OAR) is very important for treatment planning, the feasibility and accuracy of the proposed method should be reliably tested. There are five lung cancer patients with over

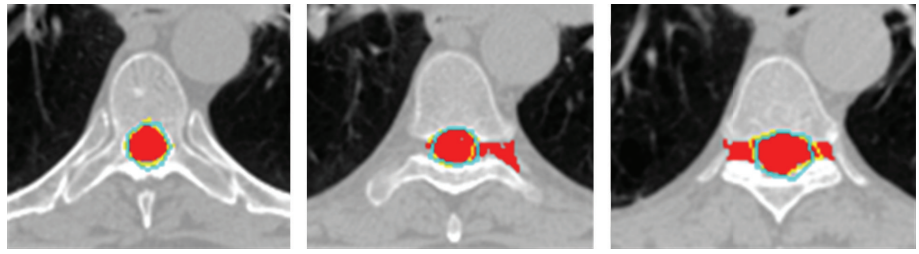

Figure 6: Three cases of delineation results conducted by our proposed method and the flood fill algorithm, respectively. The cyan contour represents the manual delineation, the yellow is automatically delineated by our proposed method, and the red region is generated by flood fill algorithm.

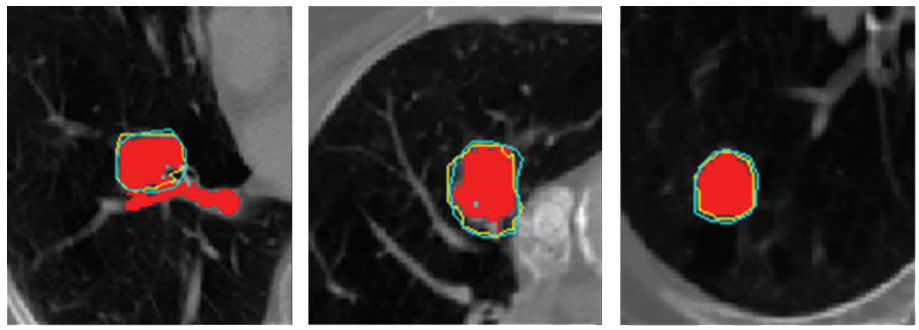

Figure 7: Three cases of lung tumor segmentation conducted by our proposed method and the flood fill algorithm, respectively. The tumors are located on the bronchia, hilus pulmonis, and lobe, respectively. The cyan contour represents the manual delineation, the yellow contour is generated by our proposed method, and the red region is generated by flood fill algorithm.

Table 1: JS comparison of five lung cancer patients by using the proposed method and the flood fill algorithm.

Patient	Target	The JS		Percentage gains
		Proposed method	Flood fill method	
Patient 1	Lung	0.9458	0.8540	9.71%
	Spinal cord	0.8520	0.7018	17.63%
	Tumor	0.9447	0.9334	1.20%
Patient 2	Lung	0.9544	0.8658	9.28%
	Spinal cord	0.8402	0.6875	18.17%
	Tumor	0.8589	0.7569	11.88%
Patient 3	Lung	0.9541	0.8320	12.80%
	Spinal cord	0.8654	0.7468	13.70%
	Tumor	0.9014	0.8654	3.99%
Patient 4	Lung	0.9440	0.8214	12.99%
	Spinal cord	0.8598	0.7025	18.29%
	Tumor	0.8958	0.6475	27.72%
Patient 5	Lung	0.9486	0.8258	12.95%
	Spinal cord	0.8475	0.6732	20.57%
	Tumor	0.8858	0.7854	11.33%

400 CT slices for the verification. The position and size of the tumors differ from patient to patient. Table 1 shows the JS by using the proposed method and the flood fill method. For patients 1 and 3, tumors are located on the lung lobe with much more apparent local features, while for the other three patients, tumors are located near the pleura, bronchia, and hilus pulmonis. Features are not apparent. It is easy to find that the JS of the first and the third patients, obtained from flood fill method, is much higher than that of the second, fourth, and fifth. On the contrary, the JS obtained from the proposed method presents small changes for all patients. When the delineation goes to the spinal cord with efferent nerves, the contour driven by flood fill tends to be less robust, and the JS between it and the manual standard becomes lower. The percentage gains of the JS between these two methods are also listed. The gains for lung and spinal cord remain steady around 0.10, but for tumor, it changes greatly among different cases. The maximum JS gain for lung, spine cord, and tumor has reached values around 12%, 17%, and 24%, respectively.

Table 2 shows the statistical value of mean and maximum of HD for lung, spinal cord, and tumor, respectively. As the tumor position and size differ from patient to patient, the HD should be listed respectively. It is clear that the HD improvement in lung is the biggest, reaching a value around 90%. The HD improvement in spinal cord can reach nearly 40%. On the contrary, for tumor, the HD improvements have a different representation. Its maximum HD improvement has, respectively, reached 90%, 45%, and 72%, according to the different tumor location. These results can be considered as a great progress in segmentation with no distinctive local feature.

Table 2: HD comparison between the proposed method and the Flood fill method.

Target	Lung	Spinal cord	Tumor				
			1	2	3	4	5
HD							
Flood fill	54.21	6.07	3.23	9.18	2.23	20.42	6.18
Proposed	5.04	3.45	3.35	2.53	2.15	5.84	4.85
Improvement (%)	90.70	43.16	−3.72	72.44	3.59	71.40	21.52
Mean HD							
Flood fill	7.58	1.71	0.63	2.85	0.83	3.38	2.61
Proposed	0.91	0.92	0.59	1.09	0.68	1.67	1.83
Improvement (%)	87.99	46.20	6.35	61.75	18.07	50.59	29.89

4. Discussions

In this work, a feature-based recursive deformable registration strategy was proposed. In routine clinical procedure, target volume and OAR for lung cancer are manually delineated. Therefore, reliable automatic contour delineation may have a substantial impact on treatment planning. The proposed method takes a manual delineated slice as prior knowledge to recursively propagate the contour slice by slice. Here, the middle slice of the whole lung has been chosen as an initial manual delineated slice; this choice doubles the propagation distance. The total 2D delineation time can be dramatically reduced compared with the conventional 3D contour segmentation. Since the initial propagated contour's quality largely depends on the similarity between two adjacent slices, slice thickness turns to be a critical factor for autodelineation.

Feature-based deformable registration [30] is used to propagate the contour since it contains both local and global feature information and can overcome the low resolution of CT image. SURF is a popular local feature detection method, which has a good robustness to variation of the scale, luminance, rotation, and blurring. After registration, an adapted Snake is employed to refine and modify the rough outline. The proposed method outperforms other fully automatic segmentation algorithms, such as the classical water-based and extensional active contour approach, as shown in Figure 5. In the picture, it also can be seen that the hilus pulmonis near the mediastinum was surrounded by our autopropagated contour as shown in Figure 4.

However, the proposed method still presents some weakness. For example, it much relies on the slice thickness. In fact, if the thickness is set excessively large, the quality of registration would decline, directly influencing the autodelineation. According to experiment measurements, 3 mm is suggested as the maximum thickness for achieving good performance. The adapted Snake should be further optimized, since the deformation still causes some instabilities. In addition, as the influence of prior knowledge would decrease with the propagation distance, the length of the propagation routine becomes more and more limited. For lung delineation, the maximum propagation distance with 20 slices has given optimal results. All in all, the delineation time was reduced drastically, while the accuracy remains high.

5. Conclusion

Automatic accurate target delineation plays an important role in radiotherapy allowing escalating tumor doses without increasing the toxicity of critical normal structures, especially in pulmonary treatment planning. The proposed method provides a novel approach combining the delineation experience from the physicists with high speed and reliability from the automatic algorithm. The advantages of the proposed method are as follows. Firstly, it largely reduces the delineation time by automatic contour propagation compared to manual delineation slice by slice. Secondly, the prior knowledge is well preserved by SURF-TPS registration increasing the accuracy of contour propagation. Thirdly, the refinement and modification by adapted Snake are beneficial for further precision upgrade. The proposed method will find practical and useful application in clinical treatment planning in radiotherapy.

Acknowledgments

This work is supported in part by Grants from the National Natural Science Foundation of China (NSFC: 81171402), the NSFC Joint Research Fund for Overseas Research Chinese, Hong Kong and Macao Young Scholars (30928030), National Basic Research Program 973 (2010CB732606) from Ministry of Science and Technology of China, Guangdong Innovative Research Team Program (no. 2011S013) of China, and the Strategic Partnership Program between Guangdong Province & Chinese Academy of Sciences Program no. 2011B090300079.

References

[1] R. Siegel, D. Naishadham, and A. Jemal, "Cancer statistics," *CA: A Cancer Journal for Clinicians*, vol. 63, no. 1, pp. 11–30, 2013.

[2] J. Staffurth, "A review of the clinical evidence for intensity-modulated radiotherapy," *Clinical Oncology*, vol. 22, no. 8, pp. 643–657, 2010.

[3] R. A. Weersink, J. Qiu, A. J. Hope et al., "Improving superficial target delineation in radiation therapy with endoscopic tracking and registration," *Medical Physics*, vol. 38, no. 12, pp. 6458–6468, 2011.

[4] C. F. Njeh, "Tumor delineation: the weakest link in the search for accuracy in radiotherapy," *Journal of Medical Physics*, vol. 33, no. 4, pp. 136–140, 2008.

[5] T. F. Cootes, C. J. Taylor, D. H. Cooper, and J. Graham, "Active shape models-their training and application," *Computer Vision and Image Understanding*, vol. 61, no. 1, pp. 38–59, 1995.

[6] T. F. Cooles, G. J. Edwards, and C. J. Taylor, "Active appearance models," *IEEE Transactions on Pattern Analysis and Machine Intelligence*, vol. 23, no. 6, pp. 681–685, 2001.

[7] M. S. Brown, M. F. McNitt-Gray, N. J. Mankovich et al., "Method for segmenting chest CT image data using an anatomical model: preliminary results," *IEEE Transactions on Medical Imaging*, vol. 16, no. 6, pp. 828–839, 1997.

[8] L. Zhang, E. A. Hoffman, and J. M. Reinhardt, "Atlas-driven lung lobe segmentation in volumetric X-ray CT images," *IEEE Transactions on Medical Imaging*, vol. 25, no. 1, pp. 1–16, 2006.

[9] A. A. Qazi, V. Pekar, J. Kim, J. Xie, S. L. Breen, and D. A. Jaffray, "Auto-segmentation of normal and target structures in head and neck CT images: a feature-driven model-based approach," *Medical Physics*, vol. 38, no. 11, pp. 6160–6170, 2011.

[10] D. L. Collins, C. J. Holmes, T. M. Peters, and A. C. Evans, "Automatic 3-D model-based neuroanatomical segmentation," *Human Brain Mapping*, vol. 3, no. 3, pp. 190–208, 1995.

[11] D. Shen and C. Davatzikos, "HAMMER: hierarchical attribute matching mechanism for elastic registration," *IEEE Transactions on Medical Imaging*, vol. 21, no. 11, pp. 1421–1439, 2002.

[12] H. Bay, T. Tuytelaars, and L. Van Gool, *Surf Speeded Up Robust Features*, Computer Vision-ECCV, Springer, 2006.

[13] F. L. Bookstein, "Principal warps: thin-plate splines and the decomposition of deformations," *IEEE Transactions on Pattern Analysis and Machine Intelligence*, vol. 11, no. 6, pp. 567–585, 1989.

[14] Y. Xie, M. Chao, P. Lee, and L. Xing, "Feature-based rectal contour propagation from planning CT to cone beam CT," *Medical Physics*, vol. 35, no. 10, pp. 4450–4459, 2008.

[15] D. G. Lowe, "Distinctive image features from scale-invariant keypoints," *International Journal of Computer Vision*, vol. 60, no. 2, pp. 91–110, 2004.

[16] Y. H. Yang and Y. Q. Xie, "Feature-based GDLOH deformable registration for CT lung image," *Applied Mechanics and Materials*, vol. 333, pp. 969–973, 2013.

[17] J. Duchon, *Splines Minimizing Rotation-Invariant Semi-Norms in Sobolev Spaces[M]//Constructive Theory of Functions of Several Variables*, Springer, Berlin, Germany, 1977.

[18] Y. Xie, M. Chao, and G. Xiong, "Deformable image registration of liver with consideration of lung sliding motion," *Medical Physics*, vol. 38, no. 10, pp. 5351–5361, 2011.

[19] L. Ibanez, W. Schroeder, L. Ng et al., The ITK software guide, 2003.

[20] G. Bradski and A. Kaehler, "Learning OpenCV: Computer vision with the OpenCV library," O'Reilly Media, Incorporated, 2008.

[21] VOLVIEW, http://www.kitware.com/opensource/volview.html.

[22] PARAVIEW, http://www.paraview.org/.

[23] T. V. Toolkit, http://www.vtk.org/.

[24] L. R. Dice, "Measures of the amount of ecologic association between species," *Ecology*, vol. 26, no. 3, pp. 297–302, 1945.

[25] K. Van Leemput, F. Maes, D. Vandermeulen et al., "Automated model-based tissue classification of MR images of the brain," *IEEE Transactions on Medical Imaging*, vol. 18, no. 10, pp. 897–908, 1999.

[26] D. P. Huttenlocher, G. A. Klanderman, and W. J. Rucklidge, "Comparing images using the Hausdorff distance," *IEEE Transactions on Pattern Analysis and Machine Intelligence*, vol. 15, no. 9, pp. 850–863, 1993.

[27] J. Lian, L. Xing, S. Hunjan et al., ". Mapping of the prostate in endorectal coil-based MRI/MRSI and CT: a deformable registration and validation study," *Medical Physics*, vol. 31, no. 11, pp. 3087–3094, 2004.

[28] A. Roy and P. Wells, "Volume definition in radiotherapy planning for lung cancer: how the radiologist can help," *Cancer Imaging*, vol. 6, no. 1, article 116, 2006.

[29] J. Mille, "Narrow band region-based active contours and surfaces for 2D and 3D segmentation," *Computer Vision and Image Understanding*, vol. 113, no. 9, pp. 946–965, 2009.

[30] W. Crum, T. Hartkens, and D. Hill, "Non-rigid image registration: theory and practice," *British Journal of Radiology*, vol. 77, supplement 2, pp. SS140–SS53, 2004.

Hindawi Publishing Corporation
BioMed Research International
Volume 2013, Article ID 461801, 8 pages
http://dx.doi.org/10.1155/2013/461801

Research Article

A Light-Field-Based Method to Adjust On-Axis Rounded Leaf End MLC Position to Predict Off-Axis MLC Penumbra Region Dosimetric Performance in a Radiation Therapy Planning System

Jia-Ming Wu,[1,2] Tsair-Fwu Lee,[3] Shyh-An Yeh,[1,4] Kuan-Yin Hsiao,[1,4] Hsin-Hsiung Chen,[2] Pei-Ju Chao,[3] and Yi-Ting Chen[3]

[1] *Department of Radiation Oncology, E-Da Hospital, Kaohsiung 824, Taiwan*
[2] *Department of Medical Imaging and Radiological Science, Central Taiwan University of Science and Technology, Taichung 411, Taiwan*
[3] *Medical Physics & Informatics Laboratory, Department of Electronics Engineering, National Kaohsiung University of Applied Sciences, 415 Chien Kung Road, Kaohsiung 807, Taiwan*
[4] *Department of Medical Imaging and Radiological Sciences, I-Shou University, Kaohsiung 824, Taiwan*

Correspondence should be addressed to Tsair-Fwu Lee; tflee@kuas.edu.tw and Shyh-An Yeh; ed100057@edah.org.tw

Received 28 June 2013; Accepted 27 August 2013

Academic Editor: Ching Chong Jack Yang

Purpose. An analytical and experimental study of split shape dose calculation correction by adjusting the position of the on-axis round leaf end position is presented. We use on-axis corrected results to predict off-axis penumbra region dosimetric performance in an intensity-modulated radiation therapy treatment planning system. *Materials and Methods*. The precise light-field edge position ($X_{\text{tang.}p}$) was derived from the on-axis 50% dose position created by using the nominal light field for geometric and mathematical manipulation. Leaf position ($X_{\text{mlc.}p}$) could be derived from $X_{\text{tang.}p}$ by defining in the treatment planning system for monitor unit calculation. On-axis offset (correction) could be obtained from the position corresponding to 50% of the central axis dose minus the $X_{\text{mlc.}p}$ position. The off-axis 50% dose position can then be derived from the on-axis 50% dose position. *Results*. The monitor unit calculation of the split shape using the on-axis rounded leaf end MLC penumbra region could provide an under-or overdose of 7.5% per millimeter without an offset correction. When using the on-axis rounded leaf end offset correction to predict the off-axis dose, the difference between the off- and on-axis 50% dose position is within ±1.5 mm. *Conclusions*. It is possible to achieve a dose calculation within 0.5% error for an adjusted MLC leaf edge location in the treatment planning system with careful measurement and an accurate on-axis offset correction. Dose calculations located at an off-axis spilt shape region should be used carefully due to noncorrectable errors which were found to be up to 10%.

1. Introduction

Multileaf collimator (MLC) systems are available on most commercial linear accelerators, for intensity-modulated radiation therapy (IMRT) treatment techniques, and many of these MLC systems utilize designs with rounded leaf ends to improve the dose profile of the geometric and transmission penumbra. The general designs of rounded leaf end MLC systems have already been described in detail by many researchers [1–8]. These MLC design considerations result in differences between the MLC 50% isodose points and the projected light-field edge locations. Before patients' treatment monitor units [9] are calculated by the treatment planning system, these differences have to be corrected. Radiation field size is defined as the lateral distance between the 50% isodose lines at a reference depth. This definition is practically achieved [10] by a procedure called beam alignment. The field-defining light is made to coincide with the 50%

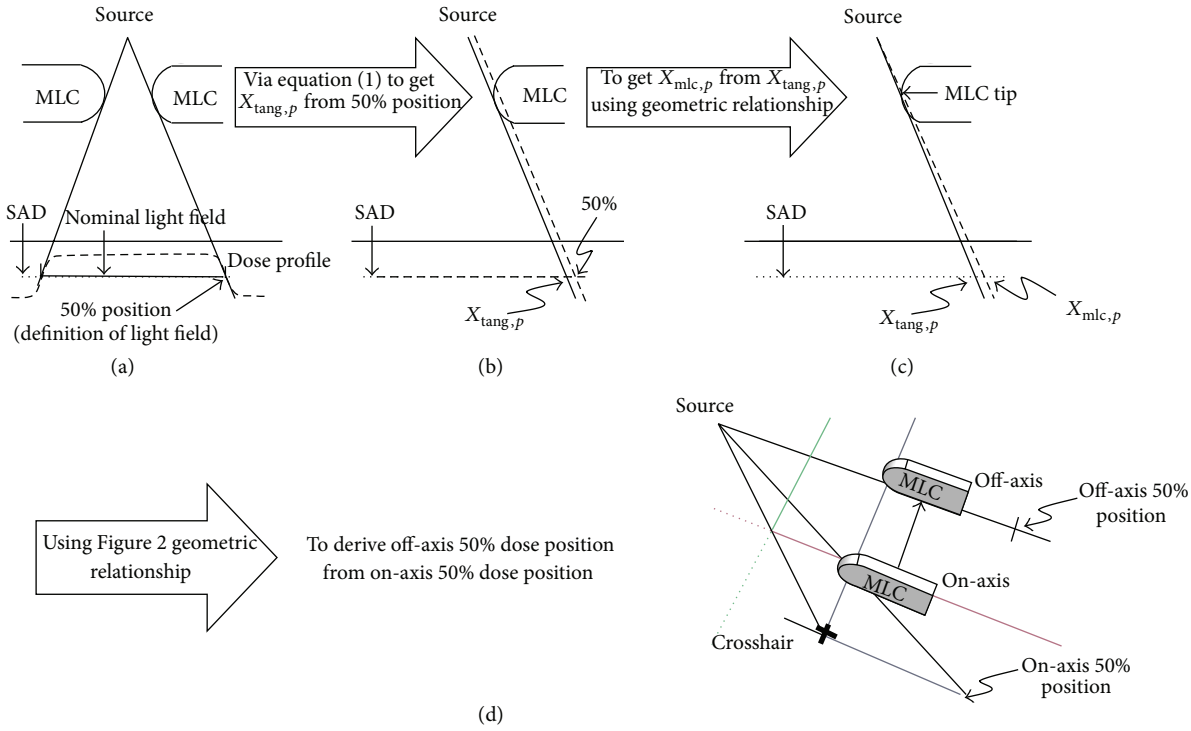

Figure 1: Summary of measurement procedures used in this study.

isodose lines of the radiation beam projected on a plane perpendicular to the beam axis and at a standard source-to-surface distance (SSD 100 cm) or source-to-axis distance (SAD 100 cm). The position of a projected split light-field edge and its relative radiation field edge of a rounded leaf end MLC needs to be measured and implemented in the computerized treatment planning system [11]. Coincidence between the 50% dose position and the split field is limited due to the nondivergent geometry found with curved leaf MLC collimator systems [12]; the 50% dose position has to be verified during MLC system acceptance.

In order to avoid under-or overdose in patients' treatment, the treatment planning system should be calibrated precisely to 50% dose position correction when the treatment monitor units are calculated in a split MLC situation.

However, radiation dose profile measurement of leaf position is usually performed in the commissioning of the MLC system on the crosshair axis. This work will illustrate some of the specific issues that should be carefully considered if dose calculation of a split shape associated with a rounded leaf end MLC system with an off-axis setup is used [13].

2. Materials and Methods

This study was performed on an Elekta Precise linear accelerator (Elekta, Stockholm, Sweden) with dual photon energies of 6 MV and 10 MV. The photon dose calculations were evaluated by using the Pinnacle v8.6 treatment planning system (Philips Healthcare, Andover, MA). Dose profiles of MLC fields were measured and the calculation results of the treatment planning system were compared for on-axis rounded leaf end MLC. The procedures of this study are given in Figure 1.

All on-axis penumbra profiles were measured with a visual light-field (nominal light-field) at an SAD of 100 cm to determine the position receiving 50% central axis dose. The projection of the nominal light-field at SAD 100 cm was adopted for dose profile measurements, but the dose profile from the nominal light-field edge could not quantitatively determine the geometry of the tangential edge ($X_{tang,p}$) for the derivation of $X_{mlc,p}$ (planning system defined by leaf position); therefore, the precise light-field edge ($X_{tang,p}$) was derived from the point corresponding to 50% of the central axis dose by geometrical and mathematical methods using (1) in this study. Leaf position ($X_{mlc,p}$, the intersection of a line from the source to the leaf tip with SAD 100 cm plane surface in Figure 2) could then be derived from $X_{tang,p}$. Once $X_{mlc,p}$ was decided, the on-axis correction "offset" could be obtained by subtraction of the point corresponding to 50% of the central axis dose from the position of $X_{mlc,p}$. The off-axis 50% dose position was then derived from the on-axis 50% dose position via the relative geometric relationship, and the off-axis offset can be predicted for comparison with the on-axis offset.

2.1. Geometry Specifications. All of the parameters described below are according to our previous study [14], a light-field-based method to adjust rounded leaf end MLC position for split shape dose calculation correction in a radiation therapy treatment planning system.

(1) Nominal light-field.

(2) $X_{\text{tang},p}$: light-field tangential edge position as a decimal value.

(3) $X_{\text{mlc},p}$: treatment planning leaf position.

(4) The 50% dose position.

(5) Direction of the MLC.

(6) Transmission penumbra.

The linear accelerators used in this study were equipped with MLCs for IMRT dose delivery devices. Many investigators have described the design and characteristics of MLCs [11, 12]. The analytical approach for optimizing the leaf design of an on-axis MLC assesses the relationship between the light-field size edge position [$X_{\text{tang},p}$, lp in (1)] and the 50% dose position [X_i or X_j, Pt_{50}(lp) in (1)].

The analytical formula of the transmission penumbra depending on leaf position will be presented in this section. In Figure 3, a schematic view of a leaf from the right bank placed at the right edge of a field is shown. If the leaf position (lp) in the field space is known, a ray line along which irradiation will drop to 50% of the initial irradiation can be defined.

By substitution of all variables in the previous study into $\text{Pt}_{50}(\text{lp}) = F \cdot \tan(\gamma_{50})$, the position of the point $\text{Pt}_{50}(\text{lp})$ is given in [14]

$$\text{Pt}_{50}(\text{lp}) = F \cdot \tan\left(\left(\arctan\left(\frac{c \cdot (\text{lp}/f) + R \cdot \cos\left(\arctan\left(\text{lp}/F\right)\right) + \left(\text{lp}/F\right) \cdot R \cdot \sin\left(\arctan\left(\text{lp}/F\right)\right)}{c}\right)\right) - \left(\arcsin\left(\frac{\sqrt{R^2 - \left(\ln\left(0.5\right)/2 \cdot \mu\right)^2}}{\sqrt{c^2 + \left(c \cdot \left(\text{lp}/F\right) + R \cdot \cos\left(\arctan\left(\text{lp}/F\right)\right) + \left(\text{lp}/F\right) \cdot R \cdot \sin\left(\arctan\left(\text{lp}/F\right)\right)\right)^2}}\right)\right)\right) \quad (1)$$

(7) Relationship of geometry and radiation position.

2.2. Measurement Devices. Radiation field size data was measured using water phantom scans and Gafchromic films (International Specialty Products, Wayne, NJ). A computer controlled water phantom scanning system (PTW MP3 Water Phantom Systems, PTW-Freiburg, Germany) was used for measurements with each field size. Photon diode detectors (PTW, Freiburg, Germany, p-type 60012, 1 mm active area) were used to measure the profile in air at SAD 100 cm. Measurements were also made with ion chamber (0.015 cm^3, Type 31016 ion chambers, PTW; Freiburg, Germany, measurement point: 1.3 mm behind the chamber tip; active cylinder length: 3.6 mm; diameter: 2.9 mm) at the isocentric plane with water depths of 10 cm. The comparison of 50% dose position measured by diode in air and by chamber at water depth of 10 cm was made for the utilization of (1) in this study. All profiles were normalized on the central axis and were normalized at the centre of the irradiated area. The field sizes were defined at the 50% intensity points relative to the central value of the profile. With the same field sizes, random measurements of water phantom scans and Gafchromic film techniques were performed for the comparison of multileaf collimated field size profiles. These field sizes measured with the film agreed with the corresponding field sizes measured with water tank scans to be within 0.2 mm. After verifying that the film method achieved the same results as the water tank method, film proved to be more efficient, so we chose to use the Gafchromic film method for this study of measurements of 50% of the central axis dose.

2.3. Film Measurement

2.3.1. Film Setup. Gafchromic film was exposed to individual rectangular fields defined by the MLC. The field sizes adopted in this experiment were generated by the nominal field size and were positioned at leaf positions from +20 cm with 1 cm increments to −12 cm (cross-over central axis −12 cm). The field size was defined at the 50% intensity points relative to the central value of the profile.

2.3.2. Film Measurement and Process. The 50% dose positions were measured by Gafchromic EBT 2 film (ISP Technology, Inc., Wayne, NJ; Log F04090901; expiry date: April 2011). A double exposure technique [9–11, 15–17] was adopted for these measurements. This was performed by giving each film an initial dose of 2 Gy and measuring the optical density before experimental irradiation was applied. A variation of 2% was observed in the optical density (OD) of the films used in the experiment due to nonuniformity in the dose response [18–22].

Calibration was carried out to convert the raw scanner signal into radiation dose. This was achieved by placing 5 cm solid water phantom slabs on top of the 3.0 cm by 3.0 cm film pieces with a field size of 10 cm by 10 cm and a source-to-axis distance (SAD) of 100 cm and irradiating them with a step size of 10 cGy in the dose range from 10 cGy to 150 cGy under an Elekta Precise medical linear accelerator machine. In this study, we used an Epson Expression 10000XL flat-bed document scanner (US Epson, Long Beach, CA). Film pieces were scanned using VariSoft software (PTW, Freiburg, Germany), with the maximum OD range and all filters and image enhancement options

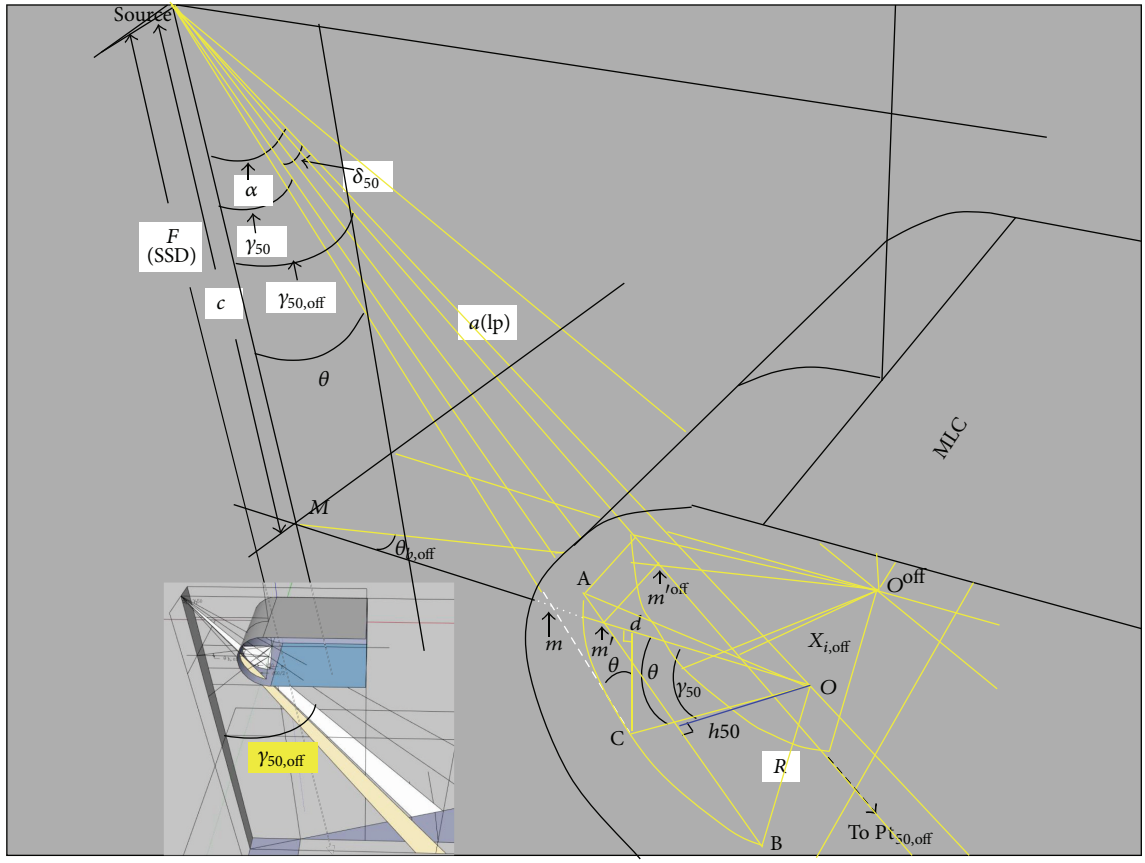

FIGURE 2: The geometric relationship for deriving the off-axis rounded leaf end MLC 50% dose position from the on-axis one.

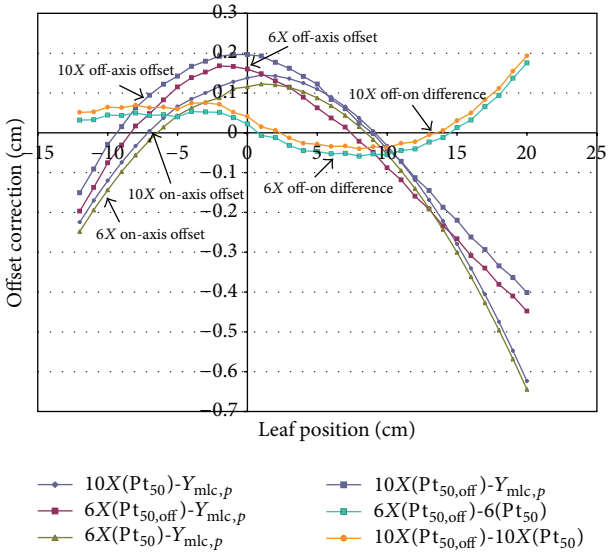

FIGURE 3: The comparison of offset correction of on- and off-axis rounded leaf end MLC.

turned off. Once the scanner is turned on, it is important to perform a preview operation in transmission mode and then to allow the scanner to warm up for half an hour. This operation turns on the upper lamp used for transmission mode and allows its temperature to stabilize. The films were scanned in the 48-bit RGB mode, with 16 bits per color, and saved as tagged image file format (TIFF) image files.

Multiple scans are performed in order to remove the scanner noise by subsequent averaging of the scanned images. The first step in the protocol is to scan the unexposed pieces of film five times. Once the five images of the unexposed film pieces have been acquired, blank scans are taken, again five times, over the same scanning region as the previously acquired images with the film pieces.

In general, scanned images of irradiated films will have a scanning region that is different from that of the unirradiated film pieces. Therefore, to remove the defective pixels in irradiated film images, five blank scans of the irradiated film scanning region are done. Then the processing of the images entails the identification of defective pixels. Since two glass plates are in the optical pathway, in addition to the examined films, the system can exhibit many imperfections. This identification was performed on the resulting images obtained by averaging five successive scans of the empty bed for both unirradiated and irradiated film images. We found that the percentage of faulty pixels was smaller than 0.4%.

The net OD of a point on the film is given by $\text{OD} = \log_{10}(S_0/S)$, where S_0 is the background (i.e., the scanner

signal for an unexposed film) and S is the scanner signal for the film at the point of interest.

2.4. Derivation of On-Axis Rounded Leaf End MLC Offset Correction. All of the parameters described below are according to our previous study [14].

(1) Attenuation coefficient: μ.

(2) Derivation of the on-axis $X_{\text{tang},p}$ from the on-axis 50% dose position.

(3) Derivation of on-axis $X_{\text{mlc},p}$ from on-axis $X_{\text{tang},p}$.

(4) The geometric derivation of $X_{\text{mlc},p}$.

According to our previous study [14], $\angle\theta$ was determined from $X_{\text{tang},p}$ as follows:

$$\angle c + \angle d = 90^{\circ},$$
$$\angle b + \angle c = 90^{\circ},$$
$$\angle b = \angle d,$$
$$\angle d = \angle\theta,$$
$$\angle a = \angle b,$$
$$\angle a = \angle\theta,$$
$$\overline{AB} = 15\,\text{cm} \times \sin\theta$$
$$(\overline{CB} = 15\,\text{cm}),$$
$$\overline{AD} = 15\,\text{cm} - 15\,\text{cm} \times \cos\theta,$$
$$\overline{DG} = \overline{BF} - \overline{AD},$$
$$\theta' = \tan^{-1}(\overline{DG}/33.5),$$
$$X_{\text{mlc}.p} = \text{SSD(cm)} \times \tan(\theta'),$$

$\overline{DE}$= penetration thickness in MLC.

(5) Offset definition.

(6) The derivation of the off-axis 50% dose position from the on-axis 50% dose position.

To derive the off-axis 50% dose position from the on-axis 50% dose position, the previous variables for finding position $\text{Pt}_{50}(\text{lp})$are used again to derive the off-axis 50% dose position ($\text{Pt}_{50,\text{off}}(\text{lp})$) in Figure 3.

3. Results

3.1. Film Results. According to our previous study [14], one of the film results of the split field is shown. Marker 1 on the film was 30 mm away from the crosshair isocentre and the MLC edge travelled to abut the crosshair central axis ray line for irradiation. After converting the OD to a dose distribution on the film, the position receiving 50% of the central axis dose was 31.38 mm away from marker 1 instead of 30 mm. The 1.38 mm discrepancy was due to the photon transmission and scatter effect.

3.2. On-Axis Offset Correction at an SAD of 100 cm. After the 50% dose position was measured from the size of the visual light-field (nominal light-field), the associated quantity of $X_{\text{tang},p}$ could be obtained by using (1). $X_{\text{mlc},p}$ could be derived from Figure 2 by implementing $X_{\text{tang},p}$, and the final offset corrections were calculated.

3.3. Off-Axis Offset Correction and the Difference between On- and Off-Axis Rounded Leaf End 50% Dose Positions. Figure 3 shows the rounded leaf end MLC uncorrectable off-axis offset correction of 10 MV and 6 MV photon beams. This figure shows three sets of curves of these two photon energies; on-axis offset correction, off-axis offset correction, and the difference of 50% dose positions between off- and on-axis rounded leaf end MLC at an SAD of 100 cm.

4. Discussion

In order to simplify the model for the transmission penumbra, the source was here approximated by a point. The coincidences of the 50% dose position measured by diode in air and the chamber with water depth 10 cm in water phantom support the utilization of transmission penumbra model in (1) in this study. The precise leaf edge position of the tangential split field ($X_{\text{tang},p}$) could be derived using the measured on-axis 50% dose position from the mathematical model and can be used to obtain the planning system defined by leaf position ($X_{\text{mlc},p}$). The on-axis offset (the 50% dose position minus the planned leaf position) could be determined for the purpose of accurate monitor unit calculation. If the MLC rounded leaf travels close to the central axis, the 50% dose position gains attenuation and will be projected outside $X_{\text{mlc},p}$ on X_j. As the MLC rounded leaf travels away from the central axis, the 50% dose position will be projected inside $X_{\text{mlc},p}$ and gain less attenuation, as shown by X_i. This offset adjustment can be of importance in clinical situations of split fields to determine overdosage or underdosage at treatment of SAD.

$X_{\text{mlc},p}$ was calculated by a mathematic analytical model at (1). According to our previous study [14], it shows one of the films in the experimental setup along with the profile result of the split light-field edge and the position receiving 50% of the central axis dose at an SAD of 100 cm with a 10 MV photon beam. Marker 1 was delineated by the jaw edge 30 mm from the crosshair isocenter, and marker 2 (used for double-checking the position setting accuracy) was 15 mm away from the centre of marker 1. Fifty percent of the central axis dose can be found via the profile through an OD-to-dose conversion; this moves away from the central axis toward the MLC shadow due to side scattering of photons and electron contributions.

This result of film measurement showed the positions of the 80% dose and the 20% dose at 26 mm and 34 mm, respectively. The width of the split field penumbra from the 80% dose to the 20% dose was approximately 8 mm and changed with the rate of dose gradient by 7.5% per mm at an SAD of 100 cm with a 10 MV photon beam. Monitor unit calculation in the treatment planning system is decided entirely by the selected point on the split field penumbra curve. When the point is selected on the descending or ascending portion between the 50% dose and the 20% dose, or between the 80% dose and the 50% dose, the results for monitor units will be over- or undercalculated.

The 50% dose position was larger at 10 MV than at 6 MV because photons have greater penetration at 10 MV. When patients treatment monitor units are calculated in a

Table 1: This table demonstrates the derivation procedures of off-axis 50% dose position from on-axis 50% dose position of 10 MV and 6 MV photon beams at an SAD of 100 cm.

1	2	3	4	5	6	7	8	9	10	11
Nominal field size	γ_{50} of nominal field	Mm' of on-axis	MO of on-axis	MO^{off}	Mm'^{off}	$\gamma_{50,\text{off}}$	$\text{Pt}_{50,\text{off}}$	$\Theta_{b,\text{off}}$	$10X$, $\text{Pt}_{50\%,\text{off}} \cdot \cos(\theta_{b,\text{off}})$	$6X$, $\text{Pt}_{50\%,\text{off}} \cdot \cos(\theta_{b,\text{off}})$
−12	−0.119	−4.018	10.081	10.625	−4.235	−0.126	−12.623	0.321	−11.977	−11.797
−11	−0.109	−3.683	10.398	10.926	−3.870	−0.115	−11.535	0.312	−10.977	−10.807
−10	−0.099	−3.347	10.719	11.232	−3.508	−0.104	−10.455	0.303	−9.977	−9.808
−9	−0.090	−3.012	11.038	11.537	−3.148	−0.094	−9.383	0.295	−8.978	−8.818
−6	−0.060	−2.006	12.010	12.470	−2.082	−0.062	−6.207	0.272	−5.978	−5.830
−5	−0.050	−1.670	12.336	12.784	−1.731	−0.052	−5.159	0.266	−4.978	−4.836
−4	−0.040	−1.335	12.669	13.106	−1.381	−0.041	−4.115	0.259	−3.978	−3.826
−3	−0.030	−0.999	12.999	13.425	−1.032	−0.031	−3.076	0.253	−2.978	−2.830
−2	−0.020	−0.664	13.332	13.748	−0.684	−0.020	−2.040	0.247	−1.978	−1.826
−1	−0.010	−0.328	13.663	14.069	−0.338	−0.010	−1.007	0.241	−0.978	−0.835
0	0.000	0.007	13.995	14.391	0.007	0.000	0.022	0.235	0.022	0.156
1	0.010	0.343	14.325	14.712	0.352	0.010	1.049	0.230	1.021	1.137
2	0.020	0.678	14.662	15.041	0.696	0.021	2.074	0.225	2.021	2.135
3	0.030	1.014	14.996	15.367	1.039	0.031	3.096	0.220	3.021	3.120
4	0.040	1.349	15.333	15.696	1.381	0.041	4.116	0.215	4.021	4.109
5	0.050	1.685	15.674	16.030	1.723	0.051	5.135	0.211	5.021	5.109
6	0.060	2.020	16.016	16.364	2.064	0.061	6.152	0.206	6.021	6.103
7	0.070	2.356	16.360	16.701	2.405	0.072	7.167	0.202	7.021	7.103
8	0.080	2.691	16.703	17.036	2.745	0.082	8.181	0.198	8.021	8.092
9	0.090	3.026	17.050	17.377	3.085	0.092	9.194	0.194	9.021	9.091
10	0.100	3.362	17.395	17.716	3.424	0.102	10.205	0.191	10.021	10.081
11	0.110	3.697	17.745	18.060	3.763	0.112	11.216	0.187	11.021	11.080
12	0.120	4.033	18.093	18.401	4.102	0.122	12.226	0.183	12.021	12.070
13	0.129	4.368	18.446	18.748	4.440	0.132	13.234	0.180	13.021	13.069
14	0.139	4.704	18.796	19.093	4.778	0.141	14.242	0.177	14.021	14.059
15	0.149	5.039	19.152	19.443	5.116	0.151	15.249	0.173	15.021	15.058
16	0.159	5.375	19.505	19.791	5.454	0.161	16.256	0.170	16.020	16.048
17	0.169	5.710	19.863	20.144	5.791	0.171	17.262	0.167	17.020	17.047
18	0.178	6.046	20.219	20.495	6.129	0.181	18.267	0.164	18.020	18.037
19	0.188	6.381	20.579	20.851	6.466	0.190	19.271	0.162	19.020	19.036
20	0.198	6.717	20.938	21.205	6.802	0.200	20.276	0.159	20.020	20.025

split field situation, the on-axis offset (50% dose position minus $X_{\text{mlc},p}$) correction should be calibrated precisely to avoid underdosage or overdosage of patients. The calculated monitor units for treatment will be less than the desired dose and lead to under-dosage due to overcorrection because the point receiving 50% of the central axis dose used for monitor unit calculation passes through the ascending portion from 50% to 80%. The 50% point used for monitor unit calculation passes through the descending portion from 50% to 20%, so the underestimated output selected in this region will lead to overcalculated monitor units and will result in over-dosage. The 50% dose position was located outside $X_{\text{mlc},p}$ (away from the source), since more attenuation leads to the positive offset correction in the range from +8 cm to −8 cm, whereas the negative offset correction is in the range from −12 cm to −8 cm and from +20 cm to +8 cm because the 50% dose position is located inside $X_{\text{mlc},p}$ (close to the source).

We expand the rounded leaf end right and left sides to simulate the off-axis MLC interaction with photon beams when leaf is at off-axis setting. Figure 3 shows the results of off-axis offset when leaf is at the leaf tip level of 6.3745 cm off-axis location ($X_{i,\text{off}}$ = 6.374 cm). The $X_{i,\text{off}}$ with a ±6.3745 cm off-axis distance at the leaf tip level (c distance level) has the extreme light-field size projection of ±20 cm at SAD 100 cm

plane (since leaf width is 1 cm at SAD 100 cm, c is 33.55 cm). This study not only shows that the 50% dose position created by the projection of MLC split edge shifts away from the central axis towards MLC shadow, but also demonstrates the same photon scatter phenomenon at off-axis distal MLC positions. The off-axis offset of the 50% dose position is located much further outside than the on-axis position when the leaf position is larger than 15 cm. This deficient tangential attenuation (off-axis 50% dose position minus on-axis 50% dose position) leads to a trend of positive curves in the upper right part of Figure 3.

Table 1 shows how to derive the off-axis 50% dose position from the on-axis 50% dose position of rounded leaf end MLC of 10 MV and 6 MV photon beams at an SAD of 100 cm.

The 50% dose position of off-axis 50% rounded leaf end MLC could be derived from the ratio of Mm'^{off} (column 6 in Table 1) and MO^{off} (column 5 in Table 1) to that of Mm' (column 3 in Table 1) and MO (column 4 in Table 1). The angle $\gamma_{50,\text{off}}$ is then $\tan^{-1}(Mm'^{\text{off}}/\text{c})$ (column 7 in Table 1), and therefore $\text{Pt}_{50,\text{off}}$ (column 8 in Table 1) is calculated by $F \cdot \tan(\gamma_{50,\text{off}})$. The identification field size (visualized field size of $\text{Pt}_{50,\text{off}}$ projection on MLC moving direction) of off-axis rounded leaf end MLC is calculated by $\text{Pt}_{50,\text{off}} \cdot \cos(\theta_{b,\text{off}})$ (column 10 and 11 in Table 1).

We set lp to be intentional from −12 cm to −11.85 cm to simulate leaf position to be in 1.5 mm error intentionally, as a result for 6 MV and 10 MV offset correction with value from −0.31337 cm to −0.26369 cm, and from −0.32337 cm to −0.27369 cm, respectively. The offset correction differences of 6 MV and 10 MV are around 0.5 cm (0.31337 cm−0.26369 cm or 0.32337 cm−0.27369 cm). The rate of dose gradient is around 7.5% per mm at an SAD of 100 cm with 10 MV and 6 MV photon beams; therefor we adopt an action level for leaf position adjustment while leaf position error is larger than 1.5 mm, because this error leads to a dose calculation error around 3.5% (7.5% divided by 2).

5. Conclusions

It is critical for high-quality radiation therapy that planned and delivered dose measurements should be at an appropriate level. In this study, we illustrate that the accumulated and planned radiation doses may not always be in agreement for MLC treatment fields at an SAD unless the offset is carefully adjusted.

With careful measurement and an accurate on-axis offset correction, it is possible to achieve dose calculation within 1.0% error for the adjusted MLC leaf edge location on-axis in the treatment planning system.

Calibration could be performed at a certain on-axis SAD to fit all off-axis offset corrections. We should keep in mind that patient treatment monitor unit calculations at extremely off-axis settings could result in significant uncorrectable underdosage or overdosage in treatment planning dose calculation.

Conflict of Interests

There is no actual or potential conflict of interests in this study.

Authors' Contributions

Jia-Ming Wu wrote the paper. Tsair-Fwu Lee and Shyh-An Yeh coordinated the study. Jia-Ming Wu, Tsair-Fwu Lee, and Shyh-An Yeh provided original idea and concept and made final revision of the paper. Jia-Ming Wu, Shyh-An Yeh, and Tsair-Fwu Lee designed and developed the study. Jia-Ming Wu, Hsin-Hsiung Chen, and Pei-Ju Chao collected data. Jia-Ming Wu, Pei-Ju Chao, Yi-Ting Chen, and Hsin-Hsiung Chen provided statistical analysis. All authors read and approved the final paper.

Acknowledgments

This study was supported financially, in part, by Grant from the National Science Council (NSC), Taiwan, (NSC-101-2221-E-151-007-MY3). This paper has not been published nor concurrently submitted for publication elsewhere.

References

[1] R. B. Hawkins, "A simple method of radiation treatment of craniospinal fields with patient supine," *International Journal of Radiation Oncology Biology Physics*, vol. 49, no. 1, pp. 261–264, 2001.

[2] W. A. Parker and C. R. Freeman, "A simple technique for craniospinal radiotherapy in the supine position," *Radiotherapy and Oncology*, vol. 78, no. 2, pp. 217–222, 2006.

[3] M. Tatcher and A. S. Glicksman, "Field matching considerations in craniospinal irradiation," *International Journal of Radiation Oncology Biology Physics*, vol. 17, no. 4, pp. 865–869, 1989.

[4] J. van Dyk, R. D. T. Jenkin, P. M. K. Leung, and J. R. Cunningham, "Medulloblastoma: treatment technique and radiation dosimetry," *International Journal of Radiation Oncology Biology Physics*, vol. 2, no. 9-10, pp. 993–1005, 1977.

[5] J. M. Galvin, A. R. Smith, R. D. Moeller et al., "Evaluation of multileaf collimator design for a photon beam," *International Journal of Radiation Oncology Biology Physics*, vol. 23, no. 4, pp. 789–801, 1992.

[6] J. M. Galvin, A. R. Smith, and B. Lally, "Characterization of a multileaf collimator system," *International Journal of Radiation Oncology Biology Physics*, vol. 25, no. 2, pp. 181–192, 1993.

[7] T. J. Jordan and P. C. Williams, "The design and performance characteristics of a multileaf collimator," *Physics in Medicine and Biology*, vol. 39, no. 2, pp. 231–251, 1994.

[8] Y. Chen, A. L. Boyer, and C.-M. Ma, "Calculation of X-ray transmission through a multileaf collimator," *Medical Physics*, vol. 27, no. 8, pp. 1717–1726, 2000.

[9] M. R. Arnfield, K. Otto, V. R. Aroumougame, and R. D. Alkins, "The use of film dosimetry of the penumbra region to improve the accuracy of intensity modulated radiotherapy," *Medical Physics*, vol. 32, no. 1, pp. 12–18, 2005.

[10] S. G. Ju, Y. C. Ahn, S. J. Huh, and I. J. Yeo, "Film dosimetry for intensity modulated radiation therapy: dosimetric evaluation," *Medical Physics*, vol. 29, no. 3, pp. 351–355, 2002.

[11] T. Cheung, M. J. Butson, and P. K. N. Yu, "Experimental energy response verification of XR type T radiochromic film," *Physics in Medicine and Biology*, vol. 49, no. 21, pp. N371–N376, 2004.

[12] J. Sun and Y. Zhu, "Study of dosimetric penumbra due to multileaf collimation on a medical linear accelerator," *International*

Journal of Radiation Oncology Biology Physics, vol. 32, no. 5, pp. 1409–1417, 1995.

[13] Q. Wu, M. Arnfield, S. Tong, Y. Wu, and R. Mohan, "Dynamic splitting of large intensity-modulated fields," *Physics in Medicine and Biology*, vol. 45, no. 7, pp. 1731–1740, 2000.

[14] J. M. Wu, T. F. Lee, C. M. Kuo, C. J. Chen, and S. A. Yeh, "A light field-based method to adjust rounded leaf end MLC position for split shape dose calculation correction in a radiation therapy treatment planning system," *Journal of Applied Clinical Medical Physics*, vol. 13, 2012.

[15] M. J. Butson, T. Cheung, P. K. N. Yu, and H. Alnawaf, "Dose and absorption spectra response of EBT2 Gafchromic film to high energy X-rays," *Australasian Physical & Engineering Sciences in Medicine*, vol. 32, no. 4, pp. 196–202, 2009.

[16] M. J. Butson, P. K. N. Yu, T. Cheung, and H. Alnawaf, "Energy response of the new EBT2 Radiochromic film to X-ray radiation," *Radiation Measurements*, vol. 45, no. 7, pp. 836–839, 2010.

[17] T. Cheung, M. J. Butson, and P. K. N. Yu, "Post-irradiation colouration of Gafchromic EBT radiochromic film," *Physics in Medicine and Biology*, vol. 50, no. 20, pp. N281–N285, 2005.

[18] X. R. Zhu, P. A. Jursinic, D. F. Grimm, F. Lopez, J. J. Rownd, and M. T. Gillin, "Evaluation of kodak EDR2 film for dose verification of intensity modulated radiation therapy delivered by a static multileaf collimator," *Medical Physics*, vol. 29, no. 8, pp. 1687–1692, 2002.

[19] W. L. McLaughlin, C. Yun-Dong, C. G. Soares, A. Miller, G. van Dyk, and D. F. Lewis, "Sensitometry of the response of a new radiochromic film dosimeter to gamma radiation and electron beams," *Nuclear Instruments and Methods in Physics Research A*, vol. 302, no. 1, pp. 165–176, 1991.

[20] W. L. McLaughlin, J. C. Humphreys, D. Hocken, and W. J. Chappas, "Radiochromic dosimetry for validation and commissioning of industrial radiation processes," *International Journal of Radiation Applications and Instrumentation C*, vol. 31, no. 4–6, pp. 505–514, 1988.

[21] B. Lynch, M. Ranade, J. Li, and J. Dempsey, "Characteristics of a new very high sensitivity radiochromic film," *Medical Physics*, vol. 31, pp. 1837–1842, 2004.

[22] L. Xu, M. McEwen, C. Cojocaru, and B. Faddegon, "Measurement of lateral dose distributions using GafChromic EBT films and PTW Starcheck 2-D array," *Medical Physics*, vol. 36, pp. 2624–2631, 2009.

Hindawi Publishing Corporation
BioMed Research International
Volume 2013, Article ID 532936, 9 pages
http://dx.doi.org/10.1155/2013/532936

Research Article

Interactive Multigrid Refinement for Deformable Image Registration

Wu Zhou and Yaoqin Xie

Shenzhen Key Laboratory for Low-Cost Healthcare, Shenzhen Institutes of Advanced Technology, Chinese Academy of Sciences, Shenzhen 518055, China

Correspondence should be addressed to Yaoqin Xie; yq.xie@siat.ac.cn

Received 17 June 2013; Accepted 5 September 2013

Academic Editor: Chung-Chi Lee

Deformable image registration is the spatial mapping of corresponding locations between images and can be used for important applications in radiotherapy. Although numerous methods have attempted to register deformable medical images automatically, such as salient-feature-based registration (SFBR), free-form deformation (FFD), and demons, no automatic method for registration is perfect, and no generic automatic algorithm has shown to work properly for clinical applications due to the fact that the deformation field is often complex and cannot be estimated well by current automatic deformable registration methods. This paper focuses on how to revise registration results interactively for deformable image registration. We can manually revise the transformed image locally in a hierarchical multigrid manner to make the transformed image register well with the reference image. The proposed method is based on multilevel B-spline to interactively revise the deformable transformation in the overlapping region between the reference image and the transformed image. The resulting deformation controls the shape of the transformed image and produces a nice registration or improves the registration results of other registration methods. Experimental results in clinical medical images for adaptive radiotherapy demonstrated the effectiveness of the proposed method.

1. Introduction

Radiotherapy is an image-guided treatment, and imaging is involved in every key step of the process. The evolution of radiation therapy has been strongly correlated with the development of imaging techniques [1]. The term of image-guided radiation therapy (IGRT) is employed loosely to refer to newly emerging techniques of radiation planning, patient setup, and delivery procedures that integrate cutting-edge image-based tumor definition methods, patient positioning devices, and/or radiation delivery guiding tools. These techniques combine new imaging tools, which interface with the radiation delivery system through hardware or software, and state-of-the-art 3D conformal radiation therapy (CRT) or intensity modulated radiation therapy (IMRT) and allow physicians to optimize the accuracy and precision of the radiotherapy by adjusting the radiation beam based on the true position of the target tumor and critical organs [2]. This increased accuracy justifies a smaller clinical target volume to planning target volume (CTV-PTV) margin, thus decreasing the consequent collateral damage to the normal tissues. While IGRT is certainly a step forward for radiation oncology, the efficacy of these image-guided treatments depends on a treatment plan optimized using these images.

One of the key questions in image guidance is how the information is used to modify treatment. If the target and organs at risk (OARs) can be delineated on online volumetric images, it is possible to generate an adaptive treatment plan. Replanning theoretically provides the highest precision and does not need specialized hardware such as the robotic couch. However, online replanning requires superior online image quality, as well as fast and robust algorithms, to perform automatic region-of-interest (ROI) delineation, dose calculation, and beamlet weight optimization. Various methods are used clinically to increase the speed of ROI delineation, including atlas-based segmentation, ROI propagation, and deformable image registration [3]. Deformable image registration is a fundamental task in medical image processing due to its potential clinical impact [4]. For instance, the advantage of deformable image registration in adaptive radiotherapy

is that the deformation field can be used for nonrigid dose accumulation [5].

The process of deformable image registration consists of establishing functional and/or spatial anatomical correspondences between different images. The term deformation is often used to denote the fact that the observed images are associated through a nonlinear dense transformation or spatially varying deformation model [6]. Deformable image registration has been studied in great detail, and numerous methods have attempted to register deformable medical images automatically, such as salient-feature-based registration (SFBR) [7, 8], free-form deformation (FFD) [9], and Demons [10, 11]. SFBR is a point-based registration approach which uses salient features that are prominent and distinctive features in the image. The features are extracted in two images using an interest point detector and are then matched for correspondence. The correspondent features are then used to interpolate a nonrigid transformation using the thin-plate-spline method [12]. In order to recover the local geometric differences well between anatomic structures by SFBR, it is also assumed that there are enough correspondent landmarks in local geometric differences areas. Typically, a large number of reliable corresponding anchor points are required for accurate registration [13]. However, it is not often fulfilled in clinical applications; for instance, in homogenous regions, the feature-based method may fail when few or no salient features locate in these corresponding regions. The Demons algorithm uses image intensity values and assumes that pixels presenting the same anatomical points on each image have the same intensity values, and thus it is appropriate for monomodality image registration. When the local geometric deformation is large or images are in multimodality, the Demons algorithm becomes difficult to handle. FFDs are one of the most common types of transformation models in medical images. The advantage of the transformation model lies in its simplicity, smoothness, and ability to describe local deformations with few degrees of freedom. However, misregistration in the difference image after such deformable registration is still viable. The main reason for this is the limited flexibility of deformation registration methods to describe complex local deformations. In addition, most of the existing methods based on energy minimization or optimization may fail in clinical settings due to the suboptimal solutions and excessive running time. Some recently proposed methods [14, 15] attempted to solve the problem of deformable registration via hierarchical subdivision. However, these methods can only be applied for monomodality registration, and local deformations are linear and small. To the best of our knowledge, no automatic method for registration is perfect, and no generic automatic algorithm has shown to work properly for clinical applications due to the fact that the deformation field is often complex and cannot be estimated well by current automatic deformable registration methods.

The aim of this study is to refine the deformable image registration by manual revision for clinical applications. The B-spline is a powerful tool for modeling 2D or 3D deformable objects. The proposed method is based on multilevel B-spline to interactively revise the misregistration regions by manipulating an underlying mesh of control points in the overlapping region between the reference image and the transformed image in RGB color model. This paper is organized as follows. Section 2 describes material and proposed registration refinement technique. In Section 3, we show the experimental results on clinical images. Section 4 concludes this paper.

2. Materials and Methods

2.1. The Framework of Interactive Multigrid Refinement Algorithm. We explored digital B-splines to devise an interactive multigrid refinement that consists of automatic process and manual process to improve the accuracy of deformable registration. As shown in Figure 1, the proposed framework of multigrid refinement algorithm consists of two steps. The first is the automatic process in which conventional automatic deformation registration methods or rigid and linear transformation model can be used to coarsely register deformable images. The second is the manual process in which multilevel B-splines are used in the overlapping region of the transformed image and the reference image in RGB model for manual revision. The misregistered areas are represented by colors and the registered areas by gray level to show alignment of the two images. If the automatic registration methods can register deformable images well, there is no need to use the second manual process. In clinical applications, however, the automatic methods often do not register well. The second step will attempt to eliminate the errors visually by manual revision in the misregistered areas. In order to describe the deformation field, we chose the B-splines to model 2D and 3D deformations. Due to the fact that misregistered areas may be large or small in different clinical cases, multilevel B-spline is designed to generate control point mesh at decreasing spacing in a coarse-to-fine manner. Misregistered areas will be reduced coarsely by dragging control points with large spacing mesh. As the misregistered areas are reduced, fine control point mesh will be generated with small spacing. Only control points in misregistered areas need to be revised in the fine level. The process will be stopped until visually satisfying registration results are displayed. Registration of the revised transformed image and the reference image will make the overlapping image in RGB model become gray. We will illustrate the proposed technique in the next sections in detail.

2.2. B-Splines and Local Deformation Model. As introduced in the previous section, the goal of interactive multigrid refinement is to reduce the local registration error of deformable registration methods. The nature of local deformation of anatomic structures can vary significantly across patients and ages. Therefore, it is difficult to describe the local deformation via parametric transformations, such as rigid transformation, or affine transformation, which can capture only the global motion of organs. Free-form deformation based on the B-splines is a powerful tool for modeling 3D deformation objects. However, optimization of a cost function associated with the global transformation parameters and the local transformation parameters in the framework

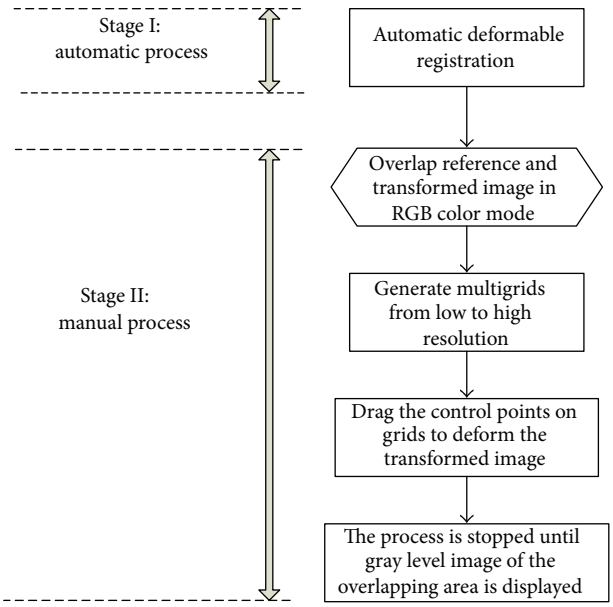

Figure 1: The framework of interactive multigrid refinement algorithm.

of free-form deformation uses an iterative multiresolution search strategy, which is often computationally expensive and prone to local minimum. Generally, the deformation results of free-form deformation contain errors which are visually distinctive from corresponding difference images. Such cases also exist in other kinds of automatic deformation registration methods. To this end, we propose a manual revision process to refine the local deformation model based on multilevel B-splines. Only the misregistration areas are revised by manipulating an underlying mesh of control points. The revision process can be fast and efficient.

To define a local deformation model, B-splines are used for modeling the deformation fields. The domain of the image volume is denoted as $\Omega = \{(x, y, z) \mid 0 \leqslant x < X, 0 \leqslant y < Y, 0 \leqslant z < Z\}$. The control lattice Φ is denoted by a mesh of control points $\Phi_{i,j,k}$ with uniform spacing overlaid on the domain Ω. Let $\Phi_{i,j,k}$ be the ijkth control point on the lattice Φ for $i = -1, 0, \ldots, X + 1$, $j = -1, 0, \ldots, Y + 1$, and $k = -1, 0, \ldots, Z + 1$. The deformation function T is defined in terms of these control points by

$$T(x, y, z) = \sum_{l=0}^{3} \sum_{m=0}^{3} \sum_{n=0}^{3} B_l(u) B_m(v) B_n(w) \Phi_{(i+l)(j+m)(k+n)}, \tag{1}$$

where $i = \lfloor x \rfloor - 1$, $j = \lfloor y \rfloor - 1$, $k = \lfloor z \rfloor - 1$, $u = x - \lfloor x \rfloor$, $v = y - \lfloor y \rfloor$, $w = z - \lfloor z \rfloor$, and $\lfloor \cdot \rfloor$ is the lower bound operator. B_l, B_m, and B_n are uniform basis functions of cubic B-spline defined as

$$B_0(u) = \frac{(1-u)^3}{6},$$

$$B_1(u) = \frac{\left(3u^3 - 6u^2 + 4\right)}{6},$$

$$B_2(u) = \frac{\left(-3u^3 + 3u^2 + 3u + 1\right)}{6},$$

$$B_3(u) = \frac{u^3}{6}, \tag{2}$$

where $0 \leq u \leq 1$. In general, the transformations that result from cubic B-splines are smooth and able to describe local deformation with few degrees of freedom. In contrast to thin-plate spline [12] or elastic body splines [16], B-splines are locally controlled; in particular, the basis functions of cubic B-splines have a limited support that changing control point $\Phi_{i,j,k}$ affects the transformation only in the local neighborhood of that control point. If any data points are added, removed, or modified, B-splines can be computationally efficient. This is the reason we chose B-spines for local deformation model.

The control points $\Phi_{i,j,k}$ are the parameters of the B-splines, and the degree of deformation field is essentially dependent on the spacing of control points. A large spacing of control points allows modeling of global deformation with large displacement, and hence, one control point will influence the deformation of large local areas, while a small spacing of control points allows modeling of local deformation within small areas. The resolution of control point mesh generally determines the degrees of freedom. Therefore, hierarchical B-spline refinement can be used to refine the deformation field. We have designed a hierarchical multiresolution B-spline refinement tool in which the resolution of control mesh is increased to revise the deformation field in a coarse-to-fine manner. Let $\Phi^1, \Phi^2, \ldots, \Phi^L$ denote hierarchical control point meshes at different spacings for deformation revision. For each control point mesh Φ^i and its associated B-spline define a local transformation T^i_{local}, and their sum defines the overall local transformation of deformation revision T_{local} as

$$T_{\text{local}}(x, y, z) = \sum_{i=1}^{L} T^i_{\text{local}}(x, y, z). \tag{3}$$

In this way, the overall local transformation of deformation revision is represented as a combination of B-splines at increasing resolution of control point mesh. For those misregistered areas, large spacing of control point mesh is generated when misregistered areas are large. After manual revision with related control points, the overall misregistered areas will be reduced. In order to refine the results further, the control point mesh is progressively refined. In this case, the control point mesh at level i is refined by inserting new control points to create the control point mesh at level $i + 1$. Therefore, the control point spacing is halved at every step. With the revision of control point at different levels, the final deformation field will be generated to make the reference image coincide with the transformed image.

2.3. Manual Refinement in RGB Model. In order to observe the misregistered area between the reference image and the transformed image well, we designed the RGB model.

Without loss of generality, we take the case of 2D image registration for explanation. In RGB model, the reference image is shown in the green band, and the transformed test image is shown in the red and blue bands of a color image. Therefore, when the images register perfectly, all three color bands at a pixel will have the same or similar values, producing gray scale. In areas where the images do not register well, the pixels will appear green or purple. Also appearing in green or purple are occluded areas. Thus, the misregistered areas will be displayed in green or purple in RGB model. The manual refinement which is based on the B-splines will revise the deformation transformation through manipulating control points in the transformed image. With the revision of the transformed image, the misregistered areas would be reduced or even eliminated because the local anatomic structures in the transformed images are revised to be aligned with the corresponding structures in the reference image. Meanwhile, the pixels in the misregistered areas that appear green or purple will become gray due to overlapping of the corresponding anatomic structures. The process of manual revision will be stopped until satisfying results are achieved. That is, the overlapping area in RGB model appears gray.

Due to the local geometric differences from large deformation or gray level change between the reference image and the test image, it is not easy to obtain perfect registration between corresponding structures. Therefore, the finally obtained overlapping area does not appear to be gray everywhere. In such case, we take the distinctive edge or salient object as the criterion for manual refinement. For example, if a distinctive edge in the transformed image is revised to be coincided with the corresponding edge in the reference image in RGB model, we consider that the manual refinement is good in such local areas around the distinctive edge. In our experiments, there is no need to revise every control point because the two images have been registered coarsely by automatic deformation registration methods and the misregistered areas are assumed to be limited. Our proposed manual revision is only used to improve the coarsely obtained registration results if the deformable registration methods do not work well. To our knowledge, the whole process of automatic deformable registration methods may not be satisfactory in clinical applications if these registration methods do not work well or if large registration errors are visible. Our proposed method provides a means to aid the process to be successful and allows the user to drag control points to get a better image alignment. If the automatic registration methods do not work well in clinical applications, the clinicians can use our tool to efficiently revise the former registered results directly.

To demonstrate the scheme of the manual refinement in RGB model, lung CT images in different respiratory phases are used for illustration. Precise targeting of lung tumors is of great importance in conformal radiotherapy, particularly stereotactic body radiation therapy (SBRT) for lung cancer. The discontinuity of the sliding behavior of the lungs makes the registration of lungs in different respiratory phases very challenging. Figure 2 shows the lung images in inhale and exhale phases of a patient's 4D CT set. Due to the local deformation of the shape of lungs, we can register the two images by our manual revision technique. As shown in Figure 2(c), the RGB model consists of three color components resulting from the test image and the reference image. Purple or green shows the misregistered area between the two images, and the well registered area appears to be gray. It should be noted that the two input images can be either two unregistered images or two images that have been previously registered, while one is the reference image and the other is the transformed image. That is to say, the proposed technique can be a manual registration tool, or it can be a revision tool to improve the registration results of other deformable registration methods by the clinician. In the control point mesh with large spacing, the mouse dragging of one control point will vary the local deformation of large areas as shown in Figure 2(d). With the decreasing of grid spacing, the revision of two or three control points will deform the transformed image locally and makes it align well with the reference image. The mesh grids can be chosen by clinicians' selection. If large misregistered areas exist in the RGB model, mesh grids with large spacing will be generated. Subsequently, the control point mesh will be progressively refined for further revision until satisfactory results are achieved.

3. Results and Discussion

3.1. Evaluation Measure. To assess the quality of the registration in images, we have calculated the mean and variance of the squared sum of intensity differences (SSD) [9]. In images before and after deformable registration and manual refinement, the SSD provides an indirect measure of the registration quality as the position of tissue changes. Since the deformation is often local between images, we have manually defined regions of interest (ROIs) around each image and then registered both ROIs independently:

$$\mathrm{SSD} = \frac{1}{n}\sqrt{\sum \left(I\left(t_0\right) - T\left(I\left(t\right)\right)\right)^2}, \tag{4}$$

where $I(t_0)$ and $I(t)$ denote the intensities of the images before and after motion and the summation includes all voxels within the overlap of both images. In addition to using the color model to represent misregistered areas visually, we calculate the SSD of the transformed image and the reference image at the same time when each step of manual revision is done. Thus, the evaluation measure SSD can supervise our interactive revision process in realtime. If the value of SSD becomes larger when the clinician is revising the control point, the moving direction of the control point should be inverted to make SSD become small. Meanwhile, the color of local areas in our RGB model is also the indication of alignment. If the local areas of misregistered become small, it is possible to reduce the stepsize to a finer grid for further refinement. The color of local areas becomes gray if registered well.

There are several reasons that we choose the evaluation metric SSD. Firstly, SSD is a good metric to evaluate the difference between two images. If two images registered well,

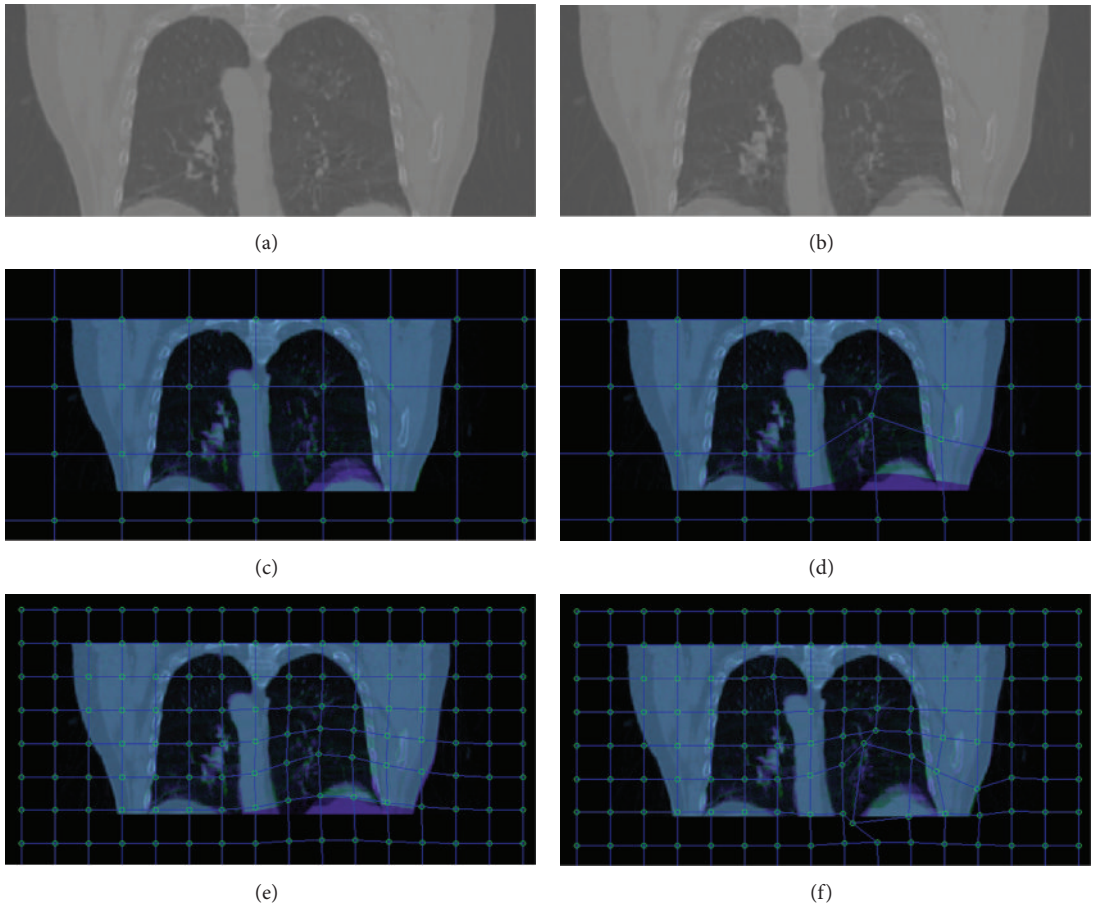

Figure 2: Manual refinement in RGB model. (a) Test image, (b) reference image, (c) overlapping of test image and reference image and large grid mesh in RGB model, (d) manually revise several related control points to reduce the misregistered area (purple or green), (e) progressively refine control point mesh and (f) manually revise related control points further.

SSD should be small. On the other hand, the evaluation metric of SSD is simple and can be calculated very fast. In our work, the value of evaluation metric should be displayed in realtime when the user is revising the local deformation. That is to say, the evaluation metric should supervise the interactive revision process. Therefore, we choose SSD for the interactive process. Other evaluation metrics, such as normalized correlation and mutual information, are very common for deformable image registration. If the interactive refinement is done, the transformed image and the reference image can be evaluated using kinds of metrics, such as SSD, mutual information, and normalized correlation.

3.2. Test Results. Two prostate images of the same patient were acquired from clinical applications. These two images contained both global and local deformations, and the gray intensities were different as well. We chose the affine transformation, FFD, and Demons for coarse registration, respectively. If the two images were registered well, the overlapping area would be in gray, and the color shows the registration errors. As shown in Figure 3, the results of these automatic registration methods all contained errors due to the large local deformable variation between the two prostate images. Affine transformation is a global mapping function for image registration, and there were large registration errors for deformation registration as shown in Figure 3(g). Typically, both FFD and Demons are commonly used deformation registration methods, and their results were much better than those of affine transformation. The color areas in overlapping images as shown in Figures 3(h) and 3(i) were much smaller than the color area in Figure 3(g). The contours of soft tissues were mostly aligned well by FFD and Demons. However, registration errors still existed around some branches of anatomic structures between the two images. The registration results can be improved further by our proposed method. Our proposed tool will generate uniform grids from larger spacing to smaller spacing, and the clinician can select the knot point for mouse draggling. Then, the local area of transformed image will be tuned with the moving of its close knots. The process will be stopped until the color region is eliminated or distinctive branches are almost aligned between two images by the interactive adjustment.

The results of manual revision for affine, FFD, and Demons deformable registration methods are shown in Figure 4, respectively. The registration errors of affine, FFD,

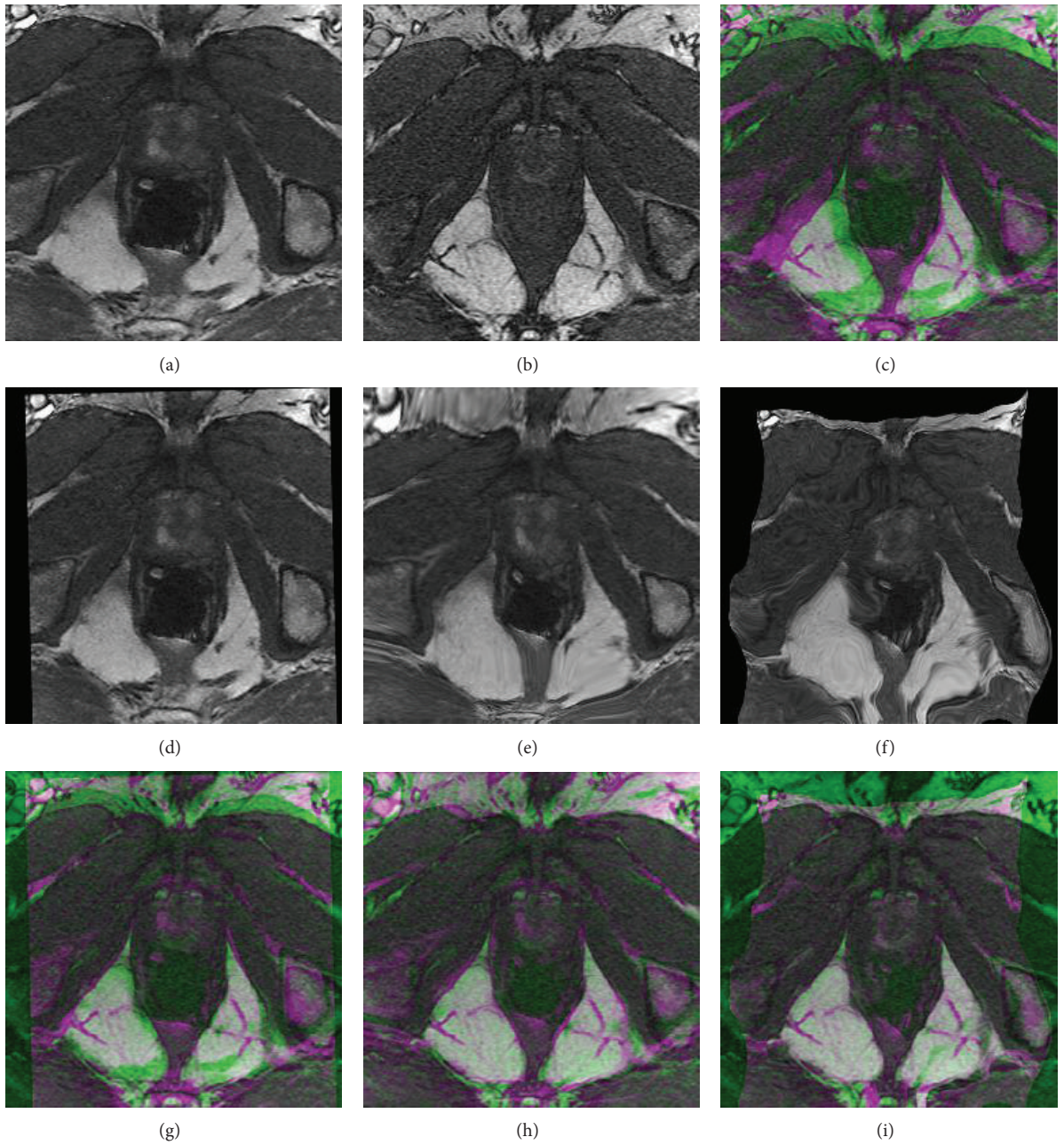

Figure 3: Registration results of affine, FFD, and Demons for two clinical prostate images. (a) Test image, (b) reference image, (c) direct overlapping of (a) and (b) in RGB model, (d) transformed image from affine transformation, (e) transformed image from FFD, (f) transformed image from Demons, (g) overlapping of affine transformed image with the reference image, (h) overlapping of FFD transformed image with the reference image and (i) overlapping of Demons transformed image with the reference image.

and Demons were reduced by manipulating progressively refined control point mesh. For affine transformation, our proposed method can improve results distinctively. Typically, the registration results of FFD and Demons were remarkably good due to the high performance of those methods. However, the proposed method can further improve the registration results and reduce registration errors. From the above experimental results, we have shown the effectiveness of the proposed method for deformable image registration in clinical applications. Although our given test data were clinical CT images, other kinds of medical modality can also be used directly. With the development of more complex deformable registration methods, our proposed tool can directly improve the registration results further.

3.3. Discussion. In this work, we tried to reduce deformable registration errors in a multigrid process. Large errors are

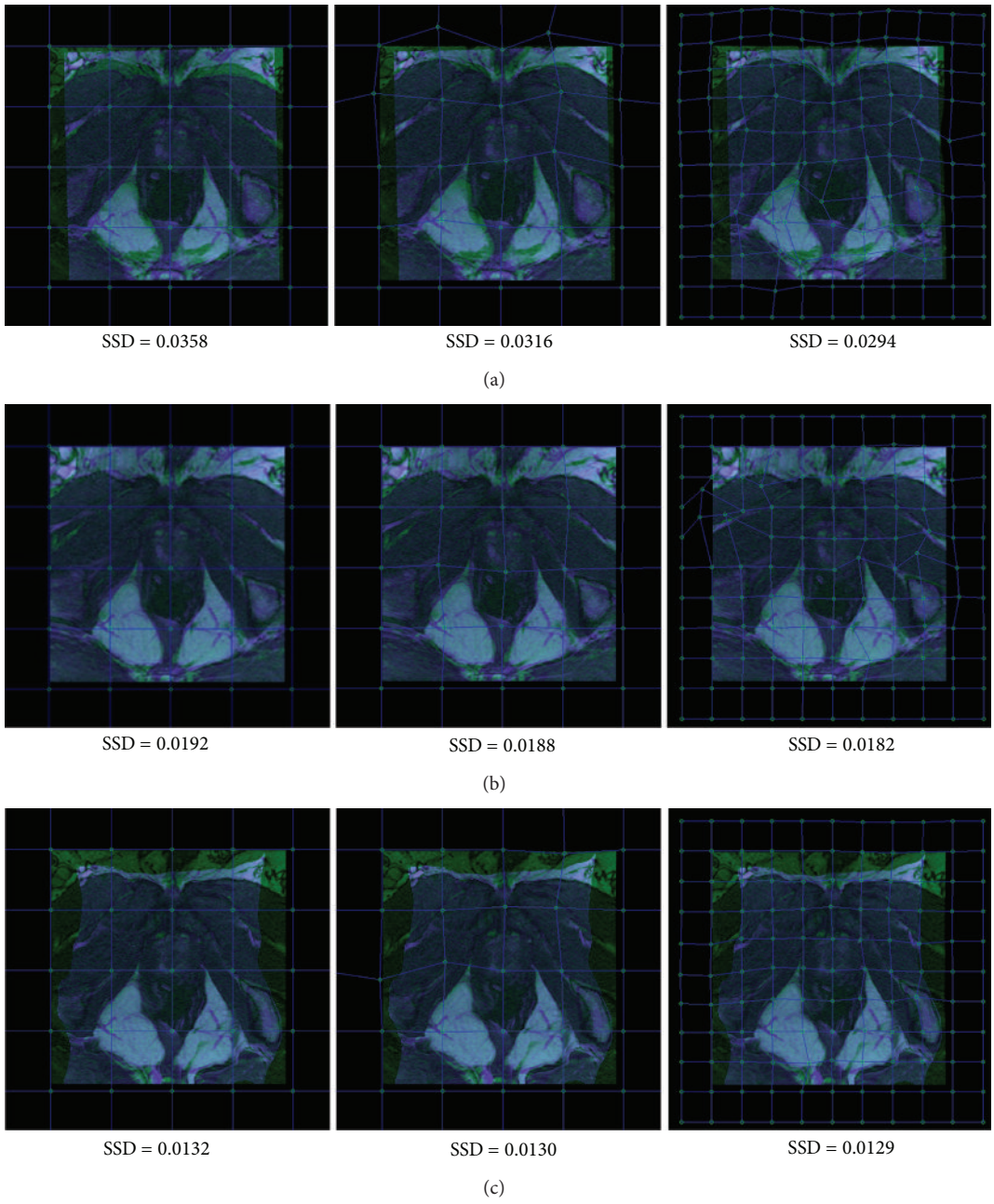

Figure 4: Registration results of manual revision of affine, FFD, and Demons for two clinical prostate images, respectively. (a) Affine, (b) FFD and (c) Demons. The value of SSD shows the performance of registration in overlapping areas. Generally, the lower the SSD, the better the registration results. Note that the SSD for Demons only calculates the areas of overlapping between two images.

reduced by revising control points in coarse grids, and small errors are reduced by revising control points in fine grids. Generally, our method is similar to multiscale image registration [17, 18], which uses hierarchical multiscale information to recover deformations. We use multigrids to recover deformation from large deformation with sparse grids to local small deformation with fine grids, and those multiscale registration methods are usually using images in different scales (or resolution) for registration, and the deformation can be recovered from global to local. However, focuses are different between our method and those multiscale image registration methods. We concentrate on how to interactively reduce errors of deformable image registration if automatic registration methods cannot work well or registration errors are distinctive in clinical applications. On the other hand, those multiscale image registration methods are trying to register images automatically in a coarse-to-fine manner, and their purposes are generally reducing computational complexity of registration and making the registration more robust and reliable.

The manual revision process may be tedious for clinicians when large misregistered areas exist. That is the truth if the

registration error is large and large areas are needed to be revised with more control points. In our work, the framework of the proposed interactive multigrid refinement algorithm consists of two steps: one is the automatic deformable registration method and the second is the manual revision process. We first of all assume that the automatic registration can obtain registration results which are not too bad. That is, the automatic deformation registration can be accurate and reliable to make the misregistered area small in clinical applications. Basically, some deformation registration methods, such as feature-based or intensity-based methods, can generate good results to some extent. Unfortunately, some areas may contain errors practically. Therefore, regions that need to be revised are often limited or very small. Hence, we provide the tool to quickly revise such errors in our proposed RGB model.

In this work, the smoothness is not considered as a metric in the interactive process which may be the limitation of our method. In general, the local deformation of the anatomic structures should be characterized by a smooth transformation [9]. It is known that SSD is a "similarity" measure, which is not the only consideration in evaluating the performance of registration. In some registration algorithms [9, 13], "smoothness" is also considered for the mapping function, but this is not included in SSD. In our interactive process, we consider how to revise the registration error conceptually from multi-grid refinement to make images align better under the evaluation metrics of SSD and color model. B-spline is smooth to some extent to make sure that the deformation field appears to be smooth. However, the "smoothness" is not easy to be considered much in the interactive process. Maybe we can add another metric of smoothness in the interactive process, like (5) in [9]. However, the balance between the similarity and smoothness may be also a problem. Therefore, the finally revised transformed image may be accurate in similarity but not much smooth by our proposed method due to the only use of SSD.

In addition, the evaluation metric of SSD is used for monomodality images. Actually, correspondent features in monomodality images are distinctive for manual revision perceptually. Therefore, the proposed method can obtain reliable and accurate results for monomodality image registration, which is suitable for monomodality images. However, it may not be good and convenient for images in different modalities because of few visual corresponding anatomic structures. If gray scale and image contrast are very different in multimodality images, the manual revision for further refinement of automatic deformable image registration will be difficult. This is also the limitation of our proposed method. In the future, we will also consider the metric of normalized mutual information for multimodality images in our proposed framework.

4. Conclusions

In this paper, we propose an interactive tool for deformable registration revision by using multigrid B-spline refinement. This technique can be used to improve registration results of other deformable image registration methods. Experimental results showed that this tool could be used to model deformation accurately and efficiently. The application of this tool can be for medical image registration in clinical cases, such as treatment planning. We believe that it will be a useful tool for clinical applications. In the future work, we will try to register multimodality images well using our proposed method by extracting salient features in the transformed image and the reference image to facilitate visualization.

Acknowledgments

The authors kindly thank D. Kroon from the University of Twente (August 2010) for sharing the code of manually warp images on the platform of Matlab file exchange, which facilitates our research. This work is supported by the Grant from China Postdoctoral Science Foundation (2013M530740) and National Natural Science Foundation of China (NSFC: 61302171)and in part by Grants from the National Natural Science Foundation of China (NSFC: 81171402), NSFC Joint Research Fund for Overseas Research Chinese, Hong Kong and Macao Young Scholars (30928030), National Basic Research Program 973 (2010CB732606) from Ministry of Science and Technology of China, and Guangdong Innovative Research Team Program (no. 2011S013) of China.

References

[1] T. M. Peters and K. R. Cleary, *Image-Guided Interventions: Technology and Applications*, Springer, Berlin, Germany, 2008.

[2] L. Xing, B. Thorndyke, E. Schreibmann et al., "Overview of image-guided radiation therapy," *Medical Dosimetry*, vol. 31, no. 2, pp. 91–112, 2006.

[3] Y. Xie, M. Chao, and L. Xing, "Tissue feature-based and segmented deformable image registration for improved modeling of shear movement of lungs," *International Journal of Radiation Oncology Biology Physics*, vol. 74, no. 4, pp. 1256–1265, 2009.

[4] Y. Xie, M. Chao, and G. Xiong, "Deformable image registration of liver with consideration of lung sliding motion," *Medical Physics*, vol. 38, no. 10, pp. 5351–5361, 2011.

[5] N. Hardcastle, W. A. Tomé, D. M. Cannon et al., "A multi-institution evaluation of deformable image registration algorithms for automatic organ delineation in adaptive head and neck radiotherapy," *Radiation Oncology*, vol. 7, p. 90, 2012.

[6] A. Sotiras, C. Davatazikos, and N. Paragios, "Deformable Image registration: a survey," Technical Report 7919, INRIA, Le Chesnay Cedex, France, 2012.

[7] S. Pszczolkowski, L. Pizarro, R. Guerrero, and D. Rueckert, "Nonrigid free-form registration using landmark-based statistic deformation model," in *Proceedings of the SPIE 8314, Medical Imaging 2012: Image Processing*, vol. 831418.

[8] N. Shusharina and G. Sharp, "Image registration using radial basis functions with adaptive radius," *Medical Physics*, vol. 39, no. 11, pp. 6542–6549, 2012.

[9] D. Rueckert, K. I. Sondoda, C. Hayes, D. L. G. Hill, M. O. Leach, and D. J. Hawkes, "Nonrigid registration using free-form deformations: application to breast mr images," *IEEE Transactions on Medical Imaging*, vol. 18, no. 8, pp. 712–721, 1999.

[10] X. Pennec, P. Cachier, and N. Ayache, "Understanding the "Demon's Algorithm": 3D non-rigid registration by Gradient

Descent," in *Proceedings of the Medical Image Computing and Computer-Assisted Intervention (MICCAI '11)*, pp. 597–606, 1999.

[11] N. D. Cahill, J. A. Noble, and D. J. Hawkes, "A Demons algorithm for image registration with locally adaptive regularization," in *Proceedings of the 12th International Conference on Medical Image Computing and Computer-Assisted Intervention (MICCAI '09)*, pp. 574–581, 2009.

[12] F. L. Bookstein, "Principal warps: thin-plate splines and the decomposition of deformations," *IEEE Transactions on Pattern Analysis and Machine Intelligence*, vol. 11, pp. 567–585, 1992.

[13] L. Zagorchev and A. Goshtasby, "A comparative study of transformation functions for nonrigid image registration," *IEEE Transactions on Image Processing*, vol. 15, no. 3, pp. 529–538, 2006.

[14] A. Andronache, M. von Siebenthal, G. Székely, and P. Cattin, "Non-rigid registration of multi-modal images using both mutual information and cross-correlation," *Medical Image Analysis*, vol. 12, no. 1, pp. 3–15, 2008.

[15] C. Buerger, T. Schaeffter, and A. P. King, "Hierarchical adaptive local affine registration for fast and robust respiratory motion estimation," *Medical Image Analysis*, vol. 15, no. 4, pp. 551–564, 2011.

[16] J. Ashburner, "A fast diffeomorphic image registration algorithm," *NeuroImage*, vol. 38, no. 1, pp. 95–113, 2007.

[17] D. Paquin, D. Levy, E. Schreibmann, and X. Lei, "Multiscale image registration," *Mathematical Biosciences and Engineering*, vol. 3, no. 2, pp. 389–418, 2006.

[18] P. Thévenaz and M. Unser, "Optimization of mutual information for multiresolution image registration," *IEEE Transactions on Image Processing*, vol. 9, no. 12, pp. 2083–2099, 2000.

Hindawi Publishing Corporation
BioMed Research International
Volume 2013, Article ID 401261, 12 pages
http://dx.doi.org/10.1155/2013/401261

Review Article

The Treatment Outcome and Radiation-Induced Toxicity for Patients with Head and Neck Carcinoma in the IMRT Era: A Systematic Review with Dosimetric and Clinical Parameters

Vassilis Kouloulias,[1] Stella Thalassinou,[1] Kalliopi Platoni,[1] Anna Zygogianni,[2] John Kouvaris,[2] Christos Antypas,[2] Efstathios Efstathopoulos,[1] and Kelekis Nikolaos[1]

[1] *Second Department of Radiology, Radiotherapy Unit, Attikon University Hospital, Medical School, Rimini 1, Xaidari, 12462 Athens, Greece*
[2] *First Department of Radiology, Radiotherapy Unit, Aretaieion University Hospital, Medical School, Vas. Sofias 76, 11528 Athens, Greece*

Correspondence should be addressed to Vassilis Kouloulias; vkouloul@ece.ntua.gr

Received 16 May 2013; Revised 8 August 2013; Accepted 22 August 2013

Academic Editor: Tsair-Fwu Lee

A descriptive analysis was made in terms of the related radiation induced acute and late mucositis and xerostomia along with survival and tumor control rates (significance level at 0.016, bonferroni correction), for irradiation in head and neck carcinomas with either 2D Radiation Therapy (2DRT) and 3D conformal (3DCRT) or Intensity Modulated Radiation Therapy (IMRT). The mean score of grade > II xerostomia for IMRT versus 2-3D RT was 0.31 ± 0.23 and 0.56 ± 0.23, respectively (Mann Whitney, $P < 0.001$). The parotid-dose for IMRT versus 2-3D RT was 29.56 ± 5.45 and 50.73 ± 6.79, respectively (Mann Whitney, $P = 0.016$). The reported mean parotid-gland doses were significantly correlated with late xerostomia (spearman test, rho = 0.5013, $P < 0.001$). A trend was noted for the superiority of IMRT concerning the acute oral mucositis. The 3-year overall survival for either IMRT or 2-3DRT was 89.5% and 82.7%, respectively ($P = 0.026$, Kruskal-Wallis test). The mean 3-year locoregional control rate was 83.6% (range: 70–97%) and 74.4 (range: 61–82%), respectively ($P = 0.025$, Kruskal-Wallis). In conclusion, no significant differences in terms of locoregional control, overall survival and acute mucositis could be noted, while late xerostomia is definitely higher in 2-3D RT versus IMRT. Patients with head and neck carcinoma should be referred preferably to IMRT techniques.

1. Introduction

Over the last years, radiotherapy has played a significant role in the treatment of head and neck cancers. 74% of head and neck cancer patients need to undergo either definitive or postoperative radiation therapy [1]. The transition from two-dimensional conventional radiotherapy (2D-RT) to three-dimensional conformal radiotherapy (3D-CRT), in addition to further technological evolutions in the field of radiotherapy, led to the successful clinical implementation of intensity modulated radiation therapy (IMRT) which constitutes an evolution of 3D-CRT [2]. The IMRT has been employed in clinical practice since 1995 resulting in a great specimen of clinical results from patients undergone this specific technique of radiotherapy [3]. The IMRT technique gives the ability to create treatment fields with varying beam intensity by using inverse planning and iterative optimization algorithms [4]. The irradiation beam can be adjusted to the irregularly shaped target volumes with extremely high precision whilst reducing the radiation delivered to the surrounding healthy tissue and critical structures such as spinal cord, brain stem, parotid glands, eyes, optic nerves, chiasma, lacrimal glands, cochlea, and mandible in case of head and neck cancer [5–7]. The ability of delivering lower doses of radiation to normal tissue while maintaining or increasing the dose in the target volume makes IMRT the most appropriate treatment option compared to 2D-RT and 3D-CRT [8–12].

Radiation therapy causes acute and late toxicities that affect various organs and functions. One of the most common acute toxicities that occurs as an injury of the mucosa of the head and neck area due to irradiation is mucositis. In the case of late toxicity, the most common characteristic is xerostomia where the considerable reduction of saliva leads to persistent dryness of mouth, oral discomfort, sore throat, dental decay, difficulty in speech, taste alteration, and impairment of chewing and swallowing functions which can lead to nutritional depletion and weight loss [13–16]. According to the published results, IMRT technique improves the toxicity profiles without compromising the efficacy [9, 12, 17–19]. The reduction of acute and late toxicities [8, 9, 12, 18, 20–22] in conjunction with comparable or superior treatment outcomes [8–10, 20, 21, 23] increases the necessity of IMRT technique for the treatment of head and neck carcinomas.

The objective of this study is to review the already published results and compare the efficacy and toxicity between patients treated with conventional RT techniques (2DRT and 3DCRT) and those treated with IMRT technique for head and neck carcinomas.

2. Materials and Methods

The literature was accessed through PubMed and Scopus (March 2000–January 2013), using the terms "radiation therapy," "head and neck cancer," "toxicity," "tumor control," and "survival." Additional papers were identified by cross-referencing bibliographies of retrieved articles. Tumor control and survival outcomes for head and neck cancers were collected from 38 studies while outcomes of acute and late toxicity were collected from 33 studies. As far as toxicity is concerned, two of the most common acute and late radiation-induced morbidity were included such as mucositis and xerostomia. The mean parotid-gland dose was also recorded as it contributes to radiation-induced xerostomia. The published results were categorized according to the radiation therapy technique which was used for the treatment of head and neck carcinomas in order to estimate the differences in clinical outcomes. The present review study focused mainly on hypopharyngeal, nasopharyngeal, and oropharyngeal tumors as well as on tumors of the larynx and the oral cavity. Furthermore, clinical outcomes for curative reirradiation were not included in the collected data.

2.1. Statistical Analysis. The analysis included a statistical correlation with spearman-rho nonparametric test between either the RT technique (IMRT versus 2-3D RT) or the mean parotid dose and the incidence of late xerostomia. For the analysis of the differences of the doses at the parotids and the mean score of xerostomia stratified by the RT technique, we used the Mann-Whitney test. The potential impact of RT technique to either survival or locoregional control rate was evaluated with the Kruskal-Wallis test. According to the bonferroni correction, the significance level was set at 0.016. Due to the efficient number of data concerning the survival and locoregional control rate of the 3-year-followup, we decided to make the analysis for the 3-year survival and locoregional rate. The statistical analysis was performed with the SPSS version 10 software (Chicago, IL, USA).

3. Results

According to the published data, the head and neck primary site was as follows: oropharynx 41%, nasopharynx 37%, oral cavity 6%, larynx/hypopharynx 15%, and other tumor site 1%. Among the studies, 2582 out of 4587 patients (56%) received concurrent chemotherapy. In terms of radiation therapy technique, IMRT was given to 3618 out of 4587 patients (79%) and 2-3D RT was given to 969 out of 4587 patients (21%). Definitive versus post-operative RT was given to 3953 out of 4587 (86%) versus 633 out of 4587 (14%) patients, respectively.

Published results on tumor control outcomes in terms of local control (LC), regional control (RC), and locoregional control (LRC) and also on survival outcomes in terms of overall survival (OS), distant metastasis-free survival (DMFS), and disease-free survival (DFS) are presented in Table 1. Relevant data are shown according to the patient sample, primary tumor site and stage, treatment intention, median followup, and the percentage of patients that received radiotherapy combined with chemotherapy. The treatment outcomes referred to head and neck cancer patients underwent radiotherapy either with conventional radiotherapy techniques or IMRT. Twenty five trials with available data were analysed in terms of overall survival and locoregional control rate. The mean 3-year overall survival for either IMRT or 2-3D RT was 89.5% (range: 64–100%) and 82.7% (71–88%), respectively. The mean 3-year locoregional control rate 83.6% (range: 70–97%) and 74.4 (range: 61–82%), respectively. The Kruskal-Wallis test revealed a significant ($P = 0.026$) correlation of overall survival with RT technique (IMRT either 2-3DRT), while there was also a significant impact of IMRT technique to locoregional rate ($P = 0.025$). However, according to the bonferroni correction, neither of the above correlations was finally significant. In Table 2, the reported acute and late toxicity rates for mucositis and xerostomia are listed according to the median followup, radiation therapy technique (IMRT or 2-3D RT), and the percentage of patients that received chemotherapy combined with radiotherapy. Few data were available for late mucositis and acute xerostomia concerning the evaluated relevant publications. In the same table, the mean parotid-gland dose is also presented in order to depict the correlation with patient-rated xerostomia. Relevant data with xerostomia grading score and dose deposited at the parotid gland were available in twenty published trials. As shown in Figure 1, the spearman-rho test showed that there was a significant correlation of late xerostomia and mean dose at the parotid gland (rho = 0.5013, $P < 0.001$). According to Figure 2, the mean score of xerostomia for IMRT versus 2-3D RT was 0.31 ± 0.23 and 0.56 ± 0.23, respectively (Mann Whitney, $P < 0.001$). The mean dose deposited in the parotid gland for IMRT versus 2-3DRT was 29.56 ± 5.45 and 50.73 ± 6.79, respectively (Mann Whitney, $P = 0.016$). By analysing thirty five relevant publications with available data with acute

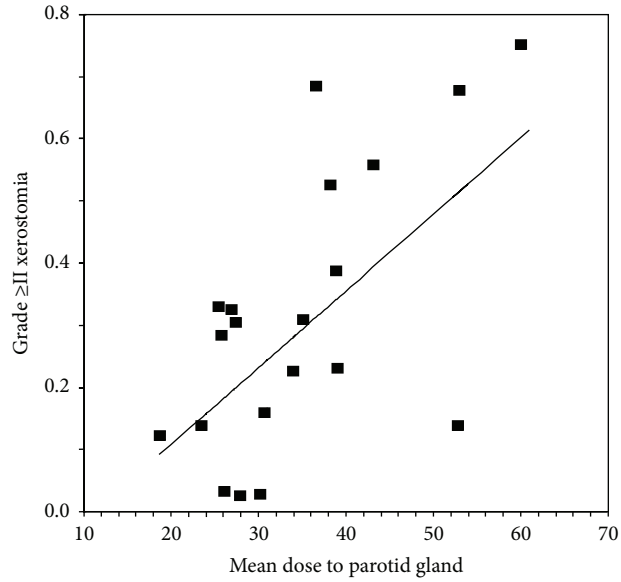

Figure 1: Linear curve estimation for grading ≥ II xerostomia related to the mean dose of parotid gland (rho = 0.5013, $P < 0.001$). The analysis was performed from 20 published trials with relevant available data.

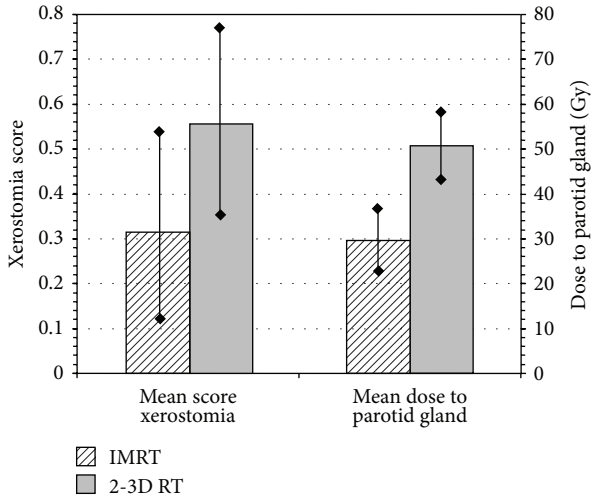

Figure 2: Comparative descriptive analysis of mean dose to parotids and mean xerostomia score stratified by RT technique. A significant difference was noted between the IMRT and conventional technique for both doses to parotids ($P = 0.016$) and xerostomia ($P < 0.001$). The related scale referring to the y-axis either right or left is presenting the dose to the parotids and the xerostomia score, respectively. Data were available from twenty published trials.

mucositis, after comparing the mean values of acute mucositis stratified by IMRT versus 2-3DRT, we found a mean score of 0.71 ± 0.23 versus 0.89 ± 0.07 (Mann-Whitney test, $P = 0.022$), respectively. However, according to bonferroni correction the difference was not significant.

At last, in Table 3 the range of tumor control and survival rates as well as the range of the acute and late toxicities rates (mucositis and xerostomia) is presented separately for each radiation therapy technique (IMRT versus 2-3D RT).

4. Discussion

With the increasing use of IMRT in head and neck carcinomas the improvement of treatment outcomes is the main concern. Several studies in the literature have reported favourable treatment outcomes for patients treated with IMRT technique [8, 9, 24, 25, 28–30, 32, 34, 37, 41, 45]. Comparable rates of LRC are observed in Table 1 among the published studies for different radiotherapy techniques as also comparable survival rates. The comparable LRC and overall survival rates were also confirmed by the descriptive statistical analysis of this study where, beyond a trend in the superiority of IMRT, the differences between the IMRT and 2-3D RT were finally statistically insignificant. However, there are significant variations in tumor control and survival outcomes which are mainly caused by differences in patient sample, tumor stage, and followup among several studies. Chemotherapy also plays a significant role in the variation of clinical results. According to numerous studies, the combination of chemotherapy with radiotherapy improves the efficacy [55–58] at the cost of increased toxicity [55, 56]. In several studies, clinical results were divided according to patients treated with definitive radiotherapy and patients treated with postoperative radiotherapy. In the study of Chao et al. [27], combined surgery and postoperative IMRT lead to improved LRC and DFS compared with definitive IMRT in patients with oropharyngeal carcinoma. Similarly in the study of Studer et al. [48], LC of patients who received definitive IMRT for oral cavity cancer was substantially lower than the LC of patients who received postoperative IMRT.

The published clinical results demonstrate equivalence or noninferiority of IMRT in terms of tumor control or survival in any head and neck site [8–10, 20, 21, 23] while IMRT plays a significant role on the reduction of radiation-induced toxicity [8, 9, 12, 18, 20–23]. According to the published data as shown in Table 3, it seems that IMRT reduces late xerostomia down to 2.3%. According to our descriptive analysis, the mean score of xerostomia was significantly lower in IMRT compared to conventional radiation therapy techniques (Mann Whitney, $P < 0.001$). The prevailing explanation for this inferior toxicity related to IMRT is that the preservation of salivary gland function itself has a protecting effect with regard to radiation-induced oral toxicity and secondary oral infections [59]. Although the data from Table 3 showed that IMRT technique can achieve a reduction of acute mucositis down to 32%, our analysis showed only a trend for the superiority of IMRT.

The mean parotid-gland doses for patients treated with IMRT were significantly lower compared with the mean parotid-gland doses of patients treated with 2-3D RT (Mann Whitney, $P = 0.016$). Furthermore, a significant correlation of late xerostomia and the mean parotid-gland dose was found (spearman test, rho = 0.5013, $P < 0.001$). Numerous studies have also reported significant correlation between the mean parotid dose and salivary flow after RT and the rate of

Table 1: Published studies with either IMRT or conventional techniques. Data included primary site, stage, intention of RT, concomitant chemotherapy or not, followup, and treatment outcome.

Study	No. of patients	Primary tumor site	TN stage	RT	Intention for RT no. of pts (%)	Concurrent chemotherapy no. of pts (%)	Median followup (Range)	Regional control (RC)	Local control (LC)	Treatment outcome % Locoregional control (LRC)	Distant metastases-free survival (DMFS)	Disease-free survival (DFS)	Overall survival (OS)
Studer et al. [24]	29	Hypopharynx	T1–T4 N0–N3	IMRT	Def: 90% Post: 10%	Yes (86%)	16 mths (4–44 mths)	93% (2yrs)	90% (2yrs)	—	93% (2yrs)	90% (2yrs)	—
Lee et al. [8]	41	Oropharynx	T1–T4 N0–N3 St: III–IVB	IMRT	Def	Yes	31 mths (20–64 mths)	94% (3yrs)	95% (3yrs)	92% (3yrs)	86% (3yrs)	82% (3yrs)	91% (3yrs)
	71	Oropharynx	T1–T4 N0–N3 St: III–IVB	2DRT	Def	Yes	46 mths (3–93 mths)	95% (3yrs)	85% (3yrs)	82% (3yrs)	85% (3yrs)	76% (3yrs)	81% (3yrs)
Garden et al. [25]	51	Oropharynx	Tx, T1-T2 Nx, N0–N3	IMRT	Def	Yes (8%)	45 mths (15–63 mths)	—	96% (2yrs)	93% (2yrs)	—	87% (2yrs)	93% (2yrs)
Daly et al. [26]	107	Oropharynx	T1–T4 N0–N3 St: II–IV	IMRT	Def: 80% Post: 20%	Yes (87%)	29 mths (4–105 mths)	—	—	92% (3yrs)	92% (3yrs)	81% (3yrs)	83% (3yrs)
Chao et al. [27]	74	Oropharynx	T1–T4 N0–N3 St: I–IV	IMRT	Def: 42% Post: 58%	Yes (23%)	33 mths (9–60 mths)	—	—	87% (3yrs)	90% (4yrs)	81% (4yrs)	87% (4yrs)
Huang et al. [28]	71	Oropharynx	T1–T4 N0–N3 St: III-IV	IMRT	Def	Yes	33 mths (3–72 mths)	94% (3yrs)	94% (3yrs)	90% (3yrs)	—	—	83% (3yrs)
Setton et al. [29]	442	Oropharynx	T1–T4 N0–N3 St: I–IV	IMRT	Def: 93% Post: 7%	Yes (88%)	36.8 mths (3–135 mths)	94.4% (3yrs)	94.6% (3yrs)	—	87.5% (3yrs)	—	84.9% (3yrs)
Schoenfeld et al. [30]	64	Oropharynx	T1–T4 N0–N3 St: I–IVB	IMRT	Def	Yes (54%)	36 mths (12–62 mths)		94% (3yrs)	90% (3yrs)	—	RFS: 86% (3yrs)	84% (3yrs)
Clavel et al. [9]	100	Oropharynx	T1–T4 N0–N3 St: III–IVB	IMRT	Def	Yes	42 mths			95.1% (3yrs)		85.3% (3yrs)	92.1% (3yrs)
	149	Oropharynx	T1–T4 N0–N3 St: III–IVB	2-3DRT	Def	Yes	42 mths			84.4% (3yrs)		69.3% (3yrs)	75.2% (3yrs)
Sanguineti et al. [31]	50	Oropharynx	Tx, T1–T4 N0–N3	IMRT	Def	No	32.6 mths (12.1–58.6 mths)	85% (3yrs)	94% (3yrs)				
De Arruda et al. [32]	50	Oropharynx	T1–T4 N0–N3 St: I–IV	IMRT	Def: 96% Post: 4%	Yes (86%)	18 mths (8.4–76 mths)	88% (2yrs)	98% (2yrs)		84% (2yrs)		98% (2yrs)
Fang et al. [10]	113	Nasopharynx	T1–T4 N0–N3 St: I–IV	IMRT	Def	Yes (57.3%)	40 mths (5–57 mths)	—	—	84% (3yrs)	83% (3yrs)	—	85% (3yrs)
	93	Nasopharynx	T1–T4 N0–N3 St: I–IV	3D-CRT	Def	Yes (54.8%)	46 mths (10–59 mths)	—	—	84.8% (3yrs)	76.7% (3yrs)	—	81.7% (3yrs)
Wong et al. [33]	175	Nasopharynx	T1–T4 N0–N3 St: I–IVB	IMRT	Def	Yes (70%)	34 mths (9–50 mths)	93.3% (3yrs)	93.6% (3yrs)		86.6% (3yrs)		87.2% (3yrs)

Table 1: Continued.

Study	No. of patients	Primary tumor site	TN stage	RT	Intention for RT no. of pts (%)	Concurrent chemotherapy no. of pts (%)	Median followup (Range)	Treatment outcome %					
								Regional control (RC)	Local control (LC)	Locoregional control (LRC)	Distant metastases-free survival (DMFS)	Disease-free survival (DFS)	Overall survival (OS)
Kwong et al. [34]	33	Nasopharynx	T1–T3 N0-N1	IMRT	Def	No	24 mths (11–42 mths)	93% (3yrs)	100% (3yrs)	—	100% (3yrs)	—	100% (3yrs)
Wolden et al. [35]	74	Nasopharynx	T1–T4 N0–N3 St: I–IVB	IMRT	Def	Yes (93%)	35 mths (3–74 mths)	93% (3yrs)	91% (3yrs)	—	78% (3yrs)	67% (3yrs)	83% (3yrs)
Kam et al. [36]	63	Nasopharynx	T1–T4 N0–N3 St: I–IV	IMRT	Def	Yes (30%)	29 mths (8–45 mths)	98% (3yrs)	92% (3yrs)	—	79% (3yrs)	—	90% (3yrs)
Tham et al. [37]	107	Nasopharynx	T1–T2 N0–N1 St: IIB	IMRT	Def	Yes (7%)	39 mths (7–77 mths)	98% (3yrs)	96.5% (3yrs)		94.8% (3yrs)	90.7% (3yrs)	95.8% (3yrs)
Lee et al. [38]	68	Nasopharynx	T1–T4 N0–N3 St: I–IVB	IMRT	Def	Yes (65%)	31 mths (6–55 mths)	90.8% (2yrs)	92.6% (2yrs)	89.3% (2yrs)	84.7% (2yrs)	72.7% (2yrs)	80.2% (2yrs)
Tham et al. [39]	195	Nasopharynx	T1–T4 N0–N3 St: I–IVB	IMRT	Def	Yes (57%)	36.5 mths		89.6% (3yrs)		89.2% (3yrs)	79% (3yrs)	94.3% (3yrs)
Lee et al. [40]	67	Nasopharynx	T1–T4 N0–N3 St: I–IV	IMRT	Def	Yes (75%)	31 mths (7–72 mths)	98% (4yrs)	97% (4yrs)	—	66% (4yrs)	—	88% (4yrs)
Liu et al. [41]	19	Nasopharynx	T1–T4 N0–N3 St: I–IV	IMRT	Def	Yes (58%)	13.0 mths (8–18 mths)	—	—	100% (13 mths)			
Luo et al. [42]	58	Nasopharynx	T1–T4 N0–N3 St: I-II	3D-CRT	Def	No	58 mths (25–92 mths)	—	—	93% (5yrs)	98% (5yrs)	91% (5yrs)	95% (5yrs)
Wang et al. [43]	300	Nasopharynx	T1–T4 N0–N3 St: IIB	IMRT	Def	Yes (83%)	47.1 mths (11–68 mths)	95.1% (4yrs)	94% (4yrs)	—	85% (4yrs)	—	86.1% (4yrs)
Sultanem et al. [44]	35	Nasopharynx	T1–T4 N0–N3 St: I–IVB	IMRT	Def	Yes (91%)	21.8 mths (5–49 mths)			100% (4yrs)	57% (4yrs)	57% (4yrs)	94% (4yrs)
Su et al. [45]	198	Nasopharynx	T1-T2 N0-N1 St: I–IIB	IMRT	Def	No	50.9 mths (12–104 mths)		97.7% (5yrs)		97.8% (5yrs)	97.3% (5yrs)	
Kim et al. [46]	21	Nasopharynx	T2–T4 N0–N2 St: III-IV	3D-CRT	Def	No	48 mths					85% (5yrs)	61% (5yrs)
Al-Mamgani et al. [47]	170	Larynx	T3 N0–N3	IMRT + 3D-CRT	Def	Yes (28.3%)	32 mths (7–172 mths)	—	73% (3yrs)	70% (3yrs)		64% (3yrs)	61% (3yrs)
Studer et al. [48]	58	Oral cavity	*Def* T2–T4 N0–N3 St: IVA-B *Post* T1–T4 N0–N2c St: II–IVA	IMRT	Def: 52% Post: 48%	Yes (78%)	Def: 19 mths Post: 12 mths		Def: 43% (2yrs) Post: 92% (2yrs)	—	—	Def: 40% (2yrs) Post: 87% (2yrs)	Def: 30% (2yrs) Post: 83% (2yrs)

Table 1: Continued.

Study	No. of patients	Primary tumor site	TN stage	RT	Intention for RT no. of pts (%)	Concurrent chemotherapy no. of pts (%)	Median followup (Range)	Treatment outcome % Regional control (RC)	Local control (LC)	Locoregional control (LRC)	Distant metastases-free survival (DMFS)	Disease-free survival (DFS)	Overall survival (OS)
Chen et al. [21]	22	Oral cavity	T1–T4 N0–N2c St: III-IV	IMRT	Post	Yes (9%)	44 mths					64% (3yrs)	67% (3yrs)
	27	Oral cavity	T1–T4 N0–N2c St: III-IV	3D-CRT	Post	Yes (2%)	44 mths					66% (3yrs)	77% (3yrs)
Yao et al. [49]	55	Oral cavity	Tx–T4 N0–N2c St: I–IV	IMRT	Def: 9% Post: 91%	Yes Def: 6% Post: 4%	23.9 mths (9.3–59.3 mths)		85% (3yrs)	82% (3yrs)	89% (3yrs)	74% (3yrs)*	68% (3yrs)
Lee et al. [50]	31	Various	T1–T4 N0–N2 St: I–IVB	IMRT	Def	Yes (65%)	26 mths (17–58 mths)		86% (2yrs)	94% (2yrs)	92% (2yrs)		63% (2yrs)
Van Gestel et al. [51]	78	Various	Tx, T1–T4 Nx, N0–N3 St: I–IVB	IMRT	Def: 62% Post: 38%	Yes Def: 63% Post: 23%	18.7 mths (0.13–51.7 mths)			Def: 66.8% (3yrs) Post: 82.2% (3yrs)		Def: 42.6% (3yrs) Post: 82.2% (3yrs)	Def: 60.3% (3yrs) Post: 85.9% (3yrs)
Peponi et al. [52]	82	Various	St: I–IV	IMRT	Def: 77% Post: 23%	Yes (85%)	55 mths		78% (3yrs)				80% (3yrs)
Gupta et al. [23]	28	Various	T1–T3 N0–N2b St: I–IV	3D-CRT	Def	Yes	40 mths (26–50 mths)			88.2% (3yrs)			70.6% (3yrs)
	32	Various	T1–T3 N0–N2b St: I–IV	IMRT	Def	Yes (90%)	40 mths (26–50 mths)			88.2% (3yrs)			68% (3yrs)
Lambrecht et al. [18]	135	Various	T1–T4 N0–N3 St: III-IV	3D-CRT	Def	Yes (80%)	68 mths (37.2–104 mths)			71% (3yrs)			61% (3yrs)
	110	Various	T1–T4 N0–N3 St: III-IV	IMRT	Def	Yes (81%)	35 mths (4.7–63.5 mths)			70% (3yrs)			64% (3yrs)
Toledano et al. [53]	208	Various	St: I–IV	IMRT	Def: 55% Post: 45%	Yes (37.5%)	25.3 mths (0.4–72 mths)	—	—	86% (2yrs)	92.7% (2yrs)	80% (2yrs)	86.7% (2yrs)
Rades et al. [22]	104	Various	T0–T4 N0–N3 St: I–IV	2DRT	Post	Yes (8%)			78% (2yrs)		79% (2yrs)		74% (2yrs)
	26	Various	T0–T4 N0–N3 St: I–IV	3D-CRT	Post	Yes (23%)			79% (2yrs)		83% (2yrs)		80% (2yrs)
	18	Various	T0–T4 N0–N3 St: I–IV	IMRT	Post	Yes (6%)			89% (2yrs)		80% (2yrs)		86% (2yrs)
Yao et al. [54]	150	Various	T0–T4 N0–N3 St: I–IV	IMRT	Def: 66% Post: 34%	Yes (45%)	18 mths (2–60 mths)		94% (2yrs)	92% (2yrs)	87% (2yrs)		85% (2yrs)

Table 2: Published studies with either IMRT or conventional techniques. Data included concomitant chemotherapy or not, follow-up, and radiation-induced toxicity.

Study	Radiation treatment	Concurrent chemotherapy No. of patients (%)	Median followup (range)	Toxicity (≥GrII)				Mean parotid-gland dose
				Mucositis		Xerostomia		
				Acute	Late	Acute	Late	
Studer et al. [24]†	IMRT	Yes (86%)	16 mths (4–44 mths)	65%	—	—	—	
Lee et al. [8]	IMRT	Yes	31 mths (20–64 mths)	66%	—	66%	12%	
	2DRT	Yes	46 mths (3–93 mths)	72%		65%	67%	
Garden et al. [25]	IMRT	Yes (8%)	45 mths (15–63 mths)	—	—	—	—	23.9 Gy
Daly et al. [26]†	IMRT	Yes (87%)	29 mths (4–105 mths)	93%	—	—	—	33.2 Gy
Chao et al. [27]†	IMRT	Yes (23%)	33 mths (9–60 mths)	86%	—	—	12%	18.6 Gy
Huang et al. [28]	IMRT	Yes	33 mths (3–72 mths)	92%	—	—	34%	25.5 Gy
Setton et al. [29]†	IMRT	Yes (88%)	36.8 mths (3–135 mths)	68%	—	28%	29%	25.8 Gy
Kwong et al. [34]	IMRT	No	24 mths (11–42 mths)	82%	—	—	40% (1yrs) 15% (2yrs)	38.8 Gy
Wolden et al. [35]	IMRT	Yes (93%)	35 mths (3–74 mths)				32% (1yrs)	35.2 Gy
Kam et al. [36]	IMRT	Yes (30%)	29 mths (8–45 mths)	92%		75%	23% (2yrs)	39 Gy
							16.7% (2yrs)	31 Gy
Lee et al. [38]	IMRT	Yes (65%)	31 mths (6–55 mths)	—	22%	—	33%	
Lee et al. [40]	IMRT	Yes (75%)	31 mths (7–72 mths)	94%	—		58%	
Liu et al. [41]	IMRT	Yes (58%)	13.0 mths (8–18 mths)	—	79%	—	53%	37.8 Gy
Luo et al. [42]	3D-CRT	No	58 mths (25–92 mths)	74%	12%		12%	52.8 Gy
Al-Mamgani et al. [47]	IMRT + 3D-CRT	Yes(28.3%)	32 mths (7–172 mths)				14.1%	23.6 Gy
Lee et al. [50]	IMRT	Yes (65%)	26 mths (17–58 mths)	48%			3.2%	26 Gy
Van Gestel et al. [51]†	IMRT	Yes Def: 63% Post: 23%	18.7 mths (0.13–51.7 mths)	100%			44%	
Peponi et al. [52]†	IMRT	Yes (85%)	55 mths				Obj: 7.3 % Sub: 3.6%	
Gupta et al. [23]	3D-CRT	Yes	40 mths (26–50 mths)	93%				53 Gy
	IMRT	Yes (90%)	40 mths (26–50 mths)	77%				34.3 Gy
Lambrecht et al. [18]	3D-CRT	Yes (80%)	68 mths (37.2–104 mths)	44%			68%	53 Gy
	IMRT	Yes (81%)	35 mths (4.7–63.5 mths)	32%			23%	34 Gy
Toledano et al. [53]†	IMRT	Yes (37.5%)	25.3 mths (0.4–72 mths)	~73%	—	—	~58%	
Clavel et al. [9]	IMRT	Yes	42 mths	75%			8% (2yrs)	
	2-3DRT	Yes	42 mths	77%			74% (2yrs)	
Vergeer et al. [20]†	IMRT	Yes (43%)	—				32% (6 mths)	27 Gy
	3D-CRT	Yes (35%)	—				56% (6 mths)	43 Gy
Chen et al. [21]*	IMRT	Yes (9%)	44 mths	87%			36%	
	3D-CRT	Yes (2%)	44 mths	89%			82%	
Nutting et al. [12]†	IMRT	Yes (43%)	44 mths	93%		71%	69%	36.5 Gy
	3D-CRT	Yes (40%)	44 mths	94%		91%	76%	61 Gy
Wong et al. [33]	IMRT	Yes (70%)	34 mths (9–50 mths)	67.4%			2.3%	30 Gy
Sultanem et al. [44]	IMRT	Yes (91%)	21.8 mths (5–49 mths)	97%			28%	
Su et al. [45]	IMRT	No	50.9 mths (12–104 mths)	73%		36%	15.4% (1yrs) 9.0% (2yrs)	31 Gy
Wang et al. [43]	IMRT	Yes (83%)	47.1 mths (11–68 mths)	33.3%		4.7%	12.3% (2yrs)	27.6 Gy

Table 2: Continued.

Study	Radiation treatment	Concurrent chemotherapy No. of patients (%)	Median followup (range)	Toxicity (≥GrII)				Mean parotid-gland dose
				Mucositis		Xerostomia		
				Acute	Late	Acute	Late	
Rades et al. [22]*	2DRT	Yes (8%)		~90%			73%	
	3D-CRT	Yes (23%)		~90%			63%	
	IMRT	Yes (6%)		~90%			17%	
Tham et al. [39]	IMRT	Yes	36.5 mths	29% (Gr3)		3% (Gr3)		
	IMRT	No	36.5 mths	20% (Gr3)				
Kim et al. [46]	3D-CRT	No	48 mths	57%			19%	
De Arruda et al. [32]†	IMRT	Yes (86%)	18 mths (8.4–76 mths)	92%		60%	33%	26.5 Gy

* Postoperative RT; † definitive and postoperative RT; all the rest: definitive RT.

Table 3: Synoptic table with ranges of treatment outcome and toxicity between IMRT versus conventional techniques.

RT	Treatment outcome					
	RC	LC	LRC	DMFS	DFS	OS
IMRT	85%–98%	78%–100%	70%–100%	57%–100%	57%–97.3%	63%–100%
2DRT-3DCRT	95%*	78%–85%	71%–93%	76.7%–98%	66%–91%	61%–95%
	Acute toxicity		Late toxicity			
	Mucositis	Xerostomia	Mucositis	Xerostomia		
IMRT	32%–100%	4.7%–75%	22%–79%	2.3%–69%		
2DRT-3DCRT	44%–94%	65%–91%	12%*	12%–82%		

* Available data from one study only.

patients suffer from xerostomia [17, 60–66]. A typical IMRT plan with parotid sparing technique for oral cavity carcinoma is shown in Figure 3. Furthermore, the direct comparison of dose volume histogram (DVH) for the right and left parotid gland between IMRT and 3DCRT is presented in Figure 4. The results clearly demonstrate the superiority of IMRT technique in terms of toxicity, mainly due to parotid-gland sparing.

In the literature, comparative studies showed differences regarding tumor control and toxicity profiles among the different radiotherapy techniques (IMRT versus 2-3D RT). In a recent study, Clavel et al. [9] reported superior outcomes (OS, DFS, and LRC) for IMRT patients treated with SIB compared to those treated with conventional radiation therapy techniques for locally advanced oropharyngeal cancer. On the other hand, the majority of the comparative studies demonstrate the equivalence of IMRT with the conventional radiation therapy techniques in regard to tumor control and survival for head and neck cancers [8, 10, 21–23]. In the study of Lee et al. [8], comparable treatment outcomes were observed for IMRT patients and patients treated with 2D conventional radiation therapy technique (2DRT) for locally advanced oropharyngeal carcinoma. Local control and survival appeared slightly superior for IMRT patients compared to 2DRT patients but this difference was statistically insignificant. Similar findings arising for head and neck cancers from the comparison between IMRT and 3DCRT confirm the equivalence in treatment outcomes of IMRT with conventional radiation therapy techniques [10, 18, 21, 23]. Rades et al. [22] compared treatments outcomes among IMRT, 3DCRT, and 2DRT for head and neck cancer patients treated with surgery followed by RT. Locoregional control

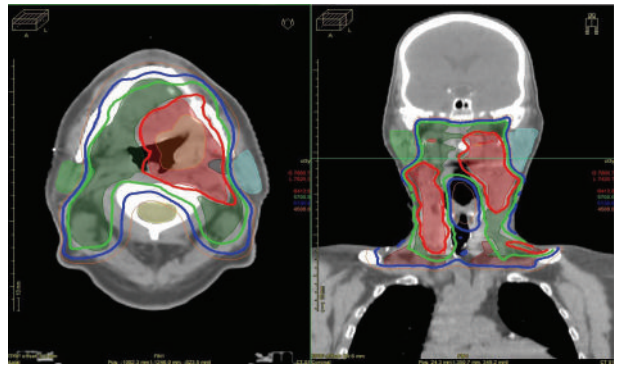

Figure 3: A typical IMRT plan with the parotid sparing technique for a carcinoma of the oral cavity. Three PTVs were contouring: primary site and all relevant lymph nodes as PTV1; primary site and clinical involved lymph nodes as PTV2; primary site only as PTV3. The technique used was integrated boost by means of 30 fractions with 1.8 Gy, 2 Gy, and 2.25 Gy per fraction by PTV1, PTV2, and PTV3, respectively (ONCENTRA, treatment planning). The isodoses shown are the 95% of the prescribed doses per PTV: 45% in orange; 51.3% in blue; 57% in green; 64,13% in red (personal archive).

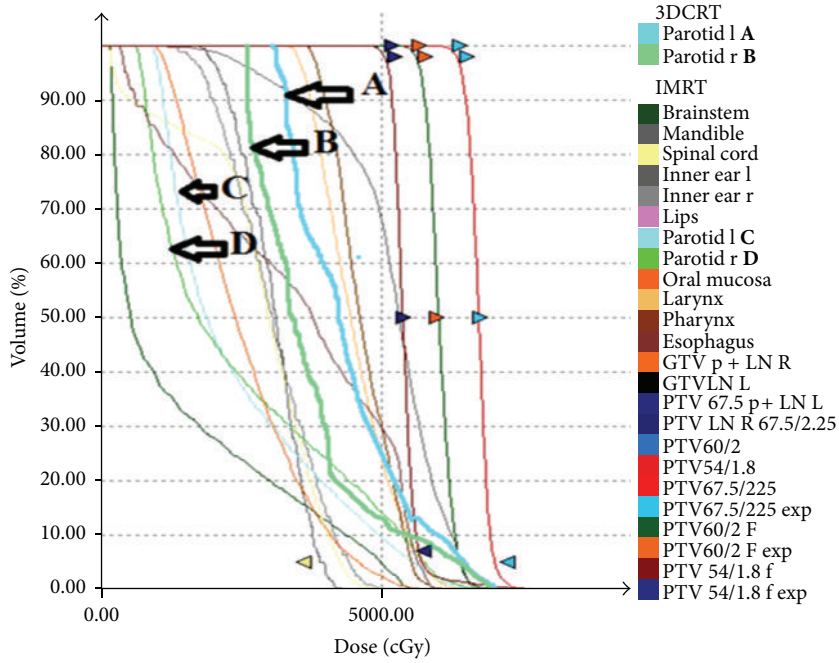

Figure 4: Comparison of the right and left parotid-gland DVHs of the same head and neck cancer patient (tumor site: oral cavity) for IMRT versus 3DCRT (3-dimensional conformal radiotherapy) technique. The arrows show the relevant DVHs for left and right parotid glands. **A** and **B** DVHs for parotids are shifted to the left (**C** and **D**) with IMRT techniques resulting in lower doses in the parotid glands (personal archive).

was similar for the three radiation techniques with IMRT being slightly superior.

As far as late toxicity is concerned, comparative studies report differences between IMRT and conventional RT techniques regarding patient-rated xerostomia [8, 9, 12, 18, 20–23]. Specifically, they demonstrate significantly less xerostomia for head and neck cancer patients treated with IMRT technique than for those treated with conventional radiotherapy techniques. In the studies of Lee et al. [8] and Lambrecht et al. [18], similar results of moderate to severe late xerostomia were observed (12% versus 67% and 23% versus 68% for IMRT and Conv RT, resp.). Clavel et al. [9] reported significant lower xerostomia for IMRT patients compared to those receiveing conventional radiotherapy techniques for locally advanced oropharyngeal carcinoma (IMRT versus conventional RT: 8%, 74%, resp.). Similarly in the study of Rades et al. [22], IMRT is associated with less xerostomia than 2-3D RT for head and neck cancers (17% versus 63% and 73%). Regarding acute toxicity, rates of mucositis for IMRT and conventional RT were reported in several studies [8, 9, 18, 20, 22, 23]. There are studies that demonstrate that patients receiving IMRT had acute toxicity comparable with those receiving 2-3D RT [8, 9, 21–23] while other studies reported that more head and neck cancer patients treated with conventional radiation therapy techniques suffered from acute mucositis compared to those treated with IMRT [18, 20].

In the case that our main concern is the reduction of xerostomia, then IMRT is the appropriate treatment option for head and neck cancer patients. However, when the main aspect is the tumor control or survival, we have to mention the lack of any randomized data to support a recommendation of IMRT over the conventional irradiation beam techniques in any head and neck site. Moreover, in our descriptive analysis, although there was a trend of better treatment outcome in favor of IMRT technique, no significant superiority was noted in terms of either overall survival or locoregional control rate. Definitely, a prospective randomized study comparing the two techniques stands in need.

5. Conclusion

The main conclusion of this study is that IMRT reduces late xerostomia compared with conventional three-dimensional conformal radiotherapy (3D-CRT) and conventional two-dimensional radiotherapy (2DRT). The trend of superiority of IMRT regarding the acute mucositis as well as the overall survival and the locoregional control should be mentioned. However, there is an absence of a clear statistical superiority of IMRT for the various tumor sites as far as tumor control and survival are concerned. A prospective randomized study exploring the potential clinical impact (treatment outcome and radiation-induced toxicity) of IMRT versus 2-3D RT stands in need in order to extract safe conclusions about the definitive superiority of IMRT for tumor control as well as for radiation morbidity. In a parallel way, a meta-analysis with raw data from all relevant publications might also give more definite results in terms of the final potential impact of IMRT for either survival or acute oral mucositis. However, the trend

of better treatment outcome in favor of IMRT deriving from our analysis should not be underestimated.

Conflict of Interests

The authors declare that they have no conflict if interests.

References

[1] G. Delaney, S. Jacob, and M. Barton, "Estimating the optimal radiotherapy utilization for carcinoma of the central nervous system, thyroid carcinoma, and carcinoma of unknown primary origin from evidence-based clinical guidelines," *Cancer*, vol. 106, no. 2, pp. 453–465, 2006.

[2] International Atomic Energy Agency, "Transition from 2-D Radiotherapy to 3-D Conformal and Intensity Modulated Radiotherapy," Tech. Rep. IAEA-TEC-DOC-1588, IAEA, Vienna, Austria, 2008.

[3] M. Bucci, P. Xia, N. Lee et al., "Intensity modulated radiation therapy for carcinoma of the nasopharynx: an update of the UCSF experience," *International Journal of Radiation Oncology, Biology, Physics*, vol. 60, pp. S317–S318, 2004.

[4] G. A. Ezzell, J. M. Galvin, D. Low et al., "Guidance document on delivery, treatment planning, and clinical implementation of IMRT: report of the IMRT subcommittee of the AAPM radiation therapy committee," *Medical Physics*, vol. 30, no. 8, pp. 2089–2115, 2003.

[5] C. Nutting, D. P. Dearnaley, and S. Webb, "Intensity modulated radiation therapy: a clinical review," *British Journal of Radiology*, vol. 73, no. 869, pp. 459–469, 2000.

[6] A. Eisbruch, "Intensity-modulated radiation therapy: a clinical perspective," *Seminars in Radiation Oncology*, vol. 12, no. 3, pp. 197–198, 2002.

[7] C.-S. Chui and S. V. Spirou, "Inverse planning algorithms for external beam radiation therapy," *Medical Dosimetry*, vol. 26, no. 2, pp. 189–197, 2001.

[8] N. Y. Lee, F. F. de Arruda, D. R. Puri et al., "A comparison of intensity-modulated radiation therapy and concomitant boost radiotherapy in the setting of concurrent chemotherapy for locally advanced oropharyngeal carcinoma," *International Journal of Radiation Oncology. Biology. Physics*, vol. 66, no. 4, pp. 966–974, 2006.

[9] S. Clavel, D. H. A. Nguyen, B. Fortin et al., "Simultaneous integrated boost using intensity-modulated radiotherapy compared with conventional radiotherapy in patients treated with concurrent carboplatin and 5-fluorouracil for locally advanced oropharyngeal carcinoma," *International Journal of Radiation Oncology. Biology. Physics*, vol. 82, no. 2, pp. 582–589, 2012.

[10] F.-M. Fang, C.-Y. Chien, W.-L. Tsai et al., "Quality of life and survival outcome for patients with nasopharyngeal carcinoma receiving three-dimensional conformal radiotherapy versus intensity-modulated radiotherapy—a longitudinal study," *International Journal of Radiation Oncology. Biology. Physics*, vol. 72, no. 2, pp. 356–364, 2008.

[11] A. M. Chen, B.-Q. Li, R. L. S. Jennelle et al., "Late esophageal toxicity after radiation therapy for head and neck cancer," *Head and Neck*, vol. 32, no. 2, pp. 178–183, 2010.

[12] C. M. Nutting, J. P. Morden, K. J. Harrington et al., "Parotid-sparing intensity modulated versus conventional radiotherapy in head and neck cancer (PARSPORT): a phase 3 multicentre randomised controlled trial," *The Lancet Oncology*, vol. 12, no. 2, pp. 127–136, 2011.

[13] J. A. Langendijk, P. Doornaert, I. M. Verdonck-de Leeuw, C. R. Leemans, N. K. Aaronson, and B. J. Slotman, "Impact of late treatment-related toxicity on quality of life among patients with head and neck cancer treated with radiotherapy," *Journal of Clinical Oncology*, vol. 26, no. 22, pp. 3770–3776, 2008.

[14] A. De Graeff, J. R. J. De Leeuw, W. J. G. Ros, G. J. Hordijk, G. H. Blijham, and J. A. M. Winnubst, "A prospective study on quality of life of patients with cancer of the oral cavity or oropharynx treated with surgery with or without radiotherapy," *Oral Oncology*, vol. 35, no. 1, pp. 27–32, 1999.

[15] E. Hammerlid and C. Taft, "Health-related quality of life in long-term head and neck cancer survivors: a comparison with general population norms," *British Journal of Cancer*, vol. 84, no. 2, pp. 149–156, 2001.

[16] E. Hammerlid, E. Silander, L. Hörnestam et al., "Health-related quality of life three years after diagnosis of head and neck cancer—a longitudinal study," *Head and Neck*, vol. 23, no. 2, pp. 113–125, 2001.

[17] K. S. C. Chao, J. O. Deasy, J. Markman et al., "A prospective study of salivary function sparing in patients with head-and-neck cancers receiving intensity-modulated or three-dimensional radiation therapy: initial results," *International Journal of Radiation Oncology. Biology. Physics*, vol. 49, no. 4, pp. 907–916, 2001.

[18] M. Lambrecht, D. Nevens, and S. Nuyts, "Intensity-modulated radiotherapy versus parotid-sparing 3D conformal radiotherapy. Effect on outcome and toxicity in locally advanced head and neck cancer," *Strahlentherapie und Onkologie*, vol. 189, no. 3, pp. 223–229.

[19] "Comparative Effectiveness and Safety of Radiotherapy Treatments for Head and Neck Cancer," no. 29, US Department of Health and Human Services, Agency for Healthcare Research and Quality, 2007.

[20] M. R. Vergeer, P. A. H. Doornaert, D. H. F. Rietveld, C. R. Leemans, B. J. Slotman, and J. A. Langendijk, "Intensity-modulated radiotherapy reduces radiation-induced morbidity and improves health-related quality of life: results of a non-randomized prospective study using a standardized follow-up program," *International Journal of Radiation Oncology. Biology. Physics*, vol. 74, no. 1, pp. 1–8, 2009.

[21] W.-C. Chen, T.-Z. Hwang, W.-H. Wang et al., "Comparison between conventional and intensity-modulated post-operative radiotherapy for stage III and IV oral cavity cancer in terms of treatment results and toxicity," *Oral Oncology*, vol. 45, no. 6, pp. 505–510, 2009.

[22] D. Rades, F. Fehlauer, J. Wroblesky, D. Albers, S. E. Schild, and R. Schmidt, "Prognostic factors in head-and-neck cancer patients treated with surgery followed by intensity-modulated radiotherapy (IMRT), 3D-conformal radiotherapy, or conventional radiotherapy," *Oral Oncology*, vol. 43, no. 6, pp. 535–543, 2007.

[23] T. Gupta, J. Agarwal, S. Jain et al., "Three-dimensional conformal radiotherapy (3D-CRT) versus intensity modulated radiation therapy (IMRT) in squamous cell carcinoma of the head and neck: a randomized controlled trial," *Radiotherapy and Oncology*, vol. 104, no. 3, pp. 343–348.

[24] G. Studer, U. M. Lütolf, and J. B. Davis, "IMRT in hypopharyngeal tumors," *Strahlentherapie und Onkologie*, vol. 182, no. 6, pp. 331–335, 2006.

[25] A. S. Garden, W. H. Morrison, P.-F. Wong et al., "Disease-control rates following intensity-modulated radiation therapy for small primary oropharyngeal carcinoma," *International Journal of Radiation Oncology. Biology. Physics*, vol. 67, no. 2, pp. 438–444, 2007.

[26] M. E. Daly, Q.-T. Le, P. G. Maxim et al., "Intensity-modulated radiotherapy in the treatment of oropharyngeal cancer: clinical outcomes and patterns of failure," *International Journal of Radiation Oncology. Biology. Physics*, vol. 76, no. 5, pp. 1339–1346, 2010.

[27] K. S. C. Chao, G. Ozyigit, A. I. Blanco et al., "Intensity-modulated radiation therapy for oropharyngeal carcinoma: impact of tumor volume," *International Journal of Radiation Oncology. Biology. Physics*, vol. 59, no. 1, pp. 43–50, 2004.

[28] K. Huang, P. Xia, C. Chuang et al., "Intensity-modulated chemoradiation for treatment of stage III and IV oropharyngeal carcinoma: the University of California-San Francisco experience," *Cancer*, vol. 113, no. 3, pp. 497–507, 2008.

[29] J. Setton, N. Caria, J. Romanyshyn et al., "Intensity-modulated radiotherapy in the treatment of oropharyngeal cancer: an update of the memorial sloan-kettering cancer center experience," *International Journal of Radiation Oncology. Biology. Physics*, vol. 82, no. 1, pp. 291–298, 2012.

[30] G. O. Schoenfeld, R. J. Amdur, C. G. Morris et al., "Patterns of failure and toxicity after intensity-modulated radiotherapy for head and neck cancer," *International Journal of Radiation Oncology. Biology. Physics*, vol. 71, no. 2, pp. 377–385, 2008.

[31] G. Sanguineti, G. B. Gunn, E. J. Endres, G. Chaljub, P. Cheruvu, and B. Parker, "Patterns of locoregional failure after exclusive IMRT for oropharyngeal carcinoma," *International Journal of Radiation Oncology. Biology. Physics*, vol. 72, no. 3, pp. 737–746, 2008.

[32] F. F. De Arruda, D. R. Puri, J. Zhung et al., "Intensity-modulated radiation therapy for the treatment of oropharyngeal carcinoma: the Memorial Sloan-Kettering Cancer Center experience," *International Journal of Radiation Oncology. Biology. Physics*, vol. 64, no. 2, pp. 363–373, 2006.

[33] F. C. S. Wong, A. W. Y. Ng, V. H. F. Lee et al., "Whole-field simultaneous integrated-boost intensity-modulated radiotherapy for patients with nasopharyngeal carcinoma," *International Journal of Radiation Oncology. Biology. Physics*, vol. 76, no. 1, pp. 138–145, 2010.

[34] D. L. W. Kwong, E. H. N. Pow, J. S. T. Sham et al., "Intensity-modulated radiotherapy for early-stage nasopharyngeal carcinoma: a prospective study on disease control and preservation of salivary function," *Cancer*, vol. 101, no. 7, pp. 1584–1593, 2004.

[35] S. L. Wolden, W. C. Chen, D. G. Pfister, D. H. Kraus, S. L. Berry, and M. J. Zelefsky, "Intensity-modulated radiation therapy (IMRT) for nasopharynx cancer: update of the Memorial Sloan-Kettering experience," *International Journal of Radiation Oncology. Biology. Physics*, vol. 64, no. 1, pp. 57–62, 2006.

[36] M. K. M. Kam, P. M. L. Teo, R. M. C. Chau et al., "Treatment of nasopharyngeal carcinoma with intensity-modulated radiotherapy: the Hong Kong experience," *International Journal of Radiation Oncology. Biology. Physics*, vol. 60, no. 5, pp. 1440–1450, 2004.

[37] I. W. K. Tham, S. Lin, J. Pan, L. Han, J. J. Lu, and J. Wee, "Intensity-modulated radiation therapy without concurrent chemotherapy for stage IIB nasopharyngeal cancer," *American Journal of Clinical Oncology*, vol. 33, no. 3, pp. 294–299, 2010.

[38] N. Lee, J. Harris, A. S. Garden et al., "Intensity-modulated radiation therapy with or without chemotherapy for nasopharyngeal carcinoma: radiation therapy oncology group phase II trial 0225," *Journal of Clinical Oncology*, vol. 27, no. 22, pp. 3684–3690, 2009.

[39] I. W.-K. Tham, S. W. Hee, R. M.-C. Yeo et al., "Treatment of nasopharyngeal carcinoma using intensity-modulated radiotherapy-the national cancer centre singapore experience," *International Journal of Radiation Oncology. Biology. Physics*, vol. 75, no. 5, pp. 1481–1486, 2009.

[40] N. Lee, P. Xia, J. M. Quivey et al., "Intensity-modulated radiotherapy in the treatment of nasopharyngeal carcinoma: an update of the UCSF experience," *International Journal of Radiation Oncology. Biology. Physics*, vol. 53, no. 1, pp. 12–22, 2002.

[41] W.-S. Liu, M.-C. Su, M.-F. Wu, H.-C. Tseng, and H.-C. Kuo, "Nasopharyngeal carcinoma treated with precision-oriented radiation therapy techniques including intensity-modulated radiotherapy: preliminary results," *Kaohsiung Journal of Medical Sciences*, vol. 20, no. 2, pp. 49–55, 2004.

[42] W. Luo, L. Ye, Z. Yu, Z. He, F. Li, and M. Liu, "Effectiveness of three-dimensional conformal radiotherapy for treating early primary nasopharyngeal carcinoma," *American Journal of Clinical Oncology*, vol. 33, no. 6, pp. 604–608, 2010.

[43] R. Wang, F. Wu, H. Lu et al., "Definitive intensity-modulated radiation therapy for nasopharyngeal carcinoma: long-term outcome of a multicenter prospective study," *Journal of Cancer Research and Clinical Oncology*, vol. 139, no. 1, pp. 139–145, 2013.

[44] K. Sultanem, H.-K. Shu, P. Xia et al., "Three-dimensional intensity-modulated radiotherapy in the treatment of nasopharyngeal carcinoma: the University of California-San Francisco experience," *International Journal of Radiation Oncology. Biology. Physics*, vol. 48, no. 3, pp. 711–722, 2000.

[45] S.-F. Su, F. Han, C. Zhao et al., "Long-term outcomes of early-stage nasopharyngeal carcinoma patients treated with intensity-modulated radiotherapy alone," *International Journal of Radiation Oncology. Biology. Physics*, vol. 82, no. 1, pp. 327–333, 2012.

[46] G. E. K. Gwi Eon Kim, J. Lim, H. C. P. Hee Chul Park et al., "A feasibility study using three-dimensional conformal boost technique in locally advanced carcinoma of the nasopharynx," *Acta Oncologica*, vol. 40, no. 5, pp. 582–587, 2001.

[47] A. Al-Mamgani, L. Tans, P. van Rooij, and P. C. Levendag, "A single-institutional experience of 15 years of treating T3 laryngeal cancer with primary radiotherapy, with or without chemotherapy," *International Journal of Radiation Oncology, Biology, Physics*, vol. 83, no. 3, pp. 1000–1006, 2012.

[48] G. Studer, R. A. Zwahlen, K. W. Graetz, B. J. Davis, and C. Glanzmann, "IMRT in oral cavity cancer," *Radiation Oncology*, vol. 2, no. 1, article 16, 2007.

[49] M. Yao, K. Chang, G. F. Funk et al., "The failure patterns of oral cavity squamous cell carcinoma after intensity-modulated radiotherapy—the university of iowa experience," *International Journal of Radiation Oncology. Biology. Physics*, vol. 67, no. 5, pp. 1332–1341, 2007.

[50] N. Y. Lee, W. O'Meara, K. Chan et al., "Concurrent chemotherapy and intensity-modulated radiotherapy for locoregionally advanced laryngeal and hypopharyngeal cancers," *International Journal of Radiation Oncology. Biology. Physics*, vol. 69, no. 2, pp. 459–468, 2007.

[51] D. Van Gestel, D. Van Den Weyngaert, D. Schrijvers, J. Weyler, and J. B. Vermorken, "Intensity-modulated radiotherapy in patients with head and neck cancer: a European single-centre experience," *British Journal of Radiology*, vol. 84, no. 1000, pp. 367–374, 2011.

[52] E. Peponi, C. Glanzmann, B. Willi, G. Huber, and G. Studer, "Dysphagia in head and neck cancer patients following intensity modulated radiotherapy (IMRT)," *Radiation Oncology*, vol. 6, no. 1, article 1, 2011.

[53] I. Toledano, P. Graff, A. Serre et al., "Intensity-modulated radiotherapy in head and neck cancer: results of the prospective study GORTEC 2004-03," *Radiotherapy and Oncology*, vol. 103, no. 1, pp. 57–62, 2012.

[54] M. Yao, K. J. Dornfeld, J. M. Buatti et al., "Intensity-modulated radiation treatment for head-and-neck squamous cell carcinoma—the University of Iowa experience," *International Journal of Radiation Oncology. Biology. Physics*, vol. 63, no. 2, pp. 410–421, 2005.

[55] A. W. M. Lee, S. Y. Tung, A. T. C. Chan et al., "Preliminary results of a randomized study (NPC-9902 Trial) on therapeutic gain by concurrent chemotherapy and/or accelerated fractionation for locally advanced nasopharyngeal carcinoma," *International Journal of Radiation Oncology. Biology. Physics*, vol. 66, no. 1, pp. 142–151, 2006.

[56] A. W. M. Lee, W. H. Lau, S. Y. Tung et al., "Preliminary results of a randomized study on therapeutic gain by concurrent chemotherapy for regionally-advanced nasopharyngeal carcinoma: NPC-9901 trial by the Hong Kong Nasopharyngeal Cancer Study Group," *Journal of Clinical Oncology*, vol. 23, no. 28, pp. 6966–6975, 2005.

[57] M. Al-Sarraf, M. LeBlanc, P. G. S. Giri et al., "Chemoradiotherapy versus radiotherapy in patients with advanced nasopharyngeal cancer: phase III randomized Intergroup study 0099," *Journal of Clinical Oncology*, vol. 16, no. 4, pp. 1310–1317, 1998.

[58] B. Baujat, H. Audry, J. Bourhis et al., "Chemotherapy in locally advanced nasopharyngeal carcinoma: an individual patient data meta-analysis of eight randomised trials and 1753 patients," *International Journal of Radiation Oncology. Biology. Physics*, vol. 64, pp. 47–56, 2006.

[59] A. Vissink, F. R. Burlage, F. K. L. Spijkervet, J. Jansma, and R. P. Coppes, "Prevention and treatment of the consequences of head and neck radiotherapy," *Critical Reviews in Oral Biology and Medicine*, vol. 14, no. 3, pp. 213–225, 2003.

[60] A. Maes, C. Weltens, P. Flamen et al., "Preservation of parotid function with uncomplicated conformal radiotherapy," *Radiotherapy and Oncology*, vol. 63, no. 2, pp. 203–211, 2002.

[61] A. Eisbruch, H. M. Kim, J. E. Terrell, L. H. Marsh, L. A. Dawson, and J. A. Ship, "Xerostomia and its predictors following parotid-sparing irradiation of head-and-neck cancer," *International Journal of Radiation Oncology. Biology. Physics*, vol. 50, no. 3, pp. 695–704, 2001.

[62] B. S. Henson, M. R. Inglehart, A. Eisbruch, and J. A. Ship, "Preserved salivary output and xerostomia-related quality of life in head and neck cancer patients receiving parotid-sparing radiotherapy," *Oral Oncology*, vol. 37, no. 1, pp. 84–93, 2001.

[63] M. W. Münter, C. P. Karger, S. G. Hoffner et al., "Evaluation of salivary gland function after treatment of head-and-neck tumors with intensity-modulated radiotherapy by quantitative pertechnetate scintigraphy," *International Journal of Radiation Oncology. Biology. Physics*, vol. 58, no. 1, pp. 175–184, 2004.

[64] A. I. Blanco, K. S. C. Chao, I. El Naqa et al., "Dose-volume modeling of salivary function in patients with head-and-neck cancer receiving radiotherapy," *International Journal of Radiation Oncology. Biology. Physics*, vol. 62, no. 4, pp. 1055–1069, 2005.

[65] M. B. Parliament, R. A. Scrimger, S. G. Anderson et al., "Preservation of oral health-related quality of life and salivary flow rates after inverse-planned intensity-modulated radiotherapy (IMRT) for head-and-neck cancer," *International Journal of Radiation Oncology. Biology. Physics*, vol. 58, no. 3, pp. 663–673, 2004.

[66] A. P. Jellema, P. Doornaert, B. J. Slotman, C. Rene Leemans, and J. A. Langendijk, "Does radiation dose to the salivary glands and oral cavity predict patient-rated xerostomia and sticky saliva in head and neck cancer patients treated with curative radiotherapy?" *Radiotherapy and Oncology*, vol. 77, no. 2, pp. 164–171, 2005.

Hindawi Publishing Corporation
BioMed Research International
Volume 2013, Article ID 657259, 6 pages
http://dx.doi.org/10.1155/2013/657259

Research Article

Effect of Adjuvant Magnetic Fields in Radiotherapy on Non-Small-Cell Lung Cancer Cells *In Vitro*

Jianguo Feng,[1,2] Huaying Sheng,[1,2] Chihong Zhu,[1,2] Hao Jiang,[1] and Shenglin Ma[3]

[1] *Cancer Research Institute, Zhejiang Cancer Hospital, No. 38 Guangji Road, Hangzhou, Zhejiang 310022, China*
[2] *Key Laboratory Diagnosis and Treatment Technology on Thoracic Oncology, Hangzhou, Zhejiang 310022, China*
[3] *Department of Oncology, Affiliated Hangzhou Hospital (Hangzhou First People's Hospital), Nanjing Medical University, No. 261 Huansha Road, Hangzhou 310006, China*

Correspondence should be addressed to Shenglin Ma; mashenglin65@gmail.com

Received 18 April 2013; Revised 12 July 2013; Accepted 12 July 2013

Academic Editor: Maria F. Chan

Objectives. To explore sensitization and possible mechanisms of adjuvant magnetic fields (MFs) in radiotherapy (RT) of non-small-cell lung cancer. *Methods*. Human A549 lung adenocarcinoma cells were treated with MF, RT, and combined MF-RT. Colony-forming efficiency was calculated, cell cycle and apoptosis were measured, and changes in cell cycle- and apoptosis-related gene expression were measured by microarray. *Results*. A 0.5 T, 8 Hz stationary MF showed a duration-dependent inhibitory effect lasting for 1–4 hours. The MF-treated groups had significantly greater cell inhibition than did controls ($P < 0.05$). Surviving fractions and growth curves derived from colony-forming assay showed that the MF-only, RT-only, and MF-RT groups had inhibited cell growth; the MF-RT group showed a synergetic effect. Microarray of A549 cells exposed for 1 hour to MF showed that 19 cell cycle- and apoptosis-related genes had 2-fold upregulation and 40 genes had 2-fold downregulation. MF significantly arrested cells in G_2 and M phases, apparently sensitizing the cells to RT. *Conclusions*. MF may inhibit A549 cells and can increase their sensitivity to RT, possibly by affecting cell cycle- and apoptosis-related signaling pathways.

1. Introduction

Lung cancer is a common malignant tumor, and its incidence is rapidly growing: 64% of patients with non-small-cell lung cancer (NSCLC) need radiotherapy (RT); 45% of these patients receive primary RT. Although RT and chemotherapy together have better therapeutic effects, patients often cannot tolerate the toxicity and side effects of the combination. Optimizing treatment result is therefore critical.

Magnetic fields (MFs) are biologically effective, and their effect on tumors has been studied since the 1970s [1–5]. Although the mechanism of how MFs affect tumors is unclear, they have been shown to inhibit cancer cell growth and induce apoptosis. Magnetic fields influence charged particles. As such, they interfere with interactions among molecules and electrons in cells and possibly harm cellular functions such as DNA synthesis, thereby inhibiting cancer cell division and growth [6]. Zhang et al. reported that a 3 Hz/picosecond electromagnetic pulse can apparently inhibit growth of cervical carcinoma Hela cells by raising intercellular Ca^{2+} concentration, inducing apoptosis, and increasing Bax protein expression while decreasing Bcl-2 expression (thus significantly increasing the Bax/Bcl-2 ratio) [7]. Lu et al. applied a low-frequency electromagnetic field on BEL-7402 hepatoma cells and found that expression of *SODD* and *Survivin* genes was significantly downregulated [8]. Wei et al. studied effects of rotational MFs combined with 5-fluorouracil (5-FU) on cell cycle and apoptosis in SP2/0 mouse myeloma cells, and found the S phase ratio was increased [9]. Magnetic fields alone cannot induce cell apoptosis, but they can sensitize cells to 5-FU toxicity, thus facilitating 5-FU-induced apoptosis. Liu et al. claimed that strong magnetic pulses significantly inhibited growth and exacerbated apoptosis in BIU-87 bladder carcinoma cells [10]. Pan et al. used microarray to measure and analyze the apoptosis-related gene-expression profile in MF-processed BEL-7402 hepatoma cells and L-02 fetus liver cells [11]. Electromagnetic field-processed cells upregulated expression

Table 1: Inhibition rates under different magnetic field durations.

Magnetic field duration (h)	Absorbance (OD value)	Inhibition rate (%)
Control	1.120 ± 0.089	0.0
1 h	1.032 ± 0.059	7.9
2 h	1.025 ± 0.065	8.5
3 h	0.990 ± 0.087	11.6
4 h	0.985 ± 0.098	12.1

of apoptosis-inducing genes and downregulated expression of apoptosis-inhibiting genes. Han et al. used pulse MFs to study drug resistance in HL60/ADR leukemia cells [12]. Pulse MFs could downregulate MRP1 gene and protein expression, while increasing accumulation of cellular Rg123, and reverse multidrug resistance in leukemia cells.

Preliminary research showed that MFs, alone or together with chemotherapy, can inhibit tumor cell proliferation. However, few studies of MFs combined with RT in lung cancer are reported. We hypothesized that cell-cycle changes induced by MFs sensitize lung cancer cells to radiation. In this study, we designed experiments to measure the effect of adjuvant MFs in chemotherapy on colony formation, cell cycle, and apoptosis in A549 cells. Microarray was employed to elucidate the molecular and cellular mechanisms.

2. Materials and Methods

2.1. Cell Lines and Reagents. Lung adenocarcinoma cell line A549 was provided by Zhejiang Cancer Hospital. Cells were cultured in RPMI1640 media with 10% bovine serum and kept in an incubator at 5% CO_2 and 37°C to promote growth. RPMI1640 was purchased from Gibco-BRL; bovine serum was purchased from HyClon.

2.2. Magnetic Field Duration and Radiation Dose. The inhibition rate was estimated by MTT assay to determine the duration of the MF effect. Using earlier research [13], 4 Gy was chosen as the radiation dose. Cells were transferred into 96-well plates at 500 cells/well and cultured for 24 hours. Four 8-well groups of cells were exposed to 0.5 T stationary MFs for 1, 2, 3, or 4 hours. After 48 hours, 20 μL 5 mg/mL MTT was added into each well. After culturing for another 4 hours, supernatant was disposed, and 200 μL was added into each well. After another 30 minutes, when brown crystals were completely dissolved, absorbance (AB) of each well was measured by enzyme-linked immunosorbent assay with 550 nm absorption wavelength. Inhibition rate of cell growth was calculated as [(Experimental AB − background control AB)/(Control AB − background control AB)] × 100%.

2.3. Colony-Forming and Surviving Curve Assay. Cells in logarithmic growth phase were digested into single-cell suspensions which were diluted and transferred into 6-well plates with 400 cells per well. After 24-hour adherent culturing, all cells were divided into 12 groups, each consisting of one plate of cells: one control group, five RT-only groups (2, 4, 6, 8, or 10 Gy), one MF-alone group (0.5 T, 8 Hz for 1 hour), and five MF-RT combination groups (0.5 T, 8 Hz for 1 hour; plus 2, 4, 6, 8, or 10 Gy). Colonies were counted after 10-hour culture. Colony-forming efficiency (CE) and surviving fraction (SF) were calculated with the following equations:

$$\mathrm{CE} = \frac{\text{Colonies observed}}{\text{Number of cells plated}}, \qquad \mathrm{SF} = \frac{\text{CE of treated group}}{\text{CE of control group}}. \tag{1}$$

Survival curves were drawn using multitarget single-hit models and linear quadratic models with SigmaPlot 10.0 software.

2.4. Superarray Gene Chip Assay. Cells at logarithmic growth phase were digested into single-cell suspensions, which were diluted and transferred into 75 mL culture flasks with 1×10^5 cells per flask. After 24-hour adherent culturing, three flasks of cells were exposed to 0.5 T, 8 Hz MF for 1 hour, and three bottles of cells were used as controls. After another 24 hours of culturing, RNA was extracted for gene chip assays for each group.

2.5. Cell Cycle and Apoptosis Assay. Cells in logarithmic growth phase were digested into single cell suspensions, which were diluted and transferred into 25 mL culture flasks with 5×10^4 cells per flask. Cells were randomly divided into four groups: controls, MF-only group (0.5 T), RT-only group (4 Gy), and combination group (0.5 T + 4 Gy). Each group provided three parallel flasks for collection at 24, 48, and 72 hours separately. Cell cycle and apoptosis rates were measured by flow cytometry with an ABC cell cycle kit (BD Biosciences) and an Annexin V-FITC apoptosis detection kit.

2.6. Data Analysis. SPSS 11.0 software was used for statistical analysis. Measurement data are expressed as mean ± standard deviation. Different groups were compared using one-way ANOVA. $P < 0.05$ was considered statistically significant.

3. Results

3.1. Inhibition Rates under Different Magnetic Field Durations Measured with MTT Assay. The inhibitory effect of a 0.5 T, 8 Hz stationary MF lasts for 1–4 hours, in a duration-dependent manner (Table 1). Although the inhibitory effect did not significantly differ with magnetic duration ($P > 0.05$), MF-treated groups had significantly greater cell inhibition than the control group ($P < 0.05$).

Table 2: Upregulated genes in A549 after 1-hour exposure to MF.

Position	Genebank	Gene name	Fold change
138	NM_003824	FADD	5.64
278	NM_006297	XRCC1	4.32
89	NM_001260	CDK8	3.42
225	NM_003839	Rank	3.11
199	NM_000963	Cox-2	2.87
261	NM_003300	CRAF1	2.81
236	NM_000043	Fas/Apo-1/CD95	2.56
227	NM_003790	DR3/Apo3	2.52
63	NM_053056	Cyclin D1	2.48
62	NM_005190	Cyclin C	2.45
244	NM_003809	TNFSF12/APO3L	2.37
43	NM_003723	Caspase 13	2.26
44	NM_012114	Caspase 14	2.14
58	NM_003914	Cyclin A1	2.12
182	NM_002392	Mdm2	2.08
61	NM_004701	Cyclin B2	2.08
70	NM_004354	Cyclin G2	2.05
48	NM_004347	Caspase-5	2.03
64	NM_001759	Cyclin D2	2.00

3.2. Colony-Forming Efficiency and Surviving Curve. The colony-forming assay showed that, for RT-only groups at 2, 4, 6, 8, and 10 Gy, the CEs were 16.4%, 13.2%, 10.2%, 7.1%, and 1.2%, respectively; SFs were 0.77, 0.62, 0.48, 0.33, and 0.24, respectively. For MF-RT combined groups at 2, 4, 6, 8, and 10 Gy, CEs were 13.7%, 8.1%, 3.3%, 1.3%, and 0.4%, respectively, and SFs were 0.64, 0.38, 0.15, 0.06, and 0.02, respectively. Cell survival decreased significantly ($P < 0.05$) with increasing RT dose in both RT groups and combination groups. Among groups with the same RT dose, the group with adjuvant MFs had a significantly smaller SF ($P < 0.05$), which suggests that A549 cells are more sensitive to RT with adjuvant MFs application. Survival curves are shown in Figure 1.

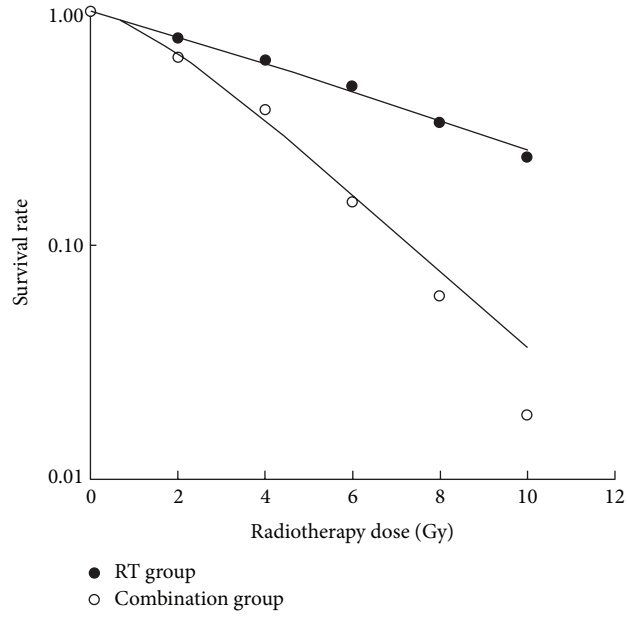

Figure 1: Cell survival rate after treatment with different dose of radiotherapy.

3.3. Gene Chip Assay. The microarray showed that after 1-hour exposure to MFs, 19 cell cycle- and apoptosis-related genes in the A549 cells had 2-fold upregulation, and 40 genes had 2-fold downregulation (Tables 2 and 3). In particular, *TNFRSF21* and CASPASE had significant upregulation, whereas expressions of *ATM*, *p53*, *p57*, *p21*, *p27*, *TNFSF12*, *TNFRSF10D*, *BAG4*, *BCL2L2*, *Mdn2*, and *XRCC1–5* were downregulated.

3.4. The Alternation of Cell Cycle and Apoptosis. Flow cytometry results showed that the MF-only group had G_2-M phase arrest. Percentages of MF-only cells at G_2-M were 24.2% for collection at 24 hours, 28.4% at 48, hours and 18.5% at 72 hours—all significantly different from the control group. The MF-only group showed no significant difference in apoptosis index compared with the control group. Both the RT-only group and the MF-RT combination group showed significant apoptosis; however, the apoptosis index of combination group was 34.6 for collection after 24 hours, which was significantly higher than that of the RT-only group (Figure 2).

4. Discussion

Repair of DNA double-strand breaks (DSBs) and cell-cycle regulation are two important factors that influence RT sensitivity of cells. ATM plays a very important role in DSB

Table 3: Downregulated genes in A549 after 1-hour exposure to MF.

Position	Genebank	Gene name	Fold change
228	NM_003820	TNFRSF14	0.03
246	NM_006573	TNFSF13B	0.09
264	NM_004620	TRAF6	0.12
96	NM_001800	p19-INK4D	0.14
232	NM_001066	TNFR2/p75	0.15
86	NM_000075	Cdk4	0.17
90	NM_000389	P21/Waf1/CIP1	0.18
221	NM_003844	TRAIL-R/DR4	0.20
88	NM_001799	CDK7	0.21
128	NM_001950	E2F-4	0.21
229	NM_001192	TNFRSF17	0.22
76	NM_004358	CDC25B	0.23
127	NM_001949	E2F-3	0.23
282	NM_021141	KU80	0.26
130	NM_001952	E2F-6	0.27
135	NM_005236	XPF	0.33
204	NM_000321	Rb	0.34
114	NM_000499	CYP1A1	0.34
262	NM_004295	TRAF-4	0.35
122	NM_004402	DFF40/CPAN	0.36
26	NM_004050	Bcl-w	0.38
279	NM_005431	XRCC2	0.41
7	NM_000051	ATM	0.41
17	NM_001188	Bak	0.41
132	NM_001983	ERCC1	0.42
22	NM_000633	Bcl-2	0.42
208	NM_003804	RIP	0.43
126	NM_004091	E2F-2	0.43
142	NM_001924	GADD45	0.44
91	NM_004064	p27Kip1	0.44
71	NM_001239	Cyclin H	0.45
27	NM_005178	BCL-3	0.45
281	NM_003401	XRCC4	0.46
256	NM_000546	p53	0.46
129	NM_001951	E2F-5	0.48
242	NM_003810	TRAIL	0.48
125	NM_005225	E2F	0.48
240	NM_001561	4-1BB	0.49
224	NM_003840	TRAIL-R4/DcR2	0.49
220	NM_000594	TNFA	0.50

repair and cell cycle regulation signaling pathways. ATM activates the G_1-S checkpoint by activating p53 and p21 genes; it activates S phase and G_2-M checkpoints by activating the chk1, chk2, cdc25, and cdc2 genes [14]. When ATM expression is deficient or decreased, cell cycle checkpoints are dysfunctional, and cell cycle arrest is hindered. Thus, ATM expression and activity are related to RT sensitivity of cells [15]. In a study of sensitivity of nasopharyngeal carcinoma cell CNE-1 to RT, Hui et al. found that an RT sensitizing agent, UCN-01, works by weakening the cell's self-repair capability, and UCN-01 can only sensitize cells with *p53* deficiency. Cyclin-dependent kinase inhibitor 1C (CDKN1C; p57, Kip2), which belongs to Cip/Kip family, can inhibit multiple G_1 cyclin/Cdk complexes and induce G_1 arrest, thus inhibiting cell proliferation. CDKN1A (p21, Cip1) can inhibit CDK2 or CDK4 complexes and regulate the cell cycle. CDKN1A is regulated by p53 and can arrest cell in G_1 phase under activating circumstances. CDKN1B (p27, Kip1), which encodes a CDK-inhibitor protein, can inhibit activation of cyclin E/CDK2 or cyclin D/CDK4 complexes and arrest the G_1 phase as

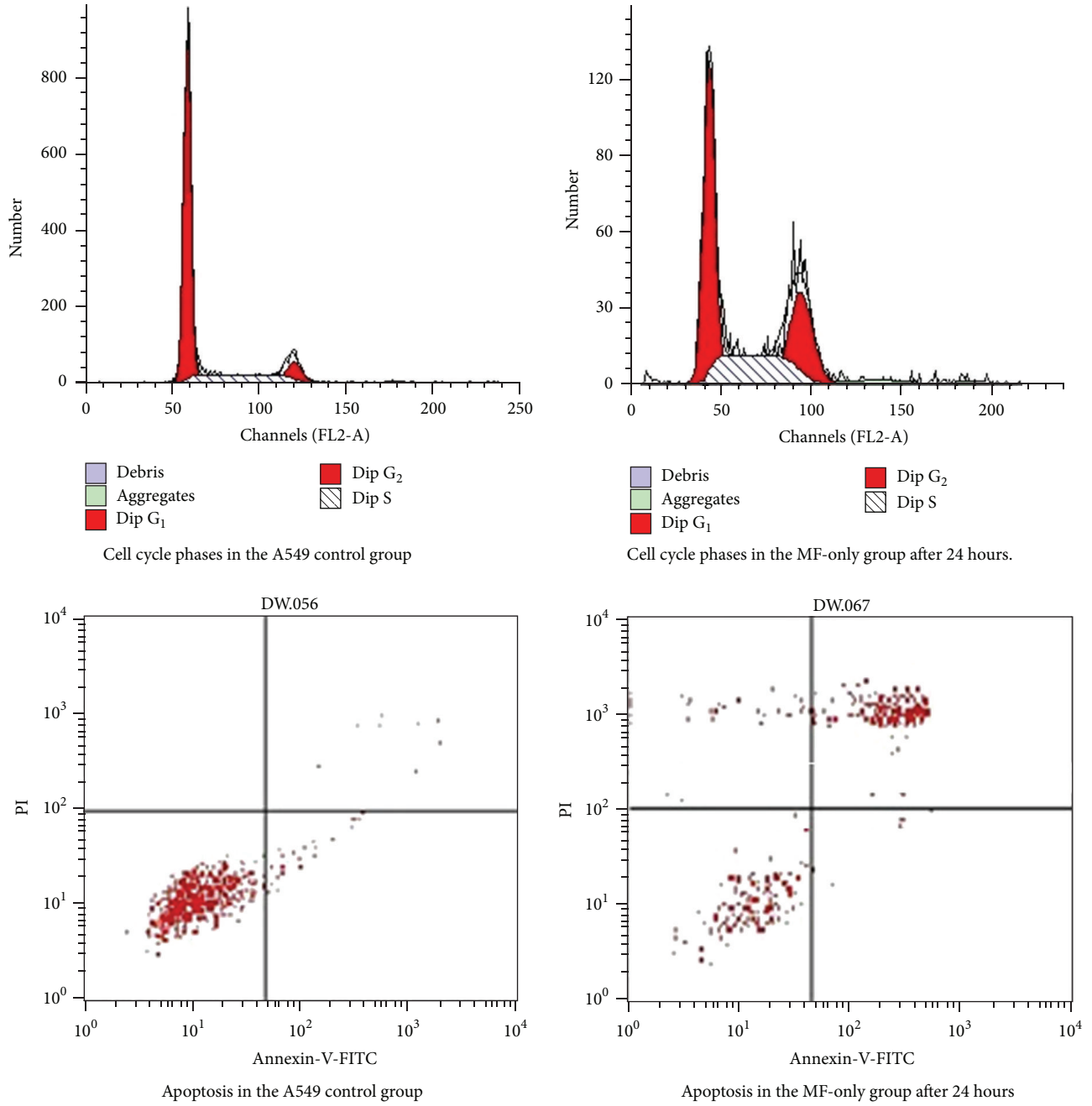

Figure 2: Changes in cell cycle and apoptosis.

well. TNFSF12, which belongs to TNF superfamily, can combine with the FN14/TWEAKR cytokine receptor, thus inducing apoptosis through multiple cell death pathways, and promote endothelial cell proliferation and migration (which are related to angiogenesis). TNFRSF21, whose functional domain activates the NF-κB and MAPK8/JNK pathways, also induces apoptosis. However, TNFRSF10D does not induce apoptosis and has been shown to play an inhibitory role in TRAIL-induced cell apoptosis. BAG4 is a member of the BAG1-related protein family. BAG4 is an antiapoptosis protein; it can interact with multiple apoptosis- and cell growth-related proteins, including BCL-2, Raf kinase, steroid receptor, growth factor receptor, and heat shock protein; it combines with TNFR1 and death receptor 3 to negatively regulate the downstream death signaling pathway. BCL2L2 belongs to the bcl-2 family; its expression induces apoptosis under cellular toxic environment. Mdn2 protein combines with and deactivates p53 and RB proteins, and it negatively regulates the *p53* gene. X-ray repair cross-complementing gene (*XRCC*) is a major mediator of mammalian gene repair [16]. XRCC1, XPD, and XRCC3 proteins are the important components of BER, NER, and DSBR, respectively. XRCC1 repairs DNA single-strand breaks, induced by RT or alkylation agents, and works with DNA ligase III, polymerase

beta, and poly(ADP-ribose) polymerase, involved in the BER pathway. XRCC2 and XRCC3 mediate RecA/Rad51-related proteins involved in homologous recombination to maintain chromosome stability and repair of double-strand breaks in DNA damage.

The gene chip results showed that, after MF exposure of A549 cells, the apoptosis-inducing gene TNFRSF21 was upregulated, as were several other apoptosis-related genes (e.g., ATM, p53, p57, p21, p27, TNFSF12, TNFRSF10D, BAG4, BCL2L2, Mdn2, and XRCC1–5). The upregulation of TNFRSF21 activated NF-κB and APK8/JNK pathways and induced apoptosis. Cellular sensitivity to RT is related to apoptosis rate [17]; higher apoptosis levels indicate higher sensitivity to RT, and rapidly apoptotic cells are more sensitive to RT. Conversely, downregulation of ATM and p53 increases apoptosis; downregulation of p57, p21, and p27 weakens cell-cycle arresting function, thus inducing apoptosis; downregulation of antiapoptotic genes (TNFSF12, TNFRSF10D, BAG4, BCL2L2, and Mdn2) also induces apoptosis. Downregulation of XRCC1–5 also weakens DNA repair function, thus leading to cell death and weakened proliferative capacity.

Our study showed that, for a 0.5 T, 8 Hz stationary MF, duration had no significant effect ($P > 0.05$); however, groups treated with MF had significantly greater cell inhibition than controls ($P > 0.05$). The surviving fraction and growth curve derived from the colony-forming assay showed that MF-only, 4 Gy RT-only and the MF-RT combination groups had inhibited cell growth; the combination group in particular showed a synergetic effect ($P > 0.01$). The microarray showed that after A549 cells were exposed for 1 hour to MFs, 19 cell cycle- and apoptosis-related genes had 2-fold upregulation, especially TNFRSF21 and CASPASE, and 40 genes, including ATM, p53, p57, p21, p27, TNFSF12, TNFRSF10D, BAG4, BCL2L2, Mdn2, and XRCC1–5, had 2-fold downregulation. Magnetic fields significantly arrested cells in the G_2 and M phases, which are the RT-sensitive phases; in this case, the cells were sensitized to RT. This study explored this sensitization effect and possible mechanisms of adjuvant MFs with RT on NSCLC at cellular and gene levels. Further study is needed to further clarify these mechanisms.

Acknowledgments

This work was supported by the Natural Science Foundation of Zhejiang Province (LY13H160028), Science and Technology Department of Zhejiang Province Key Scientific Research Projects for Social Development (2006C23018), and Zhejiang Provincial Medicine and Health Science Fund (2013KYA028).

References

[1] H. Chang, G. Li, G. Wang et al., "Report of 18 cases of the magnetic field therapy for malignant tumor," in *Biomedical Physics Research*, p. 74, Wuhan University Press, Wuhan, China, 1990.

[2] X. Xu, "Clinical observations of magnetotherapy on 10 patients with advanced malignancies," *Chinese Biomagnetism*, vol. 2, no. 1, p. 45, 1988.

[3] W. Zhao, "Four cases study on the lymphatic tumor treatment with the combination of gyromagnetic field and traditional Chinese medicine," *Chinese Biomagnetism*, vol. 5, no. 3-4, p. 124, 1991.

[4] H. Zhang, X. Zhang, C. Zhang et al., "Progress on the malignant tumor treatment with pulsed electromagnetic fields," Biomedical physics research. Atomic Energy Press, 19, 1992.

[5] F. Li, Q. Liu, Y. Ma et al., "Preliminary reports on the radioactive treatment of nasopharyngeal carcinoma with magnetic field," *Chinese Biomagnetism*, vol. 6, no. 1, p. 20, 1992.

[6] F. Zeng, "Experimental observation of the power-frequency magnetic field effects on mouse tumor," *Biomagnetism*, vol. 3, no. 4, p. 20, 1999.

[7] Y. Zhang, Z. Xiong, Y. Hua et al., "*In vitro* study of damaging effects of intense picosecond pulsed electric field on HeLa cells," *Chongqing Medicinal Journal*, vol. 41, no. 18, pp. 1785–1791, 2012.

[8] X. Lu, W. Qian, C. Xia et al., "Effects of ELF on gene expression of SODD and Survivin in hepatoma cell lines," *Journal of Soochow University*, vol. 31, no. 5, pp. 723–726, 2011.

[9] S. Wei, C. Zhang, X. Sha et al., "Effect of rotary magnetic field combining 5-fluorouracil on cell cycle and apoptosis in SP2/0 cell line," *Cancer Research on Prevention and Treatment*, vol. 37, no. 12, pp. 1367–1369, 2010.

[10] Q. Liu, Y. Ma, J. Li et al., "Effects of high pulsed magnetic field on apoptosis of human bladder cancer BIU-87 cells," *Journal of Clinical Urology*, vol. 25, no. 7, pp. 550–552, 2010.

[11] J. Pan, W. Zhao, J. Wen et al., "Effects of electromagnetic field on gene expression associated with cellular proliferation and apoptosis in hepatoma cell lines," *Jiangsu Medical Journal*, no. 6, pp. 637–639, 2009.

[12] Q. Han, X. Liu, Y. Han et al., "Mechanism of pulsed magnetic field on reversal of multi-drug resistance of the leukemic cell HL60/ADR," *Progress in Modern Biomedicine*, vol. 9, no. 1, pp. 1–4, 2009.

[13] H. Jiang, S. Ma, and J. Feng, "*In vitro* study of radiosensitization by β-Elemene in A549 cell line from adenocarcinoma of lung," *Chinese Journal of Radiological Medicine and Protection*, vol. 29, no. 04, pp. 395–396, 2009.

[14] P. J. McKinnon, "ATM and ataxia telangiectasia. Second in molecular medicine review series," *EMBO Reports*, vol. 5, no. 8, pp. 772–776, 2004.

[15] M. B. Kastan, D.-S. Lim, S.-T. Kim, and D. Yang, "ATM-a key determinant of multiple cellular responses to irradiation," *Acta Oncologica*, vol. 40, no. 6, pp. 686–688, 2001.

[16] J. Thacker and M. Z. Zdzienicka, "The mammalian XRCC genes: their roles in DNA repair and genetic stability," *DNA Repair*, vol. 2, no. 6, pp. 655–672, 2003.

[17] X. Xu and S. Yu, *Modern Radiation Oncology*, people's Military Medical Press, Peking, China, 2000.

Hindawi Publishing Corporation
BioMed Research International
Volume 2013, Article ID 568597, 6 pages
http://dx.doi.org/10.1155/2013/568597

Research Article

Development of a Modelling to Correlate Site and Diameter of Brain Metastases with Hippocampal Sparing Using Volumetric Modulated Arc Therapy

Silvia Chiesa,[1] Mario Balducci,[1] Luigi Azario,[2] Simona Gaudino,[3] Francesco Cellini,[4] Gian Carlo Mattiucci,[1] Cesare Colosimo,[3] and Vincenzo Valentini[1]

[1] *Department of Radiation Oncology, Università Cattolica del Sacro Cuore, Largo Agostino Gemelli, 8, 00168 Roma, Italy*
[2] *Department of Medical Physics, Università Cattolica del Sacro Cuore, Largo Agostino Gemelli, 8, 00168 Roma, Italy*
[3] *Department of Radiology, Università Cattolica del Sacro Cuore, Largo Agostino Gemelli, 8, 00168 Roma, Italy*
[4] *Department of Radiation Oncology, Campus Bio-Medico, 00155 Roma, Italy*

Correspondence should be addressed to Silvia Chiesa; silvia.chiesa@ymail.com

Received 15 June 2013; Revised 29 August 2013; Accepted 13 September 2013

Academic Editor: Tsair-Fwu Lee

Purpose. To correlate site and diameter of brain metastases with hippocampal sparing in patients treated by RapidArc (RA) technique on whole brain with simultaneously integrated boost (SIB). *Methods and Materials*. An RA plan was calculated for brain metastases of 1-2-3 cm of diameter. The whole brain dose was 32.25 Gy (15 fractions), and SIB doses to brain metastases were 63 Gy (2 and 3 cm) or 70.8 Gy (1 cm). Plans were optimized and evaluated for conformity, target coverage, prescription isodose to target volume, homogeneity index, and hippocampal sparing. *Results*. Fifteen brain lesions and RA plan were generated. Hippocampal volume was 4.09 cm^3, and hippocampal avoidance volume was 17.50 cm^3. Related to site of metastases, the mean hippocampal dose was 9.68 Gy^2 for occipital lobe, 10.56 Gy^2 for frontal lobe, 10.56 Gy^2 for parietal lobe, 10.94 Gy^2 for deep brain structures, and 40.44 Gy^2 for temporal lobe. The mean hippocampal dose was 9.45 Gy^2, 10.15 Gy^2, and 11.70 Gy^2 for diameter's metastases of 1.2 and 3 cm, respectively, excluding results relative to temporal brain lesions. *Conclusions*. Location more than size of metastases can adversely influence the hippocampus sparing. Further investigation is necessary to meet definitive considerations.

1. Introduction

Brain metastases are the most common intracranial tumor in adults [1]. Current treatment modalities include whole brain radiotherapy (WBRT), surgery, stereotactic radiosurgery (SRS), and chemotherapy. Whole brain radiotherapy is usually the primary treatment option for patients with multiple brain metastases, while its role remains discussed in oligometastatic patients [2].

Many studies reported serious and permanent late side effects after WBRT [3, 4].

Recent clinical studies suggest that deficits in learning, memory, and spatial information processing are related to hippocampal damage [5].

Monje et al. hypothesized that memory function is associated with the pyramidal and granule cells located in the dentate gyrus of the hippocampus [6].

Modest radiation doses cause apoptosis decline in neurogenesis in the subgranular zone and then the extinction of short-term memory [7–9].

On the other hand Li et al. [10] observed that tumor shrinkage was significantly correlated with preservation of executive function and fine motor coordination.

Ghia et al. [11] analyzed the distribution of brain metastases and observed that only 3.3% of intracranial metastases were located within 5 mm of the hippocampus; they concluded that it is reasonable to exclude this structure from WBRT when it is not involved by disease.

Modern IMRT techniques allow to deliver highly conformal dose distribution.

Several authors tested the feasibility of treating the whole brain to full dose sparing the hippocampus, using helical tomotherapy or volumetric modulated arc therapy by LINAC,

(RA or VMAT) [12]. But given the complexity of the limbic circuit and the difficulty in delineating the hippocampus on cross-sectional imaging, the peculiar features of treatment plan optimization, and physics quality assurance, this treatment may be complex and time consuming and may need of expertise.

Primary endpoint of this study was to investigate the impact of location and size of brain metastases on the feasibility of reducing the mean hippocampal dose using VMAT-RA technique; secondary endpoint was to verify if our mean hippocampal dose was close to that obtained by other investigators.

2. Methods and Materials

A model of 3 metastatic lesions for each lobe, placed in the centre of the lobe, of 1-2-3 cm of diameter was developed. A total of 15 lesions were contoured using a CT simulation scan of an adult patient.

2.1. Acquisition Image and Fusion. Patient was positioned supine in a custom-made mask and underwent a noncontrast CT simulation scan of the entire head region with 1.25 mm slice thickness (1.00 mm slice by reconstruction). The patient underwent three-dimensional spoiled gradient axial magnetic resonance imaging (MRI) scans (3D-SPGR), with standard axial and coronal fluid attenuation recovery (FLAIR), axial T2-weighted and gadolinium contrast-enhanced T1-weighted sequence acquisitions with a 1.00 mm slice thickness.

The CT images were coregistered to a gadolinium-enhanced, T1 weighted, and magnetization preparer rapid gradient-echo axial RM.

2.2. Contouring. Anatomic structures were delineated on the coregistered CT-MRI axial image sets using Varian Eclipse External Beam Planning System, version 8.9 (Varian Medical Systems).

Hippocampus, brain lobes, and deep brain structures were contoured manually with a neuroradiologist on T1-weighted MRI axial sequences according to several atlas of neuroanatomy and to guidelines [12, 13].

The hippocampus was contoured on T1-weighted MRI axial sequences, giving the preponderance of gray matter in the hippocampus, contouring focused on the T1-hypointense signal medial to the temporal horn and distinct from the T1-hyperintense parahippocampal gyrus and fimbriae, located inferomedial and superomedial to the hippocampus, respectively. Contouring began at the most caudal extent of the crescentic-shaped floor of the temporal horn and continued posterocranially along the medial edge of the temporal horn. The medial border of the hippocampus was delineated by the edge of the T1-hypointensity up to the ambient cistern. The uncal recess of the temporal horn served to distinguish the hippocampus from the gray matter of the amygdala, lying anterior and superior to the hippocampus. The postero-cranial extent of the hippocampus was defined by the curvilinear T1-hypointense hippocampal tail located just antero-medially to the atrium of the lateral ventricle. Contours terminated at the lateral edges of the quadrigeminal cisterns, before the emergence of the crus of the fornix.

Brain lobes and critical deep structures included thalamus and basal ganglia, and a single volume, separated from the lobe volumes, was generated.

The organs at risk included the eyes (whole globe and separate lenses' eye), brainstem, optic nerves, optic chiasm, and hippocampus.

Metastatic lesions were adapted to a spheroid as the metastases' shape. They were drawn in brain lobes and in the deep brain structures. The centre of these spheroids was allocated in the gravity centre of each lobe and deep brain parenchyma; it is considered a geometric representative point of whole lobe's volume. This was obtained by simulating a 3D conformal radiotherapy plan in which the target volume was represented by the lobe or deep brain contoured. On the coordinates x, y, z of the gravity centre, we contoured by brush tool circles of 1-2-3 cm of diameter. These diameters were selected according to the inclusion criteria for stereotactic therapy. Using Pythagoras' theorem we created on up and down slice, a correspondent circumference until to obtain the spheroid with selected diameter; they represented the gross tumor volume (GTV) (Figure 1).

A 5 mm volumetric margin expansion was applied to the hippocampus.

A planning target volume for each metastasis (PTV_{mts}) was outlined using a computer-automated 2 mm 3D margin expansion. The PTV_{mts} was used for concomitant integrated boost. A whole brain planning target volume (PTV_{WB}) was generated by subtracting the PTV_{mts} and the hippocampus avoidance structure from the whole brain contour.

2.3. Planning. The prescription doses were 32.25 Gy to 95% of the volume of PTV_{WB}, 63 Gy to 95% of the volume of metastases with diameter of 2.0 and 3.0 cm, and 70.8 Gy to 95% of the volume with diameter of 1.0 cm; the dose was delivered in 15 fractions. We used the schedule of Hsu et al. [14] to compare our level of dose to hippocampus using the same technique.

Dose calculations for RA optimization were performed using Varian Eclipse external Beam Planning System, version 8.9 with the AAA algorithm for dose calculation with PRO2 optimization system. The RA plans consisted of a single arc, starting at a gantry angle of 179 and rotating counterclockwise through 358 to stop at a gantry angle of 181. The falloff was 0.2. During optimization multileaf collimator (MLC)-shaped fields are progressively added throughout the arc. The gantry rotation speed and monitor units (MU) per gantry angle degree were optimized for a variable dose rate plan with a maximum dose rate of 400 MU/min, and the nominal energy of photons was 6 MV. During planning, the user defines the prescription dose to the target structures and also the dose constraints to the organs at risk. Step by step for each side and size of metastases we tried to reduce the mean dose for the hippocampus without compromising on coverage of the metastases and whole brain (Figure 2).

2.4. Treatment Planning Evaluation. The treatment plans were evaluated for the following.

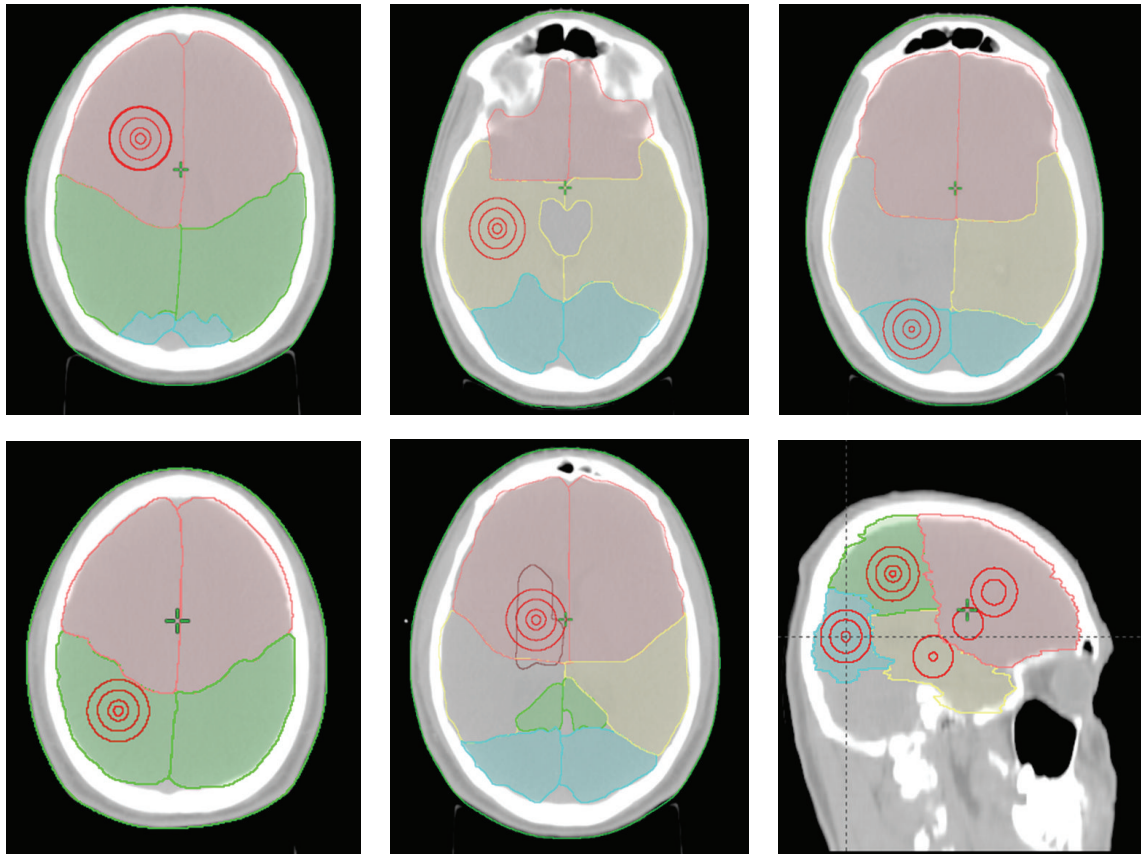

Figure 1: Concentric metastatic lesions in brain's lobes: frontal (pink), parietal (green), temporal (yellow), occipital (cyan), and deep brain structures (brown).

2.4.1. Max and Mean Hippocampal Dose. Quantifies the maximal and the mean dose of combined hippocampal volumes; doses were converted to biologically equivalent doses in 2-Gy fractions (Gy^2), assuming an α/β ratio of 2Gy.

2.4.2. Target Coverage (TC). Describes the fraction of the target volume (V_T) receiving at least the prescription dose ($V_{T\,\mathrm{presc}}$) and is defined as

$$\mathrm{TC} = \frac{V_{T\,\mathrm{presc}}}{V_T}. \tag{1}$$

According to RTOG QA guidelines, it should be kept close to 1.0.

2.4.3. Homogeneity Index (HI). Is defined as the maximum dose delivered to 2% of the target volume ($D2\%$) minus the dose delivered to 98% of the target volume ($D98\%$) divided by the median dose (D_{median}) to the target volume:

$$\mathrm{HI} = \frac{(D2\% - D98\%)}{D_{\mathrm{median}}}; \tag{2}$$

it quantifies homogeneity dose distribution in the target volumes.

2.4.4. V95. Quantifies the volume of $\mathrm{PTV_{WB}}$ receiving 95% of the prescription dose or more.

2.4.5. V105. Quantifies the volume of the $\mathrm{PTV_{WB}}$ receiving 105% of the prescription dose or more.

2.4.6. Mean Normalized Tissue Dose (NTD_{mean}). It is defined as the total dose that would have the same biological effect as the actual treatment schedule if it were given in 2-Gy fractions. This parameter allows us to compare the effects on normal tissue for two dose volume histograms. An α/β ratio of 2 Gy was assumed for the hippocampus and 3 Gy for the eyes:

$$\mathrm{NTD_{mean}}: \frac{\mathrm{Td}\,(\mathrm{Fd} + \alpha/\beta)}{(2 + \alpha/\beta)}, \tag{3}$$

where Td = total dose, Fd = dose for fraction.

3. Results and Discussion

We developed a model using 15 lesions with a diameter included between 1 and 3 cm to support the indication to stereotactic radiosurgery. We contoured 4 lobes (1 frontal, 1 parietal, 1 temporal, 1 occipital lobe), and 1 area of deep brain structures, and hippocampus for each hemisphere. Fifteen

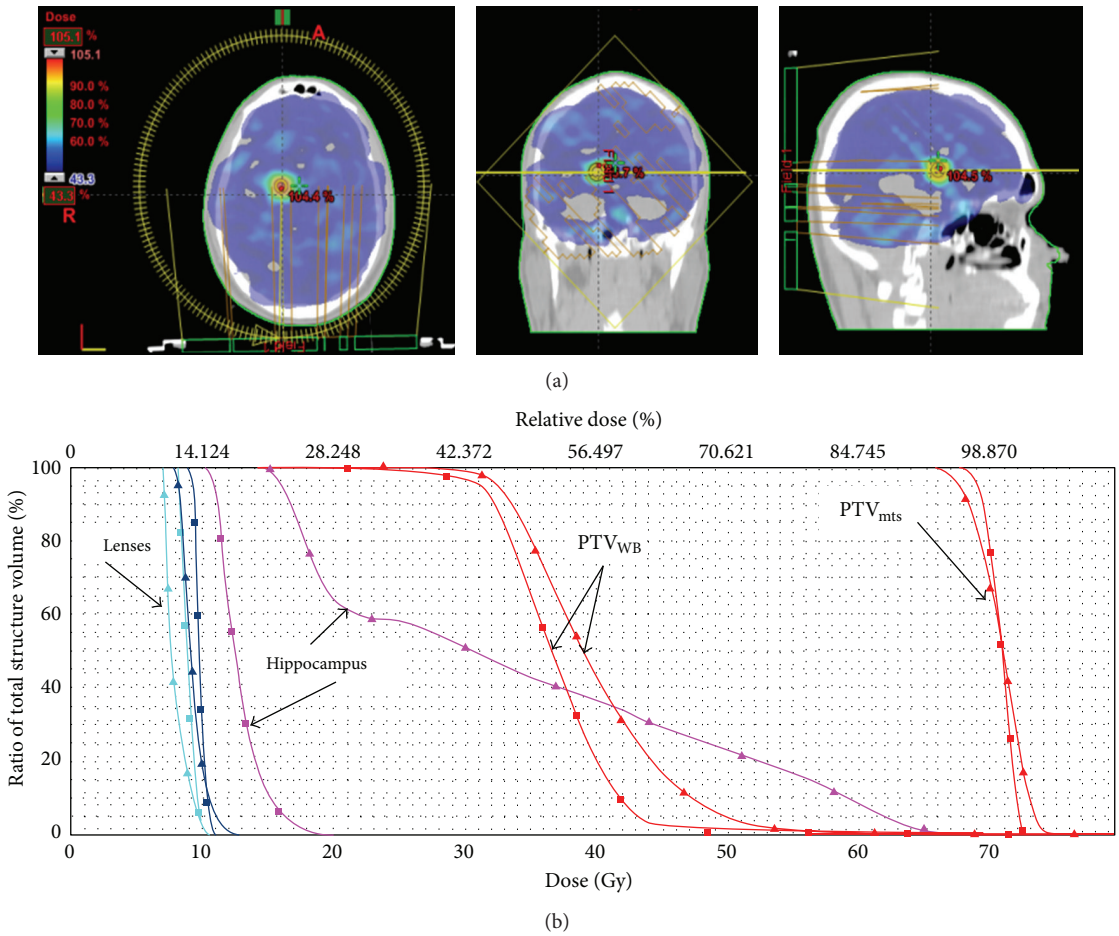

FIGURE 2: (a) Example of dose distribution of avoidance of hippocampus during whole brain radiotherapy with simultaneously integrated boost using Volumetric Modulated Arc Therapy. (b) Plan comparison cumulative, normalized dose-volume histogram (▲ temporal versus ■ occipital): hippocampus (pink), eyes (cyan/blue), and PTV_{mts} and PTV_{wb} shown. Two metastases of 1 cm of diameter prescribed to 70.8 Gy and whole brain to 32.25 Gy in 15 fractions.

brain lesions for each hemisphere were obtained: 3 for each of four lobes and 3 for deep brain critical structure. The GTV_{mts} and PTV_{mts} for diameter of 1-2 and 3 cm were 0.51–1.47 cm^3, 4.17–7.42 cm^3, and 14.11–21 cm^3, respectively. Hippocampal volume was 4.09 cm^3 and hippocampal avoidance volume was 17.50 cm^3.

Fifteen RA treatment plans were calculated. Evaluation parameters for each plan are reported in Table 1.

The mean TC was for PTV_{WB} and PTV_{mts} was 0.9 ± 0.04 and 0.52 ± 0.06, respectively.

Homogeneity for PTV_{WB} was 0.65 ± 0.18.

The mean hippocampal dose obtained in all RA plans is 10.43 Gy^2. According to the site of lesion, the mean hippocampal doses, normalized to EQD2, was 9.68 Gy^2 for occipital lobe, 10.56 Gy^2 for frontal lobe, 10.56 Gy^2 for parietal lobe, 10.94 Gy^2 for deep brain structures, and 40.44 Gy^2 for temporal lobe. According to the diameter of the lesion, excluding results relative to temporal brain lesions, the mean hippocampal dose, normalized to EQD2, was 9.45, 10.15, and 11.70 Gy^2 for 1, 2, and 3 cm metastases, respectively.

Whole brain radiotherapy remains a standard treatment for intracranial brain metastases, but patients might experience neurocognitive toxicity, correlated to effects on the limbic system [6, 7].

Ghia et al. [11] demonstrated that hippocampus can be spared because metastases are generally more than 5 mm away.

Accurate delineation of the hippocampus and its central location are two critical aspects to obtain a good intracranial control of disease without neurocognitive decline.

Integrated plans of WBRT and SIB for brain metastases have previously been already described, and several authors evaluated the dosimetric feasibility of sparing hippocampus using not volumetric IMRT technique or helical tomotherapy or VMAT [15].

At our knowledge this is the first study in which a model has been created to predict the impact of site and size of metastases on hippocampal sparing using RA technique. This can be useful because skilled users need several hours to perform image fusion, to contour structures and to develop a treatment plan, which will need another hour for physics

Table 1: Parameters of 15 RA plans.

Plan	Diameter (cm)	Mean Hippocampal Dose (Gy)	Mean Hippocampal dose (Gy^2)	HI-PTV whole brain	TC-PTV metastases	TC-PTV whole brain
DS 1	1	12.55	8.90	0.34	0.52	0.82
F 1	1	13.95	10.22	0.36	0.51	0.92
O 1	1	12.82	9.15	0.64	0.54	0.99
P 1	1	13.25	9.55	0.47	0.54	0.91
T 1	1	36.10	33.9	0.55	0.53	0.96
DS 2	2	13.46	9.75	0.78	0.55	0.92
F 2	2	13.49	9.78	0.78	0.72	0.90
O 2	2	13.68	9.96	0.53	0.52	0.92
P 2	2	14.87	11.12	0.57	0.54	0.93
T 2	2	42.00	40.27	0.68	0.48	0.90
DS 3	3	17.80	14.18	0.77	0.49	0.93
F 3	3	15.45	11.70	0.90	0.42	0.91
O 3	3	13.66	9.94	0.60	0.51	0.93
P 3	3	14.76	11.01	0.84	0.46	0.93
T 3	3	50.4	47.16	0.85	0.52	0.80

DS: deep structure; F: frontal lobe; O: occipital lobe; P: parietal lobe; T: temporal lobe; 1–3: metastases diameter (cm).

quality assurance. So knowing the feasibility of sparing hippocampus according to the site or the diameter of lesion, everyone could decide to use VMAT-RA techniques or not without spending many hours to obtain only a little sparing. Our data show that when the lesion is in temporal lobe, near the hippocampus, the feasibility of minimizing the mean hippocampal dose is lower. Ghia et al. [11] demonstrated that hippocampus can be spared because metastases are generally more than 5 mm away. According our method the temporal lesion with 2 and 3 cm in diameter are partially located into the hippocampus, while if the lesion is of 1 cm of diameter, the distance from lateral side of hippocampus is of 0.5 cm.

On the contrary, sparing hippocampus is feasible when brain lesions are in other regions, also if close to critical structures far from hippocampus. Metastases located in occipital lobe show the lowest mean hippocampal dose. The impact of size of brain lesions is lower on hippocampal dose.

Regarding hippocampus dose with helical tomotherapy (HT) technique, Gutiérrez et al. [16] showed the possibility to reduce the dose to the hippocampus until 6 Gy^2 treating the whole brain to a $D95\%$ of 32.25 Gy with SIB technique, while Marsh et al. [17] delivered 30 or 35 Gy in 15 or 14 fractions on whole brain obtaining a mean dose/equivalent uniform dose (EUD) at hippocampus of 12.5/14.23 Gy.

Gondi et al. [12] observed that HT spared hippocampus more than LINAC based IMRT, while target coverage and homogeneity were acceptable with both technologies.

Other researches tested VMAT or compared this technology to tomotherapy. Lagerwaard et al. [18] tested the efficacy of RA treatment planning to deliver WBRT with SIB in patients with multiple brain metastases, without sparing the hippocampal region, and it showed excellent coverage of planning target volume for WBRT and metastases.

Hsu et al. [14] found that VMAT was able to deliver to metastases a radiosurgical dose during WBRT. For the whole brain, the mean target coverage and homogeneity index were 0.960 ± 0.002 and 0.39 ± 0.06, respectively. The mean hippocampal dose was 5.23 ± 0.39 Gy^2; he used Varian Eclipse external Beam Planning System, version 7.1, and a pencil beam algorithm.

Prokic et al. [19] recently observed that for patients with up to 8 metastases the SIB is more effective than the WBRT + stereotactic fractionated irradiation in lowering doses to the hippocampus. In the SIB schedule, the prescribed dose was 30 Gy in 12 fraction to the WB and 51 Gy in 12 fraction to individual brain metastases. The mean dose to the hippocampus ranged from 7.55 ± 0.62 to 6.29 ± 0.62; he used Eclipse version 10.0 with an optimization system PRO3.

We obtained a mean hippocampal dose ranged from 8.90 Gy^2 to 47.16 Gy^2. In the most favourable situation, such as metastasis in the occipital lobe or diameter of 1 cm, mean hippocampal doses were 9.68 Gy^2 and 9.45 Gy^2 respectively. These data are better than those reported by Marsh et al. [17] but worse than those obtained by other authors.

The gap could be related more to algorithm for dose's optimization than to that of dose's calculation because in the brain the different accuracy between the pencil beam and the AAA algorithm could not be significant.

Regarding HI of whole brain, we found an HI that ranged from 0.34 to 0.9 with a mean of 0.65 ± 0.18; our results are more similar to those reported by Gutiérrez et al. [16] with tomotherapy (0.485 ± 0.152), comparable with those obtained by Hsu et al. [14] with VMAT (0.39 ± 0.06), Prokic et al. [19] (0.54 ± 0.04) with VMAT, and by Gondi et al. [12] with LINAC-IMRT; it is worse only them those published by Gondi et al. when used helical tomotherapy

(0.008–0.29). However, sparing the hippocampus and concomitantly boosting the metastases deliberately increases the heterogeneity for the whole brain volume for this composite plan. This makes the HI a poor measure. This is observed also by other investigators [20].

4. Conclusions

Our predictive model suggests that metastases in temporal lobe does not allow to reduce significantly the dose to hippocampus. Volumetric modulation RA is able to reduce the mean dose per fraction to the hippocampus. Different version or algorithm of VMAT-RA can influence dose's estimation to hippocampus. Further investigations are necessary to improve statistical analysis and to meet definitive considerations, modelling multiple metastasis, scanning imaging and fusion of other patients, or evaluating hippocampus as both single and paired structures.

References

[1] R. A. Patchell, "The management of brain metastases," *Cancer Treatment Reviews*, vol. 29, no. 6, pp. 533–540, 2003.

[2] H. Aoyama, H. Shirato, M. Tago et al., "Stereotactic radiosurgery plus whole-brain radiation therapy vs stereotactic radiosurgery alone for treatment of brain metastases: a randomized controlled trial," *The Journal of the American Medical Association*, vol. 295, no. 21, pp. 2483–2491, 2006.

[3] D. D. Roman and P. W. Sperduto, "Neuropsychological effects of cranial radiation: current knowledge and future directions," *International Journal of Radiation Oncology, Biology, and Physics*, vol. 31, no. 4, pp. 983–998, 1995.

[4] L. M. DeAngelis, J.-Y. Delattre, and J. B. Posner, "Radiation-induced dementia in patients cured of brain metastases," *Neurology*, vol. 39, no. 6, pp. 789–796, 1989.

[5] O. K. Abayomi, "Pathogenesis of irradiation-induced cognitive dysfunction," *Acta Oncologica*, vol. 35, no. 6, pp. 659–663, 1996.

[6] M. L. Monje, S. Mizumatsu, J. R. Fike, and T. D. Palmer, "Irradiation induces neural precursor-cell dysfunction," *Nature Medicine*, vol. 8, no. 9, pp. 955–962, 2002.

[7] I. J. Barani, L. W. Cuttino, S. H. Benedict et al., "Neural stem cell-preserving external-beam radiotherapy of central nervous system malignancies," *International Journal of Radiation Oncology, Biology, and Physics*, vol. 68, no. 4, pp. 978–985, 2007.

[8] L. G. Caceres, L. Aon Bertolino, G. E. Saraceno et al., "Hippocampal-related memory deficits and histological damage induced by neonatal ionizing radiation exposure. Role of oxidative status," *Brain Research*, vol. 1312, pp. 67–78, 2010.

[9] T. M. Madsen, P. E. G. Kristjansen, T. G. Bolwig, and G. Wörtwein, "Arrested neuronal proliferation and impaired hippocampal function following fractionated brain irradiation in the adult rat," *Neuroscience*, vol. 119, no. 3, pp. 635–642, 2003.

[10] J. Li, S. M. Bentzen, M. Renschler, and M. P. Mehta, "Regression after whole-brain radiation therapy for brain metastases correlates with survival and improved neurocognitive function," *Journal of Clinical Oncology*, vol. 25, no. 10, pp. 1260–1266, 2007.

[11] A. Ghia, W. A. Tomé, S. Thomas et al., "Distribution of brain metastases in relation to the hippocampus: implications for neurocognitive functional preservation," *International Journal of Radiation Oncology, Biology, and Physics*, vol. 68, no. 4, pp. 971–977, 2007.

[12] V. Gondi, R. Tolakanahalli, M. P. Mehta et al., "Hippocampal-sparing whole-brain radiotherapy: a "how-to" technique using helical tomotherapy and linear accelerator-based intensity-modulated radiotherapy," *International Journal of Radiation Oncology, Biology, and Physics*, vol. 78, pp. 1244–1252, 2010.

[13] B. S. Chera, R. J. Amdur, P. Patel, and W. M. Mendenhall, "A radiation oncologist's guide to contouring the hippocampus," *American Journal of Clinical Oncology*, vol. 32, no. 1, pp. 20–22, 2009.

[14] F. Hsu, H. Carolan, A. Nichol et al., "Whole brain radiotherapy with hippocampal avoidance and simultaneous integrated boost for 1-3 brain metastases: a feasibility study using volumetric modulated arc therapy," *International Journal of Radiation Oncology, Biology, and Physics*, vol. 76, no. 5, pp. 1480–1485, 2010.

[15] G. Bauman, S. Yartsev, B. Fisher et al., "Simultaneous infield boost with helical tomotherapy for patients with 1 to 3 brain metastases," *American Journal of Clinical Oncology*, vol. 30, no. 1, pp. 38–44, 2007.

[16] A. Gutiérrez, D. C. Westerly, W. A. Tomé et al., "Whole brain radiotherapy with hippocampal avoidance and simultaneously integrated brain metastases boost: a planning study," *International Journal of Radiation Oncology, Biology, and Physics*, vol. 69, pp. 589–597, 2007.

[17] J. C. Marsh, B. T. Gielda, A. M. Herskovic, J. A. Wendt, and J. V. Turian, "Sparing of the hippocampus and limbic circuit during whole brain radiation therapy: a dosimetric study using helical tomotherapy," *Journal of Medical Imaging and Radiation Oncology*, vol. 54, no. 4, pp. 375–382, 2010.

[18] F. J. Lagerwaard, E. A. P. van der Hoorn, W. F. A. R. Verbakel, C. J. A. Haasbeek, B. J. Slotman, and S. Senan, "Whole-brain radiotherapy with simultaneous integrated boost to multiple brain metastases using volumetric modulated arc therapy," *International Journal of Radiation Oncology, Biology, and Physics*, vol. 75, no. 1, pp. 253–259, 2009.

[19] V. Prokic, N. Wiedenmann, F. Fels, M. Schmucker, C. Nieder, and A.-L. Grosu, "Whole brain irradiation with hippocampal sparing and dose escalation on multiple brain metastases: a planning study on treatment concepts," *International Journal of Radiation Oncology, Biology, and Physics*, vol. 85, no. 1, pp. 264–270, 2013.

[20] P. R. M. Storchi, L. J. van Battum, and E. Woudstra, "Calculation of a pencil beam kernel from measured photon beam data," *Physics in Medicine and Biology*, vol. 44, no. 12, pp. 2917–2928, 1999.

Hindawi Publishing Corporation
BioMed Research International
Volume 2013, Article ID 436979, 8 pages
http://dx.doi.org/10.1155/2013/436979

Research Article

Evaluation of Wall Correction Factor of INER's Air-Kerma Primary Standard Chamber and Dose Variation by Source Displacement for HDR ^{192}Ir Brachytherapy

J. H. Lee,[1] J. N. Wang,[1] T. T. Huang,[1] S. H. Su,[1] B. J. Chang,[1] C. H. Su,[2] and S. M. Hsu[3]

[1] *Health Physics Division, Institute of Nuclear Energy Research, Longtan 325, Taiwan*
[2] *Department of Radiation Oncology, China Medical University Hospital, Taichung 404, Taiwan*
[3] *Department of Biomedical Imaging and Radiological Sciences, National Yang-Ming University, Taipei 112, Taiwan*

Correspondence should be addressed to S. M. Hsu; rphptw@yahoo.com.tw

Received 12 May 2013; Accepted 28 May 2013

Academic Editor: Maria F. Chan

The aim of the present study was to estimate the wall effect of the self-made spherical graphite-walled cavity chamber with the Monte Carlo method for establishing the air-kerma primary standard of high-dose-rate (HDR) ^{192}Ir brachytherapy sources at the Institute of Nuclear Energy Research (INER, Taiwan). The Monte Carlo method established in this paper was also employed to respectively simulate wall correction factors of the ^{192}Ir air-kerma standard chambers used at the National Institute of Standards and Technology (NIST, USA) and the National Physical Laboratory (NPL, UK) for comparisons and verification. The chamber wall correction calculation results will be incorporated into INER's HDR ^{192}Ir primary standard in the future. For the brachytherapy treatment in the esophagus or in the bronchi, the position of the isotope may have displacement in the cavity. Thus the delivered dose would differ from the prescribed dose in the treatment plan. We also tried assessing dose distribution due to the position displacement of HDR ^{192}Ir brachytherapy source in a phantom with a central cavity by the Monte Carlo method. The calculated results could offer a clinical reference for the brachytherapy within the human organs with cavity.

1. Introduction

In radiotherapy treatments for cancer patients it is critical to have an accurate measurement of the dose delivered to the patient. Obtaining an accurate dose involves three major steps. The first step is the establishment of primary standards of air kerma or absorbed dose to water. The second step is the use of dosimetry protocols based on ion chambers calibrated using these primary standards to establish the dose under reference conditions in a clinical therapy beam. The final step is to establish the dose distribution in individual patients specified by computed tomography (CT) data.

At present, ^{192}Ir is the most commonly used radioisotope for high-dose-rate (HDR) brachytherapy treatment. Due to the relatively short half-life of ^{192}Ir (73.827 days ± 0.013 days) [1], most radiotherapy departments change their ^{192}Ir sources every three months and medical physicists need to measure the source strength of the ^{192}Ir sources on a regular basis before an accurate treatment plan can be written. The source calibration is a main component of quality assurance programs recommended for HDR brachytherapy [2]. The recommended quantity for the specification of brachytherapy gamma ray sources is the reference air-kerma rate (RAKR), defined by the International Commission on Radiation Units and Measurements [3, 4] as the kerma rate to air, in air, at a reference distance of 1 meter, corrected for air attenuation and scattering.

To replace the interpolation techniques between air-kerma calibration coefficients of an ionization chamber for ^{192}Ir [5, 6], the Institute of Nuclear Energy Research (INER,

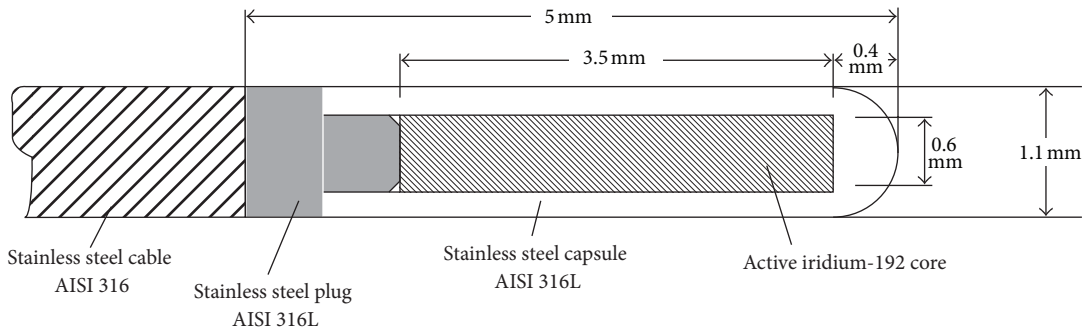

Figure 1: Geometric model of the Nucletron mircoSelectron HDR ^{192}Ir Classic source.

Taiwan) has recently developed a spherical graphite-walled cavity ionization chamber as the primary standard for direct measurement of HDR ^{192}Ir brachytherapy source strength to provide a traceable source calibration. Our primary standard is derived from measurements using the graphite-walled chamber, based on the Bragg-Gray theory. The wall correction factor k_{wall} is intended to account for the effects of attenuation and scatter of the incident primary photons in the chamber wall [7]. The k_{wall} of the primary standard chamber for HDR ^{192}Ir brachytherapy sources is the largest correction factor (approximately 80% of the total correction amounts) required to correct the measured charge for experimental perturbations. In the past, the empirical method to estimate k_{wall} has been to measure the ionization charge (or current) as a function of wall thickness for a fixed cavity size (but for wall thickness no smaller than the minimum required to exclude secondary electrons generated outside the wall). The results are then linearly extrapolated to zero wall thickness under the assumption that attenuation and scattering are thus eliminated. For more than a decade, Rogers and Bielajew suggested that the use of k_{wall} based on linear extrapolation measurements was incorrect and proposed instead the use of results from the Monte Carlo calculations [8–12].

In this research, one of the tasks was to evaluate k_{wall} of the self-fabricated chamber by the Monte Carlo photon-electron transport calculations to establish the HDR ^{192}Ir air-kerma primary standard at INER. In clinical brachytherapy treatment of the esophagus or bronchi or such organs with a cavity, the source positions tend to displace because there would be no body tissue to fix the isotope. The fact is that the position of the isotope would affect the accuracy of the output dose. So the source displacement would cause the tumor or normal tissue to receive inaccurate dose and deviate from the treatment plan and desired effect. Since the experiment of actually measuring the dose variations in the human body is not feasible, we used a simulation calculation to perform dose evaluation [13–15]. In this research, we also performed sensitivity assessment using the Monte Carlo method for the displacement of an HDR ^{192}Ir source in the cavity and explored how the related effects would affect internal doses. Hopefully the evaluation results will offer a clinical reference for brachytherapy within human organs with a cavity.

2. Materials and Methods

2.1. Wall Correction Factor Calculation for HDR ^{192}Ir Air-Kerma Standard Chamber. The INER uses a Nucletron microSelectron HDR Classic brachytherapy unit fitted with the "Classic" source, part number 096.001, manufactured by Mallinckrodt Medical B V (The Netherlands). The average photon energy for HDR ^{192}Ir brachytherapy sources is close to 0.4 MeV [16]. Figure 1 shows a schematic diagram of the HDR ^{192}Ir brachytherapy source simulated in this work. The enclosure of the radioactive material consists of a cylindrical stainless steel AISI 316L capsule (length: 5.0 mm, radial thickness: 250 μm) which is sealed by laser welding. The ^{192}Ir is contained in the capsule as a metallic ^{192}Ir cylinder (length: 3.5 mm, diameter: 0.6 mm). The stainless steel capsule is welded to a metal plug and a 1500 mm long flexible stainless steel AISI 316 cable. The other end of the capsule is welded to a steel pin (tail). The identification of the source is engraved on the long side of the tail. The nominal initial activity of the source is between 370 GBq and 550 GBq.

The INER primary standard cavity chamber for HDR ^{192}Ir sources, shown in Figure 2, is a guarded ionization chamber resulting in low leakage currents. The spherical cavity volume of the primary standard chamber was measured on two coordinate measuring machines and found to be 102 cm^3. The outside radius (3.200 cm), inside radius (2.899 cm), and wall thickness (0.301 cm) for the chamber were measured with a similar technique. In the case of ^{192}Ir, this requires a wall thick enough to stop 687 keV Compton recoil electrons generated by 885 keV gamma rays, the most energetic photons emitted by ^{192}Ir [17], neglecting three very weak lines above 1 MeV. The CSDA (continuous slowing down approximation) range of 687 keV electrons is 0.31 g cm^{-2} of graphite [18], which is equivalent to a wall thickness of approximately 1.8 mm. The graphite wall of this cavity chamber provides sufficient build-up material to ensure CPE. The computer code CAVSPHnrc, which is a user code of EGSnrc [19], is used to calculate wall correction factors of standard cavity chambers. The ionization chamber used in the calculation comprised two concentric spheres, and if ignoring the central electrode, there would be three areas including air, graphite wall, and cavity (made of air) from the outside to the inside.

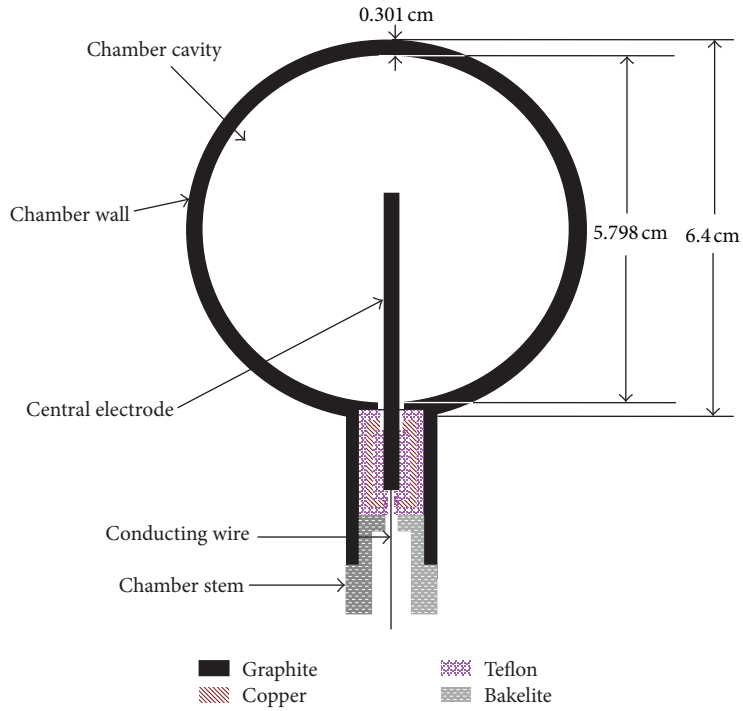

FIGURE 2: Schematic of INER primary standard cavity chamber for HDR ^{192}Ir source.

It was assumed that the ^{192}Ir source was a point source and that the distance between the source and ionization chamber was 100 cm. The simulation kept track of the wall from which the electrons entered the cavity and calculated k_{att} and k_{sc}, the correction factors for attenuation and scattering in the wall. From Figure 3 the following equations become evident:

$$k_{wall} = k_{att} \cdot k_{sc} = \frac{\langle e^{+\mu t} \varepsilon_P \rangle}{\langle \varepsilon_P + \varepsilon_S \rangle} = \frac{\langle e^{+\mu t} \varepsilon_P \rangle}{\langle \varepsilon \rangle}, \quad (1)$$

$$k_{att} = \frac{\langle e^{+\mu t} \varepsilon_P \rangle}{\langle \varepsilon_P \rangle}, \quad (2)$$

$$k_{sc} = \frac{\langle \varepsilon_P \rangle}{\langle \varepsilon_P + \varepsilon_S \rangle} = \frac{\langle \varepsilon_P \rangle}{\langle \varepsilon \rangle}, \quad (3)$$

where the primary photon collides with the chamber wall and produces electrons and a scattered photon, $\langle \varepsilon_P \rangle$ is the energy deposition caused by the primary photon, $\langle \varepsilon_S \rangle$ is the energy deposition caused by the scattered photon, and $\langle \varepsilon \rangle = \langle \varepsilon_P + \varepsilon_S \rangle$ which stands for all the energy deposition inside the chamber cavity. If the ionization chamber was wall-less, the energy deposition in the cavity would be the energy deposition of the primary photon before attenuation, that is, $\langle e^{+\mu t} \varepsilon_P \rangle$. Hence, the definition of the wall correction factor, k_{wall}, would be the ratio of the actual energy deposition $\langle e^{+\mu t} \varepsilon_P \rangle$ to the wall-less energy deposition $\langle \varepsilon \rangle$. In order to produce results that could be used for arbitrary beam spectra, calculations for the self-made chamber were done for both monoenergetic and spectral photon beams. Samples of at least 10^8 incident primary photons were used to make the relative statistical standard deviations below 0.1%.

2.2. Assessment of Dose Variation by Source Displacement for HDR ^{192}Ir Brachytherapy. Plexiglass is a useful phantom material for experimental measurement and calibration and can be easily custom-made for certain shapes and purposes. The radiation interaction properties and density of Plexiglass are similar to the human soft tissue. The Plexiglass phantom is a cylinder with a height of 14 cm and a radius of 10 cm, as indicated in Figure 4. In the center of the phantom, there is a 2 cm diameter cylindrical cavity, which in this calculation represents human organs with a cavity such as the esophagus and bronchi. At the edge of the Plexiglass phantom there are also four cylindrical cavities of the same size as that of the central one. In this calculation the cavities at the edge were not simulated and were filled with the phantom material. To simulate the movement of the ^{192}Ir HDR source in the cavity, the source was located at the cylindrical cavity surface in the calculation, at point A and point B in Figure 5. The HDR ^{192}Ir source was placed at a height of 7 cm in the cavity, which is the middle of the cavity length. As Figure 5 showed, the distance between point A and B is exactly the diameter of the cylindrical cavity. The photon and electron radiations were simulated separately with a Nucletron microSelectron Classic source with an activity of 3.552×10^{11} Bq (9.6 Ci) and then the doses due to photon and electron radiations were summed. The geometrical model of the dose monitoring positions is also indicated in Figure 5, taking the cube whose side length was 0.5 cm as a scoring volume. The monitoring positions went along as a straight line from the radius of the central cavity to the side surface of Plexiglass phantom. In this work, the doses at the same monitoring points while the ^{192}Ir source was positioned at the central axis of the cavity were

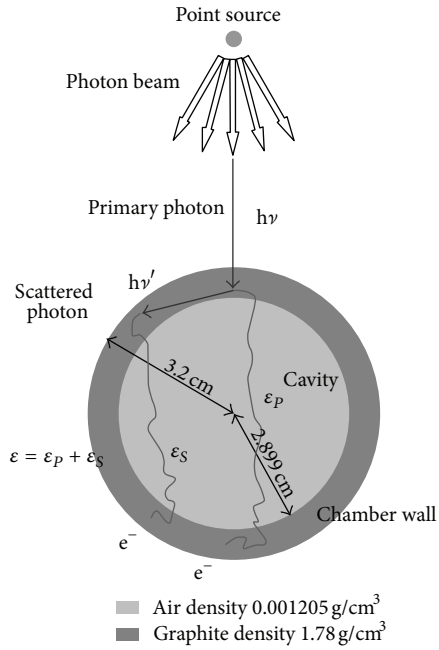

Figure 3: The Monte Carlo simulation geometry for wall correction assessment of the INER primary standard cavity chamber for HDR ^{192}Ir source.

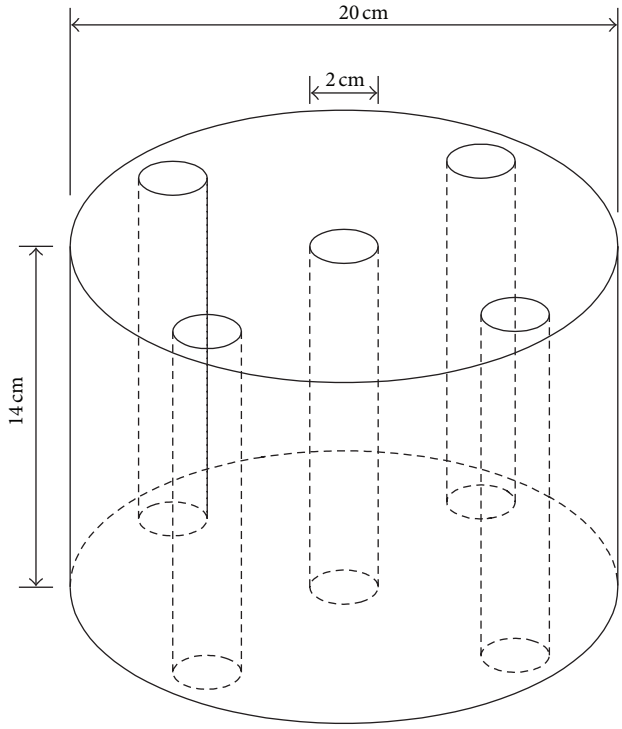

Figure 4: Diagram of Plexiglass phantom geometry.

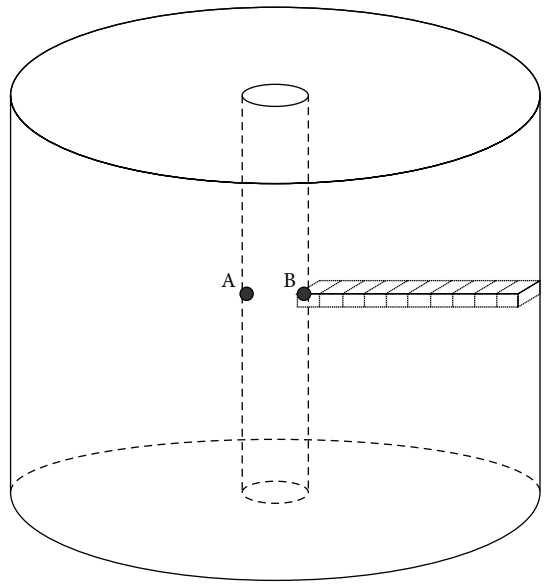

Figure 5: Geometrical indication for the positions of HDR ^{192}Ir source and dose assessment scoring volume in Plexiglass phantom.

also calculated as the comparison basis for the impact of the source displacement.

3. Results and Discussions

3.1. Calculation and Verification of the Chamber Wall Correction Factors. RAKR is determined in air at a distance of 1 m from the source axis in the plane that perpendicularly bisects the axis. The photon spectrum at the RAKR measurement point was estimated by assuming the photon emission probabilities for ^{192}Ir decay and calculating the attenuated spectrum reaching the measurement point. The calculation took into account the attenuation along all photon paths through the various materials by integrating overall source points in the cylindrical core. The photon intensity and spectrum for the source at the RAKR determination point was calculated using MCNP code version 5 [20]. In the calculation the geometry model of the HDR ^{192}Ir source was constructed and simulated in detail. The energy cut-off settings for the photon and electron transport were both 0.001 MeV. Photons were sampled uniformly in the core and were scored at the side of the HDR ^{192}Ir source. Figure 6 shows the ^{192}Ir source photon spectrum calculated in this research, with which the spectrum for the similar field from the independent Monte Carlo calculations of Rogers and Borg [21] showed a good agreement.

The ^{192}Ir source photon spectrum evaluated in Figure 6 was taken as the input data of the CAVSPHnrc code and was used to calculate the wall correction factors of INER's spherical graphite-wall cavity chamber. The k_{wall}, k_{att}, and k_{sc} calculation values and simulation uncertainty analysis for INER's HDR ^{192}Ir primary standard chamber are listed in Table 1. Figure 7(a) illustrates the wall correction factors and the related parameters of INER's spherical graphite-wall cavity chamber, k_{wall}, k_{att}, and k_{sc}, as functions of the incident photon energy. The k_{att} value reduced with the increase of energy. When compared with the mass attenuation coefficient (μ/ρ) of graphite, it showed similar variation trends (Figure 7(b)) and met the proportional relationship between

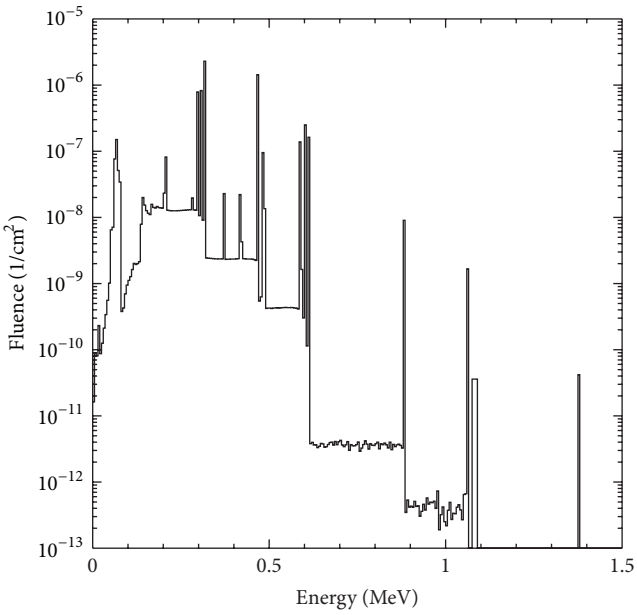

Figure 6: Fluence spectrum for the Nucletron mircoSelectron HDR ^{192}Ir Classic source at the RAKR measurement point.

Table 1: The k_{wall}, k_{att}, and k_{sc} calculation values and simulation uncertainty analysis for INER's HDR ^{192}Ir primary standard chamber.

Correction factors	k_{sc}	k_{att}	k_{wall}
Calculation values	0.9402	1.1021	1.0362
Simulation uncertainties	0.015%	0.005%	0.015%

k_{att} and $e^{+\mu t}$ in (2). k_{sc} varied inversely with the incoherent scattering cross section (Figure 7(c)) related to the energy deposition caused by the scattered photon $\langle \varepsilon_s \rangle$ in (3). The smallest k_{sc} value occurred at 0.04 MeV. The wall correction factors k_{wall} affected by the related parameters have been established in this study and will be incorporated into INER's air-kerma primary standard for HDR ^{192}Ir sources.

INER used the CAVSPHnrc code to calculate the k_{wall} values of NIST's spherical graphite primary standard chambers of different volumes for 0.40 MeV, 0.662 MeV, and 1.25 MeV photons and compared them with the results evaluated by NIST [22]. The comparison results are listed in Table 2. Table 2 shows that the k_{wall} assessment discrepancies against the NIST primary standard chambers between INER and NIST for monoenergetic photons were within 0.20%, verifying the accuracy and reliability of INER's method for evaluating the chamber wall correction factors. The Monte Carlo simulation process in this study also offered a convenient and accurate approach to evaluate the chamber wall correction factor for national metrology institutes (NMIs) in establishing their air-kerma primary standards of gamma radiation. Table 3 gives the structural information of ^{192}Ir primary standard cavity chambers for INER, NIST (50cc-1), and NPL [1, 22]. INER used the Nucletron microSelectron Classic source spectrum simulated in Figure 6 and the CAVSPHnrc code to calculate NIST's and NPL's ^{192}Ir primary standard chamber wall correction factors given in Table 4. It can be seen from Table 4 that for the assessment of wall correction factors, the difference between evaluations of NPL's standard chamber was 0.23% and between evaluations of NIST's standard chamber was 0.44%. The differences were analyzed and the root cause was found: the HDR ^{192}Ir source used by the NPL was the Nucletron microSelectron Classic type [16], which was the same type used by INER for calculation of the HDR ^{192}Ir source spectrum. On the other hand, NIST used a low-dose-rate (LDR) ^{192}Ir brachytherapy seed source to evaluate the wall correction factor [22]. With the different types of sources, INER and NIST had a larger difference in the evaluation results. Analyzing Tables 2 and 4, it can be seen that for the NIST 50cc-1 primary standard chamber for an ^{192}Ir source, the k_{wall} evaluation difference of the ^{192}Ir spectral photon beams is higher than that for the monoenergetic photons (0.40 MeV, 0.662 MeV, and 1.25 MeV).

3.2. Assessment of Dose Variation by Source Displacement. The MCNP code version 5 was adopted to evaluate the influence on the dose distribution of the phantom for HDR ^{192}Ir brachytherapy source movement in the central cavity of the Plexiglass phantom. Figure 8 indicates the photon dose, electron dose, and the total dose as a function of distance when the source was placed on the central axis of the central cylindrical cavity. It is obvious that the dominant dose contribution came from the photons of the source. At the distance of 1.25 cm from the central cavity axis, the electron dose from the source was about 1/7 of the photon dose. At other distance monitoring points, the dose contribution of the electrons was only about 1/60 of the photon dose. The difference of these compared results as a function of distance was caused by the short range of the electrons. The electrons deposit energy quickly as they transport through 0.5 cm depth of the phantom, and the electron dose at the phantom edge results from the Bremsstrahlung. The dose contribution from the Bremsstrahlung was estimated to be approximately 17% of the total electron dose summed from all monitoring points. The dose assessment in the Plexiglass phantom showed that the total dose on the surface of the phantom was as low as only 1% of that at the phantom center.

Figure 9 indicates that the total dose distribution varied with assessment distance when the ^{192}Ir source was placed at different locations in the cylindrical cavity of the Plexiglass phantom. The dominant dose contribution is still from the photons, even if the location of the ^{192}Ir source has been displaced. Table 5 lists the dose ratios at various monitoring points when the ^{192}Ir source was placed at the point A, point B, and the central axis of the phantom cavity center. It was seen that for the nearest monitoring point (1.25 cm), the dose ratios of which the source was located at point A and point B against the source located at the cavity central axis were 0.340 and 16.2, respectively. The analysis results showed that when the location of the ^{192}Ir source was displaced from point A to point B, the dose at the nearest motoring point (1.25 cm) was greater by nearly a factor of 50. The dose evaluation difference from the location of the ^{192}Ir source

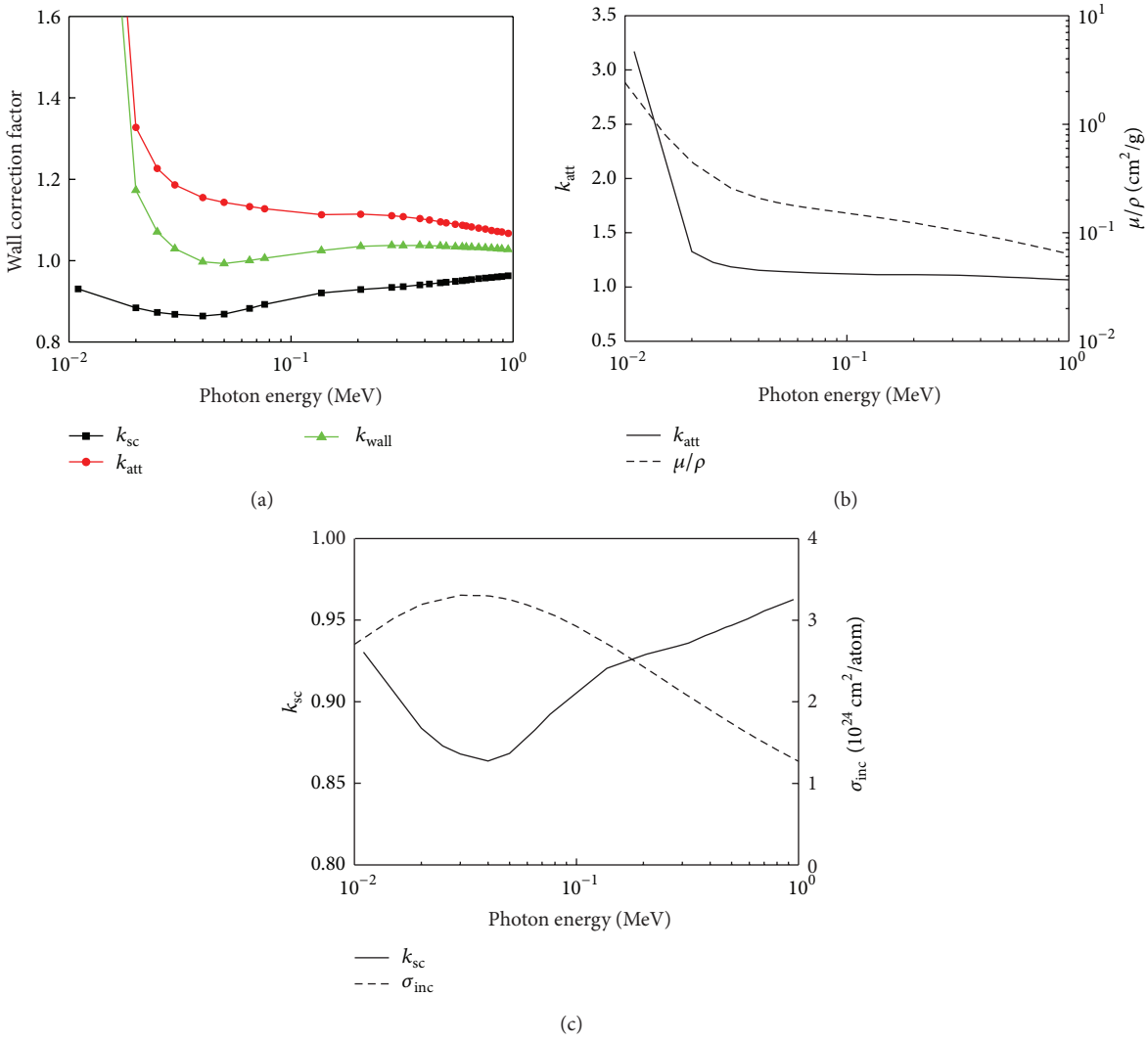

FIGURE 7: (a) Wall correction factors k_{wall}, attenuation correction factor k_{att}, and scatter correction factor k_{sc}, (b) k_{att} and mass attenuation coefficient of graphite μ/ρ, and (c) k_{sc} and incoherent scattering cross section σ_{inc} as functions of the incident photon energy.

TABLE 2: Comparison of k_{wall} values calculated by INER and NIST for NIST's spherical graphite primary standard chambers using 0.40 MeV, 0.662 MeV, and 1.25 MeV photons.

Chamber	k_{wall} (0.40 MeV)			k_{wall} (0.662 MeV)			k_{wall} (1.25 MeV)		
	NIST	INER	Difference	NIST	INER	Difference	NIST	INER	Difference
1cc	1.0312	1.0320	0.07%	1.0286	1.0287	0.01%	1.0197	1.0287	0.01%
10cc	1.0349	1.0352	0.03%	1.0314	1.0319	0.05%	1.0226	1.0319	0.05%
30cc	1.0374	1.0395	0.20%	1.0348	1.0344	−0.04%	1.0249	1.0344	−0.04%
50cc-1	1.0386	1.0402	0.16%	1.0349	1.0354	0.05%	1.0252	1.0354	0.05%

decreased as the monitoring distance increased. At the edge of the Plexiglass phantom (9.75 cm), the dose difference was reduced to 28.5%. From the above calculation results, it can be known that when performing brachytherapy for organs with a cavity, the displacement of source position could make the dose output very different from the plan. With the increase of the assessment distance, the impact from the source displacement would be greatly reduced. However, for clinical brachytherapy, the source is usually very close to the tumor. Source position displacement in organs with cavities such as the esophagus and the bronchi may cause the delivered dose to differ from the prescribed dose in the treatment plan and may bring unexpected influence to the treatment results.

4. Conclusions

We calculated k_{wall} for a self-made spherical chamber using the Monte Carlo method. The wall correction factor could

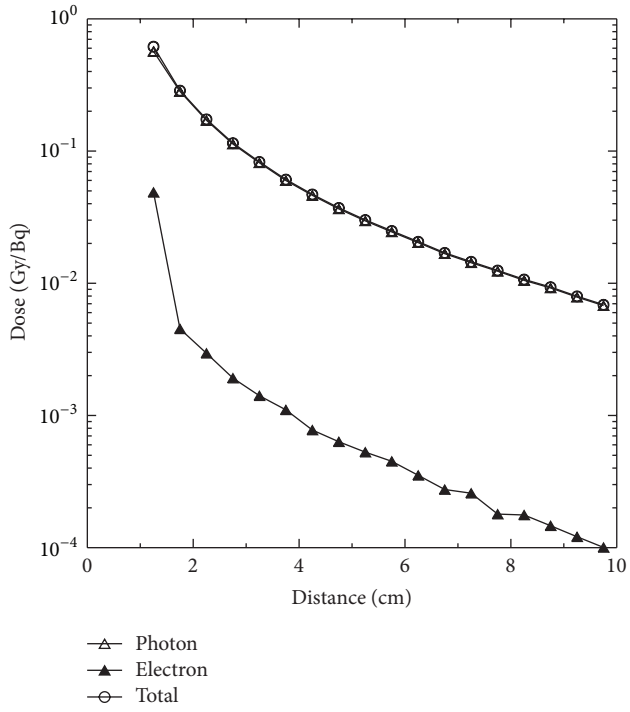

Figure 8: Indication of the dose distribution varying with assessment distance while HDR ^{192}Ir source was placed at the central axis of the Plexiglass phantom cylindrical cavity.

Table 3: Structural characteristics of ^{192}Ir primary standard cavity chambers for INER, NIST (50cc-1), and NPL.

Laboratory	Graphite density ($g\,cm^{-3}$)	Inside radius (cm)	Outside radius (cm)	Wall thickness (cm)	Cavity volume (cm^3)
INER	1.78	2.899	3.200	0.301	102
NIST	1.73	2.305	2.670	0.365	51.3
NPL	1.75	2.910	3.290	0.380	103

Table 4: Calculation comparison for wall correction factors of the ^{192}Ir primary standard chambers for NPL and NIST.

The NPL primary standard chamber for ^{192}Ir			
Wall correction factors calculated by	NPL	INER	Difference
k_{wall} values	1.0453	1.0429	−0.23%
The NIST primary standard chamber (50cc-1) for ^{192}Ir			
Wall correction factors calculated by	NIST	INER	Difference
k_{wall} values	1.0349	1.0395	0.44%

be applied in the establishment of an air-kerma primary standard for HDR ^{192}Ir brachytherapy sources. Simulation comparisons for the primary standard chamber wall corrections of different laboratories were employed to verify the accuracy of the assessment approach established by INER. The comparison results showed that INER and NPL had a better agreement with wall correction factor evaluation of NPL's standard chamber using the same type of source as compared with the different type of ^{192}Ir source used with

Table 5: Total dose distribution assessments when ^{192}Ir source was at different locations.

Distance between central axis and monitoring point (cm)	Dose ratios of monitoring points when source was at different locations		
	Point A/central axis	Point B/central axis	Point A/point B
1.25	0.340	16.2	0.021
1.75	0.445	4.57	0.097
2.25	0.530	2.86	0.185
2.75	0.592	2.25	0.263
3.25	0.633	1.91	0.331
3.75	0.676	1.74	0.390
4.25	0.700	1.62	0.431
4.75	0.726	1.52	0.478
5.25	0.764	1.46	0.525
5.75	0.784	1.39	0.565
6.25	0.783	1.36	0.574
6.75	0.825	1.31	0.628
7.25	0.797	1.29	0.618
7.75	0.844	1.27	0.666
8.25	0.842	1.26	0.668
8.75	0.860	1.24	0.696
9.25	0.797	1.22	0.652
9.75	0.848	1.19	0.715

NIST's standard chamber, which resulted in an increased discrepancy. The k_{wall} calculation data in this study will be incorporated into INER's air-kerma primary standard for HDR ^{192}Ir sources in the near future and increase the calibration accuracy in brachytherapy source strength measurements.

According to the comparison results of the dose distribution of the Plexiglass phantom for the HDR ^{192}Ir brachytherapy source, the outcome of brachytherapy will be seriously influenced by the source displacement. When dealing with clinical treatments including an internal cavity such as esophagus or bronchi, doctors and medical physicists should pay special attention to the dose output variations caused by the source that could not be exactly fixed. The MCNP simulation model used in this research hopefully could be applied to the Voxel phantom which is constructed by CT images to offer more contributions to improve clinical patient treatments.

Acknowledgments

The authors would like to thank the staff members at the Radiation Safety Assessment Group of the Institute of Nuclear Energy Research for their assistance in this study. They also extend their thanks to Dr. Lih-Yih Liao, Mr. Wei-Han Chu

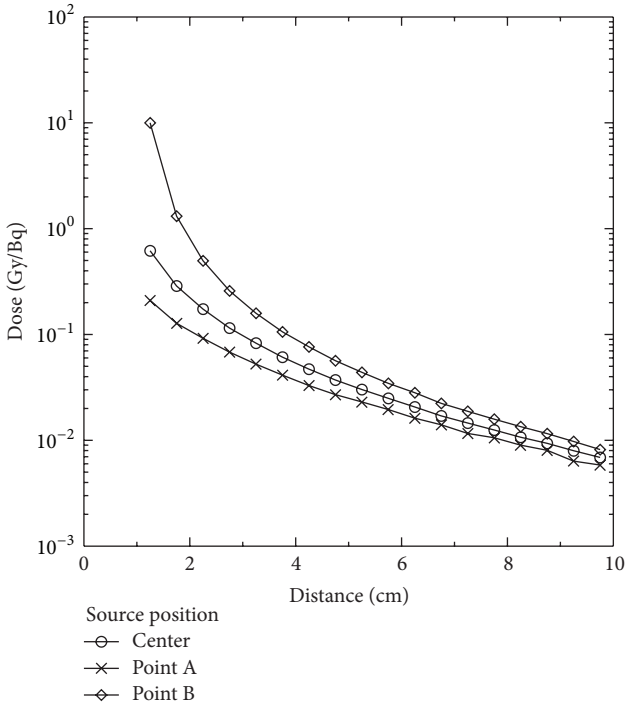

Figure 9: Indication of the total dose distribution varying with assessment distance while the HDR ^{192}Ir source was placed at different locations in the Plexiglass phantom cylindrical cavity.

and Ms. Jui-Mei Deng for their useful comments and discussions. This study was supported by Grants CMU100-S-28 and DMR-99-107 from China Medical University Hospital.

References

[1] T. Sander and R. F. Nutbrown, "The NPL air kerma primary standard TH100C for high dose rate ^{192}Ir brachytherapy sources," Tech. Rep. DQL-RD 004, Teddington National Physical Laboratory, 2006.

[2] D. Baltas, K. Geramani, G. T. Ioannidis et al., "Comparison of calibration procedures for ^{192}Ir high-dose rate brachytherapy sources," *International Journal of Radiation Oncology Biology Physics*, vol. 43, no. 3, pp. 653–661, 1999.

[3] ICRU, "Dose and volume specification for reporting intracavitary therapy in gynecology," ICRU Report 38, 1985.

[4] ICRU, "Dose and volume specification for reporting interstitial therapy," ICRU Report 58, 1997.

[5] L. Büermann, H.-M. Kramer, H. Schrader, and H.-J. Selbach, "Activity determination of ^{192}Ir solid sources by ionization chamber measurements using calculated corrections for self-absorption," *Nuclear Instruments and Methods in Physics Research A*, vol. 339, no. 1-2, pp. 369–376, 1994.

[6] E. van Dijk, I.-K. Kolkman-Deurloo, and P. M. G. Damen, "Determination of the reference air kerma rate for ^{192}Ir brachytherapy sources and the related uncertainty," *Medical Physics*, vol. 31, no. 10, pp. 2826–2833, 2004.

[7] A. Piermattei, L. Azario, A. Fidanzio et al., "The wall correction factor for a spherical ionization chamber used in brachytherapy source calibration," *Physics in Medicine and Biology*, vol. 48, no. 24, pp. 4091–4103, 2003.

[8] D. W. O. Rogers, A. F. Bielajew, and A. E. Nahum, "Ion chamber response and A_{wall} correction factors in a ^{60}Co beam by Monte Carlo simulation," *Physics in Medicine and Biology*, vol. 30, no. 5, pp. 429–443, 1985.

[9] A. F. Bielajew, "Ionisation cavity theory: a formal derivation of perturbation factors for thick-walled ion chambers in photon beams," *Physics in Medicine and Biology*, vol. 31, no. 2, pp. 161–170, 1986.

[10] A. F. Bielajew, "On the technique of extrapolation to obtain wall correction factors for ion chambers irradiated by photon beams," *Medical Physics*, vol. 17, no. 4, pp. 583–587, 1990.

[11] D. W. O. Rogers and A. F. Bielajew, "Wall attenuation and scatter corrections for ion chambers: Measurements versus calculations," *Physics in Medicine and Biology*, vol. 35, no. 8, pp. 1065–1078, 1990.

[12] D. W. O. Rogers and J. Treurniet, "Monte Carlo calculated wall and axial non-uniformity corrections for primary standards," Tech. Rep. PIRS-633, National Research Council of Canada, Ottawa, Canada, 1999.

[13] A. Angelopoulos, P. Baras, L. Sakelliou, P. Karaiskos, and P. Sandilos, "Monte Carlo dosimetry of a new ^{192}Ir high dose rate brachytherapy source," *Medical Physics*, vol. 27, no. 11, pp. 2521–2527, 2000.

[14] F. Ballester, J. Pérez-Calatayud, V. Puchades et al., "Monte Carlo dosimetry of the Buchler high dose rate ^{192}Ir source," *Physics in Medicine and Biology*, vol. 46, no. 3, pp. N79–N90, 2001.

[15] P. Papagiannis, A. Angelopoulos, E. Pantelis et al., "Dosimetry comparison of ^{192}Ir sources," *Medical Physics*, vol. 29, no. 10, pp. 2239–2246, 2002.

[16] G. Douysset, T. Sander, J. Gouriou, and R. Nutbrown, "Comparison of air kerma standards of LNE-LNHB and NPL for ^{192}Ir HDR brachytherapy sources: EUROMET project no 814," *Physics in Medicine and Biology*, vol. 53, no. 6, pp. N85–N97, 2008.

[17] S. J. Goetsch, F. H. Attix, D. W. Pearson, and B. R. Thomadsen, "Calibration of ^{192}Ir high-dose-rate afterloading systems," *Medical Physics*, vol. 18, no. 3, pp. 462–467, 1991.

[18] ICRU, "Stopping powers for electrons and positrons," ICRU Report 37, 1984.

[19] D. W. O. Rogers, I. Kawrakow, J. P. Seuntjens et al., "NRC user codes for EGSnrc," NRCC Report PIRS-702(revB), 2005.

[20] X-5 Monte Carlo team, *MCNP-A General Monte Carlo N-Particle Transport Code*, version 5, Los Alamos National Laboratory, Los Alamos, NM, USA, 2003.

[21] D. W. O. Rogers and J. Borg, "Spectra and air-kerma strength for encapsulated ^{192}Ir sources," *Medical Physics*, vol. 26, no. 11, pp. 2441–2444, 1999.

[22] S. M. Seltzer and P. M. Bergstrom, "Changes in the U.S. primary standards for the air kerma from gamma-ray beams," *Journal of Research of the National Institute of Standards and Technology*, vol. 108, no. 5, pp. 359–381, 2003.

Hindawi Publishing Corporation
BioMed Research International
Volume 2013, Article ID 717589, 11 pages
http://dx.doi.org/10.1155/2013/717589

Research Article

Helical Irradiation of the Total Skin with Dose Painting to Replace Total Skin Electron Beam Therapy for Therapy-Refractory Cutaneous CD4+ T-Cell Lymphoma

Chen-Hsi Hsieh,[1,2,3] Pei-Wei Shueng,[1,4] Shih-Chiang Lin,[5] Hui-Ju Tien,[1] An-Cheng Shiau,[1] Yueh-Hung Chou,[6] Meng-Hao Wu,[7] Jen-Yu Wang,[8] Chi-Kuan Chen,[9] and Yu-Jen Chen[3,7]

[1] *Division of Radiation Oncology, Department of Radiology, Far Eastern Memorial Hospital, No. 21, Section 2, Nanya S. Road, Banciao District, New Taipei City 220, Taiwan*
[2] *Department of Medicine, School of Medicine, National Yang-Ming University, Taipei 112, Taiwan*
[3] *Institute of Traditional Medicine, School of Medicine, National Yang-Ming University, Taipei 112, Taiwan*
[4] *Department of Radiation Oncology, Tri-Service General Hospital, National Defense Medical Center, Taipei 114, Taiwan*
[5] *Department of Hematology, Far Eastern Memorial Hospital, New Taipei City 220, Taiwan*
[6] *Department of Anatomical Pathology, Far Eastern Memorial Hospital, New Taipei City 220, Taiwan*
[7] *Department of Radiation Oncology, Mackay Memorial Hospital, Taipei 104, Taiwan*
[8] *Department of Dermatology, Mackay Memorial Hospital, Taipei 104, Taiwan*
[9] *Department of Surgical Pathology, Mackay Memorial Hospital, Taipei 104, Taiwan*

Correspondence should be addressed to Chen-Hsi Hsieh; chenciab@gmail.com

Received 1 June 2013; Accepted 31 July 2013

Academic Editor: An Liu

A 36-year-old woman was diagnosed with a therapy-refractory cutaneous CD4+ T-cell lymphoma, T3N0M0B0, and stage IIB. Helical irradiation of the total skin (HITS) and dose painting techniques, with 30 Gy in 40 fractions interrupted at 20 fractions with one week resting, 4 times per week were prescribed. The diving suit was dressed whole body to increase the superficial dose and using central core complete block (CCCB) technique for reducing the internal organ dose. The mean doses of critical organs of head, chest, and abdomen were 2.1 to 29.9 Gy, 2.9 to 8.1 Gy, and 3.6 to 15.7 Gy, respectively. The mean dose of lesions was 84.0 cGy. The dosage of left side pretreated area was decreased 57%. The tumor regressed progressively without further noduloplaques. During the HITS procedure, most toxicity was grade I except leukocytopenia with grade 3. No epitheliolysis, phlyctenules, tumor lysis syndrome, fever, vomiting, dyspnea, edema of the extremities, or diarrhea occurred during the treatment. HITS with dose painting techniques provides precise dosage delivery with impressive results, sparing critical organs, and offering limited transient and chronic sequelae for previously locally irradiated, therapy-refractory cutaneous T-cell lymphoma.

1. Introduction

Total skin electron beam therapy (TSEBT) is an effective treatment for cutaneous T-cell lymphoma affecting the superficial region [1]. One of the widely used techniques TSEBT is Stanford 6-dual field technique [2]. However, the dose in homogeneity is reported by the literatures [3, 4]. To improve this condition, a selection of patients with advanced skin disease and regional extension could be overcome by a combination of TSEBT and photon beam irradiation [5].

Helical tomotherapy (HT) has advantages in irradiating extended fields with dose painting techniques. Total marrow irradiation (TMI) via HT with low toxicities for multiple myeloma patients could be feasible [6]. According to the characteristics of HT, it is workable and feasible to replace conventional TSEBT technique by HT to increase dose homogeneity and decrease toxicities. Here, we report a successful case of therapy-refractory cutaneous CD4+ T-cell lymphoma treated with helical irradiation of the total skin (HITS) and dose painting technique to overcome the surface dose in

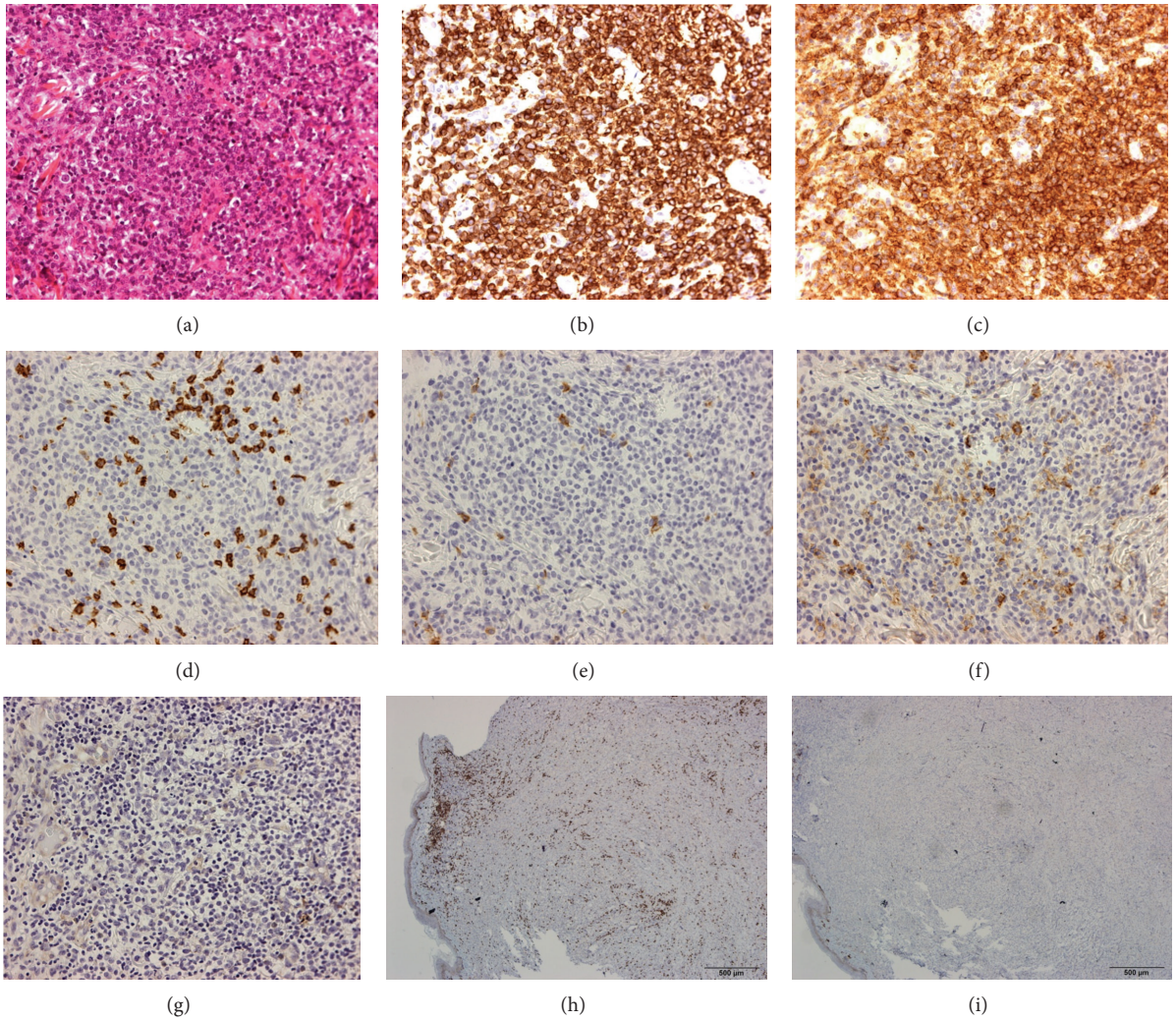

Figure 1: Pathology reports. (a) Atypical lymphoid cells infiltrated diffusely into the superficial and deep dermis. (b) Most of the atypical lymphoid cells were positive for CD3 (×200). (c) Most of the atypical lymphoid cells were positive for CD4 (×200). (d) Only a small portion of them were positive for CD8 (×200). (e) Only a small portion of them were positive for CD79a (×200). (f) Only a small portion of them were positive for CD56 (×200). (g) All negative for CD30 (×200). (h) Negative for CD3 (×40). (i) Negative for CD20 (×40) showed inflammation change without residual T-cell lymphoma.

homogeneity of conventional radiotherapy and to spare the previous irradiating area. Additionally, the data of surface dose, critical organs doses, and registration were analyzed too.

2. Materials and Methods

2.1. Patient Characteristics. In February, 2012, a 36-year-old woman visited our outpatient department due to the progression of a skin disease for several months. Eight months before visiting, she found a pruritic, noduloplaque skin rash over her trunk and extremities. Concurrently, a growing, fungating lesion 15 cm in diameter was in the left lateral chest wall. She visited one of medical center in Taiwan for help. The Ga-67 study showed intense uptake in the lateral left chest wall that was corroborated by the clinical appearance. A whole abdominal computer tomography (CT) showed several subcentimeter lymph nodes in the bilateral inguinal areas, and a biopsy was done. The pathology reports showed cutaneous CD4+ T-cell lymphoma, T3N0M0B0, and stage IIB without lymph node metastasis. Many medium- to large-sized atypical lymphoid cells infiltrated diffusely into the superficial and deep dermis (Figure 1(a)). Most of the atypical lymphoid cells were positive for CD3 (Figure 1(b)) and CD4 (Figure 1(c)). Only a small portion of them were positive for CD8 (Figure 1(d)), CD79a (Figure 1(e)), and CD56 (Figure 1(f)). They were all negative for CD30 (Figure 1(g)).

The prescriptions were interferon alpha, psoralen plus ultraviolet A photochemotherapy, and Accutane (Isotretinoin). In addition, local electron radiotherapy was delivered to the left chest wall and right axillary area with 50 Gray (Gy) in 25 fractions, respectively. After local radiotherapy, the producing newly-formed plaques over the trunk and buttock outside the radiation field were noted. Oral methotrexate

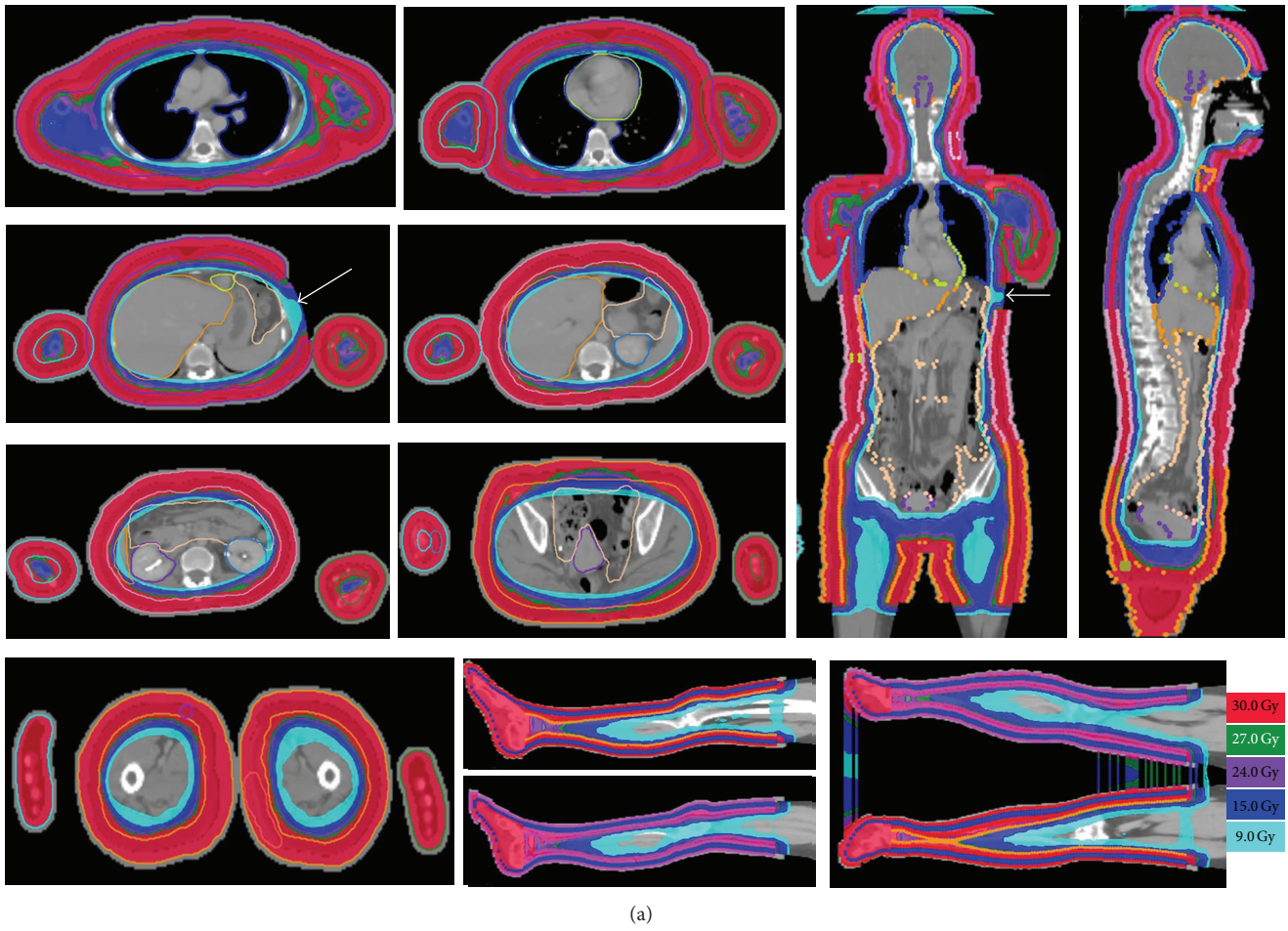

(a)

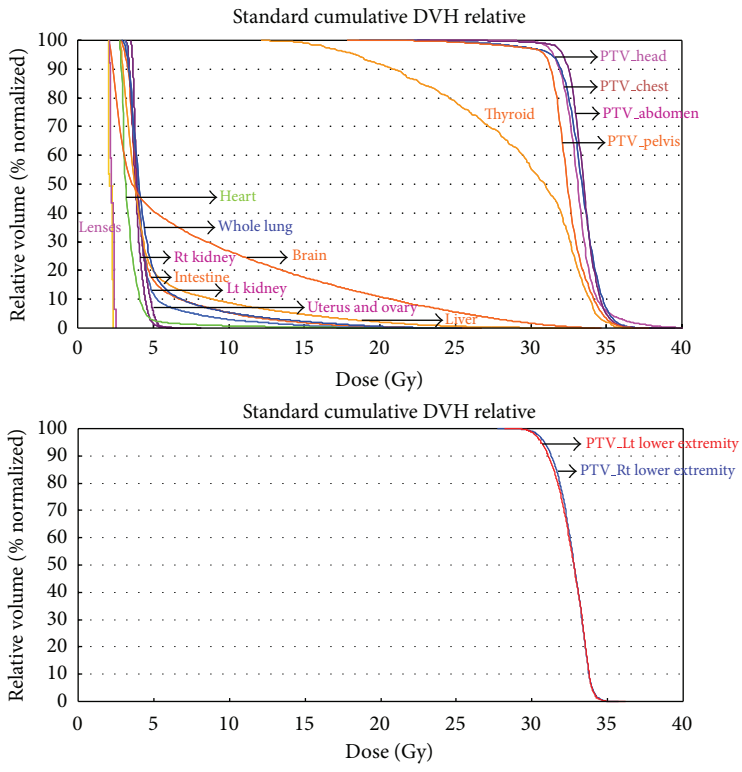

(b)

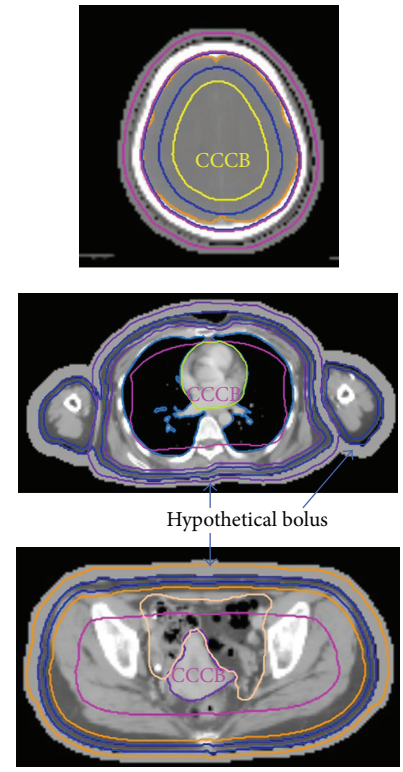

(c)

Figure 2: Continued.

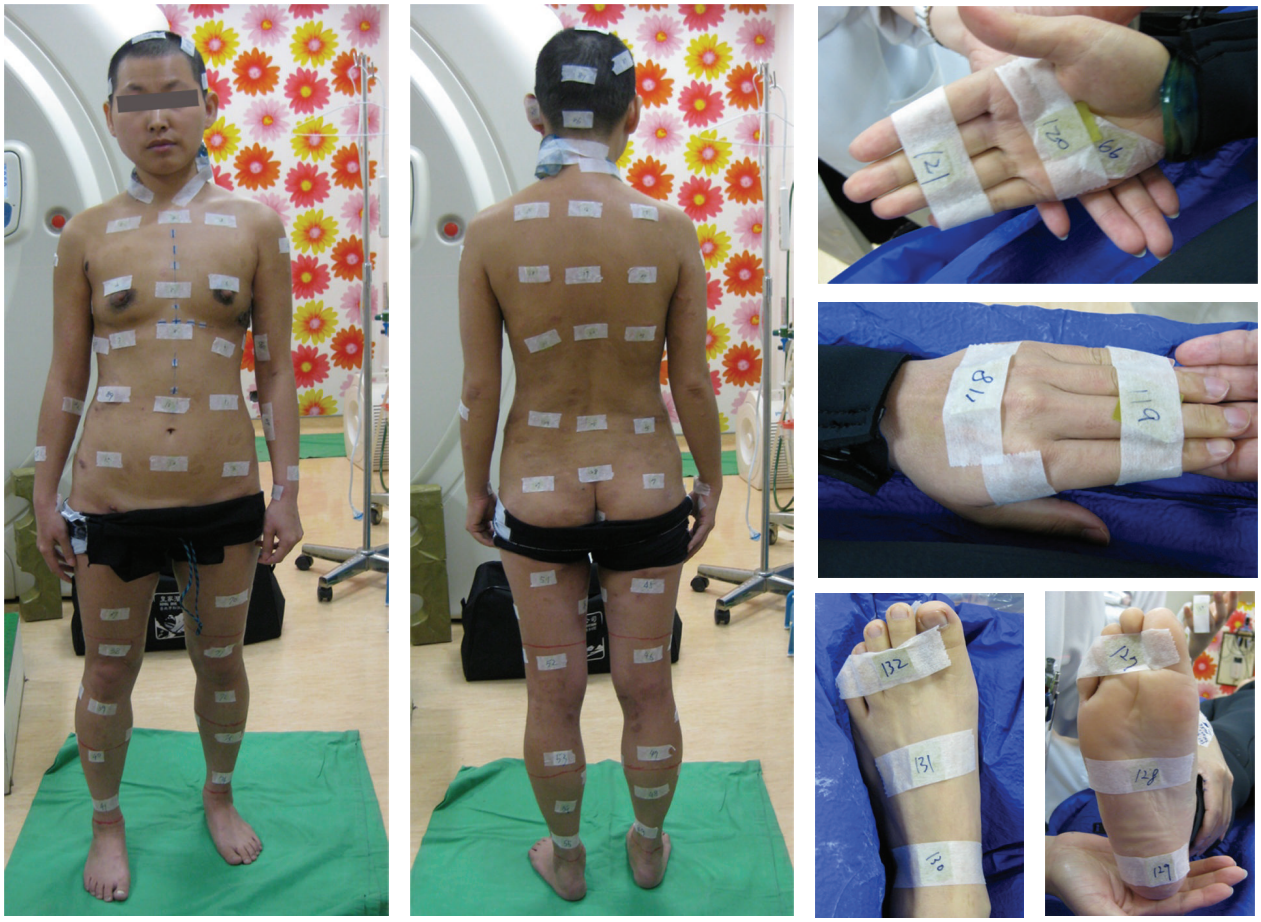

(d)

Figure 2: Irradiation techniques. (a) Helical irradiation of the total skin (HITS) with dose painting technique for total skin irradiation (white arrow indicates dose painting on the previous irradiation area). (b) The dose volume histograms (DVHs) of the target and individual organs at risk (OARs). (c) The hypothetical bolus was placed on the skin surface with 1–1.5 cm. A central core complete block (CCCB) 2.5 cm away from PTV in HITS planning. (d) The locations of radiochromic EBT2 film on the body surface.

(2.5 mg) 5 mg twice per day was prescribed immediately but disease progressed. The patient was referred to our hospital for total skin irradiation.

2.2. Regiment of Helical Irradiation of the Total Skin (HITS). HITS with dose painting techniques were applied from head to toe and avoided the previously treated areas. (Figures 2(a) and 2(b)) The patient was dressed with the diving suit (3 mm thick) to increase the superficial dose. The Polyflex II tissue equivalent material (Sammons Preston, Warrenville, IL, USA) was used as bolus for lesions over ears, fingers, and toes. The conformal bolus (R.P.D., Albertville, MN, USA) was used to cover the lesions in trunk. BlueBag immobilization system (Medical Intelligence, Germany) and thermoplastic fixation were used to fix head and neck, main trunk, and extremities. For tomotherapy treatment planning, a computed tomography (CT) image set of the whole body was required. The patients were scanned in a large bore (75 cm) CT scanner (GE, Discovery VCT PET/CT Imaging System) from head to toe. The level at 15 cm above knee was used as a reference point to separate the upper and lower set. The geometric edges of both fields were abutted at the HT treatment's 50% isodose plane.

Both image sets were using the Philips Pinnacle^3 treatment planning system for contouring. After that, the plan was transferred to the Tomotherapy *Hi Art* Planning system (v. 4.0.4. Tomotherapy, Inc., Madison, Wisconsin, USA). The clinical target volume (CTV) included the entire body surface system with subcutaneous 0.5 cm. To account for setup variability and respiratory motion, a planning target volume (PTV) was generated with a 0.5 cm margin at first. After 4 days treatment, the data of MVCT showed 0.5 cm for PTV was insufficient for some parts of body, such as shoulder, chest, abdomen, and pelvis. Therefore, the margins for PTV in these areas were changed accordingly. The anterior margin of the chest and abdomen was 1.0 cm with two-dimensional expansion and the shoulder was 0.8 cm with three-dimensional expansion, respectively. The CTV and PTV were sepacrated into five parts of head, chest, abdomen, pelvis, and upper extremities for the body plan. The hypothetical bolus was 1.0–1.5 cm in thickness from skin

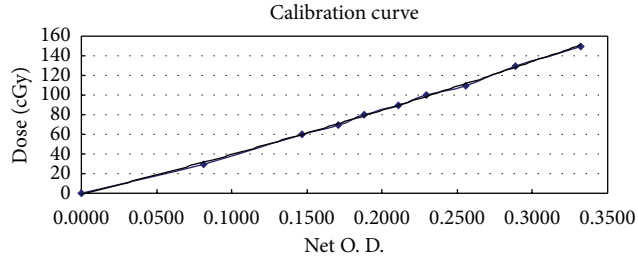

Figure 3: Calibration curve of radiochromic EBT2 film.

surface. Five mm was setting on the outer layer of PTV as hypothetical boluses during HITS plan to avoid the overhit of the inverse planning. Due to the different PTV margin used in the different part of body, the thicknesses of hypothetical boluses were variable. A central core complete block (CCCB) 2.5 cm away from PTV in HT planning system was used to restrict the photon beams to be an oblique incidence for increasing the superficial dose and reducing the internal organ dose (Figure 2(c)).

Thirty Gy with 40 fractions interrupted at 20 fractions with one week resting, 4 times per week were prescribed. Total doses of 30 Gy to 95% of the PTV were delivered to the total skin area and tumor part, respectively. The normal tissue dose constraints utilized were based on the results of the survey of the clinical outcome of the target dose and dose limits to various organs at risk (OARs). The field width, pitch, and modulation factor (MF) used for the treatment planning optimization were 2.5, 0.287 cm, and 3.5, respectively. The dose volume histograms (DVHs) were calculated for the target and individual OARs. Toxicity of treatment was scored according to the Common Terminology Criteria for Adverse Events v4.0 (CTCAE v4.0).

2.3. Image Guidance. Daily check of patient positioning was performed by the megavoltage CT (MVCT) system integrated in the tomotherapy machine. MVCT scan from head to thigh were performed to check the patient's whole body alignment. Image fusions were evaluated by the attending physician and physicist. Any translational shifts suggested by the image fusion results were applied to the final patient setup before treatment delivery. The tolerance of setup error allowed only a 5 mm difference in any of the three translation directions and 1° of difference in roll. Additional selected MVCT scans were performed after treatment to verify patient immobilization.

2.4. Dose Measurement. Radiochromic EBT2 film (International Specialty Products Inc. Wayne, NJ, USA) with thickness of 0.234 mm and effective measurement depth of 0.153 mm in a layer was used for dose measurements during HITS. Each film sheet was cut into smaller pieces as 5 × 5 cm that were placed on the lesions, head, chest, abdomen, pelvis, back, and extremities for calibration and measurement. The starting day in first period, 128 EBT2 films were measured (Figure 2(d)). In the starting day of second period, only 69 EBT2 films were putting on the important area of body to confirm the previous data. An Epson Perfection V700 flatbed scanner (Epson Seiko Corporation, Epson Seiko Corporation, Nagano, Japan) with the software of ImageJ Version 1.43 (National Institute of Health, Bethesda, MD, http://rsb.info.nih.gov/ij/) was used to scan all of the films at least 24 hours after film exposure. Films were scanned at a central scanner location and with the same orientation. The settings used were 48 bit color and 150 dpi (0.017 cm per pixel). Calibration was performed by irradiating each calibration film individually in a plastic water phantom perpendicularly to a 6 MV beam at dose levels from 0 to 150 cGy. The calibration curve was fitted using a polynomial function with the pixel value (PV) for each measurement film converted to dose accordingly (Figure 3). According to the calibration curve, the dose of the exposed EBT2 films can be measured.

3. Results

3.1. Response and Toxicities. Patient data was collected with the approval of the Institutional Review Board of our Hospital. Thirty gray were delivered to the patient from March 19, 2012 to June 29, 2012. The tumor regressed progressively over the entire body without further noduloplaques (Figures 4(a), 4(b), and 4(d)). After HITS, the following pathologic report showed only inflammation change without tumors persist (Figures 1(h) and 1(i)). Grade I dermatitis, mucositis, xerostomia, fatigue, and body weight loss (51 to 46 kg) were noted during the HITS and onycholysis during the two months following completion of the treatment (Figure 4(c)). Additionally, grade I anemia, thrombocytopenia, and grade 3 leukocytopenia were also noted during the HITS procedure (Figure 5). No epitheliolysis, phlyctenules, tumor lysis syndrome, fever, vomiting, dyspnea, edema of the extremities, or diarrhea occurred during the treatment. No abnormal liver, renal, thyroid functions, or gonadotropin hormone were noted during or after treatment (Figure 5). Transient alopecia was noted during HITS but she recovered without permanent partial alopecia 3 months later. Skin itching off and on over the trunk persisted from the beginning until the final report. Two months later, she developed grade 4 pancytopenia but recovered to grade 3 leukocytopenia and thrombocytopenia in the 3rd months after the treatment was completed. Supportive measures were provided including hematopoietic colony-stimulating factors (CSF), steroids, antioxidants, oral glutamine, and yeast-derived 1,3/1,6 glucopolysaccharide. From the treatment until now, a complete response was

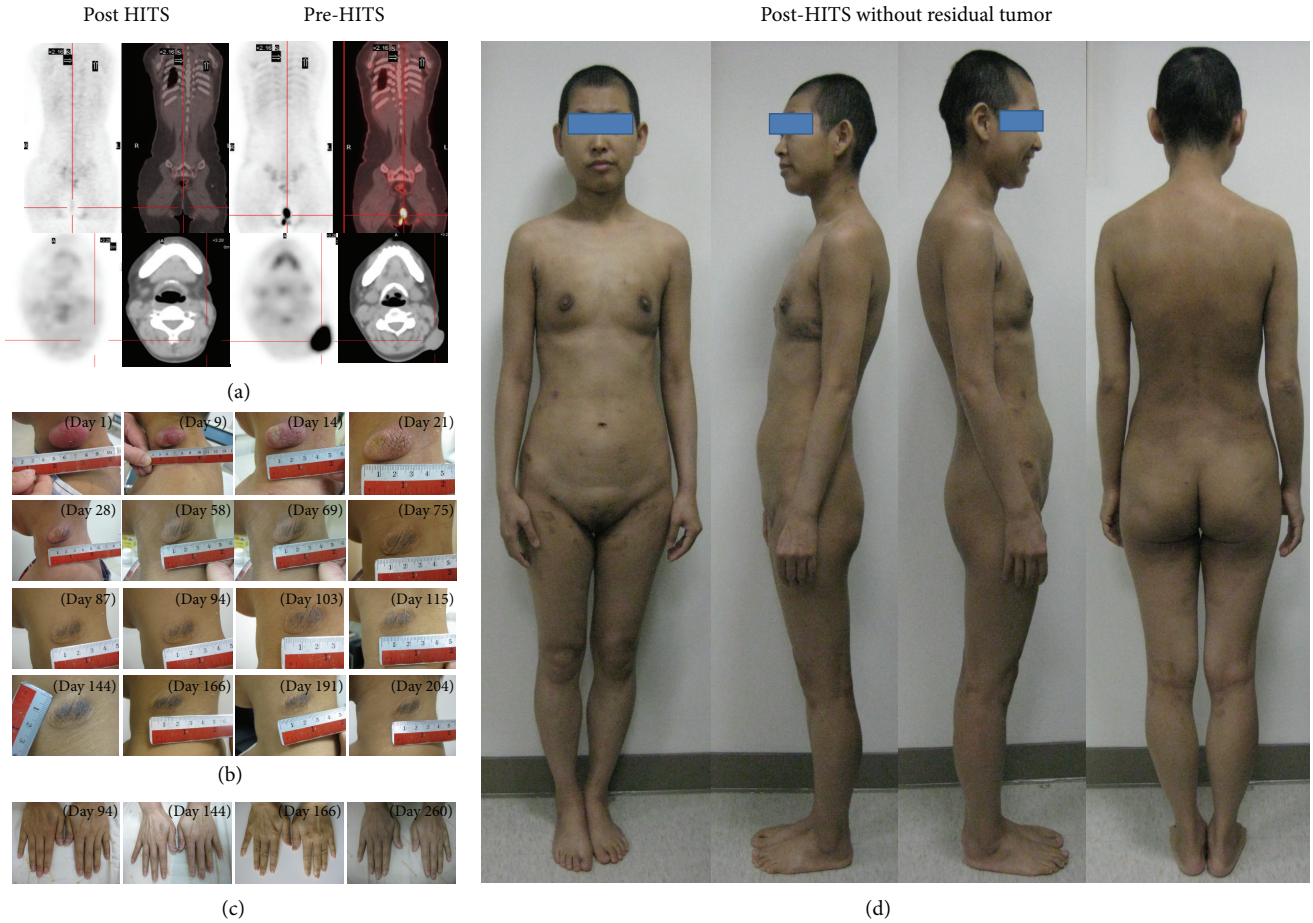

Figure 4: Treatment results. (a) Positron emission tomography study for tumor. (b) The tumor regressed progressively over the entire body without further noduloplaques. (c) Onycholysis during the two months following completion of the treatment. (d) The whole view of total body, transient alopecia was noted during HITS but she recovered without permanent partial alopecia 3 months later.

noted, with the white cell count recovering to grade 2, and the hemoglobulin and platelet counts recovering to grade 1 (Figure 5).

3.2. Dosage of Organs at Risk (OARs). Isodose distributions and dose volume histogram to the target and OARs were shown in Figures 2(b) and 2(c). The mean doses of HITS to various OARs of head, chest, and abdomen were 2.1 to 29.9 Gy, 2.9 to 8.1 Gy, and 3.6 to 15.7 Gy, respectively (Table 1(a)).

3.3. Surface Doses and the Data of Registration. The surface doses in skin were listed in Table 1(b). The mean dosage of lesions was 84.0 cGy (ranged 73.6 to 89.4 cGy). The average dosage of left side pretreated area was 32.5 cGy. In here, the dose was decreased 57%. The average beam-on time for the upper and lower part took roughly 48.1 ± 7.9 min and 8.1 ± 0.8 min, respectively. The maximum average value of registration for upper torso versus lower extremities in different translation directions were 2.8 mm versus 0.9 mm for pretreatment and 0.7 mm versus 0.6 mm for posttreatment, respectively (Table 1(c)).

4. Discussion

This is a case of cutaneous T-cell lymphoma patient refractory to multiple modality therapies with disease progression then search for further management to avoid previous irradiation area. TSEBT could be an efficient and tolerable palliative treatment for patients with cutaneous manifestations of advanced, therapy-refractory cutaneous T-cell lymphoma [7]. Consensus guidelines for delivery of TSEBT have been published by the European Organization for Research and Treatment of Cancer (EORTC) [8]. The EORTC recommends a total dose of 31 to 36 Gy prescribed to the skin surface to produce a dose of at least 26 Gy at a depth of 4mm in the truncal skin along the central axis [8]. In the report by Anacak and colleagues, data of thermoluminescent dosimetry (TLD) measurements for TSEBT demonstrated that the dose in homogeneity throughout the skin surface is around 15% [9]. However, for less radiosensitive skin lymphomas, ±15% in homogeneity is not acceptable and innovative techniques are required. In the current study, the doses were 110% (82.5 cGy) at the surface and 100% (75 cGy) at a depth of 1 cm in the HITS plan (Figures 2(a) and 2(b)), sparing the previously

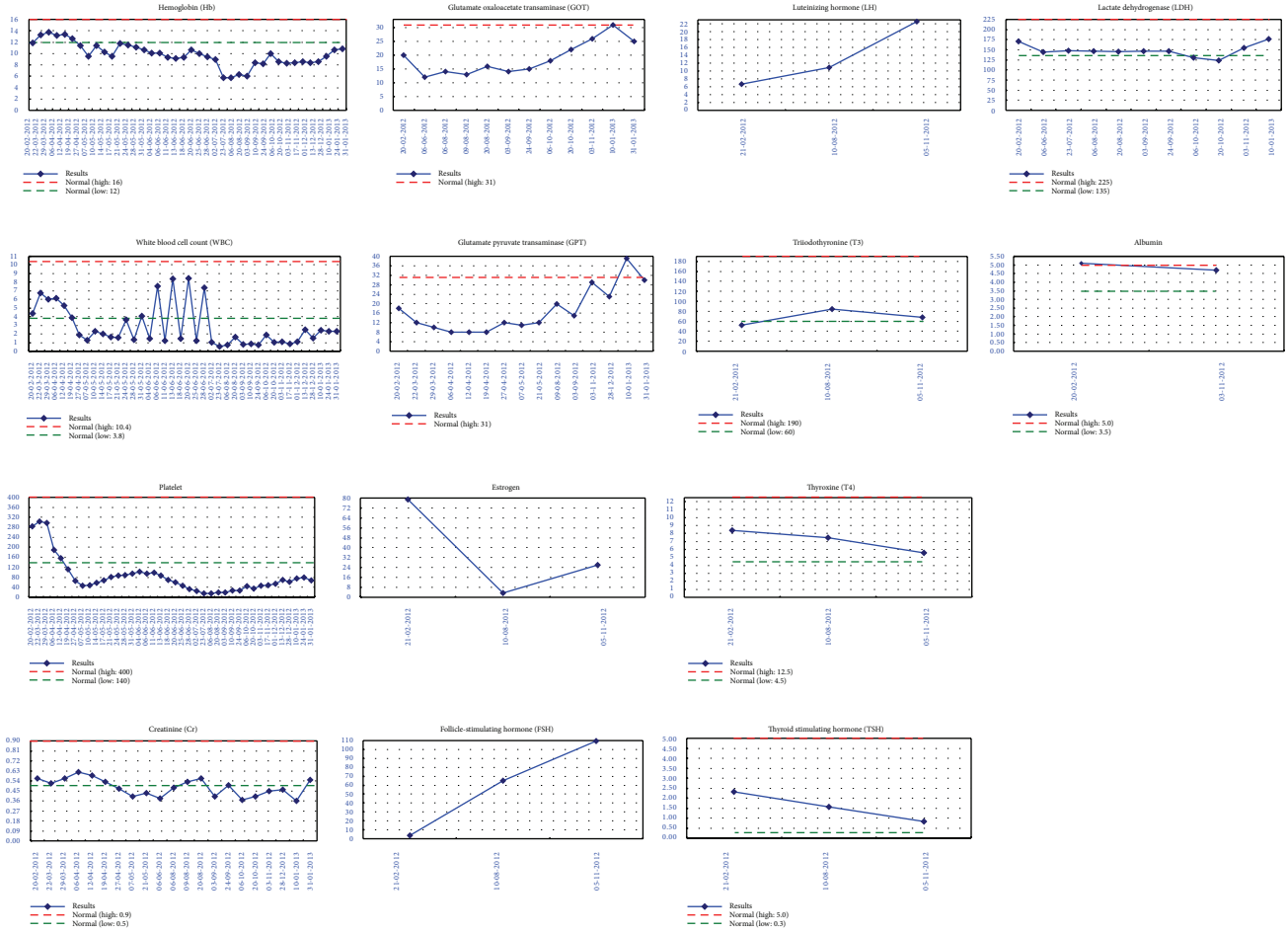

Figure 5: Laboratory results. No abnormal liver, renal, thyroid functions, or gonadotropin hormone were noted. Grade I anemia, thrombocytopenia, and grade 3 leukocytopenia were noted during the HITS procedure. Two months later, she developed grade 4 pancytopenia but recovered to grade 3 leukocytopenia and thrombocytopenia in the 3rd month after the treatment was completed.

treated area and fitting the requirement of recommendtions with high homogeneity.

The deviations of up to 40% occur from the prescription dosage and the surface dose in homogeneity can vary as much as 90% in body areas such as the perineum and eyelid [3]. Additionally, cutaneous tumors often exceed the 4 mm depth and are consequently underdosed when treated with TSEBT alone. HT has advantages in irradiating extending area that make it possible to replace total body irradiation with total marrow irradiation, lowering the toxicities, and sparing critical organs [6]. Using these characteristics of HT, HITS provides dose homogeneity with precise depth penetration and decreased toxicities. In the current study, the CTV included the entire body surface system with subcutaneous 0.5 cm. The maximum average value of registration for upper torso versus lower extremities in different translation directions were 2.8 mm versus 0.9 mm for pretreatment and 0.7 mm versus 0.6 mm for posttreatment, respectively. Generous PTV with a 0.5 cm margin, the shoulder with 0.8 cm margin, and the anterior of the chest and abdomen with 1.0 cm margin was acceptable for compensating the clinical setup variability and breathing motion (Table 1(c)). The hypothetical bolus was designed during HITS plan to avoid overhitting. Diving suit and actual boluses were used in daily practice to increase surface dose. Both hypothetical and actual boluses contributed to skin doses of whole body delivering no more than 125% and no less than 95%. The lowest and highest doses of measurement were located in left anterior lower leg (73.2 cGy) and upper-middle chest (92.6 cGy), respectively. The mean dosage of lesions was 84.0 cGy and the dosage of left side pretreated area was decreased 57% that was matched with the planning expectation (Table 1(b)). Now we have the possibility of replacing conventional TSEBT with HITS with dose painting technique, while still achieving encouraging results (Figures 1(h), 1(i), 4(a), 4(b), and 4(d)).

Common acute toxicities from TSEBT include pruritus, dry desquamation, erythema, alopecia, xerosis, bullae of the feet, edema of the hands and feet, hypohidrosis [10], hyperpigmentation of the skin [7], phlyctenules [5], and loss of fingernails and toenails [11, 12]. Rare acute side effects include gynecomastia in men and mild epistaxis or parotitis [11]. Long-term complications are typically mild and may include permanent nail dystrophy, xerosis, telangiectasias, partial scalp alopecia, and fingertip dysesthesias [8].

Table 1: (a) The doses of organs at risk in helical irradiation of the total skin (HITS) with dose painting technique. (b) The surface doses of skin from head to toes measured with radiochromic EBT2 film in helical irradiation of the total skin (HITS) with dose painting technique. (c) The mean values of registration with pretreatment and posttreatment using kVCT-MVCT fusion for helical irradiation of the total skin (HITS) with dose painting technique.

(a)

Critical organ	D10 (Gy)	D90 (Gy)	Mean dose (Gy)
Whole brain	21.5	2.3	8.0
Brain stem	3.0	2.2	2.5
Spinal cord	4.1	3.5	3.8
Right lens	2.2	2.1	2.1
Left lens	2.3	2.1	2.2
Right eye	7.7	2.1	3.8
Left eye	6.9	2.3	4.1
Right parotid gland	33.8	17.5	29.3
Left parotid gland	33.7	21.7	29.9
Lips	21.8	11.0	15.8
Oral cavity	19.8	2.6	8.7
Pharynx	11.1	2.5	5.2
Larynx	31.8	11.8	23.2
Trachea	29.9	3.1	13.7
Thyroid	31.5	17.2	24.7
Esophagus-upper part	15.2	3.3	8.1
Esophagus-middle part	3.1	2.9	3.1
Esophagus-lower part	2.9	2.8	2.9
Right lung	6.9	3.2	4.7
Left lung	5.9	3.2	4.5
Whole lung	6.4	3.2	4.6
Heart	3.9	2.8	3.3
Liver	9.7	2.9	5.2
Spleen	15.0	3.6	6.8
Right kidney	4.4	3.3	3.9
Left kidney	5.1	3.3	4.3
Bladder	16.9	5.5	11.2
Rectum	20.4	4.1	8.5
Uterus and ovary	5.4	3.7	4.3
Cervix and vagina	25.5	4.4	15.7
Intestine	6.8	3.3	4.7
Stomach	4.3	3.0	3.6
Cervical spine	10.8	3.2	5.8
Thoracic spine	17.6	3.2	6.3
Lumbar spine	4.5	3.2	4.0
Sacrum	7.8	3.4	4.8
Right iliac crest	29.8	3.6	8.9
Left iliac crest	26.9	3.5	8.5
Right femur	31.4	6.9	12.3
Left femur	14.1	6.7	10.3

(a) Continued.

Critical organ	D10 (Gy)	D90 (Gy)	Mean dose (Gy)
Right pelvic bone	23.1	3.7	13.1
Left pelvic bone	22.5	3.5	12.2

D10: The dose received to 10% of the organ volume.
D90: The dose received to 90% of the organ volume.

(b)

Site	Surface dose (cGy)/fraction			Percentage of prescription dose
	1st measurement	2nd measurement	Average	
Head				
Vertex of head	77.2	74.7	76.0	101.3%
Occipital	82.4	80.6	81.5	108.7%
Forehead	76.2	83.7	80.0	106.6%
Neck				
Anterior	73.2	73.9	73.6	98.1%
Posterior	99.8	85	92.4	123.2%
Chest				
Middle, upper	94.6	90.5	92.6	123.4%
Middle, lower	94.7	86.3	90.5	120.7%
Right axillary	89.1	89	89.1	118.7%
Left axillary	88.9	89.8	89.4	119.1%
Previous treated area (Left flank)	32.1	32.9	32.5	43.3%
Back				
Middle, upper	88.4	85.4	86.9	115.9%
Middle, lower	92.2	85.4	88.8	118.4%
Abdomen				
Middle, anterior	88.9	90.4	89.7	119.5%
Middle, posterior	99.4	86.3	92.9	123.8%
Upper extremities, right				
Upper arm	76.7	81.8	79.3	105.7%
Elbow	97.3	86.1	91.7	122.3%
Hand	84.8	80.1	82.5	109.9%
Fingers	84.7	87.1	85.9	114.5%
Upper extremities, left				
Upper arm	81.1	87.9	84.5	112.7%
Elbow	88.2	90.8	89.5	119.3%
Hand	86.2	84.5	85.4	113.8%
Fingers	85.3	87	86.2	114.9%
Right side of lower extremities				
Thigh, anterior	88	76.8	82.4	109.9%
Thigh, posterior	87.5	70.9	79.2	105.6%
Thigh, medial	88.8	76.1	82.5	109.9%
Lower leg, anterior	80.8	70.4	75.6	100.8%
Lower leg, posterior	82.3	64	73.2	97.5%
Foot	78	77.8	77.9	103.9%
Toes	90.5	88.9	89.7	119.6%

(b) Continued.

Site	Surface dose (cGy)/fraction			Percentage of prescription dose
	1st measurement	2nd measurement	Average	
Left side of lower extremity				
Thigh, anterior	86.1	74.3	80.2	106.9%
Thigh, posterior	99.6	82.4	91.0	121.3%
Thigh, medial	78	84.7	81.4	108.5%
Lower leg, anterior	81.9	61.7	71.8	95.7%
Lower leg, posterior	86.7	67.1	76.9	102.5%
Foot	79.1	83.2	81.2	108.2%
Toes	89.3	90.2	89.8	119.7%
Lesions				
Right ear lesion	85.5	74.6	80.1	106.7%
Left ear lesion	83.5	89	86.3	115.0%
Right neck lesion	92.1	78.3	85.2	113.6%
Lift neck lesion	94.4	76.7	85.6	114.1%
Buttock	75.8	71.3	73.6	98.1%
Vulva	89.5	82.4	86.0	114.6%
Right abdominal mass	91.5	87.2	89.4	119.1%
Right wrist	91.8	80.0	85.9	114.5%

(c)

Shift	Pretreatment		Posttreatment	
	Upper torso	Lower extremities	Upper torso	Lower extremities
Lateral (mm)	−2.76 ± 0.75	0.86 ± 1.18	−0.24 ± 0.37	0.61 ± 1.41
Longitudinal (mm)	0.72 ± 2.29	−0.01 ± 2.04	−0.74 ± 1.61	0.22 ± 2.18
Vertical (mm)	0.18 ± 2.17	−0.06 ± 1.99	0.28 ± 0.67	0.09 ± 1.00
Roll (degree)	0.14 ± 0.28	0.09 ± 0.10	−0.16 ± 0.32	−0.03 ± 0.09

Young patients should be thoroughly counseled regarding risks of gonadal toxicity [13]. In addition, a grade 3 erythema with bullous reaction during TSEBT was recorded in 26–32% of the cases [5, 7, 14]. The central CCCB techniques in HITS planning restrict the photon beams delivering obliquely and reduced doses of OARs (Figure 2(c)). The mean doses of thyroid, lung, liver, right kidney, left kidney, intestine, and uterine and ovary were 24.7, 4.6, 5.2, 3.9, 4.3, 4.3, 4.7, and 4.3 Gy, respectively (Table 1(a)). On the other hand, most of the toxicities during and after HITS are grade 1 with complete recovery. No destruction of the liver, renal, thyroid or gonadotropin functions was noted (Figure 5).

For TSEBT combined with photon beam irradiation, hematological complications related to the photon were a concern. Maingon and colleagues [5] noted myelosuppression (grade 2 WHO) in 17 cases. Additionally, after total body irradiation, 2/20 patients had a neutropenia below 500 granulocytes reversible without complication. Using HITS techniques, the hematological complications were reversible. Hematopoietic damages were treated with supportive measures including hematopoietic CSF [15], steroids [16], antioxidants [17], oral glutamine [18], and yeast-derived 1,3/1,6 glucopolysaccharide [19] to stimulate the granulocytes (neutrophils and eosinophils), monocytes, macrophages, and NK cell production and to modulate the immune system. The mean doses to the bone marrows (BMs) of the cervical, thoracic, and lumbar spine, sacrum, and bilateral iliac bone were 5.8, 6.3, 4.0, 4.8, and 8.7 Gy, respectively. In the future, the constraints for these BMs in the HITS plan should be stricter to diminish the possibility of hematological damages.

5. Conclusion

To our best knowledge, this is the first report of cutaneous T-cell lymphoma treated with HITS techniques to alternate TSEBT. HITS with dose painting techniques provide precise dosage delivery with impressive results, sparing critical organs, and offering limited transient and chronic sequela for advanced, previously locally irradiated, therapy-refractory cutaneous T-cell lymphoma. The proposed technique could be considered an acceptable alternative to TSEBT once the techniques are further improved to avoid the hematologic complications. Long-term followup is needed to confirm these preliminary findings.

Competing Interests

We have no personal or financial conflict of interest and have not entered into any agreement that could interfere with our access to the data on the research or upon our ability

to analyze the data independently, to prepare paper, and to publish them.

Authors' Contributions

All authors read and approved the final paper. Chen-Hsi Hsieh and Pei-Wei Shueng carried out all CT evaluations, study design, target delineations, and interpretation of the study. Chen-Hsi Hsieh drafted the paper. Shih-Chiang Lin, Meng-Hao Wu, Jen-Yu Wang, and Yu-Jen Chen took care of the patients. Hui-Ju Tien and An-Cheng Shiau made the treatment planning of HITS and carried out the evaluations. Yueh-Hung Chou and Chi-Kuan Chen provided the report of pathology.

Acknowledgment

This work was supported by the Far Eastern Memorial Hospital Grants (FEMH-2012-C-055 and FEMH 101-2314-B-418-010-MY3).

References

[1] C. Harrison, J. Young, D. Navi et al., "Revisiting low-dose total skin electron beam therapy in mycosis fungoides," *International Journal of Radiation Oncology Biology Physics*, vol. 81, no. 4, pp. e651–e657, 2011.

[2] R. T. Hoppe, Z. Fuks, and M. A. Bagshaw, "Radiation therapy in the management of cutaneous T-cell lymphomas," *Cancer Treatment Reports*, vol. 63, no. 4, pp. 625–632, 1979.

[3] R. D. Weaver, B. J. Gerbi, and K. E. Dusenbery, "Evaluation of dose variation during total skin electron irradiation using thermoluminescent dosimeters," *International Journal of Radiation Oncology Biology Physics*, vol. 33, no. 2, pp. 475–478, 1995.

[4] L. M. Gamble, T. J. Farrell, G. W. Jones, and J. E. Hayward, "Two-dimensional mapping of underdosed areas using radiochromic film for patients undergoing total skin electron beam radiotherapy," *International Journal of Radiation Oncology Biology Physics*, vol. 62, no. 3, pp. 920–924, 2005.

[5] P. Maingon, G. Truc, S. Dalac et al., "Radiotherapy of advanced mycosis fungoides: indications and results of total skin electron beam and photon beam irradiation," *Radiotherapy and Oncology*, vol. 54, no. 1, pp. 73–78, 2000.

[6] P. W. Shueng, S. C. Lin, N. S. Chong et al., "Total marrow irradiation with helical tomotherapy for bone marrow transplantation of multiple myeloma: first experience in Asia," *Technology in Cancer Research and Treatment*, vol. 8, no. 1, pp. 29–38, 2009.

[7] H. Hauswald, F. Zwicker, N. Rochet et al., "Total skin electron beam therapy as palliative treatment for cutaneous manifestations of advanced, therapy-refractory cutaneous lymphoma and leukemia," *Radiation Oncology*, vol. 7, article 118, 2012.

[8] G. W. Jones, B. M. Kacinski, L. D. Wilson et al., "Total skin electron radiation in the management of mycosis fungoides: consensus of the European organization for research and treatment of cancer (EORTC) cutaneous lymphoma project group," *Journal of the American Academy of Dermatology*, vol. 47, no. 3, pp. 364–370, 2002.

[9] Y. Anacak, Z. Arican, R. Bar-Deroma, A. Tamir, and A. Kuten, "Total skin electron irradiation: evaluation of dose uniformity throughout the skin surface," *Medical Dosimetry*, vol. 28, no. 1, pp. 31–34, 2003.

[10] N. M. Price, "Electron beam therapy. Its effect on eccrine gland function in mycosis fungoides patients," *Archives of Dermatology*, vol. 115, no. 9, pp. 1068–1070, 1979.

[11] G. Jones, L. D. Wilson, and L. Fox-Goguen, "Total skin electron beam radiotherapy for patients who have mycosis fungoides," *Hematology/Oncology Clinics of North America*, vol. 17, no. 6, pp. 1421–1434, 2003.

[12] K. R. Desai, R. D. Pezner, J. A. Lipsett et al., "Total skin electron irradiation of mycosis fungoides: relationship between acute toxicities and measured dose at different anatomic sites," *International Journal of Radiation Oncology Biology Physics*, vol. 15, no. 3, pp. 641–645, 1988.

[13] B. D. Smith and L. D. Wilson, "Cutaneous lymphomas," *Seminars in Radiation Oncology*, vol. 17, no. 3, pp. 158–168, 2007.

[14] A. Funk, F. Hensley, R. Krempien et al., "Palliative total skin electron beam therapy (TSEBT) for advanced cutaneous T-cell lymphoma," *European Journal of Dermatology*, vol. 18, no. 3, pp. 308–312, 2008.

[15] T. J. Smith, J. Khatcheressian, G. H. Lyman et al., "2006 update of recommendations for the use of white blood cell growth factors: an evidence-based clinical practice guideline," *Journal of Clinical Oncology*, vol. 24, no. 19, pp. 3187–3205, 2006.

[16] N. Watanabe, H. Narimatsu, J. Y. Noh et al., "Antithyroid drug-induced hematopoietic damage: a retrospective cohort study of agranulocytosis and pancytopenia involving 50,385 patients with Graves' disease," *Journal of Clinical Endocrinology and Metabolism*, vol. 97, no. 1, pp. E49–E53, 2012.

[17] K. N. Prasad, W. C. Cole, B. Kumar, and K. C. Prasad, "Pros and cons of antioxidant use during radiation therapy," *Cancer Treatment Reviews*, vol. 28, no. 2, pp. 79–91, 2002.

[18] P. Newsholme, L. Brennan, B. Rubi, and P. Maechler, "New insights into amino acid metabolism, β-cell function and diabetes," *Clinical Science*, vol. 108, no. 3, pp. 185–194, 2005.

[19] F. Hong, J. Yan, J. T. Baran et al., "Mechanism by which orally administered β-1,3-glucans enhance the tumoricidal activity of antitumor monoclonal antibodies in murine tumor models," *Journal of Immunology*, vol. 173, no. 2, pp. 797–806, 2004.

Hindawi Publishing Corporation
BioMed Research International
Volume 2013, Article ID 503421, 6 pages
http://dx.doi.org/10.1155/2013/503421

Clinical Study

Heart Rate Variability Is Associated with Survival in Patients with Brain Metastasis: A Preliminary Report

Yu-Ming Wang,[1,2] Hau-Tieng Wu,[3] Eng-Yen Huang,[2,4] Yu Ru Kou,[1] and Shu-Shya Hseu[5]

[1] *Institute of Physiology, National Yang-Ming University, Beitou, Taipei 11221, Taiwan*
[2] *Department of Radiation Oncology, Kaohsiung Chang Gung Memorial Hospital and Chang Gung University College of Medicine, Niao-Sung, Kaohsiung 83306, Taiwan*
[3] *Department of Mathematics, Stanford University, Stanford, CA 94305, USA*
[4] *School of Traditional Chinese Medicine, College of Medicine, Chang Gung University, Kwei-Shan, Taoyuan 33302, Taiwan*
[5] *Department of Anesthesiology, Taipei Veterans General Hospital, Beitou, Taipei 11217, Taiwan*

Correspondence should be addressed to Yu Ru Kou; yrkou@ym.edu.tw and Shu-Shya Hseu; sshseu10108@gmail.com

Received 30 June 2013; Accepted 12 August 2013

Academic Editor: Tsair-Fwu Lee

Impaired heart rate variability (HRV) has been demonstrated as a negative survival prognosticator in various diseases. We conducted this prospective study to evaluate how HRV affects brain metastasis (BM) patients. Fifty-one BM patients who had not undergone previous brain operation or radiotherapy (RT) were recruited from January 2010 to July 2012, and 40 patients were included in the final analysis. A 5-minute electrocardiogram was obtained before whole brain radiotherapy. Time domain indices of HRV were compared with other clinical factors on overall survival (OS). In the univariate analysis, Karnofsky performance status (KPS) <70 ($P = 0.002$) and standard deviation of the normal-to-normal interval (SDNN) <10 ms ($P = 0.004$) significantly predict poor survival. The multivariate analysis revealed that KPS <70 and SDNN <10 ms were independent negative prognosticators for survival in BM patients with hazard ratios of 2.657 and 2.204, respectively. In conclusion, HRV is associated with survival and may be a novel prognostic factor for BM patients.

1. Introduction

Brain metastasis (BM) is the most common intracranial malignancy, developing in 20%–40% of all cancer patients during the course of the disease. Typical BM treatments include surgical resection, stereotactic radiosurgery, and whole brain radiotherapy (WBRT) [1]. Medical professionals should choose a treatment according to the survival prognosis of the patients [2]. A widely used prognostic index, referred to as the radiation therapy oncology group recursive partitioning analysis (RPA) classification, was published by Gasper et al. [3] in 1997. Based on the RPA, patients are classified into 3 categories: RPA I includes patients who are <65 years old, with a Karnofsky performance status (KPS) ≥70, a controlled primary, and no extracranial metastasis; RPA III includes patients who demonstrate a KPS <70; all remaining patients are classified as RPA II [3]. Since 1997, several prognostic indices have been proposed, assessing the number of metastatic brain lesions, the largest intracranial lesion size, and the systemic disease status [4–6]. Although these prognostic indices are widely used in clinical settings, substantial proportion of erroneous survival prediction exists, for example, those reported by Nieder and Molls and Villà et al. [7, 8]. Erroneous prediction can eventually lead to an inadequate choice of treatment [7, 9]. Therefore, it is worthwhile to seek a novel parameter that accurately predicts survival in BM patients.

Heart rate variability (HRV) is a well-known physiological phenomenon in which the time interval between heart beats varies; in other words, the normal-to-normal beat (NN) interval sporadically varies. The HRV reflects the complexity of the physiological system that controls homeostasis in the human body. Numerous methods have been proposed to quantify and analyze the HRV, and time domain measures are widely applied. By using the standardized time domain analysis [10], several HRV indices can be generated from

the electrocardiogram (ECG), such as the standard deviation of the NN interval (SDNN), root mean square standard deviation of the NN interval (RMSSD), triangular interpolation of the NN interval histogram (TINN), number of pairs of adjacent normal-to-normal intervals differing by more than 50 ms (NN50), and the proportion of NN50 divided by total normal-to-normal intervals (pNN50) [10].

Previous studies have demonstrated that HRV provides a prognosis for various diseases including myocardial infarction, diabetes mellitus, and infection and can be used to attain the prognostic outcome in intensive care units [11–14]. Recently, scholars have examined how HRV affects cancer patients. Couck and Gidron and Kim et al. demonstrated that cancer patients possess a relatively lower HRV compared with that of healthy people [15, 16]. Among cancer patients, advanced stage patients possess a lower HRV than do those in the early stages of cancer [15]. In addition, Mouton et al. showed that low level of HRV can predict subsequent cancer progression by examining the increasing tumor markers [17]. Furthermore, impaired HRV has been correlated with a short survival time and is a poor prognosticator in patients with advanced cancer [16, 18, 19]. Although these studies have established the relationship between HRV and cancer survival, the effects of HRV on BM patients remain uninvestigated.

Based on the need for a novel prognosticator of BM patients survival, and the significant relationship between HRV and cancer survival, we conducted this prospective study to evaluate the hypothesis that time domain HRV indices are associated with survival and can be used as a prognostic factor in BM patients.

2. Materials and Methods

2.1. Patients. This prospective study was conducted between January 2010 and July 2012. Patients who were diagnosed with metastatic brain cancer and referred for palliative WBRT were enrolled in the study. To minimize the potential influence of medical treatments on HRV, patients who took antihypertensive drugs, sedatives, or antiarrhythmic drugs were excluded from the study. Patients who had undergone previous central nervous system or chest operation or radiotherapy (RT) were also excluded. For the limitation of HRV processing, patients with arrhythmia or too many premature ventricular contractions (defined as >1% of all beats) in the ECG recording were included in the study but excluded from the following analysis. The brain metastases were confirmed using contrast-enhanced magnetic resonance images or computed tomography (CT) scans. All patients underwent complete physical examination and ECG examination before WBRT was initiated. All clinical factors, previous local/systemic cancer treatment histories, and brain images were carefully reviewed for each patient. The study protocol was approved by the Institutional Review Board of Chang Gung Memorial Hospital (98-3760B), the study design was explained to each patient, and a written informed consent was obtained from all participants.

2.2. ECG Acquisition and Analysis. The ECG examinations were performed before the WBRT was initiated. The ECGs were executed after the patients had rested for 5 minutes in a quiet examination room in the supine position, and after their heartbeats and respiration rhythms had stabilized. The ECG signals were acquired using a commercialized ECG recorder (MyECG E3-80 portable ECG recorder; MSI, New Taipei City, Taiwan) for 5 minutes. The digital signals were saved at 12-bit resolution and a sampling rate of 1000 Hz. Next, the R peak of each valid QRS complex was detected using MyECG E3-80 portable ECG software (MSI, New Taipei City, Taiwan) and labeled with a time stamp. The time intervals between successful adjacent R peaks were collected for the normal-to-normal R-R interval time series. The time series were subsequently calculated using the same software according to the recommendations of the Task Force of the European Society of Cardiology and the North American Society of Pacing and Electrophysiology [10]. By using the time domain HRV analysis, several parameters were generated for further analysis including the SDNN, RMSSD, TINN, NN50, and pNN50. Because no previous reference could be used to stratify the BM patients, the values of the lower one-third of SDNN and RMSSD were used as the cutoff values for prognostic stratification.

2.3. Radiotherapy Treatment and Follow-Up. All patients were simulated by a CT simulator with slice thickness of 3.75 mm in supine position and immobilized with a thermoplastic cast. Then, patients underwent WBRT using 6- or 15-megavoltage photon irradiated via a conventional bilateral opposed helmet field. The radiotherapy dose to the whole brain was 30 Gy to 37.5 Gy in 10 to 15 daily fractions, 5 fractions per week. After completing the RT course, patients were followed at 1-2-month intervals with regular brain image surveys until their death. Patients who were unable to present at the out-patient clinic were contacted by telephone.

2.4. Evaluation of the Prognostic Factors and Statistics. The clinical factors of the patients were categorized in accordance with previously published articles [3–6]. In addition, the HRV indices including the SDNN and RMSSD were included for survival analysis. The overall survival (OS) was analyzed using the Kaplan-Meier method, and the log-rank test was used to evaluate statistical differences. A multivariate analysis was conducted for all factors by using the Cox's proportional hazard regression method. A significant difference was defined as $P < 0.05$. The analyses were all performed using the SPSS Statistics, version 17.0 (SPSS, Chicago, IL).

3. Results

3.1. Demographic Data and ECG Analysis. After the first phase of recruitment, the study comprised 51 patients. We excluded 11 patients (21.6%) with arrhythmias or with >1% premature ventricular contractions; thus, 40 patients were included in the final study.

The median age of our study participants was 61 years (range: 39–75). The most common primary cancers among these participants were nonsmall cell carcinoma originating

Table 1: Baseline patient characteristics (n = 40).

Characteristics	No.	(%)
Gender		
Female	21	52.5%
Male	19	47.5%
Age		
Median (range)	61 (39–75)	
<65	24	60.0%
≥65	16	40.0%
Primary		
NSCLC	24	60.0%
SCLC	6	15.0%
Breast cancer	4	10.0%
Others	6	15.0%
BM at diagnosis		
Not	23	57.5%
Yes	17	42.5%
KPS		
Median (range)	70 (30–80)	
<70	16	40.0%
≥70	24	60.0%
Extracranial metastasis		
Without	7	17.5%
With	33	82.5%
Primary status		
Not controlled	35	87.5%
Controlled	5	12.5%
RPA Class		
I	1	2.5%
II	23	57.5%
III	16	40%

NSCLC: Nonsmall cell lung cancer, SCLC: small cell lung cancer, BM at diagnosis: brain metastases confirmed at primary diagnosis, KPS: Karnofsky performance status, and RPA: recursive partitioning analysis.

from the lung (24/40) followed by small cell lung cancer (6/40) and breast cancer (4/40). Sixteen patients possessed confirmed brain metastases confirmed at the time of their primary cancer diagnosis. Most of the patients presented extracranial metastases, and their primary sites were not controlled. Only 1 patient was classified as RPA class I (Table 1).

3.2. HRV Analysis. Table 2 lists the results of the time domain HRV analysis. Because the NN50 was 0 in 28 patients, the NN50 and pNN50 indices were excluded from the analysis. An SDNN <10 ms or ≥10 ms and RMSSD <7 ms or ≥7 ms were used as prognostic factors in the survival analysis.

3.3. Overall Survival and Prognostic Factors. The status of each patient was tracked until death or until the end of the study. At the end of the final analysis in March 2013, 7 patients remained alive. The median follow-up time for all patients was 3.80 months, and it was 10.16 months for the patients who remained alive. In the univariate analysis, only the KPS <70 (P = 0.002; Figure 1) and SDNN <10 ms

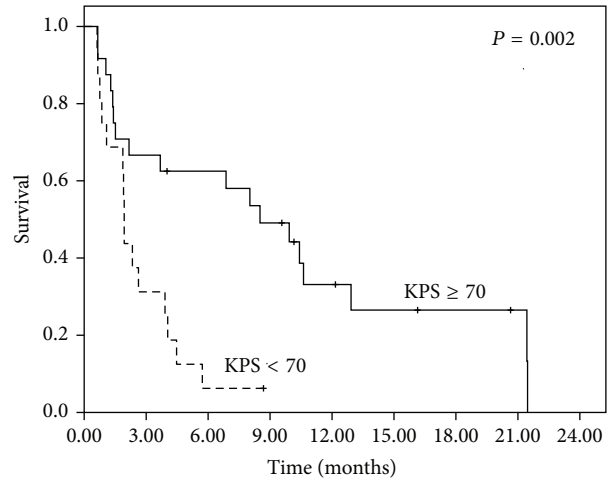

Figure 1: Overall survival of all patients stratified by KPS <70 or KPS ≥70.

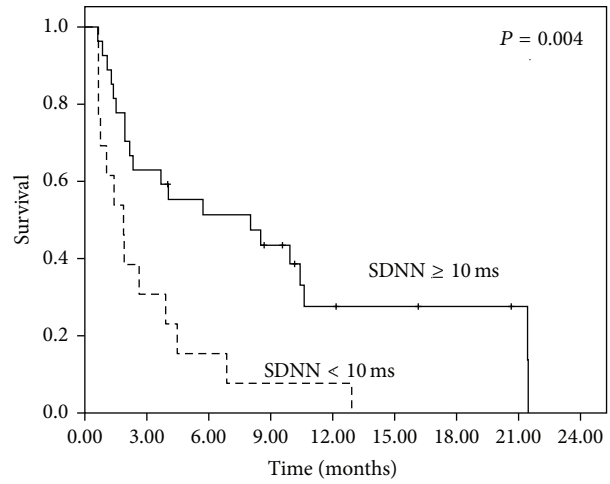

Figure 2: Overall survival of all patients stratified by SDNN <10 ms or SDNN ≥10 ms.

(P = 0.004; Figure 2) showed significance for OS (Table 3). The multivariate analysis further confirmed that the KPS <70 (P = 0.022) and SDNN <10 ms (P = 0.039) were independent prognosticators of OS, exhibiting hazard ratios of 2.657 (95% CI: 1.153–6.123) and 2.204 (95% CI: 1.046–4.733), respectively (Table 3).

4. Discussion

The results of this prospective study demonstrate that the HRV index, comprising an SDNN cutoff value of 10 ms, is a novel prognosticator for BM patients, and is independent from the commonly used prognostic indices. To the best of our knowledge, HRV has not been previously documented as a survival prognosticator for BM patients. Because HRV assessment is standardized [10], simple, noninvasive, and cost effective, the potential of this physiological measurement for daily use warrants further investigation.

Table 2: Time domain HRV analysis ($n = 40$).

HRV Indices	Mean	SD	Median	Lower one-third	Upper one-third
Mean NN (ms)	733.58	136.04	712.50	669.00	788.54
SDNN (ms)	14.30	7.68	15.00	10.06	17.06
RMSSD (ms)	11.65	7.88	10.50	6.53	15.06
TINN (ms)	76.65	28.41	78.00	63.00	94.00
NN50	2.45	5.34	0.00	0.00	0.00
pNN50 (%)	0.63	1.33	0.00	0.00	0.00

HRV: heart rate variability, SD: standard deviation, NN: normal-to-normal interval, SDNN: standard deviation of normal-to-normal interval, RMSSD: root mean square standard deviation of normal-to-normal interval, TINN: triangular interpolation of normal-to-normal interval histogram, NN50: number of pairs of adjacent normal-to-normal intervals differing by more than 50 ms, and pNN50: the proportion of NN50 divided by total normal-to-normal intervals.

Table 3: Prognostic factors for overall survival-univariate analysis and multivariate analysis.

Characteristics	Univariate analysis				Multivariate analysis	
	3M survival (%)	6M survival (%)	Median survival (M)	P value	HR (95% CI)	P value
Gender				0.711		0.604
Female	57.1	42.9	3.9		(—)	
Male	47.4	35.5	2.0			
Age				0.283		0.303
<65	54.2	45.8	3.9		(—)	
≥65	50.0	29.2	2.6			
Primary				0.160		0.333
NSCLC	54.2	48.5	3.7		(—)	
Others	50.0	29.2	1.9			
BM at diagnosis				0.996		0.775
No	50.0	36.7	2.3		(—)	
Yes	56.3	37.5	3.7			
KPS				0.002		0.022
<70	31.3	0.63	1.9		2.657 (1.153–6.123)	
≥70	66.7	62.5	8.5		Reference	
Extracranial metastasis				0.087		0.171
Without	71.4	57.1	21.4		(—)	
With	48.5	36.4	2.6			
Primary status				0.400		0.097
Not controlled	51.4	39.5	3.7		(—)	
Controlled	60.0	40.0	3.9			
SDNN (ms)				0.004		0.039
<10	30.8	15.4	1.8		2.204 (1.046–4.733)	
≥10	63.0	51.4	8.0		Reference	
RMSSD (ms)				0.100		0.868
<7	42.9	21.4	1.9		(—)	
≥7	57.7	49.7	5.7			

HR: hazard ratio, CI: confidence interval, NSCLC: Nonsmall cell lung cancer, BM at Diagnosis: brain metastases confirmed at primary diagnosis, KPS: Karnofsky performance status, SDNN: standard deviation of normal-to-normal interval, and RMSSD: root mean square standard deviation of normal-to-normal interval.

Among the participants, the median SDNN and RMSSD were 15.0 ms and 10.5 ms, respectively. These values are considerably lower than the published HRV SDNN data from health populations in previous studies [20, 21]. De Couck and Gidron published a large series HRV evaluation of cancer patients ($N = 657$) [15]. After analyzing 10-second ECG recordings, the average patient SDNN value was 21.65 ms, and the values for stage 3-4 patients were significantly lower than those of stage 1-2 patients [15]. In addition, Kim et al. [16] evaluated HRV in 68 terminal cancer patients who were referred for hospice care. The median SDNN and RMSSD were 14.40 ms and 11.35 ms, respectively [16]. The findings in the current study are compatible to these findings, as the patients demonstrated terminal statuses; extremely low HRV values were expected.

However, the mechanism that directly causes the attenuated HRV in BM patients remains unclear. Two possible rationales might explain the relationship: increased intracranial

pressure (IICP) and the "vagal-cancer" relationship. The data in previously published studies of brain injury patients have demonstrated a significant correlation between intracranial pressure (ICP) and HRV [22, 23]. In addition to ICP monitor, the authors in Winchell and Hoyt found that patients with IICP had significant attenuated HRV indices, and low HRV correlates with a poor outcome [23]. Biswas et al. reported the same findings in pediatric brain injury patients [22]. The current study did not involve evaluating ICP by the ICP monitor; however, IICP caused by intracranial masses could be expected because the BM patients had never undergone surgical resection of their metastatic tumors. This could explain their attenuated HRV.

The HRV reflects the dynamics of the complex physiological system [10]. It has been demonstrated that vagus nerve activity is highly correlated with HRV [24, 25]. Previous mouse model studies have demonstrated that induced inflammation can cause attenuated HRV through the vagus nerve [26]. It has also been reported that increased oxidative stress is related to decreased HRV [27]. Furthermore, inflammatory reactions and excessive oxidative stress can predispose cancer microenvironments and are related to impaired vagus nerve activity [28]. Based on these previous studies, it is reasonable to doubt that in patients who exhibit a disseminated cancer status and a global physiological environment altered by the cancer, HRV could be attenuated as a consequence of impaired vagus nerve activity. This "vagal-cancer" relationship may explain the low HRV levels in BM patients.

In this study, several time domain HRV indices, such as the TINN, NN50, and pNN50, were not employed for survival analysis. The TINN is an unreliable index for the current study, because a 5-minute ECG recording was not sufficiently long to evaluate this index [10]. The NN50 and pNN50 were not evaluated because 28 patients lacked NN intervals larger than 50 ms (NN50 = 0 and pNN50 = 0).

There are several limitations in this preliminary report. First, the study population was heterogeneous, and we cannot conclude how SDNN would perform in different patient subgroups. Additional studies focusing on these differences are required. Second, the metastatic location was not considered. Although previous study has indicated that intracranial metastatic location is not a survival prognosticator [3] the relationship between intracranial location and HRV remains unknown. We were unable to perform additional analysis because 31 of the participants presented both supratentorial and infratentorial lesions; this issue should be investigated in future studies. Third, the sample size was not sufficiently large and was relatively small compared to previously published studies on BM prognosis [3–6]. The limited number of cases may explain why several documented prognosticators, such as controlled primary, extracranial metastasis, and age, did not exhibit significance in terms of survival. To validate our findings regarding HRV and BM prognosis, additional large-scale studies are warranted. Finally, the HRV analysis is limited to patients who present arrhythmias and ectopic beats, and 21.6% of the patients were not analyzed for HRV. Therefore, alternative HRV analysis tools should be sought for these patients.

In conclusion, the association of HRV as a survival prognosticator in BM patients is studied. The results suggested that SDNN <10 ms may be an independent negative prognosticator of survival. Additional large-scale studies are warranted to evaluate the clinical application of SDNN in the risk stratification of BM patients and as a possible guide for selecting treatment options.

Conflict of Interests

No potential conflict of interests exists in this study.

Authors' Contribution

Yu-Ming Wang, Hau-Tieng Wu, Eng-Yen Huang, Yu Ru Kou, and Shu-Shya Hseu conceived and designed the experiments. Yu-Ming Wang and Eng-Yen Huang performed the experiments. Yu-Ming Wang, Hau-Tieng Wu, Yu Ru Kou, and Shu-Shya Hseu analyzed the data. Yu-Ming Wang, Hau-Tieng Wu, Yu Ru Kou, and Shu-Shya Hseu wrote the paper. Yu Ru Kou and Shu-Shya Hseu contributed equally to this work as co-corresponding authors.

Acknowledgment

Hau-Tieng Wu acknowledges the support of AFOSR Grant FA9550-09-1-0643. The authors thank the patients and their families for their willingness to participate in this study.

References

[1] L. R. Kleinberg, *Brain Metastasis: A Multidisciplinary Approach*, Demos, New York, NY, USA, 2009.

[2] M. N. Tsao, D. Rades, A. Wirth et al., "Radiotherapeutic and surgical management for newly diagnosed brain metastasis(es): an American Society for Radiation Oncology evidence-based guideline," *Practical Radiation Oncology*, vol. 2, no. 3, pp. 210–225, 2012.

[3] L. Gaspar, C. Scott, M. Rotman et al., "Recursive Partitioning Analysis (RPA) of prognostic factors in three Radiation Therapy Oncology Group (RTOG) brain metastases trials," *International Journal of Radiation Oncology Biology Physics*, vol. 37, no. 4, pp. 745–751, 1997.

[4] J. Lorenzoni, D. Devriendt, N. Massager et al., "Radiosurgery for treatment of brain metastases: estimation of patient eligibility using three stratification systems," *International Journal of Radiation Oncology Biology Physics*, vol. 60, no. 1, pp. 218–224, 2004.

[5] P. W. Sperduto, B. Berkey, L. E. Gaspar, M. Mehta, and W. Curran, "A new prognostic index and comparison to three other indices for patients with brain metastases: an analysis of 1,960 patients in the RTOG database," *International Journal of Radiation Oncology Biology Physics*, vol. 70, no. 2, pp. 510–514, 2008.

[6] E. Weltman, J. V. Salvajoli, R. A. Brandt et al., "Radiosurgery for brain metastases: a score index for predicting prognosis," *International Journal of Radiation Oncology, Biology, Physics*, vol. 46, no. 5, pp. 1155–1161, 2000.

[7] C. Nieder and M. Molls, "Validation of graded prognostic assessment index for patients with brain metastases: in regard to Sperduto et al. (Int J Radiat Oncol Biol Phys 2008;70:510-514),"

International Journal of Radiation Oncology Biology Physics, vol. 72, no. 5, p. 1619, 2008.

[8] S. Villà, D. C. Weber, C. Moretones et al., "Validation of the new graded prognostic assessment scale for brain metastases: A Multicenter Prospective Study," *Radiation Oncology*, vol. 6, article 23, 2011.

[9] C. Nieder and M. P. Mehta, "Prognostic indices for brain metastases—usefulness and challenges," *Radiation Oncology*, vol. 4, article 10, 2009.

[10] Task Force of the European Society of Cardiology and the North American Society of Pacing and Electrophysiology, "Standards of measurement, physiological interpretation, and clinical use," *European Heart Journal*, vol. 17, no. 3, pp. 354–381, 1996.

[11] S. Ahmad, A. Tejuja, K. D. Newman, R. Zarychanski, and A. J. E. Seely, "Clinical review: a review and analysis of heart rate variability and the diagnosis and prognosis of infection," *Critical Care*, vol. 13, no. 6, article 232, 2009.

[12] D. Almoznino-Sarafian, G. Sarafian, I. Zyssman et al., "Application of HRV-CD for estimation of life expectancy in various clinical disorders," *European Journal of Internal Medicine*, vol. 20, no. 8, pp. 779–783, 2009.

[13] R. Pop-Busui, G. W. Evans, H. C. Gerstein et al., "Effects of cardiac autonomic dysfunction on mortality risk in the Action to Control Cardiovascular Risk in Diabetes (ACCORD) trial," *Diabetes Care*, vol. 33, no. 7, pp. 1578–1584, 2010.

[14] H.-W. Yien, S.-S. Hseu, L.-C. Lee, T. B. J. Kuo, T.-Y. Lee, and S. H. H. Chan, "Spectral analysis of systemic arterial pressure and heart rate signals as a prognostic tool for the prediction of patient outcome in the intensive care unit," *Critical Care Medicine*, vol. 25, no. 2, pp. 258–266, 1997.

[15] M. De Couck and Y. Gidron, "Norms of vagal nerve activity, indexed by Heart Rate Variability, in cancer patients," *Cancer Epidemiology*, 2013.

[16] D. H. Kim, J. A. Kim, Y. S. Choi, S. H. Kim, J. Y. Lee, and Y. E. Kim, "Heart rate variability and length of survival in hospice cancer patients," *Journal of Korean Medical Science*, vol. 25, no. 8, pp. 1140–1145, 2010.

[17] C. Mouton, A. Ronson, D. Razavi et al., "The relationship between heart rate variability and time-course of carcinoembryonic antigen in colorectal cancer," *Autonomic Neuroscience*, vol. 166, no. 1-2, pp. 96–99, 2012.

[18] J.-K. Chiang, M. Koo, T. B. J. Kuo, and C.-H. Fu, "Association between cardiovascular autonomic functions and time to death in patients with terminal hepatocellular carcinoma," *Journal of Pain and Symptom Management*, vol. 39, no. 4, pp. 673–679, 2010.

[19] N. Fadul, F. Strasser, J. L. Palmer et al., "The association between autonomic dysfunction and survival in male patients with advanced cancer: A Preliminary Report," *Journal of Pain and Symptom Management*, vol. 39, no. 2, pp. 283–290, 2010.

[20] D. Nunan, G. R. H. Sandercock, and D. A. Brodie, "A quantitative systematic review of normal values for short-term heart rate variability in healthy adults," *PACE - Pacing and Clinical Electrophysiology*, vol. 33, no. 11, pp. 1407–1417, 2010.

[21] S. B. Park, B. C. Lee, and K. S. Jeong, "Standardized tests of heart rate variability for autonomic function tests in healthy Koreans," *International Journal of Neuroscience*, vol. 117, no. 12, pp. 1707–1717, 2007.

[22] A. K. Biswas, W. A. Scott, J. F. Sommerauer, and P. M. Luckett, "Heart rate variability after acute traumatic brain injury in children," *Critical Care Medicine*, vol. 28, no. 12, pp. 3907–3912, 2000.

[23] R. J. Winchell and D. B. Hoyt, "Analysis of heart-rate variability: a noninvasive predictor of death and poor outcome in patients with severe head injury," *Journal of Trauma*, vol. 43, no. 6, pp. 927–933, 1997.

[24] S. Akselrod, D. Gordon, and F. A. Ubel, "Power spectrum analysis of heart rate fluctuation: a quantitative probe of beat-to-beat cardiovascular control," *Science*, vol. 213, no. 4504, pp. 220–222, 1981.

[25] T. B. J. Kuo, C. J. Lai, Y.-T. Huang, and C. C. H. Yang, "Regression analysis between heart rate variability and baroreflex-related vagus nerve activity in rats," *Journal of Cardiovascular Electrophysiology*, vol. 16, no. 8, pp. 864–869, 2005.

[26] K. D. Fairchild, V. Srinivasan, J. R. Moorman, R. P. A. Gaykema, and L. E. Goehler, "Pathogen-induced heart rate changes associated with cholinergic nervous system activation," *American Journal of Physiology—Regulatory Integrative and Comparative Physiology*, vol. 300, no. 2, pp. R330–R339, 2011.

[27] P. Pavithran, H. Nandeesha, V. Sathiyapriya, Z. Bobby, and T. Madanmohan, "Short-term heart variability and oxidative stress in newly diagnosed essential hypertension," *Clinical and Experimental Hypertension*, vol. 30, no. 7, pp. 486–496, 2008.

[28] Y. Gidron, H. Perry, and M. Glennie, "Does the vagus nerve inform the brain about preclinical tumours and modulate them?" *Lancet Oncology*, vol. 6, no. 4, pp. 245–248, 2005.

Hindawi Publishing Corporation
BioMed Research International
Volume 2013, Article ID 321762, 7 pages
http://dx.doi.org/10.1155/2013/321762

Research Article

Total Marrow Irradiation as Part of Autologous Stem Cell Transplantation for Asian Patients with Multiple Myeloma

Shih-Chiang Lin,[1,2,3] Pei-Ying Hsieh,[1] Pei-Wei Shueng,[4] Hui-Ju Tien,[4] Li-Ying Wang,[5,6] and Chen-Hsi Hsieh[4,7,8]

[1] *Division of Medical Oncology and Hematology, Department of Internal Medicine, Far Eastern Memorial Hospital, New Taipei City 220, Taiwan*
[2] *Department of Nursing, Oriental Institute of Technology, New Taipei City 220, Taiwan*
[3] *Department of Biotechnology, School of Healthy Technology, Ming Chuan University, Taipei 111, Taiwan*
[4] *Division of Radiation Oncology, Department of Radiology, Far Eastern Memorial Hospital, No. 21, Section 2, Nanya S. Road, Banqiao District, New Taipei City 220, Taiwan*
[5] *School and Graduate Institute of Physical Therapy, College of Medicine, National Taiwan University, Taipei 100, Taiwan*
[6] *Physical Therapy Center, National Taiwan University Hospital, Taipei 100, Taiwan*
[7] *Department of Medicine, School of Medicine, National Yang-Ming University, Taipei 112, Taiwan*
[8] *Institute of Traditional Medicine, School of Medicine, National Yang-Ming University, Taipei 112, Taiwan*

Correspondence should be addressed to Chen-Hsi Hsieh; chenciab@gmail.com

Received 5 June 2013; Revised 6 August 2013; Accepted 7 August 2013

Academic Editor: Maria F. Chan

To compare the outcomes of melphalan 200 mg/m^2 (HDM200) and 8 Gy total marrow irradiation (TMI) delivered by helical tomotherapy plus melphalan 140 mg/m^2 (HDM140 + TMI 8 Gy) in newly diagnosed symptomatic multiple myeloma (MM) Asian patients. Between 2007 and 2010, nine consecutive myeloma patients who were scheduled to undergo autologous stem cell transplantation (ASCT) were studied. The patients received three cycles of vincristine-adriamycin-dexamethasone (VAD) regimen as induction chemotherapy, and if they had a partial response, peripheral blood stem cells were collected by dexamethasone-etoposide-cyclophosphamide-cisplatin (DECP). In arm A, six patients received the HDM200. In arm B, three patients received HDM140 + TMI 8 Gy. In arm B, the neutropenic duration was slightly longer than in arm A ($P = 0.048$). However, hematologic recovery (except for neutrophils), transfusion requirement, median duration of hospitalization, and the dose of G-CSF were similar in both arms. The median duration of overall survival and event-free survival was similar in the two arms ($P = 0.387$). As a conditioning regiment, HDM140 + TMI 8 Gy provide another chance for MM Asian patients who were not feasible for HDM200.

1. Introduction

The outcome of autologous stem cell transplantation (ASCT) patients for newly diagnosed multiple myeloma (MM) is superior to that of patients receiving conventional chemotherapy [1–3]. Attal et al. [1] reported that 8 Gy total body irradiation (TBI) plus 140 mg/m^2 intravenous melphalan (HDM140) improved the response rate and overall survival compared with conventional chemotherapy in patients with MM. The impact of complete response (CR) achievement has been shown with high dose preconditioning [1, 2]. To improve survival, the objective is to increase CR rates before autologous stem cell transplantation (ASCT); a total of 200 mg/m^2 melphalan (HDM200) without TBI is an alternative method [2–4]. The Intergroupe Francophone du Mye'lome (IFM) 9502 trial compared the conditioning regimen 8 Gy TBI + HDM140 and HDM200 without TBI followed by ASCT [5]. The results revealed that HDM200 could be an alternative conditioning regimen for MM.

The complications cause by TBI have been reported. The pulmonary complications were concerned by TBI position, with beam energy ($P = 0.02$) [6] and the absence of lung

shielding [7]. Helical tomotherapy (HT, Tomotherapy Hi-Art System, v. 3.2.2.35., TomoTherapy Inc., Madison, WI) is new CT-based rotational intensity modulated radiotherapy. Total marrow irradiation (TMI) with HT is designed to avoid the complications of TBI while achieving the effectiveness of TBI. Dosimetric studies showed reduced doses to adjacent critical normal organs reduced toxicity after TMI [8–10]. The advantages, acute toxicities, initial clinical experiences, and challenges of TMI were reported recently [10–12].

Recently, we reported the Asian experience with treating newly diagnosed MM patients with 8 Gy TMI by HT plus HDM140 [10]; patients subsequently received maintenance therapy with thalidomide [13] and dexamethasone. We found that HDM140 + TMI 8 Gy regimen was an acceptable conditioning regimen for MM patients. The preliminary outcomes were similar for Asians as for other races. In the current follow-up study, we compared the acute and early chronic toxicities, CR rates, very good partial response (VGPR) rates, and early results of progression-free survival (PFS) and overall survival (OS) in patients treated with HDM140 + TMI 8 Gy or HDM200 without TBI followed by ASCT.

2. Materials and Methods

2.1. Patient Characteristics. We enrolled nine consecutive myeloma patients who underwent ASCT at Far Eastern Memorial Hospital (diagnosed between 2007 and 2010). Eligibility criteria included age less than 65 years and symptomatic MM. Patients were excluded if they had the following: (1) stable stage I MM (Durie-Salmon classification [14]); (2) previous cytotoxic chemotherapy or radiotherapy; (3) severe abnormalities of cardiac, pulmonary, or hepatic function; or (4) serum creatinine levels >2 mg/dL. All patients gave informed consent, and the study was approved by the institutional ethics committee of the Far Eastern Memorial Hospital.

2.2. Autologous Stem Cell Transplantation Regimen. The treatment protocol was modified from the Intergroupe Francophone du Myélome 9502 randomized trial [5]. Briefly, the patients received three cycles of the vincristine-adriamycin-dexamethasone (VAD) regimen, as in the trial (Figure 1). If they achieved a partial response (M-protein reduced by <50%), then they received one course of dexamethasone-etoposide-cyclophosphamide-cisplatin (DECP) with granulocyte colony-stimulating factor (G-CSF) mobilization. Two weeks later, peripheral blood stem cells (PBSCs) were collected. Stem cells were collected after G-CSF priming (10 μg/kg/d) in steady state [15]. Daily apheresis was continued until at least 2×10^6 CD34 cells per kilogram were collected. No $CD34^+$ selection was performed. Two weeks after PBSC collection, the evaluation for ASCT was done. If cardiopulmonary, hepatic, and renal functions remained adequate, the patients received HDM140 + TMI 8 Gy or HDM200; the time from pre-HSCT evaluation to start of HDM140 + TMI 8 Gy or HDM200 (preconditioning) treatment was about 4 weeks. All of the patients received thalidomide for maintenance therapy after stem cell transplantation.

In arm A, HDM200 was administered for two days by infusion over 30 minutes. In arm B, patients received 8 Gy TMI by HT delivered in four fractions over a 4-day period (days 6, 5, 4, and 3) plus HDM140. HDM140 was administered for two days by infusion over 30 minutes, too. PBSC transplantation was performed on day 0. Hematopoietic growth factor support with G-CSF was provided on day 5 after transplantation until granulocyte recovery [5].

Thalidomide (50–200 mg/d) was started 100 days or later after TMI and was continued for 6 months following the achievement of complete remission, or for at least 12 months for patients with persistent evidence of residual disease [13].

2.3. Radiotherapy Technique. Details of the HT technique have been previously published [10]. Briefly, An AccuFix Cantilever Board (WFR/Aquaplast Corporation and Q-Fix Systems, LLC, Wyckoff, New Jersey, USA) with thermoplastic fixation or type-S thermoplastics head frame (MT-CHFN-C, Civco MedTec, Kalona, Iowa, USA) with mold care cushion was used for head and shoulder immobilization. A BlueBAG BodyFIX total body cushion system (Medical Intelligence, Schwabmünchen, Germany), which used a vacuum to produce a uniform pressure, was used to fix the main trunk and extremities in place.

The radiotherapy was planned with patients in a supine position for head-first upper torso therapy and with feet-first lower extremity therapy. The planning CT images were performed using dual source CT (Siemens SOMATOM Definition, Siemens Healthcare, Erlangen, Germany) where three sets of images were acquired during normal breathing, inspiration, and shallow expiration for the upper torso.

All of the CT images were sent to the Pinnacle^3 Treatment Planning System (Philips Healthcare, Madison, Wisconsin, USA) for contouring. The clinical target volume (CTV) included the entire skeletal system. The margins for the planning target volume (PTV) were 0.8 cm for CTV extremities and 0.5 cm for all other bones of the CTV. The organs at risk (OAR) included the brain, optic nerves, lenses, eyes, parotid glands, oral cavity, thyroid gland, bilateral lungs, esophagus, heart, liver, spleen, pancreases, kidneys, bowel, bladder, and reproductive organs. After contouring the targets and critical organs, the images and structure set were sent to the Tomotherapy Hi-Art Planning Station for processing (Tomotherapy, Inc., Madison, Wisconsin, USA).

The prescription dose was 200 cGy per day (in 4 fractions) for a total dose of 800 cGy to the PTV. For the planning objective, at least 95% of the volume of PTV was to receive 800 cGy, with the mean dose to the OAR reduced to 50% of the prescribed dose. The field width, pitch, and modulation factor (MF) used for the treatment planning optimization were 2.5 cm, 0.32, and 3.0 for the upper torso and 5.0 cm, 0.4, and 2.0 for the lower extremities, respectively.

2.4. Follow-Up and Response Criteria. Mandatory evaluations included physical assessment, routine hemogram, and comprehensive chemistry panel, serum protein electrophoresis every 3 months, and bone radiographs and bone marrow biopsies at 30 days and 6 and 12 months post-TMI or

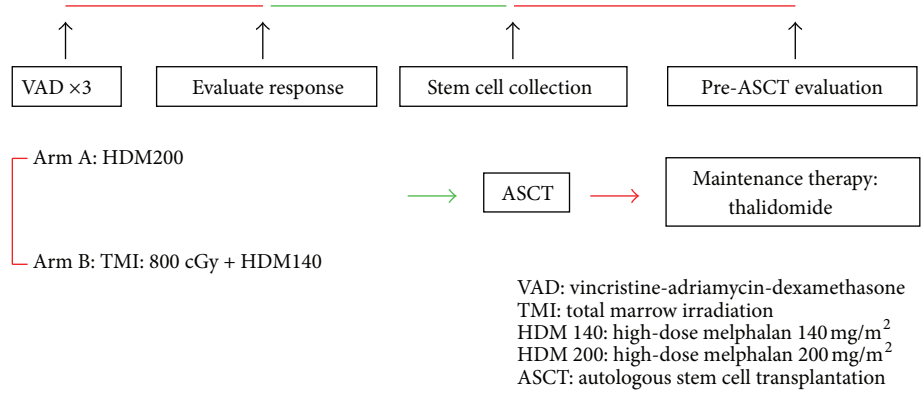

Figure 1: Study design profile.

HDM200 and yearly thereafter. Toxicity of treatment was scored according to the Common Terminology Criteria for Adverse Events v3.0. Complete response (CR) was defined as the absence of serum and urinary M-protein and no more than 5% plasma cells on bone marrow. Very good partial response (VGPR) was defined as 90% or greater decrease in bone marrow plasma cells and blood M-protein levels. Partial response (PR) was defined as 50% or greater decrease in blood and bone marrow findings. Stable disease was defined as less than 25% decrease in blood and bone marrow findings for a minimum of 3 months. Progression was defined as greater than 25% increase in M protein, greater than 25% increase in bone marrow plasma cells, or new bone lesions [11].

2.5. Analysis. Descriptive statistical analyses were applied for patient and disease characteristics, treatment features, and toxicity. All analyses were performed using the SPSS, version 12.0 (SPSS, Chicago, IL, USA).

3. Results

3.1. Patient Population. Nine patients were enrolled between 2007 and 2010. In arm A, six patients received the common conditioning regimen of 200 mg/m^2 melphalan. In arm B, three patients received the new regimen of 8 Gy TMI plus 140 mg/m^2 melphalan. All of the patients received thalidomide for maintenance therapy after stem cell transplantation.

Patient characteristics for the nine patients are given in Table 1. The median age was 54 for arm A (range: 47–62) and 55 for arm B (range: 55–56). The majority of patients were treated for stage III disease. No patient had received prior radiotherapy.

3.2. Response to Induction VAD Regimen and HDT. In arm A, one patient achieved CR and the other one achieved VGPR before ASCT. In arm B, one patient achieved VGPR before ASCT. For arm A versus arm B, the CR rate to HDT was 1/6 versus 1/3; the VGPR rate to HDT was 4/6 versus 1/3; the median OS and PFS were 1223 versus 1556 days and 982 versus 1101 days, respectively (Table 2). The PFS was similar in the two arms ($P = 0.387$, Figure 2). Each group had one patient death due to disease progression.

3.3. Toxicities. Table 3 illustrates engraftment, hospitalization time, and transplantation-related toxicities. In arm B, the duration of neutropenia was one day longer than in arm A ($P = 0.048$, Table 3). Similar side effects were noted in the two groups. However, arm B experienced a shorter duration of thrombocytopenia, fewer platelet and red blood cell transfusions, and a shorter duration of intravenous antibiotic therapy than in arm A.

4. Discussion

In newly diagnosed patients with MM treated with high-dose radiotherapy, the goal of the conditioning regimen is to achieve the best response rate with the least toxicity. The most widely used conditioning regimens are HDM200 and HDM140 + TBI [16]. The Intergroupe Francophone du Myélome 90 trial prospectively compared conventional chemotherapy with high-dose radiotherapy [1]. In this trial the conditioning regimen consisted of 8 Gy TBI plus HDM140. The CR rate after intensive therapy was 22%, and the response rate, event-free survival, and overall survival in patients with MM were improved. Furthermore, Moreau et al. [5] compared HDM200 and HDM140 + 8 Gy TBI as conditioning regimens for peripheral blood stem cell transplantation in patients with newly diagnosed MM. They reported that HDM200 could be an alternative conditioning regimen for MM.

The pulmonary complications were statistically increased by prone and supine versus lateral TBI position ($P = 0.02$) and with 15 MV versus 9 MV beam energy ($P = 0.02$) [6]. A conditioning regimen of 12 Gy TBI in 6 daily fractions induces an interstitial pneumonitis incidence of about 11% in the absence of lung shielding [7]. Fatal interstitial pneumonitis using hyperfractionated TBI with standing position was still as high as 18% [17]. Compared with TBI technique, doses to the sensitive organs in TMI techniques were reduced by 15%–70% of the target dose [11, 18] or 1.7- to 7.5-fold reduction in median organ doses [8]. Somlo et al. [12]

Table 1: Main characteristics at diagnosis of the nine patients according to treatment group.

	Arm A ($n = 6$)	Arm B ($n = 3$)	P
Age	54 (47–62)	55 (55-56)	1.000
Gender			
Female	3 (50%)	2 (67%)	0.595
Male	3 (50%)	1 (33%)	
Durie-Salmon stage			
2A	1 (17%)	0	0.643
3A	3 (50%)	3 (100%)	
3B	2 (33%)	0	
M component			
IgG	4 (67%)	3 (100%)	0.417
LCD	2 (33%)	0	
Hemoglobin	6.6 (5.5–12.5)	9.6 (8.4–11.1)	1.000
Serum calcium	8.75 (7.6–9.4)	9.6 (8.7–11.2)	1.000
Serum creatinine	1.74 (0.62–3.86)	0.93 (0.8–1.1)	0.524
Serum B2-microglobulin	2637 (1890–3033)	2143 (1515–3376)	1.000

Table 2: Response to induction vincristine-adriamycin-dexamethasone (VAD) regimen and high dose therapy (HDT).

	Arm A	Arm B	P
Median no. of course of VAD (range)	3 (3-4)	3 (3)	1.000
Response to VAD			1.000
CR	1	0	
VGPR	1	1	
PR	4	2	
Median no. of CD34 (10^6/kg) infused (range)	6.75 (3.6–9.14)	4.9 (4.12–6.21)	0.167
Response to HDT			1.000
CR	1	1	
VGPR	4	1	
PR	1	1	
Toxic death	0	0	1.000
Death due to disease progress	1	1	1.000
Overall survival, day (median)	1223 (709–1659)	1566 (737–2160)	0.515
Progression-free survival, day (median)	982 (607–1456)	1101 (677–1475)	0.387

CR: complete response; VGPR: very good partial response; PR: partial response.

Table 3: Engraftment, hospitalization time, and transplantation-related toxicity.

	Arm A	Arm B	P
Dose of G-CSF (median)	2675 (18 K–36 K)	2600 (15 K–39 K)	1.000
Duration of neutropenia, day (median)	9.5 (6–19)	10.7 (10-11)	0.048*
Duration of thrombocytopenia, day (median)	16.2 (7–23)	11.3 (10–13)	0.167
No. of platelet transfusions (median)	42 (24–72)	24 (12–36)	1.000
No. of red blood cell transfusions (median)	2.3 (0–8)	1.3 (0–4)	1.000
Duration of hospitalization, day (median)	28.2 (26–32)	29.7 (28–31)	0.226
Duration of intravenous antibiotics, day (median)	5.2 (0–13)	3.3 (0–10)	1.000

*: P value < 0.05.

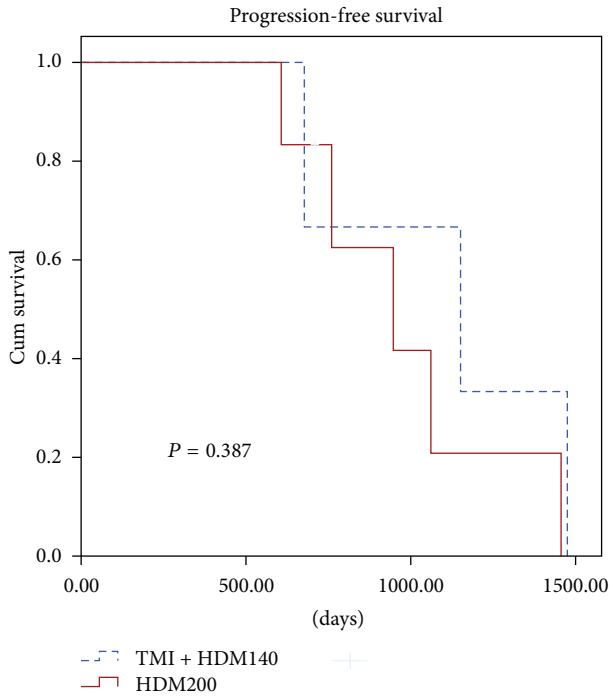

Figure 2: Cumulative (Cum) survival curves for patients treated with HDM200 or HDM140 + TMI 8 Gy. Curve for progression-free survival (according to treatment group) was illustrated. Cum survival: Cumulative survival.

reported that the estimated median radiation dose to normal organs was 11% to 81% of the prescribed marrow dose. In our previous report, the dose reduction of TMI tomotherapy to various OARs of head, chest, and abdomen relative to TBI varied from 31% to 74%, 21% to 51%, and 46% to 63%, respectively [10]. The potential advantages, acute toxicities, initial clinical experiences, and challenges of this approach were reported recently [11]. The maximum tolerated dose for TMI was 1,600 cGy (200 cGy twice daily × 4 days) [12]. Under these doses, grade 3 or 4 nausea/emesis, fatigue, and metabolic abnormality were 2/22, 2/22, and 4/22, respectively [12]. Wong et al. [8] reported that grade 2 nausea and grade 1 emesis occurred only briefly on day 2 of TMI. Skin erythema, oral mucositis, esophagitis, and enteritis were not observed. In our previous experience of TMI treatment, one with grade 1 vomiting, two with grade 1 nausea, one with grade 1 mucositis, and three with grade 1 anorexia were noted [10]. These data hit the potential dosimetric and clinical advantages of TMI. Interestingly, the outcomes for the HDM200 and HDM140 + TMI 8 Gy conditioning regimens for MM are still inconclusive. In the current study, the CR and VGPR rates for arm A and arm B were 16.7% and 33.3%, 66.7% and 33.3%, respectively. The median OS and PFS were 1223 versus 1556 days and 982 versus 1101 days, respectively (Table 2). Additionally, the PFS rate was similar (Figure 2). With similar results as HDM200, HDM140 + TMI 8 Gy provide another chance to think about for MM Asian patients who were not feasible for HDM200. However, the lower relapse probability is noted in the patients receiving the higher dose of total body irradiation [19, 20]. In the current study, the dose of TMI is only 8 Gy. There still are spaces to titrate the radiation dose for the Asian in the future.

Thalidomide has a broad spectrum of activities in multiple myeloma and is considered to improve event-free survival and OS [13, 21, 22]. The multiple effects include direct inhibition of myeloma cell growth and survival, direct stimulation of the cellular immune system, modulation of integrins compromising the adhesive interactions between the myeloma cells and bone marrow stroma, and antiangiogenic effects [23–25]. Previous studies demonstrated the impact of thalidomide maintenance of response after stem cell transplantation that improved event-free survival, complete response rate, and PFS rate [26–29]. In the current study, since the median PFS was similar between the groups, HDM140 + TMI 8 Gy appears to be as effective as HDM200 for Asians with MM.

Compared with HDM200, HDM140 + TBI had a greater toxicity regarding severe mucositis, duration of neutropenia and thrombocytopenia, number of red blood cell and platelet transfusions, number of days on antibiotics, and duration of hospitalization [5]. In the total therapy program, Barlogie et al. [30] used HDM200 for the second transplantation in responding patients. They found that HDM140 + 8.5- to 10-Gy TBI was quite toxic, and only 10% of the patients had no serious extramedullary toxicity. Treatment-related mortality was 2% with the second autotransplantation using HDM200 alone and rose to 5% with added TBI. In another retrospective evaluation, the duration of hospitalization was significantly reduced in the HDM200 cohort compared with HDM140 + TBI or HDM140 + busulfan cohort [16]. No treatment-related mortality was noted in the current study. In addition, there were no statistically significant differences between groups for engraftment, duration of thrombocytopenia, number of red blood cell and platelet transfusions, duration of antibiotic infusion days, and hospitalization time. HDM140 + TMI 8 Gy provided the similar effects and toxicities of a conditioning regimen as HDM200 dosing.

Moreau et al. [5] noted slower engraftment after HDM140 + TBI, despite the higher median number of CD34 cells infused than with HDM200 (7.3 versus 5, $P = 0.03$). Furthermore, compared with pregraft and normal control samples, patients treated with high-dose radiotherapy and autologous bone marrow transplantation revealed that conditioning regimens with TBI led more frequently to nonconfluent stromal layers [31]. Another study group analyzed fibroblast colony-forming units, the precursor compartment for the microenvironmental lineages essential to hematopoietic stem cell survival, proliferation, and differentiation [32]. The authors imply that the fibroblast damage could be due to the pretransplantation conditioning regimen. Bentley et al. [33] described patients who remained platelet and/or red cell transfusion dependent for 100 days or more after transplantation even after substantial neutrophil recovery. A significantly higher proportion of these patients had received TBI as part of their conditioning regimen. Together with these data, TBI may in some cases impair the early and late capacities of the marrow microenvironment to support transplanted stem cells. We noted similar median numbers

of CD34 cells infused and numbers of red blood cell and platelet transfusions in both groups, except for the duration of neutropenia. These data suggest a potential benefit of TMI that could diminish impairment of the marrow microenvironment and provide similar results as HDM200.

There are some limitations to our current study. First, the small case number and the retrospective study design make statistical conclusions highly tentative. However, in the current study, the percentages of stage III for both groups were more than 80%. With the similar progression-free survival days for both groups, HDM 140 + TMI regimen provided another chance for multiple myloma Asian patients who could not tolerate HDM200 regimen. Second, the follow-up time was short so that late effects are insufficiently addressed.

5. Conclusions

Based on these preliminary data, we are encouraged by the clinical results of HDM140 + TMI 8 Gy treatment of Asian patients with MM. This regimen has manageable toxicity and is at least as effective of a conditioning regimen as HDM200. Further evaluation is needed to learn what longer-term effect the regimen will have on disease control. Additionally, long-term followup is needed to characterize the long-term toxicities and assess the full impact in this new approach to ASCT pretreatment in Asian patients with MM.

Conflict of Interests

The authors declare that they have no conflict of interests.

Authors' Contribution

All authors read and approved the final paper. Chen-Hsi Hsieh and Shih-Chiang Lin carried out all CT evaluations, study design, target delineations, and interpretation of the study. Chen-Hsi Hsieh drafted the paper. Shih-Chiang Lin, Pei-Ying Hsieh, and Pei-Wei Shueng took care of patient. Hui-Ju Tien made the treatment planning and carried out the evaluations. Li-Ying Wang provided the suggestion of paper writing.

Acknowledgment

This work was supported by Far Eastern Memorial Hospital Grants (FEMH-2012-C-055 and FEMH 101-2314-B-418-010-MY3).

References

[1] M. Attal, J. Harousseau, A. Stoppa et al., "A prospective, randomized trial of autologous bone marrow transplantation and chemotherapy in multiple myeloma," *The New England Journal of Medicine*, vol. 335, no. 2, pp. 91–97, 1996.

[2] B. Barlogie, S. Jagannath, D. H. Vesole et al., "Superiority of tandem autologous transplantation over standard therapy for previously untreated multiple myeloma," *Blood*, vol. 89, no. 3, pp. 789–793, 1997.

[3] S. Lenhoff, M. Hjorth, E. Holmberg et al., "Impact on survival of high-dose therapy with autologous stem cell support in patients younger than 60 years with newly diagnosed multiple myeloma: a population-based study. Nordic Myeloma Study Group," *Blood*, vol. 95, no. 1, pp. 7–11, 2000.

[4] D. Cunningham, L. Paz-Ares, S. Milan et al., "High-dose melphalan and autologous bone marrow transplantation as consolidation in previously untreated myeloma," *Journal of Clinical Oncology*, vol. 12, no. 4, pp. 759–763, 1994.

[5] P. Moreau, T. Facon, M. Attal et al., "Comparison of 200 mg/m^2 melphalan and 8 Gy total body irradiation plus 140 mg/m^2 melphalan as conditioning regimens for peripheral blood stem cell transplantation in patients with newly diagnosed multiple myeloma: final analysis of the Intergroupe Francophone du Myélome 9502 randomized trial," *Blood*, vol. 99, no. 3, pp. 731–735, 2002.

[6] O. Thomas, M. Mahé, L. Campion et al., "Long-term complications of total body irradiation in adults," *International Journal of Radiation Oncology Biology Physics*, vol. 49, no. 1, pp. 125–131, 2001.

[7] S. Sampath, T. E. Schultheiss, and J. Wong, "Dose response and factors related to interstitial pneumonitis after bone marrow transplant," *International Journal of Radiation Oncology Biology Physics*, vol. 63, no. 3, pp. 876–884, 2005.

[8] J. Y. C. Wong, A. Liu, T. Schultheiss et al., "Targeted total marrow irradiation using three-dimensional image-guided tomographic intensity-modulated radiation therapy: an alternative to standard total body irradiation," *Biology of Blood and Marrow Transplantation*, vol. 12, no. 3, pp. 306–315, 2006.

[9] S. K. Hui, M. R. Verneris, P. Higgins et al., "Helical tomotherapy targeting total bone marrow—first clinical experience at the University of Minnesota," *Acta Oncologica*, vol. 46, no. 2, pp. 250–255, 2007.

[10] P. Shueng, S. Lin, N. Chong et al., "Total marrow irradiation with helical tomotherapy for bone marrow transplantation of multiple myeloma: first experience in Asia," *Technology in Cancer Research and Treatment*, vol. 8, no. 1, pp. 29–38, 2009.

[11] J. Y. C. Wong, J. Rosenthal, A. Liu, T. Schultheiss, S. Forman, and G. Somlo, "Image-guided total-marrow irradiation using helical tomotherapy in patients with multiple myeloma and acute leukemia undergoing hematopoietic cell transplantation," *International Journal of Radiation Oncology Biology Physics*, vol. 73, no. 1, pp. 273–279, 2009.

[12] G. Somlo, R. Spielberger, P. Frankel et al., "Total marrow irradiation: a new ablative regimen as part of tandem autologous stem cell transplantation for patients with multiple myeloma," *Clinical Cancer Research*, vol. 17, no. 1, pp. 174–182, 2011.

[13] F. Sahebi, R. Spielberger, N. M. Kogut et al., "Maintenance thalidomide following single cycle autologous peripheral blood stem cell transplant in patients with multiple myeloma," *Bone Marrow Transplantation*, vol. 37, no. 9, pp. 825–829, 2006.

[14] B. G. M. Durie and S. E. Salmon, "A clinical staging system for multiple myeloma. Correlation of measured myeloma cell mass with presenting clinical features, response to treatment, and survival," *Cancer*, vol. 36, no. 3, pp. 842–854, 1975.

[15] T. Facon, J. Harousseau, F. Maloisel et al., "Stem cell factor in combination with filgrastim after chemotherapy improves peripheral blood progenitor cell yield and reduces apheresis requirements in multiple myeloma patients: a randomized, controlled trial," *Blood*, vol. 94, no. 4, pp. 1218–1225, 1999.

[16] J. J. Lahuerta, J. Martinez-Lopez, C. Grande et al., "Conditioning regimens in autologous stem cell transplantation for multiple

myeloma: a comparative study of efficacy and toxicity from the Spanish registry for transplantation in multiple myeloma," *British Journal of Haematology*, vol. 109, no. 1, pp. 138–147, 2000.

[17] B. Shank, F. C. H. Chu, and R. Dinsmore, "Hyperfractionated total body irradiation for bone marrow transplantation. Results in seventy leukemia patients with allogeneic transplants," *International Journal of Radiation Oncology Biology Physics*, vol. 9, no. 11, pp. 1607–1611, 1983.

[18] S. K. Hui, J. Kapatoes, J. Fowler et al., "Feasibility study of helical tomotherapy for total body or total marrow irradiation," *Medical Physics*, vol. 32, no. 10, pp. 3214–3224, 2005.

[19] R. A. Clift, C. D. Buckner, F. R. Appelbaum et al., "Allogeneic marrow transplantation in patients with chronic myeloid leukemia in the chronic phase: a randomized trial of two irradiation regimens," *Blood*, vol. 77, no. 8, pp. 1660–1665, 1991.

[20] R. A. Clift, C. D. Buckner, F. R. Appelbaum, K. M. Sullivan, R. Storb, and E. D. Thomas, "Long-term follow-up of a randomized trial of two irradiation regimens for patients receiving allogeneic marrow transplants during first remission of acute myeloid leukemia," *Blood*, vol. 92, no. 4, pp. 1455–1456, 1998.

[21] I. M. Ghobrial and A. K. Stewart, "ASH evidence-based guidelines: what is the role of maintenance therapy in the treatment of multiple myeloma?" *Hematology/The Education Program of the American Society of Hematology*, pp. 587–589, 2009.

[22] M. Cavo, F. Di Raimondo, E. Zamagni et al., "Short-term thalidomide incorporated into double autologous stem-cell transplantation improves outcomes in comparison with double autotransplantation for multiple myeloma," *Journal of Clinical Oncology*, vol. 27, no. 30, pp. 5001–5007, 2009.

[23] T. Hideshima, D. Chauhan, Y. Shima et al., "Thalidomide and its analogs overcome drug resistance of human multiple myeloma cells to conventional therapy," *Blood*, vol. 96, no. 9, pp. 2943–2950, 2000.

[24] F. E. Davies, N. Raje, T. Hideshima et al., "Thalidomide and immunomodulatory derivatives augment natural killer cell cytotoxicity in multiple myeloma," *Blood*, vol. 98, no. 1, pp. 210–216, 2001.

[25] D. Gupta, S. P. Treon, Y. Shima et al., "Adherence of multiple myeloma cells to bone marrow stromal cells upregulates vascular endothelial growth factor secretion: therapeutic applications," *Leukemia*, vol. 15, no. 12, pp. 1950–1961, 2001.

[26] M. Attal, J. Harousseau, S. Leyvraz et al., "Maintenance therapy with thalidomide improves survival in patients with multiple myeloma," *Blood*, vol. 108, no. 10, pp. 3289–3294, 2006.

[27] B. Barlogie, G. Tricot, E. Anaissie et al., "Thalidomide and hematopoietic-cell transplantation for multiple myeloma," *The New England Journal of Medicine*, vol. 354, no. 10, pp. 1021–1030, 2006.

[28] B. Barlogie, M. Pineda-Roman, F. van Rhee et al., "Thalidomide arm of total therapy 2 improves complete remission duration and survival in myeloma patients with metaphase cytogenetic abnormalities," *Blood*, vol. 112, no. 8, pp. 3115–3121, 2008.

[29] A. Spencer, H. M. Prince, A. W. Roberts et al., "Consolidation therapy with low-dose thalidomide and prednisolone prolongs the survival of multiple myeloma patients undergoing a single autologous stem-cell transplantation procedure," *Journal of Clinical Oncology*, vol. 27, no. 11, pp. 1788–1793, 2009.

[30] B. Barlogie, S. Jagannath, K. R. Desikan et al., "Total therapy with tandem transplants for newly diagnosed multiple myeloma," *Blood*, vol. 93, no. 1, pp. 55–65, 1999.

[31] T. Domenech, E. Gihana, A. Dayan et al., "Haemopoiesis of transplanted patients with autologous marrows assessed by long-term marrow culture," *British Journal of Haematology*, vol. 88, no. 3, pp. 488–496, 1994.

[32] M. Galotto, G. Berisso, L. Delfino et al., "Stromal damage as consequence of high-dose chemo/radiotherapy in bone marrow transplant recipients," *Experimental Hematology*, vol. 27, no. 9, pp. 1460–1466, 1999.

[33] S. A. Bentley, M. E. Brecher, E. Powell, J. S. Serody, J. M. Wiley, and T. C. Shea, "Long-term engraftment failure after marrow ablation and autologous hematopoietic reconstitution: differences between peripheral blood stem cell and bone marrow recipients," *Bone Marrow Transplantation*, vol. 19, no. 6, pp. 557–563, 1997.

Hindawi Publishing Corporation
BioMed Research International
Volume 2013, Article ID 974614, 7 pages
http://dx.doi.org/10.1155/2013/974614

Research Article

Electrical Impedance Spectroscopy as Electrical Biopsy for Monitoring Radiation Sequelae of Intestine in Rats

Pei-Ju Chao,[1] Eng-Yen Huang,[1] Kuo-Sheng Cheng,[2,3] and Yu-Jie Huang[1,2]

[1] *Department of Radiation Oncology, Kaohsiung Chang Gung Memorial Hospital, Chang Gung University College of Medicine, No. 123, Ta-Pei Road, Niao-Sung, Kaohsiung 833, Taiwan*
[2] *Biomedical Imaging and Instrumentation Laboratory, Department of Biomedical Engineering, National Cheng Kung University, No. 1, University Road, Tainan 701, Taiwan*
[3] *Medical Device Innovation Center, National Cheng Kung University, No. 1, University Road, Tainan 701, Taiwan*

Correspondence should be addressed to Yu-Jie Huang; yjhuang@cgmh.org.tw

Received 29 June 2013; Accepted 5 August 2013

Academic Editor: Tsair-Fwu Lee

Electrical impedance is one of the most frequently used parameters for characterizing material properties. The resistive and capacitive characteristics of tissue may be revealed by electrical impedance spectroscopy (EIS) as electrical biopsy. This technique could be used to monitor the sequelae after irradiation. In this study, rat intestinal tissues after irradiation were assessed by EIS system based on commercially available integrated circuits. The EIS results were fitted to a resistor-capacitor circuit model to determine the electrical properties of the tissue. The variations in the electrical characteristics of the tissue were compared to radiation injury score (RIS) by morphological and histological findings. The electrical properties, based on receiver operation curve (ROC) analysis, strongly reflected the histological changes with excellent diagnosis performance. The results of this study suggest that electrical biopsy reflects histological changes after irradiation. This approach may significantly augment the evaluation of tissue after irradiation. It could provide rapid results for decision making in monitoring radiation sequelae prospectively.

1. Introduction

Electrical impedance is one of the most often used parameters for characterizing material properties, and it is good for use in tissue characterization. The electrical impedance of a tissue is a function associated with biological structure, including cell size, density, spacing, and the constituents of the extracellular and intracellular matrices. Besides, electrical impedance also varies with changes of applied current frequency, as employed in electrical impedance spectroscopy (EIS), revealing both the resistive and capacitive components of tissue. Schwan described the electrical properties of tissues and cell suspensions in the 1950s and concluded that electrical impedance analysis of biological media is a powerful research tool for biological research [1]. Past research has shown that variations in electrical impedance among tissues can be a good marker of pathological changes in human and animal subjects [2–11]. EIS has great potential for monitoring the tissue's change, that introduced the concept of "electrical biopsy", and this "electrical biopsy" approach may be used to complement histological examinations [12].

Radiation therapy is a definitive treatment for malignant diseases. It uses ionizing radiation for treatment. Ionizing radiation works by damaging the DNA of exposed tissue leading to cellular death [13]. The radiation affects not only the malignant cell but also normal tissue. Therefore, evaluation of the damage of normal tissue during and after radiation therapy is very important to enhance the therapeutic benefit. The pathological damage of irradiated tissue depends on tissue properties, radiation dose, and the latent period. Radiation damage mostly occurs in cells that are actively dividing. As such, the tissues of the digestive tract, especially the mucosa, are early responding tissues that injure quickly after irradiation and are the major target of clinical radiation complications [13]. In the acute phase of radiation damage in intestine tissue, the mucosa thickens and presents with ulcerations, followed by epithelial atypia. In the latent period, vascular sclerosis and intestine wall fibrosis occur [14]. Electrical

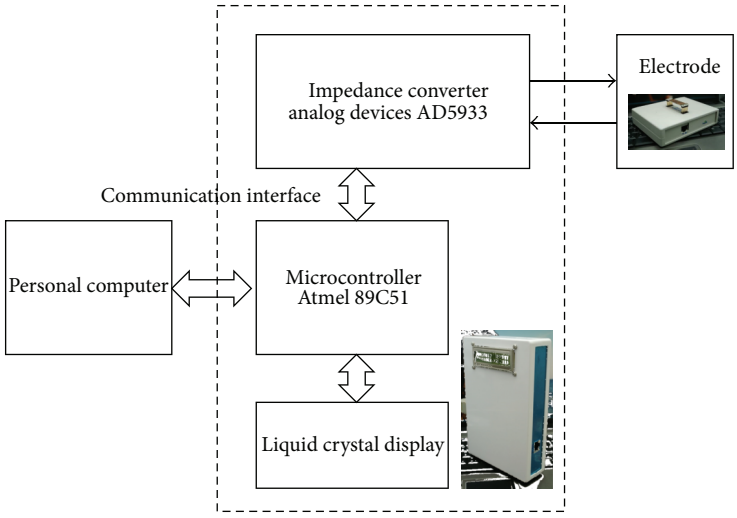

Figure 1: Block diagram and images of the electrical impedance spectroscopy (EIS) system. The components of the EIS system are shown. The electrode is connected to the device, and the device is controlled by a personal computer.

biopsy by EIS should be an idea (method) to monitor the radiation sequelae of the tissue with its' electrical characteristics.

The purpose of this study was to measure the electrical properties of intestinal tissues by electrical biopsy after whole abdomen irradiation in rats and compare them to the histology findings, for monitoring the radiation sequelae.

2. Materials and Methods

2.1. Electrical Impedance Spectroscopy System. The EIS system for the electrical biopsy of tissues was based on an electrical impedance converter chip (AD5933) acquired from Analog Devices (Norwood, MA, USA) and a microcontroller unit (MCU; 89C51) available from Atmel Corporation (San Jose, CA, USA). The MCU received the user's instruction and relayed the measurement results to a personal computer through the universal asynchronous receiver/transmitter communication interface, and the single AD5933 chip was responsible for measuring the electrical impedance. A block diagram of the device is shown in Figure 1. The detailed system design and performance evaluation are delineated in Chen, 2007 [15].

2.2. Electrodes. The electrodes are fabricated on a printed circuit board with two parallel plates of copper, and the size is the same with a glass slide. The gap between the electrode plates is 0.2 mm with a saw line to increase the effective measurement area. A sketch and photograph of the electrodes are demonstrated in Figure 2.

2.3. Animal Care and Use. Specific pathogen-free Sprague-Dawley rats (male, weighing 300–350 g) were used in this study. The rats were bred in the laboratory animal center of our institution within a specific pathogen-free environment. The rats were fed with standard forage and water and caged in pairs. The rats were anaesthetized by intra-abdomen injection of thiopental (50 mg/kg) before irradiation and EIS measurements. All procedures and measurements were performed in strict accordance with protocols approved by the Animal Care and Use Committee.

2.4. Irradiation. The rats were immobilized in the supine position on a linear accelerator couch (Varian 2100C) after anaesthetization. The prescribed radiation dose to the whole abdomen was delivered, and the rats were kept warm using a heating light until recovery. The rats in the control group were anaesthetized simultaneously with the experimental group but not irradiated.

2.5. Electrical Impedance Spectroscopy Measurements. The room temperature of the laboratory was set at 22°C. The electrodes were polished using a melamine sponge and then cleaned with an alcohol swab three times before the measurements. The rats were anesthetized by intraperitoneal injection of thiopental (50 mg/kg), and the peritoneal cavity was opened by laparotomy. The distal jejunum, traced from the cecum, was dissected. A 5 cm length of distal jejunum was sampled. Subsequently, the jejunum was dissected using scissors to expand a 5×5 mm sample. The specimen was place on absorbent paper first to eliminate extra fluid and then pasted on the electrodes with the mucosal surface down. A cover glass was used to cover the specimen with a weight load of 20 g. The electrical impedance was measured from 10 kHz to 100 kHz at 1 kHz steps. The sample was then prepared for histological examination.

2.6. Histological Examination. The specimens underwent histological examination with Masson's trichrome stain. The radiation injury score (RIS), modified from Langberg et al., was used to determine the changes in histopathology [14]. There were five items assessed for morphological evaluation regarding early and late response (Table 1).

2.7. Experiment Design. Each check point comprised eight rats. Four were for control and four were for experiment

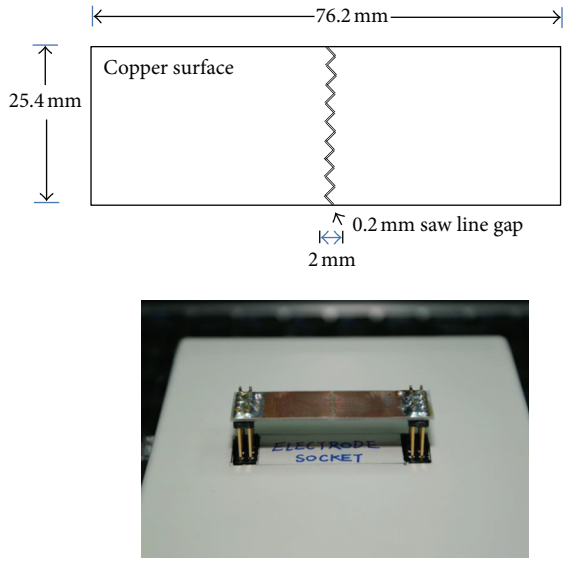

Figure 2: The electrodes for intestinal mucosa measurements.

Table 1: Morphological of assessment for evaluation of radiation injury score (RIS).

Early response
Thickening of serosa
0: None
1: Thickening of serosa; hyperplasia of peritoneal mesothelium
Mucosal ulcerations
0: Small
1: Superficial ulcerations; ulcerations involving more than half of the intestinal circumference
Epithelial atypia
0: None
1: Abnormally oriented crypts; irregular crypt regeneration with atypical epithelial cells
Later esponse
Vascular sclerosis
0: None
1: Thickening and hyalinization of vessel wall; vessel wall double normal thickness; hyalinization and stenosis; sclerosis with stenosis or complete occlusion; fibrinoid necrosis
Intestinal wall fibrosis
0: None
1: Submucosa two to four times normal thickness; broadened and hyalinized collagen fibers; abnormal collagen fibers; massive fibrosis including muscularis

group. The experimental groups were prescribed whole abdomen irradiation for 18 Gy, and the control groups were treated the same as the experimental group except that the linear accelerator was not turned on. The rats were sacrificed at the 8th hour, 3rd day, 9th day, 14th day, 21st day, 28th day, 35th day, and 40th day after irradiation for check. These 8 check points were annotated as 8Hrs, D3, D9, D14, D21, D28, D35, and D40, respectively. Totally, there were 64 rats for examinations. The intestinal tissue of the rats was assessed by electrical impedance measurements and histological examination after being sacrificed.

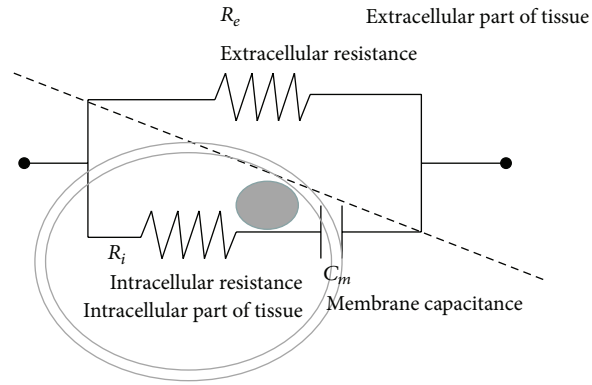

Figure 3: Simplified equivalent three-element resistor and capacitor (RC) electrical circuit model for tissues.

2.8. Data Analysis and Statistics. The simplified equivalent three-element resistor and capacitor (RC) electrical circuit model (as depicted in Figure 3) was applied for the interpretation of the EIS data. ZSimpWin Version 3.1 (Princeton Applied Research, Oak Ridge, TN, USA) was used to solve R_e (extracellular resistance), R_i (intracellular resistance), and C_m (membrane capacitance). The receiver operating characteristic (ROC) analysis was used to evaluate the diagnostic performance.

3. Results and Discussion

3.1. Results of Three-Element RC Electrical Circuit Model for Tissues. The solutions to the three-element RC electrical circuit model for each group are illustrated in Figures 4(a)–4(c). R_e was reduced after irradiation until the 9th day. R_i was decreased until the 14th day and then recovered. C_m was increased from 3rd to 21st days. The errors of solutions established by ZSimpWin were in the range of 0.92–2.08% for R_e, 1.39–2.23% for R_i, and 3.30–5.24% for C_m.

An equivalent circuit model fit derived from impedance spectroscopy can provide detailed biological information of the tissue's electrical characteristics. The most well-known model of tissue electrical characteristics is the Cole-Cole equation [16], although the parameters of this equation are not very intuitive. The three-element model, as depicted in Figure 3, is simple and easily understood from a biological viewpoint. However, the specific architecture and complex electrolytic plasma of biological tissue imply that its equivalent circuit should in principle be very complicated. The three-element model effectively eliminates any other features of the tissue and is unaware of various dispersive events. As such, all information may not be sufficiently captured by impedance spectroscopy. However, an adequate equivalent circuit model for representing tissue morphology has not been developed to date. The three-element model not only is the simplest but is often used in related studies. Although

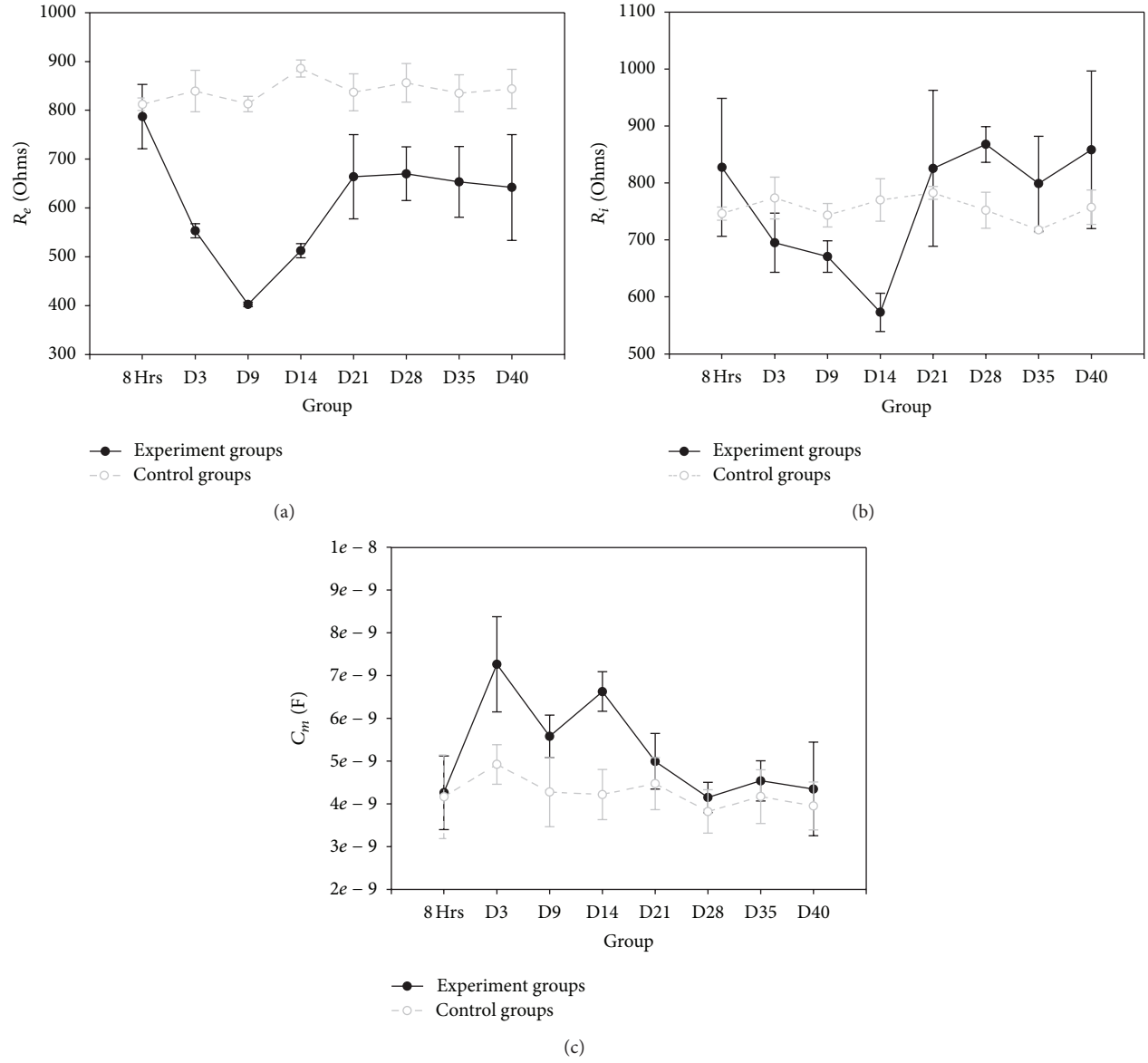

Figure 4: Symbol graphs of electrical parameters for electrical circuit model of tissue after irradiation. Symbol graphs showing error bars for each control and experimental group; (a) extracellular resistance (R_e), (b) intracellular resistance (R_i), and (c) membrane capacitance (C_m).

the three-element model used in this study may not be the most appropriate representation of irradiated tissues, it characterized some simple electrical characteristics of the tissues.

3.2. Results of Histological Examination. The results of histological examination of the control and experiment groups with RIS are shown in Figure 5. The overall RIS accumulated rapidly on the 9th day and gradually decreased after the 28th day. The early-response part of RIS subsided after the 21st day, but late-response part of RIS steadily progressed.

The vulnerability of the gastrointestinal epithelium to ionizing radiation has been well documented. Radiation enteropathy can be categorized into two stages, early and late [17]. Early radiation enteropathy occurs in the actively proliferating intestinal crypt cell compartment of intestinal mucosa, which is the primary target site of radiation injury. Stem cell depletion leads to insufficient replacement of epithelial cells in the upper crypt and villus, causing denudation of the mucosa. Following radiation exposure, the villus epithelium gradually regenerates. Late radiation enteropathy, which manifests as vascular and connective tissue damage, occurs after a variable latency period. These phenomena frequently occur in the intestinal wall instead of the mucosa. The progression of radiation injury induces morphological changes in the mucosa and the intestinal wall during the early and late stages of enteropathy, respectively. In histological examinations, as shown in Figure 5, the total postirradiation RIS score decreased after the 28th day. The acute response prevailed between the 3rd and 21st day, while

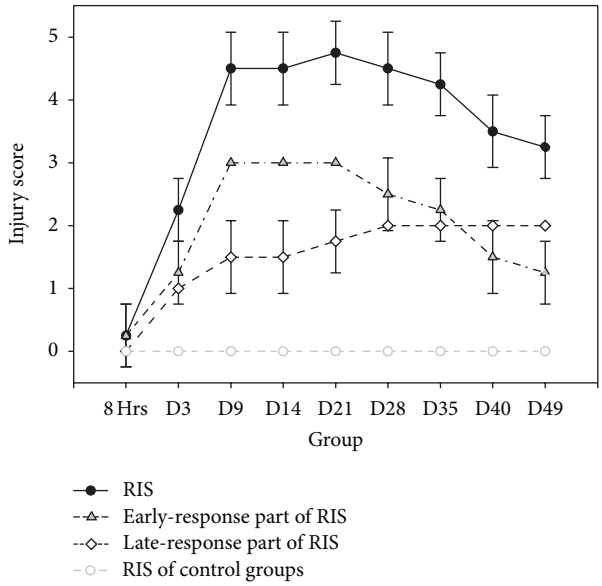

Figure 5: Symbol graph of radiation injury scores after irradiation. Symbol graph showing error bars of total, early-response, and late-response part of RIS after irradiation.

the late response steadily progressed after irradiation and persisted after 28th day, are consistent.

Comparing the results of electrical parameters and the results of histological examination of tissues, the radiation sequelae of intestine in rats could be suggested to be monitored as follows.

3.3. Extracellular Resistance for Monitoring the Start of Radiation Sequelae. The scatter plot for the R_e versus RIS is shown in Figure 6(a). According to ROC analysis, the area under curve (AUC) for R_e to marke the beginning of radiation injury (RIS ≥ 1) is 1.0. $R_e < 734\,\Omega$ could be used to check the beginning of radiation injury, the sensitivity and specificity are 1.0 and 1.0, respectively. R_e quantifies the extracellular resistance, which reflects the status of the extracellular fluid. The first morphological change after irradiation is serosa thickening, most likely a symptom of edema. The extracellular fluid accumulation leads to decreased R_e.

3.4. Membrane Capacitance for Monitoring the Dominant Early-Response Radiation Injury. The scatter plot for the C_m versus the early-response part of RIS is shown in Figure 6(b). The AUC for C_m to detect the dominant searly-response radiation injury (early response part of RIS ≥ 2) is 0.95. $C_m > 5.473 * 10^{-9}$ F could be used to teste the dominant early-response radiation injury, the sensitivity and specificity are 0.89 and 0.93, respectively. The dominant early response presents damages such as ulceration and cell atypia. C_m is increased by dysfunction of the ion channels in the cell membrane due to disturbed physiological function in this stage.

3.5. Intracellular Resistance for Monitoring the Dominant Late-Response Radiation Injury. The scatter plot for the R_i versus the late-response part of RIS is shown in Figure 6(c). R_i indicates cytoplasm resistance. Postirradiation increases in R_i could be used to check the dominant late responses, which include vascular and intestinal wall fibrosis. The cytoplasm is condensed, and fibrosis leads to decreased intra- and extracellular fluids, enhancing R_i. The AUC of R_i to reflect the dominant late-response injury (the late-response part of RIS ≥ 2) is 0.96. $R_i > 726\,\Omega$ is the threshold to examine the dominant late-response radiation injury, the sensitivity and specificity are 0.92 and 0.90, respectively.

3.6. Prospect of Electrical Biopsy to Monitor Radiation Sequelae. EIS as electrical biopsy has a great potential to monitor the tissue status. The electrical biopsy by EIS indeed reflected changes of the tissue corresponding to conventional morphological findings in a sense of conventional histological knowledge [18]. In radiation therapy, the treatment responses compete with adverse effects, and monitoring the radiation sequelae and modifying treatment planning adaptively could improve the therapeutic benefit. Osterman et al. evaluated whether EIS can noninvasively determine and quantify injury responses in soft tissue exposed to high-dose rate (HDR) irradiation [19]. Small volumes of muscle tissue were irradiated with single-dose radiation using the HDR after-loading technique (26 and 52 Gy prescribed 5 mm from the source). Impedance measurements were performed on 29 rats at 1, 2, and 3 months after irradiation at 31 frequencies in the 1 kHz to 1 MHz range. Throughout the first 3 months, the conductivity increased by 48% and 26% with a target dose of 52 and 26 Gy, respectively. EIS accurately detected responses in a fraction of the tissue probed, indicating its potential usefulness in detecting radiation damage at early postirradiation time points. In human subjects for evaluation of skin tissues after irradiation, researchers have concluded that electrical impedance measurements for dielectric constants are useful for assessing cellular changes and for providing quantitative information concerning radiation-induced skin reactions [20, 21]. At 5 weeks, the dielectric constant had decreased by 31 and 39% for the investigated skin sites of the photon and electron fields, respectively. There was a statistically significant inverse correlation between the mean dielectric constant and the clinical score of erythema. Two years later, a statistically significant positive correlation was found between the dielectric constant at the irradiated skin sites and the clinical score of subcutaneous fibrosis. These support the ability of EIS as electrical biopsy to monitor the tissue status after radiation.

In future prospect, the device for electrical biopsy in monitoring radiation sequelae should be robust and easy operating. The design should be specific for clinical examination, especially of the electrodes. The electrical biopsy also has potential and capability for in situ examination. This will be helpful in real-time monitoring and treatment decision making. The electrical circuit model for individual tissue should be established, and the changes of the electrical characteristics of tissue for pathological response should be modelled more detailedly. Moreover, electrical impedance tomography (EIT) technique could evaluate the electrical parameters of tissue in body cavity without invasive procedure instantly [22]. The progression of electrical impedance technique in biomedical

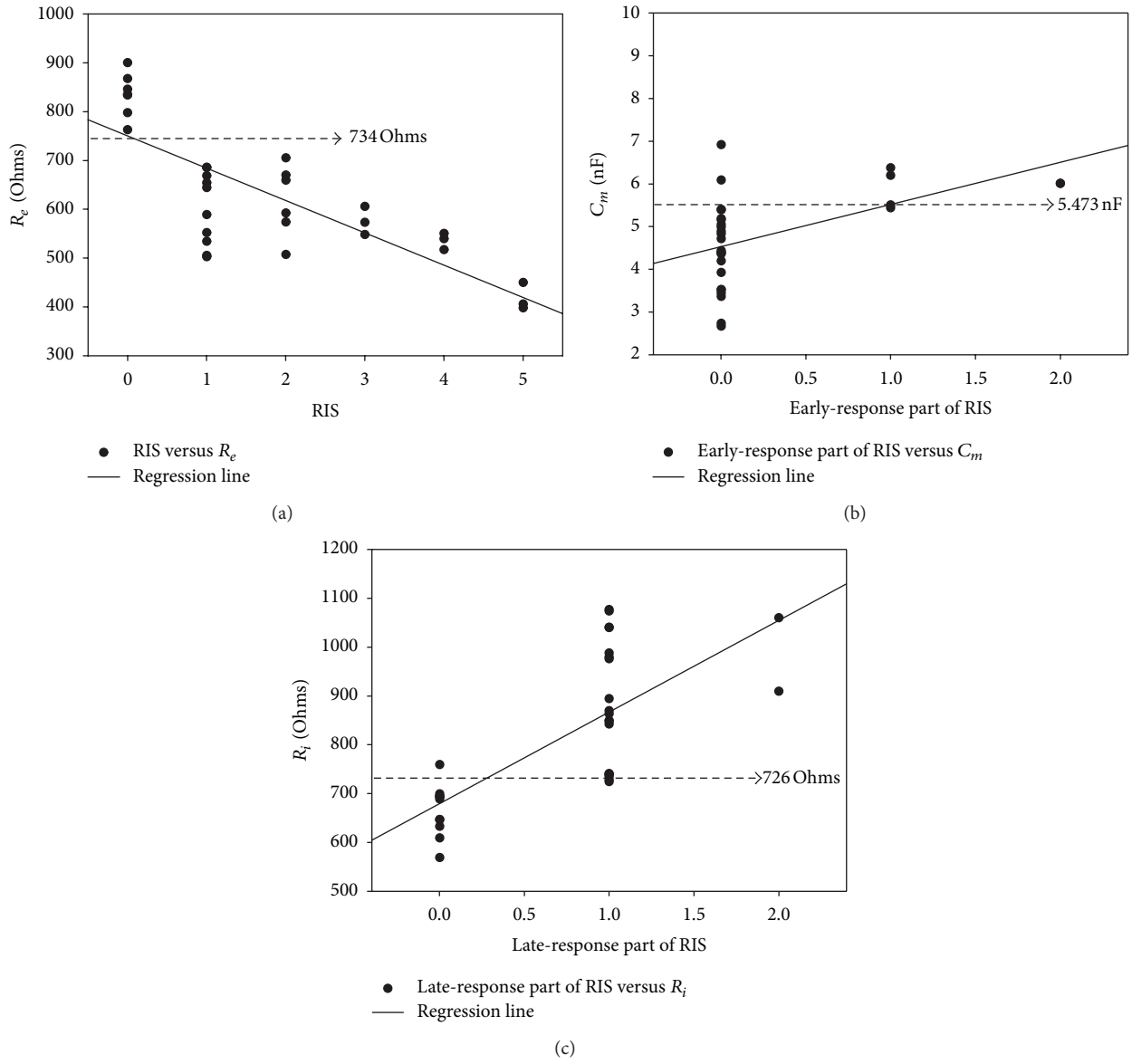

FIGURE 6: The scatter plots for electrical parameters versus radiation injury score. (a) The scatter plots for R_e versus RIS. $R_e < 734\,\Omega$ could be used to be the threshold of the beginning of radiation injury. (b) The scatter plots for C_m versus early-response part of RIS. $C_m > 5.473 * 10^{-9}$ F could be used to be the threshold of the domination of early-response radiation injury. (c) The scatter plots for R_i versus late-response part of RIS. $R_i > 726\,\Omega$ could be used to be the threshold of the domination of late-response radiation injury.

field has potential to provide a noninvasive, rapid results for decision making, that is not achievable in clinical evaluation and conventional pathological examination.

4. Conclusions

Electrical impedance spectroscopy as electrical biopsy presents as a useful method for detecting tissue injury because it reveals the electrical characteristics of tissues associated with histological change. The electrical properties were shown to accurately detect histological changes; our results demonstrated a strong diagnosis performance for radiation injury of intestine in rats. This method could be used to monitor the treatment sequelae in radiation therapy with confidence.

Acknowledgments

This work was supported by grants from the Chang Gung Memorial Hospital Research Program (CMRPG870011) and the National Science Council Research Program (NSC98-2320-B-182A-002-MY2 and NSC102-2221-E-182A-002).

References

[1] H. P. Schwan, "Electrical properties of tissue and cell suspensions," *Advances in biological and medical physics*, vol. 5, pp. 147–209, 1957.

[2] B. A. Wilkinson, R. H. Smallwood, A. Keshtar, J. A. Lee, and F. C. Hamdy, "Electrical impedance spectroscopy and the diagnosis

of bladder pathology: a pilot study," *Journal of Urology*, vol. 168, no. 4, pp. 1563–1567, 2002.

[3] D. G. Beetner, S. Kapoor, S. Manjunath, X. Zhou, and W. V. Stoecker, "Differentiation among basal cell carcinoma, benign lesions, and normal skin using electric impedance," *IEEE Transactions on Biomedical Engineering*, vol. 50, no. 8, pp. 1020–1025, 2003.

[4] C. A. González, C. Villanueva, S. Othman, R. Narváez, and E. Sacristán, "Impedance spectroscopy for monitoring ischemic injury in the intestinal mucosa," *Physiological Measurement*, vol. 24, no. 2, pp. 277–289, 2003.

[5] D. Gupta, C. A. Lammersfeld, J. L. Burrows et al., "Bioelectrical impedance phase angle in clinical practice: implications for prognosis in advanced colorectal cancer," *American Journal of Clinical Nutrition*, vol. 80, no. 6, pp. 1634–1638, 2004.

[6] C. Skourou, P. J. Hoopes, R. R. Strawbridge, and K. D. Paulsen, "Feasibility studies of electrical impedance spectroscopy for early tumor detection in rats," *Physiological Measurement*, vol. 25, no. 1, pp. 335–346, 2004.

[7] S. Abdul, B. H. Brown, P. Milnes, and J. A. Tidy, "A clinical study of the use of impedance spectroscopy in the detection of cervical intraepithelial neoplasia (CIN)," *Gynecologic Oncology*, vol. 99, no. 3, pp. S64–S66, 2005.

[8] H. S. Ahn, S. S. Yun, H. J. Shin, J. Y. Kim, and J. H. Choi, "Measurement of bioimpedance and cell viability during ischemia-reperfusion in the rat liver," in *Proceedings of the 27th Annual International Conference of the Engineering in Medicine and Biology Society (IEEE-EMBS '05)*, vol. 2, pp. 1945–1947, September 2005.

[9] A. Stojadinovic, A. Nissan, Z. Gallimidi et al., "Electrical impedance scanning for the early detection of breast cancer in young women: preliminary results of a multicenter prospective clinical trial," *Journal of Clinical Oncology*, vol. 23, no. 12, pp. 2703–2715, 2005.

[10] S. Abdul, B. H. Brown, P. Milnes, and J. A. Tidy, "The use of electrical impedance spectroscopy in the detection of cervical intraepithelial neoplasia," *International Journal of Gynecological Cancer*, vol. 16, no. 5, pp. 1823–1832, 2006.

[11] A. Keshtkar, A. Keshtkar, and R. H. Smallwood, "Electrical impedance spectroscopy and the diagnosis of bladder pathology," *Physiological Measurement*, vol. 27, no. 7, pp. 585–596, 2006.

[12] Y.-J. Huang, E.-Y. Huang, Y.-Y. Lu, C.-Y. Chen, and K.-S. Cheng, "Electrical biopsy of irradiated intestinal tissue with a simple electrical impedance spectroscopy system for radiation enteropathy in rats—a pilot study," *Physiological Measurement*, vol. 32, no. 9, pp. 1491–1504, 2011.

[13] J. Eric and A. J. G. Hall, *Radiobiology for the Radiologist*, Lippincott Williams & Wilkins, Philadelphia, Pa, USA, 2006.

[14] C. W. Langberg, T. Sauer, J. B. Reitan, and M. Hauer-Jensen, "Tolerance of rat small intestine to localized single dose and fractionated irradiation," *Acta Oncologica*, vol. 31, no. 7, pp. 781–787, 1992.

[15] C.-Y. Chen, *The Design of Multi-Frequency Bioimpedance Measuring System for Clinical Applications*, Institute of Biomedical Engineering, National Cheng Kung University, 2007.

[16] B. Rigaud, L. Hamzaoui, M. R. Frikha, N. Chauveau, and J.-P. Morucci, "In vitro tissue characterization and modelling using electrical impedance measurements in the 100 Hz-10 MHz frequency range," *Physiological Measurement*, vol. 16, no. 3, pp. A15–A28, 1995.

[17] M. Hauer-Jensen, "Late radiation injury of the small intestine. Clinical, pathophysiologic and radiobiologic aspects. A review," *Acta Oncologica*, vol. 29, no. 4, pp. 401–415, 1990.

[18] Y. J. Huang, E. Y. Huang, and K. S. Cheng, "The correlation between extracellular resistance by electrical biopsy and the ratio of optical low staining area in irradiated intestinal tissues of rats," *BioMedical Engineering OnLine*, vol. 12, article 23, 2013.

[19] K. S. Osterman, P. J. Hoopes, C. DeLorenzo, D. J. Gladstone, and K. D. Paulsen, "Non-invasive assessment of radiation injury with electrical impedance spectroscopy," *Physics in Medicine and Biology*, vol. 49, no. 5, pp. 665–683, 2004.

[20] J. Nuutinen, T. Lahtinen, M. Turunen et al., "A dielectric method for measuring early and late reactions in irradiated human skin," *Radiotherapy and Oncology*, vol. 47, no. 3, pp. 249–254, 1998.

[21] T. Tamura, M. Tenhunen, T. Lahtinen, T. Repo, and H. P. Schwan, "Modelling of the dielectric properties of normal and irradiated skin," *Physics in Medicine and Biology*, vol. 39, no. 6, pp. 927–936, 1994.

[22] P. O. Gaggero, A. Adler, J. Brunner, and P. Seitz, "Electrical impedance tomography system based on active electrodes," *Physiological Measurement*, vol. 33, no. 5, pp. 831–847, 2012.

Hindawi Publishing Corporation
BioMed Research International
Volume 2013, Article ID 574934, 8 pages
http://dx.doi.org/10.1155/2013/574934

Research Article

Control of Respiratory Motion by Hypnosis Intervention during Radiotherapy of Lung Cancer I

Rongmao Li,[1] Jie Deng,[2] and Yaoqin Xie[1,3]

[1] *Institute of Biomedical and Health Engineering, Shenzhen Institutes of Advanced Technology, Chinese Academy of Sciences, 1068 Xueyuan Anenue, Shenzhen University Town, Shenzhen 518055, China*
[2] *Zhuhai Psychological Counseling Co., Ltd, 201-40A Haisong Building, 9th Tairan Road, Shenzhen 518000, China*
[3] *Lab for Wearable Devices, Key Lab for Health Informatics of Chinese Academy of Sciences, 1068 Xueyuan Anenue, Shenzhen University Town, Shenzhen 518055, China*

Correspondence should be addressed to Yaoqin Xie; yq.xie@siat.ac.cn

Received 21 May 2013; Revised 8 July 2013; Accepted 31 July 2013

Academic Editor: Ching Chong Jack Yang

The uncertain position of lung tumor during radiotherapy compromises the treatment effect. To effectively control respiratory motion during radiotherapy of lung cancer without any side effects, a novel control scheme, hypnosis, has been introduced in lung cancer treatment. In order to verify the suggested method, six volunteers were selected with a wide range of distribution of age, weight, and chest circumference. A set of experiments have been conducted for each volunteer, under the guidance of the professional hypnotist. All the experiments were repeated in the same environmental condition. The amplitude of respiration has been recorded under the normal state and hypnosis, respectively. Experimental results show that the respiration motion of volunteers in hypnosis has smaller and more stable amplitudes than in normal state. That implies that the hypnosis intervention can be an alternative way for respiratory control, which can effectively reduce the respiratory amplitude and increase the stability of respiratory cycle. The proposed method will find useful application in image-guided radiotherapy.

1. Introduction

A prerequisite of treatment planning in thoracic radiotherapy is the accurate modeling of respiratory motion of thoracic structures [1]. Much effort has been devoted to address this issue. One of the traditional methods is that the patients are trained before treatment to make respiration as stable as possible, and the depicted planning target volume (PTV) covers the whole area of tumor motion. Another method is the gating technology, which synchronizes the treatment with the breathing cycle. The radiation at the tumor is applied only during a specific time in the cycle, typically during the deepest expiration of the patient, and the radiation is ceased once the tumor moves out of the targeted area. One of the powerful tools for gating is the respiratory position management (RPM) system [2, 3] developed by Varian, which can detect and track respiratory motion without the need to train the patient. Another respiratory trace generating (RTG) tool was also developed for tracking respiratory motion [4]. The disadvantage of gating technology is the prolonged treatment time. The third method is developed to have the patient breathe regular by a visual system which shows a standard breathing curve and the patient's real-time breathing curve in front of the patient during treatment. The intervention to the patient is inevitable in the course of the treatment, which may result in patient's discomfort. The forth method is real-time tumor tracking. In current image guided radiation therapy (IGRT), it becomes increasingly popular by using implanted metallic or radio frequency fiducials [5–9]. In this approach, stereoscopic X-ray images are taken simultaneously or sequentially during the course of dose delivery. High contrast fiducials are detected on the projection images, and a triangulation algorithm is then employed to extract the positions of the fiducials in real-time. While the fiducial marker provides a reliable way for real time tracking, implantation of fiducial markers is an invasive procedure and may result in a number of possible complications, such as pneumothorax and hemorrhage [10].

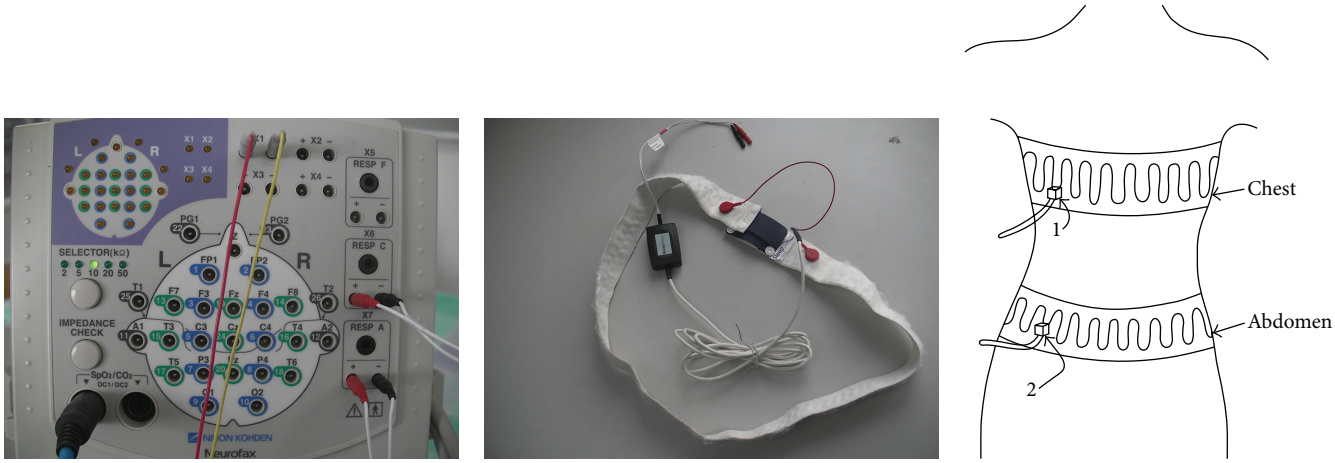

(a) (b) (c)

Figure 1: Sensors and EEG system used in the experiment, (a) the EEG system used to record the electrical signal, (b) the sleep sensor used to detect the respiration motion, (c) the schematic diagram of the method to detect the respiration motion.

In this paper, hypnosis is introduced in radiotherapy for respiratory control without any side effects. As we know, hypnosis may keep the patient in inner peace during treatment. Consequently, the respiration amplitude is reduced and becomes stable, which is an ideal state for radiotherapy. We hypothesized that hypnosis can be a helpful tool for respiratory control in various treatment procedures, such as gating and real-time tracking.

2. Materials and Methods

2.1. Hypnosis. Hypnosis is a state in which a person seems to be asleep but still can see, hear, or respond to speech directed to him [11, 12]. Hypnotherapy is hypnosis used for therapy. Under normal state, people have regular, low-amplitude, high-frequency α and uniform-frequency β brain waves, while under light hypnosis state, the amplitude of α, brain waves becomes higher, and the frequency becomes uniform. Physicians and psychiatrists may use hypnosis to treat depression, anxiety, eating disorders, sleep disorders, compulsive gaming, and posttraumatic stress. Hypnotherapy has been successfully applyied in many cases, such as fears, phobias, habit control, pain management, and psychological therapy. It is widely used in pre- and posttreatment but rarely used during treatment. In this paper, hypnosis is used to make a patient's inner peace and respiration stable during treatment.

To effectively control respiration during radiotherapy of lung cancer, we need to know whether hypnosis works well on stabilizing the respiratory motion and then develop a novel clinical scheme to apply hypnosis in radiotherapy. Several experiments have been conducted to test the influence of hypnosis on respiration. In these experiments, a professional hypnotist guides volunteers into hypnosis state.

Hypnosis technique takes part in an important role in the method. However, the technique is not suitable for all clinical cases. Based on the standard score evaluation, 10% in normal people is highly susceptible population, and 10% is marginally susceptible population. Age, imagination, self-suggestion, and other properties of the subject influence the susceptibility. So the method cannot be applied for all patients. An important work before hypnosis is to determine which patient is suitable for hypnosis therapy. Before hypnosis, several tests should be done to check the susceptibility of the patient and to select the suitable patients.

2.2. Sensors and EEG System. The electroencephalogram (EEG) system developed by Nihon Kohden Corporation is user-friendly and allows recording the electrical activity of the brain over a short period of time, as shown in Figure 1(a). It consists of a notebook PC, isolation power supply, advanced electrode junction box, and other standard accessories. There is also a full range of optional accessories. Polysmith software is the world's most all-inclusive PSG acquisition and analysis program. Patient data acquisition and analysis are integrated into a single software. As a part of EEG system, it is used in various environments and provides a comprehensive approach to analyze obtained experimental data. It is convenient for remote access from the control room [11].

The sleep sensor in Figure 1(b) is a part of the system that detects the respiration motion. It is tied on the chest and the abdomen of the volunteer. The corresponding signals are transported to the EEG system for further analysis. The inductance of the bands is exactly proportional to the transverse section encircled by the band, as shown in Figure 1(c). The inductance changes with the breathing of the patient. It is converted by the electronic circuits of the system into an electrical signal in order to accurately and reliably record the respiration waveforms. The inductive band can be easily connected to any compatible system through a dedicated interface cable.

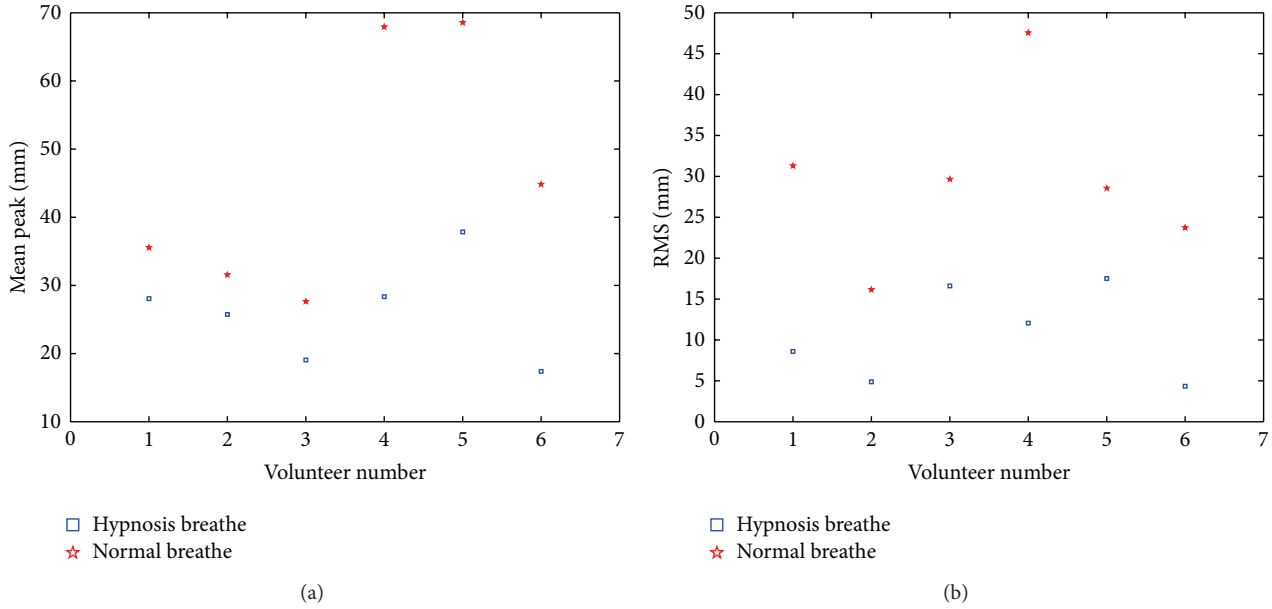

Figure 2: Peak value and maximum root mean square (RMS) of respiratory amplitude for the six volunteers in the normal state (red) and in the hypnosis state (blue), respectively.

Table 1: Physiological parameters of the six volunteers.

Parameters\volunteer no.	1	2	3	4	5	6
Age (year)	22	22	23	27	23	28
Weight (kg)	56	50	60	55	52	73
Chest circumference (cm)	89	85	91	88	75	100

The parameters setting of the sleep sensor is constant in the whole experimental procedure. The sensitivity is 10 μV/mm, the CAL voltage is 50 μV, the time constant is 0.3 s, and the high-cut filter is 50 Hz.

2.3. Experimental Procedure. Nine volunteers took part in the experiment. Among them, six volunteers were selected by the hypnotist as suitable subjects for hypnosis with a wide range of distribution of age, weight, and chest circumference, as listed in Table 1. Two experiments have been done with these 6 volunteers. One experiment was conducted under normal breathing. The volunteers peacefully lied on a bed without any motion and speaking for 15 min. Another experiment involved breathing under hypnosis. The hypnotist guided the volunteer into hypnosis state and determined whether the volunteer is under hypnosis. For each subject, it took about 10 min to enter into hypnosis and another 15 min to keep the hypnosis state. Then, the volunteer was awaken by the hypnotist. During the hypnosis procedure, the volunteer was extremely suggestible to the hypnotist. These two experiments were repeated two weeks later.

3. Experiment and Results

Figure 2 shows the mean peak value and the maximum root mean square (RMS) of respiratory amplitude for 6 volunteers in the normal state (red points) and in the hypnosis state (blue points), respectively. The definitions of mean of RMS are

$$\begin{aligned} \text{Mean}_i &\equiv \sum_j^{N_i} \frac{A_i^j}{N_i}, \\ \text{RMS}_i &= \sqrt{\sum_j^{N_i} \left(A_i^j - \text{Mean}_i\right)^2}, \end{aligned} \tag{1}$$

where i is the number of volunteers and N_i is the number of the peaks for volunteer i. It is clear from Figure 2 that the peak value in the hypnosis state is much lower than that in the normal state, so as the RMS, indicating more stable respiration in the hypnosis state. In treatment planning, PTV stands for the entire region tumor may cover. The reduction of the mean amplitudes and the RMS is a great help to protect the patient from the dose. The low mean amplitude implies the energy of the radiation more concentrated in the tumor, and the low RMS implies the more stable for treating.

Figure 3 shows the mean cycle of respiration of different volunteers under normal state and hypnosis. No obvious difference between these two states is observed.

Figure 4 shows the relative ratio between the amplitude and the time weighted average in a certain range near the peak. The parameter is defined as

$$\text{Ratio}\,(t) \equiv \frac{\sum A_i t_i}{At}, \tag{2}$$

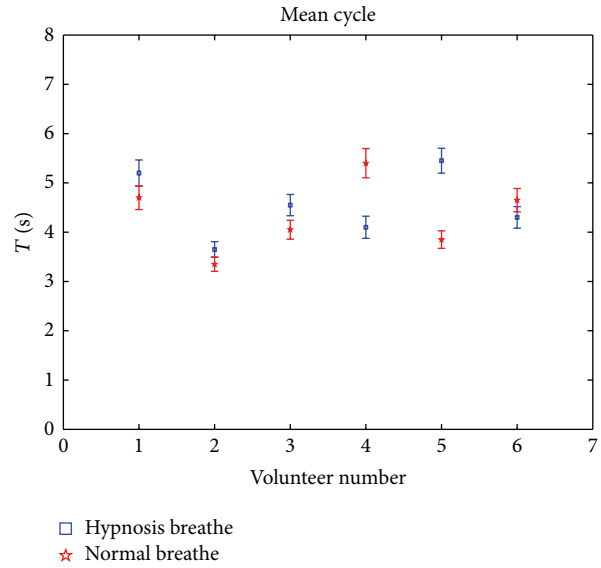

Figure 3: Mean cycle of respiration for different volunteers in the normal state (red) and in the hypnosis state (blue).

where the ratio stands for the displacement around the peak of respiratory waveform. The waveform is divided into many small time intervals, counted by i. t_i is the time interval, A_i is the corresponding amplitude of the wave during the time t, A is the amplitude of the waves, and t is the time interval of the wave near the peak. The ratio for each peak is obtained. The final ratio is the mean for all peaks.

In Figure 4, the x-axis stands for the time interval nearby the wave peak. It can be seen that the relative ratio in the hypnosis state reduced more slowly than that in the normal state. The slower the relative ratio is reduced, the more stable is the wave nearby the wave peak.

To evaluate the difference between different cycles, the γ index of passing ratio [13–15] is introduced as shown in Figure 6. Like the ratio in (2), γ passing ratio is another quantity to evaluate the similarity between different cycles. It is defined as

$$\gamma(x_m) = \min\{\Gamma(x_m, x_c)\}, \quad \forall\{x_c\}, \tag{3}$$

where

$$\Gamma(x_m, x_c) = \sqrt{\frac{x^2(x_m, x_c)}{\Delta d_M^2} + \frac{\delta^2(x_m, x_c)}{\Delta D_M^2}},$$
$$x(x_m, x_c) = |x_m - x_c|, \tag{4}$$
$$\delta(x_m, x_c) = D_m - D_c,$$

δ is the difference between different cycles with x_m and x_c. x_m is the time of the template cycle, and x_c is the time of other cycles. In the experiment, the first starting cycle is selected as the template cycle. The γ passing ratio is obtained between the template cycle and other cycles. ΔD_M is the parameter to estimate the degree of displacement, Δd_M is the parameter to estimate the degree of the time to agreement. In our experiments, 10 groups of these two parameters are set to calculate the γ passing ratios for different cycles. It can be seen from Figure 5 that the γ index is relatively stable in the area of dense curves. Therefore, the parameters of γ index are selected as 1.2% and 28%.

Similar to γ passing ratio used in the evaluation in dose distribution, γ passing ratio can also be used to estimate the similarity of two respiration cycles. As we know, respiratory motion may result in the change of dose distribution.

Figure 6 shows $\gamma_{1.2,28\%}$ index curves of passing ratio between the first cycle and the next 12 adjacent cycles in the hypnosis state (blue curves) and the normal state (red curves). Among these 6 volunteers, 5 of them show higher $\gamma_{1.2,28\%}$ passing ratio curves in the hypnosis state than that in the normal state, which means that cycles of respiration in the hypnosis state are much more stable than that in the normal state. The only opposite result as shown in Figure 6 (volunteer 5) indicates that not all the patients are suitable for respiration control using hypnosis.

4. Discussions

In this work, a novel method using hypnosis is proposed to control respiratory motion during radiotherapy of lung cancer. Since the hypnosis is comfortable for the patient and makes him peaceful, the method allows treating the patient without side effects during radiotherapy.

As we know, the traditional training method is widely applied in radiotherapy, which is a benefit to most patients. However, several uncontrollable factors still exist, such as the tension and the surrounding influence during the treating, which may trade-off the treatment effect. In the proposed hypnosis method, self-control is not needed for patients during the whole treatment procedure. Moreover, under the guidance of hypnotist, the patient could stay in peace state and feel comfortable during treatment.

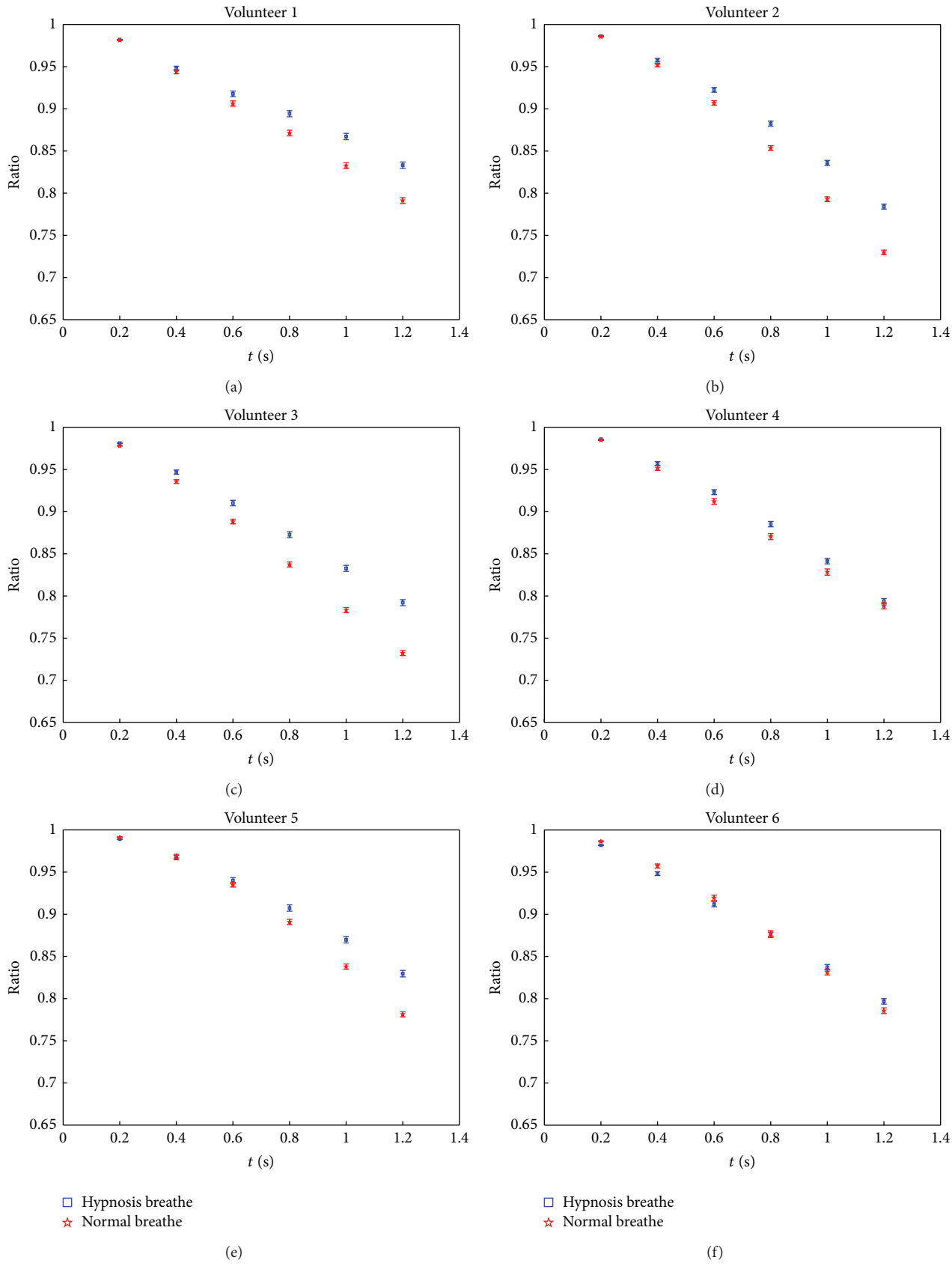

FIGURE 4: Relative ratio of the wave nearby the peak and the amplitude with time weighted. The red and blue points stand for the normal state and the hypnosis state, respectively.

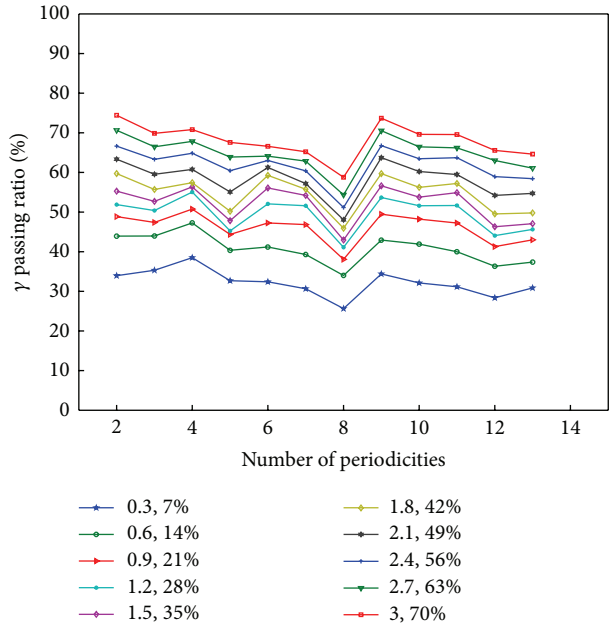

Figure 5: γ index of passing ratio between the first cycle and the other 13 adjacent cycles with ten different parameters.

It is clear that the amplitude nearby wave peak in the hypnosis state is more stable than that in the normal state, because the mean peak in the hypnosis state is much lower than that in the normal state as shown in Figure 2. If the waveforms of the two states are similar, the mean cycles for two states should have the same proportion with the mean peaks. However, the difference of mean cycle between two states is not notable as shown in Figure 3. This leads to more slow reduction of amplitude under the hypnosis state than that under the normal state, as shown in Figure 7. Again, it demonstrates the stability of respiration under the hypnosis state.

Suppose the tumor in the lung rigidly moves with respiration motion, when the tumor is irradiated at the peak of a respiration cycle, the dose in tumor is determined by the mean ratio between the displacement with time weight and the amplitude, which is the definition of ratio in (2). If the value of ratio is "1" during the whole cycle, apparently the waveform is square wave, which is an ideal state without tumor motion.

In the experiment, six volunteers were selected. It may arouse controversy that the quantity is not enough, and the age or other properties are not generally representative. However, differences always exist between the volunteers and the patients. The major contribution of the proposed method is the use of hypnosis during radiotherapy. One of the challenging problems is how to protect the hypnotist from radiation exposure, which is a key technology for the method. The ultimate goals of the method are to treat the patients with least side effects and to become applicable to a larger number of patients.

Gamma ratio is a parameter to evaluate the similarity of two distributions. As it is widely used in evaluation of dose distributions, we extend the use of gamma ratio to evaluate the difference between two respiration waveforms which may cause the change of dose distribution during radiotherapy. Therefore, we choose the gamma ratio as the evaluation metrics, although other parameters can also describe the difference.

This work is a preliminary clinical study instead of a clinical study. However, it is necessary before the further clinical application. Although it is limited to the establishment of the relationship between hypnosis and respiratory motion, this establishment has demonstrated the feasibility of the clinical application of hypnosis during radiotherapy.

5. Conclusion

In this work we found that the hypnosis can effectively stabilize respiration motion, which makes it suitable to control respiration during radiotherapy of lung cancer. Although hypnosis is not applicable to all cases, it provides an alternative way for respiratory control without any side effects. The next problem is how to use hypnosis in clinical conditions. We will propose a new scheme of respiratory control using hypnosis in radiotherapy of lung cancer. Since it is a noninvasive method, hypnosis intervention will find various clinical applications in the near future.

Acknowledgments

This work is supported in part by grants from National Natural Science Foundation of China (NSFC: 81171402), NSFC Joint Research Fund for Overseas Research Chinese, Hong Kong and Macao Young Scholars (30928030), National Basic Research Program 973 (2010CB732606) from Ministry of Science and Technology of China, Guangdong Innovative

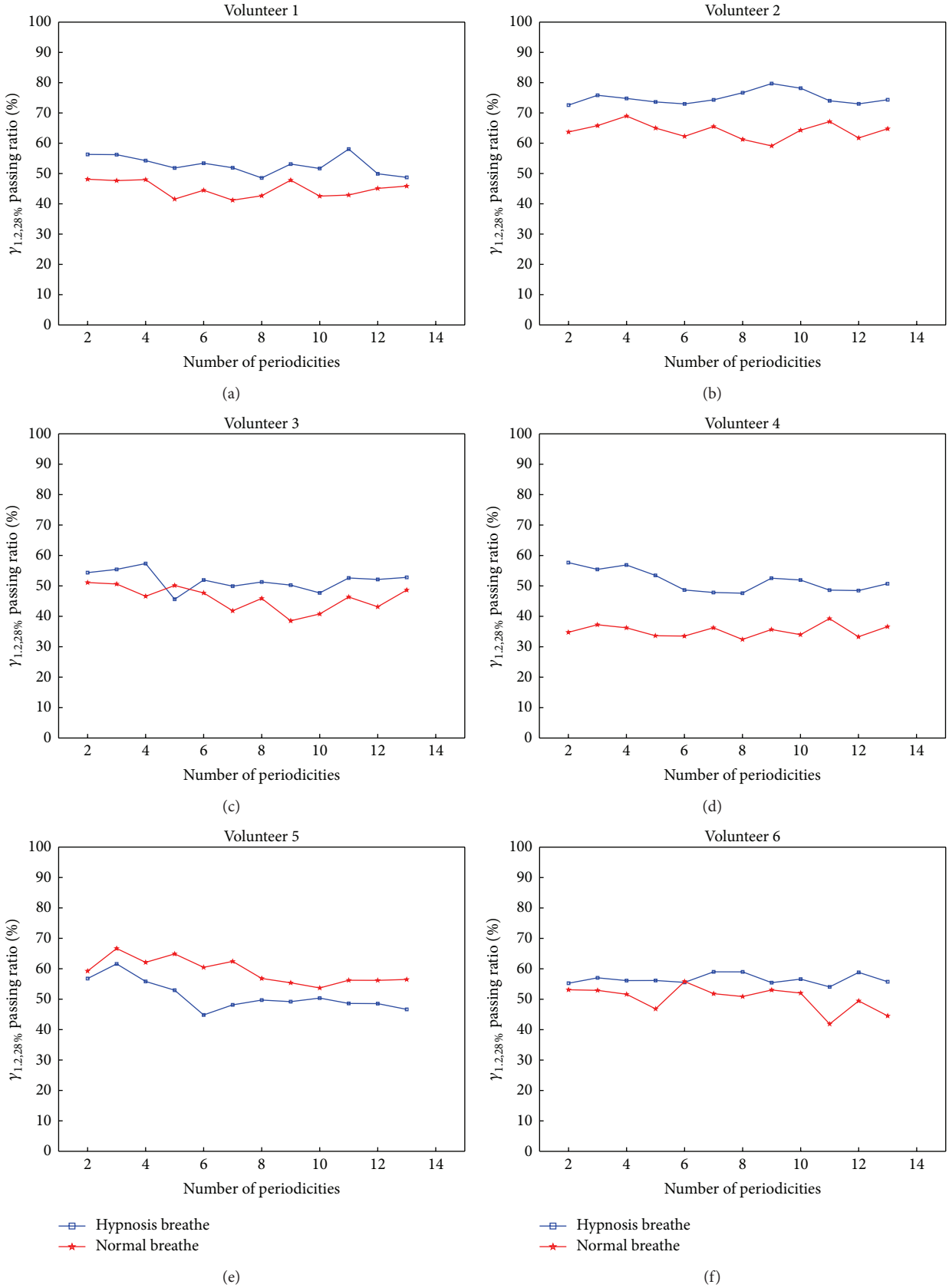

FIGURE 6: $\gamma_{1.2,28\%}$ passing ratio between the first cycle and the next 13 adjacent cycles in the hypnosis state (blue) and the normal state (red).

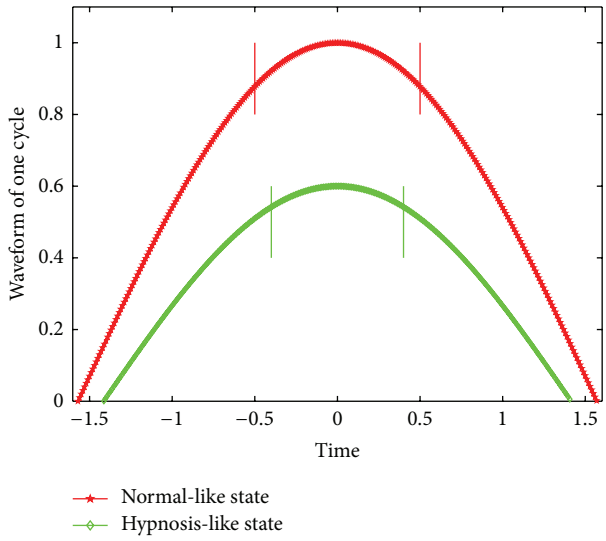

FIGURE 7: Comparison of waveforms between the hypnosis-like state (green) and the normal-like state (red); the green curve has the more stable peak than the red curve, caused by the amplitudes and the cycles of two curves.

Research Team Program (no. 2011S013) of China, Science and Technological Program for Dongguan's Higher Education, Science and Research, Health Care Institutions (Grant no. 2011108101001), grant from Comprehensive Strategic Cooperation Project of Guangdong province, and Chinese Academy of Sciences (Grant no. 2011B090300079).

References

[1] L. Xing, B. Thorndyke, E. Schreibmann et al., "Overview of image-guided radiation therapy," *Medical Dosimetry*, vol. 31, no. 2, pp. 91–112, 2006.

[2] R. Wagman, E. Yorke, E. Ford et al., "Respiratory gating for liver tumors: use in dose escalation," *International Journal of Radiation Oncology Biology Physics*, vol. 55, no. 3, pp. 659–668, 2003.

[3] S. B. Jiang, "Technical aspects of image-guided respiration-gated radiation therapy," *Medical Dosimetry*, vol. 31, no. 2, pp. 141–151, 2006.

[4] S. Quirk, N. Becher, and W. Smith, "External respiratory motion: shape analysis and custom realistic respiratory trace generation," *Medical Physics*, vol. 39, no. 8, pp. 4999–5003, 2012.

[5] R. D. Wiersma, W. Mao, and L. Xing, "Combined kV and MV imaging for real-time tracking of implanted fiducial markers," *Medical Physics*, vol. 35, no. 4, pp. 1191–1198, 2008.

[6] P. Kupelian, T. Willoughby, A. Mahadevan et al., "Multi-institutional clinical experience with the Calypso System in localization and continuous, real-time monitoring of the prostate gland during external radiotherapy," *International Journal of Radiation Oncology Biology Physics*, vol. 67, no. 4, pp. 1088–1098, 2007.

[7] W. Mao, R. D. Wiersma, and L. Xing, "Fast internal marker tracking algorithm for onboard MV and kV imaging systems," *Medical Physics*, vol. 35, no. 5, pp. 1942–1949, 2008.

[8] T. R. Willoughby, P. A. Kupelian, J. Pouliot et al., "Target localization and real-time tracking using the Calypso 4D localization system in patients with localized prostate cancer," *International Journal of Radiation Oncology Biology Physics*, vol. 65, no. 2, pp. 528–534, 2006.

[9] M. J. Murphy, "Fiducial-based targeting accuracy for external-beam radiotherapy," *Medical Physics*, vol. 29, no. 3, pp. 334–344, 2002.

[10] B. T. Collins, K. Erickson, C. A. Reichner et al., "Radical stereotactic radiosurgery with real-time tumor motion tracking in the treatment of small peripheral lung tumors," *Radiation Oncology*, vol. 2, no. 1, article 39, 2007.

[11] S. J. Lynn, O. Fassler, and J. Knox, "Hypnosis and the altered state debate: something more or nothing more?" *Contemporary Hypnosis*, vol. 22, no. 1, pp. 39–45, 2005.

[12] W. C. Coe, L. G. Buckner, M. L. Howard, and K. Kobayashi, "Hypnosis as role enactment: focus on a role specific skill," *American Journal of Clinical Hypnosis*, vol. 15, no. 1, pp. 41–45, 1972.

[13] D. A. Low, W. B. Harms, S. Mutic, and J. A. Purdy, "A technique for the quantitative evaluation of dose distributions," *Medical Physics*, vol. 25, no. 5, pp. 656–661, 1998.

[14] U. J. Yeo, M. L. Taylor, J. R. Supple et al., "Is it sensible to "deform" dose? 3D experimental validation of dose-warping," *Medical Physics*, vol. 39, no. 8, pp. 5065–5072, 2012.

[15] X. Gu, X. Jia, and S. B. Jiang, "GPU-based fast gamma index calculation," *Physics in Medicine and Biology*, vol. 56, no. 5, pp. 1431–1441, 2011.

Hindawi Publishing Corporation
BioMed Research International
Volume 2013, Article ID 264306, 8 pages
http://dx.doi.org/10.1155/2013/264306

Clinical Study

Helical Tomotherapy for Inoperable Breast Cancer: A New Promising Tool

Ciprian Chira,[1] Youlia M. Kirova,[1] Xavier Liem,[1] François Campana,[1] Dominique Peurien,[2] Malika Amessis,[2] Nathalie Fournier-Bidoz,[2] Jean-Yves Pierga,[3] Rémi Dendale,[1] Pierre Bey,[1] and Alain Fourquet[1]

[1] *Department of Radiation Oncology, Institut Curie, 26 rue d'Ulm, 75005 Paris, France*
[2] *Department of Medical Physics, Institut Curie, 26 rue d'Ulm, 75005 Paris, France*
[3] *Department of Medical Oncology, Institut Curie, 26 rue d'Ulm, 75005 Paris, France*

Correspondence should be addressed to Youlia M. Kirova; youlia.kirova@curie.net

Received 16 May 2013; Revised 7 July 2013; Accepted 11 July 2013

Academic Editor: An Liu

Background. We investigated the feasibility of helical tomotherapy (HT) for inoperable large breast tumors, after failing to achieve adequate treatment planning with conformal radiation techniques. *Material and Methods*. Five consecutive patients with locally advanced breast cancer (LABC) were treated by preoperative HT. All patients received up-front chemotherapy before HT. Irradiated volumes included breast and nodal areas (45–50 Gy) in 4 patients. One patient received a simultaneous integrated boost (55 Gy) to gross tumor volume (GTV) without lymph node irradiation. Acute toxicity was assessed with Common Toxicity Criteria for Adverse Events v.4. Patients were evaluated for surgery at the end of treatment. *Results*. Patients were staged IIB to IIIC (according to the AJCC staging system 2010). HT was associated in 4 patients with concomitant chemotherapy (5-fluorouracil and vinorelbine). Two patients were scored with grade 3 skin toxicity (had not completed HT) and one with grade 3 febrile neutropenia. One patient stopped HT with grade 2 skin toxicity. All patients were able to undergo mastectomy at a median interval of 43 days (31–52) from HT. Pathological partial response was seen in all patients. *Conclusions*. HT is feasible with acceptable toxicity profiles, potentially increased by chemotherapy. These preliminary results prompt us to consider a phase II study.

1. Introduction

Locally advanced breast cancer (LABC), defined mainly by stage III disease [1] and by a subset of stage IIB (T3N0), occurs in less than 15% of the diagnosed women [2–4] but poses a significant challenge from a treatment point of view. It requires a combined treatment approach involving anthracycline-based chemotherapy (with or without a taxane) and trastuzumab for human epidermal growth factor receptor 2 (HER-2) positive tumors, followed by surgery and radiation therapy [5]. But for patients with large volume disease whose tumors remain inoperable after primary or neoadjuvant chemotherapy (NCT) the management strategy is less clear.

Recent studies have used preoperative radiotherapy (combined with chemotherapy) in an attempt to downsize the tumor [6–11] making it amenable to surgery. However, these studies have only used conventional radiation techniques with considerable limitations in target volume coverage and sparing normal tissues.

Helical Tomotherapy (HT) is a new form of intensity-modulated radiation therapy (IMRT) that delivers a modulated fan beam using a 6 MV linear accelerator mounted on a ring gantry that rotates around the patient as he/she advances slowly through the gantry bore (Figure 1). Its advantages include: ability to correct for set-up errors, delivery of continuous craniocaudal irradiation which suppresses junction problems, and the conformality of the dose distribution

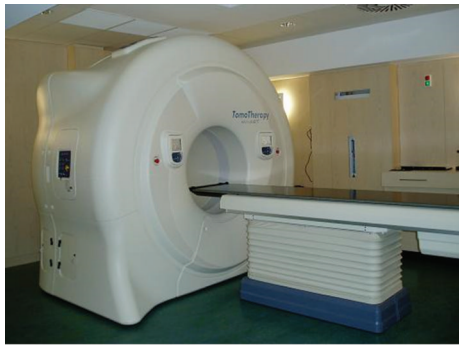

Figure 1: One of the two TomoTherapy Hi-Art treatment systems used in this study.

throughout the complex volumes formed by the lymph nodes and the breast [12].

We sought to report our early experience with the use of HT (with or without CCT) for inoperable LABC not eligible to conformal radiation techniques due to disease extension.

2. Patients and Methods

From November 2007 to February 2011 five consecutive women with stage IIB–IIIC LABC (according to AJCC staging system 2010) were seen at our multidisciplinary clinic. All patients had histological confirmation of malignancy by tumor biopsy with determination of tumor oestrogen and progesterone receptor (ER/PR) status and HER-2. The workup included history and physical examination with recording of size and location of the tumor on a diagram of the affected breast and a photo evaluation. Adequate biology lab tests were undertaken. Imaging studies included bilateral mammogram and breast ultrasound or breast magnetic resonance imaging (MRI), bone scan, thoracic-abdominal and pelvic computed tomography scan (CT), and fluorodeoxyglucose (FDG) positron-emission tomography scan (PET/CT) in one case. Genetic counseling was necessary in one patient.

All patients had advanced voluminous breast tumors judged not amenable to any form of surgery (conservative or radical). Inoperable breast cancer was defined as a combination of at least 2 of the following criteria (except for inflammatory breast carcinoma): fixation of the axillary nodes to overlying skin or deeper structures of the axilla, skin ulceration, inflammatory breast carcinoma, solid fixation of tumor to the chest wall, extensive edema of the skin (involving more than one-third of the skin over the breast), massive involvement of axillary lymph nodes (measuring 2.5 cm or more in transverse diameter), or clinically involved periclavicular lymph nodes and internal mammary metastases as evidenced by a parasternal tumor [13]. Resectability was evaluated by the breast surgeon based on the above criteria and available radiological imaging. Figure 2 illustrates the clinical assessment of one of these patients. One patient presented with a large primary (T3N0), located in the upper inner quadrant, being considered inoperable due to low probability to achieve clear surgical margins.

Table 1: Patient and tumor characteristics.

Characteristic	Value
Age Median (range)	62 (28–65)
Clinical Stage*	
IIB	1
IIIA	1
IIIB-IIIC	3
Tumor diameter in mm Median (range)	88 (75–160)
Laterality	
Right sided	3
Left sided	2
Hormonal receptors and HER2 over-expression	
ER–, PR–, HER2–	2
ER+, PR–, HER2–	1
ER+, PR+, HER2–	1
ER–, PR–, HER2+	1
Histological grade§	
2	1
3	4
Number of mitoses/10 high power field	
<11	1
>22	4
Initial chemotherapy regimen before HT	
EC + docetaxel	3
FEC + docetaxel	1
Docetaxel + trastuzumab	1
Adjuvant hormonotherapy	
Yes	2
No	3

Abbreviations: ER: oestrogen receptor, PR: progesterone receptor, HER2: Human Epidermal Growth Factor Receptor 2, *AJCC Cancer Staging Manual, Seventh Edition (2010), EC: epirubicin, cyclophosphamide, FEC: 5fluorouracil, epirubicin, cyclophosphamide, §Elston-Ellis modification of Scarff-Bloom-Richardson grading system.

All patients received up-front NCT before radiation delivery due to size and extent of disease and thus for the risk of micrometastatic disease. Chemotherapy regiments used before HT are detailed in Table 1. Clinical tumor response (defined at last week of NCT) was reported as complete if there was no palpable tumor in the breast, as partial if there was a reduction in tumor size (product of the two greatest perpendicular diameters) >50%, and as progressive disease when there was an increase >50%. Tumors not meeting these criteria were considered to be stable disease [14].

2.1. HT Planning and Radiation Delivery. In all 5 cases the choice of HT was done after careful dosimetry planning in three-dimensional conformal radiotherapy (3D CRT). An "optimized" 3D field-in-field technique, associated with internal mammary (IMN) electron-beam planning, was used,

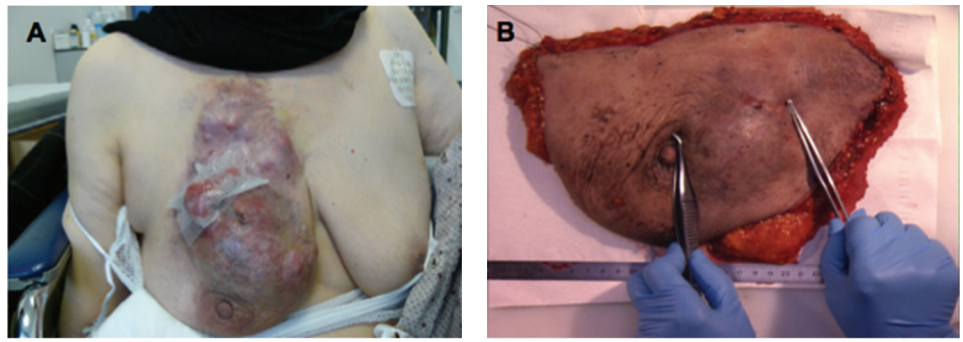

(a) (b)

Figure 2: (a) Large breast tumor in one of our patients before initiation of treatment. (b) Macroscopic residual tumor (right image) on surgical specimen from the same patient.

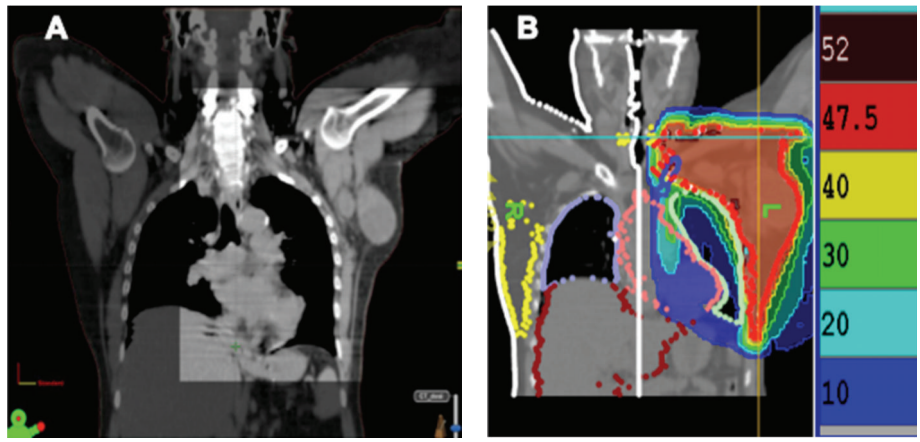

(a) (b)

Figure 3: (a) Coronal view of planning CT scan. (b) Dose colorwash of helical tomotherapy (HT) treatment plan.

which is the current standard in our department [15]. Two tangential fields with superimposed posterior borders, matching supraclavicular (SCV) and IMN fields (when indicated) were generated. For each tangent, one subfield was created with the MLC shaped to shield the 107% isodose, and the other increased the dose in the thickest part of the breast, if necessary. A more comprehensive description of this planning procedure has been published elsewhere [16]. The dosimetrical analysis using 3D CRT showed in all cases inadequate target volume coverage and unacceptable high doses to some critical organs.

The treatment planning CT scan was performed 1-2 weeks after the last cycle of NCT. Patients were placed in the supine position, on a breast board, with both arms abducted alongside the head. The palpable breast tissue contour and the tumor were delineated with radioopaque wires. Radioopaque markers were also placed along the midsternum, as well as 1-2 cm below the palpable breast limits. Images were acquired from the upper neck to the midabdomen, using a 3 mm slice thickness and separation. The CT data were transferred to a commercial treatment planning system (Eclipse 3D version 8.1; Varian Medical Systems Inc., Palo Alto, USA). The breast clinical target volume (CTV) was defined as the tissue delineated by the aforementioned radioopaque wire. In practice, on each transverse slice, the breast volume extended from the pectoralis major muscle to the skin, excluding the pectoralis muscle, ribs, or the first 3 mm of skin except in inflammatory tumors. Breast planning target volume (PTV) was generated by adding a tridimensional margin of 5 mm around the breast CTV. The gross tumor volume (GTV) was defined on the planning CT as the tissue delineated by the radioopaque wire. Margins were then added to GTV based on the information from initial clinical and radiological reports (boost CTV). Boost PTV was defined adding an additional margin of 5 mm beyond boost CTV. However, a simultaneous integrated boost (SIB) was delivered in only one patient. The regional lymph nodes (axillary (ALN), internal mammary (IMN), supraclavicular (SCV)/infraclavicular (IFC)) were delineated (whenever indicated) using our atlases [17, 18]. The heart was contoured from the level of the pulmonary trunk to the apex and included the pericardium but not the major vessels. Lungs, spinal cord, contralateral breast, esophagus, and thyroid gland were also manually delineated (Figure 3). The CT data and the structure sets were transferred to the

Table 2: Parameters for organs at risk (OAR) during HT planning.

OAR	Priority	Blocking	Importance	Histogram dose-volume points
Contralateral lung	1	Directional	1000	5%-7 Gy 30%-3 Gy 50%-2 Gy
Heart	2	Directional	1000	15%-10 Gy 5%-15 Gy
Homolateral lung	3	Directional	1000	50%-5 Gy 15%-20 Gy 5%-30 Gy
Contralateral breast	4	Directional	1000	10%-3 Gy
Spinal cord	5	Directional	300	30%-10 Gy
Liver	6	Directional	300	20%-5 Gy

tomotherapy planning station (TomoTherapy Hi-Art version 3.1.2.3; TomoTherapy Inc., Madison, USA). All plans used a jaw width of 2.5 cm, a pitch of 0.286, and a modulation factor of 2.5. Two complete blocks were created on the treatment planning system to improve HT planning. Block 1 encompassed the whole contralateral breast and hemibody, while block 2 encompassed the posterior part of the ipsilateral side of the body. The initial DVH constraints and penalties are shown in Table 2. These were adjusted during optimization to obtain adequate target volume coverage while minimizing heart, lung, esophagus and thyroid irradiation. The aim was to achieve a full PTV coverage between 95% and 107% of the prescribed dose (with the 95% isodose set as the reference isodose), to attain high target-dose homogeneity, to minimize the volume of normal tissue that received a high dose, and to keep the dose to critical structures below their tolerance. For organs at risk (OARs), the dosimetric constraints were set according to previously published toxicity data, reviewed in the QUANTEC recommendations [19]. The heart volume that received 25 Gy was limited to 10% [20], and the 20 Gy volume of both lungs was limited to 30–35% [21]. Coverage was considered adequate when the aforementioned criterion was met. Furthermore, an effort was made to reduce the treatment volume receiving more than 107% of the dose to the tumor to less than 1%.

2.2. Concomitant Chemotherapy (CCT) Regimen Used in Combination with HT. Concomitant chemotherapy (CCT) consisted of 4 cycles of 5-fluorouracil (5-FU), 500 mg/m^2/d, administered by continuous intravenous infusion over five consecutive days (d1–d5), and vinorelbine, 25 mg/m^2, short intravenous infusion on days 1 and 6. Courses were repeated every 3 weeks for a total of four courses. Radiotherapy started on day one of the second course of chemotherapy. Two cycles were prescribed during radiotherapy. This CCT protocol was tested in our institution in a phase II trial and was previously published [22, 23].

2.3. Evaluations of Toxicity and Pathological Response. Patients were seen on a weekly basis during HT. All toxicities were graded according to the Common Terminology Criteria for Adverse Events (CTCAE) v.4 [24].

Pathological response assessment on surgical specimen took into account the proportion of residual tumor cells, the location of this malignant component (invasive versus intraductal), the mitotic index in malignant cells, and the status of the metastatic axillary nodes. The response was considered as pathologically complete (pCR) when there was no residual invasive malignant epithelial cells in both the breast and the axillary lymph nodes. Tumors with an epithelial malignant residual component strictly in situ or representing less than 5% of the breast and/or axillary tumor mass and without any mitosis were also classified in the group of pCR. The response was considered as absent (pSD) when no histological modification of the tumor tissue could be related to therapy and as partial (pPR) in the remaining cases. This is according to the interpretation at the Institut Curie of the definition proposed by Sataloff and colleagues of a "total or near total therapeutic effect" [25, 26].

3. Results

Patient and initial tumor characteristics are described in Table 1. All patients had invasive ductal adenocarcinoma and had good performance status (ECOG score 0-1). Most NCT regimens were taxane- and anthracycline-based regimens (Table 1). Median number of delivered cycles was 8 (range: 6–8).

Planning with 3D CRT revealed that the doses to PTV did not attain the 95% constraint in 3 cases (<85%). Furthermore, mean (D_{mean}) and maximum dose (D_{max}) as well as V20 constraints for ipsilateral lung were not achieved with 3D CRT in 4 patients. Equally, D_{max} and V25 for the heart had not been achieved with 3D field-in-field technique in one patient with a left-sided large tumor.

Histogram dose-volume points were achieved with HT planning without deviation from the protocol for organs at risk (Table 2). Prescribed doses of radiation varied from 47.5 Gy in 25 daily fractions of 1.9 Gy to 50 Gy in 25 fractions, with simultaneous integrated boost to CTV of up to 55 Gy

in 25 fractions of 2.2 Gy. Delivered doses are described in Table 3.

There was no toxic death. Early grade 3 skin toxicity in the irradiated field was seen in 2 patients (patients numbers 4 and 5, Tables 3 and 4) both receiving CCT. These 2 patients required treatment interruption for skin care at 46 Gy/23 fx (planned dose was 50 Gy). The rest of patients experienced grade ≤2 skin events. Patient number 1 (Tables 3 and 4) had also stopped treatment at 41.8 Gy/22 fx (planned dose was 47.5 Gy/25 fx) while being scored with grade 2 skin toxicity, due to extent of lesions as well as patient desire. There was no grade >1 digestive toxicity. Grade 3 febrile neutropenia was observed in 1 patient (number 5 in Table 4). No cardiac or pulmonary toxicity was recorded during treatment and follow up.

Clinical evaluation of response to HT was judged favorable, and all patients were finally considered eligible for radical surgery. Modified radical mastectomy (MRM) with axillary lymph node dissection (ALND) of the first two levels was performed in all cases. Median time to surgery from last day of radiotherapy was 43 days (range: 31 to 52). Pathological response assessment on surgical specimen revealed pPR in all patients, according to the modified Sataloff criteria (Table 4). No patient achieved complete pathologic response.

Margins were negative in all cases (>0.7 cm in 4 cases, 5 mm in one case). No fibrosis was described in the surgical reports. One patient had wound infection and needed surgical drainage. Two patients had aspirations of lymphoceles.

Adjuvant treatments were decided according to pathological criteria and consisted of either chemotherapy (absence of complete pathological response) and/or endocrine therapy (presence of positive expression of ER/PR).

Median follow up was 15.4 months (range: 2 to 25.1). At last follow up, 2 patients were still alive and free of disease, presently undergoing endocrine therapy. One patient was lost to follow up, and 2 patients had died from metastatic disease.

4. Discussion

In the present study we have tested a relatively new form of radiation combined with sequential and/or concomitant chemotherapy. To the best of our knowledge this is the only exploratory study of HT in inoperable LABC. As it can be seen in Figure 2, these were patients requiring radiation treatment on extremely large and complex target volumes.

HT appears to improve target coverage while sparing OAR because of its ability to achieve a higher degree of conformity to the PTV. The well-known ability of HT to treat breast cancer with complex treatment volumes [12] and regional lymph nodes [27, 28] has been published before. Unfortunately, these studies are difficult to compare because dosimetric reports have different aims and different clinical situations.

In the current study, we have seen that HT can significantly spare the ipsilateral lung ($D_{max} < 40$ Gy) and reduce the lung V20 and V5 below tolerance levels. Wang et al. [29] showed the importance of the V5 which was a significant factor for the subsequent development of pneumonitis with a cut-off value of 42%. Therefore, the reduction of lung V20, V5, and mean lung dose is an important feature.

HT was also used in our series with the intention to avoid eventual cardiovascular toxicity, knowing that patients had previously received anthracycline (with or without bevacizumab) or taxane-based NCT. The reported rates of cardiac dysfunction vary from 4 to 7% in patients receiving Trastuzumab alone and up to 27% with concomitant trastuzumab, antracycline, and cyclophosphamid [30]. Epirubicine (used also in our study) is associated with 11.4% risk of cardiovascular toxicity [31]. The use of modern radiation techniques has been associated with a decline in cardiac mortality [32, 33]. In our patients, the HT plans resulted in acceptable doses to the heart. V25 Gy was negligible (<0.15 cc) with slight increase in D_{mean} compared to 3D CRT. Our results are consistent with other studies in which HT was tested in left-sided tumors with lymph node disease. Caudrelier et al. [28] also reported that cardiac dose was reduced with HT compared to 3D CRT (V30 Gy of 1.5% ± 1.9% versus 3.2% ± 2.2%). Their D_{mean} of the heart was 7.0 Gy (±2.9 Gy) versus 5.5 Gy ± 1.4 Gy ($P = 0.2$). Similar results were published by Goddu et al. [27] who reported a decrease in mean V35 Gy (from 5.6% ± 4.8% to 2.2% ± 1.5%) in the tomotherapy plans compared with 3D CRT. However, they showed an increase in D_{mean} to the heart compared to 3D CRT (12.2 ± 1.8 Gy versus 7.5 ± 3.4 Gy).

The same protective cardiac feature of HT on the heart (from high doses) was also described by Coon and colleagues [34] in patients with unfavorable cardiac anatomy. In our study none of our 5 patients (2 left-sided) experienced cardiac dysfunction during follow up.

Regarding skin toxicity, our findings indicate that the rate of severe acute events (grade ≥ 3 CTCAE) is potentially increased by CCT, high radiation dose (>45 Gy/25 fx to lymph node volumes), and outspread of target volumes (breast only versus breast and lymph nodes). Doses of 50 Gy/25 fx to whole breast seem tolerable (without CCT or lymph node irradiation) with possibility of simultaneous boost to gross tumor volume (patient number 2, Tables 3 and 4). However, in treatment of both breast and lymph nodes (especially with CCT) doses should be limited to 45 Gy/25 fx (1.8 Gy/fx) to lymph nodes and 50 Gy/25 fx (2 Gy/fx) to whole breast. The toxicity of the above CCT regimen (combined 3D CRT) has been previously evaluated [23]. Nevertheless, this study is the first to report the acute toxicity of this CCT regimen combined with HT.

One of the most current challenges for radiation oncologists treating LABC patients is the field junction problem seen with irradiation of lymph nodes around the breast. In our cohort, 4 patients received HT irradiation of lymph node areas (except patient number 2 in Table 3). These patients were initially planned with conventional multiport techniques (CMT). From our experience we know that multiple adjacent fields can lead to either hot or cold spots in target areas. Even if solutions exist to overcome this problem (asymmetric jaws to create a half beam for SCV and IMN fields and couch rotations to align tangents to SCV/IMN fields), this adds complexity for the technologists during patients setup [35]. HT has not only the ability to correct

Table 3: Description of treatment volumes and prescribed radiation doses with helical tomotherapy.

Patient number	Total doses (Gy)					Dose per fraction (Gy)				
	WB	Lymph nodes			TB	WB	Lymph nodes			TB
		IMN	SCV IFC	ALN			IMN	SCV IFV	ALN	
1	41.8	41.8	41.8	41.8	41.8	1.9	1.9	1.9	1.9	1.9
2	50				55	2				2.2
3	50		45	45	50	2		1.8	1.8	2
4	46	46	46	46	46	2	2	2	2	2
5	46	46	46	46	46	2	2	2	2	2

WB: whole breast, IMLN: ipsilateral internal mammary lymph nodes, SCV: ipsilateral supraclavicular fossa, IFC: ipsilateral infraclavicular fossa (level III axillary), ALN: ipsilateral level I and II axillary lymph nodes, TB: tumoral bed.

Table 4: Treatment characteristics and results.

Patient number	TNM stage[∬]	Tumor maximal diameter[†] (mm)	WB dose[¶] (Gy)	CCT/number of cycles	Early toxicity grade (CTCAE v.4)			Surgical specimen		Pathological response[§]
					Skin	Digestive	Other[‡]	T^* size (cm)	Nodal status	
1	T4bN2aM0	105	41.8	Yes/4	2	0	0	50	7+/11	PR
2	T4cN2aM0	160	50	No	1	1	0	64	0/13	PR
3	T3N0M0	75	50	Yes/4	2	0	1	22	0/15	PR
4	T4bN2aM0	85	46	Yes/4	3	1	0	4.5	2+/8	PR
5	T3N2bM0	88	46	Yes/2	3	0	3	17.6	1+/9	PR

[∬] AJCC cancer staging manual, seventh edition (2010), WB: whole breast, CCT: concomitant chemotherapy, CTCAE: Common Toxicity Criteria for Adverse Events v.4, [†]baseline evaluation before all treatments, [¶]delivered radiation dose, [‡]cardiovascular and/or pulmonary and/or hematological toxicity, [*]residual invasive malignant epithelial cells, [§]interpretation at the Institut Curie of the concept proposed by Sataloff and colleagues (details in article), PR: partial response.

setup errors but also the capacity to deliver a continuous craniocaudal delivery, which suppresses field junctions [36].

On the basis of the pathological analysis of surgical specimens our findings suggest that PR is achievable with HT and chemotherapy. Previous studies of LABC have reported good pathological response rates with preoperative chemoradiotherapy, but all used "conventional" radiation techniques, often via tangential fields. Matuschek et al. [11] reported a series of 315 LABC patients (cT1-cT4/cN0-N1). Preoperative EBRT delivered 50 Gy (5 × 2 Gy/week) to the whole breast, SCV/ICF nodes (255 of 315 patients), and IMC with a boost in 214 cases. Chemotherapy was administered prior to radiation in 192 patients and concomitantly in 113. Although pathologic complete tumor and nodal remission rate (pCR) was good (29.2%), in cT3 and cT4 patients it was significantly reduced (28% and 20%, resp.). Shanta and collegues [10] reported 1,117 consecutive LABC patients with stage IIB–IIIB (TNM staging, Heidelberg, Springer-Verlag; 1987) treated with neoadjuvant RT-CT (40 Gy/20 fx, 5 fx/week combined with CMF, EC, or AC). Complete pCR (pT0/pN0) was achieved in 33.7% of cases. While these studies indicate that high pCR can be achieved with conventional radiation techniques, detailed information on toxicity from these studies is scarce. Having in mind that LABC patients receive high doses of chemotherapy with potential toxicity and that conventional radiotherapy techniques have been associated with higher cardiac mortality [33], modern radiation techniques like HT should be examined.

This study has some potential limitations that need to be considered. First, this is a retrospective study with a limited number of patients, and thus treatment results should considered with caution. However, LABC is quite rare and recruiting a significant number of patients is not easy. Second, pathological response rates to our treatment may be related to both NCT as well as HT combined or not with CCT. We acknowledge the crucial role of chemotherapy in locoregional control of LABC. In fact, as mentioned before, we have previously studied the role of preoperative chemo-radiation with the CCT regimen used in this study. We showed that pathological control rates are high even with the use of conventional radiation techniques. The purpose of this study was not to assess the impact of the HT on pathological response rates but rather to test the feasibility of HT in these complex cases. Finally, breast tomotherapy needs human resources for the preparation and delivery of treatment (contouring of all target and organs-at-risk volumes, dosimetry optimization,

and quality controls). Thus, small community centers may not have sufficient financial resources for HT or human personnel for the HT workload.

5. Conclusion

Preoperative HT with or without CCT appears to be a feasible and promising alternative to highly conformal techniques in the treatment of large inoperable breast cancers. Particular attention should be given to evaluate acute skin toxicity especially in patients receiving CCT. Larger studies are warranted to better define HT doses and to evaluate long-term toxicities.

Conflict of Interests

The authors declare that they have no conflict of interests relating to the publication of this paper.

Acknowledgments

The authors thank all the members of the Breast Cancer Study Group at the Institut Curie who have contributed to the completion of this study. This work has been presented at the 2011 International Conference on Tomotherapy (ICT 2011) in Heidelberg, Germany, on September 17th (Presentation no. FC-29).

References

[1] S. E. Singletary, C. Allred, P. Ashley et al., "Revision of the American Joint Committee on cancer staging system for breast cancer," *Journal of Clinical Oncology*, vol. 20, no. 17, pp. 3628–3636, 2002.

[2] National Cancer Institute, DCCPS, Surveillance Research Program, Cancer Statistic Branch, "SEER Program Public Use tapes 1973–1998," 2000.

[3] W. A. G. El-Charnoubi, J. B. Svendsen, U. B. Tange, and N. Kroman, "Women with inoperable or locally advanced breast cancer – what characterizes them? A retrospective review of 157 cases," *Acta Oncologica*, vol. 51, no. 8, pp. 1081–1085, 2012.

[4] M. Kaufmann, G. N. Hortobagyi, A. Goldhirsch et al., "Recommendations from an international expert panel on the use of neoadjuvant (primary) systemic treatment of operable breast cancer: an update," *Journal of Clinical Oncology*, vol. 24, no. 12, pp. 1940–1949, 2006.

[5] The National Comprehensive Cancer Network (NCCN) Guidelines, http://www.nccn.org/professionals/physician_gls/pdf/breast.pdf.

[6] T. Bates, N. J. Williams, S. Bendall, E. E. Bassett, and R. S. Coltart, "Primary chemo-radiotherapy in the treatment of locally advanced and inflammatory breast cancer," *Breast*, vol. 21, no. 3, pp. 330–335, 2012.

[7] E. Touboul, L. Buffat, J.-P. Lefranc et al., "Possibility of conservative local treatment after combined chemotherapy and preoperative irradiation for locally advanced noninflammatory breast cancer," *International Journal of Radiation Oncology Biology Physics*, vol. 34, no. 5, pp. 1019–1028, 1996.

[8] E. Huang, M. D. McNeese, E. A. Strom et al., "Locoregional treatment outcomes for inoperable anthracycline-resistant breast cancer," *International Journal of Radiation Oncology Biology Physics*, vol. 53, no. 5, pp. 1225–1233, 2002.

[9] D. Lerouge, E. Touboul, J.-P. Lefranc, C. Genestie, L. Moureau-Zabotto, and J. Blondon, "Combined chemotherapy and preoperative irradiation for locally advanced noninflammatory breast cancer: updated results in a series of 120 patients," *International Journal of Radiation Oncology Biology Physics*, vol. 59, no. 4, pp. 1062–1073, 2004.

[10] V. Shanta, R. Swaminathan, R. Rama, and R. Radhika, "Retrospective analysis of locally advanced noninflammatory breast cancer from Chennai, South India, 1990–1999," *International Journal of Radiation Oncology Biology Physics*, vol. 70, no. 1, pp. 51–58, 2008.

[11] C. Matuschek, E. Bölke, S. L. Roth et al., "Long-term outcome after neoadjuvant radiochemotherapy in locally advanced non-inflammatory breast cancer and predictive factors for a pathologic complete remission: results of a multivariate analysis," *Strahlentherapie und Onkologie*, vol. 188, no. 9, pp. 777–781, 2012.

[12] R. Cendales, L. Schiappacasse, F. Schnitman, G. García, and H. Marsiglia, "Helical tomotherapy in patients with breast cancer and complex treatment volumes," *Clinical and Translational Oncology*, vol. 13, no. 4, pp. 268–274, 2011.

[13] W. Lawrence and G. H. Fletcher, "Criteria of operability in advanced breast cancer," in *Non-Disseminated Breast Cancer*, G. H. Fletcher and S. H. Levitt, Eds., pp. 5–9, Springer, Berlin Germany, 1993.

[14] M. A. Bollet, B. Sigal-Zafrani, L. Gambotti et al., "Pathological response to preoperative concurrent chemo-radiotherapy for breast cancer: results of a phase II study," *European Journal of Cancer*, vol. 42, no. 14, pp. 2286–2295, 2006.

[15] N. Fournier-Bidoz, Y. M. Kirova, F. Campana, R. Dendale, and A. Fourquet, "Simplified field-in-field technique for a large-scale implementation in breast radiation treatment," *Medical Dosimetry*, vol. 37, no. 2, pp. 131–137, 2012.

[16] C. Massabeau, N. Fournier-Bidoz, G. Wakil et al., "Implant breast reconstruction followed by radiotherapy: can helical tomotherapy become a standard irradiation treatment?" *Medical Dosimetry*, vol. 37, no. 4, pp. 425–431, 2012.

[17] P. Castro Pena, Y. M. Kirova, F. Campana et al., "Anatomical, clinical and radiological delineation of target volumes in breast cancer radiotherapy planning: individual variability, questions and answers," *British Journal of Radiology*, vol. 82, no. 979, pp. 595–599, 2009.

[18] I. Atean, Y. Pointreau, I. Barillot, and Y.-M. Kirova, "Organs at risk and target volumes: definition for conformal radiation therapy in breast cancer," *Cancer Radiothérapie*, vol. 16, no. 5-6, pp. 485–492, 2012.

[19] A. Jackson, L. B. Marks, S. M. Bentzen et al., "The lessons of QUANTEC: recommendations for reporting and gathering data on dose-volume dependencies of treatment outcome," *International Journal of Radiation Oncology Biology Physics*, vol. 76, no. 3, supplement, pp. S155–S160, 2010.

[20] G. Gagliardi, L. S. Constine, V. Moiseenko et al., "Radiation dose-volume effects in the heart," *International Journal of Radiation Oncology Biology Physics*, vol. 76, no. 3, supplement, pp. S77–S85, 2010.

[21] L. B. Marks, S. M. Bentzen, J. O. Deasy et al., "Radiation dose-volume effects in the lung," *International Journal of Radiation Oncology Biology Physics*, vol. 76, no. 3, supplement, pp. S70–S76, 2010.

[22] M. A. Bollet, L. Belin, F. Reyal et al., "Preoperative radio-chemotherapy in early breast cancer patients: long-term results of a

phase II trial," *Radiotherapy and Oncology*, vol. 102, no. 1, pp. 82–88, 2012.

[23] V. Marchand, A. Angelergues, V. Gobaux et al., "Prospective and comparative evaluation of the toxicity of adjuvant concurrent chemoradiotherapy after neoadjuvant chemotherapy for breast cancer," *American Journal of Clinical Oncology*, 2012.

[24] "Common Terminology Criteria for Adverse Events," v4.03 (CTCAE), June 14, 2010, http://ctep.cancer.gov/protocolDevelopment/electronic_applications/ctc.htm.

[25] A. Vincent-Salomon, M. Carton, P. Freneaux et al., "ERBB2 overexpression in breast carcinomasno positive correlation with complete pathological response to preoperative high-dose anthracycline-based chemotherapy," *European Journal of Cancer*, vol. 36, no. 5, pp. 586–591, 2000.

[26] A. Vincent-Salomon, A. Rousseau, M. Jouve et al., "Proliferation markers predictive of the pathological response and disease outcome of patients with breast carcinomas treated by anthracycline-based preoperative chemotherapy," *European Journal of Cancer*, vol. 40, no. 10, pp. 1502–1508, 2004.

[27] S. M. Goddu, S. Chaudhari, M. Mamalui-Hunter et al., "Helical tomotherapy planning for left-sided breast cancer patients with positive lymph nodes: comparison to conventional multiport breast technique," *International Journal of Radiation Oncology Biology Physics*, vol. 73, no. 4, pp. 1243–1251, 2009.

[28] J.-M. Caudrelier, S. C. Morgan, L. Montgomery, M. Lacelle, B. Nyiri, and M. MacPherson, "Helical tomotherapy for locoregional irradiation including the internal mammary chain in left-sided breast cancer: dosimetric evaluation," *Radiotherapy and Oncology*, vol. 90, no. 1, pp. 99–105, 2009.

[29] S. Wang, Z. Liao, X. Wei et al., "Analysis of clinical and dosimetric factors associated with treatment-related pneumonitis (TRP) in patients with non-small-cell lung cancer (NSCLC) treated with concurrent chemotherapy and three-dimensional conformal radiotherapy (3D-CRT)," *International Journal of Radiation Oncology Biology Physics*, vol. 66, no. 5, pp. 1399–1407, 2006.

[30] A. Seidman, C. Hudis, M. Kathryn Pierri et al., "Cardiac dysfunction in the trastuzumab clinical trials experience," *Journal of Clinical Oncology*, vol. 20, no. 5, pp. 1215–1221, 2002.

[31] M. Ryberg, D. Nielsen, G. Cortese, G. Nielsen, T. Skovsgaard, and P. K. Andersen, "New insight into epirubicin cardiac toxicity: competing risks analysis of 1097 breast cancer patients," *Journal of the National Cancer Institute*, vol. 100, no. 15, pp. 1058–1067, 2008.

[32] S. H. Giordano, Y.-F. Kuo, J. L. Freeman, T. A. Buchholz, G. N. Hortobagyi, and J. S. Goodwin, "Risk of cardiac death after adjuvant radiotherapy for breast cancer," *Journal of the National Cancer Institute*, vol. 97, no. 6, pp. 419–424, 2005.

[33] R. Roychoudhuri, D. Robinson, V. Putcha, J. Cuzick, S. Darby, and H. Møller, "Increased cardiovascular mortality more than fifteen years after radiotherapy for breast cancer: a population-based study," *BMC Cancer*, vol. 7, article 9, 2007.

[34] A. B. Coon, A. Dickler, M. C. Kirk et al., "Tomotherapy and multifield intensity-modulated radiotherapy planning reduce cardiac doses in left-sided breast cancer patients with unfavorable cardiac anatomy," *International Journal of Radiation Oncology Biology Physics*, vol. 78, no. 1, pp. 104–110, 2010.

[35] N. Fournier-Bidoz, Y. Kirova, F. Campana et al., "Technique alternatives for breast radiation oncology: conventional radiation therapy to tomotherapy," *Journal of Medical Physics*, vol. 34, no. 3, pp. 149–152, 2009.

[36] V. J. Gonzalez, D. J. Buchholz, K. M. Langen et al., "Evaluation of two tomotherapy-based techniques for the delivery of whole-breast intensity-modulated radiation therapy," *International Journal of Radiation Oncology Biology Physics*, vol. 65, no. 1, pp. 284–290, 2006.

Hindawi Publishing Corporation
BioMed Research International
Volume 2013, Article ID 692874, 10 pages
http://dx.doi.org/10.1155/2013/692874

Review Article

A Review on the Use of Grid-Based Boltzmann Equation Solvers for Dose Calculation in External Photon Beam Treatment Planning

Monica W. K. Kan,[1,2] Peter K. N. Yu,[2] and Lucullus H. T. Leung[1]

[1] *Department of Oncology, Princess Margaret Hospital, Hong Kong*
[2] *Department of Physics and Materials Science, City University of Hong Kong, Tat Chee Avenue, Kowloon Tong, Hong Kong*

Correspondence should be addressed to Monica W. K. Kan; kanwkm@ha.org.hk

Received 2 May 2013; Accepted 22 July 2013

Academic Editor: Maria F. Chan

Deterministic linear Boltzmann transport equation (D-LBTE) solvers have recently been developed, and one of the latest available software codes, Acuros XB, has been implemented in a commercial treatment planning system for radiotherapy photon beam dose calculation. One of the major limitations of most commercially available model-based algorithms for photon dose calculation is the ability to account for the effect of electron transport. This induces some errors in patient dose calculations, especially near heterogeneous interfaces between low and high density media such as tissue/lung interfaces. D-LBTE solvers have a high potential of producing accurate dose distributions in and near heterogeneous media in the human body. Extensive previous investigations have proved that D-LBTE solvers were able to produce comparable dose calculation accuracy as Monte Carlo methods with a reasonable speed good enough for clinical use. The current paper reviews the dosimetric evaluations of D-LBTE solvers for external beam photon radiotherapy. This content summarizes and discusses dosimetric validations for D-LBTE solvers in both homogeneous and heterogeneous media under different circumstances and also the clinical impact on various diseases due to the conversion of dose calculation from a conventional convolution/superposition algorithm to a recently released D-LBTE solver.

1. Introduction

Highly conformal photon dose distributions in various treatment sites can be achieved using different techniques of multileaf collimator-based intensity modulated radiotherapy, including static intensity modulated radiotherapy (IMRT) and volumetric modulated arc therapy (VMAT). Radiotherapy using intensity modulated techniques improves the possibility to escalate the target dose and minimize doses to critical organs when compared to three-dimensional conformal radiotherapy [1–11]. The use of IMRT or VMAT in patients usually involves many small field segments, some of which might pass through regions of low and high density media such as lung, air, and bone, depending on the location of the tumor and the surrounding normal tissues. One issue that affects the dose calculation accuracy in highly conformal planning is the ability of the algorithm to correctly account for the effects of radiation transport with the presence of heterogeneous medium.

Correction-based algorithms implemented in commercially available clinical treatment planning system include the pencil beam algorithm (PBC), collapsed cone convolution algorithm (CCC), and the analytical anisotropic algorithm (AAA). For PBC, it assumes that any collimated photon beam incident on the patient is composed of a large number of infinitely narrow pencil beams of photons. The total dose is calculated by superposition of pencil beam dose kernels at each point in space around the incident beam derived from Monte Carlo simulations. The effects of tissue variations and patient contour are usually modeled based on equivalent path length methods or the modified Batho correction method [12–14]. More advanced superposition/convolution methods such as AAA and CCC are able to incorporate electron and secondary photon transport in an approximate way for dose calculations in a heterogeneous medium. These methods use the superposition of the Monte Carlo derived dose kernels of both primary and scatter components to obtain

doses in voxels of the irradiated volume. To account for the presence of inhomogeneities, simple density scaling of the kernels is applied so that the secondary electron transport is only modeled macroscopically. Both AAA and CCC were proved to produce inaccurate dose distribution in media with complex heterogeneities in certain circumstances [14–18].

The Monte Carlo (MC) methods have been considered the most accurate methods for radiotherapy treatment planning dose calculation. They are statistical simulation methods based on random sampling. They solve the radiation transport problem stochastically by simulating the tracks of a sufficiently large number of individual particles using the random number generated probability distribution governing the individual physical processes. They are therefore capable of accurately computing the radiation dose in media under almost all circumstances [19, 20]. However, the computation time required may still limit the use of MC methods for complex intensity modulated techniques in the clinical environment.

The desire to develop a fast alternative dose calculation method with comparable accuracy to MC methods has led to the exploration of deterministic solutions to the coupled system of linear Boltzmann transport equations (LBTE) [21–26]. It was first demonstrated using the prototype software, Attila, which was a general purpose grid-based Boltzmann solver code. It was followed by Acuros developed by Transpire, Inc. (Gig Harbor, WA, USA), specially designed for radiotherapy dose calculations. Recently, a version of deterministic LBTE solver, namely, Acuros XB (AXB), has been developed and implemented in the Eclipse treatment planning system (Varian Medical Systems, Palo Alto, CA, USA). The LBTE is the governing equation that describes the macroscopic behavior of ionizing particles as they travel through and interact with matter. The electron angular fluence is first obtained by solving the LBTE, and then the dose can be generated by using the macroscopic electron energy deposition cross-sections and the density of the materials. With sufficient refinement without using any approximation, that is, if an MC algorithm simulates an infinite number of particles and a deterministic LBTE (D-LBTE) solver discretizes the variables such as space and energy into infinitely small grids, both approaches will converge on the same solution. The achievable accuracy of both approaches is equivalent and is limited only by uncertainties in the particle interaction data and uncertainties related to the transported radiation fields. Extensive efforts have been made by several investigators to validate the accuracy of D-LBTE solvers in different circumstances by comparison against MC and by experimental verification against measurements. Performed validations ranged from using a simple geometric phantom with simple fields to a complex humanoid phantom with multiple intensity modulated fields. Most studies reported that D-LBTE solvers were capable of producing comparable accuracy as MC methods and either equivalent or better accuracy than superposition/convolution algorithms [22–35]. Dosimetric impact on different media of various clinical sites due to the conversion of the currently used model-based algorithms to the newly implemented D-LBTE solvers was also investigated by several authors [32, 36–38]. This paper summarizes and discusses the findings of the most recent dosimetric evaluation for D-LBTE solvers in various treatment sites.

2. The Deterministic LBTE Solvers

More detailed description of the D-LBTE solvers can be found in the literature [21–26]. Only a summary is reported here.

The time-independent three-dimensional (3D) system of the coupled LBTE is solved to determine the energy deposition of photon and electron transport:

$$\widehat{\Omega} \cdot \overrightarrow{\nabla} \Phi^{\gamma} + \sigma^{\gamma} \Phi^{\gamma} = q^{\gamma\gamma} + q^{\gamma}, \tag{1}$$

$$\widehat{\Omega} \cdot \overrightarrow{\nabla} \Phi^{e} + \sigma^{e} \Phi^{e} - \frac{\partial}{\partial E} \left(S_R \Phi^{e} \right) = q^{ee} + q^{\gamma e} + q^{e}, \quad \overrightarrow{r} \in V, \ \widehat{\Omega} \in 4\pi, \ E > 0, \tag{2}$$

where Φ^{γ} and Φ^{e} are the photon and electron angular fluence, respectively, σ^{γ} and σ^{e} are the macroscopic photon and electron total interaction cross-sections for all materials in volume V and energies, respectively, $q^{\gamma\gamma}$, $q^{\gamma e}$, and q^{ee} represent the photon scattering source generated from photon interaction, electron scattering source generated from photon interaction, and electron scattering source generated from electron interactions everywhere in V for all angles and energies, respectively, q^{γ} and q^{e} represent the external photon and electron source from the treatment head, respectively, $\overrightarrow{r}$ is the spatial position vector, E is the energy, $\widehat{\Omega}$ is the unit vector denoting particle direction, and $\overrightarrow{\nabla}$ is referred to as the "streaming operator" which may be interpreted as the number of particles flowing into a volume dV, minus the number of particles flowing out of dV for particles travelling in a direction $d\Omega$ about Ω with energy E about dE. The second terms on the left-hand side of (1) and (2) are the "collision operators," which may be thought of as the number of particles removed from the volume by absorption or scattering. Equation (2) is the Boltzmann Fokker-Plank transport equation, which is solved for the electron transport. The third term on the left-hand side of (2) represents the continuous slowing down operator, where S_R is the restricted plus collisional radiative stopping power. Equations (1) and (2) are usually solved through discretization in space, angle, and energy. Energy discretization is achieved with the standard multigroup method. Space discretization can be achieved with a variably sized Cartesian adaptive mesh refinement technique (used by AXB) or by using a high-order Galerkin-based linear discontinuous finite-element method to solve the multigroup discrete ordinates equations on fully unstructured tetrahedral elements (used by Attila). For the former technique, the mesh is limited to refinement in factors of 2 or smaller in any direction. This allows for the use of finer resolution in higher dose and high dose gradient regions. Angle discretization for fluences and scattering sources is achieved with the standard ordinates method, where the quadrature order is adaptive by the energy group. The photon angular fluence of (1) is the summation of

uncollided (primary photon without interaction with matter) and collided fluence components (photons produced or scattered by photon interactions in the patient), where the latter is discretized using a linear discontinuous finite-element method, providing a linear solution variation throughout each element, with discontinuities permitted across element faces. After solving the electron angular fluence, the dose in any grid voxel, i, is calculated as follows:

$$D_i = \int_0^1 dE \int_{4\pi} \frac{d\widehat{\Omega}\left(\sigma_{\mathrm{ED}}^{e}\left(\overrightarrow{r}, E\right)\right)}{\rho\left(\overrightarrow{r}\right)} \Phi^{e}\left(\overrightarrow{r}, E, \widehat{\Omega}\right), \quad (3)$$

where σ_{ED}^{e} is the macroscopic energy deposition cross-section and ρ is the material density of the local voxel.

Similar to the MC methods, D-LBTE solvers also use energy cut-offs for electrons and photons. A particle is assumed to deposit all of its energy locally below the cut-off energy. For example, AXB uses an electron cut-off energy of 500 keV and a photon cut-off energy of 10 keV. Assumptions similar to those used in some MC methods are also applied to (1) and (2) of D-LBTE solvers. It is assumed that both secondary charged particles produced by pair production are electrons, not one electron plus one positron. It is also assumed that photons produce electrons, but electrons do not produce photons. The energy from photons produced by the electrons is assumed to be deposited locally. For (2), it is assumed that the Fokker-Planck operator is used for "soft" interactions leading to small-energy losses. Catastrophic interactions leading to large energy losses are represented with the standard Boltzmann scattering.

Both MC methods and D-LBTE solvers produce errors. MC methods produce stochastic errors when an insufficient number of particle histories is followed. LBTE solvers produce systematic errors due to finite discretization resolution in space, angle, and energy. Better accuracy always requires longer computation time. In addition, the achievable accuracy of MC and D-LBTE solver is limited by uncertainties in particle interaction data, patient geometry, and composition of the radiation field being modeled.

Similar to some MC methods, two options of dose reporting modes, that is, dose-to-water, D_w, and dose-to-medium, D_m, are usually provided in D-LBTE solvers. Both options calculate dose considering the elemental composition of each material in which particles are transported. The difference between them is mainly in the postprocessing step, in which D_w is obtained by rescaling D_m using the stopping power ratio of water to medium.

3. Validation in Homogeneous Water

It is important to validate a new dose calculation algorithm in basic geometrical conditions such as that in homogeneous water before going ahead for more complicated ones. The information regarding the accuracy in simple cases is important to identify the sources of errors or uncertainties in more complicated geometries. Fogliata et al. performed a comprehensive assessment of AXB in Eclipse to model photon beams of low and high energy in homogeneous water with simple geometries [26]. They also included "flattening filter free" (FFF) beams from the Varian TrueBeam machine. The use of an FFF beam significantly increases the dose rate and therefore reduces the delivery time of a treatment machine. Due to the removal of flattening filter, the physical aspects of FFF beams are different from those of conventional flattened ones, including forward peaked intensity profiles in the middle instead of uniform flat profiles across the fields, steeper dose fall-off of percentage depth doses in the exponential region, less variation of off-axis beam hardening, lower mean energy, less photon head scatter, and higher surface dose. For conventional flattened beams, the performance of AXB was determined by comparison of calculated data against measured data in water for open and wedged fields. For FFF beams, the verification tests were performed for open fields only. The overall accuracy was found to be within 1% for open beams and 2% for mechanical wedges.

Testing the performance of AXB using open fields in homogeneous water was also performed by several other investigators [27, 28, 32]. Doses calculated using AXB were compared to measured/golden beam data, data calculated using AAA and CCC, as well as MC simulated data using different field sizes for different energy beams. Output factors, percentage depth doses (PDD), and lateral dose profiles at various depths were examined. In general, the agreement between the calculated data generated by the various models and the measured/golden beam data were found to be better than or close to 2%, with slightly larger discrepancies found in the build-up and penumbra regions. The calculated penumbral widths were usually found to be slightly smaller than the measured ones.

In homogeneous water, comparable performance was found between AXB and AAA/CCC. This was expected as most commercially available correction-based algorithms, and radiation transport algorithms were capable of accurately predicting the photon beam dose distribution in homogenous water. The discrepancies between calculated data and measured data were mostly limited by the precision and spatial resolution of the beam measurement devices used, especially in regions of high dose gradient. For example, the use of ion chamber with finite size for measuring dose profiles would broaden the penumbra width.

4. Verification with Inhomogeneous Simple Geometric Phantom Using Single Open Fields

Several investigations have been performed to examine the accuracy of several different D-LBTE solvers for predicting the dose distribution in heterogeneous simple geometric phantoms using single fields of different photon energies [22, 25, 27–31]. The media of interest included soft tissue, normal lung, light lung, air, bone, aluminium, stainless steel, and titanium alloy. Most of the verifications were performed by benchmarking against the dose distributions calculated by MC methods. Table 1 summarizes the methods, phantom geometries, beam configurations, and comparison results between MC and D-LBTE solvers of some previous investigations. In general, good agreement was found between

Table 1: A summary describing information of some previous investigations for the accuracy of D-LBTE solvers in predicting the doses in heterogeneous simple geometric phantoms using single open fields.

Published investigations	Gifford et al. 2006 [22]	Vassiliev et al. 2010 [25]	Bush et al. 2011 [27]	Han et al. 2011 [28]	Kan et al. 2012 [30]	Lloyd and Ansbacher 2013 [31]
Beam energy	18 MV	6 and 18 MV	6 and 18 MV	6 and 18 MV	6 MV	6 and 18 MV
Field sizes	1.5×1.5 cm^2	2.5×2.5 cm^2 5.0×5.0 cm^2 10.0×10.0 cm^2	4.0×4.0 cm^2 10.0×10.0 cm^2 15.0×10.0 cm^2	2.5×2.5 cm^2 5.0×5.0 cm^2 10.0×10.0 cm^2	2.0×2.0 cm^2 3.0×3.0 cm^2 5.0×5.0 cm^2	10.0×10.0 cm^2
Phantom(s) geometry	One multilayer phantom: water (0–3 cm), aluminium, Al (3–5 cm), lung (5–12 cm), water (12–30 cm)	One multilayer phantom: water (0–3 cm), bone (3–5 cm), lung (5–12 cm), water (12–30 cm)	Two phantoms: (i) one with a single insert of normal lung, light lung, or air in water, (ii) a bone/lung phantom with several disk-shaped bony structures	One multilayer phantom: water (0–3 cm), bone (3–5 cm), lung (5–12 cm), water (12–30 cm)	$30.0 \times 30.0 \times 30.0$ cm^3 of water containing $5.0 \times 5.0 \times 30.0$ cm^3 of air	$20.0 \times 20.0 \times 20.0$ cm^3 of muscle cube containing $2.0 \times 2.0 \times 18.0$ cm^3 of stainless steel or titanium alloy
Monte carlo simulation	EGS4/Presta, 0.3% statistical uncertainty, resolution: $0.5 \times 0.5 \times 0.2$ cm^3 voxels	DOSXYZnrc, <0.1% statistical uncertainty, resolution: $0.2 \times 0.2 \times 0.2$ cm^3 voxels, 0.1 cm laterally in penumbra region	DOSXYZnrc ~1% statistical uncertainty in media except up to 4.5% in air, resolution: $0.25 \times 0.25 \times 0.25$ cm^3 voxels	DOSXYZnrc, <1% statistical uncertainty, resolution: $0.2 \times 0.2 \times 0.2$ cm^3 voxels for most volume, $0.1 \times 0.1 \times 0.2$ cm^3 near water/bone and bone/lung interfaces	EGS4/Presta, 2.0% statistical uncertainty, resolution: 1/10 of field dimensions with 0.2 mm bin thickness	DOSXYZnrc, ~1% statistical uncertainty, resolution: $0.2 \times 0.2 \times 0.2$ cm^3 voxels
D-LBTE solver	Attila code	Acuros (Transpire, Inc.)	AXB of version 10	AXB of version 10	AXB of version 10	AXB of version 11
Dose distribution examined	PDD	PDD and lateral profiles	PDD and lateral profiles	PDD, lateral profiles, and 3D gamma evaluation	PDD	PDD and lateral profiles
Difference between D-LBTE solver and Monte Carlo simulation	Average discrepancy is 1.4%, with 2.2% maximum discrepancy observed at water/Al interface	For 6 MV, max. discrepancy < 1.5%, with DTA < 0.7 mm in the build-up region. For 18 MV, max. discrepancy < 2.3% with DTA < 0.3 mm in the build-up region	Discrepancies were within 2% in lung, 3% in light lung, up to 4.5% in air, 1.8% in bone, with slightly larger discrepancy (up to 5%) at interfaces	For 6 MV, average discrepancy of 1.1% in PDD and 1.6% in dose profiles. For 18 MV, average discrepancy of 1.6% in PDD and 3.0% and dose profiles	Discrepancies are mostly within 2%, with slightly higher discrepancy (up to 6%) at the air/tissue interface in the secondary build-up region	In general good agreement between AXB and MC, with an average gamma agreement with a 2%/1mm criteria of 91.3% to 96.8%

D-LBTE solvers and MC, with discrepancies of better than or equal to 2% in most cases. Verification using AXB of version 10 showed that there were slightly larger discrepancies of up to about 4 to 6% found in the presence of very low density media such as light lung or air, especially at/near the interface in the secondary build-up region when small fields were used [27, 30]. The accuracy of D-LBTE solvers depends on the material assignment and the level of sampling the structure voxels to the calculation grid. Fogliata et al. showed that the version 11 of AXB gave better agreement with MC when predicting doses in the presence of air than the version 10.0 of AXB, which was due to the inclusion of air material assignment (air material was not included in version 10.0) and the provision of better resampling process of the structure voxels to the calculation grid [29].

Some of these studies also compared the accuracy of AXB with AAA [29–31], one of which performed the comparison with CCC as well [28]. All of them observed considerably larger differences between AAA and MC than those between AXB and MC in the presence of lung, air, and very high density objects especially near the interfaces. It was found that AXB could improve the dose prediction accuracy over both AAA and CCC in the presence of heterogeneities. It should also be noted that the depth dose profile data presented

by Han et al. showed that CCC produced slightly better agreement with MC than AAA in both lung and bone regions [28].

5. Verification Using Multiple Clinical Setup Fields with Humanoid Geometry

5.1. Verification by Comparison with Monte Carlo Simulation. Some investigations were performed to examine the accuracy of D-LBTE solvers by comparison against MC methods for clinical setup fields [24, 25]. One study compared the dose distributions from one prostate and one head-and-neck clinical treatment plans calculated by Attila to those calculated by MC using the DOSXYZnrc program. Both plans were generated using the CT image data set of the real patients using multiple coplanar open fields. 3D gamma evaluation showed that 98.1% and 98.5% of the voxels passed the 3%/3 mm criterion for the prostate case and the head and neck case, respectively.

Another study compared the dose distributions from a tangential breast treatment plan calculated by Acuros (Transpire, Inc.) to those calculated by MC using the DOSXYZnrc program. The plan was generated on an anthropomorphic phantom with two tangential fields using a field-in-field technique. Field shapes were defined by a multileaf collimator using both 6 and 18 MV beams. The 3D gamma evaluation showed that the dose agreement was up to 98.7% for the 2%/1 mm criterion and reached 99.9% for the 2%/2 mm criterion. The differences were mostly found in the air external to the patient and in the lateral penumbra on the inside edge of the fields.

In general, both studies showed excellent agreement between D-LBTE solvers and MC in all regions including those near heterogeneity and with the use of small fields. These studies indicated that D-LBTE solvers were able to produce similar accuracy as MC methods for complicated geometries. However, the achievable accuracy of MC approach was also limited by uncertainties of the particle interaction data, the geometry and composition of the field being modeled, and other approximations made in radiation transport. Comprehensive validations of D-LBTE solvers should also cover comparisons against experimental measurements. Treatment plans with more complex intensity modulated fields, such as IMRT and VMAT, were not included in these studies.

5.2. Verification by Comparison against Measurements. Verifications of AXB against measurements using IMRT and VMAT plans for various diseases were reported [30, 32–35]. Humanoid phantoms used include the Radiological Physics Center (RPC) phantoms, the anthropomorphic phantom (the RANDO phantom, The Phantom Laboratory, Salem, NY, USA), and the CIRS Thorax Phantom (CIRS, VA, USA). Table 2 summarizes some of the details including methods and results of each verification study. Regarding verification using thermoluminescence dosimeters (TLDs), all the calculated data matched with the measured data are within 5%, with an average discrepancy of about 2 to 3%. The positions of measurement included those inside the heterogeneous medium and near/at the interfaces.

For the gamma analysis using EBT films, the passing rate of the 3%/3 mm criterion met the recommendation (should be >90%) set by TG 119 for the studies performed in the nasopharyngeal region and the lung, where heterogeneities exist. However, the one performed using the RPC head and neck phantom, where only tissue equivalent material was involved, could only produce a passing rate of 88% for the 5%/3 mm criterion [33]. The inferior results reported might be due to the larger uncertainty of the film registration method during analysis.

All experimental validations listed also compared the accuracy between AXB and AAA. The accuracy of both when compared to TLD measurement was quite comparable except for the investigation using intensity modulated stereotactic radiotherapy (IMSRT) in locally persistent nasopharyngeal. For the IMSRT cases, AXB demonstrated better accuracy near air/tissue interfaces when compared with AAA. This might be due to the very small field segments used in IMSRT cases with the presence of air cavities. For validations performed with films, the accuracy of AXB was in general shown to be slightly better than that of AAA. When compared to TLD, films could measure a much larger number of points in a single measurement and provided better spatial resolution. This might be the reason why films could better distinguish between the accuracies of AAA and AXB even when the difference was small.

6. Dose in Medium against Dose in Water

For external photon beam radiation therapy planning, the input data used for most conventional correction/model-based dose algorithms are dose distributions and beam parameters measured in water. They usually report patient dose in terms of the absorbed dose to water (D_w) using variable electron density. On the other hand, LBTE solvers calculate the energy deposition considering radiation particle transport in different media and therefore report dose directly to patient medium (D_m). According to the recommendation from the American Association of Physicists in Medicine (AAPM) Task Group 105, MC results should allow conversion between D_m and D_w, based on the Bragg-Gray cavity theory, either during or after the MC simulation. This recommendation also applies to all other deterministic algorithms that are able to report D_m accurately for plan evaluation [39]. D_m calculated by LBTE solvers can be converted to D_w using the Bragg-Gray cavity theory by

$$D_w = D_m \left(\frac{\bar{S}}{\rho} \right)_m^w, \tag{4}$$

where $(\bar{S}/\rho)_m^w$ is the unrestricted water to medium mass collision stopping power ratio averaged over the energy spectra of primary electrons at the point of interest. It has been recently debated whether the D_m dose inherently predicted by MC methods needs to be converted to D_w. There are certain arguments between using D_m and D_w for radiotherapy treatment planning in the clinical environment.

Table 2: A summary of information on some previous experimental validations for the accuracy of D-LBTE solvers in predicting the doses in heterogeneous humanoid phantoms using multiple clinical setup fields.

Published investigations	Han et al. 2012. [33]	Kan et al. 2013 [34]	Kan et al. 2012 [30]	Han et al. 2013 [35]	Hoffmann et al. 2012 [32]
Disease of interest	Oropharyngeal tumor	Nasopharyngeal carcinoma	Locally persistent nasopharyngeal carcinoma	Lung cancer	Tumor in mediastinum
Media involved	Water equivalent materials	Tissue, air, and bone	Tissue, air, and bone	Tissue and lung	Tissue, lung, and bone
Treatment technique used	IMRT, VMAT	IMRT, VMAT	IMSRT	IMRT, VMAT	A total of 11 different plans including opposing fields, multiple fields, IMRT, and VMAT.
Phantom used	RPC head and neck phantom	Anthropomorphic phantom (RANDO)	Anthropomorphic phantom (RANDO)	RPC thorax phantom	CIRS Thorax phantom
Measurement device	TLD and EBT film	TLD and EBT film	TLD	TLD and EBT film	EBT film
LBTE solver	AXB version 11 using both D_m and D_w	AXB version 10 using both D_m and D_w	AXB version 10 using D_m only	AXB version 11 using both D_m and D_w	AXB version 10 using D_m only
Observed results	For TLD, deviation within 5%. For gamma analysis with film, 88% passed 5%/3 mm criterion for both D_m and D_w	For TLD, deviation within 5%, with an average of 1.8%. For gamma analysis with film, 91% passed 3%/3 mm criterion for D_m and 99% for D_w	For TLD, deviation within 3%	For TLD, deviation within 4.4%. For gamma analysis with film, ~97% passed 3%/3 mm criterion for D_m and 98% for D_w	For gamma analysis with film, 98.2% passed the 3%/3 mm criterion for 6 MV and 99.5% for 15 MV

Those supporting the use of D_w argued that (1) therapeutic and normal tissue tolerance doses determined from clinical trials were based on D_w as photon dose measurements and calculations were historically reported in terms of D_w, (2) calibration of treatment machines were performed according to recognized dosimetry protocols in terms of the absorbed dose to water, and (3) tumor cells embedded within any medium such as bone were more water-like than medium-like. Those supporting the use of D_m argued that (1) the dose to the tissues of interest was the quantity inherently computed by radiation transport dose algorithms and therefore was more clinical relevant and (2) the conversion of D_m back to D_w might induce additional uncertainty to the final calculated dose.

Several studies proved that the difference between using D_w and D_m for predicting photon dose distribution mainly occurred in higher density materials such as the cortical bone. The dose discrepancy could be up to 15% due to the large difference between the stopping powers of water and these higher-density materials. For soft tissues and lung, the dose discrepancy was only about 1 to 2% [33, 35, 40]. An investigation by Dogan et al. based on the MC method found that converting D_m to D_w in IMRT treatment plans introduced a discrepancy in target and critical structure of up to 5.8% for head and neck cases and up to 8.0% for prostate cases when bony structures were involved [41]. Kan et al. also observed that AXB using D_w calculated up to 4% higher mean doses for the bony structure in planning target volume (PTV) when compared to D_m in IMRT and VMAT plans of NPC cases [34]. Figure 1 shows the difference in dose volume histograms (DVHs) between D_m and D_w for different organs at risk (OAR) and PTV components (both bone and soft tissues). They were generated by AXB using both D_m and D_w for a typical VMAT plan of an NPC case. It can be seen from the DVH curves that larger dose differences were found between D_m and D_w in organs with bony structures such as mandible than those with soft tissue such as parotids.

Previous studies using Monte Carlo and AXB calculations proved that conventional model based algorithms predicted dose distributions in bone that were closer to D_m distributions than to D_w distributions [34, 42]. It is therefore better to use D_m for consistency with previous radiation therapy experience.

7. Dosimetric Impact in Clinical Cases

Various studies were performed to assess the dosimetric impact of using AXB instead of AAA for dose calculations in different clinical cases, including lung cancer, breast cancer, and nasopharyngeal carcinomas [36–38]. AXB calculations for these investigations were all performed using the D_m option, so that the capability of the algorithm to distinguish

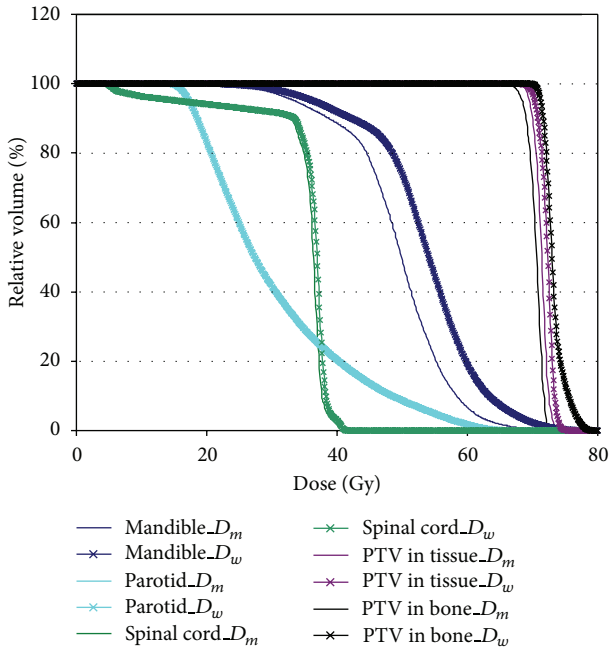

Figure 1: DVH curves for different OAR and PTV components generated by AXB with both D_m and D_w calculation options for a typical VMAT plan of an NPC patient.

between different elemental compositions in the human body could be assessed. The grid resolution for dose calculation selected was 2.5 mm. In order to evaluate the dose differences between the two algorithms due to the issue of tissue heterogeneity, the PTV were divided into components of different densities and compositions during dose analysis.

7.1. Lung Cancer. The clinical dosimetric impact for advanced non-small-cell lung cancer was assessed using three different techniques: three-dimensional conformal radiotherapy, IMRT, and RapidArc (the name of the VMAT system from Varian Medical Systems Inc., Palo Alto, CA, USA) at both 6 and 15 MV [36]. The PTVs were split into two components, namely, PTV in soft tissue and PTV in lung. The dose prescription was 66 Gy at 2 Gy per fraction to the mean target dose for each planning technique. The results demonstrated that AXB predicted up to 1.7% and 1.2% lower mean target doses in soft tissue for 6 MV and 15 MV beams, respectively, and up to 1.2% higher and 2.0% lower mean target doses in lung for 6 MV and 15 MV beams, respectively. In general, AAA overestimated the doses to most PTV components, except for PTV in lung when using IMRT at 6 MV, where the opposite trend was observed. AXB predicted up to 3% lower mean doses to OAR. The observed trend was similar for different treatment techniques.

7.2. Breast Cancer. The dosimetric impact for breast cancer was assessed using the opposing tangential field setting technique at 6 MV [37]. Doses in organs were analyzed using patient datasets scanned under two different breathing conditions, free breathing (FB, representing higher lung density), and deep inspiration (DI, representing lower lung density). The target breast was split into components in muscle and in adipose tissue. It was observed that AAA predicted 1.6% higher doses for the muscle than AXB (version 11). The difference in doses predicted by both algorithms to the adipose tissue was negligible. AAA was found to predict up to 0.5% and 1.5% higher doses than using version 11 of AXB in the lung region within the tangential field for FB and DI, respectively. The authors comparing between versions 10 and 11 of AXB found negligible differences in the predicted doses for tissue and normal lung. However, they observed that, for the lower density lung in the condition of DI, version 11 of AXB predicted an average of 1.3% higher dose than version 10. This was mainly due to the more accurate dose calculation of version 11 for very low density lung achieved by including the low density air in the material list.

7.3. Nasopharyngeal Carcinomas. The dosimetric impact for NPC was assessed using IMRT and RapidArc at 6 MV due to the use of AXB version 10 compared to AAA [38]. The PTVs with multiple prescriptions were separated into components in bone, air, and tissue. AAA was found to predict about 1% higher mean doses to the PTVs in tissue, 2% higher doses to the PTVs in bone, and 1% lower doses to the PTVs in air. AAA also predicted up to 3% higher doses to most serial organs. It should be noted that AAA predicted up to 4% higher minimum doses to the PTVs in bone, where the gross tumor volume was located.

On the whole, the various investigations for different treatment sites listed above demonstrated that in general AAA predicted higher doses to PTV and OAR, when compared with AXB. The overestimation by AAA was mostly within 2% in soft tissues such as muscle and lung and could be up to 4% in bone.

8. Discussions

Various studies showed that D-LBTE solvers were able to produce satisfactory dose calculation accuracy in the presence of heterogeneous media, even at and near interfaces of different material densities [22–35]. They were proved to produce equivalent accuracy to MC methods and better accuracy than convolution/superposition algorithms. These results are expected as D-LBTE methods model the radiation transport process in a similar manner as MC methods. There is still room for improvement in the latest version of clinically available AXB regarding accuracy in physical material assignment and calculation speed. For example, one of the limitations of AXB is the restricted material assignment range. If the CT dataset of a high density object contains HU values corresponding to a mass density greater than 3.0 g/cm^3, it is required to contain all voxels in a contoured structure with manual assignment of mass density. That means the mass density of the high density object must be known for accurate dose calculations. The validation of AXB by Lloyd and Ansbacher proved that it was able to predict the back-scatter and lateral-scatter dose perturbations accurately adjacent to very higher density objects (with density in

the range from 4.0 to 8.0 g/cm^3) [31]. However, in reality, this would be difficult for real patient planning due to the misinterpretation of HU values of high density implants introduced by shadow artifacts in CT images.

When compared to MC methods, the use of D-LBTE solvers might result in relatively shorter calculation time as explicit modeling of a large number of particle interactions is not required. Previous studies observed that the earlier D-LBTE code, Attila, performed dose calculations faster than the general purpose of MC method such as EGS4 or the EGSnrc by an order of magnitude for both external beam and brachytherapy planning [22, 24]. Acuros, which was optimized for use in radiotherapy planning, was reported to perform roughly an order of magnitude faster than Attila for various clinical cases [25]. Furthermore, the latest version of D-LBTE method, AXB, was reported to produce 3 to 4 times faster speed for VMAT planning compared to AAA [36]. The above evidence indicates that D-LBTE methods can be a fast and accurate alternative to MC methods. However, it is in fact difficult to perform direct comparison of the speed between MC and D-LBTE solvers as it depends on the hardware and the efficiency of the coding used. The computation time of D-LBTE solvers might be further reduced in the future by implementation on graphical processing units and additional refinements. On the other hand, fast MC codes have been developed to improve the speed of dose calculation for clinical use. Examples include the Voxel-based Monte Carlo (VMC, VMC++), Macro Monte Carlo, Dose Planning Method (DPM), and MCDOSE [43–50]. Continuous development of more efficient MC codes in the future may compete with currently commercial available D-LBTE methods in terms of both accuracy and speed.

Although D-LBTE solvers were proved to be more accurate than convolution/superposition algorithms, significant differences were mainly confined to certain extreme conditions. These mainly include doses near heterogeneous interfaces when using single or multiple small fields. Up to 8 to 10% higher doses near interfaces were predicted by AAA compared with AXB when stereotactic small fields were used in the presence of air cavity [30]. Smaller differences were found when using IMRT and VMAT setup fields. Several experimental verifications showed comparable dose accuracy between AXB and AAA in soft tissues within complex heterogeneous geometries for clinical intensity modulated fields [33–35]. The studies assessing the dosimetric impact of using AXB on various clinical sites also showed only about 1 to 2% lower means doses in all soft tissues predicted by AXB compared to AAA [36–38]. Slightly larger differences of about 4% were found in bony structures due to the fact that AXB reported dose to medium as default while AAA reported dose to water as default. Most of these comparison studies were confined between AAA and AXB, as both of them are implemented in the same treatment planning system. Comparison between AXB with other convolution/superposition methods such as CCC for various clinical sites is not reported. From the single field study performed by Han et al. [28] in simple heterogeneous geometry, it can be predicted that CCC may produce a closer dose distribution to AXB than AAA for clinical multiple setup fields. It is because CCC predicts more accurate doses near heterogeneous interfaces than AAA for single fields, and, like AXB, it reports dose to medium as default.

Most dosimetric studies mentioned above indicated that AAA slightly overestimated the doses to target volumes compared to AXB. If D-LBTE methods are used instead of model-based algorithms for treatment planning, it is very likely that more doses will be given to the target volumes provided that the prescribed doses by oncologists remain unchanged. Whether such conversion will bring actual clinical impact to the patients such as improvement in tumor control probability for various clinical sites requires further investigation.

9. Conclusions

On the whole, grid-based D-LBTE solvers were evaluated by extensive investigations to be accurate and valuable dose calculation methods for photon beam radiotherapy treatments involving heterogeneous materials. They were proved to produce doses in good agreement with MC methods and measurements in different clinical sites using techniques ranging from relatively simple to very complex intensity modulated treatment. The use of D-LBTE solvers is highly recommended for cases with heterogeneities. However, users must be aware of the dosimetric impact on various treatment sites due to the conversion from using model-based algorithms to D-LBTE solvers.

References

[1] M. K. M. Kam, R. M. C. Chau, J. Suen, P. H. K. Choi, and P. M. L. Teo, "Intensity-modulated radiotherapy in nasopharyngeal carcinoma: dosimetric advantage over conventional plans and feasibility of dose escalation," *International Journal of Radiation Oncology Biology Physics*, vol. 56, no. 1, pp. 145–157, 2003.

[2] W. F. A. R. Verbakel, J. P. Cuijpers, D. Hoffmans, M. Bieker, B. J. Slotman, and S. Senan, "Volumetric intensity-modulated arc therapy vs. conventional IMRT in head-and-neck cancer: a comparative planning and dosimetric study," *International Journal of Radiation Oncology Biology Physics*, vol. 74, no. 1, pp. 252–259, 2009.

[3] E. Vanetti, A. Clivio, G. Nicolini et al., "Volumetric modulated arc radiotherapy for carcinomas of the oro-pharynx, hypopharynx and larynx: a treatment planning comparison with fixed field IMRT," *Radiotherapy and Oncology*, vol. 92, no. 1, pp. 111–117, 2009.

[4] P. Doornaert, W. F. A. R. Verbakel, M. Bieker, B. J. Slotman, and S. Senan, "RapidArc planning and delivery in patients with locally advanced head-and-neck cancer undergoing chemoradiotherapy," *International Journal of Radiation Oncology Biology Physics*, vol. 79, no. 2, pp. 429–435, 2011.

[5] R. A. Popple, J. B. Fiveash, I. A. Brezovich, and J. A. Bonner, "RapidArc radiation therapy: first year experience at the University of Alabama at Birmingham," *International Journal of Radiation Oncology Biology Physics*, vol. 77, no. 3, pp. 932–941, 2010.

[6] M. J. Zelefsky, Z. Fuks, L. Happersett et al., "Clinical experience with intensity modulated radiation therapy (IMRT) in prostate

cancer," *Radiotherapy and Oncology*, vol. 55, no. 3, pp. 241–249, 2000.

[7] F. A. Vicini, M. Sharpe, L. Kestin et al., "Optimizing breast cancer treatment efficacy with intensity-modulated radiotherapy," *International Journal of Radiation Oncology Biology Physics*, vol. 54, no. 5, pp. 1336–1344, 2002.

[8] C. C. Popescu, I. A. Olivotto, W. A. Beckham et al., "Volumetric modulated arc therapy improves dosimetry and reduces treatment time compared to conventional intensity-modulaed radiotherapy for locoregional radiotherapy of left-sided breast cancer and internal mammary nodes," *International Journal of Radiation Oncology Biology Physics*, vol. 76, no. 1, pp. 287–295, 2010.

[9] P. Zhang, L. Happersett, M. Hunt, A. Jackson, M. Zelefsky, and G. Mageras, "Volumetric modulated arc therapy: planning and evaluation for prostate cancer cases," *International Journal of Radiation Oncology Biology Physics*, vol. 76, no. 5, pp. 1456–1462, 2010.

[10] I. S. Grills, D. Yan, A. A. Martinez, F. A. Vicini, J. W. Wong, and L. L. Kestin, "Potential for reduced toxicity and dose escalation in the treatment of inoperable non-small-cell lung cancer: a comparison of intensity-modulated radiation therapy (IMRT), 3D conformal radiation, and elective nodal irradiation," *International Journal of Radiation Oncology Biology Physics*, vol. 57, no. 3, pp. 875–890, 2003.

[11] S. D. McGrath, M. M. Matuszak, D. Yan, L. L. Kestin, A. A. Martinez, and I. S. Grills, "Volumetric modulated arc therapy for delivery of hypofractionated stereotactic lung radiotherapy: a dosimetric and treatment efficiency analysis," *Radiotherapy and Oncology*, vol. 95, no. 2, pp. 153–157, 2010.

[12] A. Ahnesjo, M. Saxner, and A. Trepp, "A pencil beam model for photon dose calculation," *Medical Physics*, vol. 19, no. 2, pp. 263–273, 1992.

[13] A. Fogliata, E. Vanetti, D. Albers et al., "On the dosimetric behaviour of photon dose calculation algorithms in the presence of simple geometric heterogeneities: comparison with Monte Carlo calculations," *Physics in Medicine and Biology*, vol. 52, no. 5, pp. 1363–1385, 2007.

[14] W. Ulmer, J. Pyyry, and W. Kaissl, "A 3D photon superposition/convolution algorithm and its foundation on results of Monte Carlo calculations," *Physics in Medicine and Biology*, vol. 50, no. 8, pp. 1767–1790, 2005.

[15] A. Gray, L. D. Oliver, and P. N. Johnston, "The accuracy of the pencil beam convolution and anisotropic analytical algorithms in predicting the dose effects due to attenuation from immobilization devices and large air gaps," *Medical Physics*, vol. 36, no. 7, pp. 3181–3191, 2009.

[16] L. Tillikainen, H. Helminen, T. Torsti et al., "A 3D pencil-beam-based superposition algorithm for photon dose calculation in heterogeneous media," *Physics in Medicine and Biology*, vol. 53, no. 14, pp. 3821–3839, 2008.

[17] C. Martens, N. Reynaert, C. de Wagter et al., "Underdosage of the upper-airway mucosa for small fields as used in intensity-modulated radiation therapy: a comparison between radiochromic film measurements, Monte Carlo simulations, and collapsed cone convolution calculations," *Medical Physics*, vol. 29, no. 7, pp. 1528–1535, 2002.

[18] M. W. K. Kan, J. Y. C. Cheung, L. H. T. Leung, B. M. F. Lau, and P. K. N. Yu, "The accuracy of dose calculations by anisotropic analytical algorithms for stereotactic radiotherapy in nasopharyngeal carcinoma," *Physics in Medicine and Biology*, vol. 56, no. 2, pp. 397–413, 2011.

[19] P. Andreo, "Monte Carlo techniques in medical radiation physics," *Physics in Medicine and Biology*, vol. 36, no. 7, pp. 861–920, 1991.

[20] D. W. O. Rogers, B. A. Faddegon, G. X. Ding, C.-M. Ma, J. We, and T. R. Mackie, "BEAM: a Monte Carlo code to simulate radiotherapy treatment units," *Medical Physics*, vol. 22, no. 5, pp. 503–524, 1995.

[21] T. A. Wareing, J. M. McGhee, J. E. Morel, and S. D. Pautz, "Discontinuous finite element SN methods on three-dimensional unstructured grids," *Nuclear Science and Engineering*, vol. 138, no. 3, pp. 256–268, 2001.

[22] K. A. Gifford, J. L. Horton Jr., T. A. Wareing, G. Failla, and F. Mourtada, "Comparison of a finite-element multigroup discrete-ordinates code with Monte Carlo for radiotherapy calculations," *Physics in Medicine and Biology*, vol. 51, no. 9, pp. 2253–2265, 2006.

[23] K. A. Gifford, M. J. Price, J. L. Horton Jr., T. A. Wareing, and F. Mourtada, "Optimization of deterministic transport parameters for the calculation of the dose distribution around a high dose-rate 192Ir brachytherapy source," *Medical Physics*, vol. 35, no. 6, pp. 2279–2285, 2008.

[24] O. N. Vassiliev, T. A. Wareing, I. M. Davis et al., "Feasibility of a multigroup deterministic solution method for three-dimensional radiotherapy dose calculations," *International Journal of Radiation Oncology Biology Physics*, vol. 72, no. 1, pp. 220–227, 2008.

[25] O. N. Vassiliev, T. A. Wareing, J. McGhee, G. Failla, M. R. Salehpour, and F. Mourtada, "Validation of a new grid-based Boltzmann equation solver for dose calculation in radiotherapy with photon beams," *Physics in Medicine and Biology*, vol. 55, no. 3, pp. 581–598, 2010.

[26] A. Fogliata, G. Nicolini, A. Clivio, E. Vanetti, P. Mancosu, and L. Cozzi, "Dosimetric validation of the Acuros XB advanced dose calculation algorithm: fundamental characterization in water," *Physics in Medicine and Biology*, vol. 56, no. 6, pp. 1879–1904, 2011.

[27] K. Bush, I. M. Gagne, S. Zavgorodni, W. Ansbacher, and W. Beckham, "Dosimetric validation of Acuros XB with Monte Carlo methods for photon dose calculations," *Medical Physics*, vol. 38, no. 4, pp. 2208–2221, 2011.

[28] T. Han, J. K. Mikell, M. Salehpour, and F. Mourtada, "Dosimetric comparison of Acuros XB deterministic radiation transport method with Monte Carlo and model-based convolution methods in heterogeneous media," *Medical Physics*, vol. 38, no. 5, pp. 2651–2664, 2011.

[29] A. Fogliata, G. Nicolini, A. Clivio, E. Vanetti, and L. Cozzi, "Dosimetric evaluation of Acuros XB Advanced Dose Calculation algorithm in heterogeneous media," *Radiation Oncology*, vol. 6, no. 1, article 82, 2011.

[30] W. K. Kan, L. Leung, and P. Yu, "Verification and dosimetric impact of Acuros XB algorithm on intensity modulated stereotactic radiotherapy for locally persistent nasopharyngeal carcinoma," *Medical Physics*, vol. 39, no. 8, pp. 4705–4714, 2012.

[31] S. A. M. Lloyd and W. Ansbacher, "Evaluation of an analytic linear Boltzmann transport equation solver for high density inhomogeneities," *Medical Physics*, vol. 40, no. 1, Article ID 011707, 2013.

[32] L. Hoffmann, M.-B. K. Jørgensen, L. P. Muren, and J. B. B. Petersen, "Clinical validation of the Acuros XB photon dose calculation algorithm, a grid-based Boltzmann equation solver," *Acta Oncologica*, vol. 51, no. 3, pp. 376–385, 2012.

[33] T. Han, F. Mourtada, K. Kisling et al., "Experimental validation of deterministic Acuros XB algorithm for IMRT and VMAT dose calculations with the Radiological Physics Center's head and neck phantom," *Medical Physics*, vol. 39, no. 4, pp. 2193–2202, 2012.

[34] W. K. Kan, L. Leung, W. K. So et al., "Experimental verification of the Acuros XB and AAA dose calculation adjacent to heterogeneous media for IMRT and RapidArc of nasopharygeal carcinoma," *Medical Physics*, vol. 40, no. 3, Article ID 031714, 2013.

[35] T. Han, D. Followill, J. Mikell et al., "Dosimetric impact of Acuros XB deterministic radiation transport algorithm for heterogeneous dose calculation in lung cancer," *Medical Physics*, vol. 40, no. 5, Article ID 051710, 2013.

[36] A. Fogliata, G. Nicolini, A. Clivio, E. Vanetti, and L. Cozzi, "Critical appraisal of Acuros XB and anisotropic analytic algorithm dose calculation in advanced non-small-cell lung cancer treatments," *International Journal of Radiation Oncology, Biology, Physics*, vol. 83, no. 5, pp. 1587–1595, 2012.

[37] A. Fogliata, G. Nicolini, A. Clivio, E. Vanetti, and L. Cozzi, "On the dosimetric impact of inhomogeneity management in the Acuros XB algorithm for breast treatment," *Radiation Oncology*, vol. 6, no. 1, article 103, 2011.

[38] M. K. L. Leung and P. Yu, "Dosimetric impact of using Acuros XB algorithm for intensity modulated radiation therapy and RapidArc planning in nasopharyngeal carcinomas," *International Journal of Radiation Oncology "Biology" Physics* , vol. 85, no. 1, pp. 73–80, 2013.

[39] I. J. Chetty, B. Curran, J. E. Cygler et al., "Report of the AAPM Task Group No. 105: issues associated with clinical implementation of Monte Carlo-based photon and electron external beam treatment planning," *Medical Physics*, vol. 34, no. 12, pp. 4818–4853, 2007.

[40] J. V. Siebers, P. J. Keall, A. E. Nahum, and R. Mohan, "Converting absorbed dose to medium to absorbed dose to water for Monte Carlo based photon beam dose calculations," *Physics in Medicine and Biology*, vol. 45, no. 4, pp. 983–995, 2000.

[41] N. Dogan, J. V. Siebers, and P. J. Keall, "Clinical comparison of head and neck and prostate IMRT plans using absorbed dose to medium and absorbed dose to water," *Physics in Medicine and Biology*, vol. 51, no. 19, pp. 4967–4980, 2006.

[42] C.-M. Ma and J. Li, "Dose specification for radiation therapy: dose to water or dose to medium?" *Physics in Medicine and Biology*, vol. 56, no. 10, pp. 3073–3089, 2011.

[43] I. Kawrakow, M. Fippel, and K. Friedrich, "3D electron dose calculation using a Voxel based Monte Carlo algorithm (VMC)," *Medical Physics*, vol. 23, no. 4, pp. 445–457, 1996.

[44] I. Kawrakow and M. Fippel, "Investigation of variance reduction techniques for Monte Carlo photon dose calculation using XVMC," *Physics in Medicine and Biology*, vol. 45, no. 8, pp. 2163–2183, 2000.

[45] H. Neuenschwander and E. J. Born, "A macro Monte Carlo method for electron beam dose calculations," *Physics in Medicine and Biology*, vol. 37, no. 1, pp. 107–125, 1992.

[46] H. Neuenschwander, T. R. Mackie, and P. J. Reckwerdt, "MMC—a high-performance Monte Carlo code for electron beam treatment planning," *Physics in Medicine and Biology*, vol. 40, no. 4, pp. 543–574, 1995.

[47] J. Sempau, S. J. Wilderman, and A. F. Bielajew, "DPM, a fast, accurate Monte Carlo code optimized for photon and electron radiotherapy treatment planning dose calculations," *Physics in Medicine and Biology*, vol. 45, no. 8, pp. 2263–2291, 2000.

[48] C. Ma, J. S. Li, T. Pawlicki et al., "MCDOSE—a Monte Carlo dose calculation tool for radiation therapy treatment planning," *Physics in Medicine and Biology*, vol. 47, no. 10, pp. 1671–1689, 2002.

[49] J. Gardner, J. Siebers, and I. Kawrakow, "Dose calculation validation of VMC++ for photon beams," *Medical Physics*, vol. 34, no. 5, pp. 1809–1818, 2007.

[50] K. Jabbari, "Review of fast Monte Carlo codes for dose calculation in radiation therapy treatment planning," *Journal of Medical Signals & Sensors*, vol. 1, no. 1, pp. 73–86, 2011.

Hindawi Publishing Corporation
BioMed Research International
Volume 2013, Article ID 513708, 6 pages
http://dx.doi.org/10.1155/2013/513708

Research Article

Low-Dose-Area-Constrained Helical TomoTherapy-Based Whole Breast Radiotherapy and Dosimetric Comparison with Tangential Field-in-Field IMRT

Jie Qiu, Zhikai Liu, Bo Yang, Xiaorong Hou, and Fuquan Zhang

Peking Union Medical College Hospital, No. 1 Shuaifuyuan, Dongcheng District, Beijing 100730, China

Correspondence should be addressed to Fuquan Zhang; zhangfuquan3@sina.com

Received 15 June 2013; Accepted 11 July 2013

Academic Editor: An Liu

Background and Purpose. To present a novel helical TomoTherapy-based method for whole breast radiotherapy that has better dosimetry and also has acceptable low-dose regions for lungs, heart, and contralateral breast compared with tangential field-in-field IMRT (FIF-IMRT). *Material and Methods.* Ten patients with left-side breast cancer were planned with low-dose-area-constrained helical TomoTherapy (LDC-HT) and FIF-IMRT. Dosimetry was compared for all techniques. *Results.* Coverage of the whole breast was adequate with both techniques. Homogeneity index (HI) and conformity index (CI) were better with LDC-HT. LDC-HT showed dosimetry advantages over FIF-IMRT for ipsilateral lung and heart in not only high-dose levels but also in low-dose levels such as $V_{10\,\mathrm{Gy}}$ and $V_{5\,\mathrm{Gy}}$. For contralateral lung, both techniques can provide good protection, although the mean dose of LDC-HT is higher than that of FIF-IMRT. *Conclusions.* With LDC-HT, we obtained adequate target coverage, better HI and CI of target volume, better sparing of organs at risk, and acceptably low-dose areas compared with FIF-IMRT. LDC-HT could be a feasible method in whole breast radiotherapy. Clinical benefits of LDC-HT need further investigation.

1. Introduction

Adjuvant whole breast radiotherapy following breast conserving surgery is the standard of treatment for early-stage breast cancer because it improves local control rates over breast-conserving surgery alone [1]. The standard technique for whole breast irradiation has been the delivery of two tangential fields, an approach which has not significantly changed for many decades.

Tangential 3D-CRT and field-in-field IMRT (FIF-IMRT) are commonly used tangential techniques. FIF-IMRT for whole breast irradiation is based on a standard tangential beam arrangement, employing two directly opposed fields. Subfields are added using forward or inverse planning to even out volumes of high and low doses throughout the whole breast volume; subfields are not usually used to spare the organs at risk, that is, the heart and lungs. Compared with 3D-CRT, FIF-IMRT improves dose homogeneity in whole breast radiotherapy, which correlates with less acute skin and soft tissue toxicities and better cosmesis of the treated breast in the long term [2]. But doses to heart and lungs are not significantly improved compared with 3D-CRT.

Multifield intensity-modulated radiotherapy (MF-IMRT) could achieve superior dose homogeneity and normal tissue sparing and has been applied to many tumors. It involves more complex beam arrangements and more beam angles than FIF-IMRT. High-dose regions of ipsilateral lung and heart for tumors of the left breast can be reduced compared with FIF-IMRT [3]. However, MF-IMRT is associated with an increased low-dose area, especially for organs not normally irradiated in conventional tangential radiotherapy, such as the contralateral lung and breast. Helical TomoTherapy (HT) delivers a kind of MF-IMRT. In HT treatment, a gantry continuously rotates around the patient while the patient is translated through the beam delivery plane. Hundreds of beamlets, created by passing a fan-beam through a high-speed binary collimator, can be delivered from any gantry angle. The use of all gantry angles might result in a large low-dose area in the body that would normally receive only scatter dose. The significance of this low-dose "bath" is unknown,

although it is the main concern regarding late oncogenesis. The purpose of this study is to provide a new method of helical TomoTherapy-based whole breast radiotherapy which minimizes the low-dose area.

2. Patients and Methods

2.1. Patients and Planning Images. In this study, the sample comprised 10 left-side breast cancer patients treated with breast conserving surgery and whole breast radiotherapy at Peking Union Medical College Hospital, China, in 2011-2012. All patients underwent 5 mm slice thickness computer tomography (CT) scanning in the supine position on an inclined breast board with both arms abducted above the head. Images were acquired from the lower part of neck to 5 cm below the lowest part of the breast, with radiopaque wires marking the clinically detectable ipsilateral breast borders.

2.2. Treatment Volumes and Organs at Risk. The clinical target volume (CTV) was the whole ipsilateral breast delimited within the radiopaque wires. The planning target volume (PTV) was generated by adding an 8 mm margin round CTV to allow for respiratory motion and setup errors but confined to the interior of the body outer contours reduced by 5 mm. Organs at risk (OARs) contoured were both lungs, heart, and contralateral breast.

2.3. Dose Goals. The prescribed dose fractionation for the whole breast was 46 Gy in 2 Gy daily fractions over 4-5 weeks. We required that 95% of PTV receive 95% to 105% of the prescribed dose. The treatment volume receiving more than 107% of the prescribed dose should be less than 1%. The volume of ipsilateral lung receiving more than 40 Gy ($V_{40\,\mathrm{Gy}}$), 30 Gy ($V_{30\,\mathrm{Gy}}$), 20 Gy ($V_{20\,\mathrm{Gy}}$), and 5 Gy ($V_{5\,\mathrm{Gy}}$) should be as low as possible. The volume of heart receiving more than 30 Gy ($V_{30\,\mathrm{Gy}}$) and that of the contralateral lung receiving more than 5 Gy ($V_{5\,\mathrm{Gy}}$) were also minimized.

2.4. FIF-IMRT Planning. FIF-IMRT plans were also created with Eclipse version 8.0 treatment planning software. FIF-IMRT plans used the same energies and beam angles as 3D-CRT plans. Inverse planning was used to minimize the volume receiving higher than 107% of the prescribed dose.

2.5. HT Planning. HT plans were created with TomoTherapy treatment planning software. HT plans were delivered with 6MV X-rays. HT plan parameters consisted of a 2.5 cm field width (FW), 0.287 pitch, and a modulation factor (MF) of 3.0.

A new support organ was defined for each patient as follows. A tangential line were drawn at the posterior border of traditional 3D-CRT beam, and the ipsilateral lung and heart below this line were defined as a new structure "block 1." The structure "block 1" was designated as "completely blocked." Contralateral lung and contralateral breast were designated as "directionally blocked."

2.6. Data and Statistical Analysis. Dosimetric data was extracted from each planning system. Student's t-tests were used to compare data between LDC-HT and FIF-IMRT. Differences were considered significant for $P < 0.05$.

3. Results

3.1. Patient Characteristics. Ten patients with left-sided breast cancer were selected for this study. PTV size varied from 424 cm^3 to 885 cm^3, with a mean of 630 cm^3 and a median of 650 cm^3. PTV and organs at risk (OARs) cumulative dose volume histograms (DVHs) and isodose distributions for a typical left-sided breast plan are illustrated in Figure 1.

3.2. Target Volume. The average dosimetric characteristics of the target for both techniques were presented in Table 1. Target coverage was adequate in all patients for both LDC-HT and FIF-IMRT. Mean volumes receiving at least 95% of prescribed dose for both techniques were similar (98.73% versus 98.53%; $P = 0.392$). Mean $V_{110\%}$ seemed better for LDC-HT than FIF-IMRT but not significantly (0.7% versus 15.68%; $P = 0.056$). Mean target doses were significantly lower for LDC-HT (48.28 Gy versus 49.18 Gy; $P = 0.002$), but maximum doses were not different (51.47 Gy versus 51.36 Gy; $P = 0.667$). Homogeneity index (1.08 versus 1.10; $P = 0.001$) and conformity index (0.83 versus 0.76; $P = 0.023$) were better for LDC-HT than FIF-IMRT.

3.3. Organs at Risk (OARs). The average dosimetric characteristics of the organs at risk for both techniques were presented in Table 2. LDC-HT provided significant decreases in $V_{5\,\mathrm{Gy}}$ (28% relative decrease), $V_{10\,\mathrm{Gy}}$ (30% decrease), $V_{20\,\mathrm{Gy}}$ (35% decrease), $V_{30\,\mathrm{Gy}}$ (46% decrease), $V_{40\,\mathrm{Gy}}$ (61% decrease), and mean dose (32% decrease) for ipsilateral lung. Similar results were obtained for both lungs combined. Both techniques provided very low doses to the heart, but LDC-HT was better for the heart $V_{5\,\mathrm{Gy}}$ (57% relative decrease), $V_{10\,\mathrm{Gy}}$ (59% decrease), $V_{20\,\mathrm{Gy}}$ (71% decrease), $V_{30\,\mathrm{Gy}}$ (82% decrease), $V_{40\,\mathrm{Gy}}$ (91% decrease), and mean dose (45% decrease). Both techniques yielded very low doses to the contralateral lung and contralateral breast with maximum doses less than 5 Gy. However, FIF-IMRT resulted in lower maximum and mean doses for both contralateral lung and contralateral breast.

3.4. Treatment Time. Average treatment time for LDC-HT was 718.5 s (range: 635.7–835.4 s). The treatment time did not account for the patient setup and MVCT scan time. We estimated the total treatment time per patient to be approximately 20–25 min for LDC-HT. The average beam on time for FIF-IMRT was 357.6 s (range: 309.0–391.0 s). We thus estimated the total treatment time per patient to be 12–15 min for FIF-IMRT.

4. Discussion

Whole breast radiotherapy with boost following breast-conserving surgery is the standard of care for early-stage breast cancer patients. The 2-year local control rate could

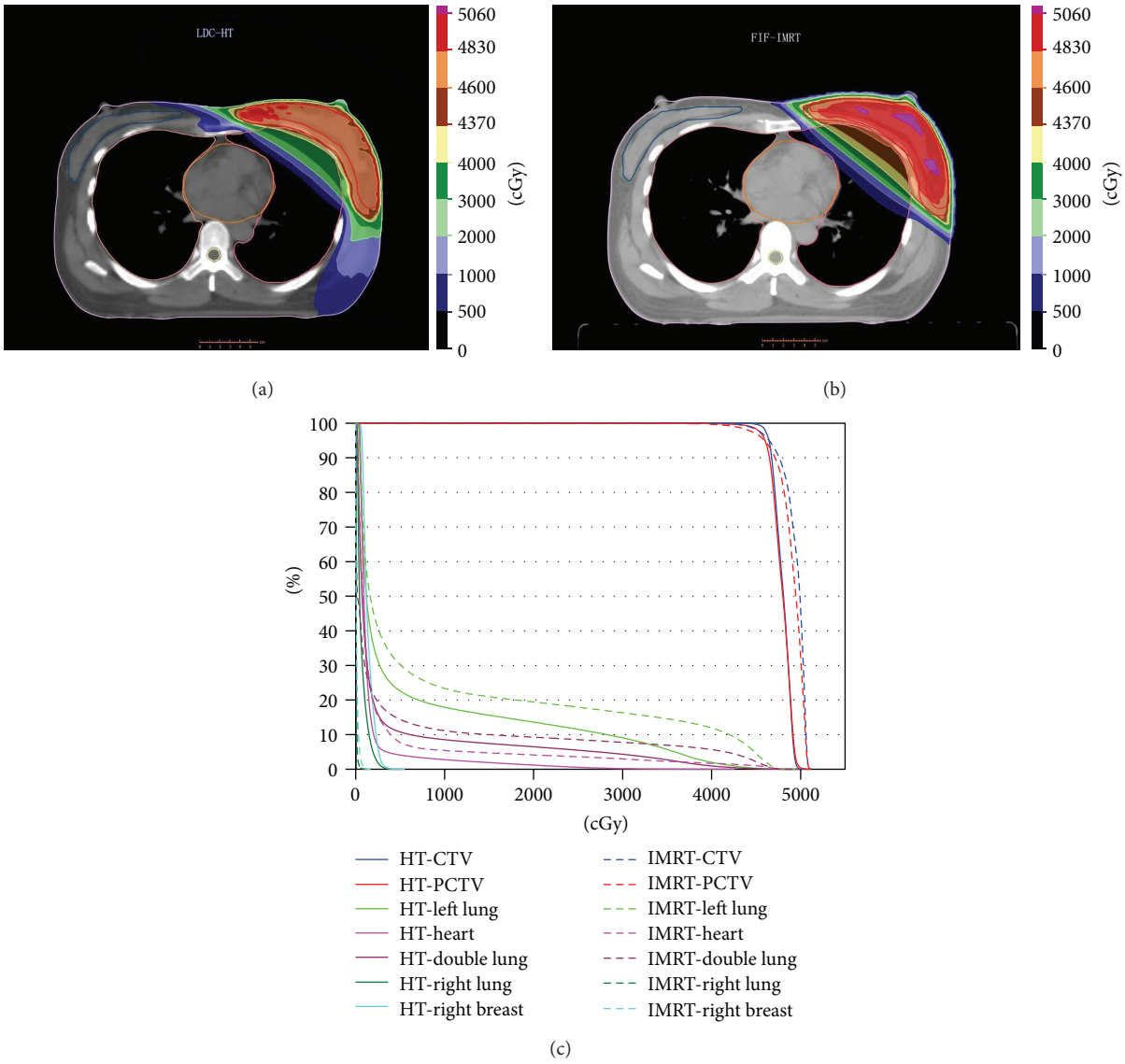

Figure 1: Isodose and cumulative DVHs for each technique.

Table 1: Average dosimetric characteristics of the target.

	LDC-HT	FIF-IMRT	*P* value
PTV (prescribed dose: 46 Gy)			
$V_{50.6\,Gy}$ or $V_{110\%}$	0.7%	15.68%	0.056
$V_{43.7\,Gy}$ or $V_{95\%}$	98.73%	98.53%	0.392
Mean dose (Gy)	48.28	49.18	0.002
Maximum dose (Gy)	51.47	51.36	0.667
Homogeneity index	1.08	1.10	0.001
Conformity index	0.83	0.76	0.023

be higher than 90% [4]. And radiotherapy reduced the 10-year risk of any (i.e., locoregional or distant) first recurrence from 35.0% to 19.3% [5]. The main concern of whole breast radiotherapy now is the reduction of patient toxicity. The tangential technique for whole breast radiotherapy has not significantly changed over many decades. FIF-IMRT in this study is a type of tangential technique. FIF-IMRT could reduce maximum target doses relative to 3D-CRT.

Multifield IMRT (MF-IMRT) has been widely used for the treatment of head-and-neck and pelvic tumors. For whole breast radiotherapy, MF-IMRT could improve dose homogeneity and reduce high-dose areas of ipsilateral lung and heart (for left-side tumors) [6–9]. However, it may result in large low-dose regions in lungs, contralateral breast, and heart that might cause late oncogenesis [10]. Helical TomoTherapy is a new radiation technology that can provide even better dosimetry than MF-IMRT by allowing radiation to be delivered from all gantry angles. But the low-dose region may spread even wider with HT.

Table 2: Average dosimetric characteristics of the organs at risk.

	LDC-HT	FIF-IMRT	P value
Ipsilateral lung			
$V_{5\,Gy}$	21.04	29.16	0.000
$V_{10\,Gy}$	15.31	21.98	0.000
$V_{20\,Gy}$	11.58	17.68	0.000
$V_{30\,Gy}$	7.95	14.65	0.000
$V_{40\,Gy}$	3.84	9.97	0.000
Mean dose (Gy)	6.12	9.02	0.000
Maximum dose (Gy)	49.98	49.12	0.069
Heart			
$V_{5\,Gy}$	4.19	9.73	0.000
$V_{10\,Gy}$	2.75	6.67	0.000
$V_{20\,Gy}$	1.45	4.96	0.000
$V_{30\,Gy}$	0.67	3.73	0.000
$V_{40\,Gy}$	0.20	2.38	0.001
Mean dose (Gy)	1.87	3.37	0.000
Maximum dose (Gy)	42.71	48.33	0.020
Contralateral lung			
Mean dose (Gy)	0.51	0.09	0.000
Maximum dose (Gy)	4.33	1.63	0.000
Both lungs			
$V_{5\,Gy}$	9.79	13.59	0.000
$V_{10\,Gy}$	7.44	10.26	0.000
$V_{20\,Gy}$	5.41	8.24	0.000
$V_{30\,Gy}$	3.66	6.83	0.000
$V_{40\,Gy}$	1.79	4.65	0.000
Mean dose (Gy)	3.15	4.25	0.000
Maximum dose (Gy)	49.98	49.12	0.069
Contralateral breast			
Mean dose (Gy)	1.02	0.12	0.000
Maximum dose (Gy)	4.89	1.89	0.000

4.1. Technical Issues. In this study, we present a novel HT-based method with similar or even better low-dose area for risk organs. Before the planning process, we divided beamlets delivered from all angles around the patient into six categories (see Figure 2).

(i) Category 1: beamlets that only pass through PTV. Obviously, these beamlets were most efficient and would cause minimum radiation to the organs at risk, and thus these beamlets were preferred in the planning process.

(ii) Category 2: beamlets that pass through PTV and then through the non-OARs body. These beamlets were less efficient than category 1 but would also cause minimum radiation to the organs at risk.

(iii) Category 3: the opposite of category 2. Beamlets pass through the non-OARs body and then PTV. These beamlets were less efficient than category 2 but were similar to category 2 in that they would not deliver dose to the organs at risk.

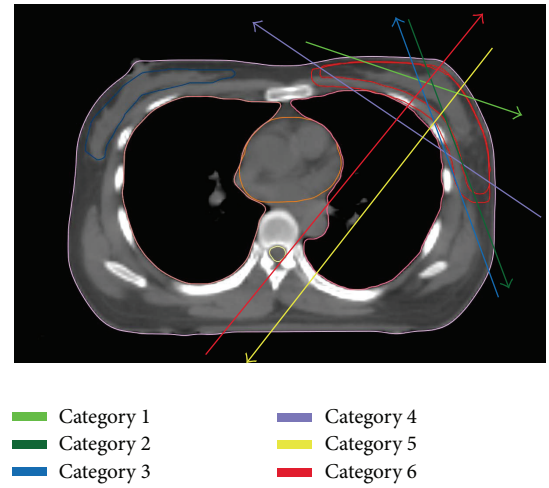

Figure 2: Schematic figure of each category.

(iv) Category 4: beamlets that pass through PTV and organs at risk and then PTV again. This category was common in tangential FIF-IMRT plans and may cause high-dose areas within OARs.

(v) Category 5: beamlets that pass through PTV and then OARs. These beamlets may be the main cause of "low-dose bath."

(vi) Category 6: beamlets that pass through OARs and then the PTV. This category is inefficient and should be avoided.

Figure 3 shows the path of X-rays for every categories described above. In the planning process, we tried to design strategies which could raise the proportion of categories 1 and 2 beamlets, reduce the proportion of categories 3 and 4 beamlets, and minimize or even eliminate the category 5 and 6 beamlets.

Given that the breast is situated over the outer border of the chest, if we place beam angles around the chest wall like the peels of an apple, the lungs, contralateral breast, and heart could be spared. The question was how to restrict beams around the chest wall. To prevent dose delivery to a structure, the structure can be designated as "completely blocked" during the planning process. We tried different types of blocks and found this method to be suitable: we draw a tangential line at the posterior border of traditional 3D-CRT beam and define the ipsilateral lung and heart below this line as a new structure "block 1." If we designate "block 1" as "completely blocked," and designate contralateral lung and contralateral breast as "directionally blocked," radiation would be delivered around chest wall as we intend, and these organs or regions would receive less radiation. Obviously, this technique could also be applied for tumors of the right breast.

4.2. PTV. Both techniques show adequate PTV coverage. LDC-HT resulted in a lower mean PTV dose than FIF-IMRT. LDC-HT is also associated with a significantly better homogeneity index and conformity index. This supports

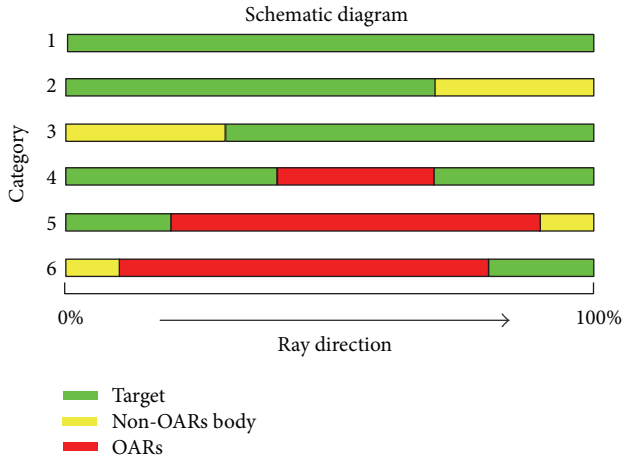

Figure 3: Path of X-ray for every category.

previous studies that have shown increased homogeneity with HT [11]. However, it is difficult to estimate if these differences would result in clinically detectable benefits such as better cosmesis or a higher local control rate.

4.3. Lungs. Radiation-induced lung injury (RILI) variously occurs after whole breast radiotherapy [12]. Most of those cases are subclinical, but about 1–5% are clinically significant radiation pneumonitis [13]. RILI is not only correlated with mean lung dose and V_{20}; the volume of the lung spared from doses of >5 Gy is an independent dosimetric factor of RILI [14]. Previous studies demonstrated that HT may reduce high-dose regions of ipsilateral lung, but increase the low-dose area [15, 16]. The low-dose "bath" of lung is the main concern of radiation oncologists considering the use of TomoTherapy for whole breast radiation.

In this study, low-dose area constrained helical TomoTherapy-based radiotherapy (LDC-HT) showed dosimetry advantages over FIF-IMRT for ipsilateral lung and heart in not only high-dose levels but also low-dose levels such as V_{10} and V_5. For contralateral lung, both techniques can provide good protection, although the mean dose of LDC-HT is higher than FIF-IMRT (0.51 Gy versus 0.09 Gy; $P = 0.000$). So, we expect even lower RILI rates for LDC-HT.

4.4. Heart. A recent case-controll study conducted by Darby et al. [17] has highlighted the importance of minimizing incidental cardiac irradiation in patients with breast cancer, as it is a known risk factor for the development of ischaemic heart disease. Importantly, no dose threshold was observed: the increased risk (relative to baseline risk) per Gy of exposure was approximately constant throughout the range of mean radiation doses to the heart studied (from as low as approximately 2 Gy to the maximum >27 Gy).

In our study, almost all dose levels of heart (V_5 56.97%, V_{10} 58.78%, V_{20} 70.70%, V_{30} 81.94%, V_{40} 91.46%, and D_{mean} 44.63%) were significantly decreased with LDC-HT compared with FIF-IMRT. So, we expect lower risk of ischaemic heart disease after LDC-HT whole breast radiotherapy.

4.5. Contralateral Breast. LDC-HT increases both D_{mean} and D_{max} of contralateral breast relative to tangential FIF-IMRT. Although the doses to the contralateral breast are very low with both techniques, the increase in maximal dose and mean dose with LDC-HT might confer an increased risk of secondary breast malignancy, especially in young women [18–21].

Although previous studies demonstrated that improved dosimetry may lead to less toxicity [22, 23], clinical benefits of LDC-HT need further investigation. A randomized phase I/II clinical trial is going on in our centre to evaluate the effect and acute toxicity of LDC-HT over FIF-IMRT.

Finally, LDC-HT had longer treatment time than FIF-IMRT. The use of a 5 cm field width instead of a 2.5 cm field width for TomoTherapy would reduce treatment time with 30–50%, but that might cause worse dosimetry and wider dose spread in the patient superior and inferior to the target. The newly available dynamic jaws capability (TomoEDGE) would eliminate the low superior and inferior doses and should give comparable plans to the 2.5 cm plans [24].

5. Conclusions

LDC-HT could have better coverage and dose homogeneity of target volume, better OAR sparing, and even better low-dose areas than 3D-CRT and FIF-IMRT. It could be a feasible method in whole breast radiotherapy. Clinical benefits of LDC-HT need further investigation.

Conflict of Interests

The authors have not had any actual or potential conflict of interests.

References

[1] P. Eifel, J. A. Axelson, J. Costa et al., "National institutes of health consensus development conference statement: adjuvant therapy for breast cancer," *Journal of the National Cancer Institute*, vol. 93, no. 13, pp. 979–989, 2001.

[2] M. E. Taylor, C. A. Perez, K. J. Halverson et al., "Factors influencing cosmetic results after conservation therapy for breast cancer," *International Journal of Radiation Oncology, Biology, Physics*, vol. 31, pp. 753–764, 1995.

[3] H. B. Ayata, M. Güden, C. Ceylan, N. Kücük, and K. Engin, "Comparison of dose distributions and organs at risk (OAR) doses in conventional tangential technique (CTT) and IMRT plans with different numbers of beam in left-sided breast cancer," *Reports of Practical Oncology and Radiotherapy*, vol. 16, no. 3, pp. 95–102, 2011.

[4] A. P. Forrest, H. J. Stewart, D. Everington et al., "Randomized controlled trial of conservation therapy for breast cancer: 6-year analysis of the Scottish trial," *The Lancet*, vol. 348, no. 9029, pp. 708–713, 1996.

[5] S. Darby, P. McGale, C. Correa et al., "Effect of radiotherapy after breast-conserving surgery on 10-year recurrence and 15-year breast cancer death: meta-analysis of individual patient data for 10 801 women in 17 randomised trials," *The Lancet*, vol. 378, no. 9804, pp. 1707–1716, 2011.

[6] D. Landau, E. J. Adams, S. Webb, and G. Ross, "Cardiac avoidance in breast radiotherapy: a comparison of simple shielding techniques with intensity-modulated radiotherapy," *Radiotherapy and Oncology*, vol. 60, no. 3, pp. 247–255, 2001.

[7] L. Hong, M. Hunt, C. Chui et al., "Intensity-modulated tangential beam irradiation of the intact breast," *International Journal of Radiation Oncology Biology Physics*, vol. 44, no. 5, pp. 1155–1164, 1999.

[8] F. A. Vicini, M. Sharpe, L. Kestin et al., "Optimizing breast cancer treatment efficacy with intensity-modulated radiotherapy," *International Journal of Radiation Oncology, Biology, Physics*, vol. 54, pp. 1336–1344, 2002.

[9] B. C. Cho, M. Schwarz, B. J. Mijnheer, and H. Bartelink, "Simplified intensity-modulated radiotherapy using pre-defined segments to reduce cardiac complications in left-sided breast cancer," *Radiotherapy and Oncology*, vol. 70, no. 3, pp. 231–241, 2004.

[10] A. Berrington de Gonzalez, E. Gilbert, R. Curtis et al., "Second solid cancers after radiation therapy: a systematic review of the epidemiologic studies of the radiation dose-response relationship," *International Journal of Radiation Oncology, Biology, Physics*, vol. 86, no. 2, pp. 224–233, 2013.

[11] H. O'Donnell, K. Cooke, N. Walsh, and P. N. Plowman, "Early experience of tomotherapy-based intensity-modulated radiotherapy for breast cancer treatment," *Clinical Oncology*, vol. 21, no. 4, pp. 294–301, 2009.

[12] L. B. Marks, S. M. Bentzen, J. O. Deasy et al., "Radiation dose-volume effects in the lung," *International Journal of Radiation Oncology Biology Physics*, vol. 76, no. 3, pp. S70–S76, 2010.

[13] Y. Seppenwolde, J. V. Lebesque, K. de Jaeger et al., "Comparing different NTCP models that predict the incidence of radiation pneomonitis," *International Journal of Radiation Oncology, Biology, Physics*, vol. 55, pp. 724–735, 2003.

[14] S.-L. Wang, Z. Liao, A. A. Vaporciyan et al., "Investigation of clinical and dosimetric factors associated with postoperative pulmonary complications in esophageal cancer patients treated with concurrent chemoradiotherapy followed by surgery," *International Journal of Radiation Oncology Biology Physics*, vol. 64, no. 3, pp. 692–699, 2006.

[15] L. K. Schubert, V. Gondi, E. Sengbusch et al., "Dosimetric comparison of left-sided whole breast irradiation with 3DCRT, forward-planned IMRT, inverse-planned IMRT, helical tomotherapy, and topotherapy," *Radiotherapy and Oncology*, vol. 100, no. 2, pp. 241–246, 2011.

[16] T. Reynders, K. Tournel, P. De Coninck et al., "Dosimetric assessment of static and helical TomoTherapy in the clinical implementation of breast cancer treatments," *Radiotherapy and Oncology*, vol. 93, no. 1, pp. 71–79, 2009.

[17] S. C. Darby, M. Ewertz, P. McGale et al., "Risk of ischemic heart disease in women after radiotherapy for breast cancer," *The New England Journal of Medicine*, vol. 368, no. 11, pp. 987–998, 2013.

[18] Y. M. Kirova, Y. De Rycke, L. Gambotti, J. Y. Pierga, B. Asselain, and A. Fourquet, "Second malignancies after breast cancer: the impact of different treatment modalities," *British Journal of Cancer*, vol. 98, no. 5, pp. 870–874, 2008.

[19] Y. M. Kirova, J. R. Vilcoq, B. Asselain, X. Sastre-Garau, and A. Fourquet, "Radiation-induced sarcomas after radiotherapy for breast carcinoma: a large-scale single-institution review," *Cancer*, vol. 104, no. 4, pp. 856–863, 2005.

[20] Y. M. Kirova, L. Gambotti, Y. De Rycke, J. R. Vilcoq, B. Asselain, and A. Fourquet, "Risk of second malignancies after adjuvant radiotherapy for breast cancer: a large-scale, single-institution review," *International Journal of Radiation Oncology Biology Physics*, vol. 68, no. 2, pp. 359–363, 2007.

[21] M. Stovall, S. A. Smith, B. M. Langholz et al., "Dose to the contralateral breast from radiotherapy and risk of second primary breast cancer in the WECARE Study," *International Journal of Radiation Oncology Biology Physics*, vol. 72, no. 4, pp. 1021–1030, 2008.

[22] A. Harsolia, L. Kestin, I. Grills et al., "Intensity—modulated radiotherapy results in significant decrease in clinical toxicities compared with conventional wedge-based breast radiotherapy ," *International Journal of Radiation Oncology Biology Physics*, vol. 68, no. 5, pp. 1375–1380, 2007.

[23] J. P. Pignol, I. Olivotto, E. Rakovitch et al., "A multicenter randomized trial of breast intensity-modulated radiation therapy to reduce acute radiation dermatitis," *Journal of Clinical Oncology*, vol. 26, no. 13, pp. 2085–2092, 2008.

[24] S. Krause, S. Beck, K. Schubert et al., "Accelerated large volume irradiation with dynamic Jaw/Dynamic Couch Helical Tomotherapy," *Radiation Oncology*, vol. 7, article 191, 2012.

Hindawi Publishing Corporation
BioMed Research International
Volume 2013, Article ID 898953, 6 pages
http://dx.doi.org/10.1155/2013/898953

Clinical Study

Stereotactic Body Radiotherapy as an Alternative to Brachytherapy in Gynecologic Cancer

Gregory J. Kubicek,[1] Jinyu Xue,[1] Qianyi Xu,[1] Sucha O. Asbell,[1] Leslie Hughes,[1] Noel Kramer,[1] Ashraf Youssef,[1] Yan Chen,[1] James Aikens,[2] Howard Saul,[3] Niraj Pahlajani,[1] and Tamara LaCouture[1]

[1] *Department of Radiation Oncology, Cooper University Hospital, One Cooper Plaza, Camden, NJ 08103, USA*
[2] *Department of Gynecology, Cooper University Hospital, One Cooper Plaza, Camden, NJ 08103, USA*
[3] *Department of Gynecology, Center for Cancer and Hematologic Disease, Marlton, NJ 08003, USA*

Correspondence should be addressed to Gregory J. Kubicek; greg.kubicek@gmail.com

Received 18 April 2013; Accepted 12 July 2013

Academic Editor: Eng-Yen Huang

Introduction. Brachytherapy plays a key role in the treatment of many gynecologic cancers. However, some patients are unable to tolerate brachytherapy for medical or other reasons. For these patients, stereotactic body radiotherapy (SBRT) offers an alternative form of treatment. *Methods*. Retrospective review of patients prospectively collected on SBRT database is conducted. A total of 11 gynecologic patients who could not have brachytherapy received SBRT for treatment of their malignancies. Five patients have been candidates for interstitial brachytherapy, and six have required tandem and ovoid brachytherapy. Median SBRT dose was 25 Gy in five fractions. *Results*. At last followup, eight patients were alive, and three patients had died of progressive disease. One patient had a local recurrence. Median followup for surviving patients was 420 days (median followup for all patients was 120 days). Two patients had acute toxicity (G2 dysuria and G2 GI), and one patient had late toxicity (G3 GI, rectal bleeding requiring cauterization). *Conclusions*. Our data show acceptable toxicity and outcome for gynecologic patients treated with SBRT who were unable to receive a brachytherapy boost. This treatment modality should be further evaluated in a phase II study.

1. Introduction

Gynecologic malignancies, mostly consisting of endometrial and cervical cancers, remain common cancers in the United States. For locally advanced cervical cancer, the standard treatment combines chemotherapy (CTX) along with conventional external-beam radiation therapy (EBRT) and a brachytherapy boost (BB) [1–5]. BB is also used in endometrial cancer, in early-stage disease as the sole treatment, and in unresectable and recurrent disease in combination with EBRT [6]. BB is a valuable treatment option because it allows for a high dose to the tumor while sparing the nearby normal structures. To treat to a tumoricidal dose using EBRT alone would lead to significant dose to nearby normal structures (mainly rectum, small bowel, and bladder), which would entail a high likelihood of acute and late toxicity. BB is ideal for treatment of gynecologic cancers because it allows the radioactive source to be placed very close to the target which receives full dose, but because of the inverse-square law (the radiation dose decreases exponentially with distance; so as distance goes from x to $2x$, the radiation dose decreases from y to $0.25y$), the nearby normal tissues receive a much lower dose; thus, BB allows for maximal tumor dose and maximal normal tissue sparing [5, 6].

While BB remains the standard treatment option for many gynecologic cancers, there are some patients who are not candidates for this treatment. Patients with comorbid conditions may not be able to tolerate BB, especially an interstitial implant. Also, for patients with unfavorable anatomy, it may not be possible to place BB even with assistance from gynecology oncologists. One possible alternative to BB is stereotactic body radiotherapy (SBRT), which entails high doses of external radiation delivered in a very conformal

fashion. While SBRT is commonly used in medically unresectable early-stage lung cancer and has a growing use in other pathologies, there are very little data regarding the role of SBRT used in place of BB.

Several retrospective clinical reports [7–12] and retrospective dosimetric reports [13] have shown that SBRT appears to be a reasonable treatment option for patients unable to receive a BB. Haas et al. [7] reported on six cervical cancer patients who had anatomic or medical conditions that precluded BB using tandems and ovoids. The patients received an SBRT boost to the cervix instead, using the doses of 20 Gy in five fractions (five patients) and 19.5 Gy in three fractions (one patient). With a median followup of 14 months, there were no reported local failures and no toxicities from the SBRT boost. Molla et al. [8] reported on 16 patients (nine endometrial and seven cervical) who had an SBRT boost to high-risk areas (14 Gy in two fractions for operated patients and 20 Gy in five fractions for nonoperated ones). With a median followup of 12.6 months, there was one patient with a central pelvic recurrence and one patient with late grade-3 rectal toxicity. A retrospective comparative analysis [12] of BB and SBRT plans found that SBRT plans had better target coverage and better dose distributions to normal structures except for bone marrow.

In order to increase the knowledge pool regarding SBRT as an alternate to BB in certain patients, we are reporting our institution's experience of this treatment modality.

2. Methods

Patients in this study were collected using an IRB-approved prospective radiosurgery database. Clinical information not contained in the database was retrospectively acquired. Eligibility criteria for the review included gynecologic patients who received SBRT but had been referred and had clinical indications for BB. All patients were initially evaluated and had been recommended to undergo a BB, and for medical or other reasons, they were unable to complete the BB and were thus treated with SBRT (Table 1). All patients were evaluated by both gynecology-oncology and radiation oncology; for patients that needed Smit's Sleeve placement, this was performed by the gynecology-oncologist. A total of 11 patients met the eligibility criteria for this review. Median age was 62 years (range: 47–81 years). Seven patients had cervical cancer, two patients had endometrial cancer, and two patients had vaginal cancer. Histology was squamous-cell carcinoma in eight patients, adenocarcinoma in two patients, and carcinosarcoma in one patient. Patients had locally advanced (seven) or recurrent cancers (four patients) but were not metastatic. All patients had conventional external-beam radiation to the pelvis prior to SBRT, three in the form of IMRT and eight in the form of 3D-CRT; dose range for previous EBRT was 45 to 50.4 Gy. Three patients had both EBRT and BB prior to SBRT, two patients had completed EBRT and BB and had local recurrence 1.4 and 1.1 years later, and the other patient had two HDR treatments, but the patient's Smit's Sleeve became misplaced after the second treatment, and when it was not able to be replaced, the patient went on to have SBRT for the remaining treatments. Three patients had surgery (hysterectomy) in addition to previous EBRT; indication for surgery in these patients was for recurrent disease.

The initial consult note and progress notes were reviewed for the treatment recommendations; in all patients, a BB was recommended. The types of BB that were indicated included tandem and ovoid BB in six patients and interstitial BB in five patients. Reasons for not being able to treat with BB are listed in Table 1.

Prior to SBRT, all patients had gold fiducial markers implanted for SBRT tracking. It was recommended that four gold-seed fiducial markers be placed, either into the cervix or into the gross tumor if visualized. CT scan for treatment planning was performed without contrast using 1.25 mm slices. Patients were instructed to have a low-residue meal prior to simulation and were coached to have a consistent fluid intake on the day of simulation and the daily treatments to maintain a regular bladder filling rate throughout the treatment. An MRI of the pelvis with contrast was obtained and fused to the planning CT scan for better visualization of the cervix and gross disease; MRI series included T2 weighting with contrast, with and without fat saturation. Prior to SBRT, 7 patients had gross disease present visible on MRI or physical exam.

SBRT target consisted of the gross tumor volume (GTV) in patients with gross disease present prior to SBRT and also a clinical target volume (CTV) for areas thought to be at high risk for residual disease. GTV consisted of gross disease noted on the MRI and physical exam. The CTV would include any extracervical disease at the time of the MRI and physical exam. CTV would also include the entire cervix for patients with cervical cancer with an intact uterus. The CTV was uniformly expanded by 5 mm to create a planning target volume (PTV) to account for a set-up error including rotation. In patients with small intestine or other critical structures adjacent to targets, the PTV was subtracted from the organs at risk to decrease dose to the organs at risk. See Table 2.

SBRT was delivered in five fractions using CyberKnife (Accuray Incorporated, Sunnyvale, CA, USA) with multiplan planning system version 3.5.4. Numerous noncoplanar beams using 6 MV photons were used for each treatment. Target tracking was performed via the CyberKnife's real-time tracking algorithm; synchrony (respiratory motion software) was not used. CyberKnife tracking, has the ability to track movements (with aid of gold fiducials), and this ability is critical since the cervix is prone to movement [14]. Treatments were delivered every other day, and we feel that normal tissues such as small bowel would tolerate every-other-day better than every-day treatments; every-other-day treatments are also similar to what is used in BB using HDR. Patients were instructed to use Simethicone (Himalaya Drug Company, Bangalore, India) during every day of treatment to reduce bowel distension. None of the patients received chemotherapy concurrent with SBRT, although chemotherapy was typically delivered with EBRT. Treatments were delivered to an isodose line that was aimed for a compromise of target coverage and sparing of the organs at risk.

Table 1: Patient characteristics.

Patient #	Diagnosis	Stage	Histology	Recommended implant	Reason that implant could not be performed
1	Cervical	Recurrent	Scc	Interstitial	Size and location
2	Cervical	Recurrent	Carcinosarcoma	Interstitial	Bleeding
3	Endometrial	Recurrent	Adenocarcinoma	Interstitial	Difficulty with interstitial, short endocervix makes tandem difficult
4	Vaginal	T2	Scc	Interstitial	Proximity to bladder and bowel
5	Vaginal	T2	Scc	Interstitial	Difficulty w visualization of tumor
6	Cervical	IIIb	Scc	Tandem and ovoid	Comorbid conditions
7	Cervical	IIIb	Scc	Tandem and ovoid	Unable to place Smits Sleeve
8	Cervical	IIIb	Scc	Tandem and ovoid	Unable to place sleeve
9	Cervical	IIIb	Scc	Tandem and ovoid	Smits Sleeve became misplaced
10	Cervical	Recurrent	Scc	Tandem and ovoid	Unable to place sleeve
11	Endometrial	T2N1	Adenocarcinoma	Tandem and ovoid	Smits Sleeve perforation through uterus

Scc: squamous cell carcinoma.

Table 2: Target and OAR definitions.

Structure	Definition
GTV	Gross tumor as visualized on MRI (T2) and physical exam
CTV	Entire cervix for most patients, including extracervical disease if present on pre-SBRT MRI
PTV	CTV plus expansion of 5 mm (using less of an expansion if adjacent to organs at risk)
Rectum	Entire rectum, superior limit will be rectosigmoid junction
Bladder	Entire bladder and contents
Small bowel	Bowel loops up to 2 cm above target

Normal tissues were contoured including large bowel, small bowel, femoral heads, sigmoid colon, rectum, bladder, and skin. See Table 2 for more information regarding contouring specifics. Note that the entire organ was contoured as opposed to just the organ wall. For patients that have had previous pelvic radiation to 45 to 50.4 Gy, the point dose limit to the sigmoid colon, rectum, and small bowel was 21 Gy; and the bladder dose limit was 24 Gy. A small volume was allowed to exceed this dose if the normal structures abutted the tumor, in which case 1-2 cc were allowed higher doses up to the target dose.

After completion of treatment, patients were followed by gynecology oncology as well as radiation oncology, and patients were typically seen 4 weeks after completion of treatment and then every 2 months for the first year; followup visit would include pelvic exam. Imaging (typically MRI) was done at 3 months posttreatment. Toxicity was physician-scored based on CTCAE 4.0. Oncologic outcomes at followup were based on combination of both the physical exam and the followup imaging.

3. Results

3.1. Radiotherapy Treatment. Ten patients had five prescribed fractions. One patient who had completed two fractions of HDR BB and then had Smit's Sleeve malposition received three fractions of SBRT. SBRT boost was completed in 10 patients. One patient suffered a stroke after the first fraction and had a subsequent decline in performance status, necessitating the treatment to be discontinued. The stroke was not felt to be related to SBRT. This patient's dosimetric information was not included in the analysis.

Median SBRT dose for patients completing the treatment was 25 Gy (range: 15–27.5 Gy); the median dose per fraction was 5.0 Gy (range: 4.8–5.5 Gy). Treatments were prescribed to the median 61% isodose line (range: 51%–81%). Median treatment volume was 9,163 cc (range: 1,665–35,740 cc). Median PTV coverage was 88% (range: 71%–94%), and median GTV coverage was 96.5% (range: 90%–97.6%). Median PTV conformality index was 1.5 (range: 1.1–2.9), where conformality index is defined as treated volume divided by PTV. Maximum rectal point dose ranged from 20.8 to 32.6 Gy (median: 23.8 Gy), median rectal dose to 1 cc was 19.6 Gy (range: 18.2 to 27.5 Gy), and median rectal dose to 2 cc was 19.3 Gy (range: 17.6–25.4 Gy). Maximum bladder point dose ranged from 16.5–36 Gy (median: 25.7 Gy), median bladder dose to 1 cc was 20.7 Gy (range: 11.1–22.9 Gy), and median bladder dose to 2 cc was 19 Gy (range: 5.6–16.9 Gy); see Table 3.

A typical SBRT plan is seen in Figure 1. One patient had SBRT after two HDR BB (Smit's Sleeve shifted out of position after the second BB). On comparing her BB and

Table 3: Treatment characteristics.

Patient	Previous RT (EBRT and HDR)	CTV volume (mm^3)	SBRT dose/Fx	SBRT dose equivalent (2 Gy/fx) alpha/beta 10	SBRT dose equivalent (2 Gy/fx) alpha beta 3
1	45 + 30 Gy HDR	254485.7	27.5/5	35.52083	46.75
2	45	9893.03	25/5	31.25	40
3	50.4	34818.04	25/5	31.25	40
4	45	19947.13	25/5	31.25	40
5	45	40721.84	22.5/5	27.1875	33.75
6	45	129132.1	5/1	6.25	8
7	45	174427.2	25/5	31.25	40
8	45	11549.91	24/5	29.6	37.44
9	45 + 12 HDR	16655.7	15/3	18.75	24
10	45+ 30 HDR	143710.1	25/5	31.25	40
11	45	45809.38	25/5	31.25	40

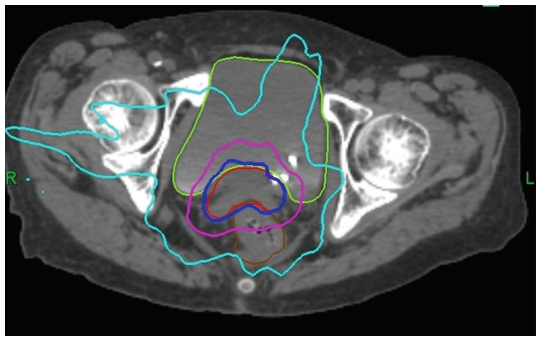

Figure 1: Sample SBRT plan. Typical SBRT plan, patient treated to 25 Gy in five fractions. Bladder, CTV, and rectal contours are shown. Isodose lines include prescription isodose line (75%), pink (50%), and light blue (20%).

SBRT treatments, maximum normal-tissue point doses were lower for the BB. For this patient, maximum dose per fraction to bladder was 5.8 Gy with SBRT versus 4.45 Gy with BB; for rectum, 5.6 Gy with SBRT versus 5.0 with BB; and for small bowel, 5.3 Gy with SBRT versus 2.8 Gy with BB. Doses to 1 and 2 cc of bladder were 5.2 and 4.9 Gy with SBRT and 5.3 and 4.7 with BB, respectively. Doses to 1 and 2 cc of rectum were 4.9 and 4.5 Gy with SBRT and 4.7 and 4.2 Gy with BB, respectively. Comparison between SBRT and HDR plans is shown in Figure 2.

The biologically equivalent dose (BED) in terms of equivalent doses given at 2 Gy per day (EQ2) was calculated using the linear quadratic (LQ) equation [15]. The α/β ratio was taken to be 10 Gy for tumor effects and 3 Gy for late effects. Median EQ2 for the tumor was 31.3 Gy (range: 18.75–35.5 Gy) for the entire group, and median EQ2 for late effects on normal tissues was 40 Gy (range: 24–46.75 Gy), Table 3.

3.2. Oncologic Outcome. At last followup, eight patients were alive. Median followup for all patients was 120 days, and median followup for surviving patients was 14 months. Of the three patients who died, two had recurrent cervical cancer and died of progressive disease; the other had locally advanced cervical cancer and had a stroke during therapy and subsequently went on to hospice care without completing the entire course of treatment. Of the eight surviving patients, one (patient no. 2) had a local recurrence 3.5 years after completion of SBRT (recurrence took place in cervical stump in the region of the previous SBRT). This patient was treated with surgical exoneration and was disease-free after salvage surgery. All of the other patients were disease-free (both local and distant) at last followup.

3.3. Toxicity. During the SBRT boost, two patients were noted to have acute toxicity (grade-2 GU and grade-2 GI, resp.). There was no grade-3 or greater toxicities during the SBRT or within 90 days after SBRT. One patient (patient no. 8) was noted to have late toxicity one year from the completion of SBRT, in the form of mild GI bleeding, and underwent cauterization of the rectal vessels, which resolved the bleeding (GI grade-3 toxicity). The patient who had GI Grade 3 toxicity had a maximum point dose to rectum of 24 Gy, 1 cc dose of 19.4, 2 cc dose of 18.6, and a mean rectal dose of 6.7 Gy, all of which were around the median for all patients treated. There were no other reported late toxicities.

4. Discussion

In the treatment of locally advanced and recurrent gynecologic cancers, chemoradiotherapy and brachytherapy boost (either ring and tandem or interstitial) remain the standard of care. This results in good disease control and acceptable toxicity. Gynecologic Oncology Group (GOG) Trial 120 [1] reported 60% overall survival at 5 years, 22% local progression, and a late toxicity rate (grade 3 or 4) of 1.7% for patients treated with chemoradiotherapy (including intracavity BB) with a median followup of 35 months. With regard to patients treated with interstitial BB, Pinn-Bingham et al. [16] have reported on 116 patients with locally advanced cervical cancer who were not candidates for intracavity BB. Following treatment with external-beam radiation and interstitial BB,

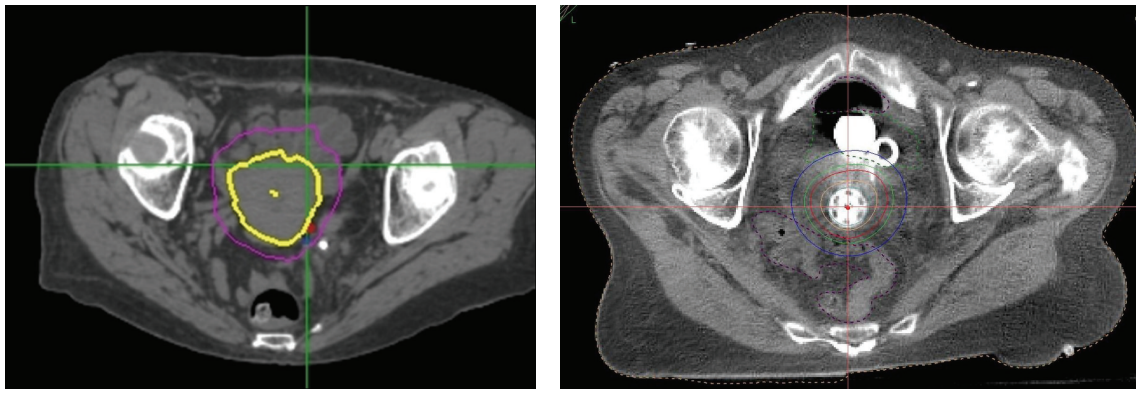

(a) (b)

Figure 2: Comparison of SBRT (a) and BB (b). Comparison of target dose using BB and SBRT for the same patient.

they found 85.3% locoregional control and 13% late toxicity rates.

For gynecologic patientss both intracavity and interstitial BB have good outcomes and are important components of the standard treatment for these patients [1–6, 16, 17]. However, some patients are unable to receive BB, because of either unfavorable anatomy or comorbid conditions. For these patients, treatment options become more limited. Conventional EBRT has been tried in place of BB with overall poor results. Barraclough et al. [18] have reported on 44 patients treated with external-beam boost instead of BB ("technical limitations" was listed as the reason for not providing BB in 73% of patients) and found a 48% recurrence rate with a median followup of 2.3 years. While this treatment is likely better than no boost at all, the importance of a high recurrence rate of the disease is secondary to dose limitations of normal pelvic tissue with conventional EBRT.

Another possible option for patients who are not BB candidates is SBRT. SBRT has advantages over conventional radiotherapy in being able to deliver higher doses while minimizing normal tissue radiation exposure. This allows the tumor to receive a higher biologically equivalent dose than with conventional radiation. Our results for SBRT showed good local control and a medically acceptable toxicity. Among the surviving patients (nine patients), only one had a local recurrence. Two patients with recurrent disease had persistent disease after SBRT, and they continued to have disease progression despite SBRT, and they subsequently died from the disease. Our toxicity results were also determined as tolerable with only one grade-3 toxicity (grade-3 GI) reported.

The data on this topic are limited to a few retrospective series, and our results mirror the available literature on SBRT in place of BB. Haas et al. [7] have reported on six cervical cancer patients treated with SBRT boost (median of 20 Gy in five fractions) after CRT. Their series did not find any local recurrences and did not report any toxicity with a median followup of 14 months. Molla et al. [8] have reported on 16 patients (nine endometrial and seven cervical cancers, while 15 patients had a hysterectomy) treated with SBRT (14 Gy in two fractions for postoperative and 20 Gy in five fractions for nonoperated patients) instead of BB. This report found one patient with late rectal bleeding (GI grade-3 toxicity) and 1 recurrence with a median followup of 12.6 months. Guckenberger et al. [12] have reported on 19 patients with recurrent cervical or endometrial cancer, who had pelvic sidewall involvement or large tumors not amenable to BB. SBRT consisted of 15 Gy in three fractions, with a median followup of 22 months. Three-year overall survival was 34%, and local control was 81%; two patients had grade-4 intestinovaginal fistulae, and one had a grade-4 small bowel ileus. Kemmerer et al. [10] reported on 11 patients with stage unresectable I-III endometrial cancer treated with SBRT boost of 30 Gy in 5 fractions; they found no late toxicity and 55% local-regional control. Higginson et al. [11] reported on a heterogeneous group of 5 with a range of SBRT doses, one of whom had late grade-3 rectal bleeding after receiving 20 Gy in 5 fractions.

All of the data to date are retrospective and heterogeneous but some trends do emerge. First of all, there appears to be good local control with this treatment modality. Secondly, the major late toxicity seen in our series and that of several others [8, 11] have been late GI toxicity, while the data thus far do not allow a precise calculation of dose tolerance for the rectum; it is important that this toxicity be discussed with patients and that there be attempts to constrain dose to the rectum.

At this point, it is not standard of practice to replace BB with SBRT in patients who are BB candidates. However, we have shown that, when BB is not an option, SBRT can be a safe and effective treatment modality. Further work in this area can be used to better define SBRT dose and to prospectively collect toxicity and outcome information on this patient subset. Our current treatment protocol is to treat to 25 Gy in five fractions using dose constraints as described previously.

5. Conclusions

Brachytherapy implants remain the standard of care as a method to deliver radiation boost for gynecological cancers.

However, for patients unable to have a brachytherapy procedure, we found acceptable toxicity and outcome with SBRT. This treatment modality should be further evaluated in a phase II study, with dose and fractionation of 25 Gy in 5 fractions, and close adherence to organ at risk limits.

Conflict of Interests

The authors declare that they have no conflict of interests.

References

[1] M. Morris, P. J. Eifel, J. Lu et al., "Pelvic radiation with concurrent chemotherapy compared with pelvic and para-aortic radiation for high-risk cervical cancer," *The New England Journal of Medicine*, vol. 340, no. 15, pp. 1137–1143, 1999.

[2] P. G. Rose, B. N. Bundy, E. B. Watkins et al., "Concurrent cisplatin-based radiotherapy and chemotherapy for locally advanced cervical cancer," *The New England Journal of Medicine*, vol. 340, no. 15, pp. 1144–1153, 1999.

[3] P. J. Eifel, K. Winter, M. Morris et al., "Pelvic irradiation with concurrent chemotherapy versus pelvic and para-aortic irradiation for high-risk cervical cancer: an update of radiation therapy oncology group trial (RTOG) 90-01," *Journal of Clinical Oncology*, vol. 22, no. 5, pp. 872–880, 2004.

[4] T. E. Schefter, K. Winter, J. S. Kwon et al., "A phase II study of Bevacizumab in combination with definitive radiotherapy and cisplatin chemotherapy in untreated patients with locally advanced cervical carcinoma: preliminary results of RTOG 0417," *International Journal of Radiation Oncology, Biology, Physics*, vol. 83, no. 4, pp. 1179–1184, 2012.

[5] A. N. Viswanathan, B. Thomadsen, and American Brachytherapy Society Cervical Cancer Recommendations Committee, "American brachytherapy society consensus guidelines for locally advanced carcinoma of the cervix—part I: general principles," *Brachytherapy*, vol. 11, no. 1, pp. 33–46, 2012.

[6] W. Small Jr., S. Beriwal, D. J. Demanes et al., "American brachytherapy society consensus guidelines for adjuvant vaginal cuff brachytherapy after hysterectomy," *Brachytherapy*, vol. 11, no. 1, pp. 58–67, 2012.

[7] J. A. Haas, M. R. Witten, O. Clancey, K. Episcopia, D. Accordino, and E. Chalas, "CyberKnife boost for patients with cervical cancer unable to undergo brachytherapy," *Frontiers in Oncology*, vol. 2, article 25, 2012.

[8] M. Molla, L. Escude, P. Nouet et al., "Fractionated stereotactic radiotherapy boost for gynecologic tumors: an alternative to brachytherapy?" *International Journal of Radiation Oncology, Biology, Physics*, vol. 62, no. 1, pp. 118–124, 2005.

[9] C. H. Hsieh, M. C. Wei, Y. P. Hsu et al., "Should helical tomotherapy replace brachy therapy for cervical cancer? Case report," *BMC Cancer*, vol. 10, article 637, 2010.

[10] E. Kemmerer, E. Hernandez, J. S. Ferriss et al., "Use of image-guided stereotactic body radiation therapy in Lieu of intracavitary brachytherapy for the treatment of inoperable endometrial neoplasia," *International Journal of Radiation Oncology, Biology, Physics*, vol. 85, no. 1, pp. 129–135, 2013.

[11] D. S. Higginson, D. E. Morris, E. L. Jones, D. Clarke-Pearson, and M. A. Varia, "Stereotactic body radiotherapy (SBRT): technological innovation and application in gynecologic oncology," *Gynecologic Oncology*, vol. 120, no. 3, pp. 404–412, 2011.

[12] M. Guckenberger, J. Bachmann, J. Wulf et al., "Stereotactic body radiotherapy for local boost irradiation in unfavourable locally recurrent gynaecological cancer," *Radiotherapy and Oncology*, vol. 94, no. 1, pp. 53–59, 2010.

[13] M. Cengiz, A. Dogan, G. Ozyigit et al., "Comparison of intracavitary brachytherapy and stereotactic body radiotherapy dose distribution for cervical cancer," *Brachytherapy*, vol. 11, no. 2, pp. 125–129, 2012.

[14] N. H. Haripotepornkul, S. K. Nath, D. Scanderbeg, C. Saenz, and C. M. Yashar, "Evaluation of intra- and inter-fraction movement of the cervix during intensity modulated radiation therapy," *Radiotherapy and Oncology*, vol. 98, no. 3, pp. 347–351, 2011.

[15] S. Nag and N. Gupta, "A simple method of obtaining equivalent doses for use in HDR brachytherapy," *International Journal of Radiation Oncology, Biology, Physics*, vol. 46, no. 2, pp. 507–513, 2000.

[16] M. Pinn-Bingham, A. A. Puthawala, A. M. Syed et al., "Outcomes of high-dose-rate interstitial brachytherapy in the treatment of locally advanced cervical cancer: long-term results," *International Journal of Radiation Oncology, Biology, Physics*, vol. 85, no. 3, pp. 712–720, 2013.

[17] S. Beriwal, A. Bhatnagar, D. E. Heron et al., "High-dose-rate interstitial brachytherapy for gynecologic malignancies," *Brachytherapy*, vol. 5, no. 4, pp. 218–222, 2006.

[18] L. H. Barraclough, R. Swindell, J. E. Livsey, R. D. Hunter, and S. E. Davidson, "External beam boost for cancer of the cervix uteri when intracavitary therapy cannot be performed," *International Journal of Radiation Oncology, Biology, Physics*, vol. 71, no. 3, pp. 772–778, 2008.

Hindawi Publishing Corporation
BioMed Research International
Volume 2013, Article ID 108794, 7 pages
http://dx.doi.org/10.1155/2013/108794

Research Article

An Attempted Substitute Study of Total Skin Electron Therapy Technique by Using Helical Photon Tomotherapy with Helical Irradiation of the Total Skin Treatment: A Phantom Result

Chi-Ta Lin,[1] An-Cheng Shiau,[1,2] Hui-Ju Tien,[1] Hsin-Pei Yeh,[1] Pei-Wei Shueng,[1,3] and Chen-Hsi Hsieh[1,4,5]

[1] *Division of Radiation Oncology, Department of Radiology, Far Eastern Memorial Hospital, New Taipei City 220, Taiwan*
[2] *Department of Biomedical Imaging and Radiological Science, China Medical University, Taichung 404, Taiwan*
[3] *Department of Radiation Oncology, Tri-Service General Hospital, National Defense Medical Center, Taipei 114, Taiwan*
[4] *Department of Medicine, School of Medicine, National Yang-Ming University, Taipei 112, Taiwan*
[5] *Institute of Traditional Medicine, School of Medicine, National Yang-Ming University, Taipei 112, Taiwan*

Correspondence should be addressed to Pei-Wei Shueng; shuengsir@gmail.com and Chen-Hsi Hsieh; chenciab@gmail.com

Received 4 May 2013; Accepted 16 June 2013

Academic Editor: Tsair-Fwu Lee

An anthropomorphic phantom was used to investigate a treatment technique and analyze the dose distributions for helical irradiation of the total skin (HITS) by helical tomotherapy (HT). Hypothetical bolus of thicknesses of 0, 10, and 15 mm was added around the phantom body to account for the dose homogeneity and setup uncertainty. A central core structure was assigned as a "complete block" to force the dose tangential delivery. HITS technique with prescribed dose (D_p) of 36 Gy in 36 fractions was generated. The radiochromic EBT2 films were used for the dose measurements. The target region with 95.0% of the D_p received by more than 95% of the PTV was obtained. The calculated mean doses for the organs at risk (OARs) were 4.69, 3.10, 3.20, and 2.94 Gy for the lung, heart, liver, and kidneys, respectively. The measurement doses on a phantom surface for a plan with 10 mm hypothetical bolus and bolus thicknesses of 0, 1, 2, and 3 mm are 89.5%, 111.4%, 116.9%, and 117.7% of D_p, respectively. HITS can provide an accurate and uniform treatment dose in the skin with limited doses to OARs and is safe to replace a total skin electron beam regimen.

1. Introduction

Radiation therapy achieves an effective treatment for cutaneous T-cell lymphoma affecting the superficial region [1]. This treatment delivers an adequate and uniform dose to the whole body superficial area. Historically, mycosis fungoides (MF) is treated mainly with total skin electron beam therapy (TSEBT). One of the most widely used TSEBT techniques was six dual fields [2]. Dosimetrically, TSEBT at energies of about 3–7 MeV at the surface of a standing patient may result in significant dose variations due to variable skin distance, self-shielding, irradiated fields overlapping, and patient motion [3, 4]. Special areas of the body, such as the perineum and eyelid [3] or inframammary fold [4], showed large deviations (up to 40%) from the prescription dose [3, 4]. Although the *in vivo* measurement of different treatment areas can realize the dose distribution in a certain region, a complicated distribution of underdosed areas can scarcely be treated with a homogeneous dose using supplemental patch fields.

Helical tomotherapy (HT) has advantages in irradiating extended volumes with treatment length of up to 160 cm, continuously in a helical pattern without the need for field junction [5]. Previous publications demonstrated it is feasible for total marrow irradiation (TMI) techniques by HT to replace total body irradiation [6] or practicing for multiple myloma patients [7]. Additionally, HT for total scalp irradiation has shown that the employment of directional and complete blocking on the inner structures can effectively force the tangential delivery of the beamlets to the planning target volume (PTV), which can limit the treatment depth successfully [8].

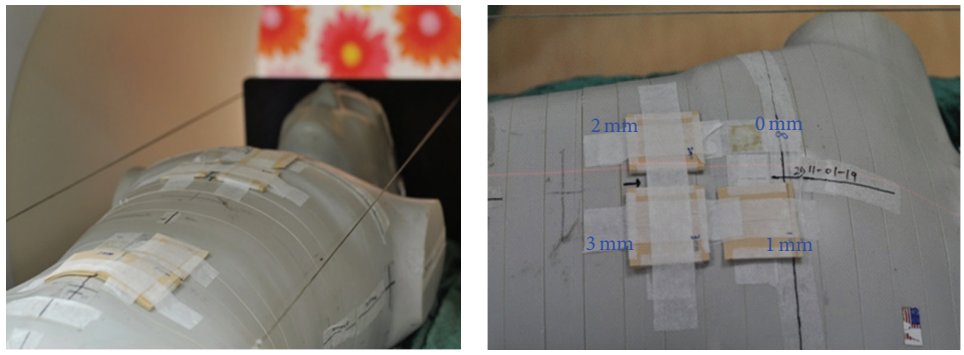

(a) (b)

Figure 1: (a) Sheets of tissue equivalent material with thicknesses of 1, 2, and 3 mm were placed on the phantom surface as a bolus. (b) The EBT2 films were placed on the phantom surface and inserted between the bolus and phantom surface for dose measurements.

Here, an anthropomorphic phantom is used to investigate the helical irradiation of the total skin (HITS) technique by HT planning system and compares with the conventional TSEBT administrated using a conventional linear accelerator. The dosimetry analysis, the uncertainty of dose calculation, the surface, and superficial doses are evaluated.

2. Materials and Methods

2.1. Treatment Plan. A treatment planning CT was taken of an anthropomorphic body phantom (ATOM 701; CIRS, Norfolk, Va), placed in the supine position and immobilized using a Vac-Lok bag (CIVCO Medical Instruments, CO, Inc., Kalona, IA). Sheets of tissue equivalent material at thicknesses of 1, 2, and 3 mm were placed on the phantom surface as a bolus for dosimetry analysis (Figures 1(a) and 1(b)). The image set was transferred to the treatment planning system (Pinnacle3 Version7.6C) using a hypothetical target volume including 5 mm depth all around the body surface contoured as the clinical target volume (CTV). The inner side of CTV plus 1.5 cm and the outer side of CTV added 0.5 cm, these areas were defined as PTV. From the shoulder to wrist and legs above ankles that areas under the skin with 0.5 cm were defined as the $CTV_{extremity}$. Hands and feet were contoured without bone sparing as CTV_{hand} and CTV_{feet}. The $PTV_{extremities}$ were defined as the volume with two dimensional expansion of 1.0 cm from the $CTV_{extremity}$, CTV_{hand}, and CTV_{feet}. A hypothetical constraint structure (HCS), 0.3 cm margin away from the inner side of PTV with 1.0–1.5 cm 2 dimensional expansion, was contoured for the dose constraint. The organs and tissues that adjacent to the inner side of HCS were contoured together as central core complete block (CCCB) and used to restrict the photon beams to be obliquely incidence for increasing the superficial dose and reducing the internal organ dose. (Figure 2) Lung, heart, liver, kidney, spleen, intestine, ovary, stomach, and spinal cord were contoured as organs at risk (OARs). Additional margins of 0, 10, and 15 mm were extended from the phantom surface individually for a different plan contoured as a hypothetical bolus to account for the dose homogeneity increase at the superficial region and setup uncertainty. The CT images and

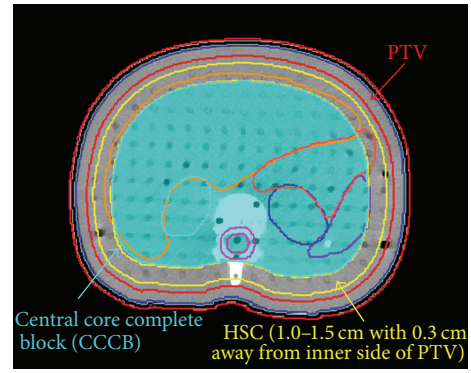

Figure 2: The phantom axial image displays the hypothetical target structure, the constraint object, and the central core structure.

structures were then transferred to the Tomotherapy Hi-ART planning system (v. 3.2.2.35. TomoTherapy Inc., Madison, WI). A plan with prescription dose (D_p) of 36 Gy in 36 fractions to 95% of the PTV and the maximum dose less than 120% of the D_p was generated. The maximum irradiation length and width for HT were 160 and 85 cm, respectively. The slice thickness, pitch, and modulation factor parameters were assigned 2.5 cm, 0.287 cm, and 3.5, respectively. The dose constraints to the OARs and the HCS were adjusted accordingly during optimization to achieve a plan with a rapid dose distribution falloff. For all measurements a predelivery megavoltage CT (MVCT) scan was taken for position alignment.

2.2. Dose Measurement. Radiochromic EBT2 film with high spatial resolution and thin configuration (thickness of 0.234 mm and effective measurement depth of 0.153 mm in a layer) has been proven a viable tool for external beam dosimetry in the superficial region [9, 10]. All of the radiochromic EBT2 films used in this study were from the same lot number (International Specialty Products, Inc. Wayne, NJ). Each film sheet of 25 × 20 cm was cut into smaller pieces (size of 5 × 5 cm) for calibration and measurement. An Epson Perfection V700 flatbed scanner (Epson Seiko Corporation,

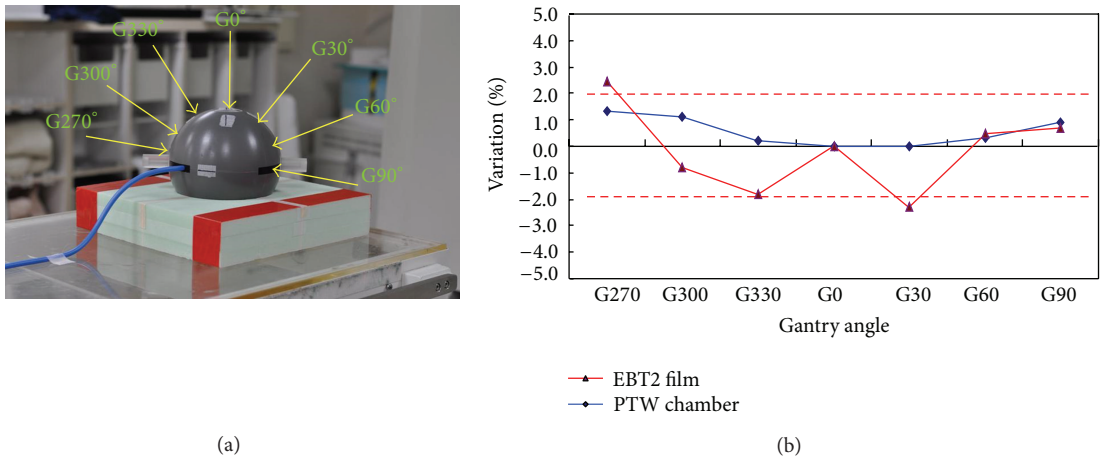

FIGURE 3: (a) PTW 31010 semiflex ionization chamber (PTW-Freiburg, Germany) as a standard without angular dependence. PTW chamber has been irradiated in spherical phantom to determine the ionization along the central axis to various gantry angles. (b) Angular dependence, measurements using EBT2 film and PTW semiflexible chamber.

Epson Seiko Corporation, Nagano, Japan) was used to scan all of the films at least 24 hours after film exposure. Films were scanned at a central scanner location and with the same orientation. The settings used were 48 bit color and 150 dpi (0.017 cm per pixel). The red channel data with 16 bit digital information were extracted and processed using the public domain software ImageJ Version 1.43 (National Institute of Health, Bethesda, MD, http://rsb.info.nih.gov/ij/). Calibration was performed by irradiating the each calibration film individually in a plastic water phantom perpendicularly to a 6 MV beam at dose levels from 0 to 300 cGy. The calibration curve was fitted using a polynomial function with the pixel value (PV) for each measurement film converted to dose accordingly.

To evaluate the buildup range of the doses on the surface and superficial regions for HITS, measurements were performed with EBT2 films placed on the phantom surface at different areas with boluses of different thicknesses of 0, 1, 2, and 3 mm added onto the films for dosimetry analysis. For clinical HITS application purposes increasing the surface dose and decreasing the unwanted air gaps under the dose buildup material, a custom-made neoprene diving suit was considered as the dose buildup material with the effective thickness relative to water evaluated. To account for the diving suit bolus effect, a piece of diving suit 3 mm thick was irradiated to a 6 MV beam to evaluate the effective thickness relative to water. To verify the calculated doses on critical organs, measurements were performed with EBT2 films inserted into the phantom at the critical organ locations.

2.3. Verification of Angular Dependence with EBT2 Film. We used spherical polystyrene phantom and PTW 31010 semiflex ionization chamber (PTW-Freiburg, Germany) as a standard without angular dependence. Reference condition was performed in 100 cm source axial distance (SAD), with field size $5 \times 5\,cm^2$ and using 6 MV photon beam 200 MU delivery. PTW chamber has been irradiated in a spherical phantom to determine the ionization along the central axis to various gantry angles. (Figure 3(a)) The ionization readings of each angle were normalized by the measurement value of normal incidence exposure. Each angle variation results will be recorded and analyzed. EBT2 film sheets have been irradiation in spherical phantom at the same position. Reference condition was performed in SAD 100 cm, with field size $5 \times 5\,cm^2$ and using 6 MV photon beam 250 MU delivery. An Epson perfection V750 PRO flat bed scanner (Epson Seiko Corporation, Epson Seiko Corporation, Nagano, Japan) was used to scan all the films at least 24 hours after film exposure. The optical density measurement position of EBT2 film was extremely small and identical to chamber exposure position. The variation of PTW ionization chamber results was compared with the EBT2.

3. Results

3.1. Angle Effect and Uncertainty in Detail. The angular dependence of EBT2 film was small and applicable to clinical surface dose measurement. In the current study, the total uncertainty was less than 2.5% (Figure 3(b)).

3.2. Treatment Plan. A homogenous dose in the target region was obtained. Ninety-five percent of the D_p was received by more than 95% of the PTV and the maximum dose was less than 116% of the D_p. (Figure 4) The calculation mean doses for the critical organs were 4.69, 3.10, 3.20, and 2.94 Gy for the lungs, heart, liver, and kidneys, respectively. The HITS plan statistics with 10 mm hypothetical bolus are shown in Table 1. The calculated dose distributions are shown in Figure 5(a). The dose delivery duration was within 45 minutes.

3.3. Dose Measurement. The dose differences between measurements and calculations for OARs were less than 0.8 Gy. In addition, the mean doses for OARs were between 2.9 and 9.1 Gy (Table 1). The dose of the vertex was 108.0%±1.2%. Due

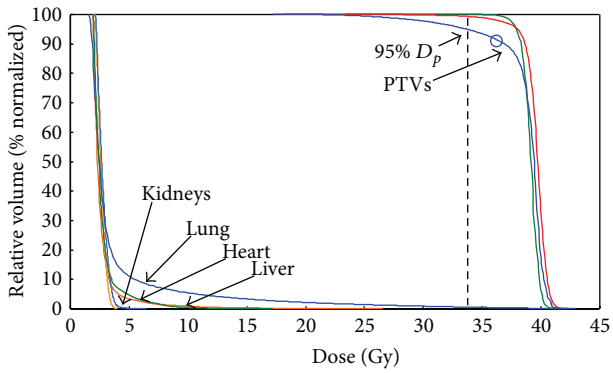

Figure 4: Dose volume histogram of helical irradiation of the total skin (HITS) with prescribed dose of 36 Gy in 36 fractions for treatment in a study phantom.

Table 1: The helical irradiation of the total skin (HITS) technique statistics with 10 mm hypothetical bolus for total skin and organs at risk (OARs).

	D_{max} (Gy)	$V_{95\%}$ (%)	$D_{mean\text{-}C}$ (Gy)	$D_{mean\text{-}M}$ (Gy)
PTV	41.88	96.0	38.83	—
Heart	28.67	—	3.10	3.25
Lung	40.96	—	4.69	3.93
Liver	25.16	—	3.20	—
Kidney	4.38	—	2.94	3.16
Spleen	6.03	—	3.11	—
Intestine	25.80	—	3.40	—
Rectum	14.83	—	9.06	—

D_{max} (Gy): maximum dose.
$V_{95\%}$ (%): target volume in % encompassed by 95% of the D_p.
$D_{mean\text{-}C}$ (Gy): TPS calculation mean dose.
$D_{mean\text{-}M}$ (Gy): measurement mean dose.

to the lack of arms and thighs for RANDO phantom, the skin dose of arms and thighs could not be measured from RANDO phantom. Therefore, the CT images of whole body of one patient who received total marrow irradiation were used to replan with HITS technique to show the workable of dose delivery to extremities (Figure 5(b)). For the TMI and HITS plans, the hand and feet were all irradiated without sparing; therefore the results of surface dose checked by EBT2 film could be similar. And the hands and plantar skin dose measured by EBT2 film of the TMI plan were 117.2% ± 2.8% and 108.6% ± 4.8%, respectively. The measurement doses on the phantom surface for plans with different hypothetical bolus thicknesses and the actual bolus were shown in Table 2. A higher superficial dose was obtained as a thicker hypothetical bolus was used. The effective thickness relative to water of the diving suit is 0.87 mm.

4. Discussion

Most TSEBT procedures are time consuming. Since patients requiring TSEBT are often elderly and weak, a long treatment time for a patient in a standing position is difficult to hold at a correct position and to ensure their safety. HITS sets patient in the supine position and immobilizes the patient with a vacuum bag, which is more stable and comfortable for a long duration treatment. Additionally, the requirement of room size for TSEBT is about 4 meters, which may restrict using the TSEBT technique. HITS do not need a large treatment room and can be performed without room size restriction.

Table 2: Measurement doses (% of D_p) of the surface and superficial regions for the helical irradiation of the total skin (HITS) technique with different hypothetic bolus thicknesses.

	Hypothetic bolus thickness		
Depth (mm)	0 mm	10 mm	15 mm
Surface	73.2	89.5	86.4
1.0	91.4	111.4	118.5
2.0	101.7	116.6	118.9
3.0	101.9	117.7	120.9

HITS employ a CCCB to force the majority of the beamlets to be delivered to the PTV tangentially. This limits the depth of the dose distribution and also makes the treatment more vulnerable to setup and respiratory motion errors. Using CCCB technique in HITS study, the mean doses for OARs, such as the lungs, heart, liver, intestine, and kidneys, were 4.7, 3.1, 3.2, 3.6, and 2.9 Gy, respectively (Table 1). Historically, whole heart doses up to 30 Gy were reasonably well tolerated [11]. In addition, limiting mean lung dose to ≤20–23 Gy can limit the risk of radiation pneumonitis to ≤20% in definitively treated patients with nonsmall-cell lung cancer [12]. Furthermore, Dawson et al. [13] reported when the mean liver dose less than 31 Gy (biologic effective dose = 30 Gy10 in 2 Gy/fraction) that was no cases of subsequent radiation-induced liver disease. Emami et al. [14] and Robert Cassady [15] suggested a total dose associated with a 5% and 50% risk of kidney injury at 5 years of 18–23 Gy and 28 Gy, in 0.5–1.25 Gy/fraction, respectively. With doses on the order of 50 Gy, late small-bowel obstruction or perforation rates of 2% to 9% had been observed after partial organ irradiation [16], concordant with the Emami et al. TD5/5 estimate [14]. According to the previous reports, HITS technique could provide safety for total skin irradiation.

Hypothetical bolus is a method to overcome setup and respiratory motion errors but the dosimetric condition is different between the planned and delivered beams. An increment in the effective hypothetical bolus thickness in a steeply inclined incidence while optimization will make the dose distributions with a significant increment in the shallow region while treatment. This increment increases with the thickness of the hypothetical bolus (Table 2). Based on this study, the measurement doses on a phantom surface for a plan with 10 mm hypothetical bolus and bolus thicknesses of 0, 1, 2, and 3 mm are 89.5%, 111.4%, 116.9%, and 117.7% of D_p, respectively. Ten mm of hypothetical bolus thickness will increase 10% of D_p to the superficial regions. Tomotherapy system delivers dose with 6 MV; the attenuation factor of this energy is about 4.5%/cm (0.45%/mm). Dosimetrically, attached boluses with thicknesses of 1, 2, and 3 mm on phantom surface will mainly affect the doses on surface.

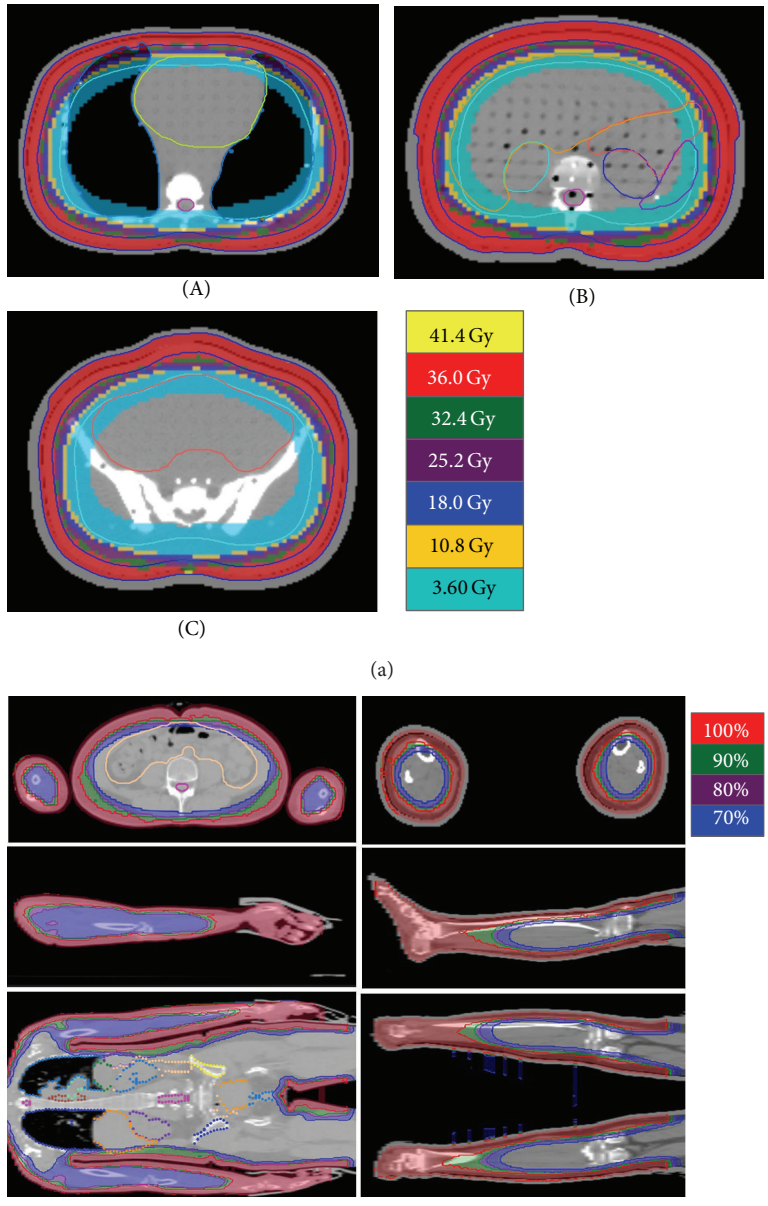

Figure 5: (a) Dose distributions at chest (A), abdomen (B), and pelvic (C) areas for helical irradiation of the total skin (HITS) treatment in a study phantom. (b) Due to our RANDO phantom without the thighs and arms, the CT images of whole body of one patient who received total marrow irradiation were used to replan with HITS technique to show the workable of dose delivery to extremities.

The differences of dosimetric effects caused by the boluses from the beam entrances away from the measurement regions will be less than 1.0%. In addition, the size of the bolus is about 1.5 cm larger than the measurement film in each side, and the film reading is accounted on the central area (about 3 × 3 cm). So, the scatter radiation can be accounted mostly in the measurement condition stated in this study. Therefore, the dose differences caused by the boluses in different thicknesses are sufficient to account for. Additionally, an appropriate hypothetical bolus thickness should be chosen according to the variations in surface positions of interfraction or intrafraction motion.

Gafchromic EBT2 film has high spatial resolution (thickness of 0.234 mm and effective measurement depth of 0.153 mm in a layer) [17], low energy dependency [18], and near tissue equivalent density (Z_{eff} = 6.84 for EBT2, Z_{eff} = 7.42 for tissue) [19]. The weak energy dependence of the EBT2 makes it most suitable for clinical use compared with other films [19]. The total uncertainty in the surface dosimetry using EBT2 film reported by Nakano et al., Hartmann et al. [20], and Richley et al. [21] are approximately 3.3%, 3.7%, and 5.5%, respectively. In the current study, the total uncertainty less than 2.5% competes with previous studies with better results (Figure 3(b)).

Consensus guidelines for delivery of TSEBT have been published by the European Organization for Research and Treatment of Cancer (EORTC) [22]. The EORTC recommends a total dose of 31 to 36 Gy prescribed to the skin surface to produce a dose of at least 26 Gy at a depth of 4 mm in the truncal skin along the central axis [22]. In our calculation, a surface dose is inadequate for HITS. To overcome this problem, a custom-made neoprene diving suit of 3 mm thickness that fits the patient's body curvature well is considered as the dose buildup material to increase the surface dose and to decrease the unwanted air gaps. The effective thickness relative to water of the diving suit is 0.87 mm, which is enough for dose buildup for HITS with 10 mm hypothetical bolus to achieve more than 110% of D_p on the skin surface (Table 2).

HITS using 6 MV photon beams generates a plan with higher internal organ dose than the TSEBT technique. A mean dose of about 3.5 Gy (9.7 cGy/fx) is received by the OARs under HITS with 36 Gy in 36 fractions. The internal TSEBT dose is contributed mainly by the contaminated X-ray, typically ranging l%–4% (1–4 cGy/fx) of the maximum electron dose received at the surface [23]. Recent reports are interesting in revisiting the effectiveness of lower dose TSEBT in the management of MF [1, 24]. Based on Harrison's report [1], the overall response rates associated with low-dose TSEBT in the 10 to <20 Gy and 20 to <30 Gy ranges are comparable to those of the standard dose (≥30 Gy). The internal organ doses from HITS might be tolerable for a 36 Gy regimen and are safer for revisiting a low-dose TSEBT regimen.

The drawback of HITS is the longer beam on time and probably the higher inner doses. Increased field width to 5.0 cm may shorten the duration significantly but the PTV coverage may reduce slightly or the maximum dose to PTV may increase by 10%–15%.

5. Conclusion

To the best of our knowledge, this is the first phantom study to prove the possibility to replace TSEBT by HT with HITS technique. HITS technique provides an accurate and uniform treatment dose to the skin area in this phantom study. The internal organ doses were effectively spared using a tangential beamlets delivery method. A diving suit of 3 mm thickness for clinical purpose is needed to increase the surface dose and to decrease the unwanted air gaps.

Conflict of Interests

All authors have no conflict of interests.

Funding

No external funding was received for this study.

Acknowledgment

This work was supported by the Far Eastern Memorial Hospital Grants (FEMH-2012-C-055, FEMH 101-2314-B-418-010-MY3).

References

[1] C. Harrison, J. Young, D. Navi et al., "Revisiting low-dose total skin electron beam therapy in mycosis fungoides," *International Journal of Radiation Oncology Biology Physics*, vol. 81, no. 4, pp. e651–e657, 2011.

[2] A. Niroomand-Rad, M. T. Gillin, R. Komaki, R. W. Kline, and D. F. Grimm, "Dose distribution in total skin electron beam irradiation using the six-field technique," *International Journal of Radiation Oncology Biology Physics*, vol. 12, no. 3, pp. 415–419, 1986.

[3] R. D. Weaver, B. J. Gerbi, and K. E. Dusenbery, "Evaluation of dose variation during total skin electron irradiation using thermoluminescent dosimeters," *International Journal of Radiation Oncology Biology Physics*, vol. 33, no. 2, pp. 475–478, 1995.

[4] L. M. Gamble, T. J. Farrell, G. W. Jones, and J. E. Hayward, "Two-dimensional mapping of underdosed areas using radiochromic film for patients undergoing total skin electron beam radiotherapy," *International Journal of Radiation Oncology Biology Physics*, vol. 62, no. 3, pp. 920–924, 2005.

[5] T. R. Mackie, T. Holmes, S. Swerdloff et al., "Tomotherapy: a new concept for the delivery of dynamic conformal radiotherapy," *Medical Physics*, vol. 20, no. 6, pp. 1709–1719, 1993.

[6] T. E. Schultheiss, J. Wong, A. Liu, G. Olivera, and G. Somlo, "Image-guided total marrow and total lymphatic irradiation using helical tomotherapy," *International Journal of Radiation Oncology Biology Physics*, vol. 67, no. 4, pp. 1259–1267, 2007.

[7] P.-W. Shueng, S.-C. Lin, N.-S. Chong et al., "Total marrow irradiation with helical tomotherapy for bone marrow transplantation of multiple myeloma: first experience in Asia," *Technology in Cancer Research and Treatment*, vol. 8, no. 1, pp. 29–38, 2009.

[8] N. Hardcastle, E. Soisson, P. Metcalfe, A. B. Rosenfeld, and W. A. Tomé, "Dosimetric verification of helical tomotherapy for total scalp irradiation," *Medical Physics*, vol. 35, no. 11, pp. 5061–5068, 2008.

[9] S. T. Chiu-Tsao and M. F. Chan, "Photon beam dosimetry in the superficial buildup region using radiochromic EBT film stack," *Medical Physics*, vol. 36, no. 6, pp. 2074–2083, 2009.

[10] S. Devic, J. Seuntjens, W. Abdel-Rahman et al., "Accurate skin dose measurements using radiochromic film in clinical applications," *Medical Physics*, vol. 33, no. 4, pp. 1116–1124, 2006.

[11] S. L. Hancock, S. S. Donaldson, and R. T. Hoppe, "Cardiac disease following treatment of Hodgkin's disease in children and adolescents," *Journal of Clinical Oncology*, vol. 11, no. 7, pp. 1208–1215, 1993.

[12] L. B. Marks, S. M. Bentzen, J. O. Deasy et al., "Radiation dose-volume effects in the lung," *International Journal of Radiation Oncology Biology Physics*, vol. 76, no. 3, supplement, pp. S70–S76, 2010.

[13] L. A. Dawson, D. Normolle, J. M. Balter, C. J. McGinn, T. S. Lawrence, and R. K. Ten Haken, "Analysis of radiation-induced liver disease using the Lyman NTCP model," *International Journal of Radiation Oncology Biology Physics*, vol. 53, no. 4, pp. 810–821, 2002.

[14] B. Emami, J. Lyman, A. Brown et al., "Tolerance of normal tissue to therapeutic irradiation," *International Journal of Radiation Oncology Biology Physics*, vol. 21, no. 1, pp. 109–122, 1991.

[15] J. Robert Cassady, "Clinical radiation nephropathy," *International Journal of Radiation Oncology Biology Physics*, vol. 31, no. 5, pp. 1249–1256, 1995.

[16] B. D. Kavanagh, C. C. Pan, L. A. Dawson et al., "Radiation dose-volume effects in the stomach and small bowel," *International Journal of Radiation Oncology Biology Physics*, vol. 76, no. 3, supplement, pp. S101–S107, 2010.

[17] M. Martišíková, B. Ackermann, and O. Jäkel, "Analysis of uncertainties in Gafchromic® EBT film dosimetry of photon beams," *Physics in Medicine and Biology*, vol. 53, no. 24, pp. 7013–7027, 2008.

[18] M. J. Butson, T. Cheung, and P. K. N. Yu, "Weak energy dependence of EBT gafchromic film dose response in the 50 kVp-10 MVp X-ray range," *Applied Radiation and Isotopes*, vol. 64, no. 1, pp. 60–62, 2006.

[19] B. Arjomandy, R. Tailor, A. Anand et al., "Energy dependence and dose response of Gafchromic EBT2 film over a wide range of photon, electron, and proton beam energies," *Medical Physics*, vol. 37, no. 5, pp. 1942–1947, 2010.

[20] B. Hartmann, M. Martišíková, and O. Jäkel, "Technical note: homogeneity of gafchromic EBT2 film," *Medical Physics*, vol. 37, no. 4, pp. 1753–1756, 2010.

[21] L. Richley, A. C. John, H. Coomber, and S. Fletcher, "Evaluation and optimization of the new EBT2 radiochromic film dosimetry system for patient dose verification in radiotherapy," *Physics in Medicine and Biology*, vol. 55, no. 9, pp. 2601–2617, 2010.

[22] G. W. Jones, B. M. Kacinski, L. D. Wilson et al., "Total skin electron radiation in the management of mycosis fungoides: consensus of the European Organization for Research and Treatment of Cancer (EORTC) Cutaneous Lymphoma Project Group," *Journal of the American Academy of Dermatology*, vol. 47, no. 3, pp. 364–370, 2002.

[23] Z. Chen, A. G. Agostinelli, L. D. Wilson, and R. Nath, "Matching the dosimetry characteristics of a dual-field Stanford technique to a customized single-field Stanford technique for total skin electron therapy," *International Journal of Radiation Oncology Biology Physics*, vol. 59, no. 3, pp. 872–885, 2004.

[24] M. R. Kamstrup, L. Specht, G. L. Skovgaard, and R. Gniadecki, "A prospective, open-label study of low-dose total skin electron beam therapy in mycosis fungoides," *International Journal of Radiation Oncology Biology Physics*, vol. 71, no. 4, pp. 1204–1207, 2008.

Hindawi Publishing Corporation
BioMed Research International
Volume 2013, Article ID 359634, 7 pages
http://dx.doi.org/10.1155/2013/359634

Research Article

Identifying the Association Rules between Clinicopathologic Factors and Higher Survival Performance in Operation-Centric Oral Cancer Patients Using the Apriori Algorithm

Jen-Yang Tang,[1,2,3] Li-Yeh Chuang,[4] Edward Hsi,[5] Yu-Da Lin,[6] Cheng-Hong Yang,[6] and Hsueh-Wei Chang[3,7]

[1] *Department of Radiation Oncology, Faculty of Medicine, College of Medicine, Kaohsiung Medical University, Kaohsiung, Taiwan*
[2] *Department of Radiation Oncology, Kaohsiung Medical University Hospital, Kaohsiung, Taiwan*
[3] *Cancer Center, Kaohsiung Medical University Hospital, Kaohsiung Medical University, Kaohsiung, Taiwan*
[4] *Department of Chemical Engineering and Institute of Biotechnology and Chemical Engineering, I-Shou University, Kaohsiung, Taiwan*
[5] *Department of Medical Research, Kaohsiung Medical University Hospital, Kaohsiung, Taiwan*
[6] *Department of Electronic Engineering, National Kaohsiung University of Applied Sciences, Kaohsiung, Taiwan*
[7] *Department of Biomedical Science and Environmental Biology, Kaohsiung Medical University, Kaohsiung, Taiwan*

Correspondence should be addressed to Cheng-Hong Yang; chyang@cc.kuas.edu.tw
and Hsueh-Wei Chang; changhw2007@gmail.com

Received 17 May 2013; Accepted 30 June 2013

Academic Editor: Tsair-Fwu Lee

This study computationally determines the contribution of clinicopathologic factors correlated with 5-year survival in oral squamous cell carcinoma (OSCC) patients primarily treated by surgical operation (OP) followed by other treatments. From 2004 to 2010, the program enrolled 493 OSCC patients at the Kaohsiung Medical Hospital University. The clinicopathologic records were retrospectively reviewed and compared for survival analysis. The Apriori algorithm was applied to mine the association rules between these factors and improved survival. Univariate analysis of demographic data showed that grade/differentiation, clinical tumor size, pathology tumor size, and OP grouping were associated with survival longer than 36 months. Using the Apriori algorithm, multivariate correlation analysis identified the factors that coexistently provide good survival rates with higher lift values, such as grade/differentiation = 2, clinical stage group = early, primary site = tongue, and group = OP. Without the OP, the lift values are lower. In conclusion, this hospital-based analysis suggests that early OP and other treatments starting from OP are the key to improving the survival of OSCC patients, especially for early stage tongue cancer with moderate differentiation, having a better survival (>36 months) with varied OP approaches.

1. Introduction

In Taiwan, betel nut chewing, cigarette smoking, and alcohol consumption have been found to be highly associated with oral cancer [1], with habitual betel nut chewers showing a particular high prevalence [2–4]. Oral cancer is one of the 10 most prevalent cancers in Taiwan, mostly classified as oral squamous cell carcinoma (OSCC) [5], which has high rates of morbidity and mortality [6] because diagnosis often only takes place in the later stages [7]. Although many tumor markers [8–10] and single nucleotide polymorphism (SNP) markers [11] have been reported as being associated with oral cancer, outcome-based studies focusing on oral cancer therapy are lacking.

The survival of OSCC patients following surgical therapy has been reported to be affected by tumor size, nodal metastasis, staging, and differentiation [12]. Some researchers have been further concerned with factors involved in outcomes for postoperative radiotherapy for OSCC patients [13]. However, the correlation between the multiple survival affecting factors for predicting the well survival of OSCC therapy is less addressed and remains a challenge.

```
01: L_1 = {l_1, ..., l_n | ∀ l ∈ large itemsets} //see Section 2.2.1
02: set k = 2
03: while (L_{k-1} ≠ Ø)
04:   C_k = apriori-gen (L_{k-1}) = {c_1, ..., c_p | c ∈ candidate k-itemsets}
      // see Section 2.2.2
05:   if (C_k = Ø)
06:     return
07:   end if
08:   for (all t ∈ D)
09:     C_t = subset (C_k, t) // see Section 2.2.3
10:     for (all c ∈ C_t)
11:       c.count++
12:     end for
13:   end for
14:   L_k = {c ∈ C_k | c.count ≥ minsup}
15:   k++
16: end while
```

Algorithm 1: Pseudocode of the Apriori algorithm.

Recently, several computational methodologies have been introduced to analyze the relationship between multiple factors and therapies for several non-OSCC diseases, including machine learning algorithms [14], data mining [15], decision tree-based learning [16], and rule-based multiscale simulations [17].

The Apriori algorithm is used here to explore the correlation between clinical factors and good survival outcomes (i.e., >36 months) in operation- (surgery-) centric treatments, including operation alone, operation/IA, and operation/IA, CT, IV, and RT, where IA, IV, CT, and RT, respectively stand for intra-arterial, intravenous, oral chemotherapies, and radiotherapy. The study aims to computationally evaluate the correlation between clinicopathological factors and survival outcomes in 493 OSCC patients treated by operation alone or by operation followed with other nonsurgical treatments.

2. Materials and Methods

2.1. Data Source. The database used to construct our cases and control groups was obtained from the chart registry of cancer center of the Kaohsiung Medical University Hospital from 2004 to 2010. Patients were excluded if they had distant metastases at presentation, did not complete the therapeutic protocol in Kaohsiung Medical University Hospital, or had incomplete records. A total of 493 patients fulfilled the requirements and were included for further analyses (the raw data set is available at http://bioinfo.kmu.edu.tw/OP_high-OP_low_groups.xlsx). The patients were followed at Kaohsiung Medical University Hospital. The last followup was recorded from the last outpatient visit or the date of death. This use of patient data and the study design were reviewed and approved by the Institutional Review Board of Kaohsiung Medical University Hospital (KMUH-IRB-EXEMPT-20130029).

2.2. Introduction of the Apriori Algorithm. The problem for association rule learning can be stated as follows. Let $I = \{i_1, i_2, \ldots, i_m\}$ be a set of literals, called items. Let transaction T be a set of items, where $T \subseteq I$. Let D be a set of transactions. The objective of the association rule is an implication of the form $A \Rightarrow B$, where $A \subset I$ and $B \subset I$, if $A \cap B = \emptyset$. The rule $A \Rightarrow B$ holds in the transaction set D with *confidence* c if c% of transactions in D that contain A also contain B. The rule $A \Rightarrow B$ has support s in the transaction set D if s% of transactions in D contain $A \cup B$. Item sets with the minimum support s are called large itemsets, and the others small itemsets.

The Apriori algorithm was proposed by Agrawal and Srikant in 1994 [18] and has been widely used for frequent itemset mining and association rule learning in databases. The Apriori algorithm aims to generate the desired rules from large itemsets. The general idea is that if items $ABCD$ are large itemsets, then any rule in $ABCD$ will have the minimum required support because $ABCD$ is large; that is, $AB \Rightarrow CD$.

The Apriori algorithm can be divided into three steps. Algorithm 1 shows the pseudocode of the Apriori algorithm. The algorithm's first pass counts item occurrences to screen the large itemsets (Section 2.2.1). The second pass generates the candidate itemsets C_k from large itemsets L_{k-1}, using the apriori-gen function (Section 2.2.2). Next, each transaction t checks whether the subsets of k-itemsets of t belong to C_k, called subset function and described in Section 2.2.3. Finally, each c counts item occurrences in C_t, and c will be stored in L_k if *c.count* minimum support. The algorithm terminates when L_k is empty; that is, no frequent set of k or more items is present in D.

2.2.1. Screening the Large 1-Itemsets. Algorithm 2 shows the pseudo code of first pass which simply counts item occurrences $I = \{i_1, i_2, \ldots, i_m\}$ to determine the large itemsets in all items. The array of *item counts* is used to count item occurrences, and elements in *Item-counts* having minimum support are included in the L_1 set.

```
01: for (all i | 1 ≤ i ≤ m)
02:   set Item-counts [i]= 0
03: end for
04: for (all t ∈ D)
05:   for (all i ∈ t)
06:     Item-counts [i]++
07:   end for
08: end for
09: L_1 = {l_i | Item-counts [i] ≥ minsup}
```

Algorithm 2: The first pass of the Apriori algorithm.

```
01: Function apriori-gen (L_{k−1})
02: set C_k ← Ø
03: for (all L_{k−1}.item_p, L_{k−1}.item_q | L_{k−1}.item_p[i] =
    L_{k−1}.item_q[i], ∀i ∈ {1, ..., k − 2})
04:   c ={L_{k−1}.item_p[1], ..., L_{k−1}.item_p[k−2], L_{k−1}.item_p
      [k−1], L_{k−1}.item_q [k−1]}
05:   if (∀L_{k−1}.item ⊂ c)
06:     C_k ← C_k∪c
07:   end if
08: end for
09: end Function
```

Algorithm 3: Pseudocode of the function apriori-gen().

2.2.2. Candidate Set Generations. The function apriori-gen (L_{k-1}) generates C_k from L_{k-1}, and it returns a superset of the set of all large k-itemsets. Algorithm 3 shows the pseudo code of the function apriori-gen (L_{k-1}). We use a set c, $c = \{L_{k-1}.item[i]\}$, for all $i \in \{1, \ldots, k-1\}$, to store the frequent $(k-1)$-itemsets in L_{k-1}. The selections of the pairs are called $L_{k-1}.item_p$, $L_{k-1}.item_q \in L_{k-1}$. For each $L_{k-1}.item_p$ in L_{k-1}, we start the search tuples in the $L_{k-1}.item_p$ and stop the search if we find $L_{k-1}.item_q$ such that 1 to $k-2$ items are not equal to the 1 to $k-2$ items of $L_{k-1}.item_p$. Only if we find an $L_{k-1}.item_q$ that satisfies $L_{k-1}.item_p[i] = L_{k-1}.item_q[i]$, for all $i \in \{1, \ldots, k-2\}$, the c does create the k-itemset = $\{L_{k-1}.item_p[i], \ldots, L_{k-1}.item_p[k-2], L_{k-1}.item_p[k-1], L_{k-1}.item_q[k-1]\}$. Finally, c checks whether the subsets of c are included in L_{k-1}.

2.2.3. Candidate Set Counts Using Hash Tree. After the candidate sets C_k are generated, the C_k are stored in a hash tree created by the function subset (C_k, t). The leaf of the hash tree comprises the pointers to C_k and the associated counters, and the leaf refers to distinct partitions of C_k. In the hash tree, the hash function can be used to insert the candidate itemsets and search the transaction subsets in C_k. The hash function is hash(i) = i mod T, $T < m$, where T is a constant, and m is the number of items. Function subset (C_k, t) is a recursive function which traverses the tree starting from the root node to the leaves, with each item in $t = \{i_1, \ldots, i_d\}$ chosen as a possible starting item of a candidate itemset. It is applied at every level of the tree. When t reaches a leaf of the tree, all candidate itemsets are checked against t and their counters are updated.

2.3. Statistics Analysis. Statistical analysis was performed with JMP version 9. All statistical tests were done at a 0.05 significance level.

3. Results and Discussion

3.1. Demographic Data and Survival

3.1.1. Age and Survival. As shown in Table 1, all patients were categorized into 2 groups based on whether the survival is greater or less than 36 months. In this regard, no difference in varied age groups can be found. This is probably because anyone who was eligible for surgical resection would have comparable survival rates.

3.1.2. Subsites and Survival. As shown in Table 1, the site distribution of the 493 cases of oral cancer patients showed common affected sites including the cheek mucosa, gum, tongue, and retromolar trigon. Postsurgical organ function and cosmetics may vary with surgical site, but no difference to survival could be found.

3.1.3. Laterality and Survival. As shown in Table 1, laterality is recorded in the database of cancer registries and is a mixed expression of clinical/pathological tumor size and location. It does not play a significant role in the surgical group.

3.1.4. Grade and Survival. As shown in Table 1, comparison of the pathological characteristics between >5-year ($n = 271$) and <5-year survival ($n = 222$) revealed better treatment outcomes for low grade tumors ($P = 0.0006$), suggesting that well-differentiated tumors are less aggressive and thus are associated with better overall survival.

3.1.5. Regional Lymph Nodes and Survival. As shown in Table 1, regional lymph node examination might express the details and quality of surgical resection. However, the number of examined lymph nodes was not found to have an effect on survival. This might be due to cross-interaction between clinical lymph node stages and overall survival.

3.1.6. Clinical Stages, Pathology Stages, Clinical/Pathology Tumor Sizes, and Survival. As shown in Table 1, neither clinical nor pathological stages were found to have an impact on 5-year survival. There might be some influencing factors between low- and high-tumor stages which cannot be simply explained by surgery. However, for clinical/pathological tumor size alone, significant differences between >5-year and <5-year groups are found ($P = 0.0004$ and $P = 0.0141$, resp.). Smaller tumor size means less tumor burden and has less surrounding tissue infiltration, which may explain improved overall outcomes.

Table 1: Demographic data of 493 enrolled patients with OSCC.

Characteristics	Survived months			P value[*1]	5-year survival (%)	P value[*2]
	Total	>36 group	<36 group			
Age				0.7786		0.5556
<30	7	3	4		71.4	
30~50	228	125	103		77.2	
50~70	236	129	107		79.2	
>70	22	14	8		63.6	
Primary Site				0.7915		0.1957
Lip	36	24	12		86.1	
Cheek mucosa	184	103	81		83.2	
Gum	42	25	17		71.4	
Tongue	175	88	87		72.0	
Mouth floor	19	11	8		68.4	
Palate	5	3	2		60.0	
Retromolar	27	15	12		77.8	
Vestibule	2	1	1		100.0	
Nonspecific	3	1	2		100.0	
Laterality[*3]				0.3965		0.8612
00	37	22	15		73.0	
01	230	123	107		79.1	
02	223	123	100		76.7	
03	3	3	0		66.7	
04	0	0	0		NA	
Grade/differentiation				0.1476		**0.0006**
01	287	156	131		80.1	
02	123	60	63		65.0	
03	7	5	2		57.1	
04	1	1	0		100.0	
09	75	49	26		89.3	
Regional lymph nodes examined				0.1550		0.1424
<5	285	160	125		80.4	
>10	134	65	69		73.1	
5~10	73	45	28		74.0	
Clinical stage group				0.0749		0.5689
Stage 0	4	0	4		75.0	
Stage 1	141	79	62		80.1	
Stage 2	73	47	26		71.2	
Stage 3	131	69	62		77.1	
Stage 4	82	50	32		72.0	
Pathologic stage group				0.2540		0.0514
Stage 0	2	2	0		100.0	
Stage 1	215	112	103		82.3	
Stage 2	92	52	40		75.0	
Stage 3	31	15	16		74.2	
Stage 4	58	24	34		67.2	
Clinical tumor size				0.3967		**0.0004**
<2 cm	162	100	62		87.0	
2~4 cm	244	134	110		71.3	
>4 cm	33	19	14		66.7	

Table 1: Continued.

Characteristics	Total	Survived months >36 group	Survived months <36 group	P value[*1]	5-year survival (%)	P value[*2]
Pathology tumor size				0.4417		**0.0141**
<2 cm	197	114	83		81.7	
2~4 cm	183	94	89		69.4	
>4 cm	25	14	11		72.0	
OP group[*4]				**<0.0001**		**<0.0001**
01	385	238	147		81.6	
02	27	14	13		66.7	
03	81	19	62		61.7	

[*1] P value for the comparison of the survival between >36 and <36 months groups.
[*2] P value for 5-year survival among the items of the same characteristics group.
[*3] 0: unknown primary site or the shape of the organ is not paired; 1: the primary site is originated from the right side; 2: the primary site is originated from the left side; 3: only one side is invaded but it is not clear which side (R't or L't) it is originated from; 4: both sides are invaded but the origin of the primary site is not clear and the chart record describes only one primary site.
[*4] OP group for 01: OP only; 02: OP → IA; 03: OP → CT, OP → CT + IV, OP → CT → RT, OP → IA → RT, OP → IV,OP → IV → RT, OP → RT, OP → RT + CT,OP → RT + IV, OP → RT → CT, OP → RT → IA, OP → RT → IV. Symbols: OP: operation; IA: intraarterial chemotherapy; CT: oral chemotherapy; IV: intravenous chemotherapy; RT: radiotherapy; →: then.

3.1.7. Surgical Modalities and Survival. As shown in Table 1, treatment modalities (OP) were further differentiated into 3 groups based on different adjuvant therapies, that is, surgery alone, surgery plus intra-arterial chemotherapy, and surgery plus concomitant chemoradiotherapy. Significant differences between groups were found ($P < 0.0001$), and further analysis of surgical modalities based on the clinical/pathological stages could produce interesting insights.

This hospital-based study followed nearly 500 patients with oral squamous cell carcinoma after surgical treatment. Results showed that age of onset and laterality of tumor location did not influence the treatment outcome. The latter might be attributed to oral cancer being a less multifocal or multicentric disease than, for example, breast cancer and, hence, laterality of the primary tumor has less influence on survival. These findings are in line with previous findings [19, 20].

Advanced tumor stage or failure of locoregional control negatively influences survival in patients with OSCC [21]. However, we did not observe a significant influence from either clinical or pathological tumor stages. Similar to our findings, Pandey et al. reported no difference in survival rates for the extent of tumor [22], and the observed difference might be due to the facts that all stages of tumor have been poured in the analysis.

In the present study, multimodality treatment proved to be a prognostic factor. Benefit from systemic or adjuvant local therapies might correlate with disease biology as the grade of tumor differentiation was also an important influencing factor.

3.2. Data Mining Results Using Apriori Algorithm. Table 2 shows the best rules for OP > 36 months. The head Y and body X represent a class association rule $X \Rightarrow Y$ which means the head Y of an association rule $X \Rightarrow Y$ (with rule body X) must be restricted to one attribute-value pair. The attribute of the attribute-value pair is thus the class attribute. The resulting rules can be evaluated according to three metrics: confidence, lift, and leverage. The minimum value of 1.5 for lift (or improvement) is computed as the confidence of the rule divided by the support of the right-hand-side (RHS). The lift represents the ratio of probability. Given a rule $X \Rightarrow Y$, X and Y occur together to the multiple of the two individual probabilities for X and Y; that is,

$$\text{lift} = \frac{\Pr(X, Y)}{\Pr(L) \cdot \Pr(Y)}. \quad (1)$$

If lift is 1, X and Y are independent. The higher lift is above 1, the more likely that the existence of X and Y together in a transaction is due to a relationship between them and not just random occurrence. Unlike lift, leverage measures the difference between the probability of co-occurrence of X and Y as the independent probabilities of each of X and Y; that is,

$$\text{leverage} = \Pr(X, Y) - \Pr(X) \cdot \Pr(Y). \quad (2)$$

Leverage measures the proportion of additional cases covered by both X and Y above those expected if X and Y were independent of each other. Thus, for leverage, values above 0 are desirable whereas values greater than 1 are desirable for lift. Finally, conviction is similar to lift, but it measures the effect of the right-hand side not being true and also inverts the ratio. Conviction is measured as

$$\text{conviction} = \frac{\Pr(X) \cdot \Pr(\text{not } Y)}{\Pr(X, Y)}. \quad (3)$$

Table 2 shows that the rule "grade/differentiation = 2 and clinical stage group = early" is associated with the rule "primary site = tongue and group = OP." The rule shows 49 patients as being grade/differentiation = 2 and clinical stage

Table 2: Ranking of the top 10 best rules found in survival larger than 36 months.

Body[*1]	No.	Head[*1]	No.	Confidence	Lift[*2]	Leverage	Conviction
Grade/differentiation = 2 Clinical stage group = early	49	Primary site = tongue Group = OP	27	0.55	1.91	0.05	1.52
Primary site = tongue Group = OP	78	Grade/differentiation = 2 Clinical stage group = early	27	0.35	1.91	0.05	1.23
Primary site = tongue Clinical stage group = early	70	Grade/differentiation = 2 Group = OP	27	0.39	1.9	0.05	1.27
Grade/differentiation = 2 Group = OP	55	Primary site = tongue Clinical stage group = early	27	0.49	1.9	0.05	1.41
Grade/differentiation = 2	60	Primary site = tongue Clinical stage group = early Group = OP	27	0.45	1.88	0.05	1.34
Primary site = tongue Clinical stage group = early Group = OP	65	Grade/differentiation = 2	27	0.42	1.88	0.05	1.3
Primary site = tongue	88	Grade/differentiation = 2 Clinical stage group = early Group = OP	27	0.31	1.81	0.04	1.18
Grade/differentiation = 2 Clinical stage group = early Group = OP	46	Primary Site = tongue	27	0.59	1.81	0.04	1.55
Grade/differentiation = 2	60	Primary site = tongue Clinical stage group = early	27	0.45	1.74	0.04	1.31
Primary site = tongue Clinical stage group = early	70	Grade/differentiation = 2	27	0.39	1.74	0.04	1.24

[*1]Stages 0 to 3 of clinical stage group and pathologic stage group as shown in Table 1 are regarded as early and stage 4 is regarded as late stage in Table 2.
[*2]The best rules with lift >1.5 were shown here.

group = early, while 27 of these 49 patients fulfill the rules "primary site = tongue and group = OP." The confidence shows the proportion of the rule "primary site = tongue and group = OP" in the rule "grade/differentiation = 2 and clinical stage group = early," that is, 27/49. The lift is 1.91, meaning the existence of rule "grade/differentiation = 2 and clinical stage group = early" and rule "primary site = tongue and group = OP" together in a transaction is not just a random occurrence. The leverage value of 0.05 means that the proportion of additional cases covered by both rule "grade/differentiation = 2 and clinical stage group = early" and rule "primary site = tongue and group = OP" are greater than those that would be expected if these two rules were independent of each other. The conviction value of 1.52 indicates the effect of the right-hand side is not being true.

From the top down in Table 2, the lift values gradually decrease but still show a high correlation between the body/head and survival of >36 months. When the Apriori algorithm-based lift value of the items listed in "body" and "head" of Table 2 is high, there is less chance of misinterpretation of the relationships between each item. Judging by the top 8 results, the same items such as grade/differentiation = 2, clinical stage group = early, primary site = tongue, and group = OP flowed between the "body" and "head". These data suggest that early stage tongue cancer with moderate differentiation will have a better survival (>36 months) with varied surgical approaches where the OP has three kinds of treatments.

Judging by the top 9 to 10 results, however, only three items are included without the group = OP and their lift values are decreased to 1.74. These results suggest that the factor of "group = OP" is not important to the top 9 to 10 results and is less strongly correlated compared with the top 8 results. It also implies that the OP plays an important role in creating a correlation with improved survival (>36 months). In clinical settings, this might be due to good treatment outcome which often accompanies surgery.

Accordingly, our proposed Apriori algorithm is a relatively simple form of rule-based computation to identify potential rules involving various factors, such as grade/differentiation = 2, clinical stage group = early, primary site = tongue, and group = OP. The algorithm can reveal the combination effect of these factors on the outcome of OSCC therapy.

4. Conclusion

This hospital-based analysis reviewed 493 patients with OSCC to mine survival factors in operation-centric patients. The results identify the importance of grade/differentiation = 2, clinical stage group = early, primary site = tongue, and group = OP in predicting higher survival for OSCC patients.

Conflict of Interests

The authors have no conflict of interests to declare.

Acknowledgments

This work was partly supported by the National Science Council in Taiwan (under Grant no. NSC101-2320-B-037-049, NSC101-2622-E-151-027-CC3, and NSC102-2221-E-151-024-MY3), by the Department of Health (DOH102-TD-C-111-002), and by NSYSU-KMU Joint Research Project (NSYSUKMU 102-034).

References

[1] Y. C. Ko, Y. L. Huang, C. H. Lee, M. J. Chen, L. M. Lin, and C. C. Tsai, "Betel quid chewing, cigarette smoking and alcohol consumption related to oral cancer in Taiwan," *Journal of Oral Pathology and Medicine*, vol. 24, no. 10, pp. 450–453, 1995.

[2] Y.-C. Ko, T.-A. Chiang, S.-J. Chang, and S.-F. Hsieh, "Prevalence of betel quid chewing habit in Taiwan and related sociodemographic factors," *Journal of Oral Pathology and Medicine*, vol. 21, no. 6, pp. 261–264, 1992.

[3] M.-S. Yang, I.-H. Su, J.-K. Wen, and Y.-C. Ko, "Prevalence and related risk factors of betel quid chewing by adolescent students in southern Taiwan," *Journal of Oral Pathology and Medicine*, vol. 25, no. 2, pp. 69–71, 1996.

[4] C.-F. Lin, J.-D. Wang, P.-H. Chen, S.-J. Chang, Y.-H. Yang, and Y.-C. Ko, "Predictors of betel quid chewing behavior and cessation patterns in Taiwan aborigines," *BMC Public Health*, vol. 6, article 271, 2006.

[5] M.-H. Chien, T.-H. Ying, Y.-H. Hsieh et al., "Tumor-associated carbonic anhydrase XII is linked to the growth of primary oral squamous cell carcinoma and its poor prognosis," *Oral Oncology*, vol. 48, no. 5, pp. 417–423, 2012.

[6] A. K. Markopoulos, "Current aspects on oral squamous cell carcinoma," *The Open Dentistry Journal*, vol. 6, pp. 126–130, 2012.

[7] I. van der Waal, R. de Bree, R. Brakenhoff, and J.-W. Coebergh, "Early diagnosis in primary oral cancer: is it possible?" *Medicina Oral, Patología Oral y Cirugía Bucal*, vol. 16, no. 3, pp. e300–e305, 2011.

[8] C.-Y. Yen, C.-H. Chen, C.-H. Chang et al., "Matrix metalloproteinases (MMP) 1 and MMP10 but not MMP12 are potential oral cancer markers," *Biomarkers*, vol. 14, no. 4, pp. 244–249, 2009.

[9] C. Y. Yen, C. Y. Huang, M. F. Hou et al., "Evaluating the performance of fibronectin 1 (FN1), integrin alpha4beta1 (ITGA4), syndecan-2 (SDC2), and glycoprotein CD44 as the potential biomarkers of oral squamous cell carcinoma (OSCC)," *Biomarkers*, vol. 18, no. 1, pp. 63–72, 2013.

[10] C. H. Lee, C. Y. Yen, S. Y. Liu et al., "Axl is a prognostic marker in oral squamous cell carcinoma," *Annals of Surgical Oncology*, vol. 19, supplement 3, pp. S500–S508, 2012.

[11] C.-Y. Yen, S.-Y. Liu, C.-H. Chen et al., "Combinational polymorphisms of four DNA repair genes XRCC1, XRCC2, XRCC3, and XRCC4 and their association with oral cancer in Taiwan," *Journal of Oral Pathology and Medicine*, vol. 37, no. 5, pp. 271–277, 2008.

[12] W.-L. Lo, S.-Y. Kao, L.-Y. Chi, Y.-K. Wong, and R. C.-S. Chang, "Outcomes of oral squamous cell carcinoma in Taiwan after surgical therapy: factors affecting survival," *Journal of Oral and Maxillofacial Surgery*, vol. 61, no. 7, pp. 751–758, 2003.

[13] J. S. Brown, R. J. Shaw, F. Bekiroglu, and S. N. Rogers, "Systematic review of the current evidence in the use of postoperative radiotherapy for oral squamous cell carcinoma," *British Journal of Oral and Maxillofacial Surgery*, vol. 50, no. 6, pp. 481–489, 2012.

[14] M. Zhu, Z. Zhang, J. P. Hirdes, and P. Stolee, "Using machine learning algorithms to guide rehabilitation planning for home care clients," *BMC Medical Informatics and Decision Making*, vol. 7, article 41, 2007.

[15] M. Toussi, J.-B. Lamy, P. Le Toumelin, and A. Venot, "Using data mining techniques to explore physicians' therapeutic decisions when clinical guidelines do not provide recommendations: methods and example for type 2 diabetes," *BMC Medical Informatics and Decision Making*, vol. 9, article 28, 2009.

[16] Y. J. Hu, T. H. Ku, R. H. Jan, K. Wang, Y. C. Tseng, and S. F. Yang, "Decision tree-based learning to predict patient controlled analgesia consumption and readjustment," *BMC Medical Informatics and Decision Making*, vol. 12, article 131, 2012.

[17] W. Hwang, Y. Hwang, S. Lee, and D. Lee, "Rule-based multi-scale simulation for drug effect pathway analysis," *BMC Medical Informatics and Decision Making*, vol. 13, supplement 1, p. S4, 2013.

[18] R. Agrawal and R. Srikant, "Fast algorithms for mining association rules," in *Proceedings of the 20th International Conference on Very Large Data Bases (VLDB '94)*, 1994.

[19] R. Yerushalmi, H. Kennecke, R. Woods, I. A. Olivotto, C. Speers, and K. A. Gelmon, "Does multicentric/multifocal breast cancer differ from unifocal breast cancer? an analysis of survival and contralateral breast cancer incidence," *Breast Cancer Research and Treatment*, vol. 117, no. 2, pp. 365–370, 2009.

[20] J.-C. Jan, W.-H. Hsu, S.-A. Liu et al., "Prognostic factors in patients with buccal squamous cell carcinoma: 10-year experience," *Journal of Oral and Maxillofacial Surgery*, vol. 69, no. 2, pp. 396–404, 2011.

[21] J. S. Cooper, T. F. Pajak, A. A. Forastiere et al., "Postoperative concurrent radiotherapy and chemotherapy for high-risk squamous-cell carcinoma of the head and neck," *The New England Journal of Medicine*, vol. 350, no. 19, pp. 1937–1944, 2004.

[22] M. Pandey, R. Bindu, and C. S. Soumithran, "Results of primary versus salvage surgery in carcinoma of the buccal mucosa," *European Journal of Surgical Oncology*, vol. 35, no. 4, pp. 362–367, 2009.

Hindawi Publishing Corporation
BioMed Research International
Volume 2013, Article ID 349437, 8 pages
http://dx.doi.org/10.1155/2013/349437

Research Article

Dose Verification in Intensity Modulation Radiation Therapy: A Fractal Dimension Characteristics Study

Jia-Ming Wu,[1,2,3] Chung-Ming Kuo,[1,4] and Ching-Jiang Chen[4]

[1] *Department of Information Engineering, I-Shou University, No. 1, Sec. 1, Syuecheng Road, Dashu District, Kaohsiung City 84001, Taiwan*
[2] *Department of Radiation Oncology, E-Da Hospital, Kaohsiung, Taiwan*
[3] *Department of medical Imaging and Radiological Science, Central Taiwan University of Science and Technology, Taichung, Taiwan*
[4] *Department of Medical Imaging and Radiological Sciences, I-Shou University, No. 1, Sec. 1, Syuecheng Road, Dashu District, Kaohsiung City 84001, Taiwan*

Correspondence should be addressed to Chung-Ming Kuo; kuocm@isu.edu.tw

Received 25 April 2013; Accepted 3 June 2013

Academic Editor: Ching Chong Jack Yang

Purpose. This study describes how to identify the coincidence of desired planning isodose curves with film experimental results by using a mathematical fractal dimension characteristic method to avoid the errors caused by visual inspection in the intensity modulation radiation therapy (IMRT). *Methods and Materials.* The isodose curves of the films delivered by linear accelerator according to Plato treatment planning system were acquired using Osiris software to aim directly at a single interested dose curve for fractal characteristic analysis. The results were compared with the corresponding planning desired isodose curves for fractal dimension analysis in order to determine the acceptable confidence level between the planning and the measurement. *Results.* The film measured isodose curves and computer planning curves were deemed identical in dose distribution if their fractal dimensions are within some criteria which suggested that the fractal dimension is a unique fingerprint of a curve in checking the planning and film measurement results. The dose measured results of the film were presumed to be the same if their fractal dimension was within 1%. *Conclusions.* This quantitative rather than qualitative comparison done by fractal dimension numerical analysis helps to decrease the quality assurance errors in IMRT dosimetry verification.

1. Introduction

Cancer has been treated by using radiation for more than a century, and, today, more than half of all cancer treatments utilize radiation therapy. Intensity modulated radiation therapy (IMRT) [1–6] is a remarkably advanced radiation therapy technique for the treatment of various kinds of cancers. The computer then optimizes the best treatment to maximize the radiation dose delivered to the tumor while minimizing the radiation dose delivered to the surrounding normal tissues [7–9]. However, not only the planning of treatment but also the dose delivery technique is more complicated than for three dimensional conformal therapy [10]. In other words, the importance of quality assurance (QA) [11] procedure in Intensity Modulation Radiation Therapy (IMRT) should be enhanced compared to that of conventional conformal radiation treatment.

The QA process usually includes verification of intensity map to radiation field coincidence by film [12]. Irrespective of the method chosen for quality assurance, dosimetric verification criteria for IMRT treatment plans are based upon either the analysis of a limited number of points in low-dose gradient areas or the measurement of distances between isodose lines in high-dose gradient areas. Radiation oncologists and medical physicists usually compare the desired dose and film measurement results by placing these transparency films side by side to visualize their discrepancy or by superimposing these films of isodose curves onto planning results to check the difference. Whatever method is used, visual inspection leads to in accordance with person to person philosophical

errors. The integrity of complexity of the IMRT dose delivery technique relies on quantification of the coincidence of the planned and delivered intensity-modulated radiation therapy dose distributions.

The aim of this study was to ascertain how to identify the coincidence of the planned and desired isodose curves and experimental film results, without visual inspection but using a mathematical method to estimate the error between the planned and measured values.

2. Materials and Methods

The treatment planning system Plato was used to implement IMRT for cancer treatment and the Elekta precise linear accelerator "step and shoot" technique was used to deliver the planned desired dose. The output was first checked before IMRT QA; this was normally performed for a standard set. Relative dosimetry was given to all subsequent measurements, which were compared to the dose at the absolute calibration point. It was not practical to check the patient dose by imitating the patient contour and anatomy case by case. Therefore, before the treatment plan was accomplished, the planning parameters were acquired from a cubic solid water phantom, from which images were acquired in advance of implementing a test planning. This was done by setting the irradiation beam onto the cubic phantom surface vertically according to the patient planning parameters portal by portal to simplify the dose distribution checking procedure.

The dose distributions adopted in the pseudocubic phantom were delivered by using a linear accelerator, and the irradiation fields were measured with a therapy verification film (Kodak, X-Omat V, Eastman Kodak Company, Rochester, NY, USA) using a standard procedure. The film was placed in a solid water phantom (PTW, white polystyrene "RW3," PTWFREIBURG, Freiburg, Germany) and developed by means of an automatic procedure. No specific calibration was made; however, the film was exposed to a dose value to guarantee that it was in the dose-density linear region of the H-D curve [13]. All films were read with an optical scanner (Vidar, VXR-12, VIDAR Systems Corporation, Herndon, VA, USA) to create the relative isodose curves. These isodose curves were acquired using Osiris (Geneva University Hospital, version 3.5) to aim directly at a single interested dose curve for fractal [14] characteristic analysis, described in detail later. All dose curves were composed of the segments, and each segment was composed of beamlets. The combination of beamlets penumbra and superimposition of tiny open fields during dose delivery led to each isodose curve having its own exclusive fractal characteristics. One of the interesting curves was selected to measure the length or area encompassed by the curve. The fundamental idea is to assume that the two quantities—the length of the curve and the scale—do not vary arbitrarily but instead are related by a law which allows us to compute one quantity from the other.

2.1. Self-Similarity Dimension. According to Figure 1, the Koch curve can be divided into four self-similar parts, which are similar to the entire curve via a similarity transformation which is reduced by a reduction factor of 3, with the relationship $A = 1/S^{\mathrm{Ds}}$ (where A represents the number of bar pieces, Ds denotes the self-similarity dimension, and S is the scale of reduction factor). Similarly, for the interested line, there is a nice power law relationship between the length of bar pieces u and the reduction factor S. This law is $u = 1/S^d$, where d is the slope in the log/log diagram. Here, we can introduce the relationship between the power law of the length measurement using different compass settings and the self-similarity dimension of a fractal curve, and use this self-similarity dimension as the identification of a curve. The relationship is simple, namely, $\mathrm{Ds} = 1 + d$, where d denotes the slope in the log / log diagram of the length of bar pieces u versus precision $1/S$; that is, $u = c/S^d$, and we simplify by choosing appropriate units of length measurements such that the factor c in the power law becomes unity, and $u = 1/S^d$.

Taking into consideration logarithms, we obtain

$$\log u = d \cdot \log \frac{1}{S}, \tag{a}$$

where, again, u is the length of bar pieces with respect to compass settings. On the other hand, we have the power law $A = 1/S^{\mathrm{Ds}}$, where A denotes the number of bar pieces in a replacement step of the self-similar fractal with scale reduction factor S. In the logarithmic form, this is

$$\log A = \mathrm{Ds} \cdot \log \frac{1}{S}. \tag{b}$$

Note that the connection between u (the length of bar) and A stands for the number of pieces, when measuring at some other scales, where the whole object is composed of a small copies each of size S, and then we measure a total length of A times S, and $u = A \cdot S$. Taking logarithms into consideration again,

$$\log u = \log A + \log S. \tag{1}$$

In this equation, we can substitute the logarithms $\log u$ and $\log A$ from (a) and (b) above.

This yields

$$d \cdot \log \frac{1}{S} = \mathrm{Ds} \cdot \log \frac{1}{S} + \log S. \tag{2}$$

Since

$$\log \frac{1}{S} = -\log S, \tag{3}$$

we get

$$-d \cdot \log S = -\mathrm{Ds} \cdot \log S + \log S. \tag{4}$$

Dividing by $\log S$ and sorting terms, we finally arrive at

$$\mathrm{Ds} = 1 + d. \tag{5}$$

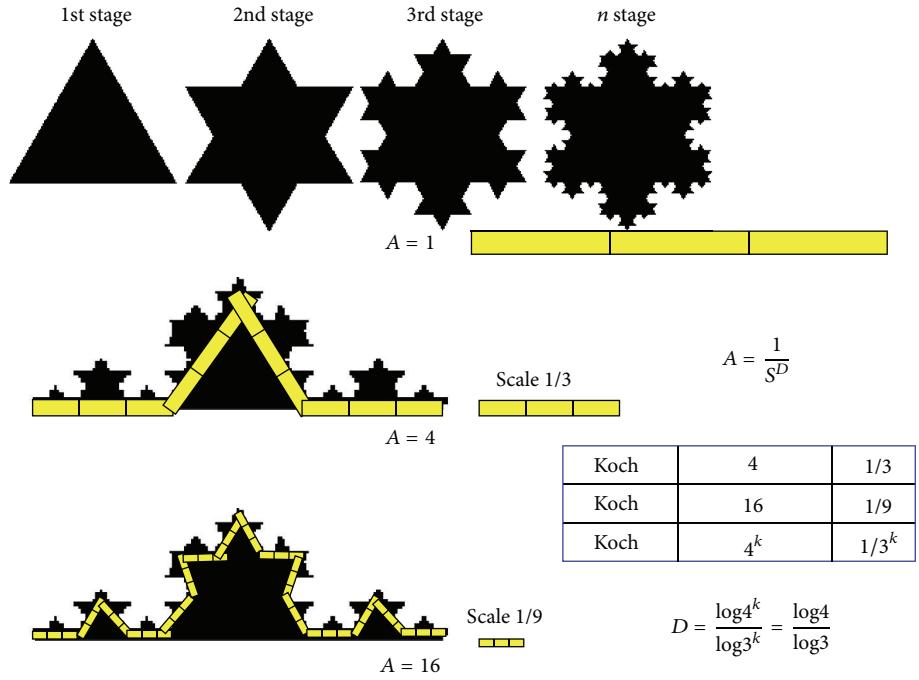

Figure 1: This figure illustrates the understanding and meaning of the power law behavior in a pure mathematical situation in Koch Island. Each Koch curve can be divided into four self-similar parts, which are similar to the entire curve via a similarity transformation which in turn is similar to the entire curve of Figure 3.

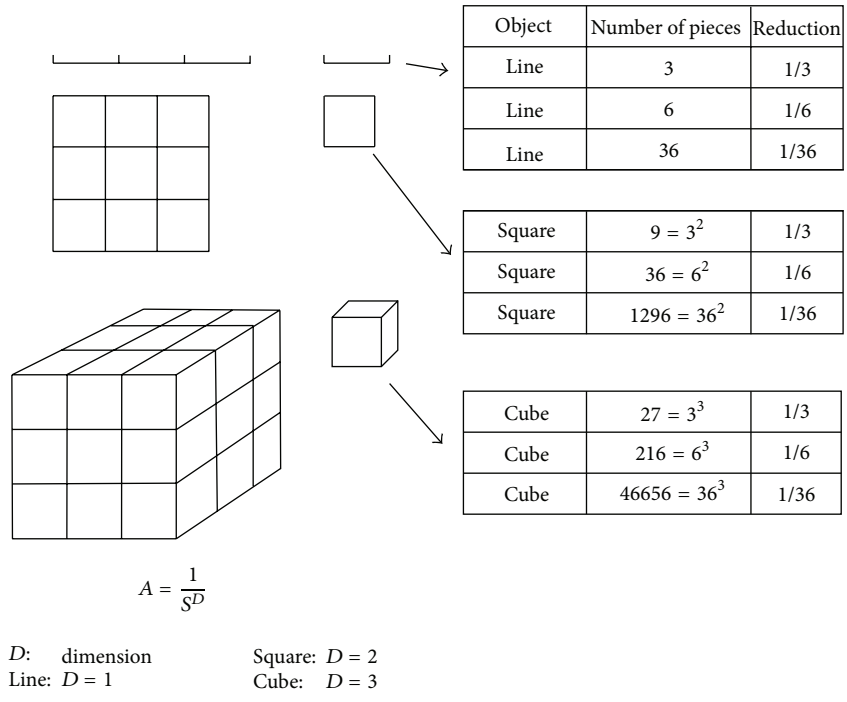

Figure 2: The relationship between the reduction factor (scaling factor) and the number of scaleddown pieces into which the structure is divided. Apparently, for the line, square, and cube, there is a nice power law relationship between the numbers of pieces, a, and the reduction factors. This law is $a = 1/S^D$ where $D = 1$ for the line, $D = 2$ for the square, and $D = 3$ for the cube.

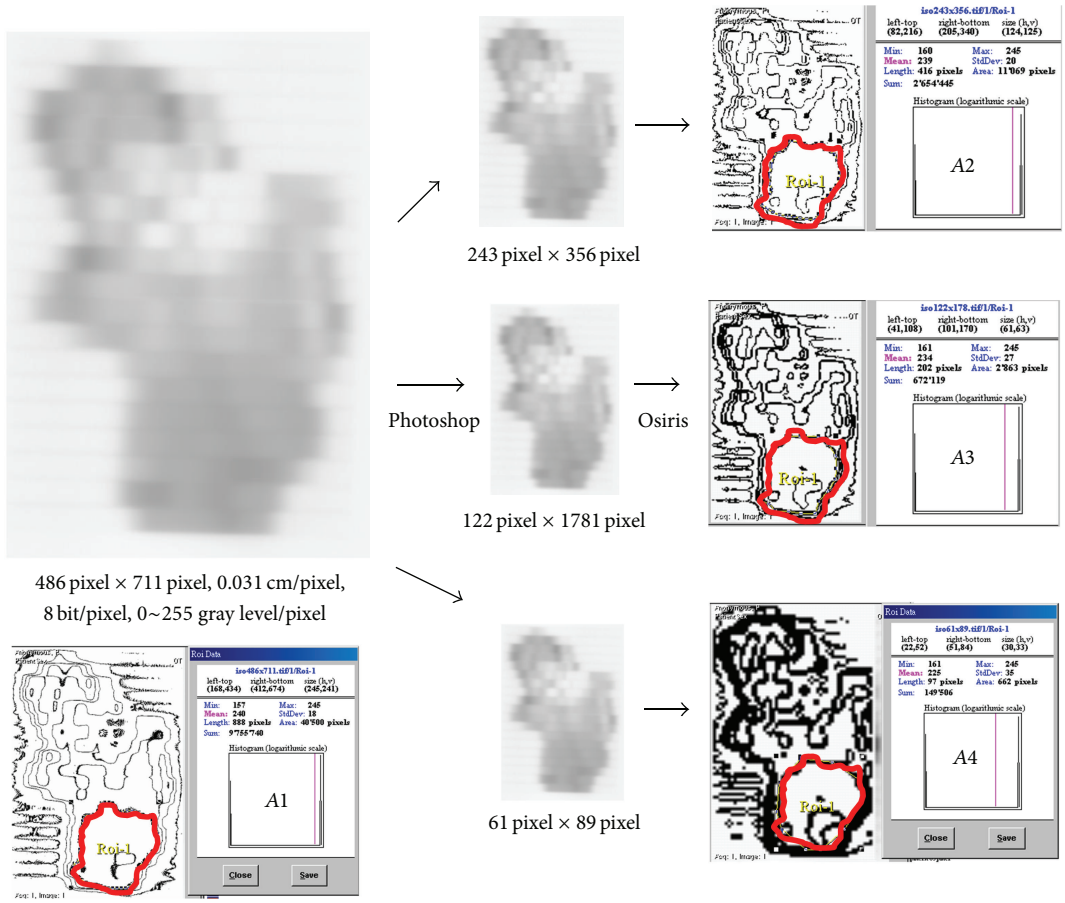

Figure 3: This figure shows how the dose curve is adopted for fractal analysis. The original resolution (left on the figure) is 486 pixels × 711 pixels with 8 bits/pixel. The scale is then reduced by 1/2, 1/4, and 1/8 (from right up to right bottom) to give 243 × 356, 122 × 178, and 61 × 89 pixels to measure the length of the same isodose curve adopted in the film. The planning dose curve Ds is then compared to that of planning result. The curve of low resolution (lower right) is coarse and big while high resolution (upper right) shows slim curves.

2.2. Reduction Factor of Geometry Structure. According to Figure 2 and the relationship between the reduction factor (scaling factor) and the number of scaled down pieces into which the structure is divided, apparently, for the line, square, and cube, there is a nice power law relationship between the numbers of pieces and the reduction factors. This is the law relationship between the number of pieces and the reduction factors. This law is

$$A = \frac{1}{S^D}, \tag{6}$$

where $D = 1$ for the line, $D = 2$ for the square, and $D = 3$ for the cube. Here we see that the reduction factor is 1/3 which is, of course, arbitrary. We could alternatively have chosen 1/2, 1/7, or 1/365. However, precisely in this fact lies the difference between these figures and the isodose curves in which we are interested (fractal structures). The reduction factors are characteristic for any fractal structures, so that the self-similarity dimension is a unique choice to represent an isodose curve.

2.3. Film Manipulation after Dose Delivery. In Figure 3, film images are acquired using Osiris from FIPS Laser densitometer at a resolution of 486 × 711 pixels with 8 bits/pixel. Consider a region of interest (e.g., an isodose curve in which we are interested), then measure the length of this curve, and reduce to the original scales of 1/2, 1/4, 1/8, which are 243 × 356, 122 × 178, and 61 × 89 pixels, respectively. It is obviously the low resolution (lower right) which reveals coarse and big curves while slim curves are shown for high resolution (upper right).

2.4. Length versus (1/Scale) Logarithms. In Figure 4, take the logarithm of the length of each region of interest and logarithm (1/scale), and then plot the log(length) against log(1/scale), where the slope is in the form $y = ax + b$. According to Figure 4, the slope of the fitted line is 0.9841 and, in accordance, $\mathrm{Ds} = 1 + d$; that is, the self-similarity dimension is equal to 1 + 0.9841.

2.5. Plan Isodose Curves Manipulation. The plan isodose curves are also acquired using Osiris for deriving their self-similarity dimension. The original format is 486 × 711 pixels with 8 bits/pixel; the scale is then reduced by 1/2, 1/4 and 1/8, which gives 243 × 356, 122 × 178 and 61 × 89 pixels to measure the length of the same isodose curve adopted in the film.

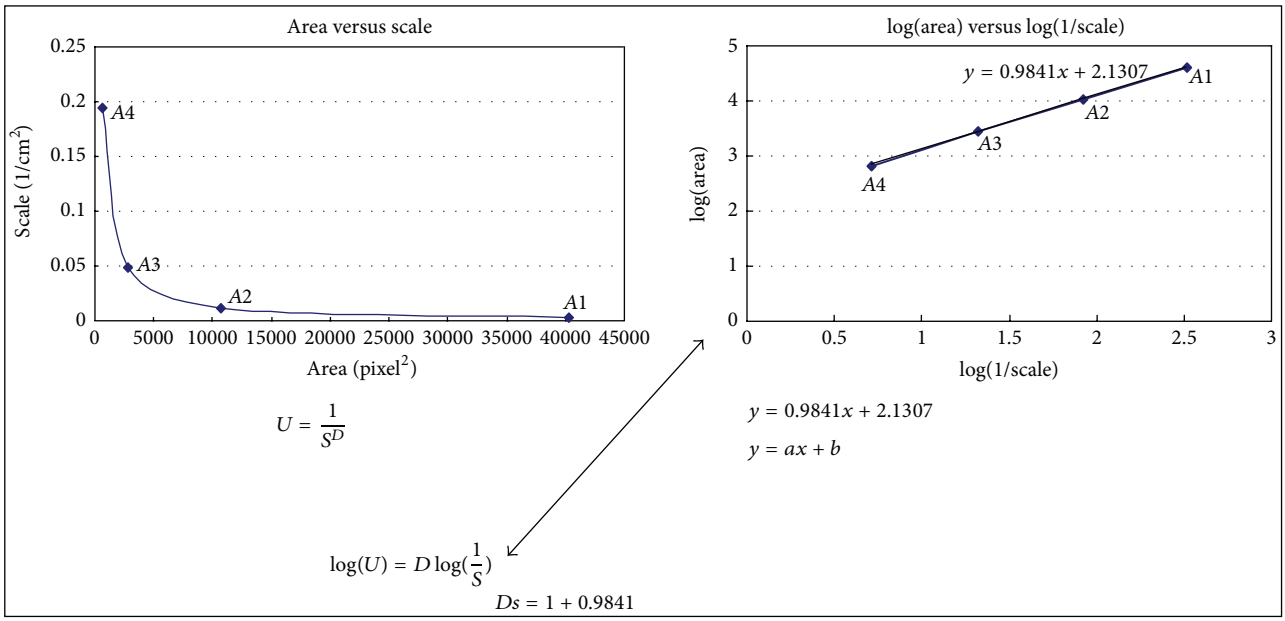

FIGURE 4: The law seems to be relevant of scale verse tarea on left hand side in this figure, which is a power law of the form $y \propto x^d$ (where y denotes the length, x denote the scale, and d is the dimension). Take the logarithm of the length of each region of interest and logarithm (1/scale), and then plot log(length) against log(1/scale); then the slope is in the form $y = ax + b$. The slope can represent the unique characteristics of the curve.

The planning dose curves, Ds, are then compared to those of the film result.

3. Results

Validation studies carried out in this manner have consistently shown point doses delivered at isocenter using Elekta medical linear accelerator to be within a maximum of 3.5% of those predicted by Plato treatment planning system in high-dose, low-gradient regions, with 99% of points in high-gradient, high-dose regions falling within 3.6 mm of predicted positions.

Phantom plans and film images were registered and normalized at the cross isocenter for further fractal study. The percentage of the pixels in high-dose low-gradient areas of the dose distribution for all analyzed phantom plans was within the 3.5% tolerance level. The percentage of the pixels throughout the entire area of the dose distribution for all analyzed phantom plans was within the 10% tolerance level.

Figure 3 shows an interesting phenomenon: dose curves are coarse and big for low resolution while slim curves are found for high resolution. When checking the length or area encompassed by the interested curve, the length or area appears as a geometric progression, followed by an increasing scale rather than an arithmetic progression.

The 85% region of the interested planning isodose curve's Ds is 1.9852, and the 85% region of the interested film isodose curve's Ds is 1.9841. The discrepancy is only 5×10^{-4}[(1.9852 − 1.9841)/1.9852] (as in Figure 5). The planning 85% isodose curve and film 85% isodose curve are supposed to be identical if the differences between their Ds values are within 1%.

4. Discussion

A fractal dimension is a ratio providing a statistical index of complexity comparing how the detail in a pattern (strictly speaking, a fractal pattern) changes with the scale at which it is measured. Consequently, it is necessary to develop sophisticated tools to compare measured and calculated dose distributions in order to verify the accuracy of the results of the planned dose distribution. Different methods have been developed to evaluate the accordance between measured and calculated doses, such as the point-to-point dose difference or the evaluation of the distance between two closed points having the same dose value. The verification method proposed by Low seems to be more complete since it takes into account both the dose difference (DD) and the distance to agreement (DTA), allowing the definition of a "score" of an interested dose distribution. The gamma value test at each point of interest gives real-time information useful for the decision making of the treatment plan. All these methods play different roles in dose verification, and this study describes how to identify the coincidence of desired planning isodose curves with film experimental results by using a mathematical fractal dimension characteristic method to avoid the errors caused by visual inspection.

4.1. Mosaic Amalgamation. When the coincidence of film and fluence map created by IMRT plan is compared, the position of light field borders is normally evaluated by visual observation [15]. It is trivial that this method is subjective, and each operator may introduce an error in locating each border. Strictly, the light field border should coincide with the 50% decrement line of the maximum central lightening, and

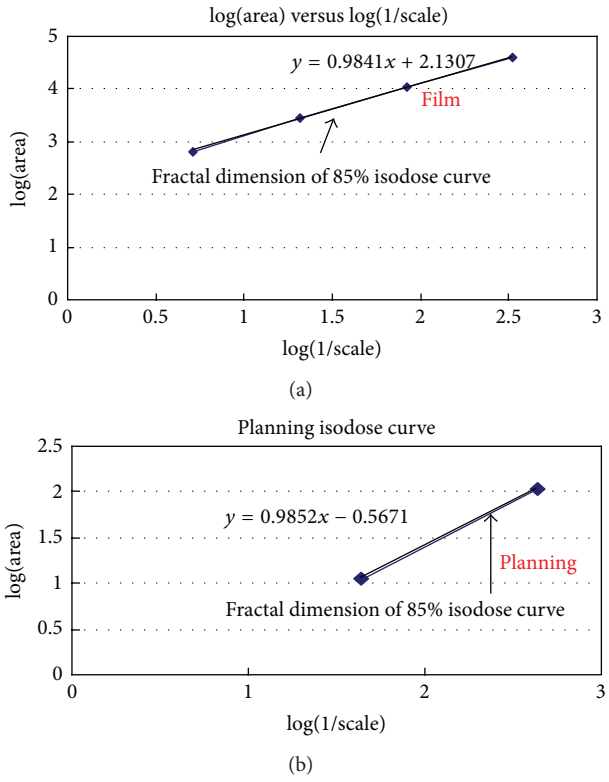

FIGURE 5: When these two dose distributions are normalized at their cross hair isocenter, the 88% region of the interested planning isodose curve's Ds is 1.9852, and the 88% region of the interested film isodose curve's Ds is 1.9841. The discrepancy is only 5×10^{-4}[(1.9852–1.9841)/1.9852]. The planning 88% isodose curve and film 88% isodose curve are supposed to be identical if the difference between their Ds values is within 1%.

this limit should be measured with the help of an appropriate device [16]. Because the human eye is not able to detect the 50% light field contour exactly, in this work, a photosensitive diode was employed to test the actual size of the light field selected on a linear accelerator. This ratiocination leads us to compare the plan and film results with unavoidable errors by a traditional method based on human observation. In order to avoid the human visualization inaccuracy with numerical manner, when the gray level films are converted to relative isodose curves, the interested isodose curve's length is measured using mosaic amalgamation. The profile (interested isodose curve) to be evaluated is overlaid by a rectangular grid, as shown in Figures 6(a) and 6(b). The square elements of the grid that sit on the boundary can be regarded as square tiles thrown onto the perimeter of the profile.

4.2. Geometric Progression. Planning dose curves were acquired using the Osiris software for further comparison with the film result described previously. First of all, planning dose curves were normalized to their cross hair isocenter, and the matrix was set to the same as the film. The interesting dose curve of 88% was then adopted for fractal dimension analysis as in Figure 5. The fractal dimension of planning 88% was 1.9852, and the discrepancy was only 5×10^{-4} when compared to that of film.

4.3. Criterion of Acceptability. According to Figure 7, the selected curve of 85% is interesting to study. Now the problem arises, when the fractal dimension of planning and films isodose curves are compared, in determining what fractal dimension variation is still acceptable in order to say that the two can be regarded as the same. In order to decide at what range of variation of fractal dimension is still acceptable, we need to check the fractal dimension variation magnitude by varying the dose curves from descending downwards and increasing upwards. If the limitation for the variation in the dose curve was set to be 2%, say 83% and 87%, then the fractal dimension of 85% varied from 1.9841 to 1.9911 and 1.9626 of 83% and 87%, respectively. The variation of fractal dimension is within 1% and the outcomes from the isodose curves descending downwards as well as increasing upwards look acceptable. The results imply that the two curves are identical only if their fractal dimension is within 1%. The fractal dimension provides an easier way to identify the two curves.

4.4. Automated Calculation of Fractal Dimension. Work is still ongoing to develop automated calculation of fractal dimension by tracing around the perimeter with an appropriate autosegmentation technique [17]. The coordinates of many points on the perimeter are transferred to the memory to generate data for the evaluation of the fractal structure of the boundary, so that a series of polygons, using a series of paced-out distances along the profile, are constructed.

5. Conclusions

Individual IMRT fields generated by the treatment planning system can be verified by film dosimetry in a cubic phantom at a depth of 5 cm. Usually, personnel is used to make side-by-side comparisons of calculated versus measured dose distributions. The calculated and measured dose distributions are compared either superimposed or side by side or by viewing the differences between the two. However, comparing shapes of isodose distributions as measured by film dosimetry and predicted by treatment planning can be more accurately done by numerical analysis as compared to visual inspection. This quantitative rather than qualitative comparison will help decrease errors in dosimetry verification.

Isodose curves measured by film and predicted by computer planning curves are identical if their fractal dimensions are the same. Therefore, fractal dimension is a unique fingerprint of each isodose curve.

Conflict of Interests

Part of this study was presented on the Sixth International Conference on Genetic and Evolutionary Computing (ICGEC-2012), August 25–28, 2012, Kitakyushu, Japan.

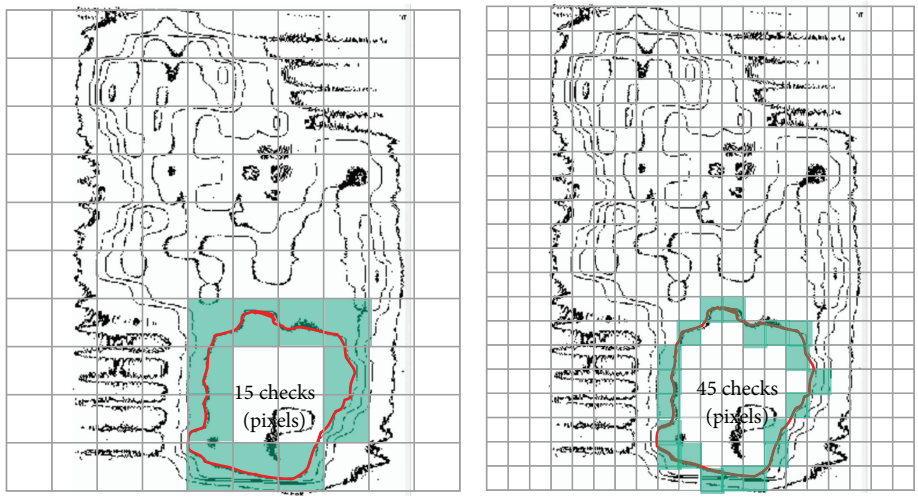

Figure 6: The relationship between length and scale (tiles size) can be implemented by transforming an image into a mosaic and regarding the elements (individual tiles) of the mosaic as being square tiles laid around the boundary. The mosaic transformation can be used to set up a procedure for evaluating the fractal structure of the boundary by a technique known as mosaic amalgamation. The perimeter estimated in (a) is smaller than (b) due to the larger scale (the length of the mosaic tile) used in (a).

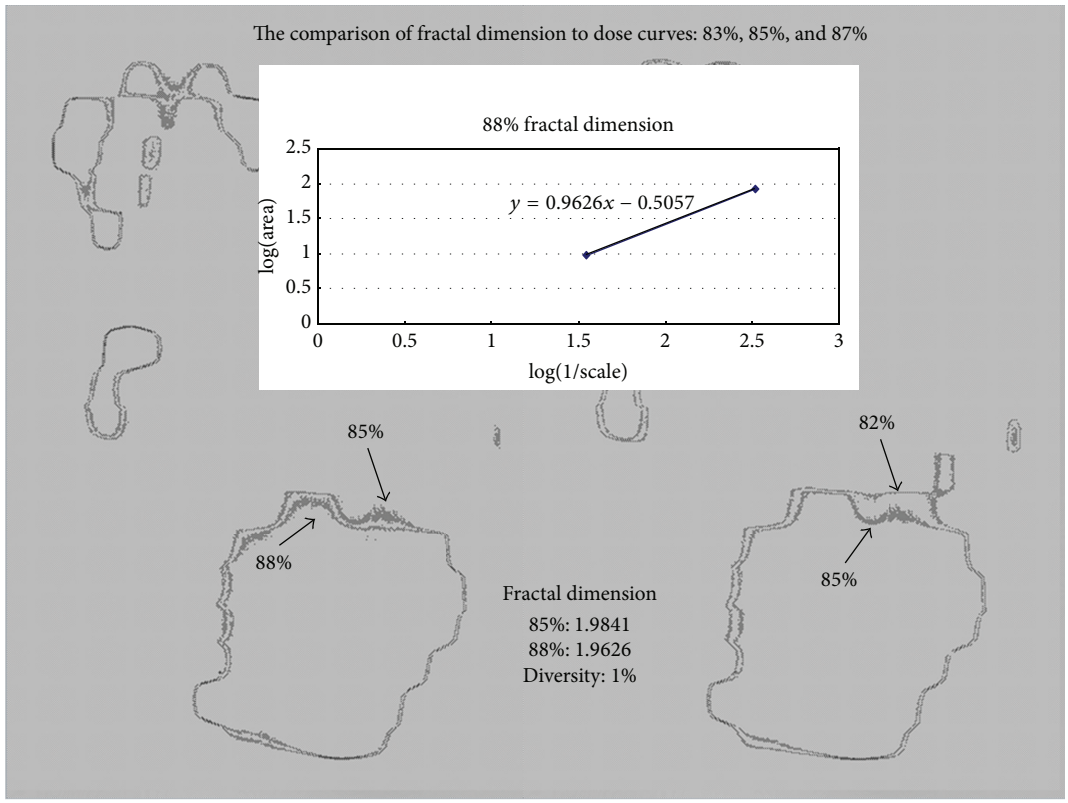

Figure 7: In this figure, the selected 85% is interesting to study. The fractal dimension magnitude criterion of acceptability between the desired planning curves and the delivered dose curves can be made by descending or increasing the isodose curves from 85% downwards or upwards to see which isodose curve is still regarded as one fractal value. When the fractal dimensions, 83% and 87%, are compared to 85% curve, the variation of fractal dimension is within 1%, which means that the two curves are identical only if their fractal dimension is within 1%.

Authors' Contribution

Jia-Ming Wu is the study coordinator. Jia-Ming Wu wrote the paper. It was the original idea and concept of Jia-Ming Wu and Chung-Ming Kuo. Jia-Ming Wu and Chung-Ming Kuo did the final revision of the paper. Jia-Ming Wu and Chung-Ming Kuo designed and developed the study. Jia-Ming Wu and Ching-Jiang Chen collected the data. Jia-Ming Wu and Ching-Jiang Chen did the statistical analysis. All authors read and approved the final paper.

References

[1] M. Nauta, J. E. Villarreal-Barajas, and M. Tambasco, "Fractal analysis for assessing the level of modulation of IMRT fields," *Medical Physics*, vol. 38, no. 10, pp. 5385–5393, 2011.

[2] T.-F. Lee, F.-M. Fang, P.-J. Chao, T.-J. Su, L. K. Wang, and S. W. Leung, "Dosimetric comparisons of helical tomotherapy and step-and-shoot intensity-modulated radiotherapy in nasopharyngeal carcinoma," *Radiotherapy and Oncology*, vol. 89, no. 1, pp. 89–96, 2008.

[3] S. Clemente, B. Wu, G. Sanguineti et al., "SmartArc-based volumetric modulated arc therapy for oropharyngeal cancer: a dosimetric comparison with both intensity-modulated radiation therapy and helical tomotherapy," *International Journal of Radiation Oncology Biology Physics*, vol. 80, no. 4, pp. 1248–1255, 2011.

[4] M. Tambasco, I. Nygren, J. Villarreal-Barajas, and A. M. Sci-Thur, "Planning-09: assessing dynamic IMRT field modulation in prostate plans," *Medical Physics*, vol. 39, no. 7, 2012.

[5] S. W. Leung, T.-F. Lee, C.-Y. Chien, P.-J. Chao, W.-L. Tsai, and F.-M. Fang, "Health-related Quality of life in 640 head and neck cancer survivors after radiotherapy using EORTC QLQ-C30 and QLQ-H&N35 questionnaires," *BMC Cancer*, vol. 11, article 128, 2011.

[6] C. M. Nutting, J. P. Morden, K. J. Harrington et al., "Parotid-sparing intensity modulated versus conventional radiotherapy in head and neck cancer (PARSPORT): a phase 3 multicentre randomised controlled trial," *The Lancet Oncology*, vol. 12, no. 2, pp. 127–136, 2011.

[7] T.-F. Lee, P.-J. Chao, C.-Y. Wang et al., "Dosimetric comparison of helical tomotherapy and dynamic conformal arc therapy in stereotactic radiosurgery for vestibular schwannomas," *Medical Dosimetry*, vol. 36, no. 1, pp. 62–70, 2011.

[8] T.-F. Lee, P.-J. Chao, H.-M. Ting et al., "Comparative analysis of SmartArc-based dual arc volumetric-modulated arc radiotherapy (VMAT) versus intensity-modulated radiotherapy (IMRT) for nasopharyngeal carcinoma," *Journal of Applied Clinical Medical Physics*, vol. 12, no. 4, pp. 158–174, 2011.

[9] T.-F. Lee, P.-J. Chao, F.-M. Fang, T.-J. Su, S. W. Leung, and H.-C. Hsu, "Helical tomotherapy for single and multiple liver tumours," *Radiation Oncology*, vol. 5, no. 1, article 58, 2010.

[10] D. L. Andolino, T. Hoene, L. Xiao, J. Buchsbaum, and A. L. Chang, "Dosimetric comparison of involved-field three-dimensional conformal photon radiotherapy and breast-sparing proton therapy for the treatment of Hodgkin's lymphoma in female pediatric patients," *International Journal of Radiation Oncology Biology Physics*, vol. 81, no. 4, pp. e667–e671, 2011.

[11] P. S. Basran and M. K. Woo, "An analysis of tolerance levels in IMRT quality assurance procedures," *Medical Physics*, vol. 35, no. 6, pp. 2300–2307, 2008.

[12] A. Niroomand-Rad, M. T. Gillin, R. W. Kline, and D. F. Grimm, "Film dosimetry of small electron beams for routine radiotherapy planning," *Medical Physics*, vol. 13, no. 3, pp. 416–421, 1986.

[13] J. Timmerman, K. Wang, S. Tang et al., "SU-ET-147: film dosimetry verification for TSE using an epson scanner," *Medical Physics*, vol. 39, no. 6, p. 3737, 2012.

[14] M. Sander, R. I. A. Patterson, A. Raj, and M. Kraft, "Comment on 'low fractal dimension cluster-dilute soot aggregates from a premixed flame'," *Physical Review Letters*, vol. 104, no. 11, Article ID 119601, 2010.

[15] A. Brahme, "Optimization of stationary and moving beam radiation therapy techniques," *Radiotherapy and Oncology*, vol. 12, no. 2, pp. 129–140, 1988.

[16] J. P. Rigaut, "Automated image segmentation by mathematical morphology and fractal geometry," *Journal of Microscopy*, vol. 150, no. 1, pp. 21–30, 1988.

[17] A. Flook, The characterization of textured and structured particle profiles by the automated measurement of their fractal dimension, 1979, 1979, p. 591.

Hindawi Publishing Corporation
BioMed Research International
Volume 2013, Article ID 216034, 12 pages
http://dx.doi.org/10.1155/2013/216034

Research Article

Total Body Irradiation with Step Translation and Dynamic Field Matching

Ho-Hsing Chen,[1,2] Jay Wu,[3] Keh-Shih Chuang,[2] Jia-Fu Lin,[1] Jia-Cheng Lee,[1,2] and Jin-Ching Lin[1]

[1] *Department of Radiation Oncology, Taichung Veterans General Hospital, 1650 Taiwan Boulevard Sect. 4, Taichung 40705, Taiwan*
[2] *Department of Biomedical Engineering and Environmental Sciences, National Tsing Hua University, Taiwan*
[3] *Department of Biomedical Imaging and Radiological Science, China Medical University, Taichung 40402, Taiwan*

Correspondence should be addressed to Jay Wu; jwu@mail.cmu.edu.tw

Received 14 April 2013; Accepted 31 May 2013

Academic Editor: Chung-Chi Lee

The purpose of this study is to develop a total body irradiation technique that does not require additional devices or sophisticated processes to overcome the space limitation of a small treatment room. The technique aims to deliver a uniform dose to the entire body while keeping the lung dose within the tolerance level. The technique treats the patient lying on the floor anteriorly and posteriorly. For each AP/PA treatment, two complementary fields with dynamic field edges are matched over an overlapped region defined by the marks on the body surface. A compensator, a spoiler, and lung shielding blocks were used during the treatment. Moreover, electron beams were used to further boost the chest wall around the lungs. The technique was validated in a RANDO phantom using GAFCHROMIC films. Dose ratios at different body sites along the midline ranged from 0.945 to 1.076. The dose variation in the AP direction ranged from 96.0% to 104.6%. The dose distribution in the overlapped region ranged from 98.5% to 102.8%. Lateral dose profiles at abdomen and head revealed 109.8% and 111.7% high doses, respectively, at the body edges. The results confirmed that the technique is capable of delivering a uniform dose distribution to the midline of the body in a small treatment room while keeping the lung dose within the tolerance level.

1. Introduction

Total body irradiation (TBI) is a type of external beam radiotherapy. It has been used in conjunction with chemotherapy to prepare patients for bone marrow transplantation (BMT) [1, 2]. A uniform dose distribution throughout the entire body during TBI is necessary to suppress immunological rejection in the recipient and to eliminate residual malignant cells. Therefore, dose impact from irregular body contour and internal tissue heterogeneity must be considered to minimize dose variation within the body [1, 3].

Parallel-opposed anterior/posterior (AP/PA) and bilateral (LAT) fields are commonly used in the conventional TBI treatment [4, 5]. For the AP/PA treatment, the patient stands in front of the wall opposite to the treatment head and is irradiated with a large treatment field. Major advantages of the AP/PA treatment are less thickness variation of the body in the superior-inferior direction and reduced radiation dose to the lungs. However, patients might find standing during treatment uncomfortable. Beams delivered bilaterally with patient sitting on the bed are more comfortable, but large thickness variation of the body requires custom designed compensators for individual patient. Shielding the lungs in the LAT position is also a challenge. It is not sufficient to reduce the lung dose by arms only [6]. Additional shieldings are required. However, boosting dose to the tissues surrounding the lungs is technically difficult. From dosimetric perspective, a treatment planning system commissioned under standard treatment condition cannot be used directly for irradiation at an extended treatment distance. Extra scatter from the floor and the wall should be considered [7–9].

Various techniques have been developed for performing TBI that deliver a uniform dose distribution. Chui et al. proposed an arc treatment with a gravity-oriented compensator

to deliver a uniform dose to a patient lying on the floor [10]. This method can be implemented in a small treatment room, but it also results in a large penumbra around the lung shielding area. The translating couch technique moves a patient horizontally beneath a vertical beam to achieve a uniform dose distribution. However, a moving couch with adjustable speed is required [11–16]. Recently, sequential beam delivery techniques have been used in TBI. Helical TomoTherapy can continually deliver a uniform dose to a patient on the treatment couch with 360° spiral gantry rotation. This can be achieved using the standard planning beam model without extra management [17–20]. In addition, linear accelerator-based intensity modulated techniques have been used to treat a large target volume with multiple isocenters under the standard treatment condition [21, 22]. The advanced field-in-field (FIF) technique uses a simple method to compensate for body contour variation with lateral beam delivery [23]. The modulated-arc total body irradiation (MATBI) technique delivers a uniform dose to the entire body by rotating gantry fields planned inversely by a new beam model commissioned at an extended source-to-surface distance [24, 25]. The aperture-modulated translating bed TBI (AMTBI) technique synchronizes the aperture with bed motion to improve dose uniformity and reduce dose to the lungs [13, 14].

The choice of TBI techniques depends on the clinical requirements, equipments availability, and practicality. In a limited treatment space, it is important to deliver a uniform dose to the entire body without extra equipment or complicated techniques while keeping the lung dose within the tolerance level.

This study presents a novel step translation dynamic field-matching (STDFM) technique to implement the TBI treatment in a small treatment room with AP/PA beams. Patients can be treated in a comfortable position without complicated bed translation, gantry rotation, and beam modulation. In addition, a uniform dose is delivered to the body, while sparing the lungs. The proposed method was verified by phantom measurement using GAFCHROMIC films.

2. Materials and Methods

A RANDO phantom was set up on the floor in supine and prone positions for the AP and PA treatments, respectively. For each AP and PA treatment, two oblique fields irradiated the superior and the inferior parts of the body. These two fields were angled obliquely so that the inferior edge of the superior field matched the superior edge of the inferior field. Moreover, through dynamic leaf motion, the matching edges were feathered over an overlapped region marked on the phantom surface. In between the superior and inferior irradiations, the phantom was translated according to these marks. The optimal overlap widths of different leaf motion lengths were investigated and used for the treatment setup. A compensator was used to modulate the slanted beam intensity due to oblique incidence of the fields. A beam spoiler was used to increase the dose in the buildup region. It also served as a platform on which the lung shielding blocks were placed. The lung shielding blocks reduced the lung dose. An additional electron beam was used to boost the dose to the chest wall.

2.1. Dynamic Field Matching. For TBI involving multiple matching fields, dose heterogeneity in the junction region [3] is a major concern. Ideally, fields abutting perfectly at the match line can provide uniform dose across the junction region. In practice, dose variation is usually observed due to setup and machine errors. Figure 1(a) illustrates an ideal case of perfect field matching which results in a uniform dose across the junction region. Figure 1(b) shows a slight overlap of the matching fields which produces a significant dose peak in the profile. Similarly, Figure 1(c) shows a gap between the matching fields which results in a cold spot. Magnitude of the dose variation depends on the magnitude of the matching error.

To deal with dose heterogeneity, a dynamic field-edge matching technique [26–28] that smears dose inhomogeneity over the field matching zone by two complementary inclined fields was used (Figure 2). In order to keep homogeneous junction dose at all depths, the matching field edges must be parallel to each other. Hence, the gantry was rotated according to the beam divergent angle to make the matching field edges aligned.

Based on the dynamic field-edge matching technique, a patient was set up on the floor in supine and prone positions. Two oblique fields with an overlapped region on the body surface were delivered by translating the patient to align the matching line with the respective dynamic field edges. As a result, a large volume can be irradiated.

2.2. Dynamic MLC Field Editing. The method of editing dynamic MLC leaf sequence files has been published previously [29]. For this study, the dynamic MLC fields were edited using the Shape Editor (Version 6.1, Varian Medical Systems, Palo Alto, CA, USA) to form a tapered field edge with the fluence decreasing gradually from the value in field to zero at the field edge. The superior dynamic field irradiated the upper part of the body with the B-leaves in motion. It consisted of two segments. The leaves of the first segment were set at the start position with dose fraction 0, and the leaves of the second segment were set at the stop position with dose fraction 1. The A-leaves were fixed at 20 cm. Similarly, the inferior dynamic field irradiating the lower part of the body was created with the A-leaves in motion. Crucially, these two dynamic fields must have the same leaf motion length. With this condition, the two adjacent inclined fields were matched complementarily to produce a uniform dose distribution in the overlapped region. Figure 3 shows the fluence distribution of the dynamic fields with the leaves moving from location 20 cm to location 17 cm.

2.3. Treatment Setup. Figure 4 shows the STDFM TBI treatment setup. A RANDO phantom was set up on the floor in the supine and prone positions beneath the gantry. A beam spoiler was placed 30 cm above the floor. The lung blocks were placed on the spoiler to shield the lung during the superior

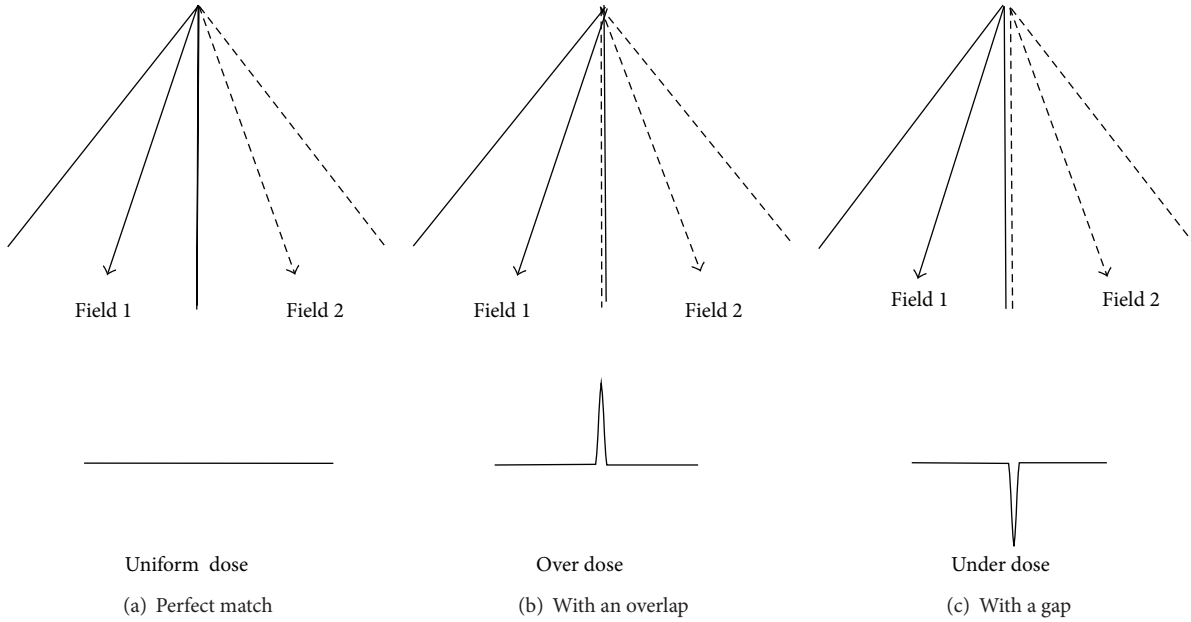

Figure 1: Two adjacent abutting fields. The setup and machine errors cause dose variation where the fields meet. (a) If the two fields are matched perfectly, they produce a uniform dose distribution at the junction. (b) When the fields overlap, an overdose is seen in the dose profile. (c) When there is a gap, an underdose is produced.

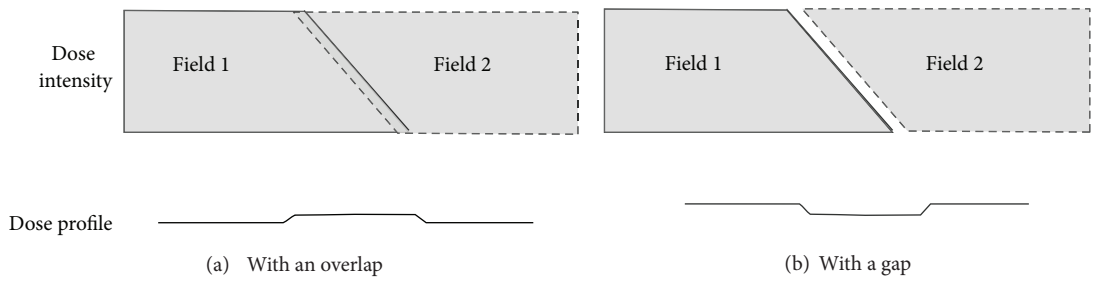

Figure 2: The dynamic field-edge matching technique generates a match zone by overlapping two fields along their border. Two complementary inclined fields smear the dose variations over a wide region. The field intensity profiles are shown with the fields (a) overlapping or (b) separated by a gap.

field irradiation. The distance from the source to the floor was 230 cm.

TBI was performed using two dynamic edge matching fields for each AP/PA treatment. The superior field was used to treat the upper part of the body and the inferior field for the lower part. Between delivery of these two fields, the phantom was translated so that these two fields covered the whole body with an overlap. In order to keep the abutting field edges parallel to each other at all depths, the gantry angle was rotated 11° clockwise for the inferior field and counterclockwise for the superior field. The 11° angle was calculated as $\tan^{-1}(20/100)$. The leaves were set at the start position of 20 cm measured at a source-to-isocenter distance of 100 cm. All treatments were delivered on a Varian 21EX linear accelerator with a 6 MV photon beam at $40 \times 40\,\text{cm}^2$ field size and 0° collimator angle.

The procedure of the two-step translation is illustrated in Figure 4. The width between the two match lines depends on the leaf motion length of the dynamic fields and is described below. The location of the overlapped region was determined by simulating the treatment conditions of the superior and inferior fields, such that the combined dynamic fields covered the entire body.

In the AP treatment, the phantom was set in the supine position. First, for the superior field, the gantry was set to 349°. The phantom was then translated to align the inferior match line with the inferior edge of the field. The beam was then turned on with the B-leaves set in motion during beam on. After completing delivery of the superior field, the gantry was rotated clockwise to 11° for delivery of the inferior field. The phantom was translated to align the superior matching line with the superior edge of the field. The beam was then turned on with the A-leaves set in motion during beam on. Using this two-step translation, the AP treatment can be delivered via the two dynamic fields. Similarly, for the PA treatment, the phantom was set in the prone position, and the same procedure was repeated as in the AP treatment.

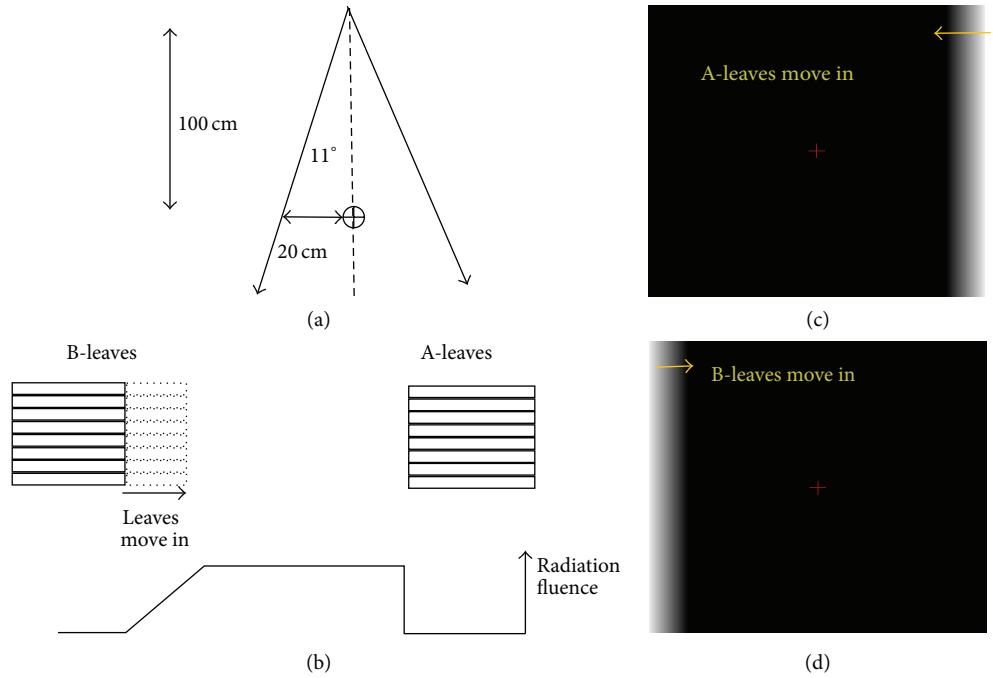

Figure 3: Dynamic MLC fields consist of inclined radiation field. (a) The field geometry is shown. (b) The radiation fluence delivered by a dynamic field. When the beam is on, the leaves move continuously from the 20 cm position to the 17 cm position. (c) The fluence map of the inferior field when the A-leaves move in. (d) The fluence map of the superior field when the B-leaves move in.

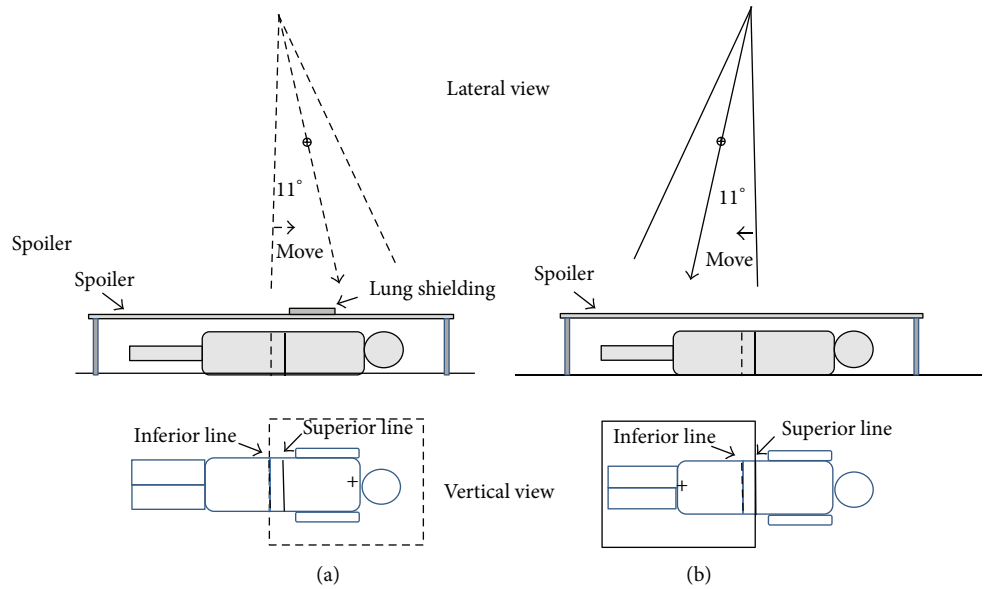

Figure 4: The setup for two-step translation dynamic field-edge matching TBI. (a) The superior field irradiates the upper body with the B-leaves moving in. The dynamic field edge is aligned with the inferior line at a gantry angle of 349° (= 360° − 11°). (b) After shifting the patient, the inferior field irradiates the lower body with the field edge of the A-leaves aligned with the superior line at a gantry angle of 11°. ⊕ indicates the isocenter of the linear accelerator. + indicates the central axis of the dynamic field.

2.4. Beam Intensity Compensator. As described above, in order to match the abutting field edges at all depths, the center lines of the two dynamic fields were incident obliquely at the body surface so that the matching edges were parallel. An oblique incident beam, however, produced a slanted dose profile. An NE-2581 farmer type ionization chamber inserted inside a 20 cm thick solid water phantom (Gammex RMI 457) at a depth of 10 cm was used to measure the dose profile at the treatment distance. Setting the gantry angle at 11° with a 40 × 40 cm^2 static field size, the transverse dose

profiles were measured with the phantom moving along the transverse direction. To modify the oblique beam fluence distribution, a beam compensator composed of a lead sheet of 1 mm in thickness was employed according to the shape of the measured dose profile. The beam compensator was placed on the blocking tray 65 cm from the source. It comprised of two parts: 12 cm width with the lead sheet and 14 cm width without the lead sheet. The transmission factor of the lead sheet was measured under the treatment conditions. Similarly, the dose profile at 10 cm depth was measured with the beam compensator mounted on the accessory mount in the same way.

2.5. Optimal Overlapping Widths in the Phantom. Dose uniformity within the field-matching zone depends on the length of leaf motion and the width of field overlap. Basically, longer leaf motion produces a slower dose gradient and a wider inclined region at the field border. Hence, a wider overlapped region is preferred for better dose uniformity. To determine the optimal overlap widths for various dynamic fields, we created leaf motion lengths of 1-, 2-, 3-, 4-, and 5-cm by the Shaper Editor. The dynamic beam profiles at field borders were measured using the Profiler (Sun Nuclear 1170).

The dose profiles were measured using the Profiler placed inside a solid water phantom on the floor at 10 cm depth with the gantry angle at 349° for a $40 \times 40\,cm^2$ and 6MV photon beams. Before the measurements, the profiler was calibrated under the treatment condition. To avoid electronic circuit damage, the dynamic field edge was aligned to detector No. 9 to keep the irradiated area away from the electronic circuit.

The measured dose profiles were exported as text files and normalized to the detector No. 40 located away from the region of leaf motion. To obtain total dose distribution in the junction area of the two dynamic fields, complementary dose profiles were created by reversing the measured dose profiles in position. Summing the measured and created dose profiles assuming different overlap widths, dose distributions in the junction region were obtained. ±10% dose variation criteria were used to screen for the optimal overlap width.

2.6. Dose Profiles in the Overlapped Region at Different Depths. Static parallel matching field edges produce a constant overlap width at all depths. However, dynamic field matching with a changing field edge during beam delivery results in variable overlap widths at different depths. Hence, dose uniformity will vary with depth. To ensure uniform dose distributions in the junction area at all depths, 1.5 cm EBT3 GAFCHROMIC film strips (ISP Corp., Wayne, NJ) was sandwiched between the solid water phantom slabs on the floor, at depths of 0, 5, 10, and 15 cm to measure the total dose profiles in the overlapped region.

The irradiated films were stored in light-tight bags and scanned 24 h later using an Epson 1680 flatbed scanner with the 48 bit RGB color transmission mode, 72 dpi resolution, and no color correction. The images were saved in the tagged image file format (TIFF), and only the red channel signals were used in subsequent readout procedures. Calibration curve fitting and signal-to-dose conversion were performed using the FilmQA software.

2.7. Total Dose Profile of the Dynamic Matching Fields. The midline dose from the two overlapping dynamic fields should be verified in the phantom with a beam compensator in place to ensure a uniform dose delivery. An ionization chamber (NE 2581) setup under the treatment condition in a 20 cm thick solid water phantom was used to measure the dose profiles at depths of 5, 10, and 15 cm. Two oblique fields, a superior field with the gantry angle set at 349° and an inferior field with the gantry angle set at 11°, delivered the dose to the phantom. Each field has a dynamic edge formed by 3 cm leaf motion, the superior field with the B-leaves moving in while the inferior field with the A-leaves moving in, which produced a 5.5 cm overlapped region on the phantom surface based on the optimal overlap width. To measure the midline dose, the superior and inferior matching lines were drawn on the phantom surface 5.5 cm apart in parallel for measurement setup. The center of the overlapped region was the center of the entire radiation field. During the measurement, the phantom was moved along the transverse axis of the beam, and the ionization chamber accumulated the doses delivered by the two matching fields. The chamber readings were normalized to the reading at the 40 cm position away from the center of the overlapped region.

2.8. Percentage Depth Dose in the Buildup Region. A 1 cm thick acrylic beam spoiler was placed 30 cm above the floor over the phantom. The spoiler-to-phantom distance depends on the thickness of the phantom, for example, 10 cm for a 20 cm thick phantom. Without the spoiler, dose deficiency in the buildup region for megavoltage photon beams results in dose inhomogeneity in the TBI treatment. With the spoiler, electrons scattered out from the spoiler increase the surface dose to near the maximum dose. A Markus parallel plate ionization chamber inserted inside a 20 cm thick solid water phantom was used to measure percentage depth doses in the buildup region for a vertical beam with and without the beam spoiler in place and for an oblique beam with the beam spoiler at the treatment distance.

2.9. RANDO Phantom Dosimetry. A RANDO phantom and GAFCHROMIC films were used to verify dose uniformity using the STDFM TBI technique. Dose distributions were measured by placing EBT3 films between RANDO phantom sections along the AP direction in several regions of interest including head, neck, lungs, abdomen, pelvis, and the overlapped region. In addition, film strips were placed in lateral direction at the abdomen and the head to investigate lateral dose distribution. All film strips were 1.5 cm in width and cut from the same batch. Radiation was delivered to the phantom with AP/PA beams following the treatment protocol described above which adopts dynamic field edges with 3 cm leaf motion, 5.5 cm field overlap, lung shielding, and a rice bag attached to the neck. Film dosimetry procedure was performed as described above.

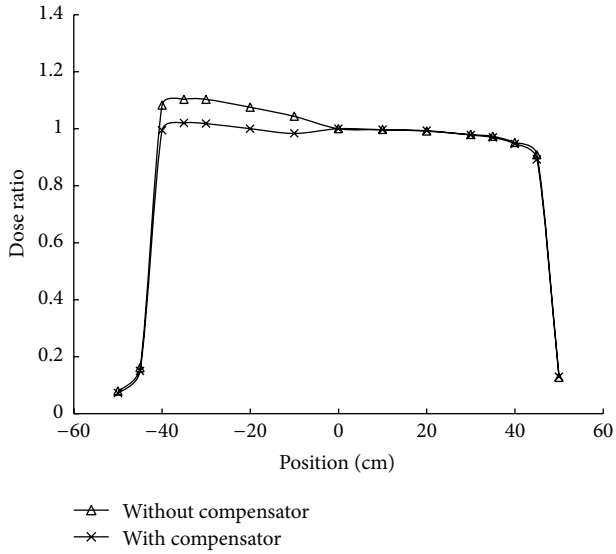

Figure 5: The dose profile measured at a depth of 10 cm with a gantry angle of 349° (= 360° − 11°) and a 40 × 40-cm^2 field. The static fields with and without a beam compensator are shown.

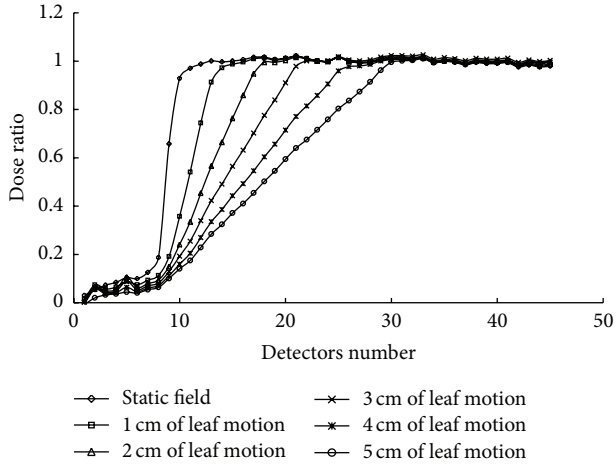

Figure 6: The field profiles were measured using a linear Profiler in solid water at a depth of 10 cm. A static field and dynamic field edges with various leaf motion lengths (measured at isocenter) are shown.

3. Results

3.1. Beam Intensity Compensator. An oblique radiation beam results in a slanted dose distribution at depths in phantom. For a 40 × 40 cm^2 static field, the transmission factor of a 1-mm lead sheet attached to the tray was 0.939. Dose variation of the profile at a depth of 10 cm for the 11° oblique beam without a compensator ranged from 0.96 to 1.10 between −40 and +40 cm. The dose ratio was normalized to the beam center. Dose variation with the beam compensator in place ranged from 0.95 to 1.02 as shown in Figure 5. The compensator smoothed the dose profile distribution and decreased the dose variation from 14% to 7%.

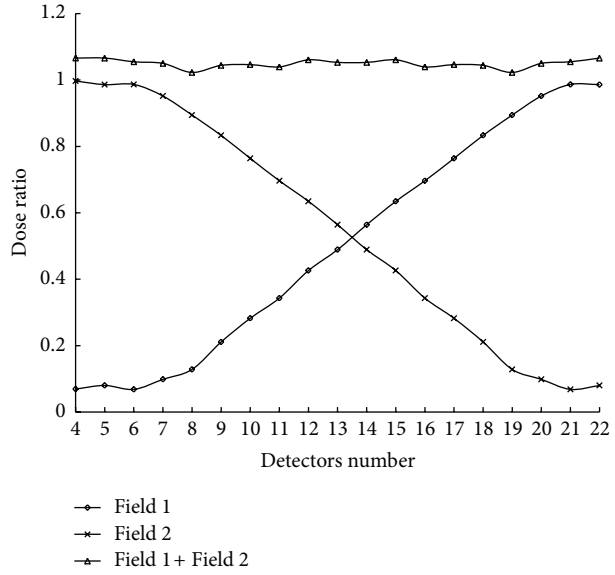

Figure 7: The summed dose profile at isocenter of two dynamic matching field edges with a 3 cm leaf motion and a 5.5 cm overlap at treatment distance. Field 1 was measured at depth of 10 cm and field 2 was the inverse of field 1 in position.

3.2. Optimal Overlap Width of Dynamic Matching Fields. Figure 6 shows dose profiles near field edges of the static and the dynamic fields with leaf motion lengths of 1, 2, 3, 4, and 5 cm. These profiles were measured with a Profiler. All measurements were made at the gantry angle of 349° with the 40 × 40 cm^2 field size at a depth of 10 cm. The horizontal axis was labeled as the number of detectors spaced 5 mm apart. The vertical axis shows the dose ratio normalized to detector No. 40, a detector far away from the field border. For dynamic field edges, the dose profiles declined gradually to the border. By comparison, the static field displayed high dose gradient at the field edge. Increases in the dynamic leaf motion length resulted in a decreased dose gradient and a broader inclined region.

Figure 7 shows the combined dose profile of two matched dynamic field edges with a 5.5 cm overlap. Field 1 was measured at a depth of 10 cm with 3 cm of leaf motion, and field 2 was the reverse of the field 1 in terms of position. The dose variation in the overlapped region ranged from 102.2% to 106.1% with the dose normalized to detector No. 40.

Figure 8 shows the total dose profiles of the two dynamic matching fields in the overlapped region at a depth of 10 cm for various lengths of leaf motion and different overlap widths. The horizontal axis is the distance from the center of the overlapped region. For a given leaf motion length, a broader overlap produced a higher dose distribution in the matching zone compared with a smaller overlap. To obtain a highly uniform dose distribution, longer leaf motion length was preferred.

Based on the results shown in Figure 8, optimal overlap width with the dose variation less than ±10% for different lengths of leaf motion was obtained (Table 1). The optimal overlap increased with the length of leaf motion. In addition,

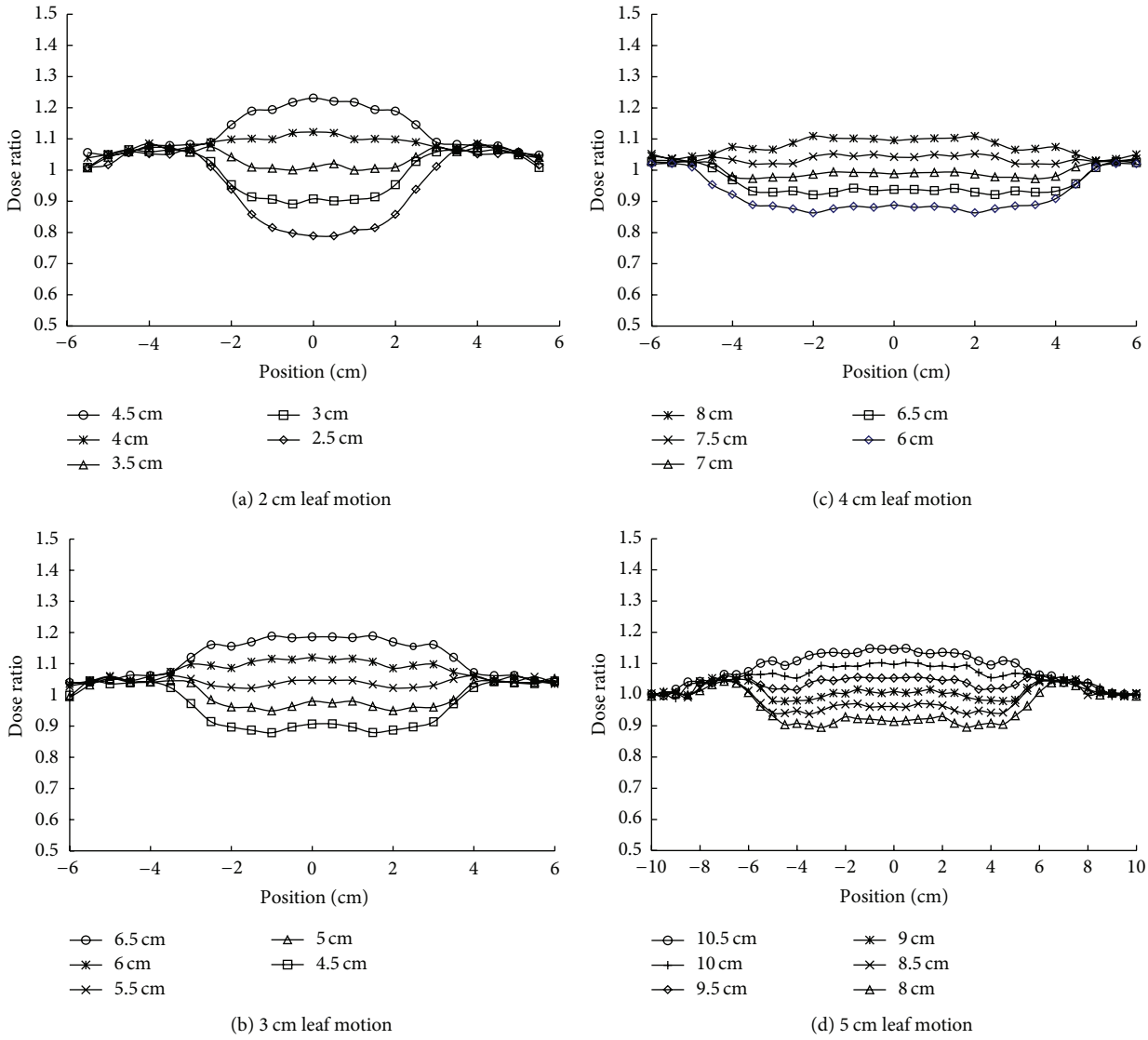

Figure 8: The dose distribution across the overlapped region of two dynamic matching field edges with various overlap widths was measured by a Profiler at 10 cm depth at the treatment distance. The dynamic fields involved leaf motion of (a) 2, (b) 3, (c) 4, and (d) 5 cm.

the range of optimal overlap was positively related to the leaf motion. For example, with 5 cm of leaf motion, the optimal width interval was 1.5 cm between 8.5 and 10.0 cm. Similarly, 3 cm of leaf motion had a 0.5 cm optimal width interval between 5 and 5.5 cm. Note that the optimal overlap changed slightly with depth (due to the change in beam divergence during leaf motion). A wider overlap has better dose uniformity, but a shorter treatment dimension. To reach a satisfied compromise between the dose uniformity and treatment dimension, 3 cm of leaf motion and 5.5 cm overlap were used in the subsequent experiments.

3.3. Dose Profiles in the Overlapped Region at Depths. The dose uniformity at different depths in the overlapped region should be maintained at an acceptable level. Dose profiles were measured with strips of GAFCHROMIC films placed in the solid water at depths of 0, 5, 10, and 15 cm as shown in Table 2. The ranges of dose variation at depths of 0, 5, 10, and 15 cm were 98.4% to 103.8%, 99.3% to 105.0%, 97.9% to 102.3%, and 98.3% to 101.2%, respectively. All the doses were normalized to that of the point 5 cm away from the center of the overlapped region. This confirmed dose uniformity requirement at different depths.

Table 1: The optimal overlap widths of the two dynamic field edges matched at a distance of 220 cm from the radiation source. When overlapped optimally, the dose variation is within ±10% at the field junction.

Leaf motion length (cm)	2	3	4	5
Optimal overlap width (cm)	3.5	5.0–5.5	6.5–7.5	8.5–10.0

3.4. Total Dose Profiles of Dynamic Matching Fields. The dose profiles of the entire irradiated volume covered by the two

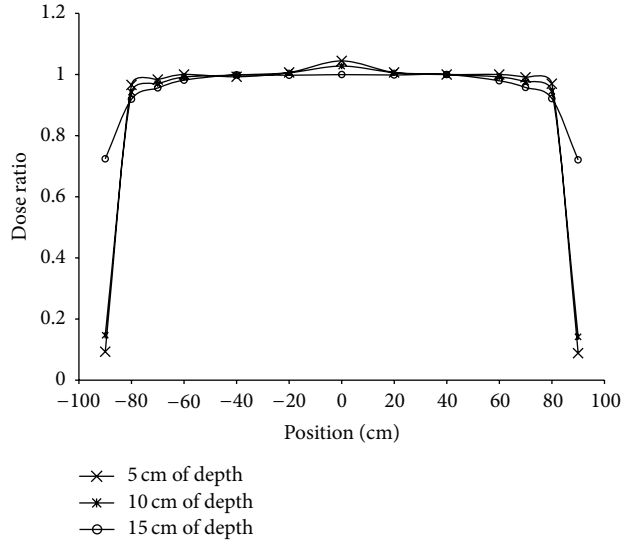

Figure 9: The total dose profiles of two oblique fields with matching dynamic field edges were measured along the transverse axis in a solid water phantom at depths of 5, 10, and 15 cm. The dose was normalized to that at the position 40 cm away from the center of the overlapped region.

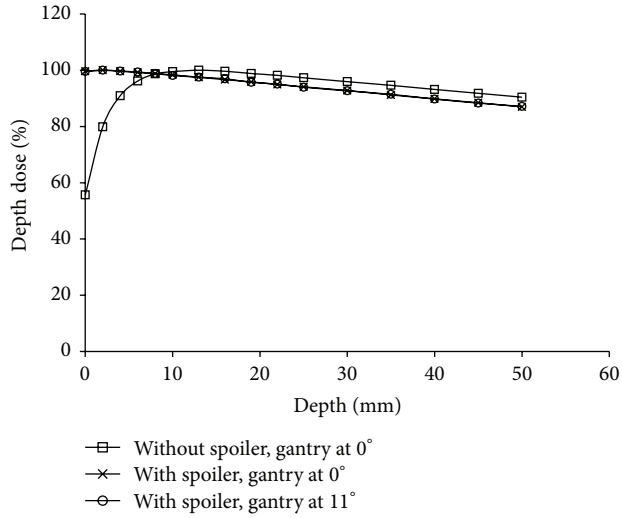

Figure 10: Percentage depth dose curves of a 6-MV, 40 × 40-cm^2 photon beam measured using a Markus parallel plate ionization chamber inserted in a 20 cm thick solid water phantom on the floor. A 1 cm thick acrylic beam spoiler was placed above the floor at a distance of 30 cm. The gantry angle was set at (a) 0° without a spoiler, (b) 0° with a spoiler, and (c) 11° with a spoiler.

oblique fields with dynamic field edges were investigated for clinical implementation. Figure 9 shows the total dose profiles measured in the solid water phantom at depths of 5, 10, and 15 cm. The dose profiles were normalized to the position 40 cm away from the center of the overlapped region. The variations of dose profiles within ±80 cm at depths of 5, 10, and 15 cm were 96.6% to 104.4%, 94.2% to 102.8%, and 91.9% to 100.0%, respectively. The dose in the overlapped region was slightly higher due to a 5.5 cm overlap for the 3-cm leaf motion. Furthermore, the dose variation decreased with depth. This result demonstrated that the dynamic matching field edges with a beam compensator produced uniform dose distribution at various depths throughout the large treatment volume.

Table 2: The dose variation in the overlapped region at various depths measured using EBT3 film strips placed in the solid water phantom slabs. Two dynamic field edges with 3 cm of leaf motion and gantry angles of 11° and 349° delivered a dose to a 20 cm-thick phantom with an overlap of 5.5 cm.

Depth (cm)	0	5	10	15
Dose variation in overlap region (%)	98.4–103.8	99.3–105	97.9–102.3	98.3–101.2

3.5. Percentage Depth Dose in the Buildup Region. A spoiler placed in front of the phantom provides extra scattered dose to the buildup region and improve the dose uniformity. The percentage depth doses of the vertical treatment field with or without the spoiler and those of the 11° oblique field with the spoiler were measured at the treatment distance, as shown in Figure 10. The use of the spoiler in the beam increased the surface dose from 57% to 99% and shifted the depth of maximum dose toward the surface from 1.3 cm to 2 mm. No significant difference was observed between the 11° oblique beam and the vertical beam with the spoiler.

3.6. RANDO Phantom Dosimetry. The dose distribution of the STDFM TBI treatment was measured with EBT3 film strips sandwiched between the RANDO phantom sections in the AP and lateral directions. Figure 11 shows measurements performed at several sites of interest: head, neck, lungs, overlapped region, abdomen, and pelvis. The two sharp peaks near the border of the profiles indicate the body surface marked on the film strips. Doses were normalized to the midpoint corresponding to the midline of the phantom of the two sharp peaks on the film strips. The smooth profiles between the peaks demonstrated good dose uniformity along the AP direction. No significant dose deficit was observed in the buildup region. The profile of the lung site showed a higher dose outside the phantom. This might be caused by the scattered radiation from the lung shielding above the phantom. Two obvious dose peaks corresponding to the location of the skull were also observed in the dose profile of the head. A larger numbers of electron motivated by the dense skull bone increased the dose absorption of the film by 4.6% compared to those of the surrounding soft tissues. There have been relatively few studies on the dose distribution in TBI affected by high-density bone compared with low-density lungs. The absorbed dose to bone depends on the ratio of the averaged mass energy absorption coefficient of the bone to that of the surrounding soft tissues over the photon spectrum. It is difficult to evaluate the influence of bone in TBI treatment because of difficulties involved in determining the beam spectrum, as well as the complex anatomical variations in volume, shape, and density [3].

Table 3: The dose variation measured in a RANDO phantom using GAFCHROMIC film strips sandwiched between sections at sites of interest. The film strips were orientated along the AP direction, except for two strips along the lateral orientation at abdomen and head. The dose ratios at midpoints of profiles inside the phantom were normalized to the midpoint dose measured between sections 27 and 28. The dose variation was normalized to the midpoint of separation in body surface for individual profile.

Sites	Head	Neck	lung[1]	Overlap region	Abdomen	Abdomen	Pelvis	Head (lateral)[2]	Abdomen (lateral)[2]
Separation (cm) of body surface	18.5	13	19	15.5	14.5	17.5	19.5	18.5	14.5
Dose ratio of midpoint	0.964	1.021	0.561	1.062	1.076	1.000	0.945	0.955	1.083
Maximum dose in profile (%)	104.6	103.4	101.2	102.8	103.2	103.3	103.3	111.7	109.8
Minimum dose in profile (%)	98.9	99.1	99.3	98.5	96.0	98.4	98.0	99.7	98.4
Between phantom section	2-3	8-9	17-18	23-24	25-26	27-28	31-32	2-3	25-26

[1]With lung shielding block. [2]Film oriented in lateral direction.

To assess the complex effects of bone in TBI, we measured the attenuated dose of the head with the skull bone and that of the abdomen in the RANDO phantom with the same thickness using an ionization chamber inserted in a 6 cm thick solid water phantom at 1.5 cm of depth. The lateral separation of the head in Section 3 of the phantom was about 15 cm. The anterior-posterior separation of the abdomen in Section 25 was about 15 cm. The measurement was made using the head site in the lateral position and the abdomen site in the AP position placed above the solid water phantom with the ionization chamber inserted in it at the treatment distance. The measured dose ratio of the head site to the abdomen site was 0.93 for the same physical thickness. The results demonstrated that the head containing the skull bone attenuated radiation to a greater extent than the abdomen. Hence, bone inhomogeneity in the head should be considered when evaluating dose uniformity for body contour variation in the TBI treatment. The lateral dose profiles of the abdomen and the head show approximately 9.8% and 11.7% higher doses at the body peripherals than at the midpoint because the body thickness is reduced laterally (Figure 12).

Table 3 shows the dose ratios at the midline along the superior-inferior axis and the dose variation along the AP and lateral directions for various anatomical sites including the overlapped region. The dose ratio was normalized to the dose at the midpoint measured between the sections 27 and 28 with a separation of 17.5 cm in the AP direction. For dose variation evaluation, dose distribution was normalized to the dose at midpoint of the individual profile inside the phantom. The dose ratios at the midline of the different sites ranged from 0.945 to 1.076, except that of the lung which has a lower value of 0.561 due to the lung shielding. The dose variation along the AP direction ranged from 96.0% to 104.6% for all sites. Two higher dose peaks were observed at the skull location with a higher density. The dose variation at the overlapped region ranged from 98.5% to 102.8%, demonstrating good dose uniformity at depths within the field matching zones.

4. Discussion

This study aimed to implement a TBI treatment technique in a small treatment room with the requirement of lower radiation exposure to critical organs, especially the lungs. Due to space limitation, it is difficult to use conventional AP/PA beams to deliver a large field. Although lateral treatment using a large field with the patient sitting on a bed in a crouched position can be employed, it is difficult to keep the organ dose below the tolerance level while delivering a sufficient dose to the surrounding tissues.

This work constructed a simple beam compensator to compensate for the slanted dose profile at oblique beam incidence. It can be easily assembled using a lead sheet and no extra work is required for individual patient. Similarly, the inclined beam intensity at the abutting field edges can be created with the dynamic MLC motion and used for all patients.

Dose uniformity in the matching zone was highly correlated with the leaf motion length of the dynamic field edges and the width of the overlapped region. A dynamic field edge with 3 cm leaf motion at the isocenter projects an approximately 6.6 cm wide region of uniform distribution at a distance of 220 cm. In theory, if a static open field has a steep square dose distribution, the linear motion of the leaves would produce a perfect inclined fluence in the field border. Consequently two complementary dynamic field edges merged with a 6.6 cm overlap should form a smooth field junction. Merging two imperfect inclined fluence distributions in the field border introduced dose inhomogeneity in the junction area. Furthermore, an additional factor affecting dose uniformity in the field junction area is the variation of the overlap widths at different depths due to the change of dynamic field-edge incident angle during beam on. We have examined the dose variation across the field junction area and determined the optimal overlap width for each dynamic field edge.

A greater leaf motion length produces a broader matching zone. Consequently, dose variation due to geometric uncertainty may be smeared and result in better dose uniformity. However, a greater field overlapped region reduces the treatment dimension. In a clinical scenario, two oblique matching fields projecting an approximately 160 cm long treatment dimension on the floor can be used to treat a 170 cm tall patient by bending the patient's legs. For taller patients whose entire body cannot be placed within the treatment field, additional conventional AP-PA fields could be given to

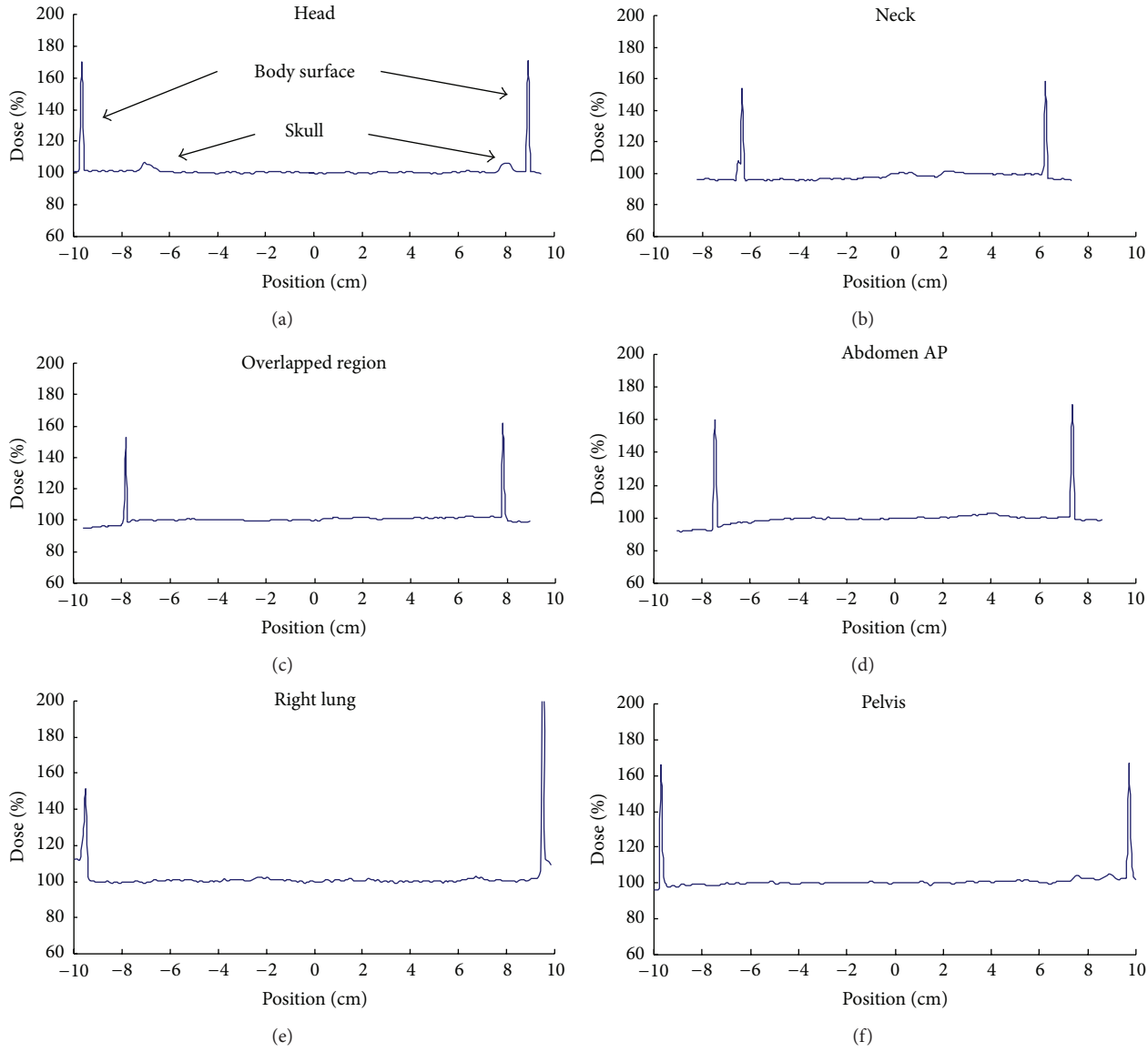

Figure 11: Dose distributions of step translation dynamic field-edge matching total body irradiation along the AP orientation are shown. They were measured with EBT3 film strips sandwiched between RANDO phantom sections. Measurements were made at several sites of interest, including head, neck, lungs, overlapped region, abdomen, and pelvis. The sharp peaks indicate the location of the body surface marked on the film strips. The dose was normalized to that at the midpoint of the two sharp peaks.

the lower extremities which are presumably less sensitive to radiation damage.

Conventional AP/PA TBI treatment has the advantage of less body contour variation compared to the lateral beam treatment, and the midline dose variation within ±10% level is recommended. Large variation in the body contour results in excessive dose variation. Although the lower limbs do not contain sensitive organs, dose delivery should still be as accurate and as uniform as possible. Yao et al. used a simple technique to improve dose uniformity in the superior-inferior axis according to patients' contours [30]. In our RANDO phantom study of dosimetry without lower limbs, a uniform dose was achieved. A slanted beam profile due to oblique incidence provides lower radiation intensity on one side of the field. The degree of slant depends on the oblique angle. For example, a beam with an 11° oblique angle results in an approximately 14% dose difference between the two opposite sides of the profile at a depth of 10 cm in the phantom study. This suggests that an oblique incidence can serve as a virtual compensator for extremities of the body.

The implications of our findings are limited because the dose distribution in the lateral axis cannot be modified using the current technique. From the lateral profiles measured in the RANDO phantom, the dose variations at the body periphery were 9.8% and 11.7% higher than at the midpoint for abdomen and head, respectively. Since variation in actual human body is great, it is important to recognize the possibility of dose variation along the lateral axis.

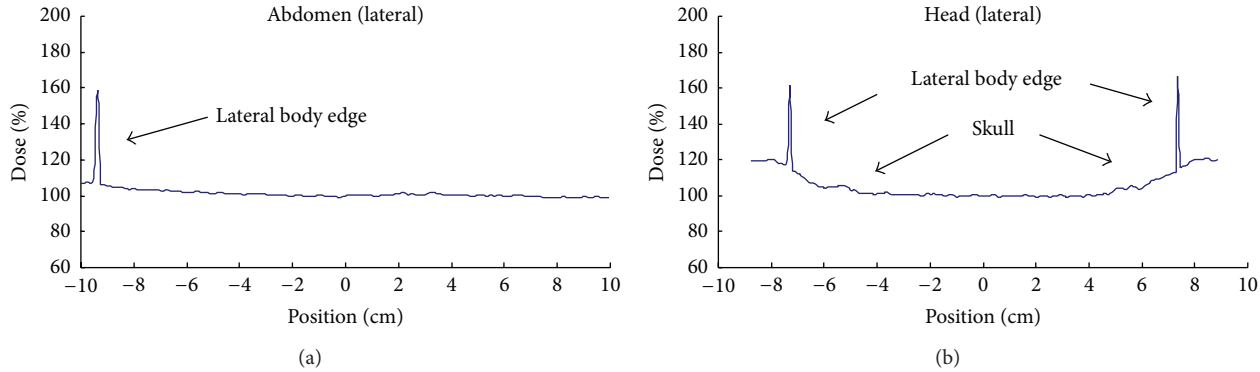

Figure 12: Lateral dose profiles measured with film strips positioned at abdomen and head along the lateral direction. The sharp peaks indicate location of the body surface.

Although dynamic TBI techniques such as dynamic beams delivered with gantry rotation and continually translating the patient during beam on can be used in a small treatment room they also introduce a broadened penumbra in the shielded region along the superior-inferior direction. If taking lung motion during breathing into account [10], the penumbra might be even larger. This might be improved by using a complicated correction method [25] or an additional process [12]. Although the lung motion during breathing makes the effect uncertain [10], the penumbra might be even larger. Therefore, fixed beam TBI techniques are preferred over the dynamic techniques for lung shielding.

Sequential field delivery TBI techniques which deliver doses with small fields sequentially might cause dose heterogeneity in the circulating blood. Molloy [31] studied this effect and concluded that the heterogeneity is acceptable in clinical practice. Our STDFM TBI technique delivers a dose with two large fields, and the effect of dose heterogeneity might be less significant than the sequential techniques.

The over response of the dose measurement in the buildup region using a parallel plate ionization chamber could be attributed to the uncertainty of the surface dose measurement in TBI. Several authors [32, 33] corrected the effect under standard treatment condition. Yao et al. [30] measured percent depth doses using a Markus parallel plate ionization chamber and concluded that the surface dose can increase to 99% when a spoiler is used in a beam. The results (Figure 11) of our phantom study also showed that the uniform dose could be achieved in the buildup region under the TBI treatment condition. To implement TBI treatment in a small treatment room with lung shielding, several techniques have been proposed [13, 24]. These techniques have the advantage of generating a highly uniform dose distribution in three dimensions. It, however, requires additional equipment and/or complex procedures.

5. Conclusions

We examined feasibility of a simple step translation and dynamic field-edge matching TBI technique using a RANDO phantom model. The method can be used to treat patients in a small treatment room, while keeping the lung dose under the desired level without using extra equipment, complex procedures, and patient-specific compensators.

Acknowledgments

This paper was supported by the Taichung Veterans General Hospital Branch Joint Research Program (TCVGH-997101B). field edges matched at a distance of 220 cm from the radiation source. When

References

[1] F. M. Khan, *Physics of Radiation Therapy*, Lippincott Williams & Wilkins, Philadelphia, Pa, USA, 4th edition, 2010.

[2] A. Stein and S. J. Forman, "Allogeneic transplantation for ALL in adults," *Bone Marrow Transplantation*, vol. 41, no. 5, pp. 439–446, 2008.

[3] J. Van Dyk, J. Galvin, G. P. Glasgow, and E. B. Pordgorsak, "The physical aspects of total and half body photon irradiation," Report of Task Group 29 of the Radiation Therapy Committee of the American Association of Physicists in Medicine 17, American Institute of Physics, New York, NY, USA, 1986.

[4] J. C. Breneman, H. R. Elson, R. Little, M. Lamba, A. E. Foster, and B. S. Aron, "A technique for delivery of total body irradiation for bone marrow transplantation in adults and adolescents," *International Journal of Radiation Oncology Biology Physics*, vol. 18, no. 5, pp. 1233–1236, 1990.

[5] R. Miralbell, M. Rouzaud, E. Grob et al., "Can a total body irradiation technique be fast and reproducible," *International Journal of Radiation Oncology Biology Physics*, vol. 29, no. 5, pp. 1167–1173, 1994.

[6] S. K. Hui, R. K. Das, B. Thomadsen, and D. Henderson, "CT-based analysis of dose homogeneity in total body irradiation using lateral beam," *Journal of Applied Clinical Medical Physics*, vol. 5, no. 4, pp. 71–79, 2004.

[7] M.-C. Lavalle, L. Gingras, M. Chrtien, S. Aubin, C. Ct, and L. Beaulieu, "Commissioning and evaluation of an extended SSD photon model for PINNACLE3: an application to total body irradiation," *Medical Physics*, vol. 36, no. 8, pp. 3844–3855, 2009.

[8] D. Abraham, V. Colussi, D. Shina, T. Kinsella, and C. Sibata, "TBI treatment planning using the ADAC pinnacle treatment

planning system," *Medical Dosimetry*, vol. 25, no. 4, pp. 219–224, 2000.

[9] B. Schaeken, S. Lelie, P. Meijnders, D. Van Den Weyngaert, H. Janssens, and D. Verellen, "Alanine/EPR dosimetry applied to the verification of a total body irradiation protocol and treatment planning dose calculation using a humanoid phantom," *Medical Physics*, vol. 37, no. 12, pp. 6292–6299, 2010.

[10] C.-S. Chui, D. P. Fontenla, E. Mullokandov, A. Kapulsky, Y.-C. Lo, and C.-J. Lo, "Total body irradiation with an arc and a gravity-oriented compensator," *International Journal of Radiation Oncology Biology Physics*, vol. 39, no. 5, pp. 1191–1195, 1997.

[11] B. Umek, M. Zwitter, and H. Habič, "Total body irradiation with translation method," *Radiotherapy and Oncology*, vol. 38, no. 3, pp. 253–255, 1996.

[12] M.-C. Lavallée, S. Aubin, M. Chrétien, M. Larochelle, and L. Beaulieu, "Attenuator design for organs at risk in total body irradiation using a translation technique," *Medical Physics*, vol. 35, no. 5, pp. 1663–1669, 2008.

[13] A. Hussain, P. Dunscombe, J. E. Villarreal-Barajas, and D. Brown, "Total body irradiation dose optimization based on radiological depth," *Journal of Applied Clinical Medical Physics*, vol. 13, no. 3, pp. 152–165, 2012.

[14] A. Hussain, J. E. Villarreal-Barajas, P. Dunscombe, and D. W. Brown, "Aperture modulated, translating bed total body irradiation," *Medical Physics*, vol. 38, no. 2, pp. 932–941, 2011.

[15] M.-C. Lavallee, S. Aubin, M. Larochelle, I. Vallieres, and L. Beaulieu, "3D heterogeneous dose distributions for total body irradiation patients," *Journal of Applied Clinical Medical Physics*, vol. 12, no. 3, p. 3416, 2011.

[16] M. Chrétien, C. Côté, R. Blais et al., "A variable speed translating couch technique for total body irradiation," *Medical Physics*, vol. 27, no. 5, pp. 1127–1130, 2000.

[17] M. Chao, J. Penagaricano, Y. Yan, E. G. Moros, P. Corry, and V. Ratanatharathorn, "Voxel-based dose reconstruction for total body irradiation with helical tomotherapy," *International Journal of Radiation Oncology Biology Physics*, vol. 82, no. 5, pp. 1575–1583, 2012.

[18] M. Sharma, T. D. Santos, N. P. Papanikolopoulos, and S. K. Huia, "Feasibility of intrafraction whole-body motion tracking for total marrow irradiation," *Journal of Biomedical Optics*, vol. 16, no. 5, Article ID 058002, 2011.

[19] A. H. Zhuang, A. Liu, T. E. Schultheiss, and J. Y. C. Wong, "Dosimetric study and verification of total body irradiation using helical tomotherapy and its comparison to extended SSD technique," *Medical Dosimetry*, vol. 35, no. 4, pp. 243–249, 2010.

[20] T. E. Schultheiss, J. Wong, A. Liu, G. Olivera, and G. Somlo, "Image-guided total marrow and total lymphatic irradiation using helical tomotherapy," *International Journal of Radiation Oncology Biology Physics*, vol. 67, no. 4, pp. 1259–1267, 2007.

[21] J. R. Wilkie, H. Tiryaki, B. D. Smith, J. C. Roeske, J. A. Radosevich, and B. Aydogan, "Feasibility study for linac-based intensity modulated total marrow irradiation," *Medical Physics*, vol. 35, no. 12, pp. 5609–5618, 2008.

[22] M. Yeginer, J. C. Roeske, J. A. Radosevich, and B. Aydogan, "Linear accelerator-based intensity-modulated total marrow irradiation technique for treatment of hematologic malignancies: a dosimetric feasibility study," *International Journal of Radiation Oncology Biology Physics*, vol. 79, no. 4, pp. 1256–1265, 2011.

[23] C. Onal, A. Sonmez, G. Arslan, S. Sonmez, E. Efe, and E. Oymak, "Evaluation of field-in-field technique for total body irradiation," *International Journal of Radiation Oncology, Biology, Physics*, vol. 83, no. 5, pp. 1641–1648, 2012.

[24] M. Held, N. Kirby, O. Morin, and J. Pouliot, "Dosimetric aspects of inverse-planned modulated-arc total-body irradiation," *Medical Physics*, vol. 39, no. 8, pp. 5263–5271, 2012.

[25] N. Kirby, M. Held, O. Morin, S. Fogh, and J. Pouliot, "Inverse-planned modulated-arc total-body irradiation," *Medical Physics*, vol. 39, no. 5, pp. 2761–2764, 2012.

[26] J. Duan, S. Shen, S. A. Spencer et al., "A dynamic supraclavicular field-matching technique for head-and-neck cancer patients treated with IMRT," *International Journal of Radiation Oncology Biology Physics*, vol. 60, no. 3, pp. 959–972, 2004.

[27] L. Hong, K. Alektiar, C. Chui et al., "IMRT of large fields: whole-abdomen irradiation," *International Journal of Radiation Oncology Biology Physics*, vol. 54, no. 1, pp. 278–289, 2002.

[28] Q. Wu, M. Arnfield, S. Tong, Y. Wu, and R. Mohan, "Dynamic splitting of large intensity-modulated fields," *Physics in Medicine and Biology*, vol. 45, no. 7, pp. 1731–1740, 2000.

[29] H.-H. Chen, J. Wu, K.-S. Chuang, and H.-C. Kuo, "Correction of respiratory motion for IMRT using aperture adaptive technique and visual guidance: a feasibility study," *Nuclear Instruments and Methods in Physics Research A*, vol. 577, no. 3, pp. 734–740, 2007.

[30] R. Yao, D. Bernard, J. Turian et al., "A simplified technique for delivering total body irradiation (TBI) with improved dose homogeneity," *Medical Physics*, vol. 39, no. 4, pp. 2239–2248, 2012.

[31] J. A. Molloy, "Statistical analysis of dose heterogeneity in circulating blood: implications for sequential methods of total body irradiation," *Medical Physics*, vol. 37, no. 11, pp. 5568–5578, 2010.

[32] D. E. Mellenberg Jr., "Determination of build-up region over-response corrections for a Markus-type chamber," *Medical Physics*, vol. 17, no. 6, pp. 1041–1044, 1990.

[33] B. J. Gerbi and F. M. Khan, "Measurement of dose in the buildup region using fixed-separation plane-parallel ionization chambers," *Medical Physics*, vol. 17, no. 1, pp. 17–26, 1990.

Hindawi Publishing Corporation
BioMed Research International
Volume 2013, Article ID 247152, 8 pages
http://dx.doi.org/10.1155/2013/247152

Review Article

^{18}F-FDG PET in the Diagnosis and Treatment of Primary Central Nervous System Lymphoma

Nobuyuki Kawai,[1] Keisuke Miyake,[1] Yuka Yamamoto,[2] Yoshihiro Nishiyama,[2] and Takashi Tamiya[1]

[1] *Department of Neurological Surgery, Faculty of Medicine, Kagawa University, 1750-1 Miki-cho, Kita-gun, Kagawa 761-0793, Japan*
[2] *Department of Radiology, Faculty of Medicine, Kagawa University, 1750-1 Miki-cho, Kita-gun, Kagawa 761-0793, Japan*

Correspondence should be addressed to Nobuyuki Kawai; nobu@med.kagawa-u.ac.jp

Received 13 March 2013; Accepted 2 June 2013

Academic Editor: Eng-Yen Huang

This paper summarizes the usefulness and limitation of positron emission tomography (PET) with ^{18}F-fluorodeoxyglucose (^{18}F-FDG) in the diagnosis and treatment of primary central nervous system lymphoma (PCNSL). The ^{18}F-FDG uptake in typical PCNSL is about 2.5 times higher than that in the normal gray matter, and the tumor can usually be identified visually. The ^{18}F-FDG uptake pattern and value provide useful information for differentiating PCNSL from other enhancing malignant brain tumors especially glioblastoma (GB). The ^{18}F-FDG uptake in typical PCNSL is usually homogenous, and the uptake value is significantly higher than that in GB. However, ^{18}F-FDG PET often fails to show the presence of tumor in the brain as ^{18}F-FDG uptake is faint in atypical PCNSL such as disseminated or nonenhancing lesions. ^{18}F-FDG PET is also useful for evaluating the treatment response at a very early stage after the initial treatment. Pretreatment and posttreatment ^{18}F-FDG uptake values may have a prognostic value in patients with PCNSL. In conclusion, ^{18}F-FDG PET is very useful in the diagnosis of typical PCNSL and can differentiate PCNSL from other malignant brain tumors. However, the usefulness of ^{18}F-FDG PET is limited in the diagnosis of atypical PCNSL.

1. Introduction

Although primary central nervous system lymphoma (PCNSL) is a rare tumor accounting for only 3–5% of all primary brain tumors, the incidence of PCNSL in developed countries is about 5 patients per 1 million person/year [1–3]. Epidemiological data have shown a continuous increase over the past three decades in the immunocompetent population, whereas the incidence seems to be decreasing in patients with acquired immunodeficiency syndrome (AIDS) since the development of highly active antiretroviral therapies [4]. PCNSL affects all age groups, with the peak incidence being in the fifth to seventh decades in non-AIDS patients. Therefore, the rising incidence of PCNSL may only represent the increasing age of the population. Recent studies have shown an encouraging improvement in the overall survival time when radiotherapy is combined with high-dose methotrexate- (MTX-) based chemotherapy [5, 6]. Young age and good Karnofsky performance score (KPS) at the time of diagnosis are reported to be associated with longer survival time [7]. Therefore, early diagnosis of PCNSL is essential to start early treatment before the patient's performance status has declined. Clinical diagnosis of PCNSL is sometimes difficult and delayed because common initial symptoms such as focal signs, raised intracranial pressure, and behavioral and personality changes especially in elderly patients are nonspecific [8]. Computerized tomography (CT) and magnetic resonance (MR) images in patients with PCNSL show single or multiple uniformly well-enhancing lesions that are usually located in the periventricular lesions and the basal ganglia and often involve the corpus callosum [8, 9]. These radiological findings are not pathognomonic for PCNSL and cannot accurately differentiate PCNSL from other

tumorous or nontumorous brain lesions. Moreover, atypical MR findings such as disseminated lesions or no lesions are more prevalent in a recent study than formally reported in immunocompetent patients with PCNSL [10].

Although CT and MR imaging are still the most important modalities in the diagnosis of PCNSL, modern metabolic imaging modalities other than conventional morphological imaging are increasingly used to improve accurate diagnosis of PCNSL. Positron emission tomography (PET) with glucose analogue ^{18}F-fluorodeoxyglucose (^{18}F-FDG) is one of the most attractive and widely used modalities for evaluating tumor metabolism noninvasively. Although PCNSL usually shows huge uptake of ^{18}F-FDG, normally high uptake of ^{18}F-FDG in the cerebral cortex, basal ganglia, and thalamus sometimes mask the presence of underlying PCNSL. Even in a rapid emerging clinical application, the role of ^{18}F-FDG PET in PCNSL is not fully defined and reviewed systemically. This paper reviews the usefulness and limitation of ^{18}F-FDG PET in the diagnosis and treatment of PCNSL.

2. Molecular Mechanism of ^{18}F-FDG Uptake

The glucose analog ^{18}F-FDG is a surrogate biomarker for glucose metabolism *in vivo* and is the most commonly used clinical PET radiotracer. The clinical applications of ^{18}F-FDG PET continue to increase, especially in the field of oncology as ^{18}F-FDG can be delivered from a hub-cyclotron center because of the relatively long half-life of ^{18}F (110 min). The molecular mechanisms of ^{18}F-FDG uptake in the cells were investigated intensively *in vitro* and *in vivo*. ^{18}F-FDG enters the cells by the same membrane glucose transporter (GLUT) as glucose. More than 10 GLUTs have been identified to date; only GLUT-1 and GLUT-3 need to be considered in the normal and tumorous brain [11]. After passing the blood-brain barrier (BBB) via the GLUT, both ^{18}F-FDG and glucose are phosphorylated by hexokinase. Unlike glucose-6-phosphate, ^{18}F-FDG-6-phosphate is not a substrate of glucose-6-phosphate isomerase and does not undergo further metabolism in the glucose pathway and is trapped in the cells. As a result, the ^{18}F-FDG uptake is a good reflection of glucose transport and phosphorylation by cells in the tumor. Several mechanisms have been shown to cause increased ^{18}F-FDG uptake in malignant tumors including high cellular density, overexpression of GLUT [12–14], and increased hexokinase activity [13, 14]. ^{18}F-FDG PET for tumor imaging is typically performed 45 to 60 minutes after an intravenous administration of ^{18}F-FDG. This interval allows the increase in tumor tracer activity due to intracellular trapping of ^{18}F-FDG-6-phosphate and the concomitant decrease in blood pool radiotracer and overall background tracer activity to improve the tumor-to-background ratio.

The degree of ^{18}F-FDG uptake is measured to perform comparison within and between different patients and disease. The standardized uptake value (SUV) is a widely used method of measuring static ^{18}F-FDG uptake in the lesion. The SUV is a semiquantitative value if all of the injected tracer is distributed evenly throughout the body and is computed as follows:

$$\mathrm{SUV} = \frac{\mathrm{FDG}_{\mathrm{region}}}{\left(\mathrm{FDG}_{\mathrm{dose}}/\mathrm{WT}\right)}, \quad (1)$$

where $\mathrm{FDG}_{\mathrm{region}}$ is the decay-corrected regional radiotracer concentration in becquerel (Bq) per milliliter, $\mathrm{FDG}_{\mathrm{dose}}$ is the administered ^{18}F-FDG dose in Bq, and WT is the body weight in kilograms. Alternatively, the tumor-to-normal brain tissue (T/N) ratio is used for evaluating ^{18}F-FDG uptake in the lesion. The T/N ratio is usually calculated by dividing the tumor SUV by the SUV value of the contralateral normal gray matter. The T/N ratio is not influenced by the injected radiotracer dose and the body weight, but the selection of normal brain tissue critically affects the calculated value.

3. ^{18}F-FDG PET in the Diagnosis of PCNSL

3.1. Primary Diagnosis and Differentiation from Nontumorous Lesions. PCNSL has a very high cellular density and increased glucose metabolism and usually shows strong uptake of ^{18}F-FDG in the tumor [15–20] (Figure 1). The semiquantitative ^{18}F-FDG uptake values measured by maximum SUV ($\mathrm{SUV}_{\mathrm{max}}$) are reported to be 14–22 in PCNSL [15–18], and this value is about 2.5 times higher than the average SUV in the normal gray matter [15–17] (Table 1). In patients with acquired immunodeficiency syndrome (AIDS), ^{18}F-FDG uptake in the lesions can be used to distinguish between human-immunodeficiency-virus-(HIV)-related brain disease such as cerebral toxoplasmosis and PCNSL [21–23] (Figure 2). The use of ^{18}F-FDG PET in the diagnosis of PCNSL is not a new concept. In 1992, Rosenfeld et al. reported a strong ^{18}F-FDG uptake in a group of 10 patients with PCNSL [19]. They also reported a patient who showed dramatic disappearance of ^{18}F-FDG uptake in the tumor with steroid therapy [19]. Hustinx et al. examined SUVs in primary brain tumors on ^{18}F-FDG PET and concluded that SUV measurements were influenced by a variety of factors, such as plasma glucose level, steroid treatment, tumor size and heterogeneity, time after injection, and previous radiation therapy [24]. Steroids have a cytotoxic effect in lymphoma cells and reduce ^{18}F-FDG uptake in the tumor significantly causing false negative results of ^{18}F-FDG PET in the diagnosis of PCNSL [15]. Moreover, nonspecific uptake of ^{18}F-FDG has been reported in patients with nontumorous brain lesions such as intracerebral hematoma [25], brain abscess [26], and multiple sclerosis [27]. Animal studies have shown that inflammatory cells significantly contribute to ^{18}F-FDG uptake in tumors. Kubota et al. reported that about 30% of ^{18}F-FDG uptake was related to the non-tumorous tissue in a malignant tumor model in mice [28]. The extent of ^{18}F-FDG uptake in the non-tumorous lesions depends on the increased density of inflammatory cells as well as disruption of the BBB in the lesion.

3.2. Differentiation from Other Malignant Brain Tumors. Recent studies have revealed that ^{18}F-FDG PET can differentiate

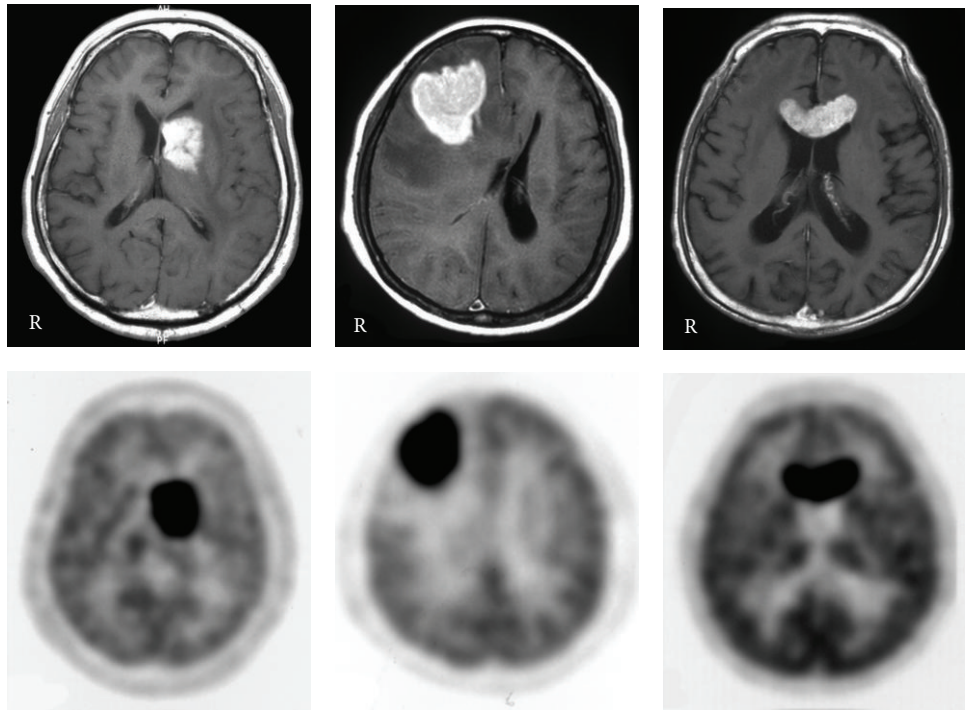

(a) (b) (c)

Figure 1: Contrast-enhanced T1-weighted MR (upper) and ^{18}F-FDG PET (lower) images in PCNSL patients with typical MR findings. MR images show a homogenous enhanced lesion in the left basal ganglia (a), the right frontal white matter (b), and the corpus callosum (c). ^{18}F-FDG PET images show a strong ^{18}F-FDG uptake in the lesions.

Table 1: Literature review: ^{18}F-FDG SUV_{max} and T/N ratio in PCNSL.

Study	*n*	Age (range)	SUV_{max}	T/N ratio
Kosaka et al. (2008) [15]	7[1]	—	22.2 ± 5.0	2.31 ± 0.70
Kawai et al. (2010) [16]	17[2]	65 (47–79)	13.5 ± 5.4	2.54
Kawase et al. (2011) [17]	13[2]	70 (54–80)	13.9 ± 5.7	2.74 ± 1.25
Makino et al. (2011) [18]	14	—	16.8 ± 7.2	—

[1]Two patients were treated with dexamethasone before PET study.
[2]Seven patients are overlapped (same institution).

PCNSL from other malignant brain tumors such as glioblastoma (GB) and metastatic brain tumor [15, 18] (Figure 3). The ^{18}F-FDG uptake in PCNSL is usually homogenous in contrast to inhomogeneous uptake in other malignant brain tumors. Kosaka et al. showed that metastatic brain tumors and GBs except for 1, case can be distinguished from PCNSL with ^{18}F-FDG PET when the cutoff value was set at 15 of SUV_{max} [15]. A recent study demonstrated the usefulness of ^{18}F-FDG PET for differentiating between PCNSL and GB showing similar MR findings. ^{18}F-FDG uptake in PCNSL (SUV_{max} of 16.8 ± 7.2) was significantly higher than that in GB (SUV_{max} of 8.2 ± 3.1; $P < 0.01$) [18]. The accuracy of ^{18}F-FDG PET for lesion differentiation was 0.86 when the cutoff value was set at 12 of SUV_{max} with a sensitivity of 100% and a specificity of 71.4% [18]. The overlying cortical gray matter sometimes shows glucose hypometabolism in PCNSL located in the deep white matter and the basal ganglia/thalamus. This finding is not a specific phenomenon in PCNSL and is reported in patients with gliomatosis cerebri due to disconnection of the cortical gray matter by tumor infiltration [29].

3.3. Diagnosis of Atypical PCNSL. PCNSL with typical radiological findings shows strong ^{18}F-FDG uptake in almost all cases, and ^{18}F-FDG PET provides valuable information in the primary diagnosis of PCNSL. However, PCNSL sometimes demonstrates atypical radiological findings such as disseminated or nonenhancing lesions (no lesions) in contrast-enhanced MR or CT images [9, 10]. Such atypical findings in non-AIDS patients with PCNSL were more prevalent in a recent study, showing that 13% of the patients had no lesions and 7% of the patients had disseminated lesions [10]. Ring-like enhancement occurs in more than 50% of the lesions in AIDS-related PCNSL, but also in 6–13% of the lesions in non-AIDS PCNSL [9, 10]. ^{18}F-FDG uptake in PCNSL with atypical

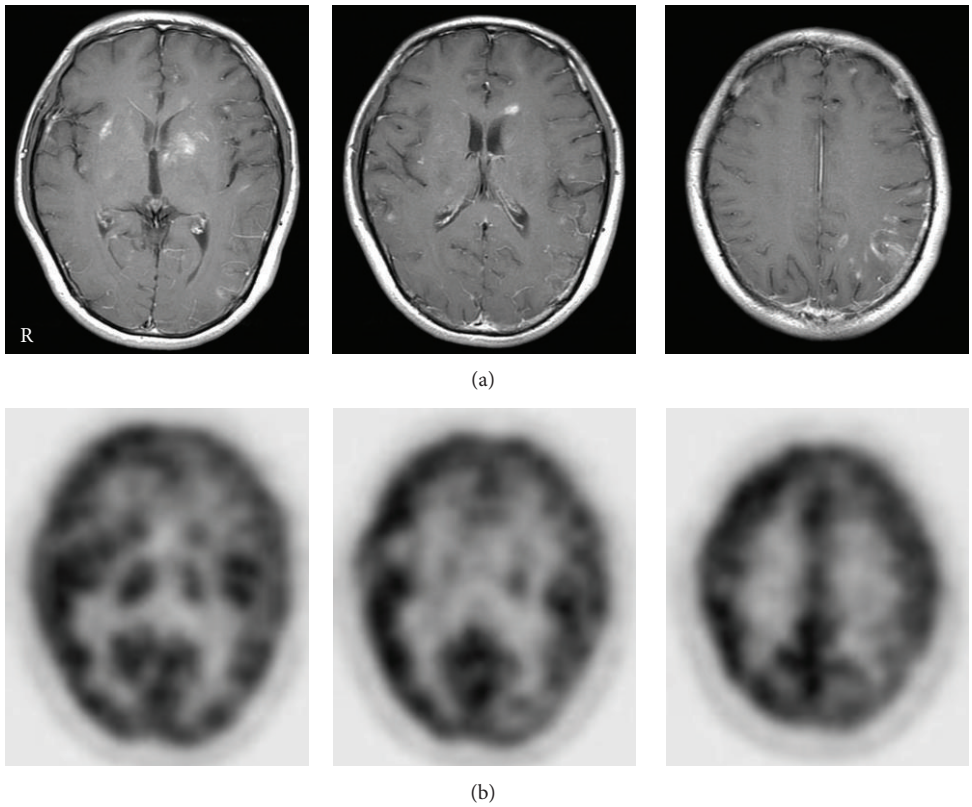

Figure 2: Contrast-enhanced T1-weighted MR (a) and ^{18}F-FDG PET (b) images in an HIV-positive patient with toxoplasmosis. MR images show multiple, small, irregular enhanced lesions in the basal ganglia and the white matter. PET images show no ^{18}F-FDG uptake in the lesions.

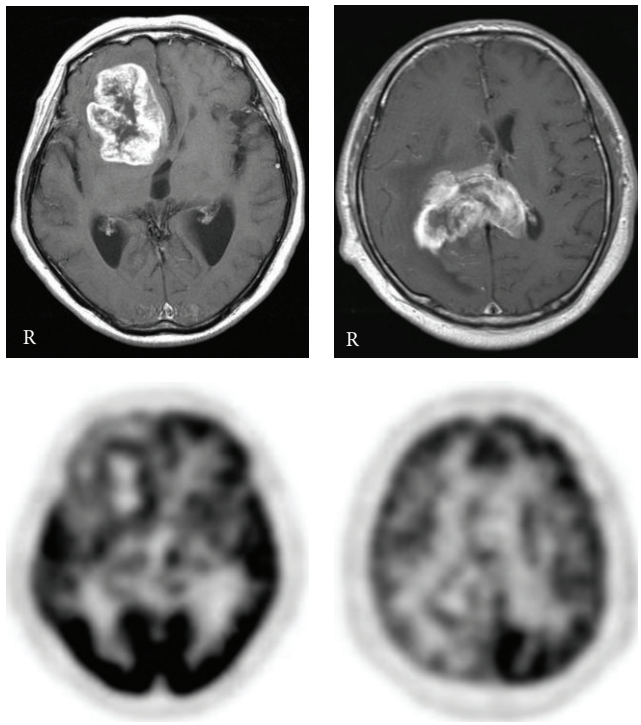

Figure 3: Contrast-enhanced T1-weighted MR (upper) and ^{18}F-FDG PET (lower) images in GB patients. MR images show a heterogeneous ring-like enhanced lesion in the right frontal lobe (a) and the splenium (b). PET images show a mild ring-like ^{18}F-FDG uptake in the lesions.

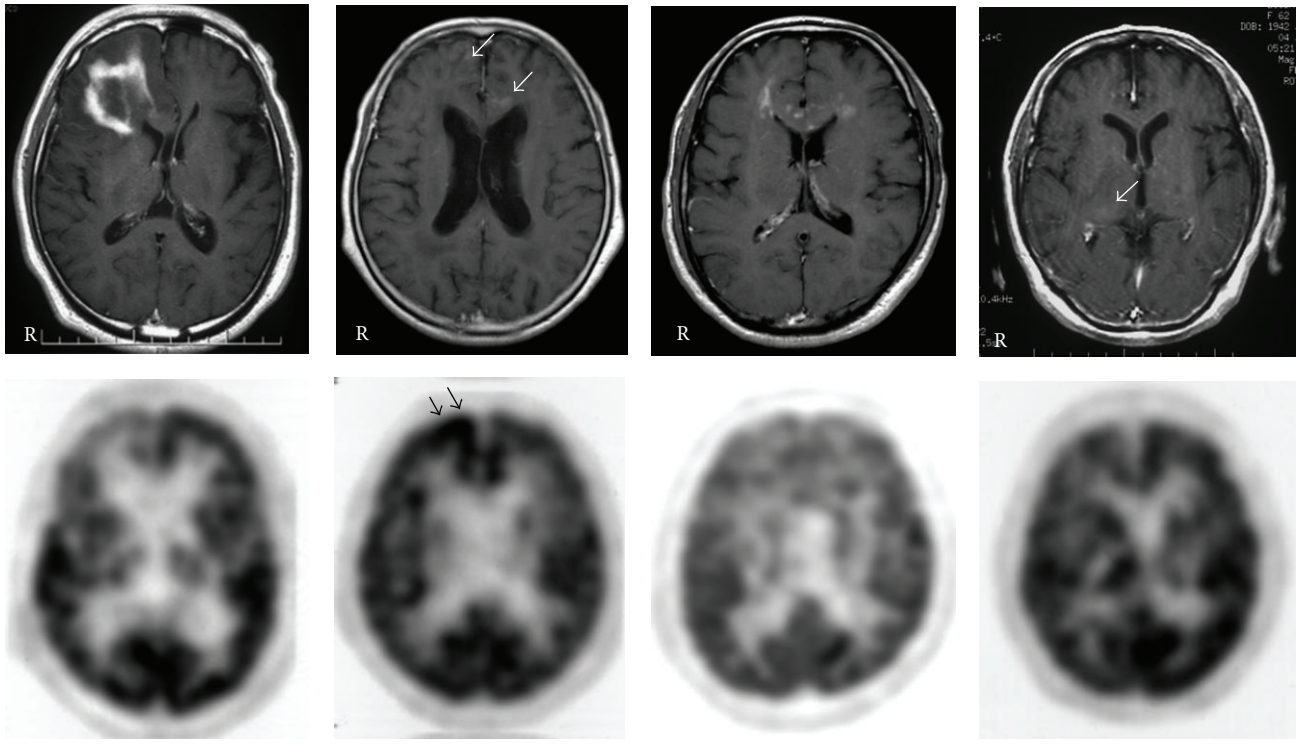

Figure 4: Contrast-enhanced T1-weighted MR (upper) and ^{18}F-FDG PET (lower) images in PCNSL patients with atypical MR findings. MR images show a ring-like enhanced lesion in the right frontal lobe (a), multiple faint enhanced lesions in the right cerebral cortex and the corpus callosum (b), multiple small enhanced lesions in the bilateral frontal white matter and the corpus callosum (c), and no enhancing lesion in the brain (d). PET images show no ^{18}F-FDG uptake in the lesions except for moderate ^{18}F-FDG uptake in the right frontal cortex (arrow) in case (b).

radiological findings is not increased sufficiently to detect the tumor visually because of normally high background uptake of ^{18}F-FDG in the brain (Figure 4). Kawai et al. revealed that 3 of the 4 ^{18}F-FDG PET failed to show the presence of PCNSL with atypical radiological findings visually [30]. Therefore, ^{18}F-FDG PET is not a perfect tool, and caution is necessary especially in the diagnosis of atypical PCNSL. To date no imaging modality can definitively diagnose PCNSL, and early tumor biopsy is still recommended when PCNSL is suspected especially with atypical radiological findings [31].

3.4. Detection of Occult Systemic Lymphoma. PCNSL is, by definition, a non-Hodgkin's lymphoma restricted to the CNS. Standard staging for PCNSL needs to examine contrast-enhanced CT of the chest, abdomen, and pelvis and sometimes bone marrow biopsy to exclude systemic lymphoma [32]. Conventional body staging in patients initially diagnosed with PCNSL showed an occult systemic lymphoma in about 4% of the patients [33]. The clinical significance of identifying systemic disease is uncertain, but at least 5% of PCNSL relapse outside the CNS [34]. ^{18}F-FDG PET may be more sensitive than conventional body staging and may disclose higher rates of concomitant systemic disease at initial PCNSL diagnosis. Mohile et al. demonstrated that 7% of patients initially diagnosed PCNSL were found to have systemic lymphoma by staging ^{18}F-FDG whole body PET scan even when body CT scans and bone marrow biopsies were negative [35]. Detection of systemic lymphoma at the time of initial PCNSL diagnosis may play important roles regarding the origin of the disease and treatment strategies.

Summary

(i) ^{18}F-FDG uptake value in PCNSL is about 2.5 times higher than that in the normal gray matter, and the tumor can usually be identified in the brain visually.

(ii) Steroid treatment significantly reduces ^{18}F-FDG uptake in the tumor and can cause false negative results of ^{18}F-FDG PET in the diagnosis of PCNSL.

(iii) ^{18}F-FDG PET can differentiate PCNSL from other malignant brain tumors such as GB and metastatic brain tumor with high sensitivity.

(iv) ^{18}F-FDG uptake in PCNSL with atypical radiological findings such as disseminated or nonenhancing lesions is not increased sufficiently to detect the tumor visually compared to the surrounding brain.

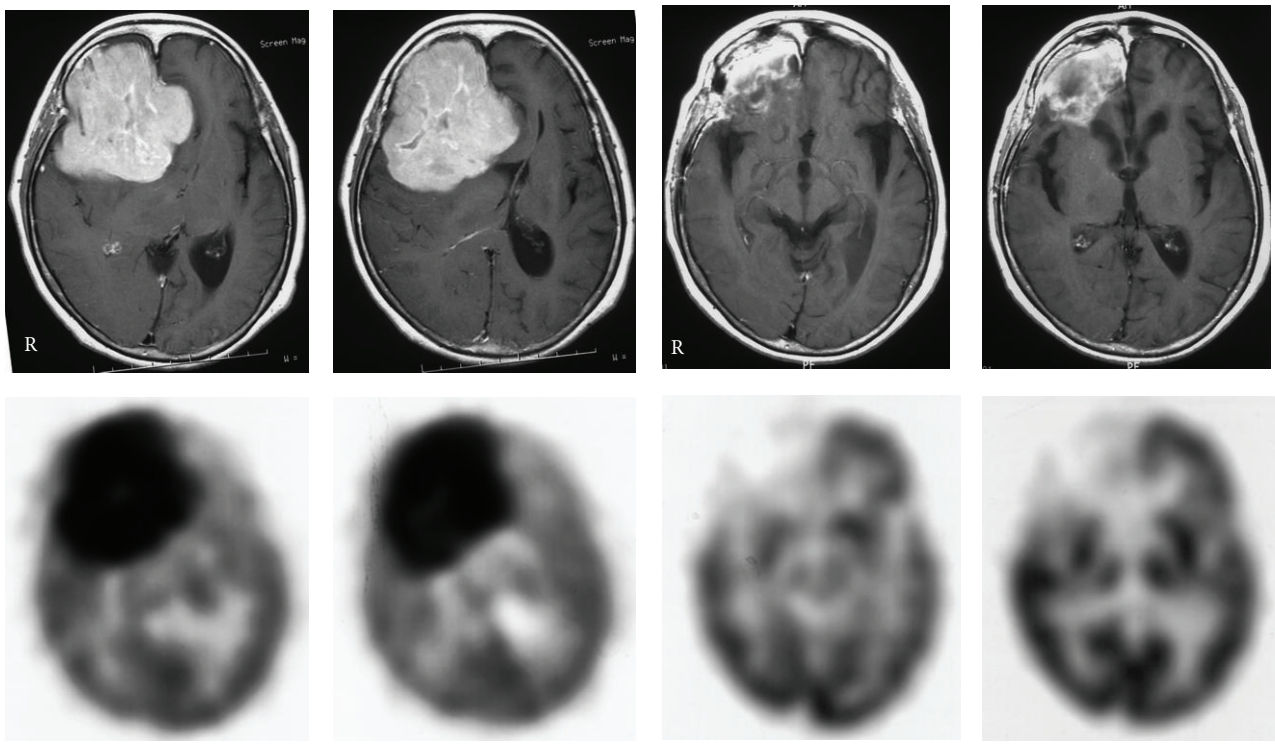

Figure 5: Contrast-enhanced T1-weighted MR (upper) and ^{18}F-FDG PET (lower) images in a patient with PCNSL in the right frontal lobe before (a) and after (b) the first cycle of chemotherapy. MR images show a well-enhanced large mass lesion in the right frontal lobe, and PET images show a huge ^{18}F-FDG uptake in the lesion before treatment (a). After the first chemotherapy, MR images show a residual enhanced lesion in the right frontal lobe; however, PET images show no increased ^{18}F-FDG uptake in the lesion (b).

(v) Conventional body scan with ^{18}F-FDG PET in patients initially diagnosed as PCNSL is occasionally useful to detect occult systemic lymphoma.

4. ^{18}F-FDG PET in the Treatment of PCNSL

4.1. Early Treatment Response. PCNSL is one of the most treatment-responsive malignant tumors in the brain. In recent years, high-dose MTX-based chemotherapy before radiotherapy has significantly extended the survival time compared to conventional chemotherapy with cyclophosphamide, adriamycin, vincristine, and prednisone (CHOP)-based regimens given either before or after radiotherapy [5, 6]. However, it is reported that about 10–35% of tumors are refractory to the high dose MTX-based regimen, and up to 60% of complete responders show tumor recurrence during follow-up [36]. Early evaluation of the initial treatment response is very important because salvage treatment may improve the outcome and quality of life [37]. Although MR imaging is the standard method for evaluating the treatment response in PCNSL [32], few studies have addressed the question of whether early tumor response, according to MRI criteria, in patients still under therapy helps to predict the long-term outcome in PCNSL [38]. In systemic lymphoma patients, an early quantitative measurement of metabolic response with ^{18}F-FDG PET was reported to provide more valuable prognostic information than conventional modalities [39]. Changes in metabolic imaging with ^{18}F-FDG PET occur soon after the initiation of therapy. Palmedo et al. studied 8 PCNSL patients with ^{18}F-FDG PET after completion of chemotherapy or after the first cycle of chemotherapy, and the results were compared with the follow-up examinations [20]. They showed that ^{18}F-FDG PET was able to predict complete remission or to diagnose tumor recurrence after chemotherapy in all patients [20]. Kawai et al. demonstrated that ^{18}F-FDG PET examined within 3 weeks of the first chemotherapy showed a significant decrease of ^{18}F-FDG uptake in the tumor compared with that before treatment [40]. The reduction of ^{18}F-FDG uptake significantly correlated with the decrease of tumor size on the follow-up MR images [40]. These results indicate that metabolic imaging with ^{18}F-FDG PET can be used to accurately evaluate treatment response at a very early stage, sometimes preceding changes on MRI (Figure 5). Early therapeutic monitoring might have an impact on deciding whether the treatment regimen should be maintained or changed. If patients with a poor early response were identified, then modification could be taken at an early stage, before many more cycles of ineffective therapy were delivered.

Again, caution is necessary in interrupting ^{18}F-FDG PET images especially after treatment because ^{18}F-FDG uptake in the tumor is not solely due to tumor cell metabolism but it also due to uptake in stromal and inflammatory cells [28].

4.2. Prognostic Considerations. A recent study showed that pretreatment ^{18}F-FDG uptake may have a prognostic value in newly diagnosed PCNSL. The overall survival time of patients with low to moderate ^{18}F-FDG uptake ($SUV_{max} < 12$) was significantly longer than that of patients with high ^{18}F-FDG uptake ($SUV_{max} \geq 12$) [16]. PCNSL with high ^{18}F-FDG uptake tended to exhibit poor treatment response compared to that with low to moderate ^{18}F-FDG uptake [16]. The ^{18}F-FDG uptake value may represent tumor aggressiveness in PCNSL. Further clinical trials are needed to define the best way to utilize ^{18}F-FDG PET information in designing true response-adapted therapies and to improve outcome in patients with PCNSL.

Summary

(i) ^{18}F-FDG PET can be used to evaluate treatment response of PCNSL at a very early stage after treatment.

(ii) ^{18}F-FDG PET is able to predict complete remission or to diagnose tumor recurrence of PCNSL after treatment.

(iii) Pretreatment ^{18}F-FDG uptake may have a prognostic value in newly diagnosed PCNSL.

5. Conclusions

The application of ^{18}F-FDG PET is currently increasing in clinical neurooncology. This review summarizes the usefulness and limitation of ^{18}F-FDG PET in the diagnosis and treatment of PCNSL. ^{18}F-FDG PET is very useful in the diagnosis of typical PCNSL, usually showing strong uptake of ^{18}F-FDG in the tumor. The uptake value is about 2.5 times higher than that in the normal gray matter, and the tumors can be identified in the brain visually. The ^{18}F-FDG uptake pattern and value provide useful information to differentiate PCNSL from other enhancing malignant brain tumors especially GB. However, the usefulness of ^{18}F-FDG PET is limited in the diagnosis of PCNSL with atypical radiological findings. ^{18}F-FDG PET is also useful for evaluating the treatment response after initial chemotherapy and determining the strategy at a very early stage. Pretreatment and posttreatment ^{18}F-FDG uptake values may have a prognostic value in patients with PCNSL. In a modern metabolic imaging era, ^{18}F-FDG PET is useful when differential diagnosis of brain tumors is difficult, and PCNSL is considered as one of the differential diagnoses, but ^{18}F-FDG PET is not a perfect tool, and early tumor biopsy is still necessary especially with atypical radiological findings.

Conflict of Interests

The authors declare no conflict of interests in this study.

Acknowledgments

This study was supported by a Grant-in-Aid for Scientific Research (B) (22390277) from the Ministry of Education, Sciences and Culture of Japan. The authors deeply appreciate the excellent technical support of the radiological technologist at their institution.

References

[1] J. E. Olson, C. A. Janney, R. D. Rao et al., "The continuing increase in the incidence of primary central nervous system non-Hodgkin lymphoma: a surveillance, epidemiology, and end results analysis," *Cancer*, vol. 95, no. 7, pp. 1504–1510, 2002.

[2] A. Behin, K. Hoang-Xuan, A. F. Carpentier, and J.-Y. Delattre, "Primary brain tumours in adults," *The Lancet*, vol. 361, no. 9354, pp. 323–331, 2003.

[3] D. Ricard, A. Idbaih, F. Ducray, M. Lahutte, K. Hoang-Xuan, and J.-Y. Delattre, "Primary brain tumours in adults," *The Lancet*, vol. 379, pp. 1984–1996, 2012.

[4] N. S. Kadan-Lottick, M. C. Skluzacek, and J. G. Gurney, "Decreasing incidence rates of primary central nervous system lymphoma," *Cancer*, vol. 95, no. 1, pp. 193–202, 2002.

[5] P. C. O'Brien, D. E. Roos, G. Pratt et al., "Combined-modality therapy for primary central nervous system lymphoma: long-term data from a Phase II multicenter study (Trans-Tasman Radiation Oncology Group)," *International Journal of Radiation Oncology Biology Physics*, vol. 64, no. 2, pp. 408–413, 2006.

[6] M. S. del Rio, A. Rousseau, C. Soussain, D. Ricard, and K. Hoang-Xuan, "Primary CNS lymphoma in immunocompetent patients," *Oncologist*, vol. 14, no. 5, pp. 526–539, 2009.

[7] L. E. Abrey, L. Ben-Porat, K. S. Panageas et al., "Primary central nervous system lymphoma: the memorial sloan-kettering cancer center prognostic model," *Journal of Clinical Oncology*, vol. 24, no. 36, pp. 5711–5715, 2006.

[8] B. Bataille, V. Delwail, E. Menet et al., "Primary intracerebral malignant lymphoma: report of 248 cases," *Journal of Neurosurgery*, vol. 92, no. 2, pp. 261–266, 2000.

[9] W. Küker, T. Nägele, A. Korfel et al., "Primary central nervous system lymphomas (PCNSL): MRI features at presentation in 100 patients," *Journal of Neuro-Oncology*, vol. 72, no. 2, pp. 169–177, 2005.

[10] I. S. Haldorsen, J. Krakenes, B. K. Krossnes, O. Mella, and A. Espeland, "CT and MR imaging features of primary central nervous system lymphoma in Norway, 1989–2003," *American Journal of Neuroradiology*, vol. 30, no. 4, pp. 744–751, 2009.

[11] R. J. Boado, K. L. Black, and W. M. Pardridge, "Gene expression of GLUT3 and GLUT1 glucose transporters in human brain tumors," *Molecular Brain Research*, vol. 27, no. 1, pp. 51–57, 1994.

[12] S. N. Reske, K. G. Grillenberger, G. Glatting et al., "Overexpression of glucose transporter 1 and increased FDG uptake in pancreatic carcinoma," *Journal of Nuclear Medicine*, vol. 38, no. 9, pp. 1344–4348, 1997.

[13] L.-C. Ong, Y. Jin, I.-C. Song, S. Yu, K. Zhang, and P. K. H. Chow, "2-[18F]-2-deoxy-D-Glucose (FDG) uptake in human tumor cells is related to the expression of GLUT-1 and hexokinase II," *Acta Radiologica*, vol. 49, no. 10, pp. 1145–1153, 2008.

[14] B. Paudyal, N. Oriuchi, P. Paudyal et al., "Clinicopathological presentation of varying 18F-FDG uptake and expression of glucose transporter 1 and hexokinase II in cases of hepatocellular

carcinoma and cholangiocellular carcinoma," *Annals of Nuclear Medicine*, vol. 22, no. 1, pp. 83–86, 2008.

[15] N. Kosaka, T. Tsuchida, H. Uematsu, H. Kimura, H. Okazawa, and H. Itoh, "18F-FDG PET of common enhancing malignant brain tumors," *American Journal of Roentgenology*, vol. 190, no. 6, pp. W365–W369, 2008.

[16] N. Kawai, H.-N. Zhen, K. Miyake, Y. Yamamaoto, Y. Nishiyama, and T. Tamiya, "Prognostic value of pretreatment 18F-FDG PET in patients with primary central nervous system lymphoma: SUV-based assessment," *Journal of Neuro-Oncology*, vol. 100, no. 2, pp. 225–232, 2010.

[17] Y. Kawase, Y. Yamamoto, R. Kameyama, N. Kawai, N. Kudomi, and Y. Nishiyama, "Comparison of 11C-methionine PET and 18F-FDG PET in patients with primary central nervous system lymphoma," *Molecular Imaging and Biology*, vol. 13, no. 6, pp. 1284–1289, 2011.

[18] K. Makino, T. Hirai, H. Nakamura et al., "Does adding FDG-PET to MRI improve the differentiation between primary cerebral lymphoma and glioblastoma? Observer performance study," *Annals of Nuclear Medicine*, vol. 25, no. 6, pp. 432–438, 2011.

[19] S. S. Rosenfeld, J. M. Hoffman, R. E. Coleman, M. J. Glantz, M. W. Hanson, and S. C. Schold, "Studies of primary central nervous system lymphoma with fluorine-18-fluorodeoxyglucose positron emission tomography," *Journal of Nuclear Medicine*, vol. 33, no. 4, pp. 532–536, 1992.

[20] H. Palmedo, H. Urbach, H. Bender et al., "FDG-PET in immunocompetent patients with primary central nervous system lymphoma: correlation with MRI and clinical follow-up," *European Journal of Nuclear Medicine and Molecular Imaging*, vol. 33, no. 2, pp. 164–168, 2006.

[21] J. M. Hoffman, H. A. Waskin, T. Schifter et al., "FDG-PET in differentiating lymphoma from nonmalignant central nervous system lesions in patients with AIDS," *Journal of Nuclear Medicine*, vol. 34, no. 4, pp. 567–575, 1993.

[22] K. Villringer, H. Jager, M. Dichgans et al., "Differential diagnosis of CNS lesions in AIDS patients by FDG-PET," *Journal of Computer Assisted Tomography*, vol. 19, no. 4, pp. 532–536, 1995.

[23] M. J. O'Doherty, S. F. Barrington, M. Campbell, J. Lowe, and C. S. Bradbeer, "PET scanning and the human immunodeficiency virus-positive patient," *Journal of Nuclear Medicine*, vol. 38, no. 10, pp. 1575–1583, 1997.

[24] R. Hustinx, R. J. Smith, F. Benard, A. Bhatnagar, and A. Alavi, "Can the standardized uptake value characterize primary brain tumors on FDG-PET?" *European Journal of Nuclear Medicine*, vol. 26, no. 11, pp. 1501–1509, 1999.

[25] S. Dethy, S. Goldman, S. Blecic, A. Luxen, M. Levivier, and J. Hildebrand, "Carbon-11-methionine and fluorine-18-FDG PET study in brain hematoma," *Journal of Nuclear Medicine*, vol. 35, no. 7, pp. 1162–1166, 1994.

[26] N. Tsuyuguchi, I. Sunada, K. Ohata et al., "Evaluation of treatment effects in brain abscess with positron emission tomography: comparison of fluorine-18-fluorodeoxyglucose and carbon-11-methionine," *Annals of Nuclear Medicine*, vol. 17, no. 1, pp. 47–51, 2003.

[27] C. Schiepers, P. van Hecke, R. Vandenberghe et al., "Positron emission tomography, magnetic resonance imaging and proton NMR spectroscopy of white matter in multiple sclerosis," *Multiple Sclerosis*, vol. 3, no. 1, pp. 8–17, 1997.

[28] R. Kubota, S. Yamada, K. Kubota, K. Ishiwata, N. Tamahashi, and T. Ido, "Intratumoral distribution of fluorine-18-fluorodeoxyglucose in vivo: High accumulation in macrophages and granulation tissues studied by microautoradiography," *Journal of Nuclear Medicine*, vol. 33, no. 11, pp. 1972–1980, 1992.

[29] P. N. Plowman, C. A. B. Saunders, and M. N. Maisey, "Gliomatosis cerebri: disconnection of the cortical grey matter, demonstrated on PET scan," *British Journal of Neurosurgery*, vol. 12, no. 3, pp. 240–244, 1998.

[30] N. Kawai, S. Okubo, K. Miyake et al., "Use of PET in the diagnosis of primary CNS lymphoma in patients with atypical MR findings," *Annals of Nuclear Medicine*, vol. 24, no. 5, pp. 335–343, 2010.

[31] Y. Z. Tang, T. C. Booth, P. Bhogal, A. Malhotra, and T. Wilhelm, "Imaging of primary central nervous system lymphoma," *Clinical Radiology*, vol. 66, no. 8, pp. 768–777, 2011.

[32] L. E. Abrey, T. T. Batchelor, A. J. M. Ferreri et al., "Report of an international workshop to standardize baseline evaluation and response criteria for primary CNS lymphoma," *Journal of Clinical Oncology*, vol. 23, no. 22, pp. 5034–5043, 2005.

[33] B. P. O'Neill, R. P. Dinapoli, P. J. Kurtin, and T. M. Habermann, "Occult systemic non-Hodgkin's lymphoma (NHL) in patients initially diagnosed as primary central nervous system lymphoma (PCNSL): how much staging is enough?" *Journal of Neuro-Oncology*, vol. 25, no. 1, pp. 67–71, 1995.

[34] K. Jahnke, E. Thiel, P. Martus et al., "Relapse of primary central nervous system lymphoma: clinical features, outcome and prognostic factors," *Journal of Neuro-Oncology*, vol. 80, no. 2, pp. 159–165, 2006.

[35] N. A. Mohile, L. M. Deangelis, and L. E. Abrey, "The utility of body FDG PET in staging primary central nervous system lymphoma," *Neuro-Oncology*, vol. 10, no. 2, pp. 223–228, 2008.

[36] M. Reni, A. J. M. Ferreri, and E. Villa, "Second-line treatment for primary central nervous system lymphoma," *British Journal of Cancer*, vol. 79, no. 3-4, pp. 530–534, 1999.

[37] R. Yamanaka, "Management of refractory or relapsed primary central nervous system lymphoma," *Molecular Medicine Reports*, vol. 2, no. 6, pp. 879–885, 2009.

[38] H. Pels, A. Juergens, I. Schirgens et al., "Early complete response during chemotherapy predicts favorable outcome in patients with primary CNS lymphoma," *Neuro-Oncology*, vol. 12, no. 7, pp. 720–724, 2010.

[39] N. G. Mikhaeel, M. Hutchings, P. A. Fields, M. J. O'Doherty, and A. R. Timothy, "FDG-PET after two to three cycles of chemotherapy predicts progression-free and overall survival in high-grade non-Hodgkin lymphoma," *Annals of Oncology*, vol. 16, no. 9, pp. 1514–1523, 2005.

[40] N. Kawai, Y. Nishiyama, K. Miyake, T. Tamiya, and S. Nagao, "Evaluation of tumor FDG transport and metabolism in primary central nervous system lymphoma using [18F]fluorodeoxyglucose (FDG) positron emission tomography (PET) kinetic analysis," *Annals of Nuclear Medicine*, vol. 19, no. 8, pp. 685–690, 2005.

Hindawi Publishing Corporation
BioMed Research International
Volume 2013, Article ID 872739, 10 pages
http://dx.doi.org/10.1155/2013/872739

Research Article

Assessment of Respiration-Induced Motion and Its Impact on Treatment Outcome for Lung Cancer

Yan Wang,[1] Yong Bao,[1] Li Zhang,[2] Wei Fan,[3] Han He,[4] Zong-Wen Sun,[5] Xiao Hu,[1] Shao-Min Huang,[2] Ming Chen,[1] and Xiao-Wu Deng[2]

[1] *Department of Radiation Oncology, State Key Laboratory of Oncology in Southern China, Cancer Center, Sun Yat-Sen University, Guangzhou, Guangdong 510060, China*
[2] *Department of Radiation Physics, Cancer Center, Sun Yat-Sen University, Guangzhou 510060, China*
[3] *Department of Nuclear Physics, Cancer Center, Sun Yat-Sen University, Guangzhou 510060, China*
[4] *Department of Radiation Oncology, The First People's Hospital of Foshan City, Foshan 528800, China*
[5] *Department of Radiation Oncology, The First People's Hospital of Jining City, Jining 272011, China*

Correspondence should be addressed to Ming Chen; chenmingdr@163.com and Xiao-Wu Deng; dengxw@sysucc.org.cn

Received 5 March 2013; Revised 18 April 2013; Accepted 25 April 2013

Academic Editor: An Liu

This study presented the analysis of free-breathing lung tumor motion characteristics using GE 4DCT and Varian RPM systems. Tumor respiratory movement was found to be associated with GTV size, the superior-inferior tumor location in the lung, and the attachment degree to rigid structure (e.g., chest wall, vertebrae, or mediastinum), with tumor location being the most important factor among the other two. Improved outcomes in survival and local control of 43 lung cancer patients were also reported. Consideration of respiration-induced motion based on 4DCT for lung cancer yields individualized margin and more accurate and safe target coverage and thus can potentially improve treatment outcome.

1. Introduction

Respiration-induced tumor motion is a significant source of geometric uncertainty in radiotherapy for thoracic malignancies [1, 2]. In the era of three-dimensional (3D) conformal radiotherapy, a tumor is usually imaged at a random time point by a free-breathing CT and encompassed by a generalized empirical respiratory-motion margin. However, in free-breathing CT, a thoracic structure can be distorted due to the motion, resulting in either lengthening or shortening of the structure in the motion direction [3]. Because of such motion artifact, the size, shape, and position of moving tumor or other organs cannot be depicted accurately. Furthermore, the conventionally used "standard safety margins" are defined without explicit measurements of the individual tumor motion [4, 5]. Recent studies show that individual, as opposed to a standard population-based margin, is essential for high-precision radiotherapy of lung cancer [2, 6–9].

Adding the fourth dimension, time, to three-dimensional CT is termed four-dimensional CT (4DCT) [10, 11]. 4DCT image data provides important spatial and temporal information including the entire range of moving targets and organs during quiet respiration [12] and has been used to characterize intrafractional respiration mobility and to determine an individualized tighter margin around the target [13]. The improved geometric accuracy would increase the therapeutic gain as it allows escalated dose to the tumor and/or improved sparing for healthy tissue [9].

Studies on the assessment of lung tumor motion using different approaches, which ranged from fluoroscopy [14], to orthogonal portal films [15], dynamic magnetic resonance imaging (MRI) [16], slow CT [7], breath-hold CT [17], and 4DCT [18–20], have been reported. The tumor motion was assessed with implanted gold markers in or near tumor [15] or by the centroid or border of tumor [7, 14, 16–21]. It was observed that the closer the tumor to the diaphragm,

the more mobile the tumor was [7, 15, 16, 18–21], because the respiration was primarily driven by the diaphragm motion. In vast majority of studies, small solitary tumors showed larger motions than bigger ones [15, 20], and the magnitude of tumor motion was always the greatest in the superior-inferior (SI) direction [7, 15, 16, 18–21].

The 4DCT is proven to be more effective and objective for the evaluation of breathing motion. This is still of great interest for more comprehensive understanding on factors associated with respiration-induced tumor motion and on its impact of treatment outcome. The main purpose of this work is, then, to determining these factors and the impact by analyzing the respiration motion and outcome data collected for 4DCT-based radiotherapy in our clinic.

2. Materials and Methods

2.1. Ethics Statement. This retrospective research was conducted according to the principle described in the *Declaration of Helsinki*. The research protocol was reviewed and approved by Ethical Review Committee of Sun Yat-Sen University Cancer Center (SYSUCC) (approval number, YP2008032).

2.2. Study Patients. After a review of medical records in our hospital, we identified 43 patients with 44 lung tumors who underwent 4DCT scans during quiet respiration between September 2005 and January 2008. Each patient had at least one pulmonary lesion with distinct boundary. Tumor staging was done by contrast-agent CT chest and abdomen, magnetic resonance imaging (MRI) of the brain, and bone scintigraphy whereas positron-emission tomography and CT were not mandatory. All patients who had local and/or regional disease, received a curative intent radiotherapy with or without chemotherapy. Karnofsky Performance Status (KPS) ≥70 and weight loss <5% in half a year were required. Exclusion criteria included previous thoracic surgery, previous radiation treatment, clinically significant pleural effusion limiting delineation of the total extent of the primary tumor, lobar atelectasis, and an inability to breathe in a reproducible manner (breath variability was more than 5%). Patients were excluded from the study in survival analysis section if their total dose was <60 Gy.

2.3. 4DCT Procedure. At SYSUCC, a 16 slice 4DCT scanner (GE Lightspeed, GE) with a respiration management system (RPM, Varian) was used to acquire respiration correlated CT. Retrospective 4DCT scanning entailed the generation of multiple slices at each relevant table position, during at least the length of a full respiration cycle (oversampling). The acquired data (about 1000 images) were sorted into 10 datasets correlating with 10 phases of the respiratory cycle. The phase 0% represents the end of inspiration, with the phase 50% for the end of expiration. The spatial resolution along the superior-inferior direction was limited by the 2.5 mm slice thickness.

2.4. Tumor Delineation and Motion Measurement. The gross tumor volumes (GTVs) on ten respiratory phases were delineated using a treatment planning system (Pinnacle^3, version 7.6c, Philips). All GTVs were delineated with an autosegmentation tool using threshold −750 to 4096 Hu first then manually modified by a single radiation oncologist. All contours were checked by two other radiation oncologists for consistency.

The GTV volumes for the ten phases were recorded as GTV-0%, GTV-20%, …, and GTV-90%. The mean GTV volume was calculated from the average GTVs of ten respiratory phases as mean GTV = 1/10 (GTV-0% + GTV-10% + ⋯ + GTV-90%). Internal gross tumor volume (IGTV) was obtained by combining the GTVs in ten phases of the respiratory cycle, that is, by the union of the 10 GTVs.

The centriods of GTVs in ten phases were determined by the planning system and were used to calculate the magnitudes of motions in three directions termed as dLR, dAP, and dSI, the distance between the two extreme positions in left-right (LR), anterior-posterior (AP), and superior-inferior (SI) direction during the respiratory cycle phases, respectively. The 3D vector was calculated as follows: 3D vector = $\sqrt{d\mathrm{LR}^2 + d\mathrm{AP}^2 + d\mathrm{SI}^2}$. Program MATLAB 7.4 (MathWorks) was used to compute and plot 3D point trajectories.

The CT set at 20% phase was chosen as reference CT to determine the relative GTV location in the lung. The location parameter consisted of three directional components, fLR, fAP, and fSI, corresponding to the relative fractional location in the lung in LR, AP, and SI directions, respectively. For example, fSI was the distance between the apex of the lung and the GTV centroid divided by the distance between the apex and the diaphragm point passing through the GTV centroid in the SI direction. For the LR and AP directions, the same method was applied except that the distance was defined from the centriod to the carina (for LR) or to the anterior boundary of the lung (for AP), and the divisor was defined as ipsilateral lung LR or AP diameter. The attachment degree to rigid structure (e.g., chest wall, vertebrae, or mediastinum, which all minimal respiratory motion) was defined as the ratio of the longest diameter attached to the rigid structure divided by longest diameter of the tumor in transversal plane.

2.5. Treatment Planning and Delivery. In the clinic, GTVs included the primary tumor (GTV-T), positive lymph nodes (GTV-N) with lymph nodes in the mediastinum with a short diameter >1 cm, or lymph nodes with positive tumor cell sampling, or clusters of small lymph nodes of short diameter <1 cm within 1 region, or ^{18}F-FDG standard uptake value >2.5 on PET/CT at initial staging. IGTV was obtained on 4DCT maximal intensity projection or ten phases. For patients who had squamous cell carcinoma, the clinical target volume tumor (CTV-T) included IGTV-T with a margin of 0.6 cm. For patients who had adenocarcinoma or histology not otherwise specified nonsmall cell lung cancer (NSCLC) or small cell lung cancer (SCLC), the CTV-T was created by IGTV-T with a margin of 0.8 cm. The clinical target volume node (CTV-N) included the positive lymph nodes region only. A 5 mm expansion uniformly around the CTV created the planning target volumes (PTV).

6–8 MV X-rays were used. All NSCLC patients underwent radiotherapy with conventional fractionation schemes. Tumors were prescribed as high as possible (not lower than 60 Gy) based on normal tissue dose-volume constraint. For locally advanced NSCLC (T3-4NxM0 or TxN2-3M0) patients, concurrent chemotherapy consisted of weekly or 2 cycles of monthly cisplatin and taxane-based regimens. For limited-stage SCLC patients, thoracic radiotherapy was administrated with a total dose of 45 Gy and at hyperfractionated technique of 1.5 Gy/fraction twice daily. The minimal interval between fractions was 6 hours. Patients received thoracic radiotherapy within the first 2 cycles of cisplatin and etoposide (EP). Patients who achieved complete remission (CR) or partial remission (PR) of tumor after the completion of chemoradiotherapy (4–6 cycles of EP plus concurrent thoracic radiotherapy) were offered prophylactic cranial irradiation (PCI), which was delivered daily to a total dose of 30 Gy over a period of 3 weeks or 25 Gy over 2 weeks.

2.6. Followup. After completion of treatment, patients were reviewed within 4–6 weeks, then every 3 months in the first 2 years, and every 4 months in the third year, every 6 months thereafter. Physical examination and CT scans of the thorax and upper abdomen were performed routinely.

2.7. Statistical Analysis. SPSS 13.0 statistical software was used (SPSS Inc., Chicago, IL). To understand what factors could be associated with and predictive of tumor motion, logistic regression (backward stepwise method) was used to test the relationship between GTV motion and clinical or anatomic factors, which were either continuous or categoric variables (e.g., gender, histology, age, GTV volume, tumor location, and attachment degree to the rigid structure). According to the results of the statistical analysis and observation of the GTV motion pattern, we calculated R^2 values to assess the possible correlation between the GTV centroid 3D vector motion and the relevant factors. Actuarial overall survival (OS), cancer-specific survival (CSS), progression-free survival (PFS), local progression-free survival, and distant metastasis-free rate were estimated by the Kaplan-Meier model, and the significances were tested by log-rank. The time for survival or failure was calculated from the first day of treatment intervention.

3. Results

3.1. Patient and Treatment Characteristics. Patient characteristics are listed in Table 1. The median age of the 38 men and 5 women was 56 years (range: 35–78 years). Twenty-seven patients had NSCLC (Stage I in 1, II in 1, IIIA in 5, IIIB in 15, and IV in 5), fifteen had limited-stage SCLC, and one had nasopharyngeal carcinoma with isolated lung metastases. The most common involved lobes were the upper lobes (36.4% left and 38.6% right). The median GTV was 45 cm^3 (range, 0.5–454 cm^3), and the median radiation dose of NSCLC was 62 Gy given in 31 fractions (range: 54–70 Gy, 2 Gy per fraction), one fraction daily. All SCLC patients received thoracic radiotherapy of 45 Gy with 1.5 Gy twice a day in 30 fractions. Most patients (39, or 82.9%) had received concurrent chemotherapy (CCRT), and the most common concurrent chemotherapy regimen was paclitaxel (45–50 mg/m^2 weekly).

Table 1: Patient and treatment characteristics of the 43 patients.

Factors	Characteristic	Number of cases	Percentage
Gender	Male	38	88.4%
	Female	5	11.6%
Age (years old)	Median	56	
	Range	35–78	
Histology	NSCLC	27	62.8%
	SCLC	15	34.9%
	Metastases	1	2.3%
Stage of NSCLC ($n = 27$)	I-II	2	7.4%
	IIIA	5	18.5%
	IIIB	15	55.6%
	IV	5	18.5%
Stage of SCLC ($n = 15$)	Limited stage	15	100%
T status*	T1	10	23.8%
	T2	7	16.7%
	T3	7	16.7%
	T4	18	42.8%
N status*	N0-1	5	11.9%
	N2	16	38.1%
	N3	21	50%
Tumor location†	Left upper lobe	16	36.4%
	Left lower lobe	1	2.3%
	Right upper lobe	17	38.6%
	Right middle lobe	4	9.1%
	Right lower lobe	6	13.6%
GTV volume (cm^3)	Median	45	
	Range	0.5–454	
Tumor attachment status†	Solitary tumor	14	31.8%
	Attached tumor	30	68.2%
Treatment dose of NSCLC (Gy) ($n = 27$)	Median	62	
	Range	54–70	
	<60	6	22.2%
	60–65	13	48.1%
	66–70	8	29.6%
Treatment dose of SCLC ($n = 15$)	45	15	100%
Concurrent chemoradiotherapy*	NSCLC	24‡	88.9%
	SCLC	15	100%

*One nasopharyngeal carcinoma patient with isolated lung metastases was not included in the T or N status calculation.
†One NSCLC patient had two lung lesions.
‡Two early patients received radiation alone. One locally advanced patient canceled chemotherapy for active tuberculosis.
NSCLC: nonsmall cell lung cancer; SCLC: small cell lung cancer; GTV: gross tumor volume.

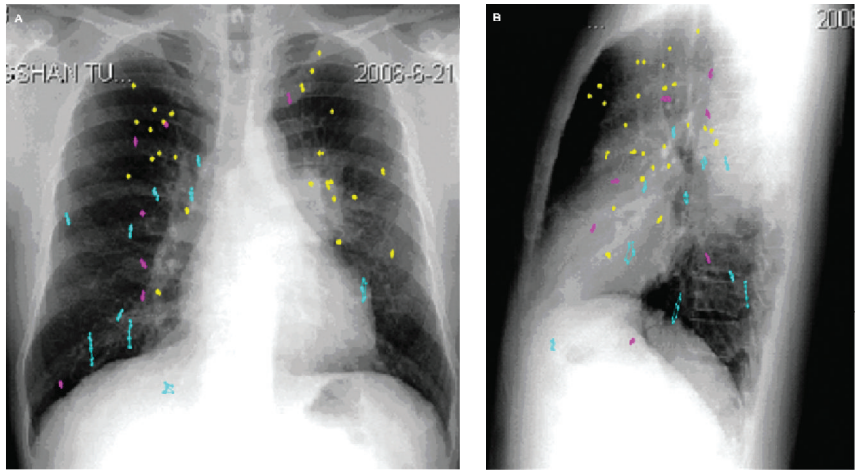

(a) (b)

Figure 1: The 3D point trajectories of GTV centroid. Green plots represent the movement of tumor center of mass is more than 5 mm in any directions (10/44), yellow points mean whose movement is less than 3 mm in three directions (27/44), and red plots represent whose is movement between 3–5 mm (7/44). (a) anterior-posterior view; (b) lateral view.

Table 2: Relationship of GTV centroid 3D vector with clinical and anatomic factors by logistic regression.

Clinical and anatomic factors	*P* value
Gender	0.198
Age	0.095
Histology	0.114
fLR	0.073
fAP	0.111
fSI	0.001
GTV volume (cm^3)	0.046
Attachment degree to rigid structure	0.008

Logistic regression suggested that the tumor centriod 3D vector was associated with GTV volume, fSI (the superior-inferior tumor location in the lung) and the attachment degree to rigid structure (e.g., chest wall, vertebrae, or mediastinum).
NSCLC: nonsmall cell lung cancer; SCLC: small cell lung cancer; fLR, fAP, fSI: fractional left-right, anterior-posterior, and superior-inferior location, respectively; GTV: gross tumor volume; attachment degree to rigid structure: the ratio of the longest diameter attached to the rigid structure divided by longest diameter of the tumor in transversal plane.

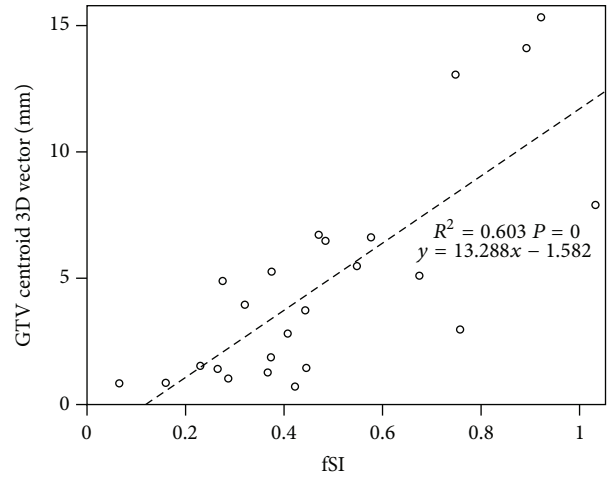

Figure 2: Relationship between vector and fSI, filtered out attachment degree to rigid structure >0.6, $y = 13.288x - 1.582$ $R^2 = 0.603$ Abbreviation: fSI: fractional superior-inferior location; 3D vector = $\sqrt{d\text{LR}^2 + d\text{AP}^2 + d\text{SI}^2}$.

3.2. GTV Centroid Movement. GTV centroid motion exceeding 5 mm was seen in 10 of 43 patients (23%), while 61% of lung tumors moving less than 3 mm (Figure 1). Maximum magnitude of the tumor centroid of 5.3 mm, 5.2 mm, and 14.4 mm was observed in the LR, AP, and SI direction, respectively. Averaged over all patients, the means and 1SD of the LR, AP, and SI motion were 1.2 ± 0.9 mm, 1.6 ± 1.1 mm, and 2.9 ± 3.4 mm, respectively. The maximum expected motion with a 95% percentile about the centroid of GTV for LR, AP, and SI direction was 2.6 mm, 4.8 mm, and 13.05 mm, respectively.

Analysis of all data revealed that the variations in GTV centroid 3D vector movement was associated with GTV size, the SI tumor location in the lung, and the attachment degree to a rigid structure, such as chest wall, vertebrae, or mediastinum (Table 2). Nonlinear relationship was observed between vector displacement and GTV volume or length, and so was the attachment degree to rigid structure. There was a weak positive correlation between centroid vector mobility and fSI, implying that patients with lower lesion disease tend to exhibit larger tumor movements. Excluding the cases with attachment degree more than 0.6, the correlation would enhance with a correlation coefficient (R) from 0.418 to 0.603 (Figure 2).

The peripheral lung tumor located near the diaphragm showed the greatest degree of motion, followed by upper-lobe posterior-segment solitary tumors. Detailed characteristics of high-mobility tumors are summarized in Table 3.

Table 3: The characteristics of high-mobility tumors (movement more than 5 mm).

Case	Tumor location	GTV (cm^3)	Longest diameter (cm)	Attachment degree	fAP	fSI	dLR (mm)	dAP (mm)	dSI (mm)	Vector (mm)
A	RUL (apicoposterior segmental)	24.9	4.6	0.5	0.56	0.37	0.8	1	5.1	5.3
B	RUL (posterior basal segmental)	31.6	5.9	0.47	0.68	0.47	2.5	2.3	5.8	6.7
C	RUL (posterior basal segmental)	2.2	1.6	0	0.46	0.54	1.4	1	5.2	5.5
D	RUL (posterior basal segmental)	2.4	1.9	0	0.61	0.57	0.7	1.9	6.3	6.6
E	RLL (lateral posterior basal segmental)	165.3	6.2	0.92	0.78	0.82	2.5	2.1	5.1	6.1
F	RLL (dorsal segmental)	0.55	1.2	0	0.76	0.51	1.4	2	6	6.5
G	LLL (lingular bronchus)	12.5	2.9	0	0.42	0.74	2.6	5.2	11.7	13.1
H	RLL (anteriorbasal segmental)	2.2	1.4	Attach to diaphragm	0.12	0.9	5.3	1.7	5.6	7.9
I	LLL (lateral posterior basal segmental)	59.6	4.9	Attach to diaphragm	0.83	0.89	1.3	1.3	13.5	14
J	RLL (lateral basal segmental)	17.0	3.7	Attach to diaphragm	0.58	0.92	1.9	4.9	14.4	15.3

GTV: gross tumor volume; RUL: right upper lobe; RLL: right lower lobe; LLL: left lower lobe; fAP, fSI: fractional anterior-posterior, superior-inferior location, respectively; dLR, dAP, and dSI: the magnitude of motion in lateral, anterior-posterior (AP), and superior-inferior (SI) direction of ten respiratory phases, respectively.

Table 4: GTV centriod movement by different positional and attachment status.

Tumor location	Magnitude of solitary tumor (mean ± SD mm) $n = 14$				Magnitude of attached tumor (mean ± SD mm) $n = 30$			
	n	Later	AP	SI	n	Later	AP	SI
Upper level	9	0.9 ± 0.3	1.5 ± 1.2	2.3 ± 2.2	20	0.9 ± 0.5	1.2 ± 0.7	1.5 ± 1.7
Middle level	1	2.6	5.2	11.7	7	1.5 ± 0.7	2.1 ± 0.9	2.2 ± 1.3
Lower level	4*	2.5 ± 1.9	2.7 ± 1.5	10 ± 4.8	3	1.5 ± 0.9	1.5 ± 0.7	3.0 ± 1.9

*This value included 3 cases whose lesions attached to diaphragm.
Upper level included right upper lobe, anterior, and apicoposterior segment in left upper lobe. Middle level included right middle lobe and lingular bronchus in left lobe. Lower level included left and right lower lobes.
SD: standard deviation; AP: anterior-posterior direction, and SI: superior-inferior direction.

The dominant displacement was in SI and/or AP directions. The rotational motions of lower lobe tumors were observed. Table 4 showed the magnitude of GTV centroid mobility with different positional and attachment status.

The more attached to the rigid structure, the less mobile of tumor was. For those tumors located to the mediastinum, movement in AP direction was a major contributor to the GTV motion, with the magnitude less than 3.5, 4, and 3.5 mm in LR, AP, and SI direction. These movements were probably associated with cardiac contraction and/or aortic pulsation.

In all 20 patients with an attachment degree to rigid structure of being more than 0.6, the magnitude was small, with 1.0 ± 0.6, 1.5 ± 0.9, and 1.5 ± 1.5 mm in the LR, AP, and SI directions, respectively. For this tumor group, there were 2 outliers with large motion in SI direction, with the magnitude of 5.1 mm and 4.5 mm. One located in lower lobe, the other in upper lobe but posterior segment. When filtered out the outliers, maximum movement observed in the LR, AP, and SI directions were 2 mm, 3.7 mm, and 2.8 mm.

For big tumor (GTV ≥45cm^3) located upper 1/3 and middle 1/3, the magnitude in AP direction was dominant. For small tumor (GTV <45cm^3), the largest motion was in SI direction.

3.3. Survival. Up to February 2013, the median follow-up duration was 32.6 months (range, 1.9–89.8 months) in all patients; 80.4 months (range: 65.6–89.8 months) in the survivors: and 20.6 months (range: 3.0–75.0 months) in patients who had died. Four NSCLC patients (Stage I in 1, IIIB in 2, and IV in 1) and four limited-stage SCLC patients are alive and free of disease. One SCLC patients is alive with local disease recurrence underwent salvage treatment. Twelve patients have died of distant metastases (NSCLC in 8, SCLC in 4). Eight patients have died of locoregional progression inside the thorax and metastases both (NSCLC in 5, SCLC in 3). One SCLC patient died of local progression inside the radiation field. Two NSCLC patients have died of treatment-related toxicity. One NSCLC patient has died with

the metastases for secondary cancer in rectum. Two patients have died as a result of other medical conditions, one for the cause of sputum jams and other for severe pneumonia. For NSCLC subgroup (Stage IIIA in 15 and IIIB in 5), the median survival time was 41.6 months. At 1-, 3- and 5-year actuarial survival was 75%, 55%, and 36.7%, whereas SCLC patients (limited-stage in 15) have a 1-, 3, and 5-year survival of 73.3%, 52.5%, and 37.5%, respectively, with the median survival time of 47.6 month (Figure 3(a)). One advanced NSCLC patient with cervical lymph node metastases who accepted definitive chemoradiotherapy has an overall survival time without progress of 89.8 months by the time of followup. At 1, 3, and 5 years, cancer-specific survival was 84.4%, 58.1%, 37.6% for Stage III NSCLC and 73.3%, 52.5%, and 45% for limited-stage SCLC, respectively.

3.4. Patterns of Treatment Failure. The median progression-free survival time was 17.1 months for NSCLC group and 34.4 months for SCLC group; 1, 3-year progression-free survival were 62.7% versus 60% and 28.5% versus 45.7% for NSCLC group and SCLC group (Figure 3(b)). Actuarial local progression-free survival at 1 and 3 years was 93.8% and 67% for NSCLC group and 79% and 60.2% for SCLC group, respectively (Figure 4(a)). The 1-, 3- and 5-year metastasis-free survival rate was 62.7%, 34.2%, and 27.4% for NSCLC and 66.7%, 57.1%, and 47.6% for SCLC, respectively (Figure 4(b)).

Of the 25 patients who experienced treatment failure or died, 4 patients (NSCLC in 1, SCLC in 3) developed local and/or regional tumor progression without distant metastases; 14 patients (NSCLC in 10, SCLC in 4) developed metastatic disease without locoregional progression; and 7 patients (NSCLC in 4, SCLC in 3) showed concurrent thoracic and distant metastatic progression during the follow-up phase.

4. Discussion

The reliability of motion results in this work was dependent on two factors, regularity in patient breathing and consistency in GTV delineation. Data from both phantoms and clinical practice demonstrated that respiratory regularity was of most importance to reduce motion artifacts during 4DCT scan [22, 23]. In our research, all patients underwent breathing training and those with breathing variability >5% were eliminated from the study. Delineation uncertainty certainly existed [24]. In order to minimize factitious factors during the delineation of GTV, we used an auto-segmentation tool with a fixed threshold and a selected window width and level. So-obtained GTVs were manually modified by a single radiation oncologist to reduce interobserver variability [25]. Before analysis, all contours were inspected independently by two radiation oncologists to ensure high contouring consistency.

It was found that tumor centroids vector movement was associated with GTV size, the SI tumor location (fSI), and the attachment degree to rigid structure. This result was intuitive but contrasted to the studies by Stevens et al. [6] and van Sörnsen et al.[7] in the early 2000s. Both studies reported that lung tumor motion was independent and cannot be predicted by any factors. Possible cause of this discrepancy included limited number of cases (the former in 22, the latter in 29), and different assessment approaches were used (the former used orthogonal radiographs; the latter was based on slow-CT images). In another study of 166 lung tumors based on 4DCT, Liu et al. [19] reported a significant correlation between tumor motion and diaphragm motion, the SI tumor location in the lung, GTV size, and disease T stage. But the related factors were not independent variables required questionable. For example, T stage sometimes included the surgery difficulty information caused by GTV size or tumor location. In the present study, our analysis revealed there was a weak positive correlation between tumor motion and the SI tumor location, but the relationship of tumor motion and GTV size or attachment status was not linear. We inferred it was because the related factors possibly had a so-call "interaction effect" and could influence each other, though they were looked at independently in our study.

Similar to the previously published studies [18, 19], besides tumors located in lower lobe, tumors in posterior side of the lung exhibited greater mobility only ranking second. The reason Maxim et al. [18] implied was that the lower lobes occupied a large proportion of the posterior thorax. Liu et al. [19] inferred that the diaphragm can exhibit a large degree of rotational movement. And another possibility appear to be that the diaphragm motion in posterior side was more moveable than that in anterior side; even upper lobe could be affected. No significant correlation was observed between centriod vector and the location in AP direction, both in our and published studies. It might partly due to small sample size.

Of the three related factors, tumor location probably weighted more than GTV size and attachment degree to rigid structure. This is supported by our original findings as follows. Firstly, the peripheral lung tumors located near the diaphragm showed the greatest degree of motion, followed by upper-lobe posterior-segment solitary tumors. Even in the tumors with an attachment degree to rigid structure of more than 0.6, which estimated very small magnitude, still can be seen cases in these two location moved more than 5 mm. Secondly, when excluding all the cases with attachment degree more than 0.6, the linear correlation between centroid vector mobility and fSI would enhance, regardless of tumor size. Thirdly, regardless of tumor attachment status, for big tumors (volume $\geq 45\ cm^3$) located upper 1/3 and middle 1/3 and those close to the mediastinum, magnitude in AP direction was dominant. Those results indicated that more consideration should focus on tumor location when determining internal margin for target mobility.

Compared with our study, Liu et al. [19] reported a higher incidence of large GTV displacements in 166 lung tumors. For 95% tumors, the magnitude of motion was less than 13.4 mm, 4 mm, and 5.9 mm in SI, LR and AP directions, respectively. In our study, the corresponding values were 13.05 mm, 2.6 mm, and 4.8 mm. In their study the proportions of tumors that moved >5 mm in SI, LR, and AP direction were 39.2%, 1.8%, and 5.4%, respectively. In our study, the corresponding percentages were 22.7%, 2.3%, and 2.3%. Two

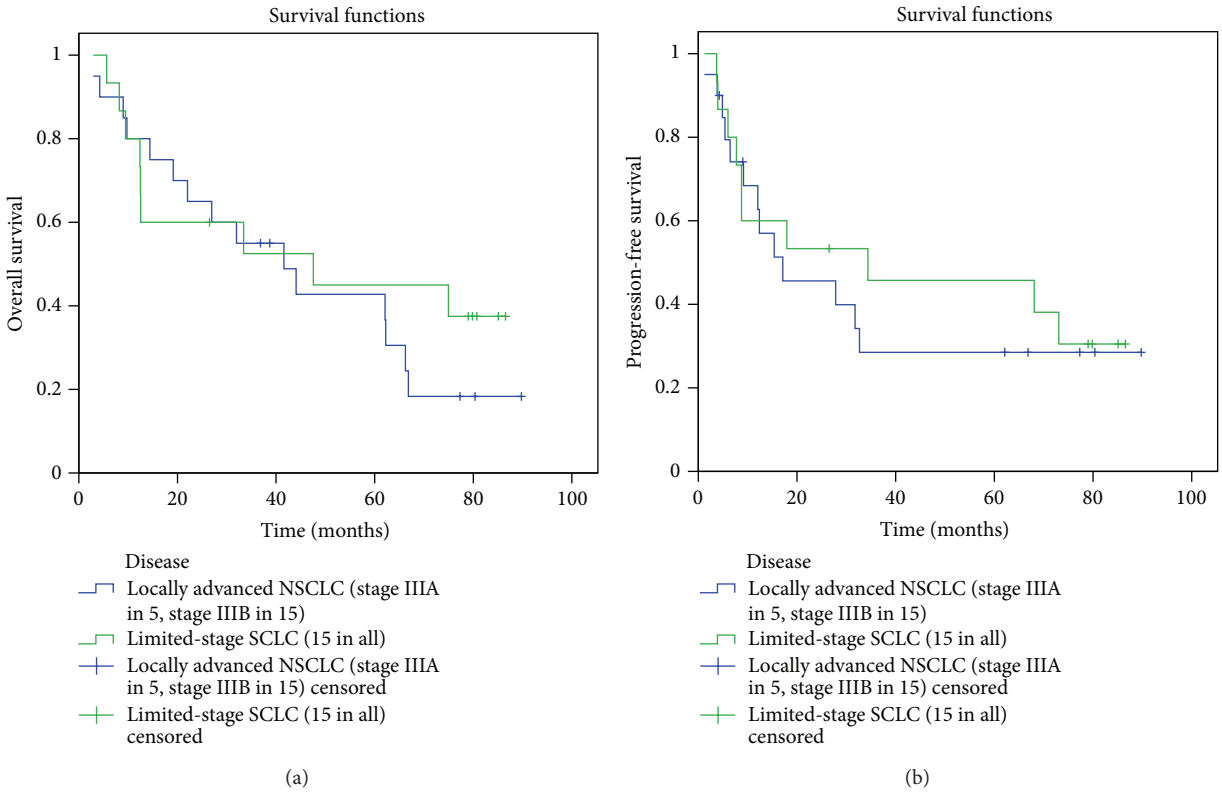

Figure 3: Overall survival (a) and progression-free survival curves (b) of local advanced NSCLC and limited-stage SCLC.

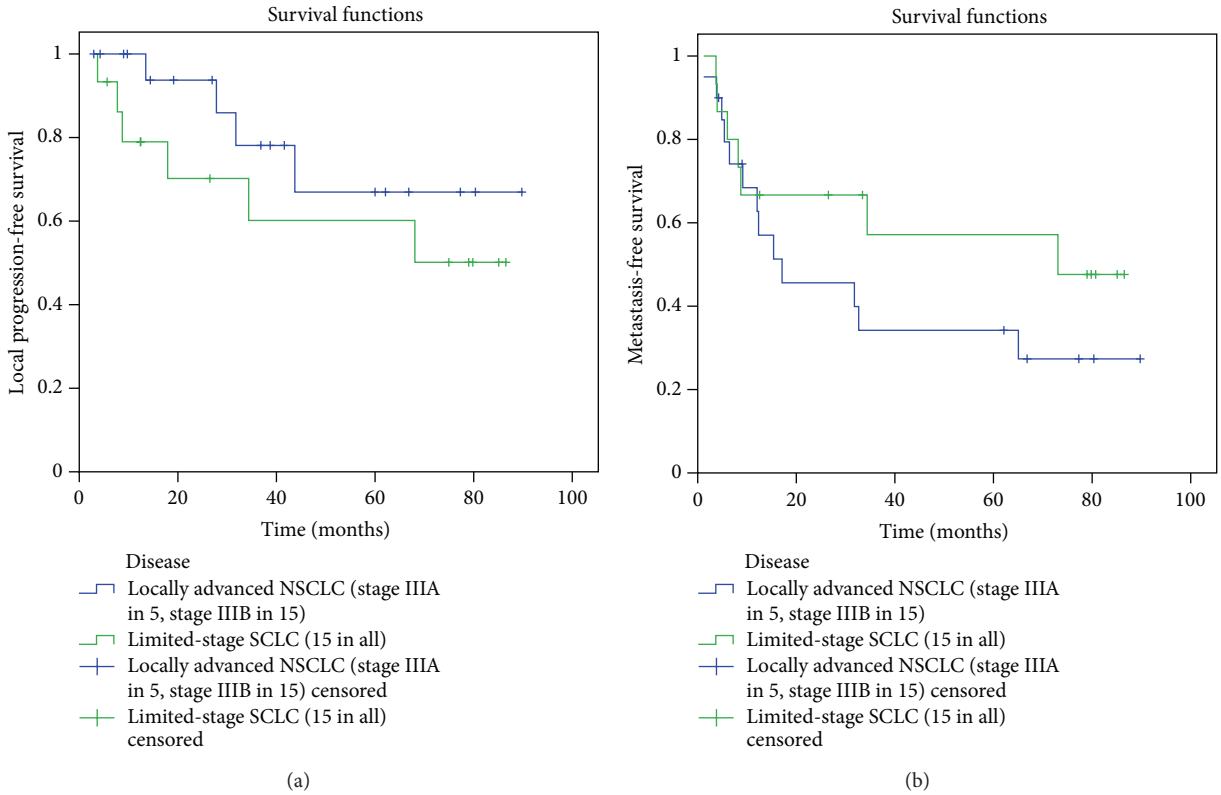

Figure 4: The local progression-free survival (a) and metastasis-free survival curve (b).

possible reasons for the slight discrepancy were the less distribution of tumor located in middle or lower lobe (25%) and the high proportion tumors attached to rigid structure (68.2%) in our study.

4DCT simulation can provide benefits in selected patients. Similar to that reported by Rietzel et al. [4]; the use of 4DCT resulted in significantly smaller and safe PTV margins than those derived using conventional 3DCT scans and the "standard" margin. It will be of clinical significance when administrating a dose to a bulky tumor, especially those limited by pulmonary or spinal toxicity without 4DCT. The smaller PTVs with 4DCT would result in less normal tissue irradiated with higher dose, thus, transforming a palliative intent to a curative one with toxicity at tolerable level. On the other hand, modern high-precision radiation delivery requires accurate knowledge for issues such as internal motion and setup. For example, the use of individualized PTV margins based on 4DCT would be essential for hypofractionated or stereotactic radiotherapy, as pointed out by Keall et al. [11].

The predominant cause of deaths for lung cancer is believed to be distant metastases and local recurrence. Local failure remains a major challenge when treating lung cancer with radiotherapy, as high as 30%–50% recurrence rate at 5 years in NSCLC [26] and 36%–52% in SCLC [27]. Animal experiments and clinical data in lung cancers indicated that improvements in local control would decrease distant metastases, as a part of the distant metastases was derived from local recurrences of the cancer [28].

In this work, we observed unexpected and promising local control and survival rate with the use of 4DCT for both NSCLC and SCLC. The 5-year overall survival rates of 36.7% for NSCLC and 37.5% for SCLC were encouraging undoubtedly, as compared to the 5-year overall survival rate of around 20% from conventional treatments for locally advanced NSCLC and limited-stage SCLC as reported in the literature and in our own clinical experience [27, 29]. Though the statistical power of this result is not strong enough to draw a firm conclusion, the positive effect of 4DCT result in accurate and safe target coverage should be given enough attention. It has the potential to improve treatment outcome. It is also believed that the geometric precision is only one of the key factors of the gain in survival and local control, but never the only one. Several other factors may contribute to clinical outcome in this study. (1) All patients with curative intent belonged to the "favorable group" (KPS $\geq$70, weight loss <5% in half a year). (2) The CCRT for locally advanced NSCLC and EP chemotherapy plus thoracic radiotherapy for limited-stage SCLC were the principle part of treatment. According to the recently meta-analyses [29], the CCRT itself can decrease locoregional progression and improve overall survival in NSCLC. (3) The start of thoracic radiotherapy in the limited-stage SCLC patients was all within 2 cycles of chemotherapy in our study, which was proved to be favorable in survival than the late start of radiotherapy [30].

Liao et al. [31] reported 91 NSCLC patients underwent CCRT with 4DCT/IMRT. The median survival times were 16.8 months for the 4DCT/IMRT group. From the survival curve, 1-year free of local-regional progression was about 87%, 1-year free of distant metastase was about 60%, and 1-year overall survival was about 70%, which were in good accordance with our study. To our knowledge, there is no study reporting survival benefit with using 4DCT for SCLC.

Although with the use of 4DCT, we can safely reduce the margin to account for intrafractional respiration motion, other components contributing to PTV margin, such as interfractional variations, set-up margin, need to be considered. While every effort was made to keep breath regular and ensure target delineation accurate, some artifacts and inconsistency were hard to eliminate. The limited number of cases analyzed is the major drawback of the current study. Our ongoing research is to increase number of the cases and to update the results in the future.

5. Conclusion

The 4DCT data in this work indicate that the peripheral lung tumors located near the diaphragm show the greatest degree of respiration motion, followed by upper-lobe posterior-segment solitary tumors. Tumor respiration motion was found to be associated with tumor location, volume, and attachment to rigid structures, with tumor location being the most important factor among the other two. The use of 4DCT resulted in the use of individualized margin to account for patient-specific breathing motion, improving the accuracy for tumor targeting during radiotherapy. This may contribute to the improved local control and overall survival as observed presently for both NSCLC and SCLC.

Conflict of Interests

All authors have no conflict of interests.

Authors' Contribution

Y. Wang and Y. Bao contributed equally to this paper.

Acknowledgments

The authors thank their patients and their families for their willingness to take part in this study. They thank the Chief of Medical Physics Professor X. Allen Li from Medical College of Wisconsin for reviewing the paper and offering helpful comments. No external funding was received for this study.

References

[1] International Commission on Radiation Units and Measurements, *ICRU Report 50: Prescribing, Recording and Reporting Photon Beam Therapy*, International Commission on Radiation Units and Measurements, Bethesda, Md, USA, 1993.

[2] J. Y. Chang, L. Dong, H. Liu et al., "Image-guided radiation therapy for non-small cell lung cancer," *Journal of Thoracic Oncology*, vol. 3, no. 2, pp. 177–186, 2008.

[3] G. T. Y. Chen, J. H. Kung, and K. P. Beaudette, "Artifacts in computed tomography scanning of moving objects," *Seminars in Radiation Oncology*, vol. 14, no. 1, pp. 19–26, 2004.

[4] E. Rietzel, A. K. Liu, K. P. Doppke et al., "Design of 4D treatment planning target volumes," *International Journal of Radiation Oncology Biology Physics*, vol. 66, no. 1, pp. 287–295, 2006.

[5] E. Rietzel, S. J. Rosenthal, D. P. Gierga, C. G. Willett, and G. T. Y. Chen, "Moving targets: detection and tracking of internal organ motion for treatment planning and patient set-up," *Radiotherapy and Oncology*, vol. 73, supplement 2, pp. S68–S72, 2004.

[6] C. W. Stevens, R. F. Munden, K. M. Forster et al., "Respiratory-driven lung tumor motion is independent of tumor size, tumor location, and pulmonary function," *International Journal of Radiation Oncology Biology Physics*, vol. 51, no. 1, pp. 62–68, 2001.

[7] J. R. van Sörnsen de Koste, F. J. Lagerwaard, M. R. J. Nijssen-Visser, W. J. Graveland, and S. Senan, "Tumor location cannot predict the mobility of lung tumors: a 3D analysis of data generated from multiple CT scans," *International Journal of Radiation Oncology Biology Physics*, vol. 56, no. 2, pp. 348–354, 2003.

[8] K. E. Sixel, M. Ruschin, R. Tirona, and P. C. F. Cheung, "Digital fluoroscopy to quantify lung tumor motion: potential for patient-specific planning target volumes," *International Journal of Radiation Oncology Biology Physics*, vol. 57, no. 3, pp. 717–723, 2003.

[9] A. Bezjak, "Harnessing radiation technology to improve survival," *Journal of Clinical Oncology*, vol. 29, no. 17, pp. 2295–2296, 2011.

[10] S. S. Vedam, P. J. Keall, V. R. Kini, H. Mostafavi, H. P. Shukla, and R. Mohan, "Acquiring a four-dimensional computed tomography dataset using an external respiratory signal," *Physics in Medicine and Biology*, vol. 48, no. 1, pp. 45–62, 2003.

[11] P. Keall, "4-dimensional computed tomography imaging and treatment planning," *Seminars in Radiation Oncology*, vol. 14, no. 1, pp. 81–90, 2004.

[12] P. J. Keall, G. S. Mageras, J. M. Balter et al., "The management of respiratory motion in radiation oncology report of AAPM task group 76," *Medical Physics*, vol. 33, no. 10, pp. 3874–3900, 2006.

[13] G. Li, D. Citrin, K. Camphausen et al., "Advances in 4D medical imaging and 4D radiation therapy," *Technology in Cancer Research and Treatment*, vol. 7, no. 1, pp. 67–81, 2008.

[14] L. Ekberg, O. Holmberg, L. Wittgren, G. Bjelkengren, and T. Landberg, "What margins should be added to the clinical target volume in radiotherapy treatment planning for lung cancer?" *Radiotherapy and Oncology*, vol. 48, no. 1, pp. 71–77, 1998.

[15] Y. Seppenwoolde, H. Shirato, K. Kitamura et al., "Precise and real-time measurement of 3D tumor motion in lung due to breathing and heartbeat, measured during radiotherapy," *International Journal of Radiation Oncology Biology Physics*, vol. 53, no. 4, pp. 822–834, 2002.

[16] C. Plathow, S. Ley, C. Fink et al., "Analysis of intrathoracic tumor mobility during whole breathing cycle by dynamic MRI," *International Journal of Radiation Oncology Biology Physics*, vol. 59, no. 4, pp. 952–959, 2004.

[17] K. E. Rosenzweig, J. Hanley, D. Mah et al., "The deep inspiration breath-hold technique in the treatment of inoperable non-small-cell lung cancer," *International Journal of Radiation Oncology Biology Physics*, vol. 48, no. 1, pp. 81–87, 2000.

[18] P. G. Maxim, B. W. Loo Jr., H. Shirazi, B. Thorndyke, G. Luxton, and Q. T. Le, "Quantification of motion of different thoracic locations using four-dimensional computed tomography: implications for radiotherapy planning," *International Journal of Radiation Oncology Biology Physics*, vol. 69, no. 5, pp. 1395–1401, 2007.

[19] H. H. Liu, P. Balter, T. Tutt et al., "Assessing respiration-induced tumor motion and internal target volume using four-dimensional computed tomography for radiotherapy of lung cancer," *International Journal of Radiation Oncology Biology Physics*, vol. 68, no. 2, pp. 531–540, 2007.

[20] E. Weiss, K. Wijesooriya, S. V. Dill, and P. J. Keall, "Tumor and normal tissue motion in the thorax during respiration: analysis of volumetric and positional variations using 4D CT," *International Journal of Radiation Oncology Biology Physics*, vol. 67, no. 1, pp. 296–307, 2007.

[21] S. C. Erridge, Y. Seppenwoolde, S. H. Muller et al., "Portal imaging to assess set-up errors, tumor motion and tumor shrinkage during conformal radiotherapy of non-small cell lung cancer," *Radiotherapy and Oncology*, vol. 66, no. 1, pp. 75–85, 2003.

[22] T. Yamamoto, U. Langner, B. W. Loo Jr., J. Shen, and P. J. Keall, "Retrospective analysis of artifacts in four-dimensional CT images of 50 abdominal and thoracic radiotherapy patients," *International Journal of Radiation Oncology Biology Physics*, vol. 72, no. 4, pp. 1250–1258, 2008.

[23] T. Neicu, R. Berbeco, J. Wolfgang, and S. B. Jiang, "Synchronized moving aperture radiation therapy (SMART): improvement of breathing pattern reproducibility using respiratory coaching," *Physics in Medicine and Biology*, vol. 51, no. 3, pp. 617–636, 2006.

[24] G. F. Persson, D. E. Nygaard, C. Brink et al., "Deviations in delineated GTV caused by artefacts in 4DCT," *Radiotherapy and Oncology*, vol. 96, no. 1, pp. 61–66, 2010.

[25] A. V. Louie, G. Rodrigues, J. Olsthoorn et al., "Inter-observer and intra-observer reliability for lung cancer target volume delineation in the 4D-CT era," *Radiotherapy and Oncology*, vol. 95, no. 2, pp. 166–171, 2010.

[26] R. Arriagada, T. le Chevalier, E. Quoix et al., "ASTRO (American Society for Therapeutic Radiology and Oncology) plenary: effect of chemotherapy on locally advanced non-small cell lung carcinoma: a randomized study of 353 patients. GETCB (Groupe d'Etude et Traitement des Cancers Bronchiques), FNCLCC (Federation Nationale des Centres de Lutte contre le Cancer) and the CEBI trialists," *International Journal of Radiation Oncology Biology Physics*, vol. 20, no. 6, pp. 1183–1190, 1991.

[27] A. T. Turrisi III, K. Kim, R. Blum et al., "Twice-daily compared with once-daily thoracic radiotherapy in limited small-cell lung cancer treated concurrently with cisplatin and etoposide," *The New England Journal of Medicine*, vol. 340, no. 4, pp. 265–271, 1999.

[28] J. Ramsay, H. D. Suit, and R. Sedlacek, "Experimental studies on the incidence of metastases after failure of radiation treatment and the effect of salvage surgery," *International Journal of Radiation Oncology Biology Physics*, vol. 14, no. 6, pp. 1165–1168, 1988.

[29] A. Aupérin, C. le Péchoux, E. Rolland et al., "Meta-analysis of concomitant versus sequential radiochemotherapy in locally advanced non-small-cell lung cancer," *Journal of Clinical Oncology*, vol. 28, no. 13, pp. 2181–2190, 2010.

[30] D. B. Fried, D. E. Morris, C. Poole et al., "Systematic review evaluating the timing of thoracic radiation therapy in combined modality therapy for limited-stage small-cell lung cancer," *Journal of Clinical Oncology*, vol. 22, no. 23, pp. 4837–4845, 2004.

[31] Z. X. Liao, R. R. Komaki, H. D. Thames Jr. et al., "Influence of technologic advances on outcomes in patients with unresectable, locally advanced non-small-cell lung cancer receiving concomitant chemoradiotherapy," *International Journal of Radiation Oncology Biology Physics*, vol. 76, no. 3, pp. 775–781, 2010.

Hindawi Publishing Corporation
BioMed Research International
Volume 2013, Article ID 749203, 9 pages
http://dx.doi.org/10.1155/2013/749203

Review Article

Quo Vadis Radiotherapy? Technological Advances and the Rising Problems in Cancer Management

Barry J. Allen,[1] Eva Bezak,[2,3] and Loredana G. Marcu[2,3,4]

[1] *Centre for Experimental Radiation Oncology, St George Cancer Care Centre, Kogarah, NSW 2217, Australia*
[2] *Department of Medical Physics, Royal Adelaide Hospital, North Terrace, Adelaide, SA 5000, Australia*
[3] *School of Chemistry and Physics, University of Adelaide, Adelaide, SA 5000, Australia*
[4] *Faculty of Science, University of Oradea, 410087 Oradea, Romania*

Correspondence should be addressed to Loredana G. Marcu; loredana.marcu@fizicaoradea.ro

Received 18 March 2013; Accepted 4 April 2013

Academic Editor: Maria F. Chan

Purpose. Despite the latest technological advances in radiotherapy, cancer control is still challenging for several tumour sites. The survival rates for the most deadly cancers, such as ovarian and pancreatic, have not changed over the last decades. The solution to the problem lies in the change of focus: from local treatment to systemic therapy. The aim of this paper is to present the current status as well as the gaps in radiotherapy and, at the same time, to look into potential solutions to improve cancer control and survival. *Methods*. The currently available advanced radiotherapy treatment techniques have been analysed and their cost-effectiveness discussed. The problem of systemic disease management was specifically targeted. *Results*. Clinical studies show limited benefit in cancer control from hadron therapy. However, targeted therapies together with molecular imaging could improve treatment outcome for several tumour sites while controlling the systemic disease. *Conclusion*. The advances in photon therapy continue to be competitive with the much more expensive hadron therapy. To justify the cost effectiveness of proton/heavy ion therapy, there is a need for phase III randomised clinical trials. Furthermore, the success of systemic disease management lies in the fusion between radiation oncology technology and microbiology.

1. Introduction

The AACR Cancer Progress Report (2011) shows that, in the USA from 1990 to 2007, death rates from all cancers dropped 22% in men and 14% in women. More than 68% of adults live five years or more after diagnosis, up from 50% in 1975. For all pediatric cancers, the five-year survival rate is 80%, compared with 52% in 1975. However, the poor survival rates from the most deadly cancers: pancreatic, ovarian, and glioblastoma multiforme (GBM) have not changed to this date.

Keyhole and robotic surgery are major developments in the surgical management of cancer. Patients suffer reduced hospitalisation, but have concomitant costs decreased? Patient quality of life has undoubtedly improved, but are patients living longer?

Pediatric leukaemia is no longer a death sentence and testicular cancer responds well to cisplatin therapy. But most chemotherapy applications are palliative in intent and associated with complications and reduction in the quality of life.

External beam radiotherapy has developed over 100 years from low energy X-rays, through Cobalt-60 gamma rays to linear accelerators producing ever-increasing photon and electron energies. Nowadays, external photon beams can be delivered to precise, irregular targets via many modalities: three-dimensional conformal (3DCRT), intensity modulated (IMRT), and image-guided (IGRT) radiotherapies. As excellent as these modalities are, they are directed not so much to the cancers that cannot be controlled but to those that can be. As such, the local control and survival achieved with these technologies do not correlate with the increasing cost of external beam radiotherapy (EBRT) (Figure 1). Still, advances in photon radiotherapy continue to be competitive with the much more expensive high energy proton and heavy ion therapy, used for their exceptional advantage in sparing critical tissues.

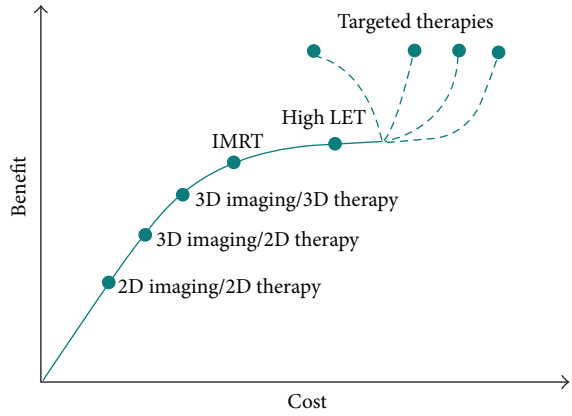

Figure 1: Cost-benefit diagram of current radiotherapy modalities.

On the imaging side, the development of computed tomography (CT), single photon emission tomography (SPECT), positron emission tomography (PET), magnetic resonance imaging (MRI), and functional MRI (fMRI) has been of immense importance in developing our ability to see into our bodies and examine function. Tumours can be identified down to a few mm in diameter with MRI and to 4-5 mm for functional images with PET. Current in vivo imaging techniques continue to resolve smaller and smaller tumours but can never resolve subclinical disease, by definition, nor tell us where micrometastases lie (see Figure 2).

Without doubt, the oncologist's job of managing cancer has been made much easier and more certain, but has this translated into improved prognoses for cancer patients? The evidence presented by the AACR suggests that the answer is in the affirmative, although early detection may be responsible for much of the improvement. External beam radiotherapy has improved markedly in terms of targeting well-defined volumes and achieving local control but can never eliminate systemic disease.

The "war on cancer" analogy is often used. But like the 21st century wars, the apparent initial success is masked by the long-term failure to control systemic disease. Few primary cancers are fatal, GBM being the standout, and it is not the primary tumour that determines outcome. It is the cancer cells released from the tumour that invade the vascular and lymphatic systems that eventually lead to multiple metastases and organ failure as normal functional tissues are crowded out by the ever populating cancer cells. Therefore, disseminated disease is the primary cause of cancer death. Yet this objective has been overlooked during the development of modern radiotherapy techniques that are focused on external beam radiotherapy.

On top of this is the rapidly developing cost of the management of cancer. Cancer causes the highest economic loss of all of the 15 leading causes of death worldwide. The World Health Organisation (WHO) note that the economic toll from cancer is nearly 20 percent higher than heart disease, the second leading cause of economic loss ($895 billion and $753 billion, resp.). Health budgets in developed countries are continually expanding and constrained by limited resources. But cost-benefit analyses to determine whether the increased cost of treatment achieves improved outcomes remain unknown. Perhaps the classic example is in the treatment of primary prostate cancer where surgery, brachytherapy, external beam photon, and proton therapies are used, all achieving similar efficacy and complications but at very different capital and running costs.

The developed nations' investment in cancer research has been growing exponentially, and the 2012 budget for the US National Cancer Institute alone will be totalling nearly 6 billion US dollars [1, 2].

For rural populations, cancer is often diagnosed at the symptomatic stage. Palliative therapy is the only course to reduce pain and increase quality of life. As a result, there is a need to provide low cost technologies appropriate for the objective of palliation. Because of the continuing shortage of trained oncologists, medical physicists, and other professionals, telemedicine must be an essential element in the development of radiotherapy care in rural regions.

We are therefore confronted with two distinct challenges:

(1) to manage and control systemic cancer,

(2) to provide cost-effective technologies.

2. Current Status and Gaps

2.1. External Beam Radiotherapy and Intensity Modulated Radiation Therapy. EBRT and IMRT are the current standards of care for radiation oncology patients. IMRT is known to be a highly conformal treatment, involving reduced treatment margins which results in improved tumour control and reduced normal tissue toxicity. However, the ability to deposit a high dose into well-defined tumours is not always desired, as too precise targeting can lead to increased local recurrences. The biology of the tumour must determine the clinical tumour volume (CTV) margin, not the resolution of beam delivery. If the CTV margin cannot be fully imaged, then this becomes the most difficult margin to be determined. The decision is typically based on clinical assessment of risk, on local clinical practice, and on historical evidence rather than the tumour spread quantified in an individual patient. Often a uniform CTV margin is used regardless of potential anisotropy in the microscopic tumour spread. The extent of the CTV margin depends on information received from imaging techniques. Such accurate, individualised CTV determinations represent one of the problems where developments in diagnostic imaging (molecular imaging techniques in particular) will improve radiotherapy treatment [3].

Other factors include problems with treatment times and dose gradients. IMRT increases the volume of normal tissue exposed to a low dose. However, what might have been thought to be a negative factor could be positive, in view of hormesis effects.

2.2. Hadron Therapy. Protons offer greatly improved and precise dose deposition and as a result lower normal tissue doses. But does proton therapy always give superior efficacy, reduced complications, improved prognosis, and lower cost therapy? While there are unique applications of proton beams

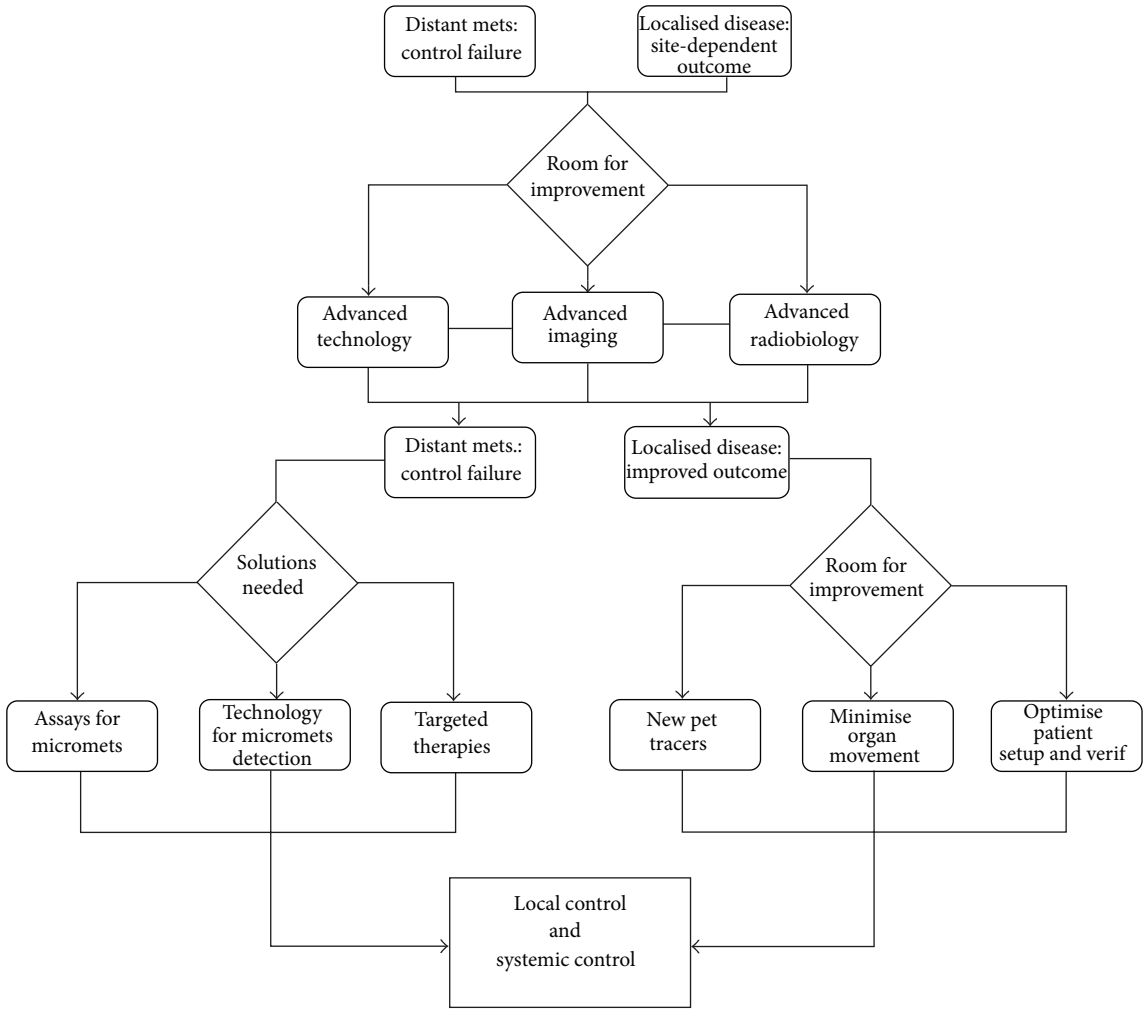

Figure 2: Building blocks of cancer management.

that give reduced adverse events, especially for pediatric cancers [4, 5], the answer appears to be negative. Prostate cancer is a major application for proton machines. But prognosis for prostate cancer is mostly set not by the primary therapy but by the initial stage of the disease on diagnosis [6, 7]. As such, low risk patients with PSA < 10 and Gleason 6 are very unlikely to succumb to the disease and will not be in need of radical therapies.

Uveal melanoma (an extremely low incidence cancer) was a long-standing application for proton therapy. However, on the basis of an intralesional skin melanoma trial of targeted alpha therapy [8], there is every reason to think that intralesional injection into the uveal melanoma will not only save the eye but could well eliminate the micrometastases arising from the primary site that lead to patient death within 5–10 years.

There is increasing evidence that improved control of the primary lesion, arising from the new modalities for protons and heavy ion (C-12) beams, translates into improved survival [9, 10]. However, care must be taken to distinguish between survival and progression-free endpoints, which are not necessarily correlated.

2.3. Cost Benefit of Proton, Heavy Ion, and Photon Therapy. The major advantage of IMRT is its low capital and running costs. While patient charges are not so much of an issue for a well-insured patient, there is a major health issue relating to the availability of radiotherapy to cancer patients. Does western society need many more IMRT units or one proton therapy facility only? Also, is proton therapy cost-effective and is there evidence in clinical trials supporting clinical gains of proton therapy versus conventional therapy? If the current evidence-based medicine standards are used for determination of clinical efficacy of proton therapy, it must be concluded that the evidence is limited and mostly based on noncontrolled studies. A Phase III clinical randomised trial has not been conducted for proton therapy.

Several studies have been though conducted trying to identify the cost-benefit of proton therapy and the type of cancer patients that might benefit from proton therapy [11, 12]. Several investigations concluded that for approximately 15% of cancer patients treated with radiation therapy, proton therapy might be cost-effective. According to Glimelius and Montelius, "This means that one proton therapy facility being able to yearly treat a reasonable number of patients

(1000–2000) is motivated for a western world population of about 10 millions. The same estimations for light ions, however, much more uncertain, came to an estimate of 50 millions" [13].

Lodge et al. [14] conducted a systematic literature review (comprising, 54 publications: 4 randomized controlled trials reported in 5 publications, 5 comparative studies, and 44 case series) on the efficacy of hadron therapy (therapies including protons, neutrons, and light and heavy ions), concentrating on external beam techniques. They found that there is insufficient clinical evidence available to justify the rapid expansion of hadron facilities as a major treatment modality and recommended that further research into the clinical and cost-effectiveness of hadron therapies was required. The authors concluded, "the current literature shows that the introduction, or significant extension, of hadron therapy as a major treatment modality—except on a minor scale for certain rare tumours (ocular, chordomas, etc.)—into standard clinical patient care cannot be supported by the evidence base currently available. There are little reliable evidence-based data available concerning the relative cost-effectiveness of hadron therapy interventions when compared with each other, with photon therapy, or with other cancer treatments."

2.4. Targeted Therapy. Although not a standard of care in radiation oncology, targeted therapies are emerging treatment techniques with the ability to control systemic disease. With advances in immunology and the development of exquisite targeting vectors, we can now engage in targeted imaging and therapy using the alpha, beta, and gamma rays emitted from radioisotope labels. However, the use of radioisotope therapy, apart from the thyroid and palliative therapy for bone cancer, has had limited effect on survival. Beta emitters have limited efficacy in the control of cancer, although new radioisotopes are finding niche applications with various targeting agents. Much more successful has been the use of gamma ray emitters for imaging with SPECT and PET.

The next generation of radioimmunotherapy may lie with alpha-emitting radioisotopes that can selectively kill targeted cancer cells. The field of targeted alpha therapy is slowly gathering momentum, with some 10 clinical trials completed, in operation, or at the planning stage around the world. This fusion of biology and medical physics suggests that we should use the term biomedical physics much more than we do.

2.5. Tumour Site-Specific Treatment Challenges. The future objectives for radiation therapy have to address the failures of current therapies. Some of the site-specific treatment challenges encountered by today's cancer management are mentioned below.

(i) *Primary prostate cancer*: there is the need to spare the nerves and rectum to reduce incontinence, impotence and rectal perforation.

(ii) *Lung cancer*: tumours can be regressed but there is the need to eliminate subclinical metastases.

(iii) *Glioblastoma multiforme*: it is fatal in the primary state, we need to improve prognosis by eliminating subclinical disease in the brain by extravascular delivery.

(iv) *Metastases to the brain*: they are invariably a fatal stage of cancer which requires elimination of subclinical metastases by vascular delivery.

(v) *Uveal melanoma*: primary treatment needs to be integrated with inhibition of lethal liver metastases.

(vi) *Advanced head and neck cancer*: it has poor outcome despite the multidisciplinary treatment approach. Around 80% of head and neck cancer patients overexpress the epidermal growth factor receptor (EGFR) which is linked to poor prognosis. Targeted molecular therapy against EGFR could play a pivotal role as adjunct therapy.

(vii) *Pancreatic cancer*: it is fatal in the primary state due to late detection. There is a need to improve prognosis by targeted immunotherapy against EGFR. While patients with mutated EGFR might benefit from Erlotinib (an EGFR inhibitor), the side effects limit the efficacy of the drug. Tumour infiltration and liver failure are ultimately the fatal stage. Another approach is to use systemic alpha therapy against uPA and/or MUC1 receptors [15].

(viii) Pretesting for patient radiosensitivity could avoid overdosing of *normal tissue* in sensitive patients and underdosing of the tumour in insensitive patients.

These problems relate to systemic cancer therapy as well as local therapy. Improved spatial dose resolution is important for tumours, but it is the ability to kill subclinical cancer cells that has become the issue. The main problems to be solved regarding systemic cancer therapy are summarised as follows.

(i) Micrometastases may be in the G0 phase and outside the cell cycle; as such these cells are insensitive to chemo- and radiotherapy and are best treated by high LET radiation.

(ii) Normal tissue radiosensitivity for high LET radiation needs to be investigated.

(iii) Systemic agents must target cancer cells via the vascular and/or lymphatic systems. The tumour capillary permeability becomes an important determinant as to whether the targeting agent can diffuse into the extravascular space.

(iv) Monitoring of systemic therapy via sequential peripheral blood analyses of circulating cancer cells.

(v) Tumour dormancy and factors responsible for inter-patient variability. The mechanisms behind cancer dormancy need to be elucidated and therapeutic targets identified. The state of dormancy needs to be indicated by biomarkers to predict outcome.

3. Current Solutions and Their Limitations

Improved treatment efficacy and/or reduced normal tissue toxicity could arise from simple changes to protocols or to complex systemic therapies. Advances in hadron therapy, targeted and molecular therapies, and well-designed predictive assays for both tumour and normal tissue might be the answer to the problems raised above.

3.1. Hadron Therapy

3.1.1. Protons and Heavy Ions. The biophysical and radiobiological properties of heavy ions render them suitable for the management of complex anatomical structures and radioresistant tumours. For example, unresectable osteosarcomas are good candidates for proton/carbon ion treatment as the dose necessary for curative radiotherapy is too large to be deliverable with photon therapy. Also, these tumours are often located in close proximity to radiosensitive organs such as the brain; spinal cord, or pelvis, therefore conventional treatment is not suitable for their management [16].

The Japanese research group from the Research Centre for Charged Particle Therapy National Institute of Radiological Sciences, Chiba [17–19], have demonstrated the efficiency of carbon ion radiotherapy on several tumour sites and types such as locally advanced head and neck tumours; early stage NSCLC and locally advanced NSCLC; unresectable locally advanced bone and soft tissue sarcomas; locally advanced hepatocellular carcinomas; locally advanced prostate carcinomas; chordoma and chondrosarcoma of the skull base and cervical spine; malignant gliomas and oesophageal cancer.

While protons do not offer clinical advantage to certain tumour sites when compared to photon treatment, for ocular tumours Lodge et al. concluded that proton therapy results in approximately 90% eye preservation rates and 50% vision preservation after 5 years. The clinical superiority of protons in ocular radiotherapy was particularly demonstrated for larger tumours and specific locations in the eye, with the benefit dropping off for smaller lesions (e.g., <4 mm).

Table 1 (modified from [14]) provides a summary of comparative clinical results for proton and ion therapy with conventional photon therapy. In base of skull chordomas, both protons and ions appear to provide superior results to photon therapy. In other central nervous system (CNS) tumours the results of photons were found to be similar to those reported for protons and ions.

There were no definitive conclusions on the relative cost-effectiveness/gains of protons and heavy ions compared to photons for head and neck cancer, gastrointestinal tumours, non-small cell lung cancer, sarcomas, cancer of the uterine cervix, and bladder cancer. Similarly, for the case of the locally advanced prostate cancer, both photons and protons resulted in similar therapeutic gains. Furthermore, while effective on well-localized tumours, hadron therapy is not a solution for the management of systemic disease.

As of 2010, there are 31 active proton therapy centers, 2 heavy ion facilities, and approximately 12 neutron therapy centers in operation [20]. There are as many as 22 new, planned, or proposed proton therapy centers, some of which are already under construction. In some of these new centers it is proposed to combine both proton and heavy ion therapy facilities.

The capital cost of a proton therapy facility is around $140 million for a large facility with four treatment rooms, reducing to approximately $50 million for a minimal facility. The cost per patient treatment is around $20–25,000. Standard radiotherapy is exceptionally cheap and perhaps should not be used for comparative purposes. One benchmark is $50,000 per life-year saved, but it is difficult to show that proton therapy actually saves lives. Costs for other therapeutic modalities are surgery ~$15,000, chemotherapy ~$30,000, and bone marrow transplant ~$70,000. However, these modalities are not associated with high capital costs.

3.1.2. Neutrons. Neutrons have been trialled in the past for various malignancies due to their high LET properties. Radioresistant, hypoxic, and/or slowly-growing tumours were found to be good candidates for neutron therapy. Although neutrons can be twice as toxic to hypoxic cancer cells as photons for the same absorbed dose (the oxygen enhancement ratio of neutrons is around 1.6 compared to OER = 3 for photons), the supporting experimental evidence for superior efficiency of neutrons as compared to photons on hypoxic tumours remains inconclusive. Salivary gland tumours and radioresistant sarcomas are probably the only cancers which were shown to benefit from fast neutron treatment.

Boron neutron capture therapy involving epithermal (for deep seated tumours) or thermal neutrons (for superficial tumours) showed promising results for a limited number of tumour sites such as the brain (glioblastoma multiforme), melanoma, and head and neck [21–23]. While the high RBE of epi/thermal neutrons implies a good outcome, the success of the method depends on the selective uptake of boron compounds by cancer cells.

In postsurgical glioblastomas the problem arises in the inability to kill cancer cells as they infiltrate in the hyaluronic acid flow through the perivascular space in the brain. For external beam radiotherapy, the therapeutic gain is less than 1, as radiation damages normal tissue cells more than the cancer cells. If high LET radiation is used, any gains from reducing cell cycle effects are lost by delayed radiation necrosis when quiescent endothelial and other cells undergo mitotic cell death. A solution to this problem would be to selectively target the GBM cells and kill them with short range cytotoxicity. BNCT had some success with this process, with a boron-10 compound being taken up by the cancer cells and activated in situ by an external beam of neutrons. However, bioavailability could be a limiting factor in controlling the cancer.

3.2. Targeted Therapies.

The next major breakthrough in cancer management lies in the fundamental biology and genetics knowledge to address the aforementioned problems rather than further improvements of physical technology which can never reach the required resolution.

Table 1: Comparative clinical results for proton and heavy ion therapy with conventional therapy (modified from [14]).

Tumour site	Proton therapy		Heavy ion therapy	
	Studies/Patients	Results	Studies/Patients	Results
Head and neck	2/62	Not conclusive	2/65	Not conclusive
Prostate	3/1751	Similar	4/201	Not conclusive
Eye	10/7708	Superior	2/1343	Similar to protons
Lung	3/156	Not conclusive	3/205	Similar to stereotactic radiotherapy
CNS	10/839	Similar	3/405	Similar to protons
Gastro-intestinal	5/369	Not conclusive	2/73	Not conclusive
Pelvic	3/80	Not conclusive	2/49	Not conclusive

Targeted alpha therapy is a novel high LET therapeutic approach which incorporates the essential elements for cancer therapy: a targeting molecule that fixes to membrane-bound molecules on the surface of cancer cells, and a cytotoxic radiation that deposits a large fraction of energy into the targeted cell.

While alpha therapy is still a work in progress, developments are being made in translating from preclinical studies to clinical trials. Alpha therapy is demonstrating efficacy in leukaemias as well as in glioblastomas, where results from intracavity administration are very promising, with a 52-week median survival. The use of peptides for targeting GMB is also under investigation [24]. However, the promise of targeted alpha therapy is greatly extended by the development of tumour antivascular alpha therapy (TAVAT) for solid tumours [25]. Metastatic melanoma results show surprising tumour regressions at doses very much below the maximum tolerated dose and, if further research is successful, could change the prognosis for end-stage cancers [26].

3.3. Molecular Imaging. Understanding of cancer genetics and biochemistry will improve with advances in molecular imaging, combining physics, chemistry, biology, and technology. In particular, developments in fluorescent imaging enable us to observe many cellular and subcellular processes in vivo. In this technique a fluorescent protein is fused with a cell protein/gene to be investigated. The composite protein/gene is inserted into the cell of interest. The cell gene/protein then performs its function while the attached fluorescent protein identifies the position of the gene within the cell by emitting fluorescent light [27].

The research into the so-called cell penetrating imaging probes (i.e., cell penetrating peptides or CPP) made visualization of biochemical processes in cells possible. These peptides can translocate (through the cell membrane) covalently attached "cargo" (i.e., molecule of interest) into a mammalian cell without requiring specific receptors.

As for the patient tumour imaging, due to significant absorption of fluorescent light this modality can only be used for very superficial dermatological tumours or tumours/tissues accessible via endoscopy. Another application involves tumour cell illumination during surgery thus enabling more accurate determination of tumour margins.

The principle of molecular imaging is also applicable to molecular therapy. A large number of different cargo molecules have been successfully delivered inside cells using cell penetrating peptides including proteins, liposomes, and nanoparticles [28]. Peptides have also been developed whose uptake into cells is triggered by enzymes typical of tumours [29]. As a result, the CPPs have potential for targeted/selective delivery of radioactive, magnetic, nanoparticle agents and therapeutic drugs into the cancerous tissues.

3.4. Individualized Treatment Planning. Personalized medicine is the "leitmotiv" of the last decade's oncology. Three major advances are emphasized to overtake traditional patient care in oncology: (1) the development and availability of drugs which inhibit oncogenetic targets; (2) the implementation of advanced technologies to allow for prediction of treatment sensitivity and risk of recurrence; (3) reclassification of malignant diseases with the aim of expanding the number of orphan molecular diseases [30]. Yet, treatment differentiation among patients based on tumour kinetodynamics, metabolism, and radiobiological characteristics remains minimal.

It is an acknowledged fact that patients with hypoxic tumours can gain from adjunct treatment with hypoxic cell sensitizers or dose "painting" to allow for higher dose delivery with conformal radiotherapy. However, patients with tumours which are better oxygenated should not be exposed to hypoxic cell cytotoxins which inevitably add to the risk of adverse events without any benefit to tumour control. Similarly, those patients that present with highly proliferating tumours were proven to gain from accelerated radiotherapy and cell cycle-specific chemotherapy, whereas patients having tumours with slow cell turnover show clinical advantage when treated with conventionally fractionated radiotherapy and cycle nonspecific chemotherapy. It is therefore important to focus on individualized treatment and to develop predictive assays which can reflect the outcome.

Biased and inconclusive clinical trial results due to inadequate patient selection have proven the need to consider radiobiological parameters such as hypoxia, proliferative ability, radioresistance, and of other epigenetic factors in their design for more eloquent conclusions. However, predictive assays trialled over the last two-three decades for oxygenation status, proliferative ability, and intrinsic radioresistance showed several limitations and they were never implemented into clinical settings (Table 2). Assays to predict normal tissue response to radiation will always be easier to understand,

Table 2: Predictive assays for tumours: past, present, and future.

Primary tumour			Systemic disease
Oxygen status	Proliferative potential	Intrinsic cellular radiosensitivity	Micrometastases tumour dormancy
Past			
(i) Electrodes (ii) Biopsy (vascular density) (iii) Endogenous markers (iv) Exogenous markers	(i) Measurement of Tpot, TS, and LI and correlation with outcome (ii) Adjustment of treatment schedule as a function of Tk	(i) Comet assay (ii) Cell survival curves (iii) Functional assays	??
Present			
(i) Oxygen-specific PET markers (FMISO, FAZA) (ii) BOLD MRI	(i) Proliferation-specific PET markers (FLT)	(i) Functional/genomic assays	(i) Immunocytochemical and molecular assays to detect occult metastatic tumour cells
Future			
(i) Oxygen-specific PET markers with higher specificity (FMISO, FAZA, FETNIM, and F-EF3,5) (ii) BOLD MRI	(i) Proliferation-specific PET markers with higher specificity (FLT, F-ISO-1)	(i) Functional/genomic assays	(i) Immunocytochemical and molecular assays to detect disseminated and circulating tumour cells (ii) Biomarkers to indicate the state of dormancy

develop, and integrate in patient care than those targeting the tumour. The challenge to "predict" treatment response is multifaceted making it difficult to establish one complex predictive parameter. There is though potential in tumour parameter-specific radioisotopes used in PET to serve as predictive assays, especially when used in combination to provide supplementary metabolic information and diagnostic specificity (such as FDG + FMISO).

Despite the fact that clinical reports strongly suggest the routine incorporation of functional imaging such as PET/CT in the management of several malignant sites [31–33], there are impediments, whether related to the health system or to physicians' conventionality, which hinder this chance for a better outcome. Besides the accurate staging, tumour-specificity, and predictive ability of PET/CT, employing functional/metabolic imaging techniques, also assists in the early detection and localization of distant metastases.

However, there are limits to detection set by the tumour size and its metabolism, such that tumours of a few mm diameter, which contain millions of cancer cells, remain subclinical. Further, improved staging improves management, but may not impact on final outcome if the therapy is inadequate. Ultimately, recurrence arises from subclinical disease.

New tumour-specific assays might be needed to complement the existing ones for a better outcome prediction. Immunocytochemical and molecular assays for detection of micrometastases via sequential peripheral blood analyses of circulating tumour cells could add to the monitoring of systemic therapy and to patients' prognosis. Studies into tumour dormancy could answer the question as to why some patients recur soon after primary treatment and others have dormant tumours for long after the completion of therapy? The most commonly accepted explanation for tumour dormancy is the failure of angiogenic switch activation, a state that maintains the balance between proliferation and apoptosis [34]. It was suggested that induction of growth arrest within small groups of tumour cells (cellular dormancy) and immunosurveillance (which prevents residual tumour cell expansion) are other mechanisms behind cancer dormancy [35]. Molecular assays for tumour recurrence and distant metastases are awaited to be developed to scrutinize the anti/proangiogenic balance within the malignant tumour, growth arrest, and adaptive response to a suboptimal microenvironment [36]. Monitoring disseminated and circulating tumour cells is the first step towards better diagnosis. However, the large number of patients that survive with disseminated tumour cells in the bone marrow indicates the need to identify additional molecular factors which characterize the microbiology of disseminated cells [37].

Consequently, the future of targeted cancer treatment to manage disseminated disease probably lies in the ability to induce cell kill of dormant tumour population, to reprogram malignant cells into growth arrest, and to develop biomarkers to indicate the state of dormancy (rather than informing about tumour recurrence).

3.4.1. Normal Tissue Radiosensitivity (RS). Variable radiosensitivity of individual patient may explain recurrent cancer as well as normal tissue damage in external beam radiotherapy. Radiosensitivity could be a double-edged sword: if patients range from high to low radiosensitivity, then extreme tissue response is seen for the former and poor tumour control in the latter. If the reasonable assumption is made that all cells in the body, including cancer cells, have the same genetic RS, then the cancer would be controlled by lower and safe doses. However, the opposite effect will also be true. Low RS means that higher but safe doses are needed to control the cancer. Pretesting of patient RS may need to be introduced as an important part of the dose planning strategy.

3.5. Healthy Tissue Protection. Healthy tissue protection and reduction of treatment-related side effects are other important considerations for the future. Chemotherapy as well as targeted agents needs to be customized, since the same drug and dosage can have minimal normal tissue toxicity in one patient and be lethal to the other. It is suggested that single nucleotide polymorphism (SNP) is a viable technique to be used for the prediction of adverse events on an individual basis and will undergo further research to be clinically validated [30].

Patients have variable radiosensitivity, such that those with high values will be overdosed for normal tissue and those with low values will be underdosed for tumour control. Adjustment to the intrinsic patient's radiosensitivity could be a far more important factor than improved dose delivery systems. As such, radiosensitivity assays need to be developed which could become an essential part of the patient workup before radiotherapy.

More in-depth studies are needed regarding low doses of radiation and their potential hormetic effect on healthy tissue. Bystander effects induced by low doses of radiation to healthy tissue surrounding the target and the consequential adaptive response to radiation have gained interest and initiated translational research from basic to preclinical studies. There is growing evidence suggesting the potential role of low dose irradiation in clinical settings. Bystander effects are expected to have an impact on systemically targeted therapies; however the limitation of existing dosimetric methods to describe dose-response relationships of various cell lines at low doses makes it difficult to assess the extent of cellular effects outside the treated area.

4. Conclusions

The future of radiation oncology technology lies in its fusion with biology. Otherwise, it is hard to see any major developments in the near future with respect to new technologies or even the need for more expensive equipment. The last decades have seen major advances in cancer imaging and external beam therapy, and such investments have already paid off in terms of achieving improved local control. However, they are not matching the current needs in the management of cancer. These needs centre on the control of systemic disease by systemic treatment. Chemotherapy has fallen short here. The fusion of biological targeting and high LET radiation may well be our best hope (although there is little evidence that funding agencies and "peer" reviewers share that opinion). Therefore, biology-driven clinical trials are expected to prevail hand in hand with the development of new targeted agents.

Based on the above-reasoned problems and possible solutions, the focus of future cancer control and management should be on the following.

(i) TAT: immunotherapy of cancer cells using high LET, short range alphas and TAVAT.

(ii) Knowledge of molecular changes in cancer which can lead to the design of therapies that target proliferation and survival of cancer cells within a tumour as well as in the surrounding tumour microenvironment (i.e., development of genetically informed cancer medicine).

(iii) The complexity of molecular interactions within and among cancer cells, and between cancer cells and normal cells, which will require refinement of multi-agent treatment approaches against cancer.

(iv) Molecular diagnostics: development of tests that will determine mutated genes in a patient's tumour, tumour expressed molecules that can be targeted, and the overall mutational gene expression profiles that can predict a response to the treatment.

(v) Individualised patient treatments: treatments will have to be modified depending on the molecular profile of a particular tumour. For each patient the optimal match between the tumour and therapeutic regimen will be identified based on biological/genetical information.

(vi) Healthy tissue protection with low doses of radiation by utilizing potential hormesis and bystander effects.

Cancer may be ultimately controlled by genetic antisense techniques that find and cancel out genetic aberrations without causing any complications. However, this ideal objective continues to elude us and, in the meantime, we need to apply less ideal techniques to improve prognosis.

Nevertheless, the majority of the world's populations are a long way from curative cancer. Their needs call for a new paradigm that brings palliative cancer therapy to the rural populations. The cost-benefit of such centers is readily apparent. They can also become centers for cancer screening and ultimately upgraded for curative therapy.

References

[1] G. Kolata, *Playing it Safe in Cancer Research*, The New York Times, 2009.

[2] http://www.nytimes.com/imagepages/2009/06/28/health/28-cancer.grafic.ready.html.

[3] N. Burnet, S. Thomas, K. Burton, and S. Jefferies, "Defining the tumour and target volumes for radiotherapy," *Cancer Imaging*, no. 42, pp. 153–161, 2004.

[4] R. Miralbell, A. Lomax, L. Cella, and U. Schneider, "Potential reduction of the incidence of radiation-induced second cancers by using proton beams in the treatment of pediatric tumors," *International Journal of Radiation Oncology Biology Physics*, vol. 54, no. 3, pp. 824–829, 2002.

[5] W. Clair, J. Adams, M. Bues et al., "Advantage of protons compared to conventional X-ray or IMRT in the treatment of a pediatric patient with medulloblastoma," *International Journal of Radiation Oncology Biology Physics*, vol. 48, pp. 727–734, 2004.

[6] M. W. Kattan, A. M. Stapleton, T. M. Wheeler, and P. T. Scardino, "Evaluation of a nomogram used to predict the pathologic stage of clinically localized prostate carcinoma," *Cancer*, vol. 79, pp. 528–537, 1997.

[7] A. W. Partin, M. W. Kattan, E. N. P. Subong et al., "Combination of prostate-specific antigen, clinical stage, and Gleason score to predict pathological stage of localized prostate cancer: a

multi-institutional update," *Journal of the American Medical Association*, vol. 277, no. 18, pp. 1445–1451, 1997.

[8] B. J. Allen, C. Raja, S. Rizvi et al., "Intralesional targeted alpha therapy for metastatic melanoma," *Cancer Biology and Therapy*, vol. 4, no. 12, pp. 1318–1324, 2005.

[9] D. Schulz-Ertner and H. Tsujii, "Particle radiation therapy using proton and heavier ion beams," *Journal of Clinical Oncology*, vol. 25, no. 8, pp. 953–964, 2007.

[10] J. P. C. Grutters, A. G. H. Kessels, M. Pijls-Johannesma, D. De Ruysscher, M. A. Joore, and P. Lambin, "Comparison of the effectiveness of radiotherapy with photons, protons and carbon-ions for non-small cell lung cancer: a meta-analysis," *Radiotherapy and Oncology*, vol. 95, no. 1, pp. 32–40, 2010.

[11] A. Ask, T. Björk-Eriksson, B. Zackrisson, E. Blomquist, and B. Glimelius, "The potential of proton beam radiation therapy in head and neck cancer," *Acta Oncologica*, vol. 44, no. 8, pp. 876–880, 2005.

[12] B. Glimelius, A. Ask, G. Bjelkengren et al., "Number of patients potentially eligible for proton therapy," *Acta Oncologica*, vol. 44, no. 8, pp. 836–849, 2005.

[13] B. Glimelius and A. Montelius, "Proton beam therapy—do we need the randomised trials and can we do them?" *Radiotherapy and Oncology*, vol. 83, no. 2, pp. 105–109, 2007.

[14] M. Lodge, M. Pijls-Johannesma, L. Stirk, A. J. Munro, D. De Ruysscher, and T. Jefferson, "A systematic literature review of the clinical and cost-effectiveness of hadron therapy in cancer," *Radiotherapy and Oncology*, vol. 83, no. 2, pp. 110–122, 2007.

[15] B. J. Allen, S. M. Abbas Rizvi, C. F. Qu, and R. C. Smith, "Targeted alpha therapy approach to the management of pancreatic cancer," *Cancers*, vol. 3, no. 2, pp. 1821–1843, 2011.

[16] C. Blattmann, S. Oertel, D. Schulz-Ertner et al., "Non-randomized therapy trial to determine the safety and efficacy of heavy ion radiotherapy in patients with non-resectable osteosarcoma," *BMC Cancer*, vol. 10, article 96, 2010.

[17] H. Tsujii, J. E. Mizoe, T. Kamada et al., "Overview of clinical experiences on carbon ion radiotherapy at NIRS," *Radiotherapy and Oncology*, vol. 73, no. 2, supplement, pp. S41–S49, 2004.

[18] J. E. Mizoe, H. Tsujii, A. Hasegawa et al., "Phase I/II clinical trial of carbon ion radiotherapy for malignant gliomas: combined X-ray radiotherapy, chemotherapy, and carbon ion radiotherapy," *International Journal of Radiation Oncology Biology Physics*, vol. 69, no. 2, pp. 390–396, 2007.

[19] M. Kano, S. Yamada, I. Hoshino et al., "Effects of carbon-ion radiotherapy combined with a novel histone deacetylase inhibitor, cyclic hydroxamic-acid-containing peptide 31 in human esophageal squamous cell carcinoma," *Anticancer Research*, vol. 29, no. 11, pp. 4433–4438, 2009.

[20] http://ptcog.web.psi.ch/.

[21] R. F. Barth and H. Joensuu, "Boron neutron capture therapy for the treatment of glioblastomas and extracranial tumours: as effective, more effective or less effective than photon irradiation?" *Radiotherapy and Oncology*, vol. 82, no. 2, pp. 119–122, 2007.

[22] R. Henriksson, J. Capala, A. Michanek et al., "Boron neutron capture therapy (BNCT) for glioblastoma multiforme: a phase II study evaluating a prolonged high-dose of boronophenylalanine (BPA)," *Radiotherapy and Oncology*, vol. 88, no. 2, pp. 183–191, 2008.

[23] A. Wittig, L. Collette, K. Appelman et al., "EORTC trial 11001: distribution of two 10B-compounds in patients with squamous cell carcinoma of head and neck, a translational research/phase 1 trial," *Journal of Cellular and Molecular Medicine*, vol. 13, no. 8 B, pp. 1653–1665, 2009.

[24] S. Kneifel, D. Cordier, S. Good et al., "Local targeting of malignant gliomas by the diffusible peptidic vector 1,4,7,10-tetraazacyclododecane-1-glutaric acid-4,7,10-triacetic acid-substance P," *Clinical Cancer Research*, vol. 12, no. 12, pp. 3843–3850, 2006.

[25] B. J. Allen, C. Raja, S. Rizvi, E. Y. Song, and P. Graham, "Tumour anti-vascular alpha therapy: a mechanism for the regression of solid tumours in metastatic cancer," *Physics in Medicine and Biology*, vol. 52, no. 13, pp. L15–L19, 2007.

[26] B. J. Allen, "Future prospects for targeted alpha therapy," *Current Radiopharmaceuticals*, vol. 4, no. 4, pp. 336–342, 2011.

[27] T. Jiang, E. S. Olson, Q. T. Nguyen, M. Roy, P. A. Jennings, and R. Y. Tsien, "Tumor imaging by means of proteolytic activation of cell-penetrating peptides," *Proceedings of the National Academy of Sciences of the United States of America*, vol. 101, no. 51, pp. 17867–17872, 2004.

[28] C. Foerg and H. P. Merkle, "On the biomedical promise of cell penetrating peptides: limits versus prospects," *Journal of Pharmaceutical Sciences*, vol. 97, no. 1, pp. 144–162, 2008.

[29] R. Etzioni, N. Urban, S. Ramsey et al., "The case for early detection," *Nature Reviews Cancer*, vol. 3, no. 4, pp. 243–252, 2003.

[30] T. Tursz, F. Andre, V. Lazar, L. Lacroix, and J. C. Soria, "Implications of personalized medicine-perspective from a cancer center," *Nature Reviews Clinical Oncology*, vol. 8, no. 3, pp. 177–183, 2011.

[31] J. Bussink, J. H. A. M. Kaanders, W. T. A. Van Der Graaf, and W. J. G. Oyen, "PET-CT for radiotherapy treatment planning and response monitoring in solid tumors," *Nature Reviews Clinical Oncology*, vol. 8, no. 4, pp. 233–242, 2011.

[32] J. Corry, D. Rischin, R. J. Hicks, and L. J. Peters, "The role of PET-CT in the management of patients with advanced cancer of the head and neck," *Current Oncology Reports*, vol. 10, no. 2, pp. 149–155, 2008.

[33] V. Grégoire, K. Haustermans, X. Geets, S. Roels, and M. Lonneux, "PET-based treatment planning in radiotherapy: a new standard?" *Journal of Nuclear Medicine*, vol. 48, no. 1, supplement, pp. 68S–77S, 2007.

[34] G. N. Naumov, J. Folkman, and O. Straume, "Tumor dormancy due to failure of angiogenesis: role of the microenvironment," *Clinical and Experimental Metastasis*, vol. 26, no. 1, pp. 51–60, 2009.

[35] J. A. Aguirre-Ghiso, "Models, mechanisms and clinical evidence for cancer dormancy," *Nature Reviews Cancer*, vol. 7, no. 11, pp. 834–846, 2007.

[36] N. Almog, "Molecular mechanisms underlying tumor dormancy," *Cancer Letters*, vol. 294, no. 2, pp. 139–146, 2010.

[37] K. Pantel, C. Alix-Panabières, and S. Riethdorf, "Cancer micrometastases," *Nature Reviews Clinical Oncology*, vol. 6, no. 6, pp. 339–351, 2009.

Hindawi Publishing Corporation
BioMed Research International
Volume 2013, Article ID 371819, 7 pages
http://dx.doi.org/10.1155/2013/371819

Clinical Study

Involved-Field Radiotherapy versus Elective Nodal Irradiation in Combination with Concurrent Chemotherapy for Locally Advanced Non-Small Cell Lung Cancer: A Prospective Randomized Study

Ming Chen,[1] Yong Bao,[2] Hong-Lian Ma,[3] Xiao Hu,[2] Jin Wang,[3] Yan Wang,[2] Fang Peng,[2] Qi-Chao Zhou,[2] and Cong-Hua Xie[1]

[1] *Department of Radiation and Medical Oncology, Zhongnan Hospital, Hubei Cancer Clinical Study Center, Wuhan University, Wuhan 430071, China*
[2] *Department of Radiation Oncology, Sun Yat-sen University Cancer Center, State Key Laboratory of Oncology in South China, Guangzhou 510060, China*
[3] *Department of Radiation Oncology, Zhejiang Cancer Hospital, Hangzhou 310022, China*

Correspondence should be addressed to Cong-Hua Xie; xiechdr@163.com

Received 10 March 2013; Accepted 14 April 2013

Academic Editor: An Liu

This prospective randomized study is to evaluate the locoregional failure and its impact on survival by comparing involved field radiotherapy (IFRT) with elective nodal irradiation (ENI) in combination with concurrent chemotherapy for locally advanced non-small cell lung cancer. It appears that higher dose could be delivered in IFRT arm than that in ENI arm, and IFRT did not increase the risk of initially uninvolved or isolated nodal failures. Both a tendency of improved locoregional progression-free survival and a significant increased overall survival rate are in favor of IFRT arm in this study.

1. Introduction

Nowadays the combined chemoradiotherapy has been established as a standard treatment modality for patients with unresectable locally advanced non-small cell lung cancer (LA-NSCLC). However, overall survival remains poor with median survival time 16–20 months because of both local and distant failure [1]. Studies have confirmed that improved local control and overall survival are associated with dose escalation in patients with LA-NSCLC. But the use of traditional elective nodal irradiation (ENI) will limit dose escalation because of pulmonary and esophageal toxicities [2]. So some investigators used involved-field radiotherapy (IFRT) in order to accomplish dose escalation [3–5]. However, rare data from large sample sizes, prospective, randomized studies were available to support the use of IFRT. Whether IFRT could replace ENI or not has been a controversial topic for years [6]. Therefore, we have initiated this prospective randomized study on IFRT versus ENI in combination with concurrent chemotherapy for LA-NSCLC since July 2002, with a primary objective of the locoregional progression and failure patterns, as well as the impact of failure patterns on overall survival (OS).

2. Materials and Methods

2.1. General Clinical Data. Inclusion criteria were as follows. Patients were eligible when histologic or cytologic of NSCLC verified and stage IIIA or IIIB confirmed radiographically (according to the 6th AJCC/UICC staging system) with no pleural effusion (including brain magnetic resonance imaging, contrast-enhanced chest and abdomen CT, and bone scintigraphy, while positron-emission tomography was not mandatory). The patients were aged 18–75 years without

previous thoracic radiotherapy or chemotherapy. Karnofsky performance status was ⩾70 and had measurable or assessable disease, neutrophilic granulocyte $\geqslant 1.5 \times 10^9$/L, hemoglobin ⩾100 g/L, and platelet count $\geqslant 100 \times 10^9$/L. Serum creatine and bilirubin were <1.5 × the upper normal limit (UNL). Aminotransferase was <2 × UNL. Weight loss was less than 10% within 6 months before diagnosis. Written informed consent was required from all patients.

Exclusion criteria were as follows. Patients were ineligible when they had a history of other malignant diseases except for non-melanomatous skin cancer, carcinoma in situ of the cervix, or any contraindications for chemoradiotherapy, malignant pleural, and/or pericardial effusion.

2.2. Interventions. Chemotherapy. Patients were randomized into IFRT arm or ENI arm. Induction chemotherapy consisted of paclitaxel (175 mg/m^2 on day 1) and carboplatin (AUC = 5~6 on day 1) administered intravenously at 21-day intervals for 2 cycles. Three to four weeks after induction chemotherapy, thoracic radiotherapy was administered concurrently with weekly paclitaxel (40 mg/m^2) as a radiosensitizer to end radiotherapy [7]. During chemotherapy, 5-hydroxytryptamine receptor antagonists, dexamethasone, cimetidine, and diphenhydramine were used prophylactically. Meanwhile, electrocardio-guardianship was applied.

Radiotherapy. All patients were immobilized in a supine position on a vacuum bag with both arms above the head; a contrast-enhanced CT simulation was performed from the fourth cervical vertebra to the second lumbar vertebra, using a maximal slice thickness of 5 mm. A three-dimensional treatment planning system of Pinnacle (version 7.0~8.0) was applied to the radiotherapy plan. Radiotherapy was performed with a linear accelerator using 6~8 MV photons. After induction chemotherapy, patients who did not develop metastasis continued to receive concurrent chemoradiotherapy. The targets were contoured in accordance with the International Commission on Radiation Units and Measurements (ICRU) 50 guidelines. Gross tumor volume (GTV) included the gross tumor volume-tumor (GTV-T) and gross tumor volume-node (GTV-N) defined as lymph nodes in the ipsilateral hilum and mediastinum with a short diameter ⩾1 cm, or lymph nodes with positive tumor cell sampling, or clusters of small lymph nodes of short diameter <1 cm within one region, or 18F-FDG standard uptake value ⩾2.5 on PET/CT at initial staging. The lymph node regions originally involved before induction chemotherapy were included in the radiation fields for both arms even when the lymph nodes disappeared after induction chemotherapy. The clinical target volume-tumor (CTV-T) included the GTV-T with a margin of 0.6 cm or 0.8 cm, depending on squamous cell carcinoma or otherwise in all patients [8]. For patients who were randomized to IFRT arm, the clinical target volume-node (CTV-N) included the prechemotherapy positive lymph nodes with a margin of 0.5 cm and ipsilateral hilum. For patients who were randomized to ENI arm, the CTV-N included the ipsilateral hilum, mediastinum (from the inferior head of the clavicle to 3~5 cm below the carina), and the bilateral supraclavicular fossa. CTVs (include CTV-T and CTV-N) were edited according to the anatomic structure borders. Planning target volumes (PTV) involved CTVs with a margin of 1.0 cm~1.5 cm. Under the condition of V20 (percent volume of bilateral lung receiving ⩾20 Gy) ⩽35% and the maximal dose to spinal cord ⩽50 Gy, thoracic irradiation consisted of 2.0 Gy once a day for consecutive 5 days a week to a maximal tolerable dose in IFRT arm. In ENI arm, a dose of 40~46 Gy was delivered to the elective nodal areas. Then an escalated dose was delivered to GTV to a maximal tolerable dose.

2.3. Follow-Up. Patients took chest X-ray exam every 2 weeks during irradiation period. After completion of treatment, patients were reviewed within 4~6 weeks, then every 3 months in the first 2 years, every 4 months in the third year, and every 6 months thereafter. Physical examination and CT scans of the thorax and upper abdomen were performed routinely.

2.4. Response and Toxicity Criteria. Tumor response was evaluated with thoracic CT scans after induction chemotherapy and concurrent chemoradiotherapy were completed, in accordance with Response Evaluation Criteria in Solid Tumors Group 1.0 (RECIST1.0). An elective nodal failure (ENF) was defined as a nodal failure of elective irradiation region in ENI arm and an uninvolved nodal failure out of irradiation field in IFRT arm. Involved-field nodal failure (IFNF) was defined as a nodal failure in the irradiation region with dose escalation in ENI arm and a nodal failure in irradiation field in IFRT arm. Locoregional failure included primary tumor failure, ENF and IFNF. Local progression-free survival (LPFS) was recorded from the beginning of induction chemotherapy to the time of primary tumor failure, ENF or IFNF. During radiotherapy, acute radiation-induced pneumonitis and esophagitis as well as body weight change of each patient was recorded, and a complete blood count was performed at least once a week. Acute hematologic toxicities and weight loss were classified in accordance with the National Cancer Institute Common Toxicity Criteria (CTCAE) version 3.0. Acute and late toxicities of lung and esophagus were evaluated according to RTOG criteria [9].

2.5. Study Design and Statistical Analysis. This study was designed as a prospective, randomized trial. The primary endpoint was locoregional progression. We hypothesized that the 3-year local control rates for IFRT arm and ENI arm were 45% and 30%, respectively; sample sizes of 123 in each group achieved 80% power to detect a risk ratio of 0.65. A statistical software package SPSS 15.0 (IBM, Somers, New York) was applied, and the Kaplan-Meier method was used to estimate survival data. The distribution of survival time between arms was tested by log-rank method; a Student t-test was used for comparison of means. Fisher exact test was used for comparisons of categorical data. All P values were based on a 2-sided test, and the differences were regarded as statistically significant when $P < 0.05$. The protocol was approved by the clinical ethics committee of Sun Yat Sen University Cancer Center before study activation.

Table 1: Patient characteristics.

Characteristic	IFRT arm ($n = 45$)		ENI arm ($n = 54$)		P
	n	%	n	%	
Gender					0.343
Male	37	82.2	48	88.9	
Female	8	17.8	6	11.1	
Age, y					0.385
Median	56		55.5		
Range	27~71		38~71		
KPS					0.744
80–90	8	17.8	11	20.4	
90–100	37	82.2	43	79.6	
Weight loss					0.771
<5%	34	75.6	44	81.5	
5%–10%	10	22.2	9	16.7	
>10%	1	2.2	1	1.9	
TNM stage					0.420
IIIA	15	33.3	14	25.9	
IIIB	30	66.7	40	74.1	
Tumor position					0.363
Central	33	73.3	35	64.8	
Peripheral	12	26.7	19	35.2	
PET/CT examination	13	28.9	10	18.5	0.224
Histology					0.668
Adenocarcinoma	23	51.1	27	50.0	
Squamous cell carcinoma	19	42.2	23	42.6	
Adenosquamous carcinoma	1	2.2	0	0.0	
Undifferentiated carcinoma	2	4.4	4	7.4	

3. Results

3.1. Patient Characteristics. Between July 2002 and June 2011, a total of consecutive 99 patients with LA-NSCLC were enrolled onto the study. The characteristics of the 99 eligible patients were well balanced in 2 arms (Table 1). Eight patients were ineligible because of distant metastasis during chemoradiotherapy and were not included for local control analysis.

3.2. Treatment Results. Forty and 48 patients had completed radiation plan in IFRT arm and ENI arm, respectively. Eight patients developed distant metastasis during radiotherapy received palliative treatment. Of the 3 patients who discontinued radiation plan, one emerged acute left ventricular failure when irradiated to 40 Gy in IFRT arm, one developed severe acute respiratory syndromes when irradiated to 46 Gy, and one refused treatment because of grade 2 radiation-induced esophagitis when irradiated to 32 Gy in ENI arm. The media radiation dose were 60 Gy (range: 38~74 Gy) and 60 Gy (range: 32~70 Gy) in IFRT arm and ENI arm, respectively. Thirty-six (87.8%) and 40 (80.0%) patients received dose of ⩾60 Gy, respectively ($P = 0.426$). More patients in IFRT arm received ⩾62 Gy than those in ENI arm (48.9% versus 25.9%, $P = 0.018$). Rank sum test was used for comparing dose distribution between the two arms. Dose delivered in IFRT arm was higher than that in ENI arm. The mean rank order was 51.84 and 41.21 in IFRT arm and ENI arm, respectively ($P = 0.042$). The average total cycles of concurrent chemotherapy administered in IFRT arm and ENI arm were 5.5 ± 1.4 and 5.9 ± 1.1, respectively ($P = 0.168$).

3.3. Locoregional Failure, Distant Metastasis, and Survival. Patients who developed distant metastasis after induction chemotherapy were not included in analysis for locoregional but for distant failure. At last follow-up, 14 (34.1%) patients in IFRT arm and 15 (30%) patients in ENI arm experienced locoregional failure ($P = 0.673$). Among them, 9 (22%) and 12 (24%) encountered primary tumor failure in IFRT arm and in ENI arm, respectively. ENF in combination with involved-field nodal failure (IFNF) or primary recurrence was present in 2 and 3 patients, respectively. Only one patient experienced isolated-ENF in ENI arm. Twenty-four (53.3%) patients in IFRT arm and 31 (57.4%) cases in ENI arm experienced distant metastases.

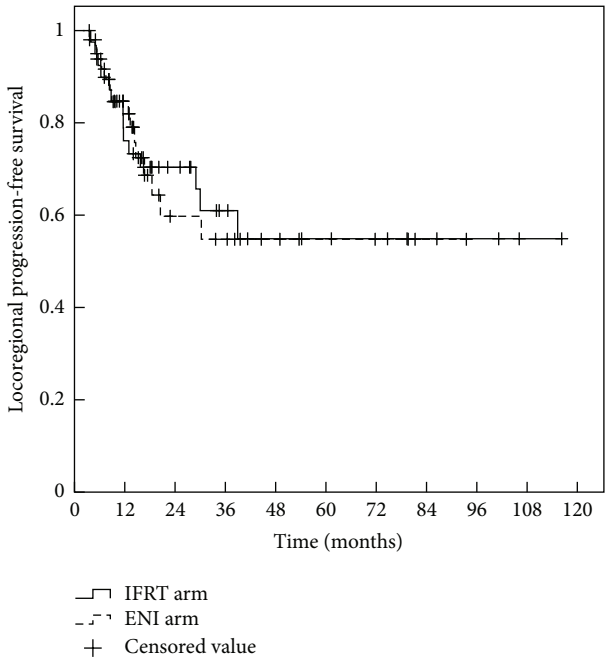

Figure 1: Local progression-free survival curves for patients with IFRT or ENI. The 1-, 2-, and 3-year local tumor progression-free survival rates in the IFRT arm were 78.1%, 72.6%, and 62.9% compared with 85.5%, 61.2%, and 56.1%, respectively, in the ENI arm. There was no statistically significant difference in local progression-free survival between the two arms ($P = 0.895$).

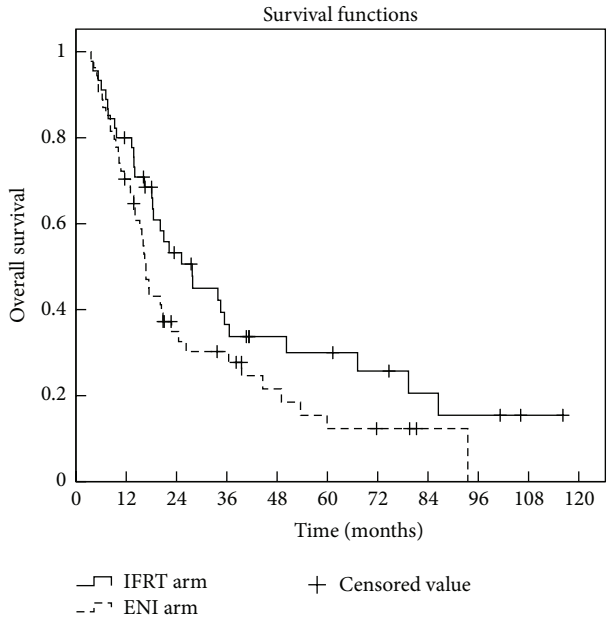

Figure 2: Overall survival curves for patients with IFRT or ENI. The 1-, 2-, and 3-year overall survival rates in the IFRT arm were 80.0%, 53.3%, and 36.6% compared with 70.4%, 34.9%, and 30.3%, respectively, in the ENI arm. There was no statistically significant difference in local progression-free survival between the two arms ($P = 0.08$).

Twenty-five patients remained alive at the time of analysis, with a median follow-up of 33.6 months in survivors (4.8 months~112 months). The median LPFS time was not available. The 1-, 2-, and 3-year LPFS rates were 78.1%, 72.6%, and 62.9%, respectively, in IFRT arm, versus 85.5%, 61.2.0%, and 56.1% in ENI arm ($P = 0.895$ by log-rank test) as shown in Figure 1. The median survival time was 27.8 months in IFRT arm (95% confidence interval (CI), 18.0~37.5 months) and 16.7 months (95% CI, 15.0~18.4 months) in ENI arm. The 1-, 2-, and 3-year OS rates were 80.0%, 53.3%, and 36.6%, respectively, in IFRT arm, versus 70.4%, 34.9%, and 30.3% in ENI arm ($P = 0.08$ by log-rank test) as shown in Figure 2. The 1-, 2-, and 3-year OS rates were 95.5%, 75.7%, and 46.6%, respectively, in IFRT arm when radiation dose ⩾62 Gy, much better than that of those patients who received radiation dose <62 Gy in both arms, and that in ENI arm when radiation dose was greater than or equal to 62 Gy ($P = 0.013$ by log-rank test) as shown in Figure 3.

3.4. Toxicity. (i) *Acute Toxicities.* Hematologic and nonhematologic acute and late toxicities are summarized in Table 2. Hematologic toxicity was mild to moderate in both arms; one patient developed grade III radiation-induced pneumonitis in each arm and 1 patient encountered grade IV radiation-induced pneumonitis in IFRT arm. No severe esophageal toxicity was observed in two arms. There were no significant differences in acute nonhematologic toxicities between the arms.

(ii) *Late Toxicities.* Late toxicities of radiotherapy were mainly mild-to-moderate pulmonary and esophageal injury. No patients developed grade III~IV pulmonary injury in both arms. Late spinal cord toxicity was not observed. Our study showed no significant differences in toxicity in patients treated with IFRT or ENI using three-dimensional conformal radiotherapy (3D-CRT) technique for LA-NSCLC.

4. Discussion

In order to avoid missing the targets, ENI was applied and relatively decreased the failure rate of mediastinal lymph nodes in 2-dimensional radiotherapy era. However, with the advent of three-dimensional conformal radiotherapy (3D-CRT), ENI considerably increased exposure of normal tissues, led to significant toxicities, and prevented dose-escalation. RTOG 9311 [10] was a phase I~II dose-escalation study for patients with inoperable NSCLC treated with 3D-CRT. Elective nodal regions were not intentionally irradiated. The radiation dose was safely escalated to 77.4 Gy when V20 was between 25% and 36% and to 83.8 Gy when V20 <25%. The 2-year locoregional control rate was 50% ~78%. Although postoperative pathologic upstaging to N2 was reported in approximately 20% of patients with presurgery diagnosis as N0/1 [11, 12], micrometastases were detected in 20.4% of patients with pathologic N0 when immunohistochemical staining was used [13]. The isolated-ENF rate of 7% was reported in Stage T1-2N0 M0 NSCLC patients treated with stereotactic body radiation therapy (SBRT) [14]. Several

Table 2: Treatment toxicities according to treatment arms.

	IFRT arm (n = 41)		ENI arm (n = 50)		P
	n	%	n	%	
Acute toxicities					
Hematologic toxicity ≥grade 3					
Leucopenia					0.384
III	31	75.6	38	76.0	
IV	3	7.3	2	4.0	
Anemia					0.499
III	1	2.4	0	0.0	
IV	1	2.4	0	0.0	
Weight loss					0.256
I	8	19.5	4	8.0	
II	2	4.9	2	4.0	
Pneumonitis					0.385
I-II	23	56.1	22	44.0	
III-IV	2	4.8	1	2.0	
Esophagitis					0.839
0-I	27	65.9	35	70.0	
II	14	34.1	15	30.0	
Late toxicities					
Pulmonary injury					0.925
I-II	19	46.3	23	46.0	
III–V	0	0.0	0	0.0	
Esophageal injury					0.142
I-II	3	7.3	4	8.0	
III-IV	0	0.0	0	0.0	

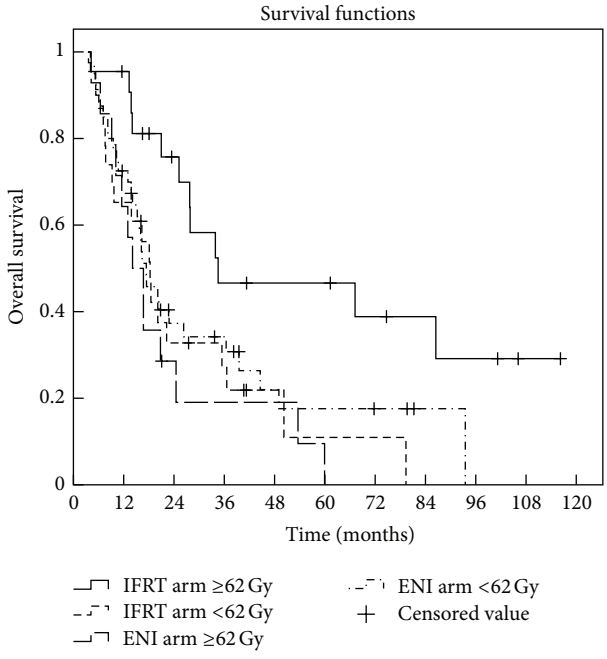

Figure 3: Overall survival of patients irradiated at dose of ⩾62 Gy in IFRT arm, much better than that of those patients who received radiation dose <62 Gy in both arms and that when radiation dose was greater than or equal to 62 Gy in ENI arm (P = 0.013).

studies have reported that the ENF rate was less than 10% in patients with NSCLC treated with IFRT [3, 5, 15–18].

Fernandes et al. [19] retrospectively analyzed 108 patients with locally advanced NSCLC treated with 3DCRT and concurrent or sequential chemotherapy. The IFRT group received higher radiation doses than the ENI group (60~84 Gy versus 54~72 Gy, $P < 0.001$). There were no significantly differences in ENF rate between the 2 groups. To our knowledge, there are few prospective studies available comparing ENI with IFRT in patients with LA-NSCLC at present. Only one randomized trial specifically addressed this issue [20]. In this trial, 68~74 Gy radiation doses were prescribed for patients in IFRT arm, while 60~64 Gy for the ENI arm. ENF rate was 7% and 4% in IFRT arm and ENI arm, respectively (P = 0.352). Patients in the IFRT arm achieved better 5-year local control (LC) rate (51% versus 36%, P = 0.032) and better 2-year survival rate (39.4% versus 25.6%, P = 0.048) than those in the ENI arm.

Because the prescribed dose to IFRT arm was higher than that to ENI arm, it remained unclear if the better outcome from IFRT was due to the higher radiation dose or the use of IFRT in the study above. Therefore, our study is designed uniquely in that we delivered radiation dose as high as possible provided that the organs at risk could tolerate. Under the condition of that V20 was ⩽35% and the maximum dose to spinal cord was ⩽50 Gy, dose delivered between the IFRT

arm and ENI arm was significantly different. Patients in IFRT arm received dose of ⩾62 Gy which was much more than that in ENI arm (48.9% versus 25.9%, $P = 0.018$), which indicated that with IFRT, higher dose could be delivered. It was the same as the results of many studies on radiation dose escalation [4, 10, 18, 21].

Sura et al. [22] discovered that when the dose delivered was <60 Gy or ⩾60 Gy in NSCLC patients treated with IFRT, 75% patients and 33% patients developed recurrence within the GTV, respectively ($P < 0.05$). Rengan et al. [23] reported that the 1- and 2-year local failure rates were 27%, 47% and 61%, 76%, respectively, for stage III patients treated with 64 Gy or higher, and less than 64 Gy ($P = 0.024$). Both studies suggested that administration of higher doses using 3D-CRT improved local control in NSCLC patients. In our study, only one patient developed isolated-ENF in ENI arm. Two patients in IFRT arm and 3 in ENI arm had ENF accompanied with IFNF or primary tumor failure. Less patients developed ENF in IFRT arm than in ENI arm (4.9% versus 8.0%), which suggests that a decrease in ENF may be achieved when involved-field control rate increased due to a higher prescription dose delivered in the IFRT arm. The preliminary results have showed that the median overall survival in IFRT arm was longer than that in ENI arm (27.8 months versus 16.7 months). In addition, the overall survival rate of patients treated with IFRT at dose of ⩾62 Gy is significantly higher than that in both arms at dose of <62 Gy and that in the ENI arm at dose of ⩾62 Gy as showed in Figure 3 ($P = 0.013$). These results indicate that irradiation dose could be successfully escalated with IFRT and then overall survival rate is expected to be increased.

However, at the 53rd Annual Meeting of the American Society of Radiation Oncology, Bradley et al. [24] reported the result of RTOG 0617 study that the higher radiation dose of 74 Gy could not produce an overall survival benefit compared with 60 Gy. These findings are counterintuitive and run counter to a large body of evidence showing that higher radiation doses lead to better tumor control at numerous sites. Moreover, the toxicity rates difference was not significant statistically between the two dose groups. However, there were 17 patients died in the 74-Gy arms and 7 in the 60-Gy arms. Cox [25] reviewed considerable evidence that supports the hypothesis that the pulmonary or cardiopulmonary effects of thoracic radiotherapy can contribute to death and considered that as the most likely explanation of the findings from the RTOG 0617. So we could still presume that if the death-related toxicities can be restrained in higher dose arms, dose escalation remains produce survival benefit. In our study, dose to organs at risk was restrained in both arms, so there was no significant deference in toxicities between the two arms. Even if the final result of RTOG 0617 study would confirm that higher radiation dose could not improve survival, delivered with same dose, irradiation with IFRT could decrease normal tissues damage due to less normal tissues irradiation exposure than that with ENI. Then treatment prevalence would be increased and a survival benefit even to be produced.

In summary, our preliminary results showed that IFRT did not increase the risk of initially uninvolved or isolated nodal failures and locoregional failure. Meanwhile, higher radiation dose could be effectively administered with IFRT, which is expected to improve overall survival.

The current sample size has not met the designed requirements; caution must be taken when adopting the conclusions. Further investigations are warranted. In addition, CT scan was used to assess the treatment effect and failure patterns for all patients. Undetected occult recurrence and micrometastasis of mediastinal lymph node maybe exist as the intrinsic limitation of accuracy using CT scan [26]. Nowadays, PET/CT scans are available generally, which is superior to CT for assessment of stage III NSCLC after chemoradiation [27]. In future studies, we hope to ideally incorporate information from PET/CT scans for diagnosis and assessment.

5. Conclusions

These preliminary results indicated that IFRT did not increase locoregional failure related to ENF. With IFRT, higher radiation dose could be administered compared with ENI and it is expected to improve survival. Further investigation is warranted.

Authors' Contribution

Ming Chen, Yong Bao, and Hong-Lian Ma contributed equally to this article.

References

[1] E. E. Vokes, J. E. Herndon II, M. J. Kelley et al., "Induction chemotherapy followed by chemoradiotherapy compared with chemoradiotherapy alone for regionally advanced unresectable stage III non-small-cell lung cancer: cancer and leukemia group B," *Journal of Clinical Oncology*, vol. 25, no. 13, pp. 1698–1704, 2007.

[2] J. D. Bradley, S. Wahab, M. A. Lockett, C. A. Perez, and J. A. Purdy, "Elective nodal failures are uncommon in medically inoperable patients with Stage I non-small-cell lung carcinoma treated with limited radiotherapy fields," *International Journal of Radiation Oncology ∗ Biology ∗ Physics*, vol. 56, no. 2, pp. 342–347, 2003.

[3] K. E. Rosenzweig, S. Sura, A. Jackson, and E. Yorke, "Involved-field radiation therapy for inoperable non-small-cell lung cancer," *Journal of Clinical Oncology*, vol. 25, no. 35, pp. 5557–5561, 2007.

[4] J. A. Hayman, M. K. Martel, R. K. Ten Haken et al., "Dose escalation in non-small-cell lung cancer using three-dimensional conformal radiation therapy: update of a phase I trial," *Journal of Clinical Oncology*, vol. 19, no. 1, pp. 127–136, 2001.

[5] F. M. Kong, R. K. Ten Haken, M. J. Schipper et al., "High-dose radiation improved local tumor control and overall survival in patients with inoperable/unresectable non-small-cell lung cancer: long-term results of a radiation dose escalation study," *International Journal of Radiation Oncology ∗ Biology ∗ Physics*, vol. 63, no. 2, pp. 324–333, 2005.

[6] J. S. A. Belderbos, L. Kepka, F. M. (Spring) Kong F.-M., M. K. Martel, G. M. M. Videtic, and B. Jeremic, "Report from the International Atomic Energy Agency (IAEA) consultants'

meeting on elective nodal irradiation in lung cancer: non-small-cell lung cancer (NSCLC)," *International Journal of Radiation Oncology ∗ Biology ∗ Physics*, vol. 72, no. 2, pp. 335–342, 2008.

[7] H. Choy, H. Safran, W. Akerley, S. L. Graziano, J. A. Bogart, and B. F. Cole, "Phase II trial of weekly paclitaxel and concurrent radiation therapy for locally advanced non-small cell lung cancer," *Clinical Cancer Research*, vol. 4, no. 8, pp. 1931–1936, 1998.

[8] P. Giraud, M. Antoine, A. Larrouy et al., "Evaluation of microscopic tumor extension in non-small-cell lung cancer for three-dimensional conformal radiotherapy planning," *International Journal of Radiation Oncology ∗ Biology ∗ Physics*, vol. 48, no. 4, pp. 1015–1024, 2000.

[9] J. D. Cox, J. Stetz, and T. F. Pajak, "Toxicity criteria of the Radiation Therapy Oncology Group (RTOG) and the European organization for research and treatment of cancer (EORTC)," *International Journal of Radiation Oncology ∗ Biology ∗ Physics*, vol. 31, no. 5, pp. 1341–1346, 1995.

[10] J. Bradley, M. V. Graham, K. Winter et al., "Toxicity and outcome results of RTOG 9311: a phase I-II dose-escalation study using three-dimensional conformal radiotherapy in patients with inoperable non-small-cell lung carcinoma," *International Journal of Radiation Oncology ∗ Biology ∗ Physics*, vol. 61, no. 2, pp. 318–328, 2005.

[11] A. N. J. Graham, K. J. M. Chan, U. Pastorino, and P. Goldstraw, "Systematic nodal dissection in the intrathoracic staging of patients with non-small cell lung cancer," *Journal of Thoracic and Cardiovascular Surgery*, vol. 117, no. 2, pp. 246–251, 1999.

[12] T. Koike, M. Terashima, T. Takizawa, T. Watanabe, Y. Kurita, and A. Yokoyama, "Clinical analysis of small-sized peripheral lung cancer," *Journal of Thoracic and Cardiovascular Surgery*, vol. 115, no. 5, pp. 1015–1020, 1998.

[13] J. Wu, Y. Ohta, H. Minato et al., "Nodal occult metastasis in patients with peripheral lung adenocarcinoma of 2.0 cm or less in diameter," *Annals of Thoracic Surgery*, vol. 71, no. 6, pp. 1772–1778, 2001.

[14] N. Andratschke, F. Zimmermann, E. Boehm, S. Schill, C. Schoenknecht et al., "Stereotactic radiotherapy of histologically proven inoperable stage I non-small cell lung cancer: patterns of failure," *Radiotherapy and Oncology*, vol. 101, no. 2, pp. 245–249, 2011.

[15] E. P. Sulman, R. Komaki, A. H. Klopp, J. D. Cox, and J. Y. Chang, "Exclusion of elective nodal irradiation is associated with minimal elective nodal failure in non-small cell lung cancer," *Radiation Oncology*, vol. 4, article 5, 2009.

[16] D. De Ruysscher, S. Wanders, E. van Haren et al., "Selective mediastinal node irradiation based on FDG-PET scan data in patients with non-small-cell lung cancer: a prospective clinical study," *International Journal of Radiation Oncology ∗ Biology ∗ Physics*, vol. 62, no. 4, pp. 988–994, 2005.

[17] K. E. Rosenzweig, S. E. Sim, B. Mychalczak, L. E. Braban, R. Schindelheim, and S. A. Leibel, "Elective nodal irradiation in the treatment of non-small-cell lung cancer with three-dimensional conformal radiation therapy," *International Journal of Radiation Oncology ∗ Biology ∗ Physics*, vol. 50, no. 3, pp. 681–685, 2001.

[18] J. S. A. Belderbos, W. D. Heemsbergen, K. De Jaeger, P. Baas, and J. V. Lebesque, "Final results of a phase I/II dose escalation trial in non-small-cell lung cancer using three-dimensional conformal radiotherapy," *International Journal of Radiation Oncology ∗ Biology ∗ Physics*, vol. 66, no. 1, pp. 126–134, 2006.

[19] A. T. Fernandes, J. Shen, J. Finlay et al., "Elective nodal irradiation (ENI) versus involved field radiotherapy (IFRT) for locally advanced non-small cell lung cancer (NSCLC): a comparative analysis of toxicities and clinical outcomes," *Radiotherapy and Oncology*, vol. 95, no. 2, pp. 178–184, 2010.

[20] S. Yuan, X. Sun, M. Li et al., "A randomized study of involved-field irradiation versus elective nodal irradiation in combination with concurrent chemotherapy for inoperable stage III nonsmall cell lung cancer," *American Journal of Clinical Oncology*, vol. 30, no. 3, pp. 239–244, 2007.

[21] J. S. A. Belderbos, K. De Jaeger, W. D. Heemsbergen et al., "First results of a phase I/II dose escalation trial in non-small cell lung cancer using three-dimensional conformal radiotherapy," *Radiotherapy and Oncology*, vol. 66, no. 2, pp. 119–126, 2003.

[22] S. Sura, C. Greco, D. Gelblum, E. D. Yorke, A. Jackson, and K. E. Rosenzweig, "(18)F-fluorodeoxyglucose positron emission tomography-based assessment of local failure patterns in non-small-cell lung cancer treated with definitive radiotherapy," *International Journal of Radiation Oncology ∗ Biology ∗ Physics*, vol. 70, no. 5, pp. 1397–1402, 2008.

[23] R. Rengan, K. E. Rosenzweig, E. Venkatraman et al., "Improved local control with higher doses of radiation in large-volume stage III non-small-cell lung cancer," *International Journal of Radiation Oncology ∗ Biology ∗ Physics*, vol. 60, no. 3, pp. 741–747, 2004.

[24] J. D. Bradley, R. Paulus, R. Komaki et al., "A randomized phase III comparison of standard-dose (60 Gy) versus high-dose (74 Gy) conformal chemoradiotherapy +/- cetuximab for stage IIIA/IIIB non-small cell lung cancer: preliminary findings on radiation dose in RTOG 0617," in *Proceedings of the 53rd Annual Meeting of the American Society of Radiation Oncology*, Miami, Fla, USA, October 2011.

[25] J. D. Cox, "Are the results of RTOG, 0617 mysterious?" *International Journal of Radiation Oncology ∗ Biology ∗ Physics*, vol. 82, no. 3, pp. 1042–1044, 2012.

[26] E. M. Toloza, L. Harpole, and D. C. McCrory, "Noninvasive staging of non-small cell lung cancer: a review of the current evidence," *Chest*, vol. 123, supplement 1, pp. 137S–146S, 2003.

[27] R. J. Cerfolio, A. S. Bryant, and B. Ojha, "Restaging patients with N2 (stage IIIa) non-small cell lung cancer after neoadjuvant chemoradiotherapy: a prospective study," *Journal of Thoracic and Cardiovascular Surgery*, vol. 131, no. 6, pp. 1229–1235, 2006.